The Tephrostratigraphy of Three, Late Quaternary, Mediterranean Marine Cores

Christopher George Satow

Submitted for the Degree of Doctor of Philosophy at Royal Holloway College, University of London.

September 2012

Institution of study:

Department of Geography

Royal Holloway, University of London

Declaration

This thesis presents the results of original research undertaken by the author and none of the results, illustrations or text are based on published or unpublished work of others, except where specified and acknowledged

Signature: Christopher Satow

Date: 10.09.2012

Abstract:

Isochronous tephra layers provide the potential for the precise correlation of environmental records and, in the case of tephra layers of known age, for the importation of age estimates into sequences that lack independent ages, or for which the chronology is equivocal. This PhD project explored this potential for three important late Quaternary core sequences from the Mediterranean Sea: ODP975, which lies close to the Balearics in the western Mediterranean; LC21 in the Aegean Sea, close to Crete; and OPD967 in the far eastern Mediterranean, close to Cyprus. Each sequence was investigated for the presence of visible volcanic ash and cryptotephra layers. Very low amounts of volcanic glass shards were found in the ODP975 sequence, while 15 discrete tephra layers were found in core LC21 and 5 in the ODP967 sequence. These were geochemically analysed for constituent major and trace element ratios using EPMA-WDS, LA-ICP-MS and SIMS micro-analytical methods. Correlations of tephra layers were based on graphical comparison of the resulting geochemical data-sets to a developing data-base of the representative glass chemical compositions of European proximal and distal tephra deposits. The results reveal evidence for 19 separate volcanic eruptions spanning the last 166 ka, originating from Campania, Pantelleria, Santorini, Yali/Nisyros and Kos, and possibly also from Central Anatolia and Iceland. 12 of these eruptions were previously unknown and thus are here characterised for the first time.

The results add to the tephrostratigraphical record of the eastern Mediterranean, but also demonstrate that further progress requires some crucial procedural problems to be addressed first. Several chronologically distinct tephra layers have identical elemental abundances, which complicates their applicability as robust stratigraphic and chronological markers. In addition, proximal and distal deposits derived from the same eruption phase may have different geochemical attributes, and some evidence suggests a degree of chemical heterogeneity between different distal components of the same eruption. If confirmed, these findings have serious implications for assigning distal tephra layers to a contemporaneous proximal deposit, and hence impede the reliable transfer of age estimates obtained from proximal layers to distal tephra and environmental records.

These problems notwithstanding, the discovery of 12 previously unknown tephra layers demonstrates that the tephrostratigraphical record of the eastern Mediterranean is far from complete, and highlights the need for further research of this type. In particular, rhyolitic eruptions from Santorini are here shown to be more common than were previously thought. These findings therefore have importance for augmenting the history of volcanic activity in the region, especially as a contribution to understanding magma recharge rates and eruption frequencies and their relevance for developing more robust hazard assessments.

Acknowledgements.

This thesis is the result of a large collaborative research project, and as such many people have contributed invaluably to its completion. My supervisors Prof. John Lowe, Dr Simon Blockley, Prof. Martin Menzies and Prof.Eelco Rohling have all questioned, advised and encouraged my work over the last four years. John has patiently and meticulously reviewed this text throughout its ten months of development. Simon has advised me with the possibilities for the research and has facilitated many stimulating discussions about age modelling and geochemistry. Martin has been unfailingly positive in the face of my doom-laden geochemical woes and has frequently reminded me that an unexpected result is often an opportunity rather than a disappointment. Eelco has made me most welcome at the National Oceanographic Centre and has discussed with me an invaluable oceanographic context for this thesis.

I would like to thank my co-workers, without whom this project could not have been completed and without whom it would have been considerably less enjoyable. Katharine Grant has been unbelievably patient with my requests for samples and information, and together we conquered many a translation and sampling surprise on our Bremen trip. Thanks are due also to Jenny Stanford who survived a frenetic and surreal sampling trip to Bremen with me and co-produced the XRF data for ODP975.

My geochemical work would not have been possible without Vicki Smith in Oxford and Emma Tomlinson and Christina Manning at Royal Holloway. They have all put in a great deal of time, skill and expertise to allow me to produce the geochemical analyses presented here and I am greatly indebted to them for all their hard work. Christopher Bronk-Ramsey built the excellent software from which the bi-plot charts in this thesis were made.

Alison Macleod, Ian Matthews, Simon Armitage, Adrian Palmer, Anna Bourne, Elaine Turton and Robyn Christie have all helped and advised for the considerable laboratory work which has culminated in this thesis. Their contributions have been invaluable and I thank them for the work they have done on my behalf, and the advice they have given to make this research project possible. Mark Hardiman has been my tephra colleague and housemate for all these four years. Our enthused debates over geochemistry, hypothesised correlations and the philosophies of age models have precipitated many of the ideas in this thesis.

Finally I'd like to thank my family for encouraging me to complete this PhD and for supporting my university studies for so long. In particular I'd like to thank John and my Mum for their unfailing support and understanding and also alterting me to the existence of Druitt et al. (2012) research paper which has been central to the interpretation of some of the more perplexing data presented here. Amy has wonderfully and patiently helped me through the tough months of writing up, with encouraging words, helpful days off and unfailing cheer and I am so grateful to her. In addition, I thank the many friends who have given me encouragement, interest, good company and pub visits during these four years.

This work was entirely funded by the Natural Environment Research Council, who provided excellent training opportunities in addition to the considerable financial backing. I am very grateful for this comprehensive financial support

Table of Contents

Chapter 1- General Introduction and Project Scope..... 20

1.1 The RESET Project- General Scope and Aims. 20

1.1.1 WP 1- Neanderthals and modern humans in Europe (60 to 25 ka BP)..... 21

1.1.2 WP 2- The Impact of abrupt environmental transitions on early modern human populations in North Africa..... 21

1.1.3 WP 3- Re-populating Europe after the Last Glacial Stage..... 21

1.1.4 WP 4- Geochemical fingerprinting of proximal volcanic deposits. 21

1.1.5 WP 5- Abrupt environmental transitions and tephras in marine sediment cores. 22

1.1.6 WP 6- Abrupt environmental transitions and tephras in continental records 22

1.1.7 WP 7- Data synthesis and age modelling..... 23

1.2 Aims of the thesis..... 25

Chapter 2- Synopsis of the archaeological, environmental and oceanographic contexts..... 26

2.1 Archaeological context relevant to RESET. 26

2.2 Terrestrial environmental context relevant to RESET. 28

2.3 The Quaternary oceanography of the Mediterranean Sea. 30

2.3.1 Introduction. 30

2.3.2 Deep water formation 32

2.3.3 Mediterranean Sapropels. 33

2.3.4 Mechanisms of sapropel formation. 34

2.3.5 Short term climatic fluctuations in Mediterranean Marine Proxy Records..... 36

2.3.6 Available oceanographic proxies. 40

Chapter 3- Background information on the Volcanic systems of the Mediterranean. 42

3.1 Santorini: background..... 42

3.1.1 Geological Setting and Style of Volcanism on Santorini. 42

3.1.2 History of Volcanism on Santorini- the Volcanic Stratigraphy..... 44

3.1.3 Interplinain activity between the Cape Thera and Minoan eruptions 46

3.1.4. Santorini distal tephra reported in the literature. 47

3.2 Campanian System: Background 48

3.2.1 Geological Setting and Style of Volcanism in the Campanian System 48

3.2.2 History of volcanism in the Campanian system- the volcanic stratigraphy. 48

3.2.3 Campanian distal tephra reported in the literature 49

3.3 Kos/Yali/Nisyros System: background. 50

3.3.1 Geological setting and style of volcanism 50

3.3.2. Volcanic stratigraphy. 51

3.4 Pantellerian System: Background 52

3.4.1 Geological Setting and Style of Volcanism on Pantelleria 52

3.4.2 The Volcanic Stratigraphy of Pantelleria 52

3.4.3 Distal tephra originating from Pantelleria 53

3.5 Aeolian Islands 53

3.6 Anatolian/Turkey 54

3.6.1 Eastern Anatolian Volcanic System 54

3.6.2 Central Anatolian Volcanic System 54

3.6.3 Western Anatolian Volcanic System 55

3.7 Critical review of existing distal tephra records for the Mediterranean Sea, methods used and sites examined 55

3.7.1 Introduction. 55

3.7.2 The Tyrrhenian Sea and the Western Mediterranean. 56

3.7.3 Ionian Sea 58

3.7.4 Adriatic Sea. 59

3.7.5 The Aegean Sea and Far Eastern Mediterranean. 61

3.7.6. Methods of tephra identification and dating. 62

Chapter 4- Core/ site selection and background. 64

4.1 Core Selection Rationale 64
4.2- Core ODP975 – Western Mediterranean- Balearic Basin. 65
4.2.1- Location and previous work 65
4.2.2- Core lithostratigraphy and existing proxy records. 66
4.2.3- Age models for ODP975. 68
4.2.4. Potential sources of tephra shards which may be found in ODP975. 70
4.3 Core LC21 - South East Aegean Sea 71
4.3.1- Location and previous work 71
4.3.2- Core lithostratigraphy and existing proxy records. 72
4.3.3- Age models for LC21 73
4.3.4- Potential Sources of tephra for LC21. 75
4.4 Core ODP967- Far Eastern Mediterranean 76
4.4.1- Location and previous work 76
4.4.2- Core lithostratigraphy and existing proxy records 77
4.4.3- Age models for ODP967. 81
4.4.4- Potential sources of tephra for ODP967. 82
4.5 Lago Grande di Monticchio. 82
Chapter 5- Methodology 93
5.1 Sediment core treatment proceedures. 93
5.1.1 Core Sub-sampling Strategy and Sample Storage 93
5.1.2 Sub-sampling for tephra analyses 93
5.2 Sample Processing and slide mounting. 95
5.2.1 Sample processing 95
5.2.2 Slide mounting and shard counting 96
5.2.3 Mounting samples for elemental analysis. 96
5.3. Geochemical analysis methods 100
5.4 Wavelength Dispersive Spectrometry-Electron Probe Microanalysis 101

5.4.1 WDS-EPMA Method Theory.....101
5.4.2 Data production from the WDS EPMA.....108
5.4.3. EPMA Data production and filtering.....111
5.5 LA-ICP-MS Laser ablation inductively coupled plasma mass spectrometry. 117
5.5.1 LA-ICP-MS Theory. 117
5.5.2 Data Production and Analytical setup. 120
5.5.3 Data Filtering and Processing.....125
5.5.4 Analytical Precision and Accuracy.....128
5.6. SIMS. 128
5.6.1 SIMS theory.....128
5.6.2 Analysis Parameters for SIMS. 132
5.6.3 Data filtering and processing 133
5.7 Correlation Methods and Principles 133
5.7.1 Reference Data- the proximal data.....133
5.7.2 Correlations Background- Correlation methods in the literature.....134
5.7.3 Adopted Identification Procedure for This Thesis 135
5.7.4 Reproducibility and Analytical uncertainty in correlations.....136
Chapter 6- Results.....149
6.1 LC21 results.....149
6.1.1 Results of Shard counting 149
6.1.2 Modelled ages for LC21 tephra samples.....152
6.1.3 Results of Geochemical Analyses.....156
6.2 ODP967-Results. 176
6.2.1 Shard count results. 176
6.2.2 Results of Geochemistry from ODP967 181
6.3 ODP975 Results.....193
6.3.1 Shard count results. 193

6.3.2 Results of Geochemistry from ODP975 (from EPMA only). 197

6.4 Lago Grande di Monticchio results. 200

7. Discussions 205

7.1 Defining Source Volcanic Systems for an Unknown Tephra Sample. 205

7.2 – Discussion for tephra layers found in LC21. 207

7.3 Discussion for tephra layers found in ODP967. 244

7.4 Discussion of tephra shards found in ODP975. 258

7.5 Correlations and integration with literature data. 265

7.5.1 Tephras originating from Santorini. 267

7.5.2 Tephras originating from Campania. 291

7.5.3 Tephras originating from Yali/Nisyros. 301

7.5.4 Tephras originating from Kos or Central Anatolia 303

7.5.5 Tephras originating from Pantelleria. 306

7.5.6 Tephras of Unknown Origin. 308

8. Synthesis, suggestions for further work and conclusions. 309

8.1 Reappraisal of the thesis aims. 309

8.2. The contribution of this thesis to the earth sciences. 311

8.3 Problems encountered during the research 312

8.3.1 Multiple tephra layers with identical geochemical compositions. 312

8.3.2 Differences between the geochemical analyses of proximal and distal tephra deposits. 313

8.3.3 Differences in the geochemical composition of deposits from a single eruption between sites. 313

8.3.4 The absence of deposits from apparently very voluminous, Plinian eruptions in a marine core close to the source volcano. 314

8.4 Suggestions for further work 314

8.4.1 Construction of volcanic stratigraphies. 314

8.4.2 Tephra investigations in the Western Mediterranean Sea. 315

8.4.3- Contribution to the RESET project and suggestions for the progression of the project. 315

8.5 Conclusions. 316

References. 318

Appendix 1 Standard analyses for EPMA analyses. 341

Appendix 2 - Atho-G standard analyses (bias corrected) from LA-ICP-MS. 346

Appendix 3- details of the construction of the chronology for core LC21 through correlation with the Soreq Cave speleothem. 356

Appendix 4- Section 3 (base of core LC21) scanning XRF data. 360

List of Figures.

Chapter	Title	Page Number
Chapter 1	**General Introduction and Project Scope**	
Fig 1.1	Map of RESET sites and marine cores investigated in this thesis.	**24**
Chapter 2	**Synopsis of the archaeological, environmental and oceanographic contexts.**	
Fig 2.1	A conceptual summary of typical Mediterranean vegetation change during the glacial-interglacial cycles for the middle and upper Pleistocene age	**29**
Fig 2.2	A bathymetric map of the Mediterranean Sea	**31**
Fig 2.3	A schematic diagram showing both sapropel forming and non sapropel forming circulatory states in the Mediterranean Sea	**33**
Fig 2.4	The generalised sapropel stratigraphy for the last ~200ka in the eastern Mediterranean Sea	**35**
Fig 2.5	An interpreted proxy record for the western Mediterranean Sea	**37**
Fig 2.6	Short term climatic changes coincident with a solar minimum (the Homeric Minimum) discovered in the proxy record of Meerfelder Maar, Germany	**39**
Chapter 3	**Background information on the Volcanic systems of the Mediterranean.**	
Fig 3.1	The tectonic setting of the major Mediterranean volcanic systems	**42**
Fig 3.2	The second explosive cycle stratigraphy of Santorini	**43**
Chapter 4	**Core/ site selection and background.**	
Fig 4.1	Map showing locations of marine cores studied in this thesis	**65**
Fig 4.2	The stable isotope stratigraphy of core ODP975	**68**
Fig 4.3	Age vs depth models for core ODP975 based on orbital tuning of the sapropel and isotope stratigraphies	**69**
Fig 4.4	Lithostratography for core LC21 from the on-ship initial report.	**73**
Fig 4.5	LC21 isotope stratigraphy and age model.	**74**
Fig 4.6	Composite 14C age vs depth model for LC21 for the last ~17ka	**75**
Fig 4.7	The stratigraphy of core ODP967	**79**
Fig 4.8	The 3Ma dust record from core ODP967	**80**
Fig 4.9	Barium, Sulphur, Iron and Titanium stratigraphies for ODP967	**81**
Fig 4.10	A precession tuned, sapropel based age model for core ODP967	**82**
Fig 4.11	The visible tephrostratigraphy of Lago Grande di Monticchio	**84**
Fig 4.12	Vegetation changes recorded in Lago Grande di Monticchio over the last 105ka	**92**

Chapter 5	**Methodology**	
Fig 5.1	Three methods for mounting tephra onto epoxy resin stubs	**98**
Fig 5.2	Schematic diagram of the EPMA-WDS system	**102**
Fig 5.3	Schematic diagram of the focusing of the electron beam in the EPMA-WDS system	**104**
Fig 5.4	The production of X-rays within a sample under the EPMA-WDS system	**105**
Fig 5.5	The decomposition of mineral structures under the EPMA-WDS system	**107**
Fig 5.6	Comparison of ZAF and PAP correction procedures	**112**
Fig 5.7	A schematic representation of the LA-ICP-MS system	**117**
Fig 5.8	An example output from the LA-ICP-MS system	**123**
Fig 5.9	Example plots of analyses of tephra shards using the LA-ICP-MS system	**127**
Fig 5.10	Schematic diagram of the SIMS analytical system	**131**
Fig 5.11	A conceptual assessment of the errors in gechemical analysis	**138**
Fig 5.12	A comparison of duplicate analyses of two samples using the EPMA	**140**
Fig 5.13	Comparisons of values and errors resulting from different beam sizes on the LA-ICP-MS	**142**
Fig 5.14	A comparison of duplicate analyses of a sample using the LA-ICP-MS	**145**
Fig 5.15	A comparison of LA-ICP-MS values using different values of SiO2 in the callibration	**145**
Fig 5.16	The effect of applying correction factors to analyses of trace elements using the LA-ICP-MS	**146**
Fig 5.17	A comparison of SIMS BCR 2G standard analyses to the accepted values	**148**
Chapter 6	**Results**	
Fig 6.1	Results of shard counting for LC21	**150**
Fig 6.2	Photomicrographs of shards recovered from LC21	**151**
Fig 6.3	Construction of the LC21 age model through correlation with soreq cave.	**154**
Fig 6.4	Geochemical classification diagrams for all tephra layers found in LC21	**156**
Fig 6.5	Major element bi-plots for samples LC21 (0.940) and LC21 (0.010)	**158**
Fig 6.6	Trace element bi-plots for samples LC21 (0.940) and LC21 (0.010)	**159**
Fig 6.7	Major element bi-plots for samples LC21 (2.005), LC21 (3.225) and LC21 (3.775)	**160**
Fig 6.8	Trace element bi-plots for tephra layers LC21 (2.005), LC21 (3.225), LC21 (3.775) and LC21 (4.285)	**161**
Fig 6.9	Alkali and CaO vs FeOt plots for all four samples taken from the visible tephra layer at 4.925m depth in core LC21	**164**
Fig 6.10	Major element analyses of samples from LC21 (4.925), LC21 (5.145), LC21 (7.915) and LC21 (9.575)	**165**
Fig 6.11	Trace element bi-plots of samples from LC21 (4.925), LC21 (5.145), LC21 (7.915) and LC21 (9.575)	**166**
Fig 6.12	Comparison of shard morphologies and chemical signatures for sample LC21 (7.915)	**169**
Fig 6.13	Major element bi-plots of tephra shards from samples LC21 (9.709), LC21 (10.345) and LC21 (11.190)	**170**
Fig 6.14	Trace element bi-plots of tephra shards from samples LC21 (9.709) and	**172**

	LC21 (11.190)	
Fig 6.15	Major element bi-plots of tephra shards from samples LC21 (12.245), LC21 (12.625), LC21 (13.275), LC21 (13.405) and LC21 (13.485)	**174**
Fig 6.16	Trace element bi-plots of tephra shards from samples LC21 (12.245), LC21 (12.625), LC21 (13.275), LC21 (13.405) and LC21 (13.485)	**175**
Fig 6.17	ODP967 proxy stratigraphy with the locations of samples processed for crypto-tephra	**178**
Fig 6.18	Shard count results for ODP967	**179**
Fig 6.19	Photomicrographs of shards recovered from ODP967	**180**
Fig 6.20	Geochemical classification diagrams for all tephra layers found in ODP967	**183**
Fig 6.21	Major element bi-plots for samples ODP967 (1.540), (1.620), (1.730), 1.810), (1.850) and (1.880)	**184**
Fig 6.22	Trace element bi-plots for samples ODP967 (1.810), (1.850) and (1.880).	**185**
Fig 6.23	Geochemical classification plots for samples ODP967 (1.730), (1.810) and (1.850)	**187**
Fig 6.24	Geochemical classification plots for samples ODP967 (1.880), (5.560) and (7.610)	**189**
Fig 6.25	Major element bi-plots for samples ODP967 (5.560), (7.610), (8.460) and (8.870)	**190**
Fig 6.26	Trace element bi-plots for samples ODP967 (7.610) and (8.870)	**191**
Fig 6.27	Geochemical classification plots samples ODP967 (8.470) and (8.870)	**193**
Fig 6.28	Stratigraphic positions of possible tephra shards extracted from ODP975.	**195**
Fig 6.29	Photomicrographs of possible tephra shards extracted from ODP975	**196**
Fig 6.30	Geochemical classifaction of the two tephra shards found in ODP975	**198**
Fig 6.31	Major element bi-plots of the tephra layers from Lago Grande di Monticchio	**201**
Fig 6.32	Trace element bi-plots of the teprha layers from Lago Grande di Monticchio	**202**
Chapter 7	**Discussions**	
Fig 7.1	The principles of using High Field Strangth Elements to define the source of an unknown tephra.	**206**
Fig 7.2	Zr vs Nb plots for LC21 samples to define their source volcano	**209**
Fig 7.3	Major element comparison of LC21 (0.010) and (0.940) to the proximal stratigraphy of Santorini.	**210**
Fig 7.4	Trace element comparison of LC21 (0.010) and (0.940) to the proximal stratigraphy of Santorini.	**211**
Fig 7.5	Major element comparison of LC21 (2.005) to the proximal stratigraphy of Santorini.	**213**
Fig 7.6	Trace element comparison of LC21 (2.005) to the proximal stratigraphy of Santorini.	**214**
Fig 7.7	Major element comparison of LC21 (3.225) to the proximal stratigraphy of Santorini	**216**
Fig 7.8	Trace element comparison of LC21 (3.225) to the proximal stratigraphy of Santorini	**217**
Fig 7.9	Major element comparison of LC21 (3.775) to the proximal stratigraphy of Santorini	**219**

Fig 7.10	Trace element comparison of LC21 (3.775) to the proximal stratigraphy of Santorini	**220**
Fig 7.11	Major element comparison of LC21 (4.285) with proximal deposits of the Yali-2 pumice, the Nisyros Upper Pumice and the Nisyros Lower Pumice.	**222**
Fig 7.12	Trace element analyses of sample LC21 (4.285) with analyses from proximal deposits of Yali and Nisyros: the Yali-2 pumice, the Nisyros Upper Pumice and the Nisyros Lower Pumice.	**223**
Fig 7.13	Major element comparison of LC21 (4.925) to Plinian eruptions from the proximal stratigraphy of Campania.	**225**
Fig 7.14	Trace element comparison of LC21 (4.925) to Plinian eruptions from the proximal stratigraphy of Campania.	**226**
Fig 7.15	K2O vs SiO2 plot for all four samples of Campanian Ignimbrite in LC21	**227**
Fig 7.16	Bar chart showing the percentage Upper Flow in each sample of the Campanian Ignimbrite in LC21	**227**
Fig 7.17	Major element comparison of the silica saturated shards from LC21 (5.125) to the proximal stratigraphy of Santorini.	**228**
Fig 7.18	Trace element comparison of the silica saturated shards LC21 (5.125) to the proximal stratigraphy of Santorini.	**229**
Fig 7.19	Major element comparison of the silica saturated shards from LC21 (7.915) to the proximal stratigraphy of Santorini.	**230**
Fig 7.20	Trace element comparison of the silica saturate shards LC21 (7.915) to the proximal stratigraphy of Santorini.	**231**
Fig 7.21	Major element comparison of silica under-saturated shards from LC21 (7.915) to the proximal stratigraphy of Campania.	**232**
Fig 7.22	Trace element comparison of silica under-saturated shards from LC21 (7.915) to the proximal stratigraphy of Campania.	**233**
Fig 7.23	Major element comparison of LC21 (9.575) to the proximal stratigraphy of Santorini	**235**
Fig 7.24	Trace element comparison of LC21 (9.575) to the proximal stratigraphy of Santorini.	**236**
Fig 7.25	Major element comparison of LC21 (9.709) to the proximal stratigraphy of Santorini	**237**
Fig 7.26	Trace element comparison of LC21 (9.709) to the proximal stratigraphy of Santorini	**238**
Fig 7.27	Plot showing 5 shards of LC21 (10.345) classified in the Pantellerite geochemical field	**239**
Fig 7.28	Major element comparison of LC21 (10.345) (without Pantelleria component) to the proximal stratigraphies of Central Anatolia, Nisyros, Yali and Kos (using LC21 12.465).	**240**
Fig 7.29	Major element comparison of LC21 (11.190) to the proximal stratigraphy of Santorini	**241**
Fig 7.30	Trace element comparison of LC21 (11.190) to the proximal stratigraphy of Santorini.	**242**
Fig 7.31	HFSE (Zr vs Nb) plots for all ODP967 with trace element analyses	**245**
Fig 7.32	Major element geochemistry of ODP967 (1.810) and crypto-tephra layers above and below this visible tephra.	**246**
Fig 7.33	Santorini proximal deposit major element bi-plots with ODP967 (1.810), ODP967 (1.850) and ODP967 (1.880).	**248**
Fig 7.34	Trace element plots showing proximal Santorini deposits and the tephra samples from ODP967 at 1.810, 1.840 and 1.880m	**249**

Fig 7.35	Major element analyses of the two tephra shards from sample ODP967 (5.560) shown with proximal deposits from Santorini.	**252**
Fig 7.36	Major element analyses of ODP967 (7.610), (8.460) and (8.870) plotted with proximal data from three eruptions from Acigol, central Anatolia	**254**
Fig 7.37	Trace element analyses from proximal deposits on Acigol (Central Anatolia), LC21 (12.465) considered in this study to represent the Kos Plateau Tuff, and ODP967 (7.610) and (8.870).	**255**
Fig 7.38	Trace element analyses for samples LC21 (12.465) and ODP967 (8.870), and their corresponding standard values.	**257**
Fig 7.39	Major element data from Late Holocene eruptions from the Aeolian Islands and ODP967 (0.040).	**259**
Fig 7.40	Major element analyses of Late Holocene eruptions from Iceland and sample ODP975 (0.040	**260**
Fig 7.41	Alkali ratio vs SiO2 plot for si-saturated, Late Holocene eruptions from the Iceland and the Aeolian Islands with ODP975 (0.040),	**261**
Fig 7.42a	FeOt vs CaO plot for ODP975 (2.240) and proximal data from the Azores and Campania	**263**
Fig 7.42b	Total alkali vs Silica plot for ODP975 (2.240) and proximal data from the Aeolian Islands and Campania.	**263**
Fig 7.43	Major element plots for ODP975 (2.240) and data from major Plinian eruptions from Campania.	**264**
Fig 7.44	Comparison of the major element geochemistry of the distal Minoan tephra deposits, as defined in the literature, to that defined in this study, sample LC21 (0.940).	**268**
Fig 7.45	Literature and RESET project reported discoveries of shards originating from the Minoan eruption of Santorini, from the RESET database	**268**
Fig 7.46	Major element analyses of distal tephra shards attributed to the Cape Riva eruption of Santorini published in the literature and available on the RESET database together with ODP967 (1.810) from this study and proximal data from the Cape Riva eruption (Tomlinson, unpublished).	**270**
Fig 7.47	Map showing reported occurrences of the Cape Riva tephra from this study and the literature (	**270**
Fig 7.48	The Druitt et al. (2012) model of magma production for the Minoan eruption of Santorini	**273**
Fig 7.49	HFSE comparison of Santorini type 1 (dacitic) and type 2 (rhyolitic) magmas of (Druitt et al. 2012) with proximal deposits, and deposits from LC21	**275**
Fig 7.50	Figure 7.49 with the addition of data representing the Kos Plateau Tuff and the Central Anatolian volcanic system	**278**
Fig 7.51	Use of figure 3 from Druitt et al. (2012) to attain an estimate of the plagioclase composition (%An) and thus the depth of the rhyolitic magma batch (batch M1) which contributed to the eruption represented by LC21 (0.940) in LC21	**279**
Fig 7.52	Use of figure 3 from Druitt et al. (2012) to attain an estimate of the plagioclase composition (%An) and thus the depth of the rhyolitic magma batch (batch M1) which contributed to the eruption represented by LC21 (2.005) in LC21	**280**
Fig 7.53	Use of figure 3 from Druitt et al. (2012) to attain an estimate of the depth of the plagioclase composition (%An) and thus the magma batches (batches F1 and F3) which contributed to the eruption	**281**

represented by LC21 (3.225) in LC21
Fig 7.54 Use of figure 3 from Druitt et al. (2012) to attain an estimate of the plagioclase composition (%An) and thus the depth of the magma batch (batch F3) which contributed to the eruption represented by LC21 (3.775): **282**
Fig 7.55 Use of figure 3 from Druitt et al. (2012) to attain an estimate of the plagioclase composition (%An) and thus the depth of the rhyolitic magma batches (batches F1 and F3) which contributed to the eruption represented by LC21 (5.125) in LC21 **285**
Fig 7.56 Use of figure 3 from Druitt et al. (2012) to attain an estimate of the plagioclase composition (%An) and thus the depth of the rhyolitic magma batch (batch M1) which contributed to the eruption represented by LC21 (7.915) in LC21 **284**
Fig 7.57 Use of figure 3 from Druitt et al. (2012) to attain an estimate of the plagioclase composition (%An) and thus the depth of the magma batch (batch M2) which contributed to the eruption represented by LC21 (9.575) in LC21 **285**
Fig 7.58 Use of figure 3 from Druitt et al. (2012) to attain an estimate of the plagioclase composition (%An) and thus the depth of the magma batch (batch F1) which contributed to the eruption represented by LC21 (9.709) in LC21 **286**
Fig 7.59 Use of figure 3 from Druitt et al. (2012) to attain an estimate of the plagioclase composition (%An) and thus the depth of the magma batch (batch F2 or M1) which contributed to the eruption represented by LC21 (11.190) in LC21 **287**
Fig 7.60 Use of figure 3 from Druitt et al. (2012) to attain an estimate of the plagioclase composition (%An) and thus the depth of the magma batch (batch F2) which contributed to the Cape Riva eruption represented by the tephra layer ODP967 (1.810). **288**
Fig 7.61 A proposed magma batch model for Santorini, with reference to Kos/Yali/Nisyros system and the Central Anatolian System **289**
Fig 7.62 Major element omparison of LC21 (4.925) to Campanian Ignimbrite proximal deposits and the Campanian Ignimbrite of Bourne et al. (2010)- PRAD 1-2 (1653). **292**
Fig 7.63 Major element analyses reported for the Campanian Ignimbrite from the literature (from the RESET database), this study LC21 (4.925). **293**
Fig 7.64 Map showing the reported occurrences of the Campanian Ignimbrite tephra from the literature and reported by the RESET consortium **293**
Fig 7.65 Trace element analyses of tephra shards attributed to the Campanian Ignimbrite, from the RESET database. **294**
Fig 7.66 Three likely hypotheses for the correlation of the tephras in and around sapropel S4 in the Ionian, Adriatic and Aegean Seas and the TM24 tephra layers of Lago Grande di Monticchio **298**
Fig 7.67 Major element data from 'X5' assigned tephras from various cores in the Adriatic, Aegean and Ionian Seas, and Lake Ohrid in Macedonia (Vogel et al. 2010) plotted with the data from TM24 tephra samples from Lago Grande did Monticchio produced in this study **300**
Fig 7.68 Major element comparison of LC21 (4.285) with the geochemical data from shards attributed to the Yali-2 eruption of Yali from the literature **302**
Fig 7.69 Map showing the reported extent of the Yali-2 tephra from Federman **303**

	and Carey (1980), updated with the identification of the tephra in cores MAR-03-24 (Aksu et al. 2008), KB-33 (Vinci et al. 1985) and as a crypto-tephra in LC21	
Fig 7.70	Major element comparison of tephra shards from LC21 (12.465), ODP967 (8.870) and the Kos Plateau Tuff from Lesvos Island	**305**
Fig 7.71	Major element comparison of shards attributed to the P-11 tephra from Lake Ohrid, tephra layers ODP2,3 and 4 from Tamburrion et al. (2012) and shards derived from Pantelleria, in LC21 (10.345)	**307**
Fig 7.72	A composite tephrostratigraphy for the Aegean and the Eastern Mediterranean Sea, merging the work of Aksu et al. (2008) and Vinci et al. (1985) with this study	**308**
Chapter 8	**Synthesis, Suggestions for Further Work and Conclusions**	
No Figures		

List of Tables

Table	Title	Page number
2.1	Common paleaoceanographic proxies	**40**
3.1	Visible tephra deposits found in the Tyrrhenian Sea	**58**
3.2	Visible tephra deposits found in the Ionian Sea	**59**
3.3	The Adriatic Sea tephrostratigraphy	**60**
3.4	The Aegean Sea tephrostratigraphy	**62**
4.1	Cores selected for inclusion in this thesis	**64**
4.2	The tephrostratigraphy of Lago Grande di Monticchio	**91**
5.1	Operating conditions and primary standards for the EPMA analyses	**108**
5.2	Secondary glass standard accepted values for EPMA analyses	**109**
5.3	Four theoretical senarios applied to the proximal and distal deposits of one eruption.	**116**
5.4	Analytical setup parameters for the LA-ICP-MS analyses	**121**
5.5	Analytical conditions for the SIMS analyses	**132**
5.6	Assessment of the potential sources of natural variation or analytical uncertainty on tephrochronology	**137**
6.1	The ages of tephra layers in LC21 defined by the age model of Grant et al. 2012.	**155**
6.2	The predicted depths in ODP967 of the tephra layers found in LC21.	**177**
6.3	Summary of possible tephra shards recovered from ODP975	**194**
6.4	EPMA Standard analyses for a single shard found in ODP975.	**199**
7.1	Summary of data available for comparison to the tephra layers discovered in cores LC21 and ODP967	**266**
7.2	Summary of how the eruptions of Santorini relate to the fractionationtrends or mixing trends of the volcano.	**277**

Chapter 1- General Introduction and Project Scope.

1.1 The RESET Project- General Scope and Aims.

This thesis forms one component of a large research project funded by the UK's Natural Environment Research Council; the RESET (RESponse of humans to abrupt Environmental Transitions) project. This RESET consortium project aims to investigate the relationships between humans and their environment during the past 100,000 years or so, using tephra layers to precisely link various archaeological records to terrestrial and marine environmental records in Europe. Teams from Royal Holloway, University of London, the University of Oxford, the National Oceanography Centre, Southampton and the Natural History Museum, London all contribute a different set of skills and research experience to the group's endeavours.

Precise alignments of human developments and the environmental changes of the Late Quaternary have previously been constrained by the limitations of the dating and concomitant correlation methods available. In general the temporal errors and uncertainties associated with the current dating techniques are greater than the temporal resolution needed to answer questions of cause and effect, such as: did Neanderthals and Modern Humans cohabit (and if so for how long), were human populations directly influenced by sudden climatic changes. What are the temporal relationships between the evolution of archaeological tool industries and the environmental conditions? Each of these questions requires the highly precise synchronisation of the relevant records to one another. As the often widespread product of volcanic eruptions, tephra layers can provide a basis for secure correlations. As a volcanic eruption is essentially a geologically instantaneous event, the tephra layers can be used to synchronise records. Thus, where the ash is identified in an environmental or archaeological record, its temporal uncertainty is limited only by the sampling resolution and not, as with correlations made using other dating techniques, by analytical uncertainties and assumptions.

The RESET project consists of seven work packages (WPs) that are described briefly below. This PhD thesis forms the bulk of the contribution made by WP5- the marine tephrochronology component.

1.1.1 WP 1- Neanderthals and modern humans in Europe (60 to 25 ka BP)

The key hypothesis for WP1 is to assess whether or not Neanderthal and Anatomically Modern Human (AMH) populations in Europe were influenced by abrupt environmental transitions. Assessing this relationship may clarify the causes of the disappearance of the Neanderthals from the fossil record. Possible contributing factors for their demise, absorption into modern human populations, extinction through disease or warfare, an inability to compete for resources with AMHs, the impacts of adverse climate changes, or possibly the impacts of large volcanic eruptions themselves (e.g. Golovanova et al. 2010).

1.1.2 WP 2- The Impact of abrupt environmental transitions on early modern human populations in North Africa

All major cultural transitions in North Africa during the period 130-20ka BP occur in Modern Humans rather than Neanderthals. This work package is thus focused on deducing the causes for significant changes in industry type associated with AMH and whether these changes are co-incident with abrupt environmental transitions?

1.1.3 WP 3- Re-populating Europe after the Last Glacial Stage

The period from 20-6 ka BP is (approximately) the period from the Last Glacial Maximum in Europe to the establishment of global environmental conditions similar to the present day. For human populations this period of warming encouraged the repopulation of Europe as the boundaries of glacial conditions receded northwards. The key research focus for this WP is thus to assess the fine-scale temporal relationships between inferred abrupt environmental transitions and the timing of the repopulation of Europe.

1.1.4 WP 4- Geochemical fingerprinting of proximal volcanic deposits.

This work package forms the fulcrum of the RESET consortium. It's primary goal is to define the geochemical compositions of the major volcanic eruptions of Europe, over the past 100ka or so (the period of time of primary interest to the other work packages). It is to this reference dataset that all the tephras found by the other work packages will be compared. Comprehensive sampling of the volcanic stratigraphies on Europe's major volcanic centres ensures that this dataset covers the largest possible geochemical range of products for each eruption. A major output of RESET is a comprehensive database of all the tephra

layers investigated and their geochemical analyses. This will allow assessments of their origins, dates and distributions.

1.1.5 WP 5- Abrupt environmental transitions and tephras in marine sediment cores.

This work package aims to detect visible and crypto-tephra layers in the marine sediment cores of the Mediterranean Sea. A range of new proxy records for these cores are being generated by Katharine Grant and Eelco Rohling at the National Oceanography Centre, Southampton. These proxy records will be synchronised with the RESET archaeological records (WP 1 and 2) and the terrestrial environmental records (WP 6) principally using the tephra layers they have in common to each sequence. The specfic objectives of WP5 are:

1. To resolve more precisely the sequence of Abrupt Environmental Transitions (AETs) which affected Mediterranean and Red Sea proxy records during the past 160ka.

2. To synchronise the marine proxy records of the Mediterranean and Red Seas using tephra layers.

3. To test assumptions about synchronous changes affecting land and sea and to define and quantify any significant leads and lags in the response of different proxy records to abrupt environmental changes.

This thesis represents the entirety of the tephra results from the Mediterranean Sea for this work package. Cores from the Red Sea were processed by Christine Lane and Vicky Cullen of the University of Oxford.

1.1.6 WP 6- Abrupt environmental transitions and tephras in continental records

WP 6 is concerned with terrestrial environmental records obtained from sites in Europe and North Africa. Tephras layers found in lakes and peat bogs are being used to test the assumption that environmental transitions are synchronous over large distances (continental scale), and over various altitudes. WP6 links with WPs 1,2,3 and 5 to establish

the full range of tephra layers that are common to archaeological, marine and terrestrial records.

1.1.7 WP 7- Data synthesis and age modelling

WP7 is a synthesis work package designed to combine the data from all the other work packages and generate age models that assimilate all age-depth information from all studied sites. The overall aim is to test the extent to which archaeological data can be synchronised with environmental events.

The common aim of these seven work packages is to establish a series of robust isochrons that link European and North African archaeological and environmental records, and which can be used as a reference framework to assess the relative timings of events in the records. The collective of sites investigated by RESET during the past five years are shown in a map in figure 1.1.

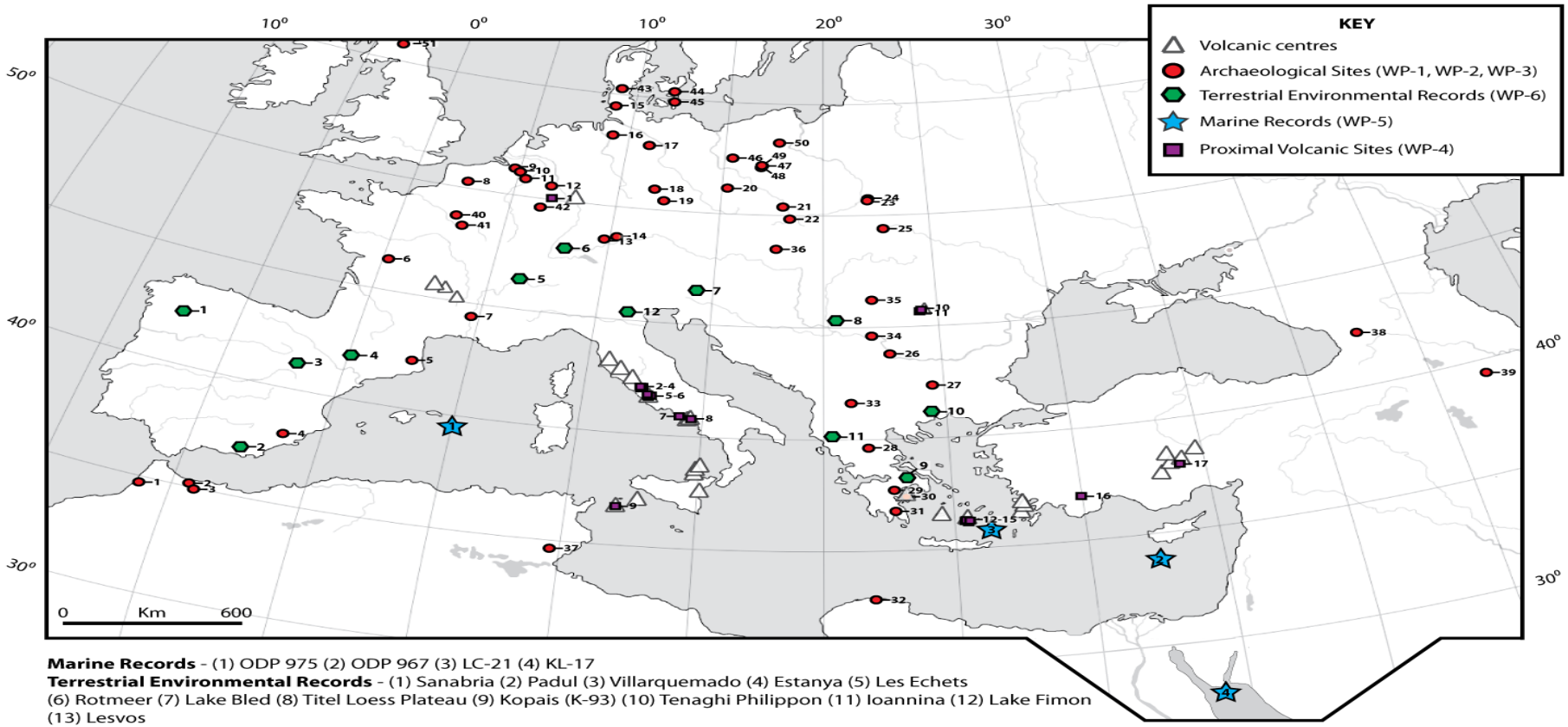

Figure 1.1 Map showing the selected ocean cores for the marine tephrochronology component of the RESET project (blue stars). Sites 1,2 and 3 were completed for this thesis. Site 4 was completed by another investigator.

1.2 Aims of the thesis.

This thesis forms the bulk of the **WP 5 tephra contribution** to RESET. The specific aims of the project reported in this thesis were:

1 - to augment knowledge of the geographical extent of Mediterranean volcanic products in marine sediment sequences. The distribution of the tephra found in this investigation will be placed within the context of those already known from the literature.

2 - to initiate the development of a regional tephrostratigraphy for the Eastern Mediterranean. At the start of this project very few distal tephra layers had been reported from the Eastern Mediterranean Sea. The aim is to generate new data that will help to link the marine core environmental records into a regional tephrostratigraphic framework. Such a lattice could allow an assessment of the synchronicity (or otherwise) of some of the environmental events or archaeological information in the various records.

3 - to develop and test a regional tephrochronology for the Eastern Mediterranean. The lattice referred to in 2 would, if proxy independent dates can be established for the tephra layers, allow dates to be imported into all other records where the known tephras are found. If radiometric dates are not available for the tephra layers the age models may provide initial age estimates for the often poorly dated volcanic events of the region. This aim therefore has both an environmental and a volcanological application.

4- to develop synchronised age models for each of the core sequences investigated and thereby to establish more reliable ages for oceanographic events reflected in the proxy records.

Chapter 2- Synopsis of the archaeological, environmental and oceanographic contexts.

2.1 Archaeological context relevant to RESET.

The RESET project is primarily concerned with linking archaeological sites to environmental records using tephra layers. A brief archaeological summary is given here to set the marine tephra study of WP5 within the broader research context.

One of the major archaeological events of the past 200ka in Europe was the disappearance of Neanderthals from the archaeological record and the persistence of Anatomically Modern Humans (Klein 2003, Straus 2005). This replacement was gradual and appears to have occurred over a period of perhaps 10,000 to 15,000 years, from about 40 to 25ka BP (Banks et al. 2008).The exact timing of the process is difficult to constrain due to both uncertainties in dating and in the attribution of different stone tool technologies to the two hominid species (Pettitt and Pike 2001). Due to these uncertainties, it has been very difficult to infer how the two species may have interacted, and also how (if at all) they were affected by the abrupt climatic fluctuations of the time.

Greenland ice cores and North Atlantic sediment records reveal multiple abrupt climatic changes over this timeframe (Bond et al. 1993, Appenzeller et al. 1998), but to what extent these changes impinged directly on hominid populations in Europe is as yet unclear. Rapid climatic changes are also recorded in the sediments of the Mediterranean Sea (e.g. Cacho et al. 2002, Piva et al. 2008b, Tzedakis et al. 2009, Muller et al. 2011), and attempts have been made to link these changes with archaeological events, such as the Neanderthal extinction. Jimenez-Espejo et al. (2007), for example, inferred that the Neanderthal extinction could have been caused by abrupt environmental changes in Southern Iberia.

Other causes for the demise of the Neanderthals have been proposed. Banks et al. (2008) produce a model of Anatomically Modern Human (AMH) and Neanderthal migration during MIS 3 (approximately 60-30ka BP), and conclude that the Neanderthal extinction was coincident with the migration of AMH into Northwest Europe and that it was the consequent competition for resources, not climatic factors *per se*, which forced the Neanderthals to extinction. It is difficult to know what sort of evidence in the fossil record

would imply competition between the two species (Shea 2003). Tzedakis et al. (2007) conclude that two industry changes in Neanderthal sites can be chronologically related to climatic shifts, but that their final extinction most likely occurred before one of the most pronounced climatic shifts (Heinrich event 2), and thus might have been precipitated by some other factor. For example Gilligan (2007) suggests that the Neanderthals may have had clothing that improved their resilience to modest cold (middle MIS 3), but that the severe cold at the end of MIS 3 could have pushed the population to a tipping point. This idea is loosely supported by archaeological evidence but is presently closer to speculation than to a testable hypothesis (Banks et al. 2008).

There are also propositions suggesting medical factors which may have accelerated the extinction of the Neanderthals. Stormer and Mysterud (2006) implicate air pollution from cave fires as a possible driver of population extinction. The cave smoke could have induced a variety of debilitating health defects. Another plausible but currently untestable hypothesis is expounded by Underdown (2008), who speculates that the disease of transmissible spongiform encephalopathies may be at least partly responsible. This disease is associated with cannibalistic behaviour, which the Neanderthals are thought to have engaged in (Alban Defleur 2006). It is not intuitively obvious however why these afflictions would only assume an importance from ~40-25 ka BP and not before this time. These papers also pose the question of how much interaction (aggressive or passive) there was between Neanderthals and AMH. Could cultural ideas, industries or diseases have been exchanged between the two species?

There is some evidence supporting theories of interaction between Neanderthals and AMH. The most robust is the recently exposed evidence of gene flow from Neanderthals into AMH (Green et al. 2010), suggesting that the two species may have interbred. It is therefore not improbable that the Neanderthals were simply assimilated into the AMH gene pool (Trinkaus 2007). Further evidence for interbreeding may be found in an apparently hybrid skeleton found in Portugal (Duarte et al. 1999).

In addition, some archaeological evidence may indicate a transfer of technologies from AMH to Neanderthals (Hublin et al. 1996), as the use of bone, ivory and body ornaments (the Neanderthal Chatelperronian culture) appeared suddenly with the arrival of modern humans and their highly similar Aurignacian culture into Europe. However a counter-explanation is provided by d'Errico et al. (1998), who argue that the similarities in the

artefacts are not sufficient to imply acculturation. Nevertheless it seems highly unlikely that the Neanderthal transition away from their 300,000 year old Mousterian culture was not in some way precipitated by the coincident arrival of AMH into Europe (Herrera et al. 2009).

The most recent proposition for the extinction of the Neanderthals is that of Golovanova et al. (2010) who implicate the Campanian Ignimbrite eruption as the cause of a volcanic winter. This climatic event imposed, they propose, such a strain on the Neanderthals of eastern Europe (possibly indirectly though reduction of their staple foods), that they were driven to extinction. The hypothesis is contradicted by the archaeological evidence that Neanderthals persisted in sites in Eastern Europe for several thousand years after the Campanian Ignimbrite eruption (Lowe et al. 2012). A variant on this idea is that the ash and ecological impact of the eruption drove Neanderthals out of parts of Europe, leaving the territory free for subsequent colonisation by AMH (Giaccio et al. 2006), or perhaps triggered more gradual in situ cultural and evolutionary changes, enabling AMH to out-compete and finally replace the Neanderthals (Banks et al. 2008).

Many of these research questions rely on the precise order of events being established between archaeological sites, and the temporal relationships of the archaeological sites to the terrestrial and marine environmental sites. It is this highly resolved integration of the various records which the RESET project hopes to initiate using tephrostratigraphy.

2.2 Terrestrial environmental context relevant to RESET.

The RESET project also seeks to link the marine environmental records to the terrestrial environmental records that have been studied within another of the RESET Work Packages (WP6). If successful, this will allow for the first independent, high resolution comparisons between marine and terrestrial proxy archives to be made. This may lead to the identification of leads and lags in the ecological or climatic systems between the ocean and the land. Here, a summary of the relevant terrestrial proxy records from the literature is provided to illustrate potential types of comparisons and therefore which hypotheses may be tested.

Detailed, high resolution, continuous terrestrial environmental records are generally preserved in either lake sediments or peat bogs. Terrestrial geomorphological features and lithological facies also give information on climatic change, but tend to be discontinuous, difficult to date, and of much lower resolution than that needed to answer in any precise

manner the questions that RESET wishes to address and thus are not considered further here.

Lake and peat bog sediments yield pollen data from which flora ecology and by extension humidity and temperature can be inferred. Ostracod/diatom/insect data provide information on fauna ecology and by extension temperature and salinity, with isotopic data providing an additional proxy for temperature (Lowe and Walker 1997). In the Mediterranean there are several highly resolved records of terrestrial environmental change which are briefly reviewed here. Some of these records also include existing tephrochronological data while for others the tephra work is being completed by work packages in the RESET consortium. The sites are shown on figure 4.2 (chapter 4).

Pollen studies reaching back to the last interglacial are concentrated in southern Europe. In northern Europe sediments dating from before the last glacial stage have been either removed or reworked by glacial ice. The general model of pollen zone succession typical of glacial-interglacial cycles in southern Europe is shown in figure 2.1 (fig. 3 from Beaulieu et al. (2007)).

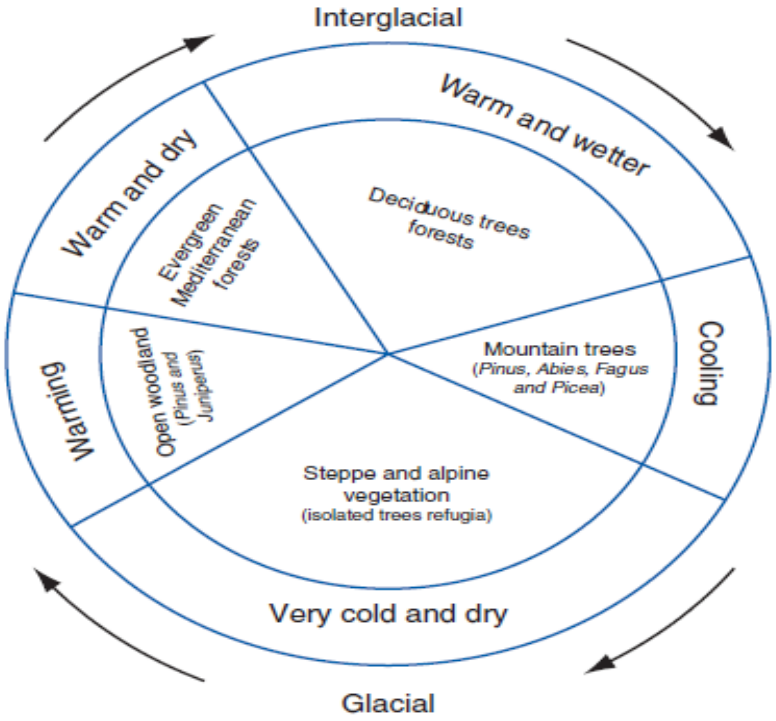

Figure 2.1 a conceptual summary of typical Mediterranean vegetation change during the glacial-interglacial cycles for the middle and upper Pleistocene age (according to Beaulieu et al. 2007). Warmer and wetter climes (interglacials) are indicated by deciduous tree pollen while alpine vegetation indicates the very cold and dry environment of glacial periods.

Pollen sequences show both orbital (Tzedakis et al. 2006, Tzedakis 2005), and sub-orbital scale variations in vegetation (Allen et al. 2010, Tzedakis 2005). The broad picture is that the large North Atlantic cyclic climatic changes (glacial-interglacial) are also manifested in Mediterranean records (Tzedazis et al. 2006). The detail is more complicated. Several authors suggest that Heinrich events and Bond cycles registered in North Atlantic sediment sequences were also propagated into Mediterranean climes (e.g. Allen et al. 1999, Caucho et al. 2002, Sanchez Goni et al. 2002, Rohling et al. 2003, Margari et al. 2009). However Allen et al. (1999) also identified fluctuations of a higher frequency than those shown in the north Atlantic records in the Italian pollen record of Lago Grande di Monticchio, implying that there may be an additional control on the vegetation/climate of the Mediterranean. Margari et al. (2009) surmised that the arboreal pollen changes on Lesvos Island (Greece) were synchronous with the Heinrich events of the North Atlantic. Tzedakis (2005) however revealed an apparent lag in the Eemian terrestrial vegetation responses to climatic changes with respect to the proxy marine records. This lag could be as large as 6000 years (Tzedakis 2005). There are significant environmental gradients across Europe which complicate the synchronisation of pollen records over large distances (Beaulieu et al. 2007). A major problem is that many ideas remain untestable due to a lack of reliable and precise dating work: much of the period lies beyond the range of radiocarbon dating.

It is hoped therefore that the tephra investigations presented in this thesis will allow terrestrial climatic records to be synchronised with the marine environmental proxies to test for leads and lags between them and, if relevant, to estimate their durations. Such information might prove to be important in predicting how ecosystems could react to future climatic changes.

2.3 The Quaternary oceanography of the Mediterranean Sea.

2.3.1 Introduction.

The oceanographic context of the Mediterranean is determined by several forcing factors, some internal and some external to the basin. The interpretation of proxies in this semi-enclosed marine system is thus complicated, and there is no single variable which controls each proxy throughout time. The various proxies (isotope stratigraphies, mineralogies, magnetic measurements or geochemical logs) must be interpreted as a synthesis, rather than individually, as each of the forcing factors may vary in its influence on each proxy through time (Henderson 2002).

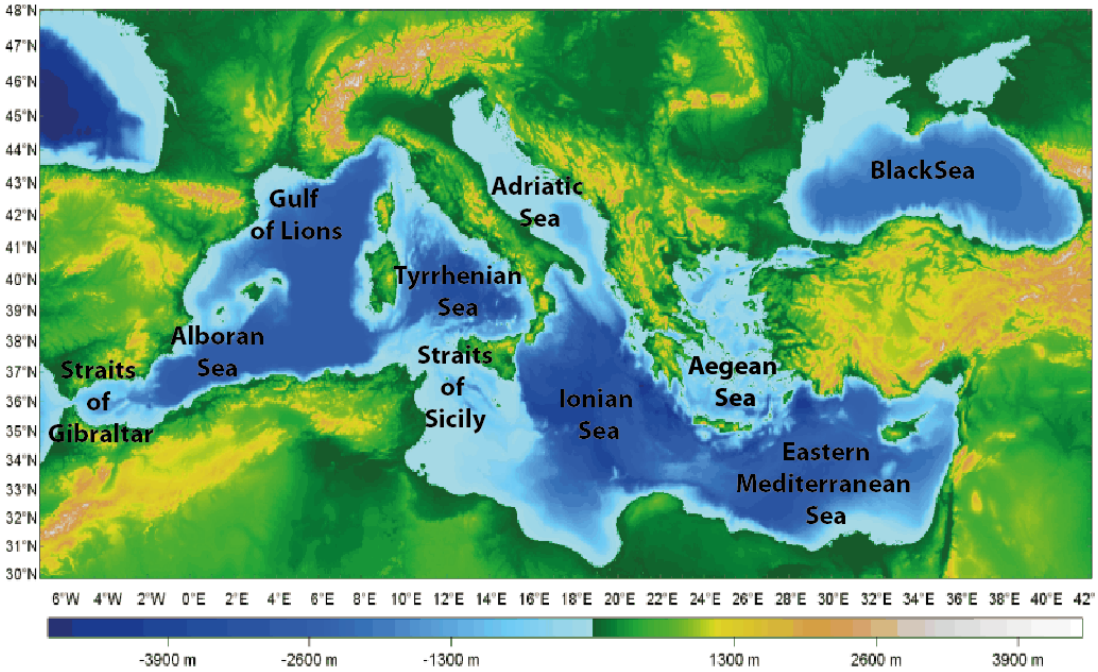

Figure 2.2 A bathymetric map of the Mediterranean Sea (adapted from map at www-3.unipv.it/webcib/edu_Mediterraneo_uk.) with the locations for the regions most pertinent to palaeoceanography, which are described in the text.

An understanding of the circulation of water in the Mediterranean is important to interpret the marine core proxies, as the major changes recorded in the sediment cores are thought to be a function of fundamental changes in the oceanographic regime. This circulation is controlled by factors internal and external to the basin. The main external forcing factor for short timescale variations (monthly to decadal) is the North Atlantic Oscillation, where changes in the atmospheric pressure gradient between the Azores high and the Iceland low influence the surface water currents (Tsimplis and Josey 2001). On longer timescales, the Western Mediterranean appears to be the area most affected by these changes in the North Atlantic as the growth and decay of the global ice sheets controls the rate of inflow and outflow across the Gibraltar Sill (Cramp and O'Sullivan 1999). Centennial to millennial changes in the water circulation are also thought to be implemented by latitudinal changes in the position of the Inter-tropical Convergence Zone (ITCZ) (Rohling et al. 2002). It is the Eastern Mediterranean (E.Med Sea, Aegean and Ionian Seas) circulation which is most profoundly affected by these monsoonal variations as the formation of deep water in this area is inhibited by high fluxes of freshwater into the Eastern Mediterranean Sea via the Nile Estuary (Rohling 1994).

The circulation of water in the basin as a whole is controlled by both the surface winds through wind shear (Rohling et al.2009), and by thermohaline circulation (Casford et al.

2003 and Rohling et al.2009). The present day circulation of the main basin overall can be described as anti-estuarine (water entering the Mediterranean from the Atlantic on the surface, and leaving in the sub-surface). This mechanism is driven by the increase in the salinity of the surface water due to evaporation as it travels from West to East. By the time the water reaches the far Eastern Mediterranean, the salinity (and therefore density) is high enough for it to sink and return west as a sub-surface flow.

The flows of the surface waters in the Mediterranean's accessory basins (Adriatic and Aegean Seas, fig 2.2) are driven by local winds. In the winter, cold, dry northern air masses penetrate these basins through the valleys in the Alps. In the summer and the autumn air (and thus water) is driven southwards in these marginal basins (Rohling et al.2009).

2.3.2 Deep water formation

Deep water formation in the Mediterranean is thought to be important in maintaining the "non-sapropel" state of sedimentation, where the bottom water is constantly refreshed and thus does not so easily become anoxic. Deep water formation occurs where the water mass is dense enough by virtue of its salinity and temperature to sink below all the other water already present. In the Mediterranean, it occurs in several regions.

The main sink region for the western basin is the Gulf of Lions, south of France. In this region Western Mediterranean Deep Water (WMDW) forms as a result of cool dry, cyclonic winds passing over it in winter. Crudely, this creates a 'plug hole' effect in the previously stratified water column, where surface waters penetrate downwards into the intermediate and deep water strata (Rohling et al.1998).

In the Eastern Mediterranean deep water formation presently occurs in 3 places- the Adriatic Sea, the Aegean Sea and the far Eastern Mediterranean basin (fig.2.2). In the Adriatic, cold north-easterly winds cause intense cooling of the shelf waters. This drives their density to a point where it can sink to the bottom of the Adriatic and contribute to the main deep water of the Mediterranean by outflowing at the southern end of the Adriatic. The Aegean Sea is more sporadic in its production of Eastern Mediterranean Deep Water- contributing only when its regional, winter climate becomes cold enough (Klein et al. 1999) to create water dense enough to sink below the highly evaporated saline waters of the Eastern Mediterranean. In the Eastern Mediterranean Sea, off the coasts of Syria and Lebanon, the surface waters (originating from the Straits of Gibraltar) have become so

dense due to the evaporation of freshwater water that they sink to the base. In this way the bottom waters are constantly refreshed and remain oxygenated.

The combined flow patterns of water in the Mediterranean Sea (as described briefly above) inter-link to create the present day pattern of circulation where the bottom water is penetrated by surface waters allowing delivery of oxygen to the deepest parts of the sea. This situation appears to have endured for the majority of the Late Quaternary, but was periodically interrupted for brief periods, resulting in the formation of sapropels; considered next.

2.3.3 Mediterranean Sapropels.

Figure. 2.3 shows the implied situation during the formation of sapropels. These organic layers are thought to have formed during times of bottom water anoxia and have been the focus of paleaoceanographic research in the Mediterranean Sea since their discovery in 1946-47 (Rohling et al. 2009, Rohling and Thunell 1999).

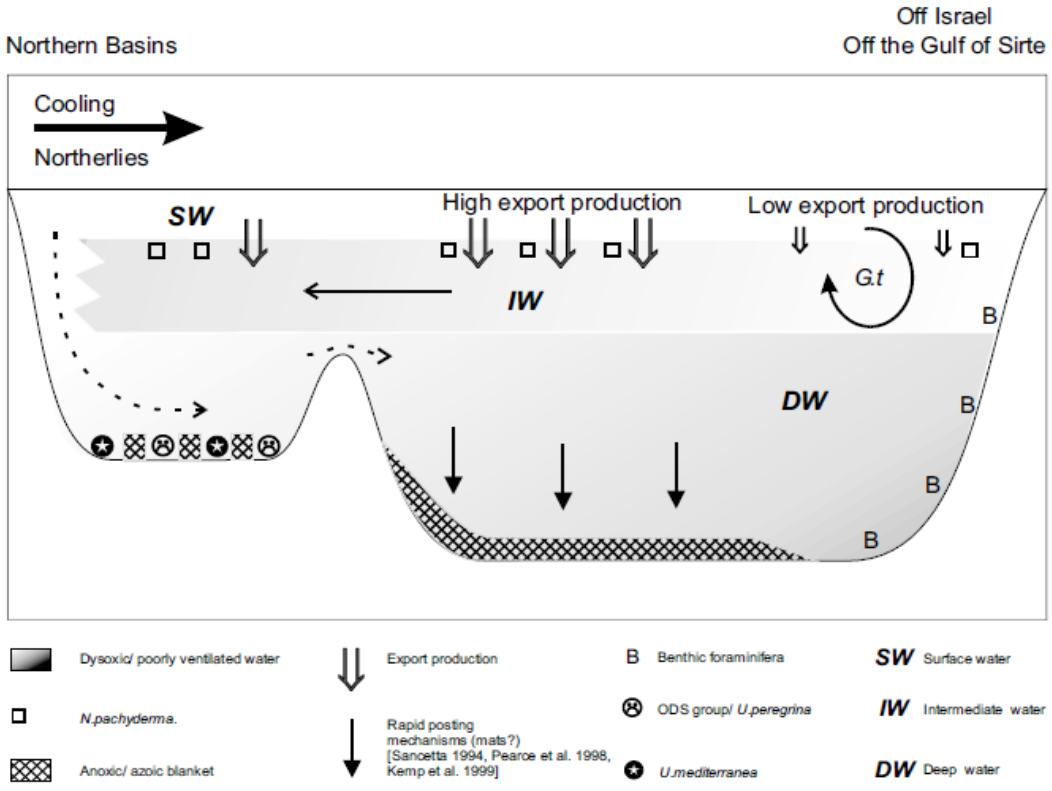

Figure 2.3 A schematic illustration of the mechanism of transition between sapropel producing state of the Mediterranean, and the non-sapropel producing state. In the sapropel producing state the deep water is anoxic, allowing the accumulation of organic matter on the sea floor. This is shown by the anoxic blanket in the diagram. In the non-sapropel state, the deep water is ventilated by cold dense water from the Aegean and Adriatic seas, and the far eastern Mediterranean (dotted arrow). The diagram illustrates the restricted nature of the anoxic blanket (sapropel inducing water) in both space and time (Casford et al.2003).

These are unconsolidated organic deposits composed of algae and other organic detritus (Rohling 1994). They are thought to primarily reflect changes in the circulation and associated productivity of the Mediterranean Sea (Cramp and O'Sullivan 1999). There is however still a great deal of uncertainty regarding the precise causes of the formation of sapropels, particularly between the different basins of the Mediterranean Sea. They are best developed and most thoroughly studied in the eastern Mediterranean and Aegean (e.g. Rohling et al. 1994, Casford et al. 2002, 2003, 2007), but also occur in the western basins (e.g. Cramp and O'Sullivan 1999 or Capotondi and Vigliotti 1999). 'Sapropel like' layers also occur in the Adriatic (Piva et al.2008b). Understanding the rates of sedimentation acting during deposition of a sapropel, may help to clarify its mode of formation. In addition, relating sapropels in different locations via isochronous regional tephra layers could also help to assess the importance of any climatic or oceanographic components in the process of sapropel formation. A brief overview is given here, but more comprehensive synopses are given by Pedersen and Calvert (1990), Rohling (1994), Rohling and Thunell (1999), Casford et al. (2003). The RESET consortium project aims to synchronise regional environmental events such as the formation of sapropels and abrupt oceanographic changes to the archaeology surrounding the Mediterranean Sea using tephra layers.

2.3.4 Mechanisms of sapropel formation.

The literature describes two end member mechanisms for the formation of sapropels in the Mediterranean region. These are a) anoxia of the bottom waters and b) surface productivity increase (fig. 2.3). The broad sapropel stratigraphy, within the timespan relevant to this thesis is shown in figure 2.4, with a composite $\delta^{18}O$ stratigraphy and an approximate age scale. The sapropels are referred to by the prefix S and the number referring to their position in the stratigraphy (S1 is the youngest).

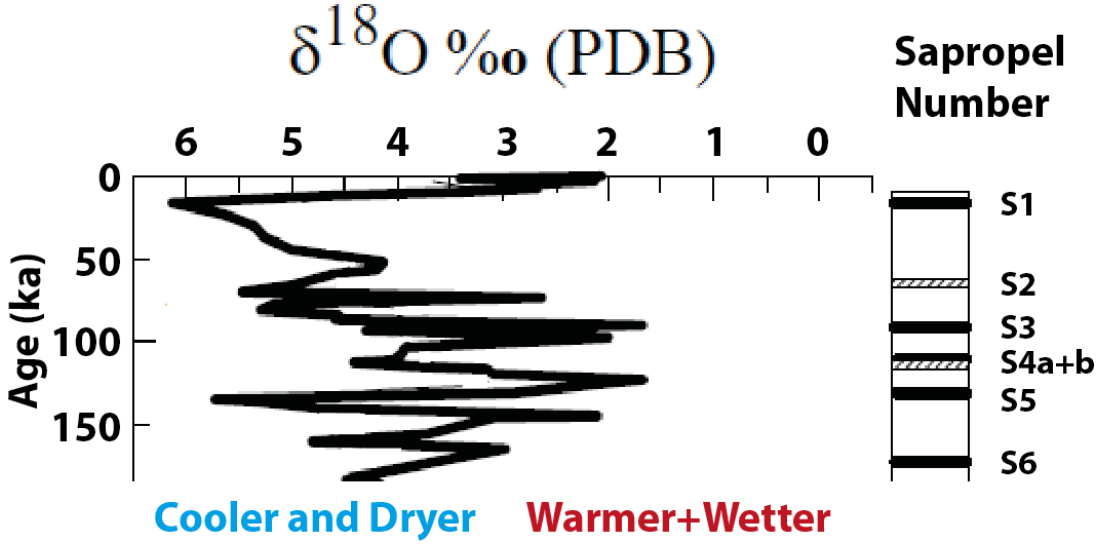

Figure 2.4. The generalised sapropel stratigraphy for the last ~200ka in the eastern Mediterranean sea (adapted from Kroon et al.1998). The $\delta^{18}O$ record is from Eastern Mediterranean core ODP967. Sapropels 2 and 4b are considered "ghost sapropels", preserved only weakly in most cores and in other cores not at all.

1 a) Anoxia induced by Glacial meltwater.

Most of the Mediterranean sapropels (including S_1) occur at times of climate warming (Cramp and O'Sullivan 1999), as defined by isotope stratigraphy in the region (e.g. Piva et al.2008) as shown in figure 2.4. Several studies have thus proposed that anoxic conditions could be produced in bottom waters as a result of a high flux of fresh water from Alpine glaciers (e.g. Emeis et al.1991). This influx of fresh water would create a large density gradient and a slow replenishment of bottom water, which thus becomes anoxic. An anoxic environment is not conducive to the breakdown of organic matter causing sapropels accumulate. In this scenario sedimentation rates would probably increase because while the flux of organic matter remains the same, its rate of breakdown on the sea floor would reduce (Rohling 1994).

1 b) Anoxia induced by increased rainfall.

Another way to create a lens of freshwater on the surface and the concomitant anoxic bottom water is to increase the flux of rainwater into the basin (Kallel et al. 2000, Zanchetta et al. 2007). This could be a result of the strengthening of the African monsoon (Cramp et al. 1988 or Perissoratis and Piper 1992) or the Indian Monsoon (Rohling 1994). Ground-breaking work by Rossignol-Strick (1985) strongly implied that the sapropels were synchronous with periods of strong African Monsoons. The implication is that the increased runoff through the Nile, and other now extinct North African river systems diluted the

surface and intermediate waters of the Eastern Mediterranean to such an extent that the deep water ventilation (previously maintained by the thermo-haline circulation) was switched off. This hypothesis is strongly supported by the close association of a rainfall signal from a speleothem in Soreq Cave, Israel (Bar-Matthews et al.2000) with the sapropel stratigraphy. The dates for the sapropels (estimated by orbital tuning of the $\delta^{18}O$ stratigraphy) and the inferred high rainfall event dates (obtained using U-series dating) in Israel are broadly coincident.

2) Sapropel formation by increased surface productivity.

Sapropels may in part represent times of increased surface productivity (Ganssen and Troelstra 1987). The flux of material may be too great for the organic C to be disseminated by biological and diagenetic processes on the seafloor. Sancetta (1994) proposed a "mat-sedimentation" mechanism to produce sapropels. In this scenario one would expect to see an increase in the sedimentation rate at the start of the sapropel. Such changes could be identified in an age model where tephra layers are incorporated as dates.

There are various lines of evidence to support both these mechanisms (increased anoxia or increased surface productivity) and in reality the two may form end members, each contributing a different component depending on the sapropel in question and the exact geographical location. Accurate dating and correlation of records is vital to assess the duration and initiation of sapropel formation, and it is hoped that the tephrochronology produced in this thesis can contribute strongly to this goal.

2.3.5 Short term climatic fluctuations in Mediterranean Marine Proxy Records.

Short term fluctuations in the Earth's climate were highlighted in the data obtained from the Greenland ice cores (see Barker et al.2011 and references therein). Short term fluctuations have also been inferred from the proxy records obtained from Mediterranean marine deposits (e.g. Casford et al.2002). The causes for these fluctuations are not yet well defined. There are suggestions that these rapid fluctuations could be related to the Heinrich layers (fig.2.5) in the North Atlantic sediments (e.g. Cacho et al.1999, 2000, 2001) and Dansgaard-Oeschger cycles in the Greenland ice cores (Cacho et al. 2000) particularly in the northern and western waters of the Mediterranean (Capotondi and Vigliotti 1999).

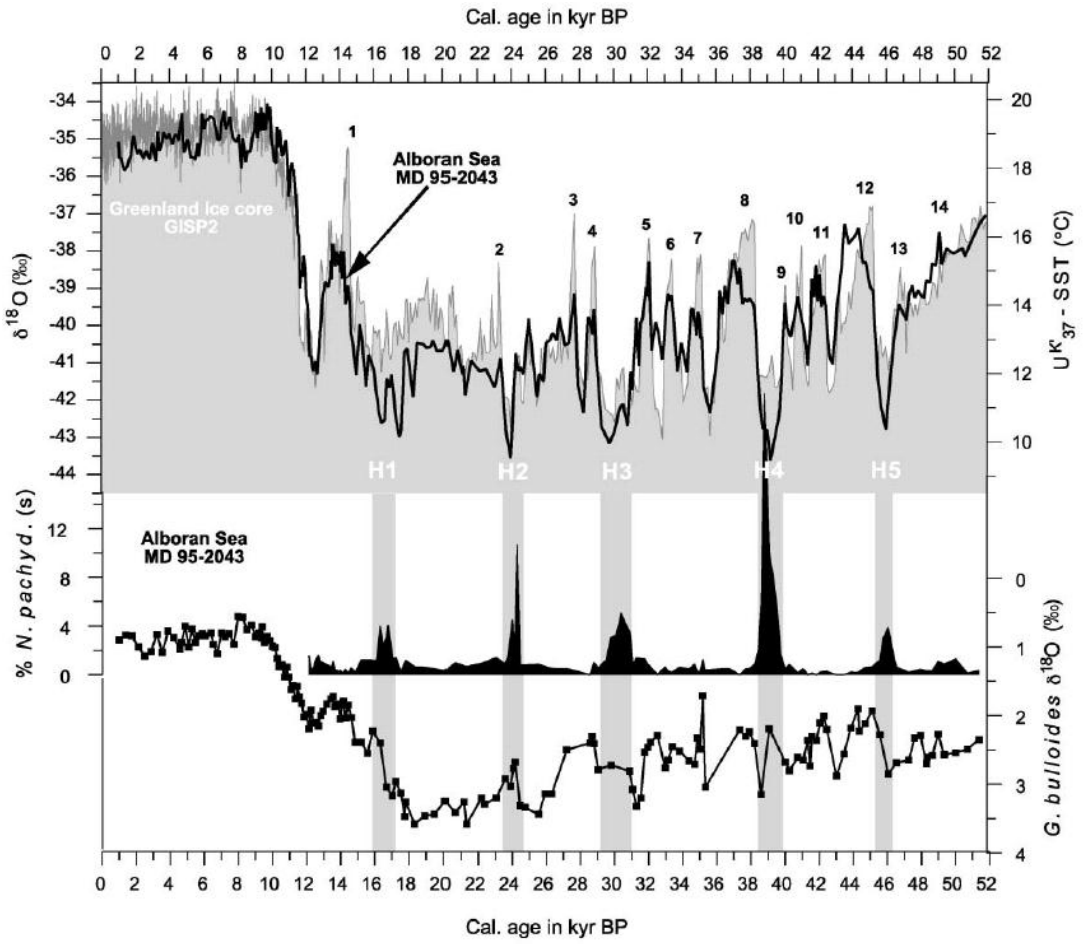

Figure 2.5 Upper panel: a reconstruction of sea surface temperatures in the Alboran Sea for the last 50,000ka, calculated using the alkenone $U^{k'}_{37}$, plotted against an atmospheric temperature record from Greenland GISP2 (Cacho et al. 2002). The authors correlate cold events in the Alboran Sea with Heinrich events evidenced in the North Atlantic, which are denoted by the numbers 1-14. The abundance of the Polar foram species *N.Pachyderma* in the Alboran Sea core is also shown, in the middle panel. The lower panel shows the $\delta^{18}O$ concentration of the planktonic foram *G.Bulloides* from the Alboran Sea. Interestingly changes in the $\delta^{18}O$ signal do not consistently correspond to changes in the sea surface temperature, indicating that the proxy is complex and requires careful interpretation.

The short term interruptions seen in the formation of sapropels 5 and 1 are chronologically associated with arid periods in northern Africa (Sanchez-Goni et al.2002, Tzedakis et al.2004), implying that the high frequency fluctuations in the proxy records are not just controlled by the North Atlantic/European climate, but also by climate of North Africa and thus, by inference, the strength of the African Monsoon.

Rohling et al. (2002) infer an apparent manifestation of the North Atlantic climate variations in the Holocene sea surface temperature proxy records of the Aegean (core LC21, also investigated in this study). They invoke the propagation of polar continental air into the Mediterranean basin as the linking mechanism and, by extension, variations in solar output as the root cause. The study hinges on the chronology of both the Greenland

and Aegean records, and recognises that an uncertainty of about 400 years in the comparison is unavoidable given the correlation techniques.

While short term, high frequency variations in climate are evident from these studies, uncertainty remains over the precise timing and therefore the causal mechanisms for these changes. Tephrochronology has recently begun to contribute to an understanding of the timings of these abrupt climatic shifts, in central Europe. Martin-Puertas et al. (2012) infer that decadal scale changes in the Holocene atmospheric circulation of Northern Europe (most likely the North Atlantic Oscillation) are coincident with a ~200 year duration solar minimum event, about 2800 years ago. Their evidence (fig 2.6) from Lake Meerfelder Maar in Germany is constrained using a varve and tephra supported chronology. This example shows how high precise dating is required to determine the root causes of rapid environmental transitions.

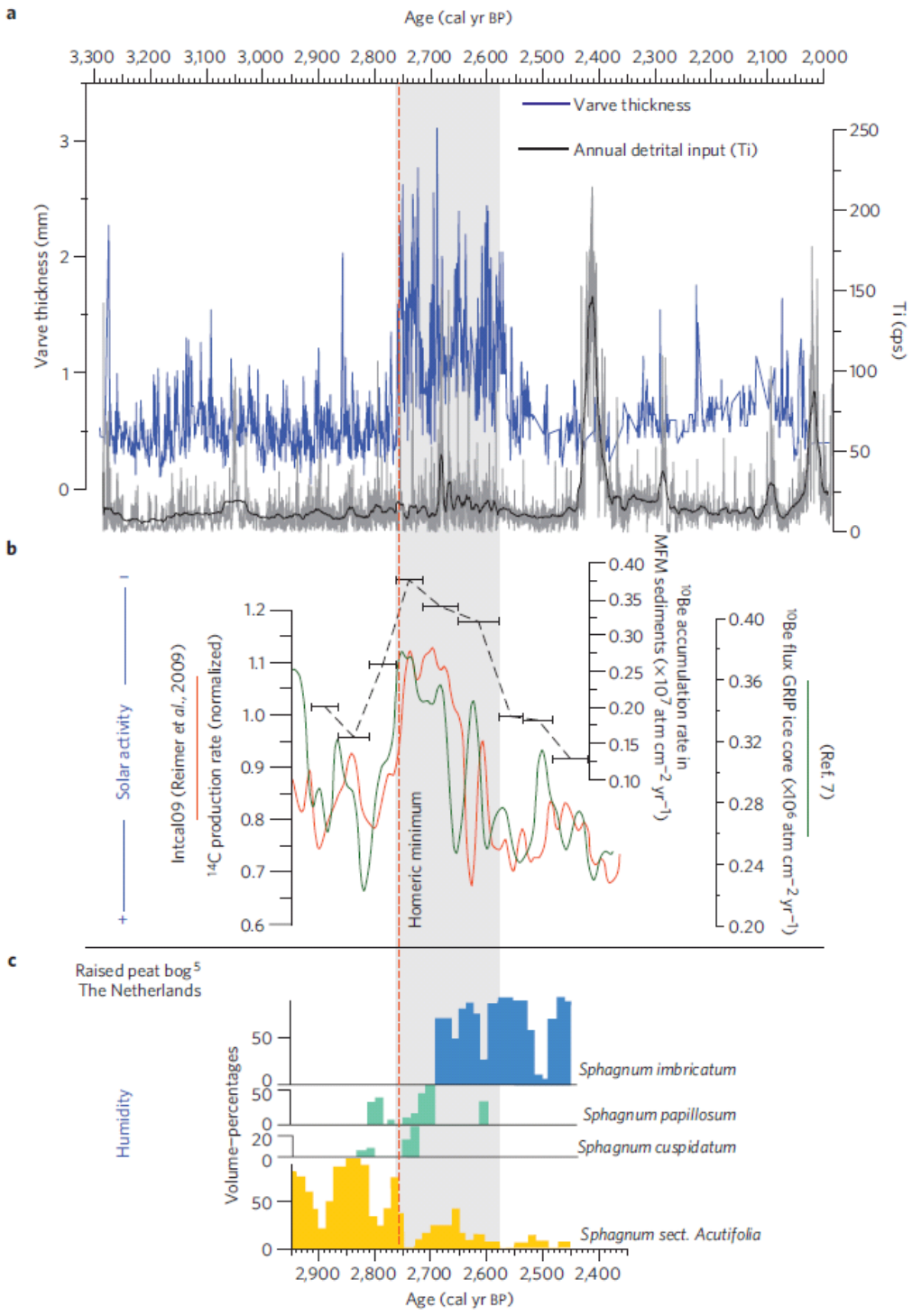

Figure 2.6. Short term climatic changes coincident with a solar minimum (the Homeric Minimum) discovered in the proxy record of Meerfelder Maar, Germany. a) Varve thickness (mm) and annual detrital input variability (Titanium in counts per second from scanning XRF), b) Proxies for solar activity: ^{10}Be accumulation rate in Meerfelder Maar in flux units and normalised ^{14}C production rate from Greenland ice cores (Muscheler et al. 2005) with the horizontal error bars indicating the uncertainty in the dating of the sediments. c) raised bog-based humidity proxy for the Netherlands, interpreted to show evidence for the 'Homeric climate oscillation' in Western Europe (Van Geel et al. 1996). The chronology for the study is created from the varve records of Meerfelder Maar and anchored to an absolute timescale using tephrochronology. From Martin-Puertas et al. (2012).

Absolute stratigraphic correlation of the Mediterranean marine cores with proxy records from both the North Atlantic and Greenland using tephra markers could robustly test the hypotheses concerning the Dansgaard-Oeschger and Heinrich events. Hypotheses relating the Mediterranean marine proxy records to the African Monsoon could also be tested using tephra layers which might be common to both of those regions.

2.3.6 Available oceanographic proxies.

Table 2.1 shows the available oceanographic proxies commonly employed in paleaoceanographic research and their accepted interpretation in Mediterranean marine records.

Proxy	Interpretation	Example references
$\delta^{18}O$ Planktonic Foram (generally *G.ruber*)	Local SST + global ice volume	Henderson (2002), Marino et al. (2009)
V/Rb	Redox state of bottom waters (circulation)	Henderson (2002)
Ba/Rb	Productivity	Henderson (2002)
Smectite/kaolinite clay ratio	Saharan dust input/Nile sediment input- dry/wet north Africa.	Sandler and Herut (2000)
Palaeomagnetic stratigraphy	Redox state of bottom waters	Roberts et al. (1999), Capotondi & Vigliotti (1999)
$\delta^{13}C$ Planktonic Foram (generally *G.ruber*)	Dissolved Inorganic Carbon content of the water (nutrients)	Marchitto et al. (2007)
Foram species assemblages	Sea surface temperature +salinity	Cacho et al. (2002)
Alkenone content	Sea surface temperature.	Cacho et al. (2002)
Benthic foram $\delta^{13}C$	Nutrient content of water	Cacho et al. (2002)

Table 2.1 Widely employed palaeoceanographic proxies used to investigate sediment sequences in the Mediterranean Sea.

The proxy record of the Mediterranean is complicated as it is influenced by a number of factors, both internal and external to the Mediterranean, which cannot be assumed to be synchronous across the region, or consistent through time. This complexity means it is very

difficult to determine the causes of specific events, and to establish the chronological relationships between marine sites and terrestrial (e.g. Allen et al.1999, or Margari et al.2009) proxy records across the region.

It is hoped therefore that the work presented in this thesis can help to relate the proxy records from different basins in the Mediterranean Sea to one another and also to terrestrial records, with chronologically absolute tephra markers. This could expose any currently hidden leads and lags between the abrupt climatic changes of the different parts of the Mediterranean basin, informing how the Mediterranean ecological and oceanographic systems work and how they relate chronologically to archaeology, the terrestrial ecology, North Atlantic and North African proxy records and the orbital and solar parameters.

Chapter 3- Background information on the Volcanic systems of the Mediterranean.

Mediterranean geology of the past 30Ma has been defined by the convergence of the African and Eurasian plates. The complicated tectonic setting of the Mediterranean has induced many volcanic centres (fig 3.1). The subduction of the Tethyan oceanic lithosphere underneath Europe is the feeding mechanism for some of these volcanic systems such as the Hellenic Arc or the Massif Central. Other systems such as the Campanian region in Italy are a result of back-arc tectonic extension or local extension fault systems which accommodate the complex systems of micro-plates in the Mediterranean basins. An in depth review of the tectonics of the Mediterranean is given by Carmenati and Doglioni (2004). The volcanic systems associated with this tectonic regime are shown on fig 3.1.

3.1 Santorini: background

3.1.1 Geological Setting and Style of Volcanism on Santorini.

The Island of Santorini (36° 24', 25° 24') is located in the Southern Aegean Sea, approximately 150km North of the Island of Crete (see fig. 3.1).

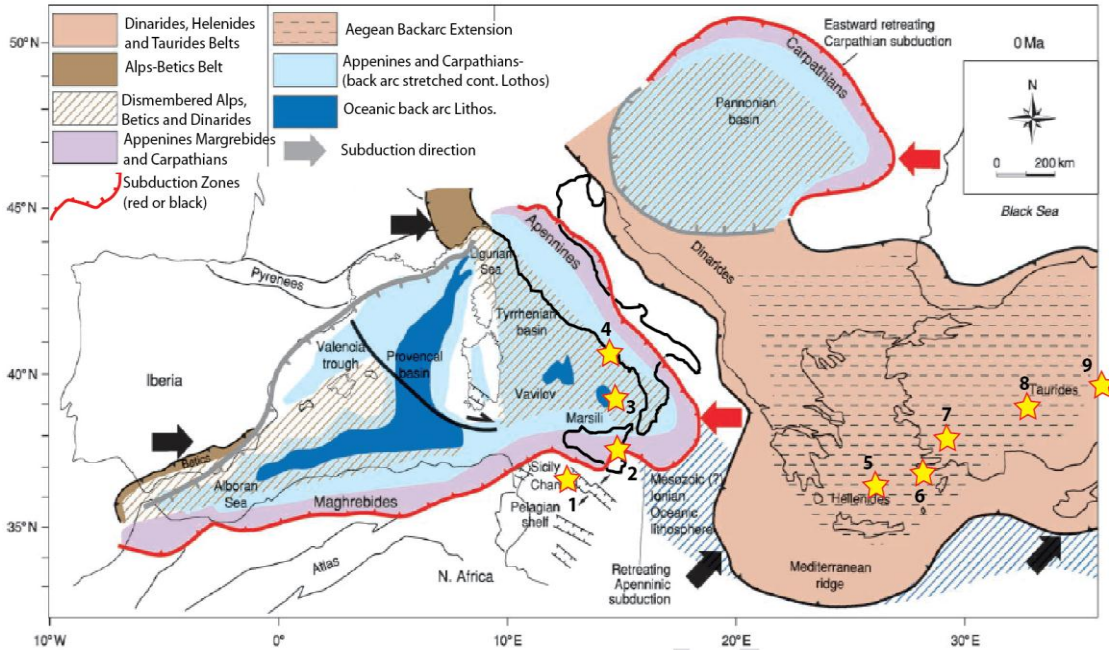

Figure 3.1 Tectonic setting of the major Mediterranean volcanic systems (shown as yellow stars). 1. Pantelleria, 2. Etna, 3. Aeolian Islands, 4. Campanian system, 5. Santorini, 6. Kos/Yali/Nisyros, 7, Western Anatolia, 8. Central Anatolia, 9.Eastern Anatolia. (adapted from Carminati and Doglioni 2004).

Figure 3.1 shows that Santorini is located in a supra-subduction zone setting. Early Tertiary to mid-Miocene volcanism was the result of subduction of the African Plate under the European plate (Carminati and Doglioni 2004). This island arc volcanism is still manifest today in the Hellenic Arc islands of Santorini, Kos, Yali and Nisyros (fig. 3.1). Back-arc extension has precipitated very minor alkaline volcanism in the Aegean islands of Psathoura and Kalogeri. It is normal in supra-subduction zone settings for volcanoes to produce calc-alkali type, silica-saturated magmas and this is the case for Santorini. The eruptions of Santorini are set within a cyclic framework (Druitt et al.1999), consisting of Plinian and interplinain activity, ending with a caldera collapse phase and recharging of the magma system. The Plinian activity is described by Druitt et al. (1989) and Martin et al. (2010) while the inter-Plinian activity is investigated by Vespa et al. (2006). The schematic stratigraphy of the Santorini proximal deposits is summarised in figure. 3.2.

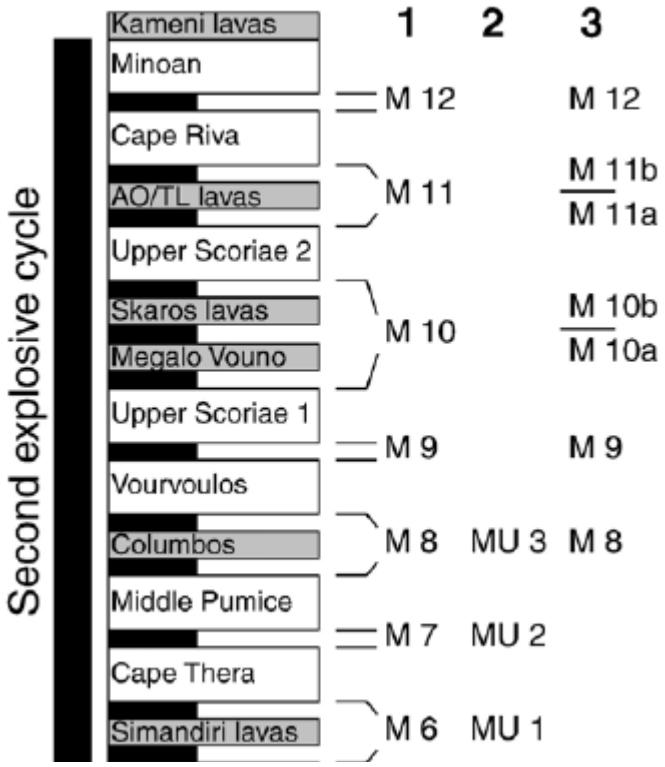

Figure 3.2 The second explosive cycle stratigraphy of Santorini (from Vespa et al.2006). The units are named by different authors 1= Druitt et al. (1999), 2= Edwards et al. (1994) and 3= Vespa et al. (2006). Black units indicate effusive interplinian activity, grey units indicate interplinian lavas and cinder cones, white layers indicate major explosive eruptions.

The volcano has had 12 major individual eruptions in the past 200ka, interbedded with minor explosive eruptions (Druitt et al.1989) and interplinian activity (Vespa et al.2006). Two cycles of volcanic activity are inferred from the deposits on Santorini based on the

repetition of pumice compositions and eruptive styles in the caldera-wall successions (Druitt et al. 1989). Each of these started with explosive eruptions of andesitic or dacitic magma, and culmulated in two large pyroclastic eruptions of dacitic to rhyolitic tephra. (Druitt et al.1989).

3.1.2 History of Volcanism on Santorini- the Volcanic Stratigraphy

While the island preserves a well-defined volcanic succession (fig. 3.2), the absolute chronology of the deposits has not been well constrained, presumably due to a paucity of both K bearing phases for ^{40}Ar:^{39}Ar dating or charcoal for ^{14}C radiometric dating. Using these deposits in marine cores may therefore be limited to assessing the relative timing of events between cores which share the same tephras, rather than importing absolute dates into a core to refine the chronology. It is however possible that eruptions could be dated using an age model generated for a marine core, based on other tephras of known ages sourced from other volcanoes. The time between eruptions can also be assessed much more easily using the tephra isochrons in a marine core, as the deep sea bottom is less prone to erosion than are most terrestrial deposits. (Clift and Blusztajn 1999).

Plinian eruptions produce very important, widespread isochrons within detailed proxy sequences. In the case of Santorini, the most abundantly studied eruption is also the most recent. The Minoan eruption (fig. 3.2) (3344.9+/-7.5 BP, Manning et al. 2006) has been studied by both volcanologists and archaeologists, due to its association with the demise of the Minoan culture on Crete (Cashman and Giorando 2008 and references therein).

The Minoan eruption vented about 36km^3 of magma (Driutt et al.1989) and generated a widespread tephra layer (Sparks et al.1984). If the other major eruptions were of comparable size, or larger, then the eruptive products from Santorini should be abundant in environmental records throughout the Eastern Mediterranean as a visible or micro-tephra layer. Studies of the other proximal deposits are restricted to overview papers by Druitt et al. (1989,1999), Vespa et al. (2006) and Martin et al. (2010); these eruptions are presumably considered to have less archaeological significance. They could however be far more important than the Minoan tephra in constraining age models for marine and terrestrial archives, or may even contribute to solutions to other important chronological problems in the archaeology of the Eastern Mediterranean.

The Cape Riva eruption is stratigraphically below the Minoan eruption in the proximal Santorini stratigraphy (fig.3.2) (Druitt et al.1989, 1999) where it comprises four units. It has been assigned a ^{14}C date of ~21ka (Druitt et al.1999) or 21.95ka (Wulf et al.2002). This Plinian eruption has been identified as a visible layer in cores in the Sea of Marmara (Wulf et al.2002) and the eastern Mediterranean cores ODP967,968 (Clift and Blusztajn 1999) and 84MD648 (Dacassou et al. 2007), indicating a dispersal to both the north east and the south east. As this tephra is found in both the Aegean and the Eastern Mediterranean, it offers the potential for linking cores from both regions to test assumptions about the synchronous (or otherwise) nature of oceanographic events.

The Upper Scoria 2 deposits underlie the Cape Riva deposits, and also comprise four units (Druitt et al. 1989). The best available date for the Upper Scoria 2 deposits is from Druitt et al. (1989) who cite an unpublished ^{14}C date of 37 +/- 1.8ka from associated charcoal, although Druitt et al. (1999) cite a whole rock ^{40}Ar:^{39}Ar age of 54+/- 3ka. This latter date would be valid if the crystals all held the same closure age, but Martin et al. (2010) demonstrate that the Upper Scoria 2 has two populations of crystals. As a result, 54+/-3ka is likely to be a compromise of the 'old recycled' crystal ages and the 'real' crystal ages; the eruption age. This whole rock method must therefore give a radiometric date which is too old and so 54ka +/-3ka which should be regarded as a maximum age limit for the Upper Scoria 2 eruption.

The age (albeit approximate and poorly defined) of the Upper Scoria 2 could also make it an important eruption for the dating and correlation of archaeological sites in the area where the tephra can be found as this is a period in which the remains and artefacts of Neanderthals and/or Anatomically Modern Human populations are found in the Eastern Mediterranean.

The Upper Scoria 1 eruption is exposed below the Upper Scoria 2 and is also comprised of 4 units. It is separated from the Upper Scoria 2 by minor tephras and palaeosols (Druitt et al.1989). It is ^{14}C dated at 54.0+/- 0.7ka by Druitt et al. (1989) from charcoal found within Unit B. This date is however at the limit of the ^{14}C method and is thus likely to be a minimum. The Upper Scoria 1 has not yet been identified for certain in marine cores, though the "Group 2" tephra of Aksu et al. (2008) has a very similar chemistry and thus may originate from the Upper Scoria 1 eruption.

The Vourvolous eruption deposited thin proximal deposits comprising two units: a pumice fall deposit (unit A) with overlying surge deposits and ignimbrite (unit B) (Druitt et al.1999). As the thickness of these deposits on Santorini is less than each of the four eruptions previously described, it might be expected that the associated tephra layers would not be found as widely dispersed; it appears to be the most minor explosive eruption in the proximal stratigraphy of Santorini. No dates are reported in the literature for the Vourvolous deposit. If tephra associated with the eruption could be identified in a marine core then a modelled date could be imported as the date for the proximal eruption deposits and thus as a maximum age for the overlying palaeosols and interplinian activity (M9 of Vespa et al.2006).

The Middle Pumice series of pumice, tuff, breccias, and pyroclastics lies below the Vourvolous deposits (Vespa et al.2006, Druitt et al.1989). The Middle Pumice has been correlated with the W2 marine tephra (Federman and Carey 1984) and from the oxygen isotope stratigraphy has been assigned a date of ~150ka. The W2 tephra has been found as a visible layer as far east as marine cores south of Cyprus (84MD637 and 84MD638-Dacassou et al.2007), meaning it may be found throughout the eastern Mediterranean, and possibly (as a crypto-tephra layer) even further east.

The earliest of the Santorini second explosive cycle eruptions is represented by the **Cape Thera eruption.** This eruption has a pumice fall unit (unit A) and an ignimbrite deposit (unit B) (Druitt et al.1999). The pumice deposit is only a maximum 85cm thick on the island, and thus it is unlikely, but not impossible that this eruption generated a regionally significant tephra marker layer. S. Sparks (pers. comm.) suggests that the maximum thickness of some fall deposits can occur far from the central vent of an eruption.

3.1.3 Interplinain activity between the Cape Thera and Minoan eruptions

The Plinian stratigraphy of Santorini is intercalated with inter-plinian deposits (IPDs) as summarised by Vespa et al. (2006). This inter-plinian activity persists between plinian eruptions for between 17 and 45ka (on the chronology of Druitt et al. 1999). These deposits are from non-caldera forming eruptions, and Vespa et al. (2006) classify all of these as Strombolian magnitude events. This diminished explosivity status does not however preclude these eruptions from producing ash clouds, and so this inter-plinian activity is also considered very briefly here.

In general, the inter-Plinian deposits are composed of pumice fall and scoria fall deposits. Ash deposits are a minor component of the overall volume of the interplinian stratigraphy (Vespa et al. 2006). Silicic fall deposits are more common at the start of the 2nd eruptive cycle and decrease to almost none between the Vourvoulos and the Upper Scoriae 2 eruptions, during the formation of the Skaros lavas and the Megalo Vouno cinder cone (see fig. 3.2). They then increase again in frequency towards the top of the eruptive cycle (the Cape Riva and Minoan Plinian eruptions) (Vespa et al.2006).

3.1.4. Santorini distal tephra reported in the literature.

Terrestrial finds of Santorini tephra in the literature have been restricted mainly to tephra from the Minoan and the Cape Riva eruptions. This is likely due to the former's significance with respect to archaeological investigations and the latter's age of ~21ka (Druitt et al. 1999); which dates approximately to the coldest period in Europe during the last 100ka. Margari et al. (2007) for example, have found tephra shards from the Cape Riva eruption on the island of Lesvos, (Greece), while Sullivan (1990) found the tephra shards from the Minoan eruption in lake deposits in Eastern Turkey.

Marine tephra studies have however been more comprehensive in their chronological scope. Guichard et al. (1993) have found the Minoan tephra in the Black Sea and Wulf et al. (2002) reported the Cape Riva in the Sea of Marmara. Aksu et al. (2008) detected the Minoan, Cape Riva, the uncorrelated Y4 (implied by them to be from Santorini) and a further tephra which they interpret as originating from the Aeolian Islands, but from its thickness in the marine core (12cm) and the similarity of its trace element contents other Santorini-derived tephras in that paper, it is more likely from Santorini. Vinci (1985) presented a first synthesis of Eastern Mediterranean deep sea tephra layers, identifying 7 visible tephra layers from Santorini, including deposits she correlates to the Minoan, Cape Riva, and Middle Pumice eruptions. The furthest discovery of Santorini tephra from the island is by Dacassou et al. (2007) who identified the Cape Riva ash in the Northern part of the Nile Delta. This discovery suggests that distal material from Santorini eruptions may be found in North of Africa and in the eastern Mediterranean Sea as micro-tephra. These regions are important, both for archaeology and oceanography respectively.

3.2 Campanian System: Background

3.2.1 Geological Setting and Style of Volcanism in the Campanian System

The Campanian Volcanic system is located on the Tyrrhenian Sea coast of Italy, in the Bay of Naples (fig. 3.1). It comprises the volcanic centres of Vesuvius, the Campi Flegrei, Procida-Vivara and Ischia Island.

The position of this volcanic system on the western edge of the Apennines is due to the extensional (back-arc) tectonic setting in this region (Vezzani et al.2010 and fig. 3.1). The resultant alkaline magma migrates to the surface via a series of NE-SW and NW-SE trending normal faults in the Campanian region, and the lava has collected at between 10 and 3km depth below the land surface (Pabst et al. 2008 and references therein). The fault geometry has created 3 major, currently active volcanic areas within the Campanian system: Somma-Vesuvius, the Campi Flegrei and Ischia Island (Paterne et al.1990).

The general model for the Campanian system is one of small magma chambers that contribute to the more minor eruptions, with a large magma chamber below them. It is the evacuation of this large chamber which causes the larger caldera-forming eruptions (Pabst et al. 2006).

3.2.2 History of volcanism in the Campanian system- the volcanic stratigraphy.

While these three volcanic centres have erupted regularly (~118 times within the last 200ka, Paterne et al. 1990), two major caldera forming eruptions from the Campi Flegrei dominate the local volcaniclastic, and distal tephra stratigraphies. These are the Campanian Ignimbrite eruption (the CI) at~39ka (De Vivo et al.2001) and the Neapolitan Yellow Tuff (NYT) at ~15ka (Deino et al.2004). The CI is thought to be the largest eruption in the Mediterranean region in the last 200ka with an estimated volume of up to 210km^3 of magma erupted (Pyle et al.2006). The tephra from the eruption is distributed over a wide region, reaching South-East Russia (Pyle et al.2006) and thus this eruption has the most widespread tephra layer of any known eruption in the Mediterranean during the last 200ka.

The complicated volcanic event stratigraphy for this system is probably best represented in records distal to the caldera itself, as the events are more easily distinguished stratigraphically from one another, and because much of the proximal Campi Plegrei stratigraphy is now submerged below sea level. Wulf et al. (2004), Bourne et al. (2010) and Paterne et al. (2008) probably provide the most comprehensive stratigraphic successions revealing the sequence of eruptions for this region.

Volcanism in the Campanian system began before 150ka (Poli et al.1987) on Ischia Island. Here, a highly explosive period of volcanic activity persisted until it was replaced by a period of relative quiescence and lava dome growth until about 75ka (Poli et al.1987). Two major pyroclastic deposits were created after 75ka: the Tufo Verde Epomo (~56ka) and the Citara Formation (from 48-33ka). The island then returned to a lava dome building period from 28ka to the present day.

The Campi Phlegrei caldera preserves deposits dating from 60ka (Orsi et al. 1996 and Pappalardo et al. 1999), although explosive volcanism most likely began prior to this date, as tephra layers strongly resembling these caldera products have been found preserved in many distal archives extending further back in time than 60ka (Wulf et al.2004, Bourne et al.2010). The most prominent of these is a widespread marine tephra (the X5 tephra) dated to ~105ka. (Bourne et al.2010 and references therein and Wulf et al. 2012).

The famous volcanic vent of Vesuvius which looms over the city of Naples is the most recent vent of the Somma-Vesuvius complex, which was initiated ~25ka. Since then, 4 major caldera forming eruptions (Cioni et al.1999) have reshaped the geography of the complex, and contributed tephra to the regional tephra record (Wulf et al.2004). Since the last caldera forming event (the Pompeii eruption of 79AD), the activity of Vesuvius has been comprised of intermittent Strombolian or Vulcanian scale eruptions. The composition of the eruptive products from Vesuvius has been highly variable, but always Si under-saturated (Cioni et al.1999) and often containing xenoliths and high CO_2 levels from the assimilation of limestone, the local country rock.

3.2.3 Campanian distal tephra reported in the literature

As outlined above, the most widespread of the Campanian tephras are those associated with the two caldera forming eruptions of the Campi Phlegrei; the Campanian Ignimbrite and the Neapolitan Yellow Tuff eruptions. The Campanian Ignimbrite has been found as a

distal visible or crypto-tephra as far away as Kostenki in Western Russia (Pyle et al.2006), Lesvos in Greece (Margari et al.2007), in several marine cores in the Eastern Mediterranean (Asku et al.2008) and to the west in the Tyrrhenian Sea (Roberta et al.2008, Paterne et al.1986). This tephra, having been assigned a highly precise date from ^{39}Ar:^{40}Ar of 39.3 ±0.1 ka (De Vito et al.2001), is therefore an important marker horizon for Italian and Eastern Mediterranean palaeoclimatic and archaeological records.

The Neapolitan Yellow Tuff has a more limited extent, but is found in marine sediments of the Adriatic Sea (Bourne et al.2010, Calanchi et al.1998, Siani et al.2003), and in lake sediments in southern Italy (Munno and Petrosino 2007, Wulf et al.2004). It has not yet been reported in the Aegean or Ionian Seas, or on land in Greece. It has also been reported as a crypto-tephra in Slovenia (Lane et al.2011), where it was found with an Icelandic tephra layer and thus relates the timings of eruptions from the two volcanic systems.

Two other tephras from the Campanian system may be regionally significant, both of these being found initially in marine sediments. The X5 tephra is thought to originate from the Campi Flegrei and is dated at ~105ka (Bourne et al.2010 and references therin). This tephra has been found in the Adriatic Sea (Bourne et al.2010) and the Ionian Sea (Paterne et al.1998). The Y3 tephra has an uncertain origin, but is also likely to originate from the Campanian System (Munno et al.2004). It is found in the Tyrrhenian Sea (Munno et al.2004) and in the Adriatic (Bourne et al.2010) and Ionian (Keller et al.1978) seas.

Other tephra layers originating from the Campanian system are more limited still. The most comprehensive record of the eruptive history must be from Lago Grande di Monticchio, in Southern Italy (Wulf et al.2004), where 313 eruptions from the Campanian system over the past ~100ka are evidenced by the tephra layers. These apparently more geographically limited tephra horizons may still be present in more distal locations, and may be found in the future by crypto-tephra sample processing.

3.3 Kos/Yali/Nisyros System: background.

3.3.1 Geological setting and style of volcanism

The Islands of Kos, Yali and Nisyros are located in the Aegean Sea, southwest of Turkey (36°34', 27°10') and as with Santorini are a product of northwards subduction of the

African Plate below the Aegean microplate and the European Plate (fig. 3.1). The three Islands are considered to be three exposed manifestations of the same magmatic system (Bachmann et al.2010), separated by only 30km or so. The positions of the vents for the past eruptions are not precisely known (Allen et al.1999) and the eruptions are therefore named after the island upon which they are found in most abundance. The system has been periodically exposed above, and hidden below sea level resulting in both sub-aerial and sub-marine eruptions (Allen and McPhie 2000).

The composition of the volcanic products of Kos is highly homogenous, and silica-rich (Bachmann et al.2007). These observations lead to the hypothesis that the magmatic compositions are strongly influenced by contamination from the crust or a partially consolidated magma chamber (Oppenheimer and Pyle 2009).

The eruptive products of the neighbouring islands of Nisyros and Yali are more chemically heterogenous but have also been thought to have been contaminated by a crustal source (Buettner et al.2005). Francalanci et al. (2007) state that the crustal component of the isotopic signature in the Nisyros+Yali eruptive materials could be due to the inclusion of crustal material on the subducted slab into the mantle wedge where the magma originates, rather than assimilation of the ambient continental crust.

3.3.2. Volcanic stratigraphy.

The literature documents 4 major ash producing eruptions during the last 200ka, the Kos Plateau Tuff, Nisyros Upper and Lower Pumice eruptions, and the Yali-2 (or Yali-C eruption) in stratigraphic order.

The Kos Plateau Tuff was one of the largest eruptions in the Mediterranean in the last 200ka (Bachmann et al.2010), releasing an estimated 60km^3 of magma in a Plinian eruption (Allen et al.1999), or perhaps as much as >100km^3 (Francalanci et al.2007). The products of this large rhyolitic eruption are likely to be widely distributed in the Eastern Mediterranean Sea, although as many palaeoceanographic studies have focused on sapropels S1 and S5, the Kos Plateau Tuff tephra has not been widely reported from marine cores previously studied. Only Dacassou et al. (2007) report the Kos Plateau Tuff as a visible tephra in cores (84MD648 and 84MD638) from the Nile Delta south of Cyprus.

The Nisyros Upper and Lower pumices are described by Hardiman et al. (1999). These two eruptions do not appear to be widely spread in the deep sea surrounding Nisyros

(Hardiman et al.1999), and so are unlikely to create regional tephra horizons. Aksu et al. (2008) have however correlated a tephra layer in the Central Aegean, predating the Campanian Ignimbrite tephra, to the Nisyros Lower Pumice. Margari et al. (2007) assign a tephra from Lesvos Island in the Northern Aegean Sea to Nisyros. From these samples, this eruption appears to have a NW dispersal.

The stratigraphy of Yali consists of 4 units: Yali 1,2,3 and 4. Of these Yali 1 and 2 are submarine pumice breccias, and Yali 4 is a lava flow event. The only event likely to have produced significant airborne tephra is represented by the Yali 2 deposit. The Yali 2 Pumice (Yali C of Federman and Carey 1980, Yali 2 of Hardiman 1999 and Asku et al.2008, Yali 2a+ of Buettner et al.2005) is also found on Nisyros, above both the Nisyros Upper and Lower Pumice layers (Volentik et al.2002) and thus postdates these two eruptions. Federman and Carey correlate a tephra from cores up to ~300km SE of Yali to this Yali 2 Pumice, and Asku et al. (2008) assign a tephra in a Gokova Bay core (between Kos and the Turkish mainland) to this eruption also. These occurrences indicate dispersal to the SE for the Yali Pumice eruption, meaning that it is also likely to occur as either a visible or micro-tephra layer in the eastern Mediterranean Sea.

3.4 Pantellerian System: Background

3.4.1 Geological Setting and Style of Volcanism on Pantelleria

Pantelleria is an Island volcano located in the Straits of Sicily, 100km SW of Sicily and 70km N of Tunisia (fig 3.1). The volcanism on the island is a manifestation of Neogene/Quaternary extension and concomitant rifting in the Sicily Channel. The island itself is located on a region of crust with a strongly positive “Bouguer anomaly” and high heat flows, suggesting upwelling asthenosphere, and a basaltic melt ‘pond’ under the volcano (Della Vedova et al.1995).

3.4.2 The Volcanic Stratigraphy of Pantelleria

The volcanic products are very variable, from alkaline mafic lavas to peralkaline pantellerite tuffs and ignimbrites. The oldest deposits are lava flows dating from about 324ka to 239ka (White et al.2009), which probably mark the start of volcanic activity on Pantelleria. The first evidence of explosive activity is a welded tuff dating to ~189ka (Mahood and Hildreth 1986). This was followed by welded tuffs at ~175 and 164ka, and ignimbrites at 133, 106, 94, 79 and 70ka (Mahood and Hildreth 1986) although it is not clear from the literature

how these dates were obtained. The last known major Plinian eruption on the island occurred at 45-50ka (Cornette et al.1983, White et al.2009, Avanzinelli et al.2004) and is named the Green Tuff.

3.4.3 Distal tephra originating from Pantelleria

Distal tephra from Pantelleria is easily recognised due to its unusual FeOt (very high) and Al_2O_3 (very low) values. Tephra layers from Pantelleria have been found as far east as the island of Lesvos- Greece (Margari et al.2007). In Margari et al. (2007) this tephra is attributed to the Green Tuff (~45ka), although the age model presented there and using this date requires a massive change in the sedimentation rate of the record. Consistency in the sedimentation rate would more sensibly imply a date of about 130ka (Vogel et al.2010). A Pantelleria tephra (P11) dated at 133ka is found in the Ionian Sea (Paterne et al.2008).

Another Pantelleria tephra (TM22) has been detected in the Lago Grande di Monticchio lake sequence by Wulf et al. (2004) dated at 85,320 by their varve supported chronology, and attributed to the proximal Pantelleria deposits of the Ante-Green Tuff. The later eruption of the Green Tuff has distal products which have been identified in Lake Ohrid, Albania/Macedonia, by Vogel et al. (2010), and in the Ionian Sea as the Y-6 tephra by Keller et al. (1978). Two tephras from Pantelleria are thus established as regional stratigraphic reference points- the P-11 tephra at ~130ka (which may correlate to the proximal Unit P, of the Pantelleria stratigraphy- Tamburrino et al.2012) and the Green Tuff, dated at ~45ka. The oldest Pantellerian tephras found so far in the Mediterranean are described in the Tyrrhenian and Ionian Seas (Paterne et al.2008) and are dated at 163.6ka (P-12), 192.5ka (P-13 and P-14), 197.4ka (P-15) and 198.4ka (P-16).

3.5 Aeolian Islands

The Aeolian Islands are a group of volcanic islands and seamounts located to the north of Sicily and to the west of the toe of Italy, in the Tyrrhenian Sea. The system is a manifestation of subduction of the Ionian Plate beneath the Calarian plate (Lustrino and Wilson 2007) and produces both silica saturated and silica under-saturated eruptive products (Albert et al. 2012). Eruptions have been mainly Strombolian and range from basic to highly evolved. The stratigraphy of the islands relative to one another has not yet been defined in the literature, although a first attempt was made by Albert et al. (2012) using a marine core. This paper describes 11 major eruptions within the last 30ka.

3.6 Anatolian/Turkey

Turkey has several volcanic provinces, each related to intra-plate fault zones. These fault zones have been created and maintained by the complex relative movements of the Eurasian Plate (and the Anatolian Block), and the African and Arabian plates (Kocyigit and Beyhan 1998). It is appropriate to divide the Turkish volcanic into 3 geographically removed systems; the West, Central and Eastern Anatolian volcanic systems.

3.6.1 Eastern Anatolian Volcanic System

The Eastern Anatolian volcanic system (fig 3.1) produces alkaline volcanic products and has been active throughout the Quaternary (Notsu et al.1995). There have been several phases of eruptive products described by Karaoglu et al. (2005), however, no good dating exists for these deposits. Two trachytic deposits thought to represent the Plinian eruptions of the complex have been analysed by the RESET team (E. Tomlinson pers.com.) These are; a pre-caldera ignimbrite and the caldera causing eruption ignimbrite (Nemrut Ignimbrite-Karaoglu et al.2005). The rest of the Quaternary stratigraphy consists only of basaltic, trachybasaltic and trachyandesitic lavas and minor scoria deposits (Karaoglu et al.2005) which are unlikely to have associated, widespread tephra layers.

3.6.2 Central Anatolian Volcanic System

Volcanism in this region is again related to faulting caused by the complex tectonic motions of the Arabian, African and Eurasian plates (Kocyigit and Beyhan 1998) (fig. 3.1) This system produces calc-alkaline volcanic products (Sen et al.2003). The stratigraphy is divided into two eruptive cycles by Sen et al. (2003), separated by a caldera forming eruption at ~2.7ka. They describe Plinian activity at ~115ka and postdating 83ka, but once again the dating control is poor. 3 ignimbrite deposits have been analysed by the RESET team (Tomlinson pers.com). These are the Kara Gulu and Perikartini eruptions (~7ka) and the Dikkarin eruption at ~8.8ka. This eruption is considered to be the most likely source for marine tephra found by Hamann et al. (2010) in the Eastern Mediterranean Sea. In addition, ignimbrite forming eruptions from the Acigol vent have been cited at ~14ka and 29ka (Bigazzi et al.1993).

3.6.3 Western Anatolian Volcanic System

Late Quaternary volcanism in Western Turkey is currently maintained in the Kula region by extensional, strike-slip rifting (Aydar 1998) (fig 3.1). The system began producing explosive calc-alkaline eruptions within a compressional context in the Early Miocene, probably as a result of subduction of oceanic lithosphere (Innocetti et al. 2005) and developed into the current extensional volcanic system upon the initiation of slab roll-back. The system has not produced any explosive eruptions in the Late Quaternary: the only extrusive products are very locally distributed alkaline lavas (Alici et al. 2002). This system is thus not considered to be a likely contributor to the Mediterranean Sea tephrostratigraphy.

The complexity of the tectonic arrangement in this region also initiates subduction volcanism. The Golcuk volcano is found to the South of the Kula volcanic system and has, in contrast, produced several explosive eruptions over the past 200ka. Platevoet et al. (2008) produced a chronology which defines explosive, phretomagmatic eruptions at 206 ± 9.8ka , 173 ± 7.4ka, 72.7 ± 4.7ka and 53.5±2.7ka. These eruptions have produced tephriphonolitic products incuding dome growth and pyroclastic flows. This volcano is therefore here considered as a possible source of regional tephra layers in the Eastern Mediterranean Sea

3.7 Critical review of existing distal tephra records for the Mediterranean Sea, methods used and sites examined.

3.7.1 Introduction.

The most comprehensive review of distal Mediterranean marine tephrostratigraphy is currently that of Narcisi and Vezzoli (1999). Much work has been done however, since this paper was published. In particular the stratigraphy and the extent of specific tephras has been extended by the use of micro/crypto-tephra extraction techniques. It is convenient to report the current state of the tephra work in the Mediterranean by dividing it into areas. In this way it is possible to have some idea of how fruitful tephrostratigraphy could be when considering a particular region.

The initial stratigraphy, to which researchers owe the nomenclature attached to the Mediterranean marine tephra layers, was published by Keller et al. (1978). This paper defined 20 visible tephra layers from cores taken from the Ionian and Eastern Mediterranean Seas and labelled them according to the fauna defined “bio-zone” in which they were found, zone Z being the most recent and zones X,Y,W etc. being progressively

older. Thus individual tephra layers were labelled Z-1, Z-2, X-1, X-2, X-3 e.t.c. with the highest number indicating the oldest tephra layer in each bio-zone. This system was intuitive at the time, but cannot accommodate tephras subsequently found between these first defined layers. In addition, the system could be misleading if two near-simultaneous eruptions deposited tephra layers in geographically distinct places. If they are chemically similar, all near-synchronous tephras could be assigned the same name, if not found in the same core.

It is now customary to name tephra layers after the core and the depth in that core in which they were found (e.g. Bourne et al. 2010), and then assign them geochemically to another sample from the marine realm or preferably (if available) from a proximal location on land. The biostratigraphic labels of Keller et al. (1978) still abound in the literature however, as they provide the broad "master" stratigraphy of the most widespread eruptions, and have been widely employed.

3.7.2 The Tyrrhenian Sea and the Western Mediterranean.

The known tephrostratigraphy of the Tyrrhenian Sea consists exclusively of visible tephra layers. Paterne et al. (1986) identified 10 deposits listed in table 3.1 below, and identified the sources of 8 of these. Mollisso et al. (2010) identify an additional 8 Holocene tephras from the Bay of Naples and Salerno Bay, and Paterne et al. (2008) extend the Tyrrhenian sea record back to 200ka with a further 21 tephras, making the total discovered so far for the Tyrrhenian sea 39 tephra layers dating from the present day back to 200ka (table 3.1).

Name of ash layer	Date given in paper	Volcanic Event assigned in literature	Reference
tS1	AD 1745+/-80	AD 1822 eruption of Vesuvius	Mollisso et al. (2010)
tS1-α	AD 1690+/80	AD 1631 eruption of Vesuvius	Mollisso et al. (2010)
tS1-β		AD 787 or 685 eruption of Vesuvius	Mollisso et al. (2010)
tS1-γ	AD 542 +/-50	AD 685, or 512 eruption of Vesuvius	Mollisso et al. (2010)
tS2		AD 79 eruption of Vesuvius	Mollisso et al. (2010)
tS3	3300+/-100	Interplinian of Vesuvius	Mollisso et al. (2010)

tS3-α	3700+/-110	Interplinian of Vesuvius	Mollisso et al. (2010)
tS4	4350+/-90	Astroni- Campi Flegrei	Mollisso et al. (2010)
C-2	12.3 +/-0.3	Neapolitan Yellow Tuff (Phlegrean Fields)	Paterne et al. (1986)
E-2	12.97 +/-0.18	Pollara (Salina Island)	Paterne et al. (1986)
C-4	19.62 +/-0.27	Solchiaro (Procida Island)	Paterne et al. (1986)
C-9	Unknown		Paterne et al. (1986)
C-10 (Y-3 of Keller et al.1978)	33.5 +/-1.5	Campanian Ignimbrite (Phlegrean Fields)	Paterne et al. (1986)
C-11	33+/-1.8	Ciglio-Serrara (Ishia)	Paterne et al. (1986)
C-13 (Y-5 of Keller et al.1978)	40+/-2	Citara (Ischia)	Paterne et al. (1986)
C-16	51+/-2.2	Barano (Ischia)	Paterne et al. (1986)
C-17	55.4 +/-2.2	Epomeo (Ischia)	Paterne et al. (1986)
C-18	unknown	unknown	Paterne et al. (1986)
C-22 (X1 of Keller et al.1978?)	89.80-90.20ka	Campania	Paterne et al. (2008)
C-26	100.6-101ka	Ischia (35J in Poli et al.1987?)	Paterne et al. (2008)
C-27 (X-5 of Keller et al.1978?)	103.3-103.6ka	Campania	Paterne et al. (2008)
C-31 (X-6 of Keller et al.1978?	107.-107.95ka	Campania	Paterne et al. (2008)
C-36	123.2ka	Ischia/Roccamonfia?	Paterne et al. (2008)
C-39	134.6ka	Ischia/Roccamonfia?	Paterne et al. (2008)
C-41	144.1ka	Roman/Vesuvius?	Paterne et al. (2008)
C-42	148.4ka	Vico/Vulsini?	Paterne et al. (2008)
E-24	148.4ka	Eolian Islands	Paterne et al. (2008)
C-44	160.8ka	Ischia/Roccamonfia	Paterne et al. (2008)
C-48	174.5-176.7ka	Campania	Paterne et al. (2008)
C-50	181.5-181.7ka	Campania	Paterne et al. (2008)
C-51	183ka	Campania	Paterne et al. (2008)
C-52	185-189.4ka	Campania	Paterne et al. (2008)
C-53	189.2ka	Campania	Paterne et al. (2008)

C-54	192.4ka	Campania	Paterne et al. (2008)
C-55	193.4ka	Campania	Paterne et al. (2008)
C-56	196.4ka	Campania	Paterne et al. (2008)
P-15	197.4ka	Pantelleria	Paterne et al. (2008)
P-16	198.4ka	Pantelleria	Paterne et al. (2008)
C-57	202.8ka	Campania	Paterne et al. (2008)

Table 3.1 visible tephra deposits in the Tyrrhenian sea (from Paterne et al.1986, 2008 and Molisso et al.2010)

No crypto-tephra work has yet been published for the Tyrrhenian Sea so it is reasonable to assume (from evidence in other parts of the Mediterranean) that there may be even more eruptions represented as crypto-tephras. Given the large number of visible tephras identified in the marine cores of the Tyrrhenian Sea, it is not unreasonable to suppose that some of these tephras may have reached west of the islands of Sardinia and Corsica, and may be hidden as crypto-tephras in cores from that region. The selection of core ODP975 from just East of Menorca in this thesis tests this hypothesis and is the first crypto-tephra investigation to be undertaken from the a core sequence located in the Western Mediterranean Sea.

3.7.3 Ionian Sea

The Ionian Sea is where the tephrostratigraphy of Keller et al. (1978) was first defined. The stratigraphy in this area is best defined by Narcisi and Vezzoli (1999) who updated the Keller et al. (1978) stratigraphy. This is shown along with some additions reported in more recent papers in table2.3.

Tephra name	Age years BP	Volcanic event assigned in literature	Reference
Z-1	3360	Avellino-Vesuvius	Narcisi & Vezzoli (1999)
Y-1	15000	Biancavilla, Montalado Ignimbrite- Etna	Narcisi & Vezzoli (1999)
Y-3	25001	Campanian	Narcisi & Vezzoli (1999)
Y-5	35000	CAMPANIAN IGNIMBRITE	Narcisi & Vezzoli (1999)
Y-6	45000	Green Tuff (Green Ignimbrite)	Narcisi & Vezzoli (1999)

Y-7	50000	Campanian	Narcisi & Vezzoli (1999)
Y-8	55000	Aeolian Islands	Narcisi & Vezzoli (1999)
X-1	70000	Aeolian Islands	Narcisi & Vezzoli (1999)
X-2	70001	Campanian	Narcisi & Vezzoli (1999)
X-3	90000	Aeolian Islands	Narcisi & Vezzoli (1999)
X-4	90001	Etna	Narcisi & Vezzoli (1999)
X-5	105000	Campania	Narcisi & Vezzoli (1999)
X-6	110000	Campania	Narcisi & Vezzoli (1999)
C-35	121,500	Campania	Paterne et al. (2008)
P-11	130,600	Pantelleria	Paterne et al. (2008).
W-1	140,000	Roman	Narcisi & Vezzoli (1999)
P-12	163,600	Pantelleria	Paterne et al. (2008).
V-2	170,000	Roman	Narcisi & Vezzoli (1999)
E-25	171,000	Eolian Islands	Paterne et al. (2008).
C-49	175,800	Roman/Campanian?	Paterne et al. (2008).
P-13	192,500	Pantelleria	Paterne et al. (2008).
P14	192,500	Pantelleria	Paterne et al. (2008).

Table 3.2 Visible tephra layers found in the Ionian Sea.

Table 3.2 lists 22 principle known tephras that have been detected in the Ionian Sea sediments, although it should be noted that there are over 100 tephras which are chemically characterised from core sequences all over the central Mediterranean (Narcisi and Vezzoli 1999). Only the most widespread (either geographically or in the literature) and shown here.

3.7.4 Adriatic Sea.

The tephrostratigraphy of the Adriatic is best summarised by Bourne et al. (2010) and Calanchi et al. (1998). Several of the layers featured in this basin have been correlated by the authors to deposits in the Tyrrhenian Sea (see above) or on the mainland of Italy. The known stratigraphy is outlined in table 3.3 and includes crypto-tephra layers (Bourne et al.2010) as well as visible tephras (Calanchi et al.1998 and Bourne et al.2010).

Tephra name	Age BP from literature.	Volcanic event assigned in literature	Reference
PRAD 055	4690-4300	AMST	Bourne et al. (2010)
PRAD 120		Fondi di Baia	Bourne et al. (2010)
PRAD 203		Pomici Principali	Bourne et al. (2010)
PRAD 218	14320-13900	Neapolitan Yellow Tuff	Bourne et al. (2010)
Y-1	14.2	Biancavilla- Etna	Calanchi et al. (1999)
PRAD 268		unknown	Bourne et al. (2010)
PRAD 324		Campania	Bourne et al. (2010)
PRAD 404		Campania	Bourne et al. (2010)
PRAD 480		unknown	Bourne et al. (2010)
PRAD 650		Lago Amendolare	Bourne et al. (2010)
PRAD 784	19396-19020	Greenish	Bourne et al. (2010)
PRAD 845		unknown	Bourne et al. (2010)
PRAD 875	22240-21150	Pomici di Base	Bourne et al. (2010)
PRAD 1100		Faro di Punta Imperatore	Bourne et al. (2010)
PRAD 1332	30300+/-200	Y-3 Campania	Bourne et al. (2010)
PRAD 1494		Codola (Base)	Bourne et al. (2010)
PRAD 1653	39280+/-110	Campanian Ignimbrite	Bourne et al. (2010)
C-14	41.8	Unknown Campania	Calanchi et al. (1998)
PRAD 1752		SMP-1a	Bourne et al. (2010)
PRAD 1870	56000+/-4000	Monte Epomeo Green Tuff Y-7	Bourne et al. (2010)
PRAD 2040		Pignatiello Formation	Bourne et al. (2010)
C-20	67.5	Unknown Campania	Calanchi et al. (1998)
PRAD 2375		unknown	Bourne et al. (2010)
PRAD 2517	105000+/-2000	X-5	Bourne et al. (2010)

Table 3.3 The Adriatic Sea tephrostratigraphy compiled from Bourne et al. (2010) and Calanchi et al. (1998).

3.7.5 The Aegean Sea and Far Eastern Mediterranean.

The tephra record of the Aegean Sea has been significantly understudied in comparison to those of the Ionian, Adriatic and Tyrrhenian Seas. This may be because there are fewer volcanoes active in the Quaternary in the Aegean region than in the seas surrounding Italy.

The current tephrostratigraphy reported in the literature is limited to visible layers and is best summarised in the composite stratigraphy of Aksu et al. (2008) in which data from 12 marine cores are synthesised into a single record spanning approximately 0-70ka. This stratigraphy is extended by Aksu et al. (2008) using the work of Hardiman (1999) and Pe-Piper and Piper (2002) to include several tephra layers dating back to approximately 161ka, and by Hamann et al. (2010) who found a rhyolitic tephra layer thought to originate from Turkey, and chronologically associated with Holocene sapropel S1. The integrated tephrostratigraphy of 16 tephra layers derived from these reported records is shown in table 3.4.

Tephra name	Age estimate BP from literature.	Volcanic event assigned in literature	Reference
Z-2	3000	Minoan- Santorini	Asku et al. (2008)
S1 tephra	9600-6500	Dikkartin-Erciyes Dag	Hamann et al. (2010)
Y-2	20000	Cape Riva- Santorini	Asku et al. (2008)
Unknown Santorini tephra	>20000	Unknown Santorini	Vinci (1985).
Kal	?	Kalogeri	Asku et al. (2008)
Y-4	30000	? Santorini	Asku et al. (2008)
Yali	30000	Yali-2 Yali	Asku et al. (2008)
Y-5	35000	Campanian Ignimbrite Campania	Asku et al. (2008)
Nisyros	41000-44000	? Nisyros	Asku et al. (2008) and Hardiman et al. (1999)
X-1	70000	?	Asku et al. (2008)
W-1	140000		Pe-Piper and Piper (2002) in Asku et al. (2008)
W-2	150000	Middle Pumice- Santorni	Pe-Piper and Piper (2002) in Asku et al. (2008)

W-3	160000	Kos Plateau Tuff	Pe-Piper and Piper (2002) in Asku et al. (2008)
V-1	170000	Santorini	Pe-Piper and Piper (2002) in Asku et al. (2008)
V zone rhyolite	170000	?	Pe-Piper and Piper (2002) in Asku et al. (2008)
V-3	180000	Hellenic	Pe-Piper and Piper (2002) in Asku et al. (2008)

Table 3.4 Compiled tephrostratigraphy for the Aegean Sea, for the last ~180ka.

3.7.6. Methods of tephra identification and dating.

The tephrostratigraphies described above have in the main been constructed only from visible tephra layers with the exception of the Adriatic Sea (Bourne et al. 2010). Occasionally researchers use data obtained from down-core logging techniques, such as magnetic susceptibility or XRF core-scanning to aid identification of very fine tephra layers. Bourne et al. (2010-figure 15) show that a number of significant tephras can evade detection by these logging techniques and that tephrostratigraphies can be significantly augmented when using crypto-tephra extraction techniques (reviewed in Lowe 2011 and exemplified by Lane et al. 2011, Bourne et al.2010). This method also extends the geographical range of the some tephra isochrons which can be used for the direct comparison of the timings of events within these diverse records (within the chronological resolution of the sampling intervals).

Furthermore, the chemical characterisation of tephra layers has usually been based only on the major elements, using wavelength dispersive, or energy dispersive electron microprobe techniques. These techniques generally derive the concentrations of 9-11 elements to discriminate tephras from one another and to define their origins. In volcanically profuse regions however, discriminating between the different eruptions can be very difficult using only these elements (Pearce et al. 2007). Clift and Blusztajn (1999) and Asku et al. (2008) have shown that trace element abundance data can easily discriminate between sources of similar major element chemistry. Given also that trace element analyses can yield a further 20 to 22 elements to add to the 9 to 11 quantified from the major element analyses, this

technique also gives much more scope to discriminate different eruptions originating from a single source (e.g. Tomlinson et al.2010).

In light of these developments, trace element analyses will be used in this study to help determine the source region for individual distal tephra layers in this study. Then the data are considered in the context of the proximal eruptive stratigraphy from the source region. This will define the specific eruption represented in the marine core.

Also in this study, where possible, independent dates for distal ashes are imported from the proximal volcanic stratigraphies into the marine records to test and improve age models. Until recently many studies have used the orbital tuning of the marine proxy records to estimate dates of the tephra layers. While his practice may provide a broad scale age control for the tephra layers, it ignores the principle that all tephra deposits from a single eruption must form an isochron, and can result in the same tephra being assigned different dates in different records. For example, the Y-1 tephra from Etna is assigned an age of 15ka by Keller et al. (1987) and 14.2ka in Calanchi et al. (1999). These differences probably reflect the inherent uncertainties in the orbital tuning method (which are currently unquantifiable) but the implied diachronic deposition of tephra violates the fundamental principle of tephrostratigraphy. It is the stratigraphic changes in the proxy records that could be diachronous over a wide geographical area, not the volcanic eruption and its deposits.

Tephra layers are still very powerful as a correlation tools even if they have no proximal correlative and no date attached to them. If found and matched in several records, they allow the relative timings of events in those records to be determined. Subtle differences in the timings of palaeoclimatic or paleaoceanographic events from core to core could therefore be resolved by the careful use of tephrostraigraphy. It can be especially important where other dating or correlation methods fail to resolve the sequence of events due either to large dating uncertainties, or lack of independence from tuning procedures that assume correlation between two events. This thesis aims to derive correlation and age determinations that are truly independent of such assumptions and that are based on reliable procedures for establishing the chemistry and origin of individual tephra deposit.

Chapter 4- Core/ site selection and background.

4.1 Core Selection Rationale

Three core sequences were selected for tephrostratigraphical investigation. These were selected with a compromise between 1) oceanographic relevance, 2) archaeological relevance and 3) potential to contain tephra. The cores chosen would, by compromising geographical spread with an intuitive assessment of their potential to preserve tephra, allow all of the aims detailed in chapter 1.2 to be addressed. The following section describes briefly the research histories of the selected cores, thereby elucidating the respective rationales for their inclusion in this investigation.

Core name	Date extracted	Chief Scientist	Location	Water Depth	Core Stored at……..
LC21	1994	Guy Rothwell	South East Aegean (35°40'N, 26°35'E)	1522m	BOSCORF- Southampton
ODP 975	1995	Maria Comas & Rainer Zahn	South Balearic Margin (38°54'N, 43°1'E)	2415m	BCR- Bremen.
ODP 967	1995	K-C. Emeis, Robertson.A.H.F. Richter.C.	South of Cyprus (34°04'N, 32°43'E)	2687.1m	BCR- Bremen.

Table 4.1 Cores selected for inclusion in this thesis. A literature review and a rationale for each are provided in the text.

These cores constitute an east-west transect across the Mediterranean Sea. Each core is in a position at which a reliable chronology (based on tephra layers) would be critical to addressing some of the specific questions of work package 5 (marine stratigraphies) of the RESET consortium project (see chapter 1.1). All the cores were thought to extend from the present day to at least 150ka, the period of time of interest to the RESET consortium. This information is based almost entirely on orbital tuning, average sedimentation rates and isotope stratigraphies, with few independent radiometric dates available to test these chronologies. The broad core location rationale was to select key Mediterranean sites of importance to palaeoceanography which also had the potential to yield tephra layers.

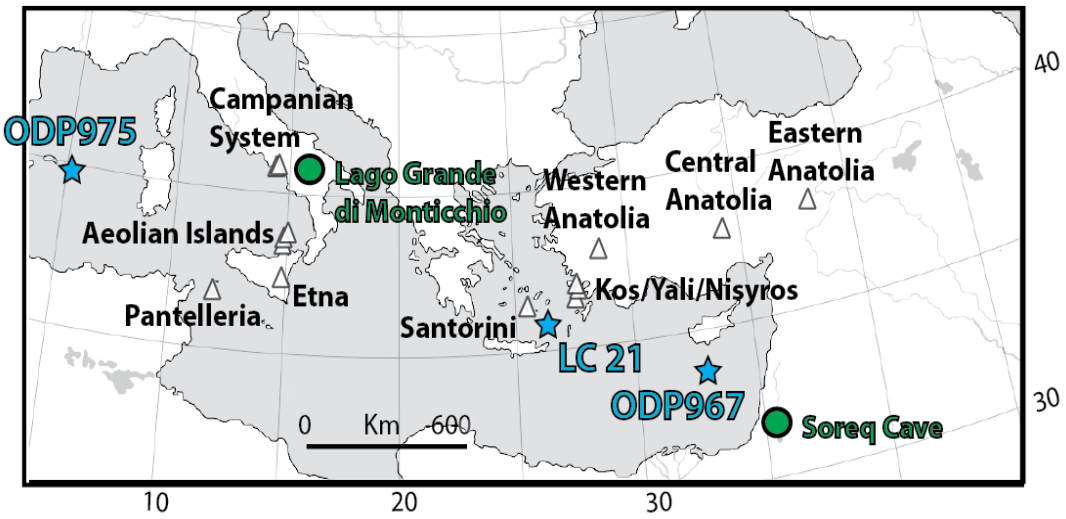

Figure 4.1 Map showing the 3 marine cores included in this study: ODP975, LC21 and ODP967, together with the location of all the volcanic regions referred to in the text and the location of the Lago Grande di Monticchio lake environmental record from which 4 samples analysed in this thesis were taken. Also shown is the location of the Soreq Cave speleothem record which is also referred to in the text. NB: scale bar is only approximate, as the map is not an equal area projection.

4.2- Core ODP975 – Western Mediterranean- Balearic Basin.

4.2.1- Location and previous work

This core is situated in the Western Mediterranean Sea in the Balearic Sea (fig. 4.1). It thus represents the most western extent of the geographical region relevant to aim 1 of this thesis which is to contribute to an assessment of the geographical extent of tephra in the Mediterranean Sea marine sediments and to establish broadly where in the Mediterranean Sea detailed tephra investigations (including crypto-tephra) might be most fruitful. The site was initially selected by the Ocean Drilling Project (ODP) by virtue of its position in a small sub-basin on the Menorca Rise which is conducive to preserving ponded sediments relatively free of turbidites (Comas et al.1996). It is perfectly positioned to record both the flow of Atlantic water into the Mediterranean Sea, and Mediterranean water out into the Atlantic. Variations in these two parameters initiate changes in the circulatory regime of the Mediterranean Sea (Cacho et al. 2000).

ODP975 is also relevant archaeologically too. The RESET consortium has investigated many archaeological records in Northwest Africa and Southwest Europe which would benefit from a comparison with relevant climatic record (fig. 1.1, and online at http://c14.arch.ox.ac.uk/reset/embed.php?File). Indeed, the core has already been used for this purpose by Jimenez-Espejo et al. (2007). They have concluded from the study of

multiple proxies and an age model based on ^{14}C and graphical correlation to a nearby, well dated marine core in the Alboran Sea, that Neanderthals inhabited Southern Iberia only during humid periods. This kind of study relies very heavily on the accurate chronological correlation of two or more records of different types. Such correlations could be tested by tephra horizons, if at least one was common to all of the records, while age models for each record might be improved if any tephra layer was found within them. Finding tephra in this region would help to reduce the uncertainties inherent in ^{14}C or orbitally-tuned chronologies.

The core isotope stratigraphy is shown for the top 18m of the core (approximately the last 200ka according to the age model of de Kaenel et al. 1999) in figure 4.2.

4.2.2- Core lithostratigraphy and existing proxy records.

The stratigraphy of ODP975 is composed of nannofossil ooze, calcareous or nannofossil clay and silty clay, and organic sapropel layers (Comas et al. 1996). The sedimentation rate for the Holocene and Pleistocene part of the core is estimated to be about 68.28 m/Ma or ~146 years/cm (Alvares –Marron, 1999). The high sedimentation rate and the presence of sapropels in this Western Mediterranean core, make it an excellent core for high-resolution paleaoceanographic research.

The core contains sapropels. The formation of these organic deposits is thought to be well understood in the Eastern Mediterranean, but less well studied in the West. Sapropels are thought to have formed as a result of either bottom water stagnation, or high levels of surface organic productivity (Rohling and Thunnell 1999), although some studies indicate that the mechanisms for their formation may be different in the West than in the East (e.g. Weldeab et al.2003). If the same tephras could be found in both Eastern and Western Mediterranean marine sediments the relative timings of the sapropel events in both regions could, for the first time, be directly assessed. This would allow hypotheses about their consanguinity (or otherwise) to be addressed. The same concept could also be applied to any of the other oceanographic proxies and their associated phenomena, circumventing the problems associated with ^{14}C (e.g. unknown marine reservoir effects or the commonly employed oceanographic method of dating by orbital tuning, or 'wiggle-matching' to another core. Doose et al. (1999) state that while sapropels in both the east and the west of the Mediterranean appear to occur during warm, wet periods, the question of single or different controls on the proxy records of the Eastern and Western Mediterranean Sea is

not yet resolved. The variation in the parameters used in the orbital tuning dating process is too great to assess the synchronicity or otherwise of anoxic conditions in the different basins.

During the tenure of this PhD studentship, K.M. Grant at the National Oceanography Centre, Southampton produced a bulk foraminifera isotope stratigraphy for both $\delta^{18}O$ and $\delta^{13}C$. This is shown in figure 4.2 together with the FeO and CaO data derived from XRF core scanning (generated by the author and J. Stanford- University of Southampton, using the XRF core scanner of the MARUM centre, University of Bremen, Germany). These datasets are the only contiguously sampled, high resolution proxy work yet undertaken on core ODP975. Other studies address the whole core at very low resolution.

Gonzalez-Donoso et al. (2000) produced a planktonic fauna-stratigraphy for ODP975 and for core ODP976 located in the Alboran Sea. Their study implied that there are leads and lags between the seasonality evident in the fauna records of the two sites and the insolation signal, but that these could not be quantified. An independent chronological method is needed to test this hypothesis and tephrostratigraphy may be able to fulfil this role. Similarly Haywood et al. (2009) also completed a study of the benthic foraminifera fauna in ODP975 (for the entire core to ~5Ma) and other western Mediterranean marine cores. They concluded that the re-colonisation of benthic species following an extinction event (such as the Messinian Salinity Crisis or an anoxic event) is geographically sporadic and thus a-synchronous. Such differences in the timing of events could perhaps also be quantified using tephrochronology.

Magneto-stratigraphic, micro-fauna data and total organic carbon (TOC) and sulphur content data have been presented by Capotondi and Vigliotti (1999) for core ODP975. Using these data they identified the sapropels which are such visually prominent features of the eastern Mediterranean sediments in western Mediterranean sediments. This conclusion is corroborated by the work of Murat (1999) who also produced a TOC record and a comparison to the stratigraphy of the Eastern Mediterranean. Capotondi and Vigliotti (1999) also note the presence of rapid cooling episodes in the micro-fauna of ODP975. They suggest that these events may correspond to the Heinrich layers which are so prominent in North Atlantic sediments. This hypothesis is also proposed by Cacho et al. (2001,2002) for cores from the Alboran Sea, and could be tested should ODP975 contain tephra layers that are also found in a North Atlantic marine core.

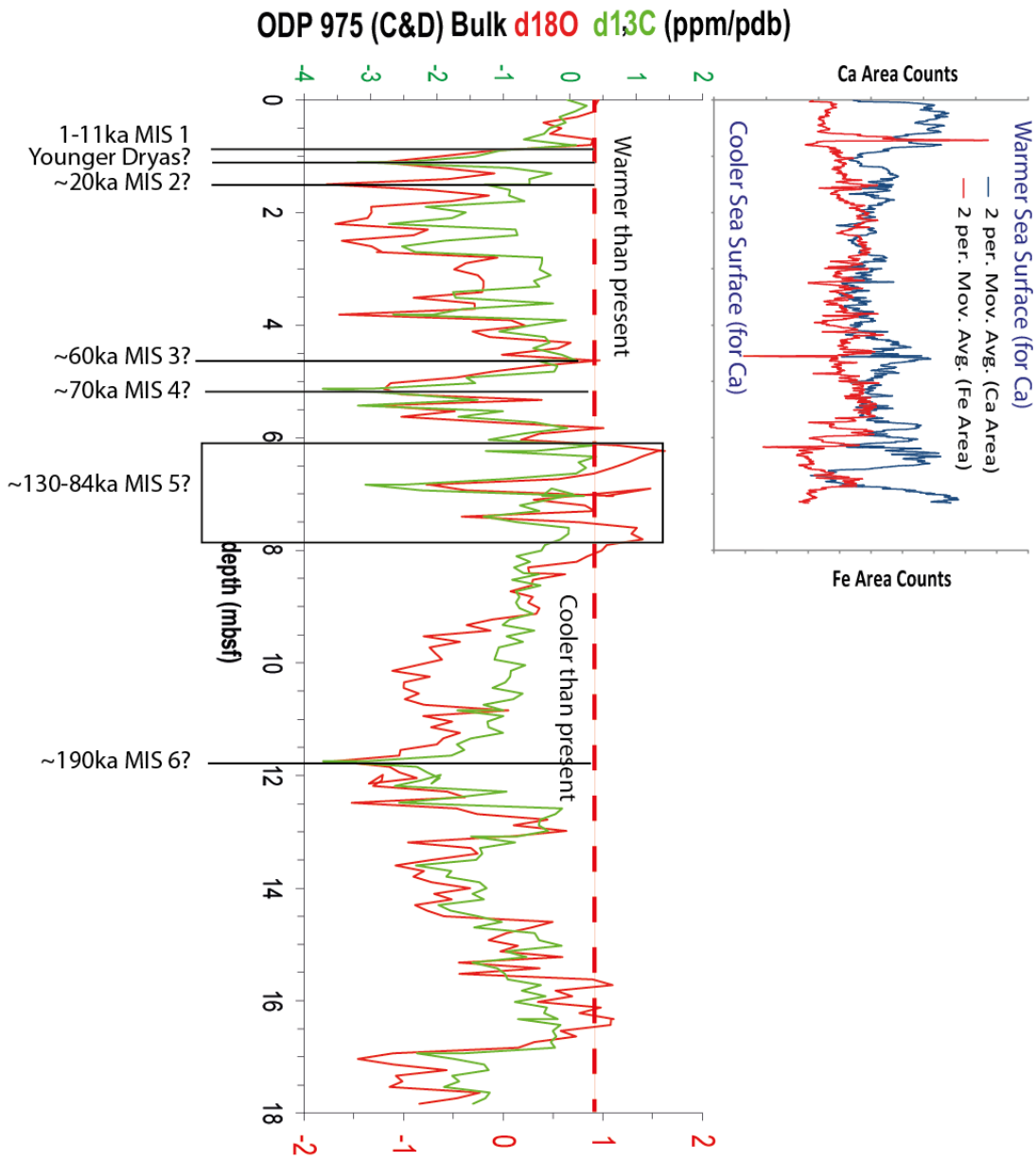

Figure 4.2- the stable isotope stratigraphy of core ODP975- showing the bulk $\delta^{18}O$ from foraminfera for the top 18m of the core, and the FeO and CaO counts from scanning XRF. The Ca values to the right indicate warmer sea surface temperatures for the top 8m of the core. The estimated chronology of the isotope stratigraphy is shown on the left and related to the Marine Isotope Stages. This estimated chronology is created from visual alignment only with approximate dates of the Global Marine Isotope Stages (MIS) derived from Thompson and Goldstein (2006).

4.2.3- Age models for ODP975.

Two age models proposed for ODP975 Pierre et al. 1999) have been constructed by orbitally tuning of both the sapropel layers within the sequence (de Kaenel et al. 1999) and the principle $\delta^{18}O$ variations (Pierre et al. 1999). These two models are shown in figure 4.3

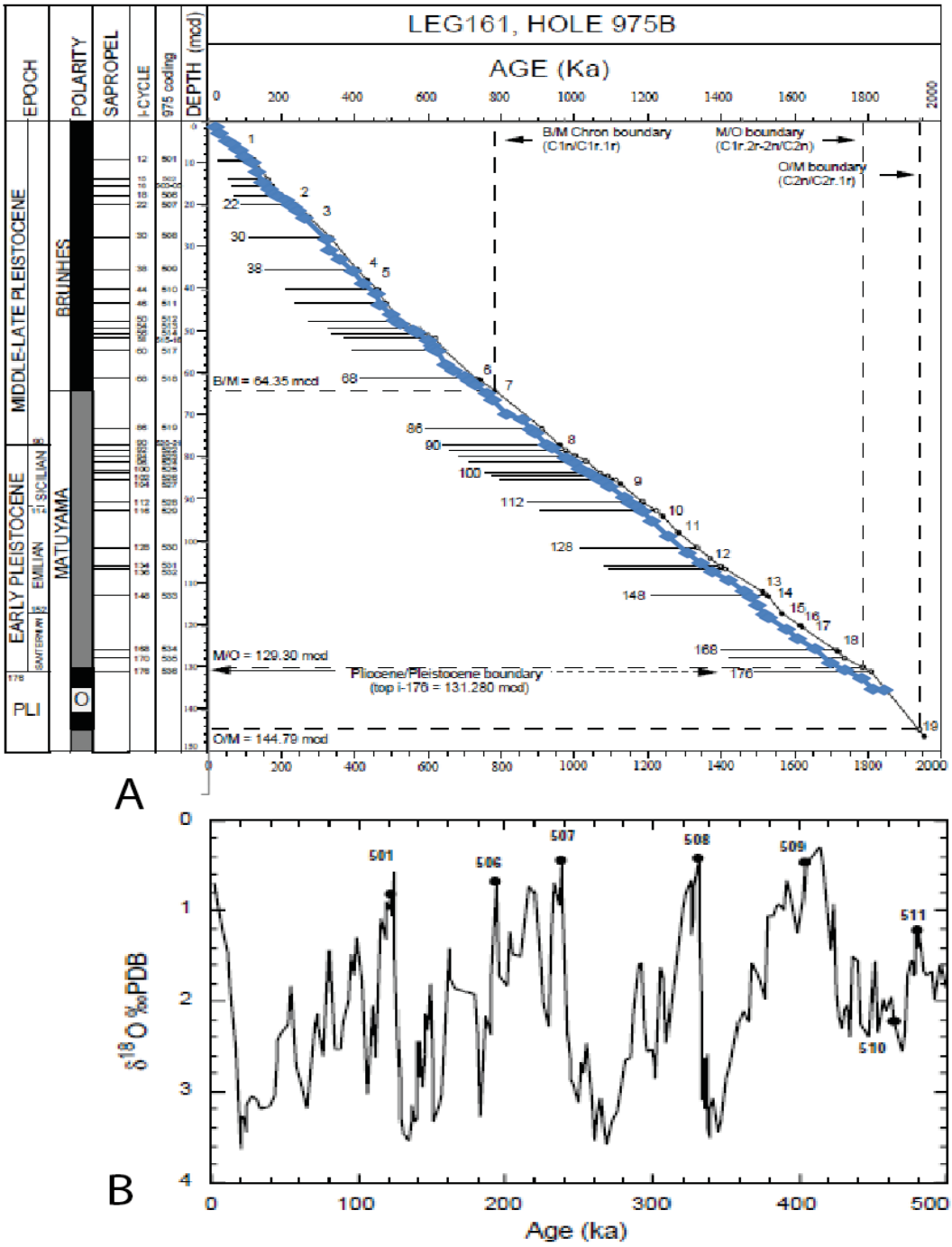

Figure 4.3 A) Age vs depth model for ODP975 based on orbital tuning of the sapropel stratigraphy (black spots and lines- de Kaenel et al. 1999) and an age vs depth model based on orbital tuning of the isotope stratigraphy (blue spots and lines- Pierre et al. 1999), for the top 145m of the core (~2Ma). B) the orbitally tuned isotope stratigraphy for the last 500ka for ODP975 (Pierre et al. 1999).

Both of these age models are tuned to an insolation record defined by orbital parameters. This precludes an independent chronological comparison of the proxy record to the orbital forcing mechanisms of eccentricity, obliquity and precession. The two age models are indistinguishable for the top 18m of the core (the section studied in this thesis) where the ages differ by less than 1%. This similarity is likely to occur because of similar assumptions

and parameters used to make both models. It is hoped that any tephra layers found by this investigation could test these two age models and their assumptions and possibly link this western Mediterranean core to cores ODP967 or LC21 in the east. Even if there were no tephras common to both the Eastern and Western Mediterranean, the tephras could in theory be able to date sediment much older than the ~50ka limit of radiocarbon dating. The resultant, independently derived, chronologies could then still be justifiably compared.

4.2.4. Potential sources of tephra shards which may be found in ODP975.

While there are no visible tephra layers in ODP975, there here are several potential sources for tephra which might be preserved as crypto-tephra layers. Possible Italian sources for the tephra layers include the Campanian system, the Aeolian Islands and Pantelleria has been found extensively in the Tyrrhenian Sea, as visible layers (Munno and Petrosino 2004, Molisso et al.2010 and Paterne et al.1986). Core ODP975 is located ~800km from the Campanian and Pantelleria volcanic systems and ~750km from the Aeolian Islands. It is not unreasonable to suppose that ash from these eruptive centres could reach this core and be preserved as a crypto-tephra. Other possible sources are located further away but are upwind of the core. The Azores have been active during the past 100ka (Moore 1991) but are located 2600km to the west of ODP967, in the Atlantic Ocean. Tephra shards may reach ODP975 but likely only in very small quantities. The same is true for the Canary Islands which have also produced many explosive eruptions within the last 100ka (Carracedo et al.1998), and are ~2,250km away.

Volcanism has also occurred closer to the core. The Massif Central in France is located ~725km away from ODP975. The region has been abundantly active during the late Pleistocene and Holocene (Juvigne 1992). The Eiffel district of Germany also produced a widespread tephra: the Laacher See tephra at approximately 13ka (Schminke et al.1999). This tephra is found throughout Central Europe (Schminke et al.1999).

Finally, Iceland has produced several large eruptions, which are demonstrably preserved in European post-glacial sediments (e.g. Lane et al. 2011). Modern eruptions in recent years have shown that Icelandic tephra can reach southern Europe (Davies et al. (2010) while Lane et al. (2011) have shown that Icelandic ash can be preserved, and identified, in stratigraphic sequences in Southern Europe and geochemically characterised. At ~3000km

distance from the source, if tephra from Iceland were found in ODP975, it would be the furthest recorded occurrence so far.

This site will thus be used to ascertain the potential for crypto-tephra studies in the Western Mediterranean in accordance with aim 1 of this thesis. If tephra were to be found in the core it could allow correlation of the Western Mediterranean sea proxies with the Atlantic sediments, or the sediments of the Eastern Mediterranean Sea. For the former this is important to explore the expression of Atlantic Heinrich events in the Mediterraean Sea (Cacho et al.2002) and for the latter it would allow the sapropel layers to be chronologically related across the basin.

4.3 Core LC21 - South East Aegean Sea

4.3.1- Location and previous work.

Core LC21 was collected by the RV Marion Dufresne in 1995 for the EC-MAST2 PALAEO-FLUX program and was located at 35°40'N,26°35'E at a present day water depth of 1522m. The core was selected for this investigation because of its oceanographic importance (as described above) and its proximity to the important archaeological sites of the Aegean region (fig 4.1). The most important consideration in the selection of this core was however, its position close to several of the major volcanic centres of the Hellenic arc (fig 4.2), offering the possibility of finding tephra layers and hence augmenting the tephrostratigraphy for the Eastern Mediterranean. The enlargement of such a stratigraphy for the past 150ka or so is the second aim of this thesis.

Most studies on LC21 to date have not included tephra in their chronological framework, although there are visible tephra layers in the core. Casford et al. (2002) used a ^{14}C AMS dating to conclude that there is a lag between Aegean sapropel formation and stratification of the water column. In a study of Mediterranean wide planktonic foram faunas spanning the last glacial cycle (including LC21), Hayes et al. (1999) also concluded that biostratigraphy should not be used as a correlation tool over large regions. There are significant environmental gradients in the Mediterranean which induce spatial variation in marine ecologies. Marino et al. (2007) also concluded, through an investigation of S5 in LC21 that the formation of anoxic bottom waters (an inducing condition for sapropels) is probably not synchronous across the whole of the Mediterranean Sea. They concluded, through a comparison with Eastern Mediterranean core ODP971A, that the Aegean Sea is a

driver of circulation and ecological changes in the Eastern Mediterranean, leading by 300+/-120 years with a chronology based on orbital tuning. Such hypotheses could be tested using tephrostratigraphy. Clearly, as synchronous and regional stratigraphic markers, tephras have an important role to play in Mediterranean palaeoceanography.

Rohling et al. (2002b) attempted to match LC21 with the GISP2 Greenland ice core and thereby infer a link between the sea surface temperature of the Aegean and the climate of Greenland. They attempted to link the records using a combination of ^{14}C and the GISP2 chronology. It was thought that some tephra shards and a peak in sulphur in the ice core could originate from the Minoan eruption of Santorini (Zielinski and Germani 1998), but the shards were subsequently re-attributed to a late Holocene eruption from Alaska (Pierce et al.2004) which indicates importantly, that Santorini tephras are unlikely to be found in the Greenland ice-core record.

RESET is investigating a very important archaeological site in Northeast Africa (see fig. 4.1) called Haua Fteah. This site is famous for its long record of Neanderthal and Modern Human occupation, and thus is highly relevant to the central principle of the consortium: to assess the relationship between these species and climatic impacts. It is located ~450km southwest of LC21 and so the core will provide a relevant oceanographic proxy record for correlation to this site.

4.3.2- Core lithostratigraphy and existing proxy records.

The sequence in LC21 is composed of hemi-pelagic sediment, organic-rich sapropel layers and visible tephra layers and has been a fulcrum of palaeoceanographic research in the Eastern Mediterranean since it was collected in 1995. Studies have in general focused on the Holocene Sapropel S1 and the Eemian Sapropel S5. S1 is the most amenable to precise ^{14}C dating while S5 has been inferred to represent an insolation maximum and concomitant phase of strong African monsoon (Bar-Matthews et al.2000, Rohling et al.2002a).

The core material (fig. 4.3) comprises hemipelagic nannofossil ooze with four sapropel layers and nine visible tephra layers and the average sedimentation rate is estimated by Casford et al. (2007) to be ~21cm/ka (1cm ~47years). This high sedimentation rate makes the core ideal for the construction of both proxy records and tephrostratigraphy.

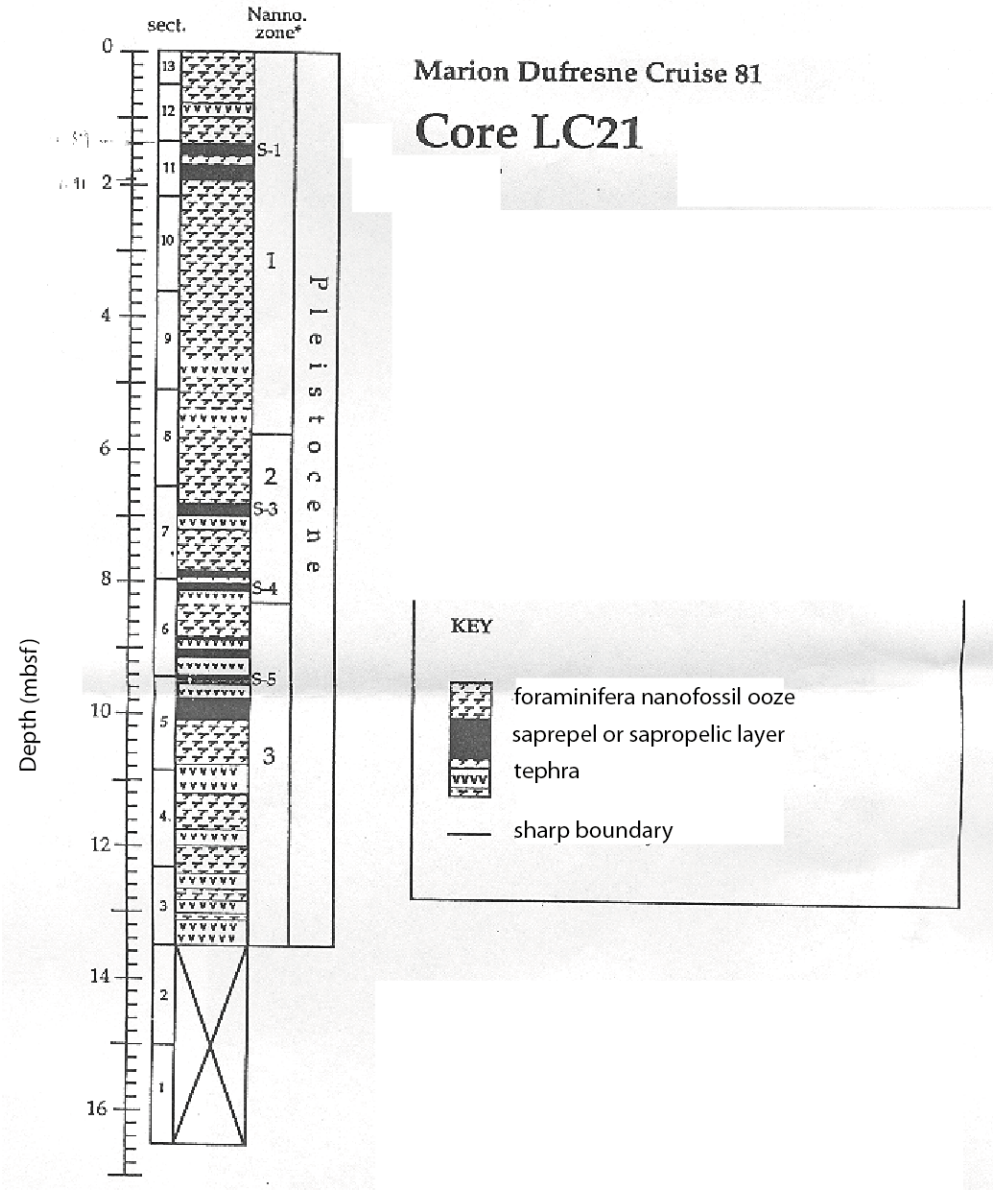

Figure 4.4 litho-stratigraphy for LC21 from on-ship initial report.

4.3.3- Age models for LC21

The most complete age model for the LC21 sequence is constructed from a high-resolution planktonic foraminiferal (*Globigerinoides ruber*) δ18O record from core LC21 ("δ18O ruber") (Grant et al. 2012), which has been correlated to the extensively U series dated Soreq Cave (Bar-Matthews et al. 2000, 2003) speleothem $\delta^{18}O$ record. The strong signal similarity between these records reflects their common source water and permits their visual synchronisation, and this in turn allows a robust, radiometric chronology to be transferred to core LC21 (Grant et al. 2012). Two additional, robust chronostratigraphic markers are provided by the conclusive identification of the Minoan (Rohling et al. 2002b,

Marino et al. 2009) and the Campanian Ignimbrite (CI) tephra layers (this study and Lowe et al. 2012) tephra horizons in core LC21. The precision of this LC21 age model is further improved by the application of a Bayesian depositional model to the LC21 chronostratigraphy (Grant et al. 2012) using the OxCal software (Bronk Ramsey. 2008). A significant advantage of this approach is that it yields a modelled chronological uncertainty for every tie-point. The age model is also in very good agreement with existing, independent radiocarbon dates from Casford et al. (2007).

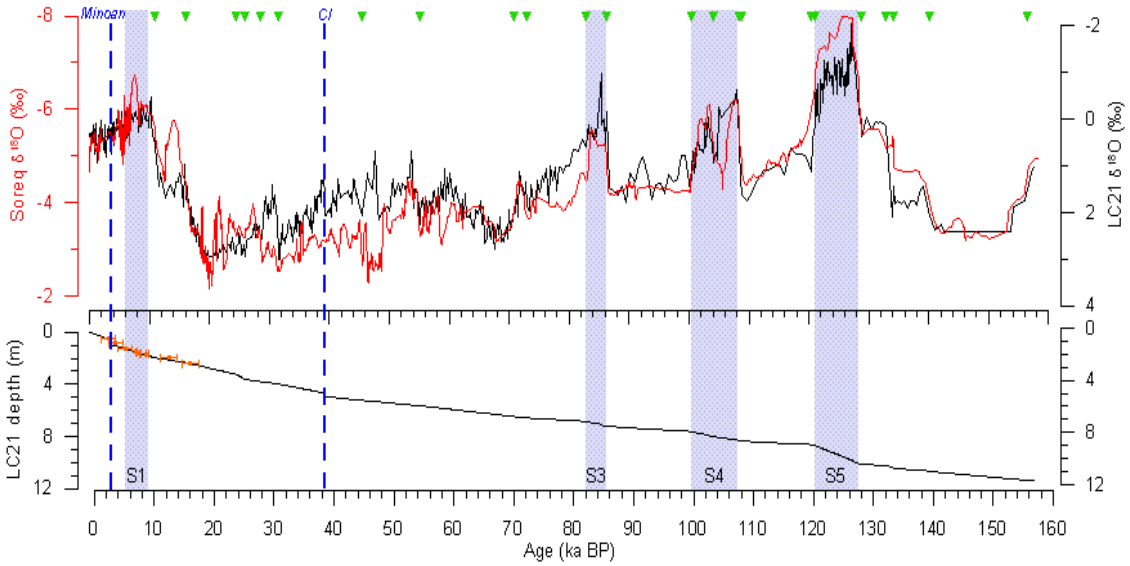

Figure 4.5 The LC21 full core isotope stratigraphy (top panel) and age model (bottom panel). The age model has been created by Grant et al. (2012) through the correlation of the LC21 $\delta^{18}O$ stratigraphy to that of Soreq Cave speleothem in Israel (fig. 4.1) through tie points (green triangles) and by the identification of the Campanian Ignimbrite and Minoan tephra layers (dashed blue vertical lines). These attributions are discussed and demonstrated in the results and discussions section of this thesis. The age model is corroborated with the ^{14}C dates of Casford et al. (2007) which are shown by the red points in the lower panel.

Other age models exist for discrete sections of the core. Casford et al. (2007) created a composite age model for the Eastern Mediterranean Sea based on the ^{14}C dates shown in figure 4.5 and ^{14}C dates from other cores in the region. The model was generated for the last 17ka only and is shown in figure 4.6.

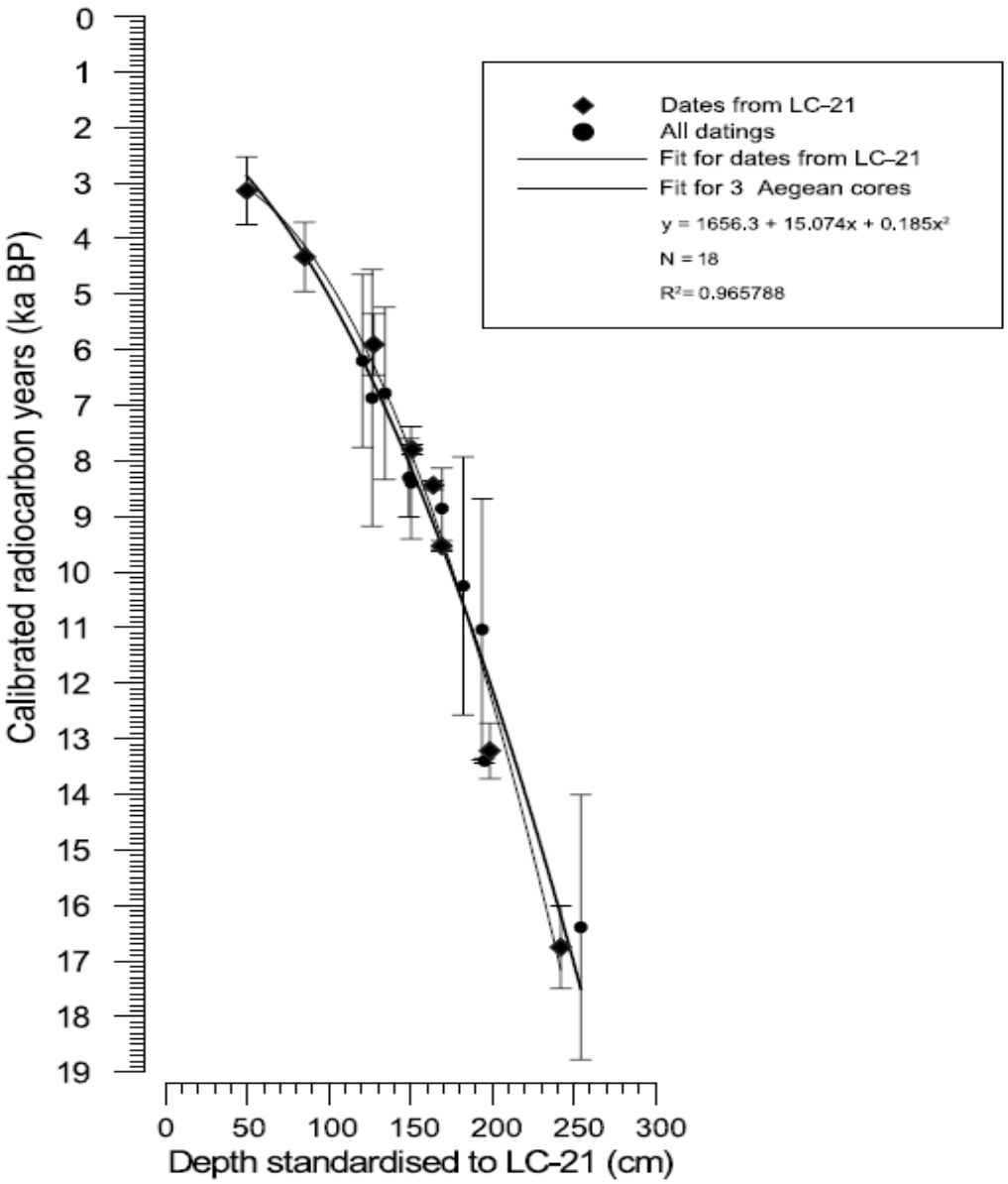

Figure 4.6 Composite age vs depth model for LC21 for the last ~17ka, using ^{14}C dates from the core and other eastern Mediterranean cores (from Casford et al. 2007)

These age models could both be tested with any tephra layers, with radiometric dates associated with them, which may be found in LC21.

4.3.4- Potential Sources of tephra for LC21.

The volcanic sources closest to and therefore most likely to contribute to an eastern Mediterranean tephrostratigraphy are the island of Santorini and the Kos/Yali/Nisyros volcanic system (fig. 4.1). Both these sources have been active, and generating Plinian eruptions within the last 200ka (see sections 3.1 and 3.3), and can therefore be expected to form the backbone of a new tephrostratigraphy for the Eastern Mediterranean. The Bronze

age Minoan eruption of Santorini has been identified previously in LC21 (Rohling et al. 2002).

Other potential sources of tephra include the Campanian System in Italy (~1150km to the west, thesis section 3.2), the Anatolian system in Turkey (~450km to the east, section. 3.6), the Island of Pantelleria in the Straits of Sicily (~1200km to the west, section 3.4) and the Aeolian Islands of Italy (~1500km to the west, section 3.5). The Campanian Ignimbrite tephra layer has already been identified in LC21 (Lowe et al. 2012).

4.4 Core ODP967- Far Eastern Mediterranean

4.4.1- Location and previous work

ODP967 is located approximately 60km south of Cyprus. This core was taken on ODP leg 160 primarily to address questions relating to the tectonics of the Eastern Mediterranean, where the Eratosthenes Seamount impinges on the crust underlying Cyprus (Emeis et al. 1996). As a result, the sequence is long enough to extend into the Late Cretaceous. It is the top 10m or so (fig. 4.4) of this ~140m core which are investigated in this study. The core is also in a perfect position to record the relationship between freshwater input into the Mediterranean Sea via the Nile, and the formation (or otherwise) of high salinity, Eastern Mediterranean deep water. It is this relationship which is thought to control the development of the organic-rich sapropel layers in the sediment, at least in the Eastern Mediterranean (Rohling et al.1999). Morigi et al. (2009) used the core as an Eastern Mediterranean type-site sequence to investigate the spatial variation of bottom water ventilation during the deposition of the Eemian sapropel S5. Their conclusion, that the oxygen content is dependent on the basin type and depth, could be tested using the synchronisation of ODP967 with a core from another basin (such as LC21), via tephrostratigraphy.

The core also contains a record of dust supply (haematite content) into the Mediterranean Sea, from Northeast Africa and thus, by inference, a record of aridity in this region (Larrasoana et al. 2003). This record was used by Trauth et al. (2009) to deduce that major changes in the evolution of North African mammals (including hominins) occurred during wetter periods, in step with the insolation maxima in the low latitudes. Herein lies the connection of this marine core to the archaeological component of the RESET consortium. The Levant is thought to be a key corridor for the migration of hominins from Africa into

Europe (Frumkin et al. 2011). ODP967 is located only ~200km from the Levant coastline (fig. 4.1) and thus can provide a highly relevant and high resolution proxy record for this region.

The core has also been used to assess the relationship of vegetation to hydrological changes in the Mediterranean region. Joannin et al. (2008) investigated the early Pleistocene of ODP967, to compare the vegetation record of Southeast Italy to the prevailing hydrological conditions of the day. They concluded that the wetness of the region was driven by the earth's precession and that it dictated the vegetation signal evident in the pollen records. Menzel et al. (2004) concluded from their study of alkanes in several Eastern Mediterranean marine cores (including ODP967) that the circum-Mediterranean landscape had much more vegetation during the wet periods associated with sapropel deposition. These studies are forced to use orbital tuning methods to constrain their chronologies as they are beyond the time range of radiocarbon dating. This approach appears to work well, but has the drawback of assuming particular forcing factors for particular events, and assuming absolute synchronicity of the signal from one site to the next. The latter assumption precludes the discovery of subtle leads and lags in different sites. If present, these could be discerned by using the known synchronous deposition of tephra layers.

Core ODP967 therefore represents a good compromise between archaeological relevance, oceanographic/climatic importance and proximity to major volcanic regions. Those volcanic regions (most likely to contribute tephra) are Santorini and Kos/Yali/Nisyros, the Campanian region, the Aeolian Islands, Pantelleria, and the Anatolian province of Turkey. Indeed Wulf et al. (2002) have already identified the Cape Riva tephra from Santorini in ODP967. An early Holocene Turkish tephra was identified in a marine core close to the coast of Israel (Hamann et al. 2010), indicating that Turkish tephra may also be found in ODP967. The known range of the Campanian Ignimbrite also covers the location of the core (Pyle et al. 2006). This core could be the first location in the Mediterranean to record eruptions from the Hellenic Arc, Italy and Turkey.

4.4.2- Core lithostratigraphy and existing proxy records

The core photographs for core ODP967 are shown in figure 4.4. The site comprises six bore holes (four of which are used here), each divided into sections, and thus site ODP967 is a composite stratigraphy. There is therefore some potential for slight depth uncertainties to

be introduced into the comparison of various studies or proxies. To minimise this effect the samples for tephra analysis taken in this study were taken co-linearly with samples for the proxy record (in prep. K Grant), to ensure a common absolute depth scale (Larrasoana et al. 2003) was applied.

The core material consists of nannofossil ooze, nannofossil clays, mud turbidites and sapropels, with some bioturbation. The sedimentation rate estimated by Emeis et al. (1996) is between 5 and 57m/Ma (~175-2000 years per cm). The core thus provides a high resolution marine record in the Mediterranean, but detailed sedimentological work is required to construct a realistic age model which accommodates the turbidites and sapropels. It is hoped that this tephra investigation can contribute to such an age model.

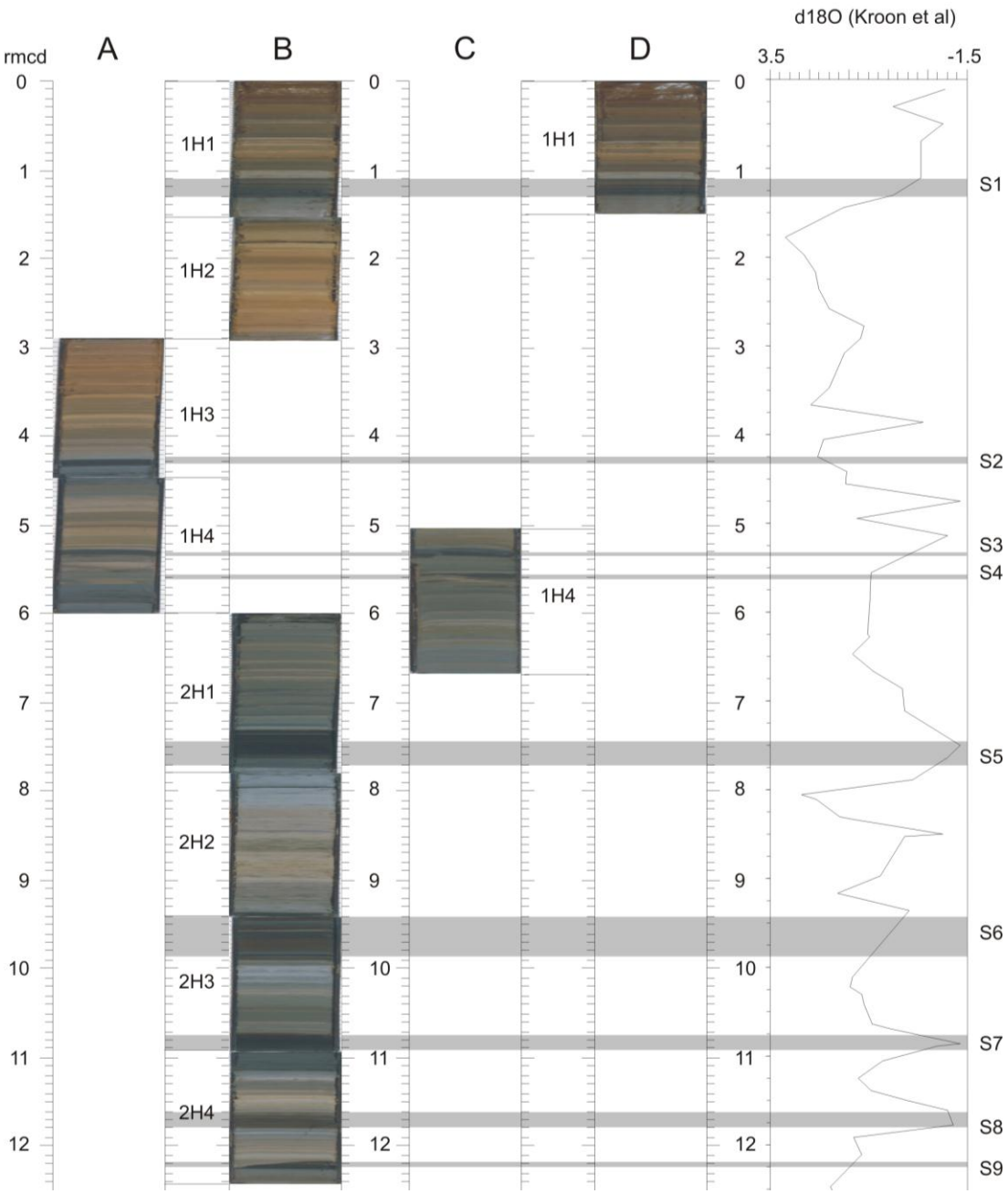

Figure 4.7 The stratigraphy of site ODP967. Only sections relevant to this study are shown. The stratigraphy is a composite of 4 bore holes A,B,C and D. Each sequence has core sections denoted by the notation 1H1, 1H2 etc. The sapropelic layers (as defined by Kroon et al. 1998) are set against the low resolution isotope stratigraphy (ppm-PDB) of Kroon et al. (1998). The depth in the composite core stratigraphy is indicated on the left in meters below the sea floor. The approximate dates of the sapropels are: S1~8ka, S2~55ka, S3~0.81, S4~102ka, S5~124ka, S6~172ka, S7~195ka, S8~217ka, S9~240ka

Some studies have produced proxy data for small sections of the core; predictably the sapropels have attracted stable isotope and alkenone temperature studies (Emeis et al. 1998 and Menzel et al. 2004). The only contiguous proxy record so far published is the dust record (haematite content) of Larrasoana et al. (2003) and Trauth et al. (2009). This is

shown in figure 4.8 for the past 3Ma. The eastern Mediterranean is an important destination for North African dust and therefore ODP967 yields a record of the aridity of North Africa.

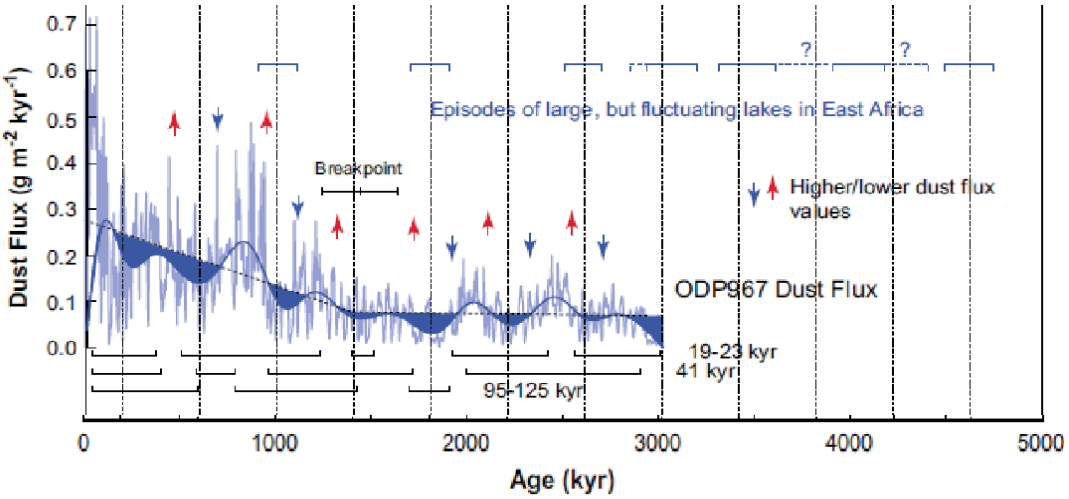

Figure 4.8 The 3Ma dust record of Larrasoana et al. (2003) and Trauth et al. (2009), and its relationship to North African lake systems. The diagram implies that low dust flux to the eastern Mediterranean is coincident with episodes of large lake development in North Africa.

K.M. Grant (NOCS) has produced an initial $\delta^{18}O$ record using the planktonic foraminifera *G.Ruber* and the author and K.M. Grant produced contiguous scanning XRF data to produce a geochemical stratigraphy, for the top 13m of the core (possibly to sapropel 9 which is dated to ~252-253ka by Emeis et al. (1998). The $\delta^{18}O$ record and the Fe, Ti, Ba and S stratigraphies are shown together with a high resolution dust record (from magnetic susceptibility measurements) which was also produced by K.Grant.

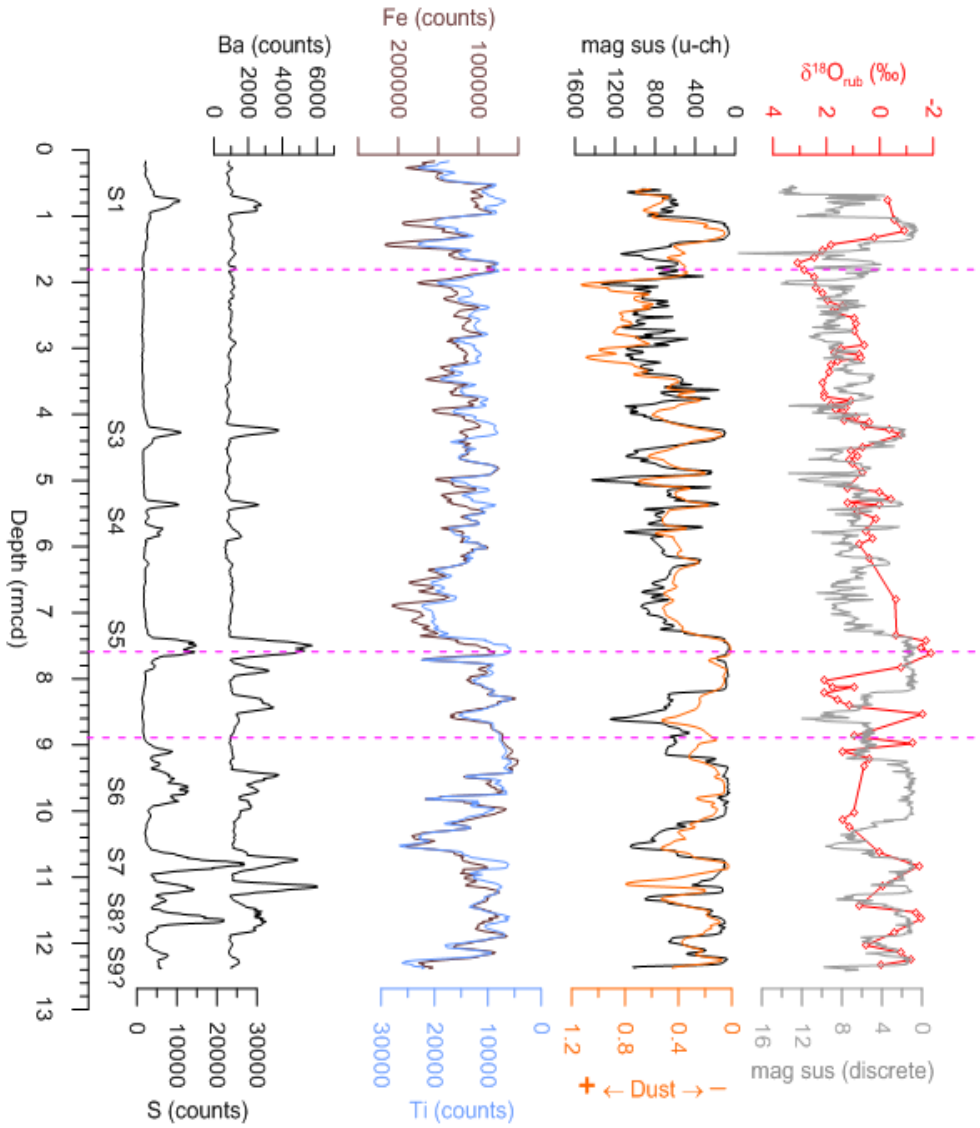

Figure 4.9 Variations in Ba and S stratigraphies highlight the sapropel layers, Fe and Ti stratigraphies (measuring terrigenous content), scanning mag sus measurements as a proxy for dust content and $\delta^{18}O$ measurements from *G.Ruber* samples together with discrete magnetic susceptibility measurements.

4.4.3- Age models for ODP967.

The ODP967 age models have been constructed by tuning the proxy records to the dust record of Larrasoana et al. (2003). This in turn has been produced by tuning the dust haematite content of the sediments (the North African dust record) to the orbital precession cycle and using the age model of Kroon et al. (1999) for tie points relating to the sapropels. The age model of Kroon et al. (1999) is based on the orbital tuning of the sapropels to insolation maxima. The resulting composite age model is shown in figure 4.10

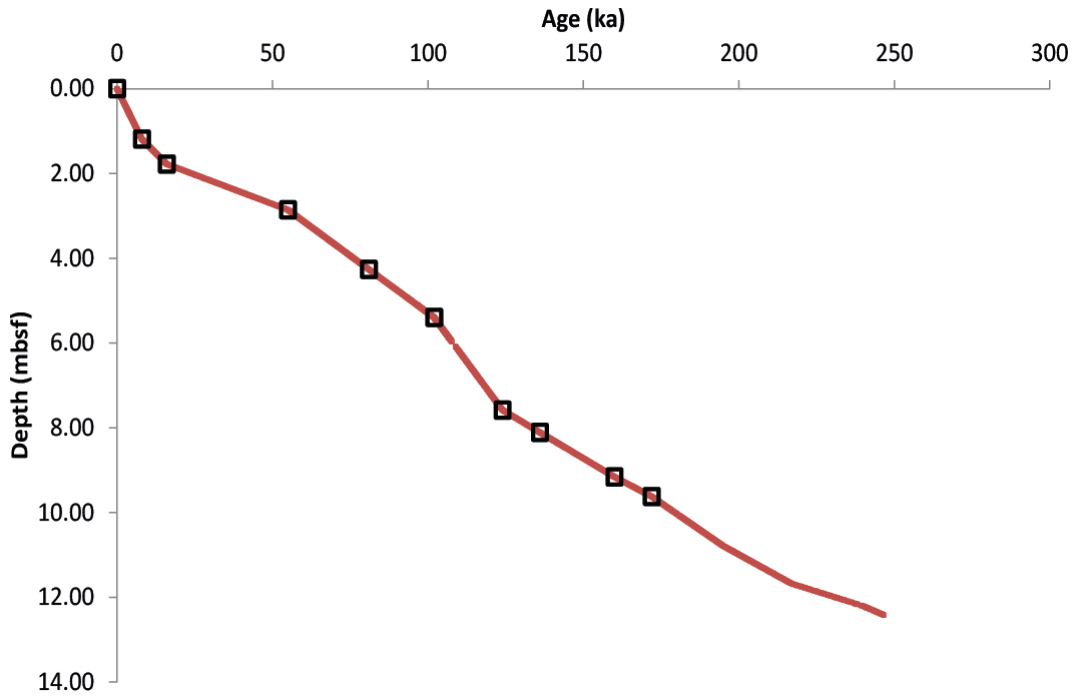

Figure 4.10 the age model of Larrasoana et al. (2003) (red line), constrained by the precession tuned sapropel age model of Kroon et al. (1999) (black cubes).

Tephra layers found in this core could help to test this age model, particularly if their associated proximal deposits a have precise radiometric dates. If the tephra implied that the age model was incorrect, the assumption upon which the Larrasoana et al. age model is based (that the North African dust record is controlled by, and in phase with, orbital precession) would also have to be challenged.

4.4.4- Potential sources of tephra for ODP967.

The most likely sources for tephra which may be found in the eastern Mediterranean Sea are Anatolia, Santorini, Kos, Yali and Nisyros. These sources are the closest and are upwind of core site ODP967.

4.5 Lago Grande di Monticchio.

During the period of this study, several tephra layers likely to originate from the Campanian Region of Italy were found which did not have equivalent proximal equivalents. As the most comprehensive record of Italian volcanic activity is that of the Lago Grande di Monticchio lake sediment sequence (Wulf et al.2004, 2008), several samples of tephra layers from this stratigraphy were kindly donated by S. Wulf (Potsdam) for geochemical analysis, to assist in the identification of tephra layers identified in this PhD project.

Lago Grande di Monticchio is a maar lake in central southern Italy (fig. 4.1) located at 15°25'E, 40°56'N at an elevation of 656m OD. It has a maximum depth of 36m, but an average depth of only 8.6m. It circulates in a eutrophic to polytrophic state and as a result is partially organically varved.

The 72.5m composite sequence for Lago Grande di Monticchio consists of four sediment cores (Zolitschka and Negendank 1996). The sediments are organic to minerogenic or calcareaous in composition and mostly laminated, although organic varves only comprise about 10% of the length of the core (Zolitschka and Negendank 1996, Wulf et al. 2004). Palaeoecological and palaeoclimatic studies have also been conducted on the lake sequence (Zolitschka and Neggendank 1996, Allen et al. 2010). This site therefore not only provides an excellent tephrostratigraphy for comparison to the results of this PhD study but the available palaeoclimate record (fig. 4.12) could also be directly compared with the proxy records available for LC21, ODP967 and ODP975 using any tephra layer which the records may have in common.

The high resolution pollen record of LGdM features the major climatic shifts which are recorded in the Greenland ice cores (Allen et al. 1999) at sub millennial (to 200year) time resolution. Prior to about 65ka, however, the high resolution of the sequence also reveals additional climatic shifts which are not shown by the Greenland records. These changes are thought by Allen et al. (1999) to indicate the better resolution of the pollen over the ice core records during this period. In addition the record illustrates differences in the duration of climatic events between southern Europe and Greenland with marine isotope stage 5b being shorter in duration in the LGdM record than in the ice cores. This conclusion was reached through the use of independent age models rather than 'wiggle matching' techniques. Allen et al. (1999) thus demonstrate how independent age models can reveal previously unresolvable climatic disparities between records.

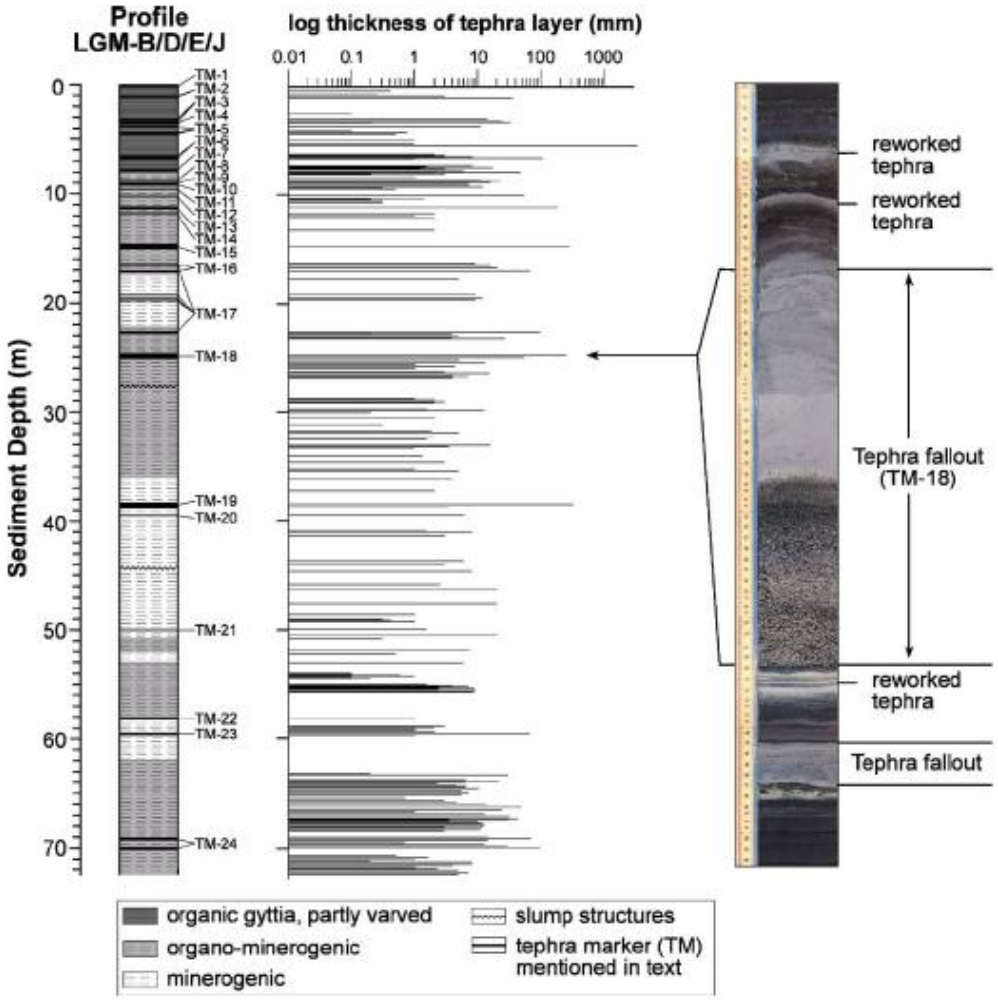

Figure 4.11 the visible tephra layer record for Lago Grande di Monticchio (from Wulf et al 2004). The sequence also has a chronology supported by varve counting and radiometric ages for the tephra layers. The sequence covers the present day to tephra TM24 which is dated at ~102.5ka. These dates are given in table 4.2 The lake has also recorded a very high resolution vegetation record (fig 4.13)

No.	Tephra	Age (new chronology) (years BP 1950)	Thickness (mm)	Tephra bottom depth (cm)	Source	Volcanic event
1	TM-1	88	9.00	6.00	S.Vesuvius	1631 AD
2	TM-1-1	818	0.40	50.00	S.Vesuvius	AS?
3	TM-1-2	1072	0.25	75.80	S.Vesuvius	AS?
4	TM-2a	1416	3.00	112.00	S.Vesuvius	MI 1, 512 AD
5	TM-2b	1441	35.00	116.50	S.Vesuvius	Pollena 472 AD
6	TM-2-1	3042	0.10	252.50	Ischia Island	Cretaio ?
7	TM-2-2	3939	1.00	311.00	S.Vesuvius	AP6
8	TM-3a	3994	22.00	315.70	S.Vesuvius	AP4
9	TM-3b	4018	24.00	320.20	S.Vesuvius	AP3
10	TM-3c	4146	14.00	332.30	S.Vesuvius	AP2
11	TM-3c	4153	17.00	334.00	S.Vesuvius	AP2
12	TM-4	4313	6.00	352.60	S.Vesuvius	Avellino
13	TM-5a	4619	11.00	374.10	Campi Flegrei	Astroni 1-3

14	TM-5b	4663	3.00	378.00	Campi Flegrei	Astroni 1-3
15	TM-5c	5393	0.75	426.80	Campi Flegrei	AMST
16	TM-5cd1	5502	0.10	433.00	Campi Flegrei ?	reworked
17	TM-5cd2	5635	0.70	445.00	Campi Flegrei	AMST
18	TM-5d	5675	0.50	448.00	Campi Flegrei	AMST Unit
19	TM-5-1a	6581	1.00	507.50	Ischia Island?	Piano Liguori?
20	TM-5-1b	6588	1.00	508.00	Ischia Island	Piano Liguori
21	TM-5-1c	6592	0.50	508.50	Ischia Island	Piano Liguori
22	TM-5-2	7151	1.00	544.00	Ischia Island	Cantariello
23	TM-6a	9620	1.00	644.50	S.Vesuvius	Mercato
24	TM-6b	9678	106.00	658.60	S.Vesuvius	Mercato
25	TM-6-1a	9894	1.00	667.00	Campi Flegrei	Fondi di Baia?
26	TM-6-1b	9958	3.00	668.80	Campi Flegrei	Fondi di Baia?
27	TM-6-2a	11187	0.10	725.60	Palinuro	Palinuro
28	TM-6-2b	11207	0.10	726.50	Palinuro	Palinuro
29	TM-6-3a	11501	0.40	737.00	Ischia Island	Selva del Napolitano
30	TM-6-3b	11516	0.50	737.50	Ischia Island	Selva del Napolitano
31	TM-6-3c	11522	0.40	738.00	Ischia Island	Selva del Napolitano
32	TM-6-4a	11668	17.00	745.70	Campi Flegrei	Soccavo 4
33	TM-6-4b	11888	1.00	760.00	Campi Flegrei	Soccavo 4
34	TM-6-4c	11983	3.00	765.30	Campi Flegrei	Soccavo 4
35	TM-6-5a	12072	1.00	768.00	Campi Flegrei	APP reworked
36	TM-6-5b	12073	2.00	768.30	Campi Flegrei	APP reworked
37	TM-6-5c	12074	2.00	768.70	Campi Flegrei	APP reworked
38	TM-7a	12169	6.00	775.10	Campi Flegrei	Pomici Principlai
39	TM-7b	12181	47.00	780.70	Campi Flegrei	Pomici Principali
40	TM-7c	12184	2.00	781.20	Campi Flegrei ?	Pomici Principali ?
41	TM-7-1a	12591	0.20	805.30	Campi Flegrei	Gaiola ?
42	TM-7-1b	12592	0.10	805.40	Campi Flegrei ?	Gaiola ?
43	TM-7-2	12643	0.30	807.90	Campi Flegrei	La Pigna ?
44	TM-7-3	12765	0.10	812.90	Campi Flegrei	LP-NYT units 1-6 ?
45	TM-7-4	12905	0.30	817.80	Campi Flegrei ?	LP-NYT units 1-6 ?
46	TM-8	14106	4.00	857.40	Campi Flegrei	NYT
47	TM-8	14113	11.00	858.50	Campi Flegrei	NYT
48	TM-8	14115	7.00	859.50	Campi Flegrei	NYT
49	TM-9	14557	18.00	877.30	Campi Flegrei	Tufi Biancastri, GM1
50	TM-10a	15028	4.00	896.80	Campi Flegrei	Lagno Amendolare
51	TM-10b	15215	7.00	903.70	Campi Flegrei	Lagno Amendolare
52	TM-10c	15296	1.00	910.30	Campi Flegrei	Lagno Amendolare
53	TM-10d	15551	4.00	917.70	Campi Flegrei	Amendolare
54	TM-10-1	15822	12.00	927.00	Ischia Island	Faro di Punta

						Imperatore
55	TM-11	16444	0.50	953.00	Etna	Biancavilla, Y-1
56	TM-12	17560	55.00	1002.00	S.Vesuvius	Verdoline
57	TM-12-1	17976	1.40	1019.00	Etna	Ante-Biancavilla
58	TM-12-2a	18496	0.30	1043.30	Campi Flegrei	Tufi Biancastri ?
59	TM-12-2b	18538	0.20	1044.10	Campi Flegrei	Tufi Biancastri ?
60	TM-13	19282	182.00	1107.00	S.Vesuvius	Pomici di Base
61	TM-14a	21071	2.00	1166.00	Procida?	Solchiaro CD1-b?
62	TM-14b	21259	1.00	1171.50	Procida	Solchiaro, white facies
63	TM-14-1	21353	2.00	1174.70	Ischia Island	Faro di Punta Imperatore?
64	TM-14-2	22249	2.00	1202.00	Alban Hills	Peperini
65	TM-14-3	25366	2.00	1326.50	Campi Flegrei	?
66	TM-15	27256	286.00	1458.00	Campi Flegrei	Y-3, SMP1-e
67	TM-17a	29920	9.00	1632.40	Alban Hills	Peperini
68	TM-17b	29998	7.00	1636.70	Alban Hills	Peperini
69	TM-16a	30237	16.00	1648.00	Campi Flegrei?	Codola Top
70	TM-16b	31121	68.00	1724.50	Campi Flegrei?	Codola Base
71	TM-17bc	31830	5.00	1792.50	Alban Hills	Peperini
72	TM-17c	33768	9.00	1930.00	Procida	Fiumicello
73	TM-17d	33920	12.00	1962.40	Procida	Fiumicello
74	TM-17e	33962	9.00	1993.30	Procida	Fiumicello
75	TM-17f	34528	97.00	2344.50	Alban Hills	Peperini
76	TM-17-1a	34862	1.00	2365.80	Ischia Island	?
77	TM-17-1b	34956	4.00	2370.50	Ischia Island	?
78	TM-17-1c	34980	5.00	2372.80	Ischia Island	?
79	TM-17-2	35531	27.00	2417.50	Campi Flegrei ?	Schiava, C-9
80	TM-18	36773	257.0	2637.00	Campi Flegrei	IC
81	TM-18-1a	36843	56.00	2649.20	Campi Flegrei?	SMP1-a
82	TM-18-1b	36943	5.00	2657.00	Campi Flegrei?	SMP1-a
83	TM-18-1c	37059	4.00	2667.80	Campi Flegrei?	SMP1-a
84	TM-18-1d	37363	13.00	2705.60	Campi Flegrei?	SMP1-a
85	TM-18-2	37586	1.00	2722.70	Ischia Island	Citara
86	TM-18-3	37809	4.00	2729.00	?	?
87	TM-18-4	38603	15.00	2779.00	Campi Flegrei	TLm
88	TM-18-5a	38833	7.00	2804.00	Ischia Island	Citara
89	TM-18-5b	38858	4.00	2805.60	Ischia Island	Citara
90	TM-18-5c	38878	3.00	2814.50	Ischia Island	Citara
91	*TM-18-6*	*39245*	*?*	*?*	*Campi Flegrei*	*?*
92	TM-18-7	40170	1.00	2823.10	Procida ?	?
93	TM-18-8a	40557	3.00	2940.00	Campi Flegrei	TGm
94	TM-18-8b	40568	2.00	2940.80	Campi Flegrei	TGm
95	TM-18-9a	41423	1.50	2992.00	Ischia Island	Citara
96	TM-18-9b	41472	0.90	2996.20	Ischia Island	Citara
97	TM-18-9c	41506	0.50	2997.40	Ischia Island	Citara
98	TM-18-9d	41521	1.00	2997.80	Ischia Island ?	Citara ?

99	TM-18-9e	41694	13.00	3005.20	Ischia Island	Citara
100	TM-18-9f	41934	0.20	3015.50	Ischia Island	Citara
101	TM-18-10a	43281	2.00	3062.10	Campi Flegrei	TGl
102	TM-18-10b	45834	1.30	3159.80	Campi Flegrei	ME039p2, TGl
103	TM-18-10c	45870	1.80	3162.10	Campi Flegrei	TGl
104	TM-18-10d	46459	5.00	3182.90	Campi Flegrei	TGl
105	TM-18-11	47312	2.00	3211.50	Procida ?	?
106	TM-18-12a	48113	1.50	3239.60	Campi Flegrei	Santa Lucia
107	TM-18-12b	49409	16.00	3285.00	Campi Flegrei	Santa Lucia, C-15
108	TM-18-13	49631	3.50	3296.00	Procida ?	?
109	TM-18-14a	50260	1.00	3345.40	Ischia Island	Citara
110	TM-18-14b	50315	0.20	*3337.60*	Ischia Island	Citara
111	TM-18-14c	50362	0.30	3338.50	Ischia Island	Citara
112	TM-18-15a	51948	1.30	3371.00	Campi Flegrei	TL f
113	TM-18-15b	53529	3.00	3445.20	Campi Flegrei	TL f
114	TM-18-15c	53580	1.00	3447.10	Campi Flegrei	TL f
115	TM-18-16	54729	1.00	3478.50	?	?
116	TM-18-17a	55614	5.00	3508.50	Campi Flegrei	CA1-a, C-16
117	TM-18-17b	57289	4.00	3587.70	Campi Flegrei	CA1-a, C-16
118	TM-19	60055	332.00	3831.00	Ischia Island	TVEss
119	TM-19-1	60235	3.50	3846.50	Campi Flegrei	TLc
120	TM-20	61371	6.00	3923.80	Ischia Island	SC2-a, C(i)6
121	TM-20-1a	64047	1.50	4062.60	Ischia Island	Y-7
122	TM-20-1b	64136	8.00	4067.60	Ischia Island	Y-7
123	TM-20-1c	64470	3.00	4104.70	Ischia Island	Y-7
124	TM-20-2a	68619	6.00	4351.30	Campi Flegrei	C-18, SA3-a/SA3-b
125	TM-20-2b	69463	3.00	4393.20	?	666-04
126	TM-20-2c	69517	1.00	4394.50	?	666-04
127	TM-20-3	69585	0.20	4396.00	Ischia Island	?
128	TM-20-4a	70367	8.00	4443.60	?	?
129	TM-20-4b	72107	2.50	4616.40	Campi Flegrei	?
130	TM-20-5	72942	20.00	4657.00	Ischia Island	Pignatiello
131	*TM-20-6*	*74085*	*?*	*?*	*?*	*?*
132	TM-20-7	75351	20.00	4780.20	Ischia Island	Pignatiello
133	TM-20-8	76467	1.00	4810.00	Campi Flegrei	?
134	TM-20-9	77237	0.30	4916.63	Ischia Island	Parata
135	TM-20-10	77552	1.00	4937.50	Campi Flegrei	?
136	TM-21	78341	1.50	5012.00	Eolian Islands	Y-9
137	TM-21-1a	79414	20.00	5071.80	Campi Flegrei	?
138	TM-21-1b	79514	0.30	5106.00	Campi Flegrei	?
139	TM-21-2a	80985	7.50	5236.20	Ischia Island	Monte Vico
140	TM-21-2b	81427	0.50	5258.00	Ischia Island	Monte Vico
141	TM-21-2c	81949	6.00	5339.70	Ischia Island	Monte Vico
142	TM-21-3a	82626	0.60	5405.00	?	?
143	TM-21-3b	82656	0.10	5405.50	?	?
144	TM-21-4	83410	0.10	5474.20	?	?
145	TM-21-5	83421	1.00	5474.50	?	?
146	TM-21-6	84089	0.20	5492.80	?	
147	TM-21-6a	85690	0.20	5559.40	Campi Flegrei	?
148	TM-21-6b	85710	4.00	5563.00	Campi Flegrei	?
149	TM-21-6c	85753	1.50	5564.50	Campi Flegrei	?
150	TM-21-6d	85768	0.20	5564.80	Campi Flegrei	?

151	TM-21-6e	85809	0.30	5565.50	Campi Flegrei	?
152	TM-21-7a	85934	5.00	5568.00	Campi Flegrei	?
153	TM-21-7b	86060	8.50	5575.60	Campi Flegrei	?
154	TM-21-7c	86287	7.00	5581.80	Campi Flegrei	?
155	TM-21-8a	86645	1.90	5594.00	Campi Flegrei	?
156	TM-21-8b	86862	9.00	5600.20	Campi Flegrei	?
157	TM-21-8c	86863	8.00	5601.20	Campi Flegrei	?
158	TM-21-9	86910	1.50	5602.00	Campi Flegrei	?
159	TM-21-10a	86987	0.10	5602.80	Campi Flegrei	?
160	TM-21-10b	87081	5.80	5605.30	Campi Flegrei	?
161	TM-21-10c	87492	0.75	5611.00	Campi Flegrei	?
162	TM-22	89126	1.00	5840.00	PA	Ante Green Tuff (P-10)
163	TM-22-1a	89248	3.00	5902.10	Campi Flegrei	?
164	TM-22-1b	89288	2.00	5916.30	Campi Flegrei	?
165	TM-23	89473	66.00	5982.50	SA	Tufo di Baccano
166	TM-23-1a	89479	2.00	5984.00	?	?
167	TM-23-1b	89486	1.00	5985.50	?	?
168	TM-23-2a	91070	30.00	6369.70	Campi Flegrei	?
169	TM-23-2b	91331	0.20	6373.30	Campi Flegrei	?
170	TM-23-3a	92942	2.00	6431.60	Campi Flegrei	?
171	TM-23-3b	92947	6.50	6432.60	Campi Flegrei	?
172	TM-23-3c	92949	22.00	6436.30	Campi Flegrei	?
173	TM-23-4	93034	1.00	6438.00	Campi Flegrei	?
174	TM-23-5	93312	2.30	6450.80	Eolian Islands	Piano Caldera
175	TM-23-6a	93369	0.60	6458.90	? (Etna)	?
176	TM-23-6b	93372	0.10	6459.10	? (Etna)	?
177	TM-23-7a	93424	1.50	6459.50	Campi Flegrei ?	?
178	TM-23-7b	93598	0.80	6463.50	Campi Flegrei	?
179	TM-23-7c	93607	4.50	6464.30	Campi Flegrei	?
180	TM-23-7d	93617	2.50	6478.30	Campi Flegrei	?
181	TM-23-7e	93618	2.50	6479.00	Campi Flegrei	?
182	TM-23-7f	93619	3.50	6479.90	Campi Flegrei	?
183	TM-23-8a	93637	4.00	6485.10	Campi Flegrei	?
184	TM-23-8b	93639	6.50	6486.60	Campi Flegrei	?
185	TM-23-8c	93641	2.00	6487.30	Campi Flegrei ?	?
186	TM-23-8d	93644	10.50	6489.00	Campi Flegrei	?
187	TM-23-8e	93654	1.30	6489.30	Campi Flegrei	?
188	TM-23-9	93680	0.80	6489.70	Campi Flegrei	?
189	TM-23-10	93997	2.50	6495.00	Campi Flegrei	?
190	TM-23-11a	95166	5.00	6528.70	Campi Flegrei	?
191	TM-23-11b	95169	3.50	6529.00	Campi Flegrei	?
192	TM-23-11c	95170	2.00	6529.40	Campi Flegrei	?
193	TM-23-11d	95172	7.00	6530.50	Campi Flegrei	?
194	TM-23-11e	95177	4.00	6532.10	Campi Flegrei	?
195	TM-23-11f	95179	4.00	6532.60	Campi Flegrei	?
196	TM-23-11g	95181	5.50	6533.80	Campi Flegrei	?
197	TM-23-12a	95598	0.10	6543.00	Campi Flegrei ?	?
198	TM-23-12b	95623	0.10	6543.40	Campi Flegrei	?
199	TM-23-12c	95798	0.20	6547.30	Campi Flegrei	?
200	TM-23-13	95843	0.20	6548.50	Campi Flegrei	?

201	TM-23-14	96164	0.70	6589.20	Ischia Island	?
202	TM-23-15	97010	0.40	6610.00	Campi Flegrei	?
203	TM-23-16	97477	4.60	6625.00	Ischia Island	Monte S. Angelo
204	TM-23-17	97794	0.10	6629.70	Campi Flegrei	?
205	TM-23-18a	97866	3.00	6630.60	Campi Flegrei	?
206	TM-23-18b	97944	0.20	6642.00	Campi Flegrei	?
207	TM-23-18c	97982	0.50	6643.40	Campi Flegrei	?
208	TM-23-18d	98079	14.00	6649.90	Campi Flegrei	?
209	TM-23-18e	98083	48.00	6657.80	Campi Flegrei	?
210	TM-23-19a	98117	1.00	6659.00	Campi Flegrei ?	?
211	TM-23-19b	98159	0.50	6660.70	Campi Flegrei	?
212	TM-23-19c	98180	1.30	6661.00	Campi Flegrei	?
213	TM-23-19d	98251	0.50	6661.50	Campi Flegrei	?
214	TM-23-19e	98293	0.90	6662.00	Campi Flegrei	?
215	TM-23-19f	98348	0.10	6662.80	Campi Flegrei	?
216	TM-23-19g	98593	0.10	6664.80	Campi Flegrei ?	?
217	TM-23-20a	99140	24.00	6685.90	Ischia Island	Monte S. Angelo
218	TM-23-20b	99466	1.00	6708.50	Ischia Island	Monte S. Angelo
219	TM-23-21a	99653	13.00	6754.00	Campi Flegrei	?
220	TM-23-21b	99654	8.00	6755.10	Campi Flegrei	?
221	TM-23-21c	99656	12.00	6756.90	Campi Flegrei	?
222	TM-23-21d	99658	6.00	6759.70	Campi Flegrei	?
223	TM-23-21e	99660	5.00	6760.30	Campi Flegrei	?
224	TM-23-21f	99661	32.00	6765.10	Campi Flegrei	?
225	TM-23-21g	99670	30.00	6779.90	Campi Flegrei ?	?
226	TM-23-22	99733	0.20	6781.00	Campi Flegrei	?
227	TM-23-23	100105	0.50	6787.00	Ischia Island	Monte S. Angelo
228	TM-23-24a	100115	2.50	6787.30	Campi Flegrei	?
229	TM-23-24b	100329	1.50	6792.50	Campi Flegrei	?
230	TM-23-24c	100527	3.50	6800.90	Campi Flegrei	?
231	TM-23-24d	100857	10.00	6815.50	Campi Flegrei ?	?
232	TM-23-24e	100880	4.50	6815.90	Campi Flegrei ?	?
233	TM-23-24f	100881	2.00	6817.50	Campi Flegrei ?	?
234	TM-23-24g	100884	2.50	6820.00	Campi Flegrei ?	?
235	TM-23-24h	100910	12.00	6840.40	Campi Flegrei	?
236	TM-23-24i	100912	13.00	6841.80	Campi Flegrei	?
237	TM-23-25	100917	4.00	6844.90	Campi Flegrei ?	?
238	TM-23-26a	101056	1.40	6873.50	Campi Flegrei ?	?
239	TM-23-26b	101058	11.00	6878.80	Campi Flegrei	?
240	TM-23-26c	101059	3.00	6879.30	Campi Flegrei	?
241	TM-23-26d	101077	2.50	6888.60	Campi Flegrei	?
242	TM-23-26e	101157	3.00	6894.30	Campi Flegrei	?
243	TM-23-26f	101159	0.80	6895.10	Campi Flegrei	?

244	TM-23-26g	101169	1.10	6895.30	Campi Flegrei	?
245	TM-23-27	101211	2.00	6896.50	Campi Flegrei	?
246	TM-24a	101572	70.00	6952.30	Campi Flegrei	X-5
247	TM-24a	101573	3.20	6955.90	Campi Flegrei	X-5
248	TM-24a	101574	6.50	6956.50	Campi Flegrei ?	X-5
249	TM-24a	101575	14.40	6958.00	Campi Flegrei ?	X-5
250	TM-24a	101577	3.60	6958.50	Campi Flegrei	X-5
251	TM-24a	101589	1.25	6959.20	Campi Flegrei ?	X-5
252	TM2-4Alban Hills-1a	101622	2.00	6960.20	Campi Flegrei	?
253	TM-24Alban Hills-1b	101639	4.40	6961.40	Campi Flegrei	?
254	TM-24Alban Hills-1c	101653	3.20	6962.00	Campi Flegrei	?
255	TM-24Alban Hills-2a	101761	0.80	6967.40	Campi Flegrei	?
256	TM-24Alban Hills-2b	101890	0.20	6970.80	Campi Flegrei ?	?
257	TM-24Alban Hills-2c	101896	12.00	6972.90	Campi Flegrei	?
258	TM-24Alban Hills-3	102322	0.70	7001.90	Campi Flegrei	?
259	TM-24b	102537	2.00	7012.50	Campi Flegrei	X-5
260	TM-24b	102538	0.40	7012.70	Campi Flegrei	X-5
261	TM-24b	102539	3.00	7013.20	Campi Flegrei	X-5
262	TM-24b	102540	5.00	7014.20	Campi Flegrei	X-5
263	TM-24b	102541	1.00	7016.50	Campi Flegrei	X-5
264	TM-24b	102542	5.00	7017.70	Campi Flegrei	X-5
265	TM-24b	102543	12.00	7020.60	Campi Flegrei	X-5
266	TM-24b	102544	1.00	7024.40	Campi Flegrei	X-5
267	TM-24b	102545	1.50	7024.70	Campi Flegrei	X-5
268	TM-24b	102546	2.00	7025.10	Campi Flegrei	X-5
269	TM-24b	102548	13.00	7027.50	Campi Flegrei	X-5
270	TM-24b	102549	12.00	7030.20	Campi Flegrei ?	X-5
271	TM-24b	102552	29.00	7033.00	Campi Flegrei	X-5
272	TM-24b	102553	9.00	7036.00	Campi Flegrei	X-5
273	TM-24b	102556	97.00	7077.50	Campi Flegrei	X-5
274	TM-24b	102569	1.00	7158.70	Campi Flegrei	?
275	TM-24-1a	102798	1.60	7178.50	Campi Flegrei	?
276	TM-24-1b	102924	0.50	7182.00	Campi Flegrei	?
277	TM-24-1c	102947	0.10	7184.90	Campi Flegrei	?
278	TM-24-2a	103460	0.20	7217.00	Campi Flegrei ?	?
279	TM-24-2b	103556	8.00	7223.50	Campi Flegrei ?	?
280	TM-24-2c	103602	0.20	7225.00	Campi Flegrei ?	?
281	TM-24-3a	103748	2.60	7238.50	Ischia Island	Punta Imperatore
282	TM-24-3b	103803	8.00	7243.60	Ischia Island	Punta Imperatore
283	TM-24-3c	104040	2.00	7263.10	Ischia Island	Punta Imperatore
284	TM-24-3d	104047	0.20	7264.10	Ischia Island	Punta Imperatore

285	TM-24-3e	104120	4.00	7271.50	Ischia Island	Punta Imperatore
286	TM-24-4	104326	1.00	7281.80	Campi Flegrei	?
287	TM-24-5a	105007	2.30	7304.90	Campi Flegrei ?	?
288	TM-24-5b	105013	0.70	7305.10	Campi Flegrei ?	?
289	TM-24-5c	105018	4.80	7305.70	Campi Flegrei	?
290	TM-24-6a	105042	0.20	7312.40	Campi Flegrei ?	?
291	TM-24-6b	105062	0.10	7313.20	Campi Flegrei	?
292	TM-24-6c	105080	0.10	7313.50	Campi Flegrei	?
293	TM-24-7a	105187	0.10	7316.40	Campi Flegrei	?
294	TM-24-7b	105228	1.50	7316.70	Campi Flegrei	?
295	TM-24-7c	105269	0.20	7317.30	Campi Flegrei	?

Table 4.2 Names, ages (from varve supported chronology), thicknesses, depths and assigned source and volcanic event for 295 tephra layers found in the Lago Grande di Monticchio sequence (from S.Wulf).

The chronology deveoloped for the core sequence, integrates data from varve counting, sedimentation rates, ^{14}C dating and ^{39}Ar:^{40}Ar dating of the tephra layers (Allen et al.2010). The ages of tephra layers not dated directly by ^{39}Ar:^{40}Ar have been interpolated using this composite chronology. Tephra samples in this sequence are named according to their stratigraphic order and the prefix “TM” from stratigraphically highest to lowest e.g. TM12, TM13a-1, TM13a-2, TM14 etc. In this study tephra geochemical data were generated for 4 tephra samples from Lago Grande di Monticchio; TM24a-1, TM24a-3+4, TM24b-15 and TM27.

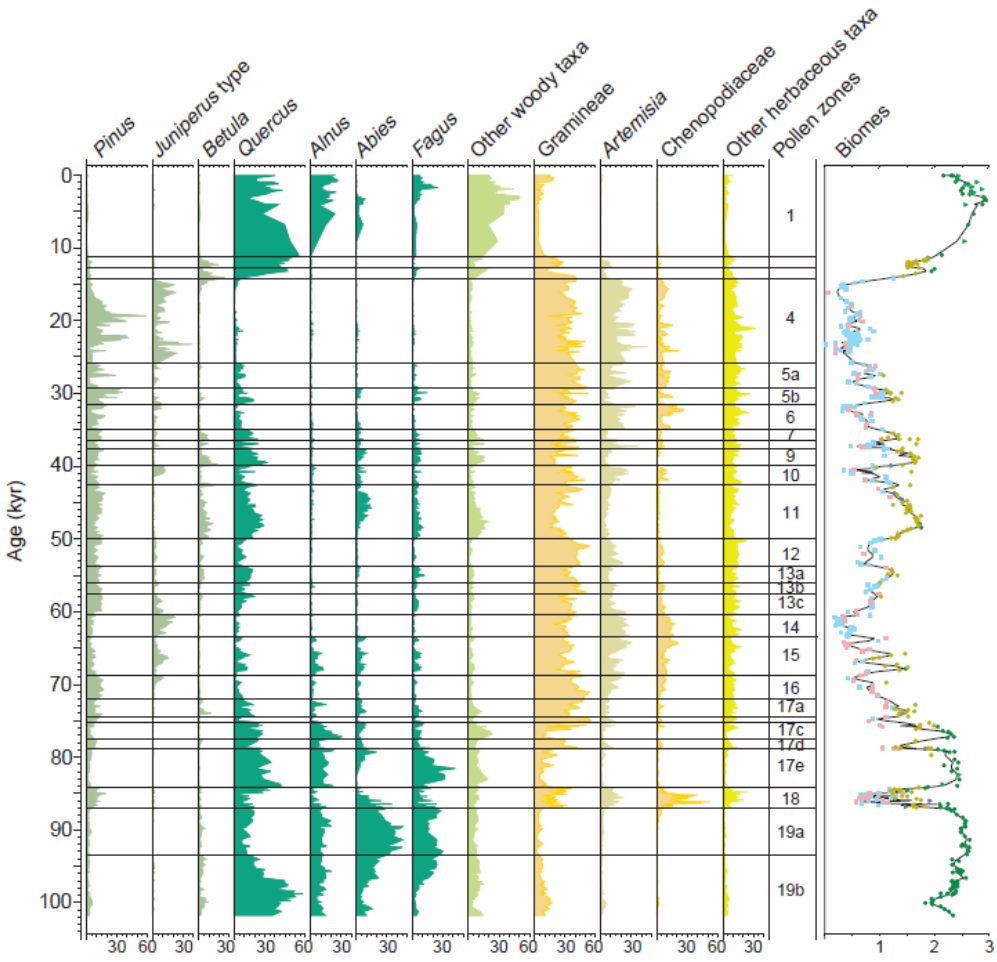

Figure 4.12 Vegetation changes recorded in Lago Grande di Monticchio for the last 105ka, the same period of time as figure 4.11 (from Allen et al. 1999). The sequence contains a total of 340 tephra layers, through which comparisons can be made from other environmental archives to the high resolution environmental record.

Chapter 5- Methodology

5.1 Sediment core treatment procedures.

5.1.1 Core Sub-sampling Strategy and Sample Storage

The marine sediment cores were sub-sampled using U-channels to attain a continuous stratigraphy for tephra analysis. U-Channels were cut out of the cores using a ceramic knife and nylon fishing wire. Metal cutting tools were avoided as the cores were to be used for magnetic measurements. Each of these U-Channels was marked with the "0" point for the core section from which it was taken, to allow all depth measurements to be related back to the original core. Magnetic susceptibility logs were taken (at NOCS) to reinforce the depth relations between the sets of U-Channels, ensuring that the various analyses performed on the different sets (foraminifera stratigraphy, organic geochemistry, tephra etc.), could be accurately related to one another. For core LC21, 3 U-channels were taken concurrently to ensure parity of depth measurements between each of the sets. For ODP cores 975 and 967 two sets of U-channels were taken concurrently. These U-channels were subsequently and concurrently sliced into 1cm deep samples to ensure that the tephra samples could be precisely related to the proxy records.

U-channel samples were stored horizontally in cold stores at either BOSCORF or RHUL. 1cm block samples were stored in 1x1x2 cm plastic boxes in the same cold stores.

5.1.2 Sub-sampling for tephra analyses

The LC21 and ODP967 core sequences contained visible tephra layers while ODP975 contained no visible tephra layers. Fragments of these layers were extracted from the U-channel using a spatula. Some layers less than 1cm in thickness were sampled to include all of their depth. Other layers were visible for up to 30 or 40 cm depth. In these cases it was not possible to sample the whole depth of the deposit as the volume of material would have made processing and handling of the sample very difficult. These deposits were therefore sampled only from the bottom 1cm, which would intuitively represent the first fall of ash from the eruption. The first fall of ash is likely to be the most geographically widespread geochemical composition of all the geochemistries produced in an eruption (Martin Menzies pers. com.) It is recognised however that there could be chemical heterogeneity in these layers and that particularly from a volcanological perspective they deserve more comprehensive sampling. The matching of these layers to proximal deposits

should not be affected by this method, as the proximal deposits should display the full range of chemical compositions, and thus include the composition sampled in the marine core.

Where there was no visible tephra, the U-channels were sub-sampled for cryptotephra. The size of the sample depended on the author's expectation of how tephra-rich the core may be, the time available to process the samples and the amount of material available for this destructive sampling. Approximately 1 gram of material is appropriate for micro-tephra analysis in cores where tephra is likely to be found (Blockley et al.2005). Core LC21 was considered likely to contain many cryptotephra layers, and so a long time was set aside for processing and analysis (approximately 1 year), with all the material in half a U-channel being available for sampling. A resolution of 5cm was therefore considered appropriate for LC21.

Once a cryptotephra layer had been detected within a 5cm sample, the sampling procedure was repeated at 1cm resolution within that 5cm interval. If tephra was detected in two sequential 5cm samples, then the entire 10cm section was re-sampled at 1cm, not just the 5cm section which contained the most tephra. This ensured that if the peak in shard content lies on the boundary between two samples, the entire distribution of tephra shards could still be detected. In addition, in some cases (e.g. LC21 section 9C) this procedure resolved multiple peaks within the initial 5cm sample.

Sites ODP957 and ODP967 were considered less likely to contain large amounts of tephra shards, given their large distances from Quaternary active volcanoes from these sites (see figs. 4.1 and 4.2).

For ODP975 the core was sampled at 5cm resolution, as it was considered that the quantities of tephra likely to be found at this site may be so small that shards recovered in the scans might have to be used for chemical analysis, in addition to any material subsequently recovered from the 1cm samples. A 5 cm sample would contain a higher concentration of shards than a 10cm sample. Furthermore, where shard concentrations in the sediment were so low as to be found in the scans but not replicated in the 1cm samples, then 5cm resolution is better than 10cm.

ODP967 also lies very far from any volcanic source (figs. 4.1 and 4.2). It was however known prior to the cryptotephra sampling that there are two visible tephra layers in this

core. So it is likely that only the very largest eruptions would be represented in this core. This core was chosen to test the tephrostratigraphy already derived for core LC21, but a very limited period of only 11 weeks was available for its investigation, further constrained by limited access to the EPMA and LA-ICP-MS analytical equipment. For these reasons sections of the core were prioritised and investigated based on the knowledge of the existing tephrostratigraphy from LC21 together with the known visible layers in ODP967, relevant data published in the literature (Hamann et al.2010) and the positions of the sapropels in both cores were used to identify regions of the core which might contain tephra. Sections of the core considered likely to contain tephra on this basis were sampled at 5cm resolution. For reasons of time efficiency, regions of the core considered less likely to contain tephra were analysed at 10cm resolution.

5.2 Sample Processing and slide mounting.

5.2.1 Sample processing

For all cores, the visible tephra layers were sampled initially. As described above, all material to be investigated was sampled continuously at 10 or 5cm resolution. For these 10 or 5cm samples, the organic-rich layers (sapropels) were burnt in a furnace for 3.5 hours at 550°C. The samples were then immersed in 10%HCL for 30 minutes to dissolve carbonates, rinsed and then sieved through 125 and 25 micron meshes to remove large detritus and clays respectively. Each was then floated in a centrifuge, first at 1.95kg/l (to remove organic matter) and then at 2.55kg/l to separate any floating glass shards from the remaining mineral matter. The floated material was then mounted onto a slide using Euparol if the slide was intended to be permanent, or Glycerol if it were to be only temporary, and examined under a petrological microscope for tephra content.

Where tephra was found in these scan samples the cores were re-sampled at 1cm resolution to define peaks in shard concentrations more precisely and to extract shards for chemical analysis. This re-sampling procedure was a replication of the 5cm sampling in all respects, with the exception that none of the samples were burnt to remove organics. This was to preserve the chemical composition of the shards. In place of burning off the organic layers, an extra 2 preliminary floats of 1.95kg/l were employed to remove the organic matter. The method conforms broadly to that of Blockley et al. (2005).

5.2.2 Slide mounting and shard counting

The tephra counts for micro-tephras are important as they define the position of the eruption event in the sediment stratigraphy, and potentially reveal evidence of reworking or re-deposition which may have occurred after the initial deposition event. Shard counts must always be expressed as shards/gram of dry sediment, in order to account for different sample sizes and variable amounts of water in the sediment.

If present in large quantities (as evident from the amount of material seen in the bottom of the centrifuge tube, or under examination in a well slide) tephra shards may be counted by proxy using a *Lycopodium* pollen spike. The tablet containing a known number of pollen grains is dissolved with the sample in the centrifuge tube and mixed thoroughly. A portion of the mix is then mounted onto a slide and the lycopodium grain and the tephra grains are both counted. The ratio between the two, together with the known amount of grains in the *Lycopodium* tablet can be used to make an estimate of the number of tephra shards present in a unit volume of the sediment sample.

Alternatively, where the amount of material to be examined is low, an accurate count of all the tephra in the sample can be made simply by counting the shards on a slide mounted using Euparol under a high-power, petrological microscope.

5.2.3 Mounting samples for elemental analysis.

The samples to be analysed by one of the three geochemical methods (EPMA, LA-ICP-MS or SIMS) used in this thesis were required to conform to the following criteria: The mounting medium must not react with the sample or any of the conductive coatings (e.g. carbon or platinum), which may be applied prior to analysis. The mounting medium must also be stable under vacuum and over time. The size of the mounting stub must be that which is standard for the holders in each of the required machines (in this case a cylinder of 25mm diameter and not more than 20mm height). The surface of the stub must also be flat enough to allow the sample which will sit on it, to be subsequently sectioned and polished. The difference in height of the stub must therefore not be more than the height of the sample shards. As a result, samples with large/thick shards do not require a mounting surface as flat as those with very thin/flat shards. Stubs can usually be flattened to within 30µm using a hand grinder and silicon carbite paper. In addition, the sample must be set up on the stub in a manner which allows the same shard to be re-located on a number of different analytical systems.

Three methods of shard mounting (fig 5.1) were used in this thesis, all of them using Specifix 40 epoxy resin stubs and coverings. Specifix 40 sets in the oven at 55° for 3.5 hours.

1) Line scoring and filling- in this process, the flattened stub had a line scored onto the top surface with a scalpel. This line was then filled with sample by dusting the tephra over the line and removing the excess with a small paintbrush. The sample was the covered in epoxy resin, set, and then cut and polished. This process produced a stub with a line of tephra shards 2-3 shards wide on the top. This line, together with reflected light photomicrographs, allows the analyst to easily revisit the same shard surfaces on any system. It does however require material abundant enough to fill the line and some in excess to be wasted and so this method is only really suitable for visible tephras. In addition photographing of the surface does take a considerable time to complete (perhaps 1-2 hours per sample), but allows the analyst the luxury of being able to see (and subsequently measure) the shard after analyses have been completed.

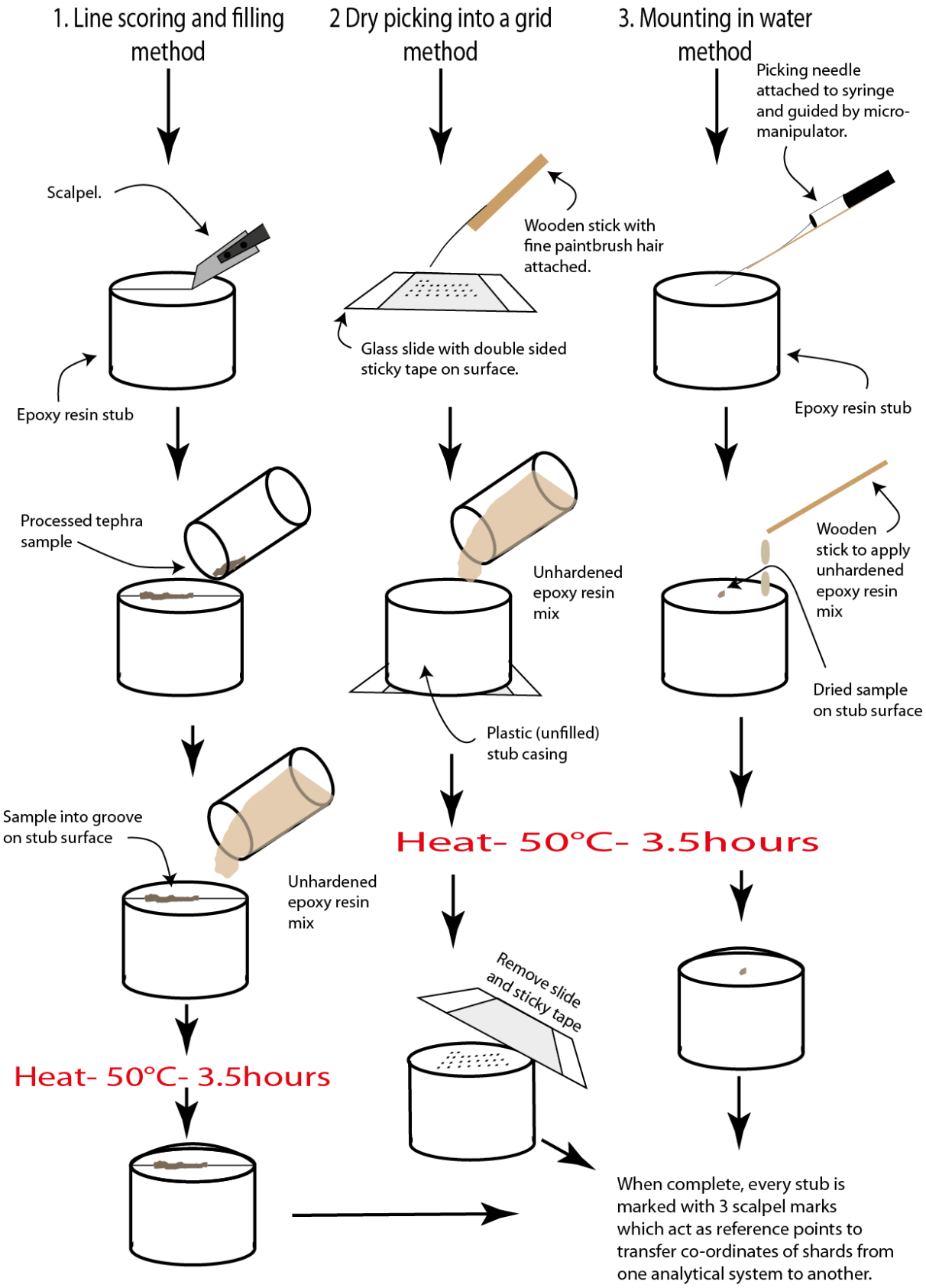

Figure 5.1 3 stub mounting methods developed and used in this investigation. All stubs were made using Specifix 40 epoxy resin.

2) Picking into a grid- If large enough (>100µm), the shards can be picked onto a stub using either a human hair or a hair from a fine paintbrush taped to a wooden stick. Under a low power binocular microscope the shards can be arranged in a grid fashion onto a piece of double sided sticky tape attached to a microscope slide. Once complete, the grid can be surrounded by a plastic ring, and backfilled with Specifix 40 resin to create the stub. Once set in the oven, the sicky tape and slide can be removed from the base of the stub, leaving behind the shards arranged in a grid. In this way, and with a reference point on the grid, the analyst knows which shard is which and can find them easily on any analytical system. This method is quick and neat, but also leaves out smaller shards which may contain important chemical information. The method is also only suitable for visible layers, as the shards in microtephra layers tend to be too small to be manipulated with a hair (the static is usually too great).

3) Mounting in water/picking in water - Extracted shards were mounted onto pre-flattened (to within 30µm) Specifix 40 resin stubs, transferred in a medium of water. The water was then dried off the stub on an aluminium tray on a warm hotplate. Layers with very low concentrations of tephra, or high concentrations of organic material remaining after processing, were mounted with the aid of a micro-manipulator and syringe to pick the shards and thus to ensure as pure a tephra sample as possible. Once covered with Specifix 40 and set, the samples were then sectioned and polished. The tephra shards were then analysed for major and (where possible) trace element concentration determinations. The scoring three marks on the surface of the polished stub with a scalpel allowed the same shards to be located on all analytical systems, via a Cartesian co-ordinates transfer. This method is the most efficient use of sample, as none is wasted. It also, by individual shard picking, allows different shards from one sample to be mounted onto different sample stubs, to resolve hypotheses relating morphology to chemistry.

In this investigation, all three of these methods were tried, to determine which of them is most convenient for the samples in question. Method 1 has the limitation of being only suitable for large volume samples. Method 2 has a restriction in terms of shard size (very small shards are difficult to manipulate with a hair). Method 3 is the most efficient in terms of material and time, and still fulfils all the requirements of a stub prepared for use with multiple analytical systems, and thus was employed for the majority of this investigation.

Polishing of samples and coating with conductive medium.

For EPMA analysis, shard surfaces must be very highly polished and flat, as accuracy relies heavily on a consistent take off angle for the X-Rays and a known volume of material being analysed. A flat surface is important for SIMS too, as this analytical method relies heavily on a known sample volume, which could be uncertain for a shard with a bumpy surface. LA-ICP-MS is in theory not so reliant on a flat shard surface, as in general the volume ablated is much greater than in the other two methods. In this investigation however, the shards were still highly polished for this analysis, as often the shards can be thin so the amount of material ablated is still relatively small. In these cases the component of the signal from an uneven surface would be larger than would otherwise be expected.

Samples were cut to produce a flat surface using a hand grinder, silicon carbine paper (of various grades) and inspection under a high power, reflective light microscope. Cutting was stopped when the sample showed an optimum number of shards with large surface areas at the surface of the stub.

After cutting the sample stubs were polished using a 9µm diamond paste and then a P4000 silicon carbide paper. They were then further polished using a 3µm diamond paste and 0.3 µm corundum (Al_2O_3) powder, until all scratches were removed from the shard surfaces. Care was taken to avoid "doming" of the shard surfaces; occasionally the resin can be preferentially removed from around the edges of the shards, leaving the shard surfaces domed. This imperfection can be seen as a thick line around the edge of the shard. Ideally, the line around the shard should be as thin as possible.

5.3. Geochemical analysis methods

Several methods are available for the geochemical analysis of tephra (Gill. 1997, Lowe. 2010). The selection of a method is a compromise between required elements required precision, availability and cost. Sections 5.4, 5.5 and 5.6 describe in detail the three methods used in this thesis. It is vital to understand the detailed mechanisms of analysis and data production for each of these methods to fully appreciate possible sources of uncertainty. An assessment of the uncertainty is crucial in an investigation which relies on the fair comparison of one sample with another.

Three analytical methods are used in this study and each of these is comprehensively described below. These are 1) Wavelength dispersive Spectrometry-Electron Probe

Microanalysis (WDS-EPMA), 2) Laser Ablation Inductively Coupled Plasma Mass Spectrometry (LA-ICP-MS), and 3) Secondary Ion Mass Spectrometry (SIMS).

5.4 Wavelength Dispersive Spectrometry-Electron Probe Microanalysis

The chemical composition of glass tephra shards can be determined by several methods. Each of these techniques uses the differing physical attributes of each of the elements to define that element's abundance within the sample.

5.4.1 WDS-EPMA Method Theory

The WDS-EPMA system is a versatile and widely used method of determining the elemental composition of many materials in Earth Science. The basis of the EPMA system is that a generated electron beam interacts with the sample surface, to produce X-Rays. These X-rays can be detected, and are characteristic of certain elements present within the sample. The counts of the X-Rays at either different wavelengths (Wavelength Dispersive- WD EPMA) or energies (Energy Dispersive-ED EPMA) represent the abundances of their associated elements. This investigation uses the WDS system and not the EDS system, as it has higher peak to background ratios (therefore lower detection limits) and better spatial resolution in the spectra (therefore more accurate determinations of elemental concentrations) (Reed 1996).

EPMA is fundamentally a simple system. Electrons are generated by an electron gun through the process of thermo-emission. These electrons are directed towards, and focused upon, the sample surface (the tephra shard). The sample then has a volume of interaction, comprising the area of focused electrons on the surface, and a "bulb shaped" volume below this. Within this volume, interactions of the electrons with the atoms of interest in the sample produce X rays. These X-Rays are counted by a spectrometer and these counts are then converted into a %wt value for each element by a computer.

A schematic diagram of the main body of the EPMA is shown in figure 5.2.

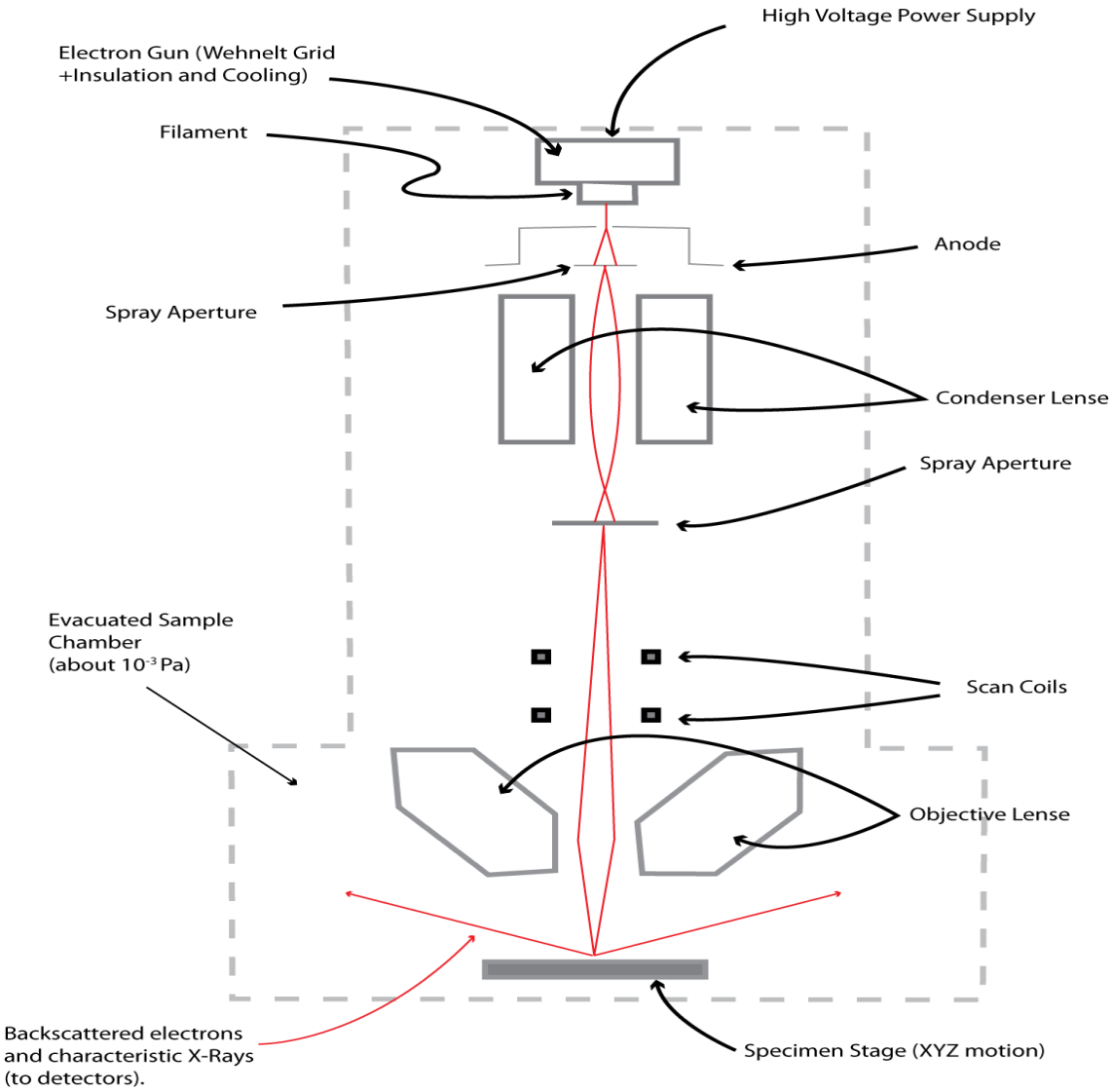

Figure 5.2 A schematic diagram of the WDS-EPMA setup. The function of each of the component parts is described below.

1.a) **Electron Gun.**

Free electrons are generated by the electron gun, through the process of thermo-ionic emission from the filament. This filament is made from Tungsten and heated to about 2400°C. At such a temperature the electrons have a greater energy than that which binds them to the filament surface. They are accelerated by the anode (which provides a voltage gradient together with the Wehnelt Grid). The resulting stream of electrons is the electron beam.

To create X-Rays from the sample, the voltage needs to be approximately 15-30keV. This beam also needs to be high enough to achieve a stable beam current but not too high as to

burn out the filament too frequently. Thus there is a compromise between beam stability and filament temperature (Gill 1997, Ghorbel et al. 1995). The operation of the filament voltage between 15 and 30keV means that the beam current is saturated (stable) and the filament has an optimum lifetime.

1.b) Focusing Lenses.

The "lenses" to concentrate the beam onto a spot (perhaps 10-20µm diameter) are actually cylindrical electromagnets. These create an electric field which focuses the beam at various points in the path from the Tungsten element to the sample surface. In addition to the condenser and objective lenses, the set up includes two (or sometimes more) spray apertures. These are positioned to reduce spherical aberration. This is the effect of electrons which pass closer to the electromagnet-cylinder being refracted more than those which pass closer to the centre. This creates a poorly focused beam. Thus, removing parts of the beam which have resulted from spherical aberration improves the focus of the beam on the sample.

The arrangement means that the focal length of the beam is controlled by the current in the objective lens, while the beam current can be controlled by the current in the condenser lens (combined with the Spray Aperture). These principles are shown in figure 5.3 below.

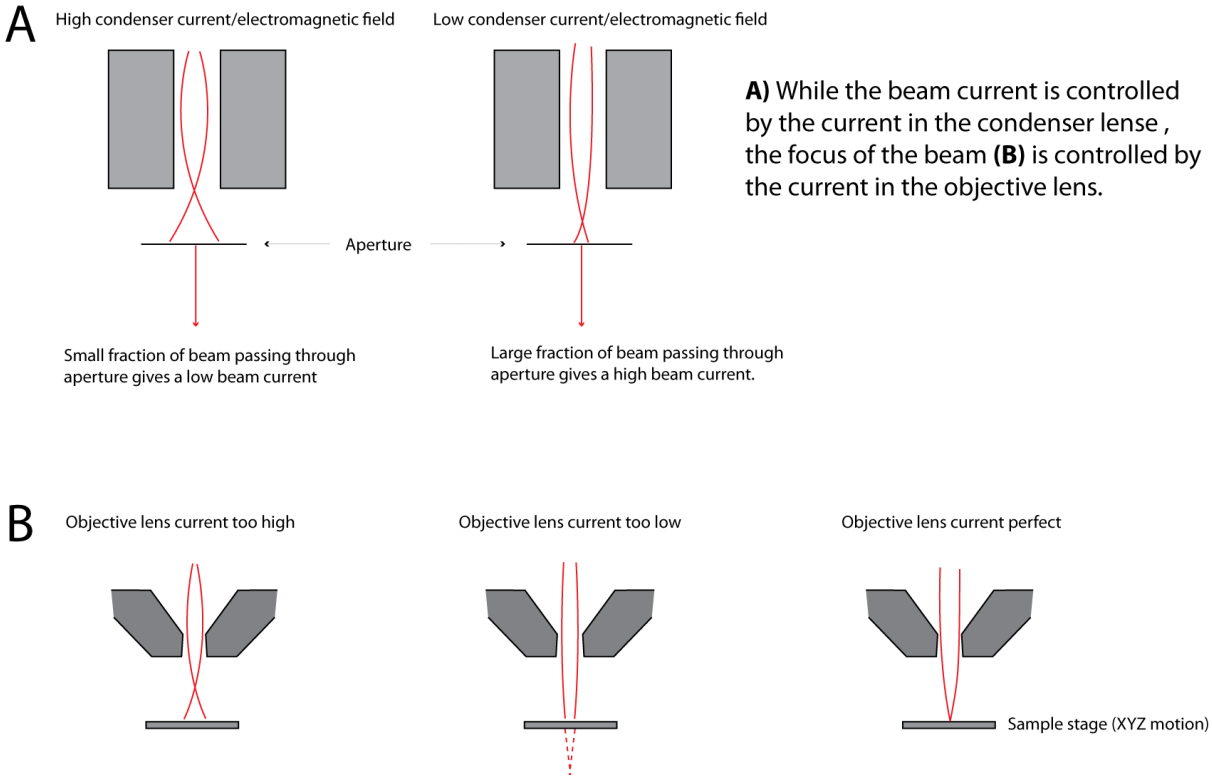

Figure 5.3, schematic diagram of the focusing of the electron beam on the sample surface. Good focus is essential for high quality data acquisition.

1.c. Interaction of the electron beam with the sample

The entire operation of the EPMA system depends upon the interaction of the electrons with the sample. The inference is that the counts detected by the X-Ray detectors are basically a function of the chemical composition of the sample. The X-rays are produced by the physical interaction of the electron beam with the atoms of the sample. It is therefore necessary to understand these physical phenomena, at least conceptually.

Back-scattered Electrons.

A small fraction of the incident electrons do not enter the sample at all. The outer surface of the sample is effectively a shield of electrons. This causes a small proportion of the electron beam to simply bounce back off the surface. This is just a consequence of the surface and the beam having effectively the same charge. As the efficiency of this repulsion increases with mean atomic number of the area under the beam (Z), these *Backscattered Electrons* can be used to produce a first approximation of the composition of the surface of the sample. This effect can be used to pick out compositional anomalies such as inclusions

within tephra shards (which should in theory be homogenous). Most modern machines are equipped with Backscatter Electron imaging equipment.

Interactions of the beam and the sample

Most of the electrons in the beam penetrate the sample surface and follow statistically random trajectories within the sample; consequently they lose energy and are eventually deposited in the sample matrix. Ghorbel et al. (2005) describe the numerical modelling of these electrons within the sample. They follow essentially random pathways (Monte Carlo Modelling), but overall define a bulb shaped "X-Ray generation volume", from which the X-Rays the analyst is interested in are produced (summarised in fig 5.4.).

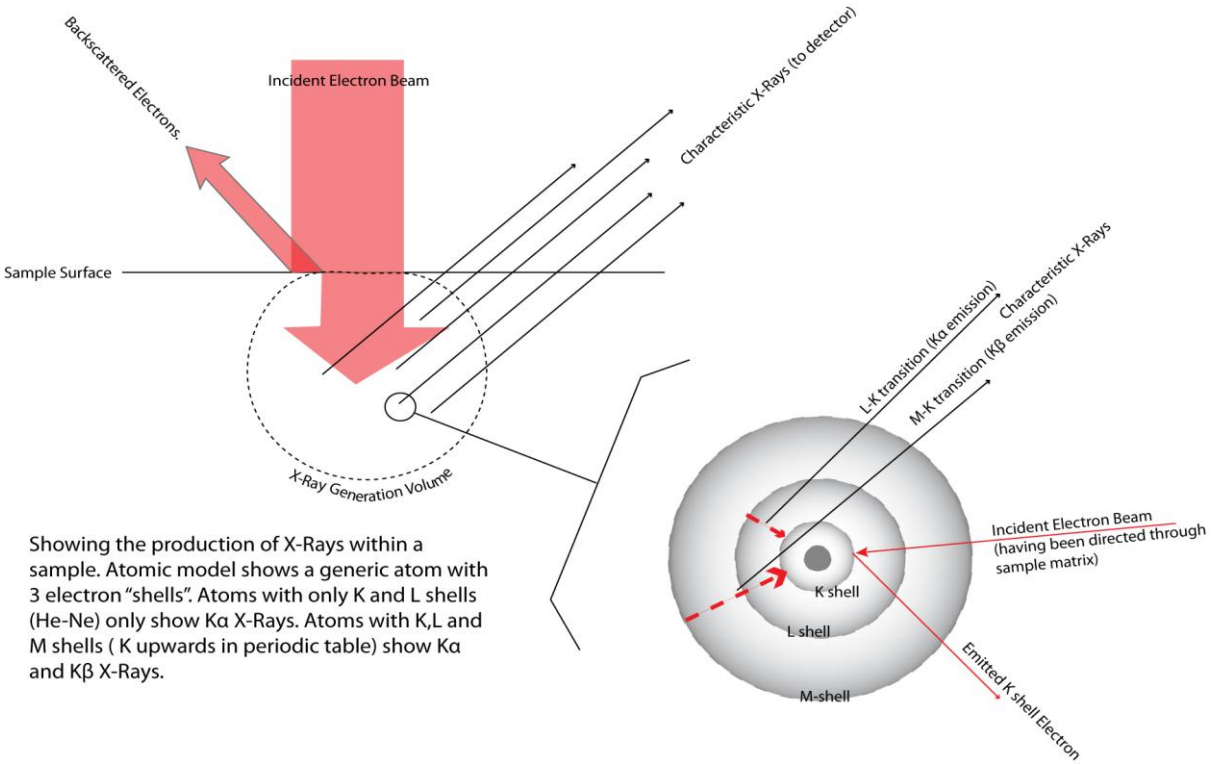

Figure 5.4. The production of X-rays within a sample. The conversion of the resulting secondary X-Rays into totals for each of the major elements relies on assumption about these processes.

The production of X-Rays from the sample as a whole is more complex than that shown in the simple atomic model of figure 5.4. Assuming the incident electron beam remains stable and the beam remains focused on the sample surface, the signal recorded by the X-Ray detectors is a function of:

1) The amount of electrons back-scattered which is dependant on the charge on the surface of the sample and the mean atomic mass (Z);

2) Secondary X-Rays produced by interaction of the primary X rays with the ambient sample matrix (dependent on the composition of the matrix, and the path length of the X-Rays in within the sample); and
3) Absorption of the primary X-Rays by the ambient sample matrix (dependent on the composition of the matrix and the path length of the X-Rays within the sample).

These three "matrix" effects must be corrected for if an accurate qualitative assessment of the composition of our sample is to be attained. Unfortunately all three effects are functions of the chemical composition of the sample, which is exactly what is being determined. The answer to this problem is iteration, through a series of statistical corrections called the ZAF corrections (Z=mean atomic mass, A= Absorption, F= Fluorescence). This ZAF correction assumes that the path length of the produced X-Rays in the sample is known with a low uncertainty, and is thus one reason why the sample should be polished as flat as possible during preparation. ZAF correction algorithms are either integral to the software accompanying a machine, or are provided online.

Other Phenomena in EPMA.

1) Heat build up.

With electrical energy from the beam being concentrated upon a small area of the sample (maybe 10µm diameter), a large amount of heat can build up. This is particularly true for samples with poor thermal conductivity. Temperature rises can range from 1°C to >300°C, depending on the beam current, spot size and analysis time (Potts 1987). The larger the temperature rise, the more the risk of structural alteration and element mobility within the sample. These changes are thermal effects.

2) Thermal Effects.

Materials most likely to be affected seriously by thermal effects are those which contain appreciable amounts of structural water (clays, hydrated minerals or shards), structural CO_2 or other gas (tephra shards may contain S or CO_2 in the matrix), or glass/minerals with high amounts of mobile cations (notably K^+ and Na^+).

The effect on the calculated elemental values from the loss of water and other volatiles through heating is intuitive. These volatiles escape through heating and the signal from the remaining matrix elements is relatively increased. Element mobility is not such a simple

concept. Generally the inferred concentrations of these elements decreases with heating (Neilsen and Sigurdsson 1981, Spray and Rae 1995, and Morgan and London 1996), simply because of a local thermodynamic disequilibrium. This effect must be considered however, together with the build up in charge within the X-Ray generation volume which could *attract* cations to the beamed volume.

The significance of decomposition due to thermal effects depends upon the composition of the glass or mineral (Potts 1987), and the amount of heating (the time exposed and the beam current, Nielsen and Sigurdsson 1981). This is shown diagrammatically below in figure 5.5 for various minerals.

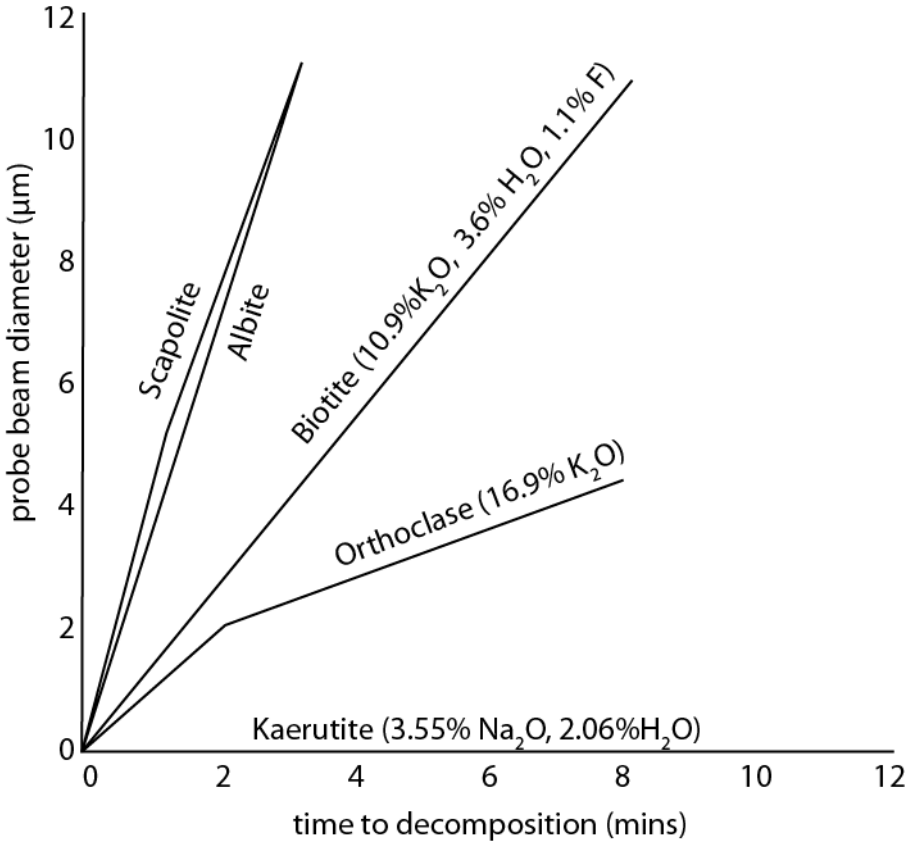

Figure 5.5 the decomposition of mineral structures dependent on probe diameter and time of exposure to the X-Ray beam, assuming a constant beam current. Unfortunately timescales for the decomposition of glasses have not yet been defined.

3) Contamination.

Samples should be clean, flat and, if non-conducting, coated with a conducting medium. Contamination can still however be a problem. The organic oil used in the vacuum pumps in the microprobe is present in trace amounts within the sample chamber. This oil is

cracked by interaction with the electron beam, and the Carbon can then be absorbed into the surface of the sample, building up at a rate of about 0.1-1.0nm per second (Cambell and Gibbons 1966 and Ong 1966, in Potts 1987). This contamination is mostly an issue when analysing light elements, because of absorption of the low energy X-Rays associated with these elements. It is reduced by installing a conducting device such as a copper plate or bar adjacent to the sample to deflect the condensation of these Carbon vapours.

5.4.2 Data production from the WDS EPMA

Calibration and analytical standards

Before the analysis of a batch of 7 samples, the WDS EPMA is calibrated to an external reference (primary) standard. This reference standard is different for each of the 9 (or 11) elements which are to be analysed. These standards are mounted on a single primary standard block, and are described in table 5.1. A suite of secondary standards is also available, together with an accepted range of values for each of the elements, in order to test the calibration. These secondary standards are also analysed regularly (every 20-30 analyses, or every 2-3 hours) during the analytical run to detect any drift or monitor changes in performance in the instrument. Secondary standards used are shown together with their accepted values in table 5.2.

Oxford University (RLAHA) Jeol8600 superprobe (4 spectrometers).		
Acceleration Voltage		15kV
Current		6nA (15nA for calibration)
Element analysis times	Na	10s
	P+Cl	60s
	Si,Ti,Al,Mn,Mg,Ca,Fe,K	30s
Beam Diameter		10µm
Correction Procedure		PAP
Primary Standards	Na	Wollastonite
	Ti	Rutile
	Al	Corrundum
	Fe	Haematite
	Mn	Fowlerite
	Mg	Periclase
	Ca	Wollastonite
	Na	Jadite
	K	Orthoclase
	P	Apatite

Table 5.1 Operating conditions and primary standards for EPMA analysis (Jeol8600 superprobe).

MPI-DING StHs6/80-G: fused andesite glass, Mt St Helens

	SiO2 %m/m	TiO2 %m/m	Al2O3 %m/m	FeO(t) %m/m	MnO %m/m	MgO %m/m	CaO %m/m	Na2O %m/m	K2O %m/m	total	P2O5	Cl (ppm)
EPMA average:	63.12	0.70	17.75	4.37	0.07	1.96	5.30	4.39	1.30	98.96		
EPMA stdev:	0.32	0.01	0.47	0.10	0.02	0.05	0.06	0.19	0.03			
EPMA min	62.80	0.69	17.28	4.27	0.06	1.92	5.24	4.20	1.27			
EPMA max	63.44	0.71	18.22	4.46	0.09	2.01	5.36	4.59	1.34			
All Systems Preferred value:	63.70	0.70	17.80	4.37	0.08	1.97	5.28	4.44	1.29	99.63	0.16	231.00
All systems uncertainty (95%CL)	0.50	0.02	0.20	0.07	0.00	0.04	0.09	0.14	0.02		0.02	50.00
All systems max	64.20	0.72	18.00	4.44	0.08	2.01	5.37	4.58	1.31		0.18	
All systems min	63.20	0.68	17.60	4.30	0.07	1.93	5.19	4.30	1.27		0.15	

MPI-DING ATHO-G: fused rhyolite glass, Iceland

	SiO2 %m/m	TiO2 %m/m	Al2O3 %m/m	FeO(t) %m/m	MnO %m/m	MgO %m/m	CaO %m/m	Na2O %m/m	K2O %m/m	total	P2O5	Cl (ppm)
EPMA average:	75.67	0.23	12.23	3.26	0.11	0.10	1.68	3.31	2.65	99.24		
EPMA stdev:	1.08	0.03	0.25	0.13	0.01	0.01	0.07	0.58	0.20			
EPMA min	77.84	0.29	12.72	3.52	0.13	0.11	1.82	4.48	3.04			
EPMA max	73.50	0.18	11.74	2.99	0.08	0.09	1.54	2.15	2.26			
All Systems Preferred value:	75.60	0.26	12.20	3.27	0.11	0.10	1.70	3.75	2.64	99.62	0.03	2430.00
All systems uncertainty (95%CL)	0.70	0.02	0.20	0.10	0.01	0.01	0.03	0.31	0.09		0.00	
All systems max	76.30	0.27	12.40	3.37	0.11	0.11	1.73	4.06	2.73		0.03	
All systems min	74.90	0.24	12.00	3.17	0.10	0.09	1.67	3.44	2.55		0.02	

Table 5.2. Secondary glass standard average values and 2 standard deviation uncertainties for Atho-G and StHs6/80, from Jochum et al. (2006), from both WDS-EPMA only, and from all analytical systems combined (including highly precise systems such as ID-TIMS) for the analysis of magmatically evolved glass shards by WDS-EPMA. These two standards were chosen as the matrix is similar to that of the material being analysed (mid-high Silica volcanic glass).

Accuracy

After the microprobe was calibrated, the calibration was tested using the secondary standards. This process incorporates the PAP matrix correction (as applied to the unknown samples) and is thus used as an assessment of the accuracy of the EPMA. As the accepted MPI-DING values for the secondary standards (table5.4.2) are a conglomeration of the values measured by different laboratories, it is reasonable to use them as a communal assessment of the "true" values. However, Jochum et al. (2006) note that there are some minor, systematic differences for the measured values of certain elements, between different labs, on the same secondary standards. Such differences could give the illusion of a real compositional difference between two samples, or conversely show two compositionally different samples to be the same. Thus, in this investigation, which relies on the chemical discrimination (or otherwise) of two or more samples, where possible, all samples obtained from the sediment cores, and used in the reference database were analysed using the same WDS-EPMA system (Oxford University-RLAHA Jeol8600 superprobe). One sample was an exception due to the very small shard size involved. This was sample ODP975 (0.04) which was analysed using a 3µm beam on the Cameca SX100 probe at the University of Edinburgh. Details of this analysis are given in the results section (chapter 6).

Precision

There is no way to assess the precision of an individual, unknown tephra shard, because only one analysis of the shard can be made. The standards are therefore used to assess the overall precision of the WDS-EPMA. The precisions of the standards, over the entire period of the data acquisition for this project, are shown visibly in appendix 1.

EPMA Analytical procedure

Sample stubs were prepared and highly polished as described previously. Sample stubs were carbon-coated in a spatter coater. This carbon coat is necessary to dissipate the charge which would otherwise build up on the sample surface during bombardment with electrons. The samples (up to 7) were then mounted into the EPMA sample holder with both the primary and secondary standards (tables 5.1 and 5.2). Once loaded into the sample chamber of the EPMA, and the vacuum restored (fig. 5.2) the analyst then selects individual tephra shards for analysis, and spots on the secondary standards (to monitor the

performance of the microprobe). The coordinates of these shards and standard spots, when selected, are stored on the computer. Shard selection was made with the LA-ICP-MS in mind, thus larger shard surfaces were selected for the first 20 hits of a sample (to subsequently accommodate the minimum 25µm laser beam), and the last 10 hits were selected on smaller surfaces (indifferent to this 25µm limit), to ensure that the full range of shard sizes were accounted for with the EPMA.

Once this process is complete, the EPMA is started and left to run overnight. The coordinates of three points prepared on the surface of each stub were also recorded. These coordinates allow the transfer of the shard coordinates to a different system (such as the LA-ICP-MS). In this way the major and trace element analyses are, where possible, taken from the same shards and thus can be directly related to one another.

5.4.3. EPMA Data production and filtering.

For compositionally simple analytes (such as the primary standards- in table 5.1), the relationship between the concentration of an element and the intensity of the X-rays detected at each element's peak X-Ray spectrum is a nearly linear relationship. For compositionally complex samples (such as natural glasses) however, this relationship is not simple. As the sample is composed of many different elements, there is a "matrix effect" component to the X-ray counts. This is the reason why, during the calibration of the machine, secondary standards of a similar composition (matrix) to the samples to be analysed must be used (table 5.2). A matrix correction calculation is employed at this stage.

There are two correction algorithms widely used in the literature; the ZAF correction and the PAP correction. Hunt and Hill investigated the effect of using each of these two algorithms on the same analyses data, to produce two sets of data. The results are significantly different for each of the procedures and are shown in figure 5.6. The difference of 1% in silica shown here could be very significant in the comparison of two tephra samples, particularly as Si is used as an internal standard for the correction of bias in LA-ICP-MS analysis (see section 5.5).

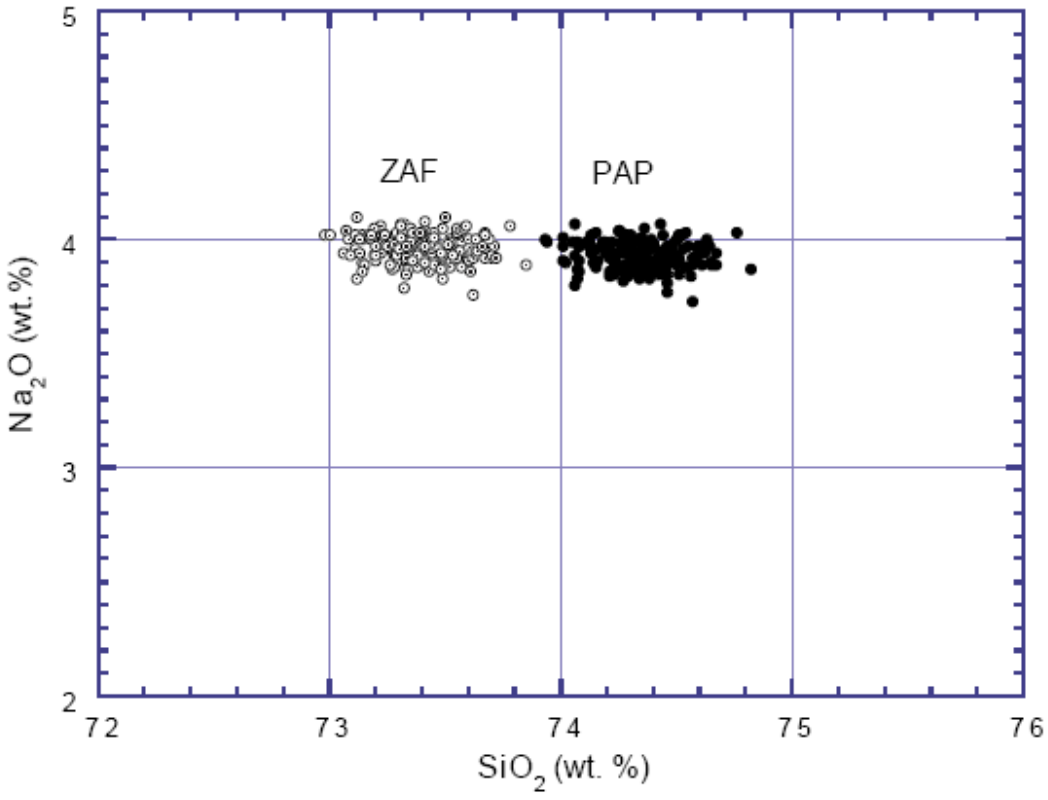

Figure 5.6. (Hunt and Hill 1998). Comparison of the final wt% oxides using ZAF or PAP corrections, for the Lipari obsidian secondary standard.

In this investigation the PAP correction algorithm was used consistently for all the the marine core samples to ensure a valid comparison to proximally derived geochemical data which was also produced using this method.

Data filtering.

Once the concentrations (in %Oxide) have been calculated for each of the analyses, the data can be filtered to remove 1) data yielding low analytical totals, 2) analyses containing a component of a mineral (rather than glass), or 3) samples bracketed by standards which fall outside the accepted range for the "EPMA only" standards (table 5.2, appendix 1)

1) Low analytical totals

1) Low totals can in theory be due to

a) Poor polish; b) Poor focus of the electron beam.; c) Charge build-up; d) Migration of Na; e) Hitting a mineral within the glass; f) Hitting a vesicle or the edge of a shard; g) high water contents.

If the low totals in the samples were due reasons a,b,c or d this effect would be seen in the secondary standards too, as they are subject to the same mechanisms of polishing, focus and charge dissipation and would be equally as susceptible to Na migration, since they have a similar matrix. This is not the case, because as the standards which are essentially water-free (Atho-G= 0.014%, StHls6/80-G= 0.025% H_2O), nearly always have totals of ~99%. It is therefore estimated that only ~1% of the difference in the total from 100% in the tephra samples could be due to reasons a-d. Factor e can be avoided by using the electron backscatter facility on the microprobe to identify phenocrysts, and also, should one be hit unwittingly, by the identification of anomalously high values of particular elements in the analysis results. Reason F can be avoided too, through careful selection of, and aim onto, the shard surface- vesicles and the edge of the shard are clearly identifiable under the focusing microscope.

It is thought therefore that most of the low totals (90-100%) are due to the un-quantified water/volatile content in the shards. Some studies advocate the removal of samples which show analytical totals of less than 95% (e.g. Wulf et al.2004, Pollard et al.2006, Turney et al.2008, Bourne 2010,), This cut off is arbitrary, however and has no geological basis. This assertion is supported by quantified water contents of up to 8.76% in other tephra studies (Pearce et al.2008 and references therein). Clearly removing analyses with totals of less than 95% in these cases could remove valid and valuable data. As a result, all glass analyses with totals greater than 90% in this investigation are included in the datasets. This cut off of 90% is based on the empirically derived value that 10% of the analytical total can be lost due to un-quantified water contents (either primary or secondary- Yang and Kirkpatrick 1990, Shane 2000, Pierce et al.2008,) and is consistent with the procedures adopted by WoldeGabriel et al. (2005) and Pierce et al. (2008).

2) Removing analyses with mineral components.

Analysis of mineral inclusions can usually be avoided using the backscatter electron facility on the EPMA. However, occasionally a mistake can be made by the operator, or a mineral can be hidden just under the surface of the glass. Such analyses are unwanted in a comparison of glass-to-glass chemistry. They can be identified by anomalously high values of Al, K and Na (feldspars or amphiboles), Ca or Fe (pyroxenes) or Si (diatoms, or quartz), and removed.

2) Detecting systematic EPMA inaccuracy.

Occasionally the performance of the EPMA may drop over the time of the sample run. This deviation can be detected by using the analyses of the secondary standards. Where the data obtained from the secondary standards fall outside the accepted EPMA value ranges, the analyses they bracket should be rejected. Of course, it may be that some of the elements fall outside the EPMA accepted limits while others are acceptable. This is particularly the case for the lower abundance elements such as Mn , Mg and Ti. In this situation, these elements should be used with great caution in any correlations which may be tested by them.

4) <u>Normalisation of data to 100%.</u>

All analyses in this study are recalculated to an anhydrous basis of 100% to remove the dilution effect of secondary water, and restore the chemistry back to as near as possible- the pre deposition ratios.

Normalising to compensate for primary (magmatic) water

There has been considerable debate in the literature as to whether or not the analyses should be normalised to 100% (Pollard et al.2007, Pierce et al.2008). It is implicitly assumed in comparing data from two samples that the primary (magmatic) water content should be similar in all shards from one eruption, just as it is assumed that the concentrations of each element are similar for all shards from one eruption. Thus, normalising to 100% for primary water content will adjust both samples by the same amount, and therefore not have any effect on whether or not they match (table5.3)

Normalising to compensate for secondary (ambient) water.

It is not necessarily so that all tephra shards from an eruption will contain the same amount of secondary (absorbed from surroundings) water, as deposits in different environments will have been subjected to different ambient conditions (c.f. shards on the floor of the sea to shards in a cave setting.) Hence normalising to 100% to remove this component of the shortfall from 100% may adjust the elemental values by different amounts in two separate deposits, depending on the context in which the shards have been preserved. However, this adjustment is necessary to enable the shard obtained from different sedimentary environments to be compared on their pre-depositional geochemical basis. This statement

is valid as the hydration of glass, up to about 10% H_2O, is a dilution process rather than an alteration process (Shane 2000, Pierce et al.2008, Yang and Kirkpatrick 1990) and so the relative proportions of the elements should not have changed.

After this process was complete, the data (both normalised to 100% and non-normalised) was compiled in a personal database, before the non-normalised data was uploaded to the online communal database for the RESET consortium. This integrated database provides the facility to assign an identity to the eruption, once the analyst has correlated it to a proximal setting or other known and named tephra horizon. There is a five-star rating system for the correlations which allows the analyst to assign a degree of certainty to the identity of each geochemical sample- 5stars indicated near certainty in the correlation- 1 star indicates only that the correlation is hypothetical and that there are significant problems with the tephra layer's identification.

Senario	Distal tephra water content		Analytical total for distal tephra	proximal tephra water content		Analytical total for proximal tephra	Outcome if Normalised to 100% i.e. all water content ignored.	Outcome if raw values are used i.e. primary and secondary water included.
1) proximal and distal deposits have no hydration	Primary -1%	Secondary- 0%	99%	Primary -1%	Secondary- 0%	99%	Correct Match	Correct Match
2) proximal deposit has no hydration- distal has some hydration.	Primary -1%	Secondary- 6%	93%	Primary -1%	Secondary- 0%	99%	Correct Match	Incorrect distinguishing of distal and proximal deposits.
3) proximal and distal deposits have different amounts of hydration	Primary -1%	Secondary- 6%	93%	Primary -1%	Secondary- 3%	96%	Correct Match	Incorrect distinguishing of distal and proximal deposits.
4) proximal and distal deposits have the same amount of hydration	Primary -1%	Secondary- 6%	93%	Primary -1%	Secondary- 6%	93%	Correct Match	Correct Match

Table 5.3 Four theoretical scenarios applied to the proximal and distal deposits of one eruption. Assumptions are 1) that the initial composition of the proximal and distal glass deposits is identical (a central assumption of tephrostratigraphy), 2) that the primary (magmatic) water content in the glass is the same in all cases, and 3) that the uptake of secondary water (up to 10% total H_2O) does not affect the composition of the glass, and acts only as a diluting effect (see Yang and Kirkpatrick 1990).

5.5 LA-ICP-MS Laser ablation inductively coupled plasma mass spectrometry.

5.5.1 LA-ICP-MS Theory.

Laser Ablation Inductively Coupled Plasma Mass Spectrometry is the technique used here for determination of the trace element abundances in tephra shards. The general principle of mass spectrometers, regardless of the sample input procedures, is that they distinguish ions of particular elements on their mass: charge ratio. The inductively coupled plasma is the mechanism by which the sample is converted from molecular and particle form, into an ionic form suitable for mass spectrometry. Laser ablation removes a small part of the sample by vapourisation and then transfers this sub-sample into the plasma. This method was pioneered by Gray (1985) and Pearce et al. (1992).

LA-ICP-MS is particularly well suited to the analysis of tephra shards. The shards may have an area of only 200µm^2 or so, and are of course in the solid state. In comparison to the SIMS system (Secondary Ion-Microprobe Spectrometry), the LA-ICP-MS system is cheaper, quicker and more readily available. It should be noted though that the procedure requires a known internal standard. In this project therefore the analysis by EPMA (non-destructive) was performed prior to the LA-ICP-MS measurement to derive an internal element standard (in this case SiO_2) for the destructive LA-ICP-MS procedure. The general layout of the LA-ICP-MS is shown schematically in figure. 5.7.

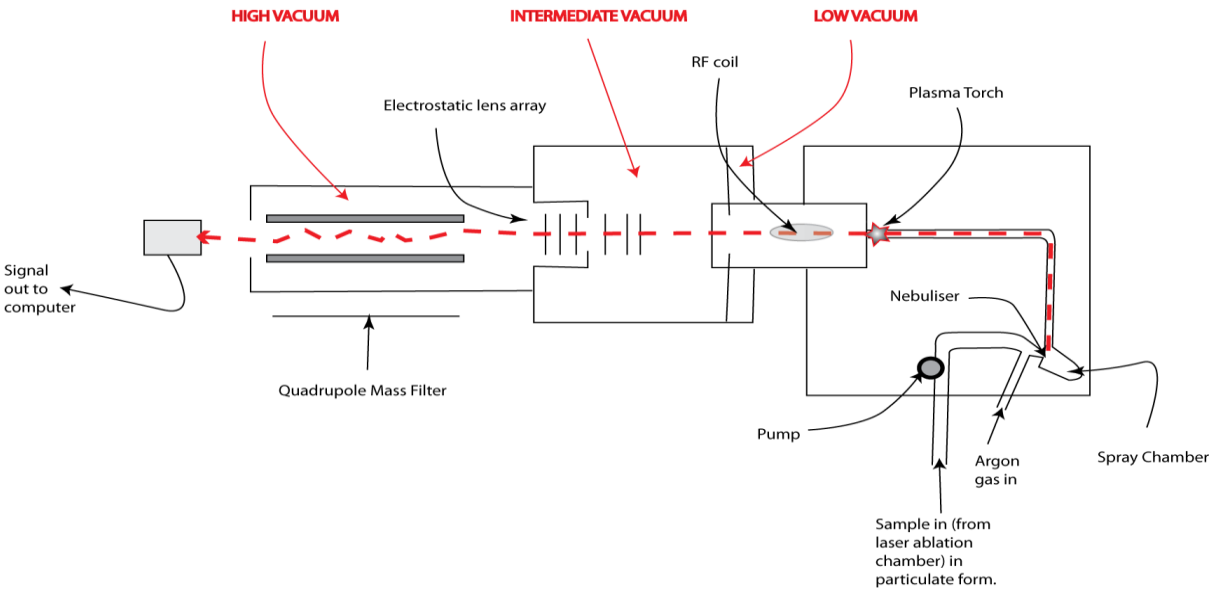

Figure 5.7 Schematic representation of an LA-ICP-MS system, starting from the injection of the sample from the laser ablation chamber.

The ICP-MS system was developed in the early 1980's (Houk et al.. 1980), with the addition of solid sample introduction by laser ablation occurring in 1985 (Gray 1985). The basic principles can be understood with reference to figure 5.7: a schematic layout of the LA-ICP-MS.

The laser removes a small part of the sample by ablation. This is pumped to the spray chamber, which acts as a sorting area, preventing larger droplets/particles (>10µm) from entering the plasma torch (Schaldach 2003). This plasma torch is held at approximately 6000°C (Pearce et al. 2007) and atmospheric pressure. It is within this plasma that the sample disassociates into its constituent ions.

Part of the core of the plasma is siphoned off through a nickel cone (the sampling cone), by a pressure difference imposed by vacuum systems. This plasma sample is focused by a series of electrostatic lenses into the mass spectrometer.

Many laser ablation systems use a quadrupole mass spectrometer, which contains four rods, each exerting an electric field onto the ions if the sample. The ion separation is achieved by the mass/charge ratio (m/z). The system produces a mass band filter so that only ions in a limited m/z range are transmitted to the detector. Continuous variation of the electric field within the quadrupole means that many elements can be measured simultaneously.

While the basic principles are relatively simple, there are several complications which must be considered in the design of the machine, and by the analyst in its set up.

Element fractionation effects.

There are two places where element fractionation can occur in the LA-ICP-MS system. LA works by vaporising the sample. Potentially, therefore, some elements may be more easily ablated and thus preferentially fractionated from the sample. Fractionation may also occur in the plasma. The technique assumes that all the elements which enter the mass spectrometer do so in their ionic form. If this ideal condition is not satisfied, elements will have either the wrong mass or the wrong charge (or both) to be allowed through the mass spectrometer to the detector (see sections on polyatomic ions and refractory oxide ions below).

Fractionation during ablation.

The count rate for an element during LA-ICP-MS can vary considerably depending on whether or not the laser is kept on one part of the sample (static measurement) or is moved over the sample surface during analysis (raster measurement) (Pearce et al. 2007). In the latter case, the laser will always be hitting fresh, unheated sample. In the former, there may have been partial ablation and heating previous to the period of analysis. For large samples, the surfaces can be treated with a "pre-ablation" phase, as the signal tends to stabilize after about 2 minutes of exposure to the laser. For the analysis of cryptotephra shards however, unfortunately there is often insufficient material for this. They may be less than 100µm diameter and even less than this in thickness, due to the cutting and polishing preparation. The analysis of micro-tephra is thus inevitably complicated by fractionation effects during the ablation process.

Polyatomic Ions.

In theory the plasma should have sufficient energy to prevent the ions flocculating back into atomic forms. In practice, however, *polyatomic ions* can form from the most abundant ion species. In LA-ICP-MS these will generally involve Argon as this is the analytic support gas. Examples are ArO^+ or ArH^+. The formation of these polyatomic, ionic species is determined by the internal enthalpy of the plasma (Zahran et al. 2003). This is a function of the internal energy (temperature and composition dependent) the volume of the plasma and the pressure gradient confining the plasma. Thus the operating conditions of the plasma should ideally be kept in a state such as to minimise the potential for polyatomic ion formation.

Formation of polyatomic ions can lead to interferences with the counts for elements with the same atomic mass. Fortunately these interferences generally apply to the light elements with a m/z below 40; no significant species are produced above m/z=80 (Jarvis 1997). The m/z ratio of 40 is the Ar dimer (Ar_2^+), which is of course the carrier gas for the ICP-MS. The elements most severely affected during routine analyses are V and As (in the presence of Cl). S can also be problematic.

Refractory Oxide Ions

Spectral interferences can be caused by oxide ions. These are in the form MO^+, MO^{2+} and MO^{3+} where M is any particular offending element. As they all contain oxygen, the interference forms at 16, 32 or 48 mass units above the mass number of the conjoined

element. The plasma is usually stable enough in modern instruments to avoid refractory oxide abundances of more than 1.5% (Oxide to element M abundance) (Jarvis 1997). This is therefore more of a problem when analysing both major and trace elements in a single runs; as oxides of the major elements may interfere with measurements of the low abundance trace elements. This effect is an important consideration in tephra studies as a major element is used as a standard. REE often form significant refractory oxide ions (Barrat et al. 2007).

5.5.2 Data Production and Analytical setup.

The instrumentation and operating parameters for the Laser Ablation system at Royal Holloway, University of London are shown in table 5.4. Tephra studies are generally conducted using a UV laser as this gives the best absorption in natural glasses.

Laser Parameters: Resonetrics 193nm ArF excimer.	
Energy density on target.	3.0J/cm^{-2}?
Pulse duration	20ns
Repetition Rate	5 Hz
Laser spot size	25-44µm appropriate to the shard surface area
He cell gas flow	850ml min^{-1}
N_2 trace gas flow (after cell exit)	6ml min^{-1}
Sampling strategy	Spot analysis
ICP-MS Tuning strategy	Raster analysis
count time on sample	40s
blank before + after sample	20s
ICP-MS Settings: Agilent 7500.	
Plasma gas flow	15L min^{-1}
Carrier Gas flow	Optimised between 0.40 and 0.50L min^{-1}
RF power	Optimised between 1150 and 1200 W
Lens	Ce
Cones	Ni

External Callibration Standard	NIST612
Bias Correction standard	StHs6/80-G
Internal Standard Isotope	^{29}Si
Isotopes Analysed	^{29}Si, ^{43}Ca, ^{45}Sc, ^{47}Ti, ^{51}V, ^{55}Mn, ^{60}Ni, ^{85}Rb, ^{88}Sr, ^{89}Y, ^{90}Zr, ^{93}Nb, ^{138}Ba, ^{139}La, ^{140}Ce, ^{141}Pr, ^{146}Nd, ^{147}Sm, ^{153}Eu, ^{157}Gd, ^{163}Dy, ^{166}Er, ^{172}Yb, ^{175}Lu, ^{181}Ta, ^{208}Pb, ^{232}Th, ^{238}U.

Table 5.4- Analytical setup parameters for the LA-ICP-MS used in this thesis.

Sampling method for LA-ICP-MS

This investigation adopted the principle of generating data from single tephra shards EPMA values, rather than using average internal standard values. The data obtained from the LA-ICP-MS were therefore obtained from the same shards as those analysed on the EPMA. This is particularly important when there is a broad range of chemistries is displayed for a sample, or where two chemically-distinct tephras appear to have been mixed (by sedimentary processes, or through synchronous deposition in the same record). In order to achieve this 'single-shard' rule, two approaches were employed. For larger shards (greater than perhaps 250µm), it is possible to pick the shards onto a piece of sticky tape and arrange them into a grid, prior to their preservation on a resin stub (fig. 5.1). This grid together, potentially, with photographs of each EPMA analysed shard allows each shard to be identified by its position, and thus easily relocated for measurement using several different analytical systems. This approach is often used with proximal volcanic samples (Pearce et al. 1999, or Tomlinson et al. 2010).

It is not possible to pick very small shards (20-250µm) in this manner and transfer them into a coherent grid on a piece of sticky tape. The shards are too small to manipulate with a pair of tweezers or needle and the relief on the tape surface is often greater than the depth of the shards, meaning that the shards will all be at different heights for cutting. Furthermore, the application of the resin is likely to displace the shards from their predefined places. To circumvent this problem, it is possible to mount the shards directly onto a set resin stub (as used routinely in distal tephrochronology- e.g. Bourne et al. 2010). The sectioned stub can then be marked with three reference points, using a scalpel. These three reference points can be inserted into a Cartesian coordinate transfer spread-sheet (kindly provided by N. Charnley of the University of Oxford) to convert the coordinates

recorded for the shards on the EPMA to those on the LA-ICP-MS system (or any other system). The coordinate transfer accounts for any rotation of the stub between the different systems and the different scale used by the LA-ICP-MS or SIMS apparatus. The LA-ICP-MS or SIMS coordinates of the shards can be calculated as soon as the coordinates for the reference points on both systems are known, allowing the shards to be easily relocated. This latter method is the one employed most frequently in this investigation.

Acquisition of data from the LA-ICP-MS.

The LA-ICP-MS is conceptually a simple system. The sampling unit (the laser ablation unit) is connected to the analysis unit (the mass spectrometer), with a tube carrying an inert carrier gas (argon) which transports material to the Mass Spectrometer (fig 5.7). As the sample is not sampled continuously (the laser is pulsed), to avoid a pulsed or spiky signal on the mass spectrometer, a series of loops of different lengths can be inserted into the carrier tube to smooth out the pulsed signal from the Laser into a smooth signal in the spectrometer. This means that the analysis of the signal can be maintained over the whole period of ablation of the shard.

The mass spectrometer measures all the elements simultaneously. The signal for each shard was maintained for 40 seconds, with a 20 second blank before and after each analysis (40seconds between successive analyses), to allow the next shard to be positioned under the laser, and to flush the mass-spectrometer clean of aerosols. As the mass spectrometer is analysing continuously, a chart of spectrometer counts against time is produced (fig. 5.8). This can be viewed as the analysis is running.

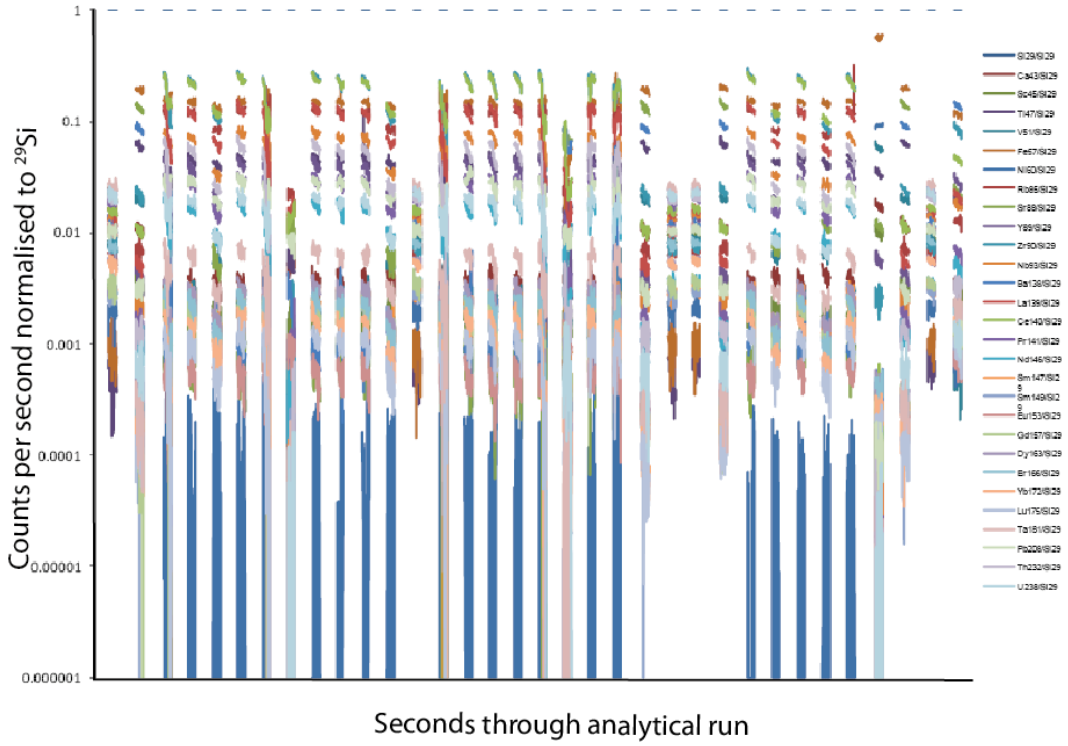

Figure 5.8 An example output from the LA-ICP-MS, showing counts per second against seconds (time of LA-ICP-MS run). Each colour represents a different element, each peak represents a different analysis (as picked out by the vertical lines).

This output was input into a Microsoft Excel macro program (provided by E. Tomlinson), to produce a plot such as that in figure 5.8. The first 8 seconds of the ablation are deleted to remove the initial rise (from background) in counts in the mass spectrometer, and to include only the stable ablation section of the analysis. The concentrations are then determined by the macro as follows:

The counts are determined using the following formula (Tomlinson et al. 2010).

$$C_i^{sample} = \frac{I_i^{Sample}}{I_{IS}^{Sample}} \times \frac{C_i^{Ref}}{C_{IS}^{Ref}} \times \frac{I_{IS}^{Ref}}{I_i^{Ref}} \times C_{IS}^{Sample}$$

Where C is the concentration (in ppm), I is intensity (in counts per second), i is the element to be determined, IS is the internal standard (here ^{29}Si), and Ref is the external calibration standard (here NIST612).

The measurements are also calibrated specifically for different beam diameters (sample volumes). It is therefore crucial to bracket shard analyses of certain beam diameters with

internal standards analysed with the same beam diameter. The data are calibrated to an average of the standards bracketing that analysis. It also accommodates the known values of SiO_2 (the internal standard derived from the EPMA analysis) for the individual shards, by correcting for these.

Once this calculation is complete for each of the time slices in the run, a mean value for the concentration of each of the elements in each shard or standard analysis is calculated. It is also possible to calculate an uncertainty weighted average. This approach would weight each of the time slice readings according to the uncertainty associated with it (the greater the uncertainty, the lower the weighting), and thus reduce the uncertainty associated with the final compositional value. This approach however, cannot distinguish between natural variability in the sample and imposed uncertainty from the analytical process. It is therefore not recommended for the analysis of tephra shards (Tomlinson et al. 2010).

The data must then be also be manually edited to remove sections of the analysis which represent inclusions or vesicles, or where the laser has ablated all the way through the shard. This process is described in section 5.5.3. below.

Bias.

A bias exists between the values obtained for secondary standards and the known values for those standards (Tomlinson et al. 2010). This bias varies with the SiO_2 content of the secondary standard; and is greater with more basic (lower SiO_2) secondary standards. To account for this bias a correction factor can be applied to the concentration values for the shards. The value of this correction factor should be quantified using a major element value from the standards that is known with good accuracy from the EPMA. The best candidates for a tephra study are Si and Ca, as they are measured both on the EPMA and on the LA-ICP-MS, they are relatively abundant in the standard of choice (here StHs 6/80) and they are not volatile under the EPMA beam and so the values are reliably accurate on both systems. As Si must be used as the internal standard for rhyolitic samples (because they do not contain sufficient Ca), it cannot be used for the bias correction. Ca from the secondary standard StHs6/80-G is therefore used here to quantify the bias, which is calculated as follows:

$$\%\text{bias} = \frac{100 \times (C_{det} - C_{ref})}{C_{ref}}$$

and the correction factor is quantified as:

$$f_{cor} = \frac{Ca_{ref}}{Ca_{det}}$$

Where Ca_{det} is the LA-ICP-MS determined Ca concentration, Ca_{ref} is the known reference concentration for the standard of choice (here StHs6/80). F_{cor} is the correction factor. The %bias appears to be independent of beam size (Tomlinson et al. 2010).

After this correction factor has been applied a final, average concentration for each shard can been determined.

5.5.3 Data Filtering and Processing.

Tephra shards may not be homogenous glass; they may contain vesicles or mineral inclusions which could be unintentionally included in the material ablated from the shard. In order to make valid comparisons between two different samples, only the glass component of the signal should be included in the calculation of the elemental concentrations. Fortunately the time-dependant nature of the LA-ICP-MS output allows the analyst to visually pick out sections of the shard analyses which have components of vesicles or minerals, or the mounting resin where the aim of the laser was poor or the shard depth has been completely ablated. Homogenous glass will be represented by parallel lines for all of the elements. Figure 5.9 (Tomlinson et al. 2010) shows examples of counts vs time charts for samples with a resin component and mineral components.

The sections of these analyses which contain inhomogeneous compositions can be removed from the calculations of the final average compositions. It is important to note however that this process is qualitative, and to some extent, analyst dependent. Tephra shards may contain small variations in the glass chemistry which are natural and not a potential source of error. It is the job of the analyst to distinguish between major deviations in chemistry which are indicative of minerals, vesicles or the resin, and the small heterogeneities which occur within the glass matrix. Analyses which show consistent enrichment in certain groups of elements are indicative of certain minerals. For example,

enrichment in Ba, Sr, Eu and U, and a decrease in all other elements indicates an alkali feldspar inclusion.

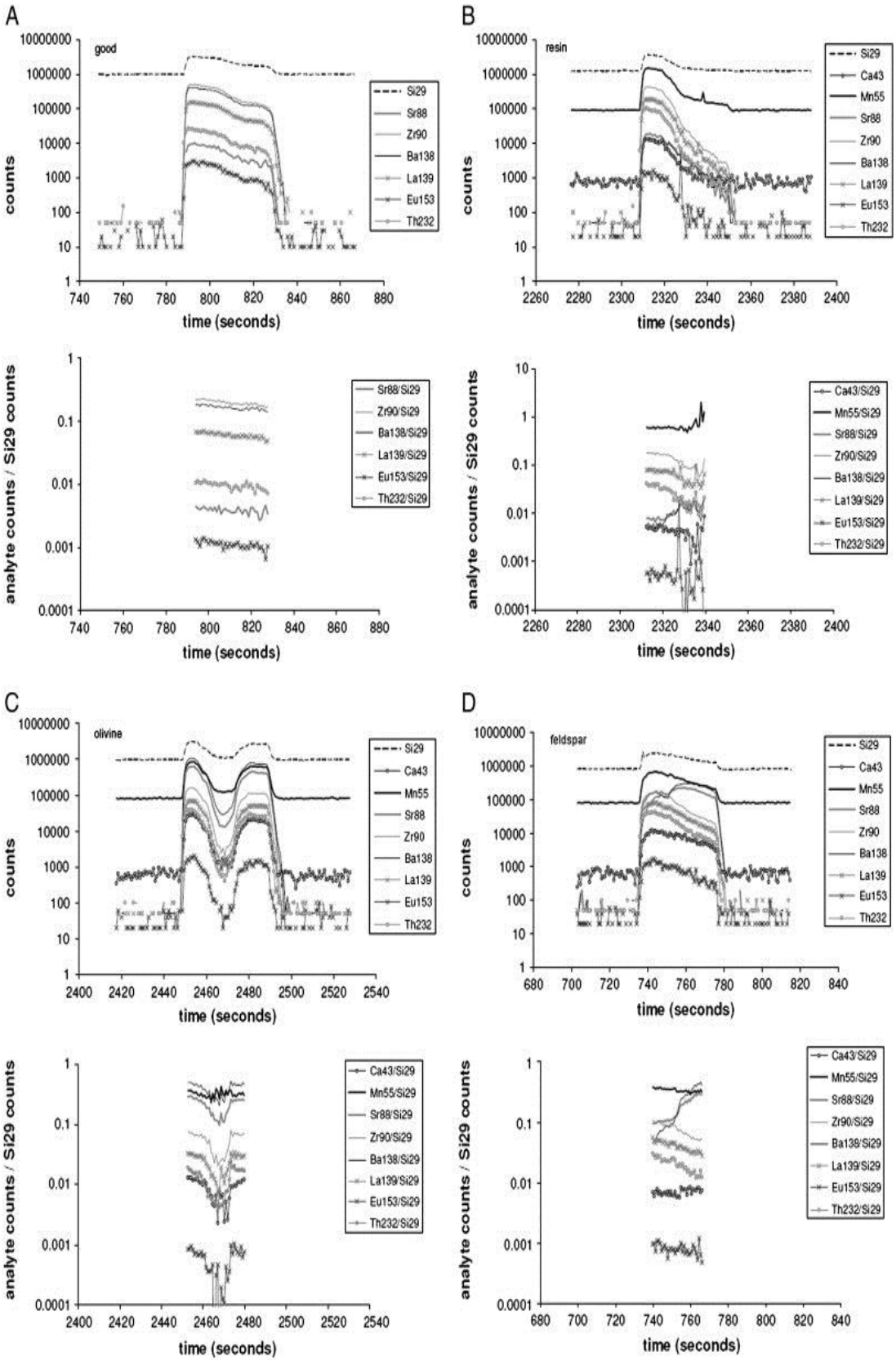

Figure 5.9 Example plots of results of analyses of tephra shards, showing A) good homogenous glass, B) an analysis with a vesicle inclusion, or where the shard has been ablated through, C) an inclusion of olivine, D) an inclusion of an alkali feldspar in the analysis (from Tomlinson et al. 2010). Elements that deviate from parallel lines with the other elements indicate ablation of non-homogenous material.

Lower Limit of Detection.

The lower limit of detection (LLD) in LA-ICP-MS is determined by the background count in the mass spectrometer, and its sensitivity. Ideally, the sensitivity should be high, while the background count is low (Pierce et al. 2007). The higher the sensitivity to background ratio, the smaller the sample volume can be (the smaller the spot size can be). In this investigation the LLD was taken as 6 times the standard deviation for the background, to ensure that the data for a shard does not contain a component from the background count. Analyses yielding values below the LLD were removed from the dataset.

5.5.4 Analytical Precision and Accuracy.

Analytical precision increases with increasing counts in the mass spectrometer for each element (fig. 8 in Pierce et al. 2007). The precision is therefore better for the more abundant elements than for the least abundant elements, for any particular shard. The analytical precision (the variability of the measured composition of a sample) can be estimated using the 2SD of the standards values. This is discussed further in section 4.6.4.

Accuracy.

Accuracy is assessed by comparison of the measured values of standards, to the reference values of those standards. A comparison of the values for StHls6/80-G generally shows a negative bias, i.e. the measured values are lower than the accepted values (Tomlinson et al. 2010). If this can be quantified, then a correction can be applied, as has been done in this work and is discussed previously in section 5.52.

5.6. SIMS.

5.6.1 SIMS theory.

Secondary ion mass spectrometry is a method used to obtain trace element data. It is particularly suited to small, rare or fragile samples, as it is only slightly destructive, and so a sample can be small and thin, and still be mainly preserved. The impact of a SIMS analysis extends only ~10nm into the surface of the sample, and the beam can be reduced to about 3-5 microns (depending on the elements of interest).

The SIMS setup is illustrated in figure 5.10 (from the website of the SIMS laboratory-Pavia, Italy). The principles of secondary ion mass spectrometry are conceptually simple but complex in their detail.

SIMS basics.

When beam of primary ions (typically $^{16}O^-$) is incident on the sample surface, the primary ions penetrate the sample surface and their energy is transferred to the atoms within the sample matrix, causing them to move around. If an atom at the surface has acquired more than its binding energy it will be released from the surface of the sample (McPhail 2006). Such particles may be charged ions or uncharged atoms or molecules. Only the ions are required by the mass spectrometer, and so these are removed from the sample chamber and efficiently directed to the mass spectrometer by a Dynamic Transfer System (a charged extraction lens- see 6 in figure 5.10). Only about 1% of the particles which are removed from the surface of the sample are ions (Macrae 1995). The most efficient extraction lenses remove typically 50% of the sputtered ions. The mass spectrometer then sequentially detects the numbers of the ions which are removed from the chamber for each element, and these counts are converted into ppm concentrations through a series of calculations. These calculations incorporate (just as with LA-ICP-MS) the limit of detection, the primary standards (for calibration) and the internal standard (in this case the 100% normalised Si value of the shard, as measured on the EPMA), detailed below (equations 1-3).

The full quantification of trace elements requires a translation of the number of counts received at the mass spectrometer's detector, into a value for the concentration of the element in the sample. In SIMS, the complex nature of the sputtering process means that this relationship is different for each element, and is poorly understood. There are two factors which affect this translation:

1) Matrix effects in the sample- the nature of the matrix determines how many ions of a particular element are sputtered out of the surface of the sample, given a known set of beam parameters. This factor is sample dependent.

2) Transfer efficiency and detection sensitivity- how efficiently the equipment transports the ions to the detector and how sensitive the detector is on any given day.

These two factors are accommodated in the equation by 1) using a standard with a very similar matrix to that expected in the sample (which is already known from the EPMA analysis), and 2) performing a calibration directly before an analysis, to ascertain how efficiently the system is working that day. The following equations (McPhail 2006) describe

the translation of counts at the detector into ppm concentration in the sample, and account for factors 1 and 2 above.

$$\mathbf{N^{*}_{(X+)} = (\alpha_{(X+)}\, T_{(X+)})\, \rho X\, (Az)}$$

Where

$\mathbf{N^{*}_{(X+)}}$ is the number of X ions actually detected by the mass spectrometer: the count.

$\boldsymbol{\alpha_{(X+)}}$ is the ionisation probability for X atoms (unknown)

$\mathbf{T_{(X+)}}$ is the transmission coefficient, i.e. the proportion of atoms which make it from the sample chamber to the detector (also unknown)

ρX is the concentration of element X in the sample (known in standards, unknown in sample)

Az is the analytical volume in the sample. This is a function of the incident ion beam energy and is thus known.

In this equation, the term $\mathbf{(T_{(X+)}\alpha_{(X+)})}$ summarises two unknowns (which cannot be known separately) in the equation and can be summarised as the "translation coefficient" between the number of atoms of X in the sample volume (**ρX(Az)**) and the number of ions of X that reach the detector ($\mathbf{N^{*}_{(X+)}}$). This term is quantified directly before the sample of interest by analysis of standards with a similar matrix to that the sample of interest.

The full quantification of trace elements on the SIMS system is thus dependent on using appropriate standards. There is, nevertheless, a good agreement between results attained on the LA-ICP-MS system, and those attained on the SIMS (Lane 2009).

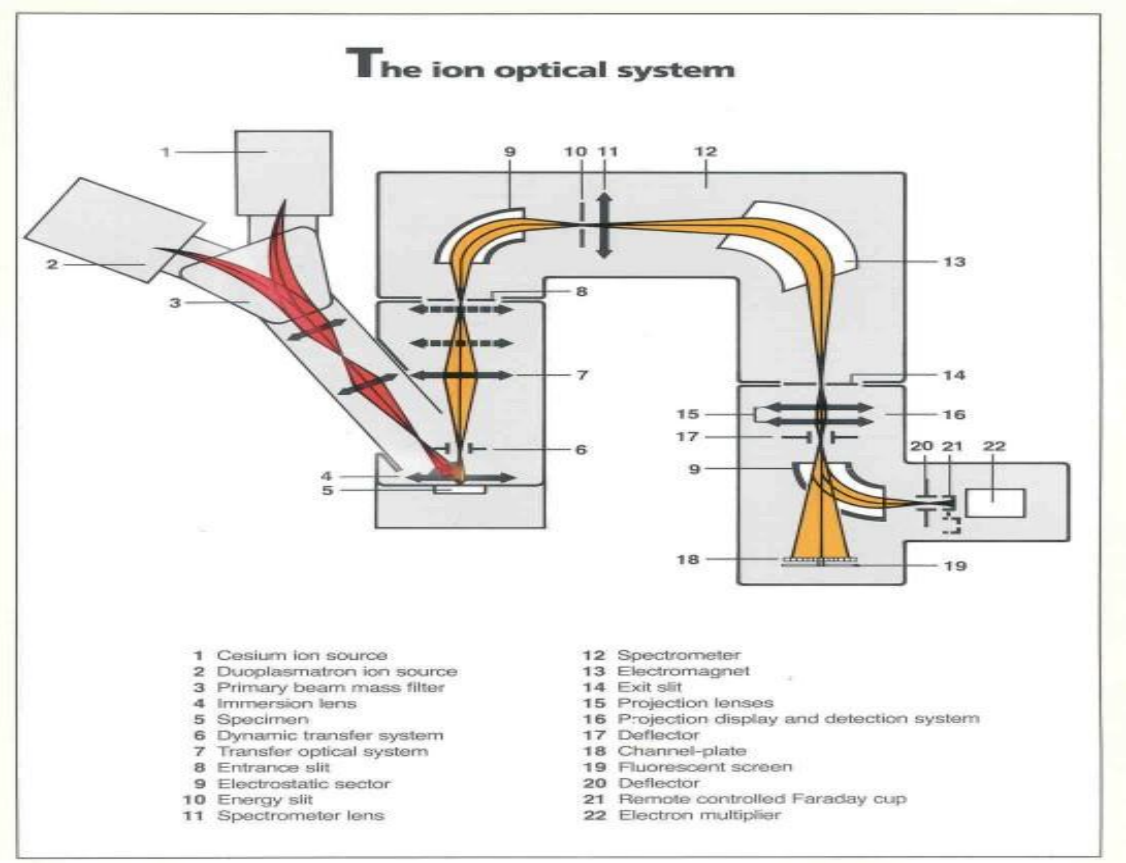

Figure 5.10 The setup of the ion microprobe system. (from the website of the SIMS laboratory-Pavia, Italy)

It is because of the small volume of material analysed, the low numbers of secondary ions produced and the efficiency limitations of the extraction lens that the analysis of one tephra shard using the SIMS takes much longer than either the EPMA or LA-ICP-MS systems. The analysis of one tephra shard for the full available range of trace elements takes about one hour, including calculation times and procedures. The price of the analysis is also high, owing to the extended analysis time and can be as much as £90 per tephra shard, depending on the elements of interest and the specific terms of a particular contract. These factors combined mean that the SIMS was reserved in this investigation only for the samples with shards which could not be analysed on the LA-ICP-MS and which were crucial to constraining identification for a tephra layer.

Accuracy in SIMS.

The accuracy of SIMS measurements on tephra shards cannot be precisely known, as calibration depends on the analysis of a standard with a similar matrix. Thus, the accuracy is to some degree assured by the analyst (Luisa Ottolini, University of Pavia). Repeat measurements comparing SIMS to LA-ICP-MS show that the data are highly comparable

(Lane 2009) and the secondary standards may be compared to the internationally agreed values.

Precision in SIMS.

Precision in SIMS can be quantified by repeat analysis of a known standard. The standards used in this investigation were NIST-SRM 610, BCR-2G, the intra CNR-IGG standard BB basalt glass and WY1 basaltic glass and the precision of the results is discussed further in section 5.7.4.

5.6.2 Analysis Parameters for SIMS.

The Secondary ion microprobe system at CNR-IGG, Pavia was used to attain trace element abundances on samples with shards too small for the minimum 25µm diameter on the LA-ICP-MS. A $^{16}O^-$ beam (0.8-1.2nA current) of between 5-8µm was used, appropriate to the shard size. Width of the energy slit was 50eV and the voltage offset applied to the accelerating voltage (+4500 V) was -100 V. The standard used for calibration interference was NIST-SRM 610. Trace element concentrations for both the unpublished proximal data and the published distal shard data were calculated using 100% Normalised (water free) SiO_2 values of the same shards from the EPMA analysis.

Ion Microprobe	Cameca ims 4f (at CNR-IGG Pavia, Italy)
Primary Ion Beam Current	0.8-1.2nA ($^{16}O^-$)
Energy slit width	50eV
Voltage offset	-100V (to accelerating voltage of 4500V).
Image field size	25µm
Ion beam spot diameter	5-8µm
Elements Analysed for Time- (4 cycles) 2 seconds	Si, K
4 seconds	Ti
5 seconds	Li, Be, Sc, V, Cr, Rb, Sr, Y, Zr, Nb,
8 seconds	Cs, Ba
10 seconds	La, Ce, Nd,
15 seconds	Sm, Er, Yb,
20 seconds	Dy,Th, U

Table 5.5 Analytical conditions applied to the secondary ion mass spectrometer (SIMS) analyses obtained in this study.

5.6.3 Data filtering and processing

Data produced from the SIMS were obtained from the same shards as those analysed for major elements on the EPMA. Because the tiny volume of material analysed during SIMS, and the major element analysis attained from the EPMA, it is highly unlikely that any non-glass grains would have been analysed. Nonetheless, the data was manually screened for anomalous elemental values which would indicate a mineral component to be removed.

5.7 Correlation Methods and Principles

5.7.1 Reference Data- the proximal data

One of the central aims of this project was to make correlations, where possible, between the tephras found in the marine cores and deposits proximal to the source volcanic systems. Proximal volcanic deposits in theory provide the best opportunities to establish robust volcanic stratigraphies, and to import radiometric dating for individual source eruptions into the marine core stratigraphy. This is desirable because minerals required for dating (e.g. sanidine) are much more abundant in proximal deposits than in more distal ash deposits.

Investigations into the volcanic deposits of Santorini, the Campanian Region, Pantelleria, Iceland and Turkey were conducted by Emma Tomlinson of the Department of Earth Sciences, Royal Holloway, University of London. Deposits on the Aeolian Islands were investigated by Paul Albert (also of Earth Sciences, RHUL). The Nisyros volcanic stratigraphy was analysed by Helen Kinvig (Dept Earth Sciences, University of Bristol). The Yali-2 pumice sample from the Nisyros caldera was analysed by the author of this thesis, as were three deposits from the Lago Grande di Monticchio sequence, TM24a, TM24b and TM27.

The RESET consortium has an online database, in which the data generated the various analysts are shared. The proximal data produced by other members of the consortium was obtained using same machines and using the same standards to ensure a secure comparison between the analyses. Other data were added to the database from investigations already published. These analyses are considered here if they are generated using WDS-EPMA and LA-ICP-MS or SIMS, but are excluded where they were determined using EDS-EPMA or Solution ICP-MS, because the former are of lower precision while the latter are not grain specific, and may contain mineral material.

5.7.2 Correlations Background- Correlation methods in the literature.

Data obtained from a single tephra sample may include measurements made from as many as 20 or 30 shards, each with major and trace element data (20-30 elements). As a result it is often difficult to present data in a transparent and useful but nevertheless concise way in an academic paper. Authors have used several methods to present data, and thus demonstrate the consanguinity or otherwise of two samples.

Correlation coefficients

One way to compare two or more samples geochemically is to take the average values of both of the samples to be compared, and divide the mean values for each element by the same element in the other sample. If the values are close to one, the two samples can be said to be similar to one another. The ratio of the two can be expressed as a percentage, and the analyst can set a numerical limit as a basis for supporting or rejecting a correlation, or they can entertain various possibilities for correlations and settle for the paring which has the values closest to 100%. This method is used by Federman and Carey (1980) and Margari et al. (2007). The method is concise, but it averages data which may not be normally distributed and summarises what may be a large variability within the data into one value. If proximal deposits show greater variation than their distal equivalents then they would produce a different average value. There is also a temptation to draw a false correlation where two deposits are very similar, but where the volcanic eruption stratigraphy is (perhaps unknowingly) incomplete.

Multi-variant analysis

The multi-elemental nature of tephra geochemical data might intuitively lend itself well to multivariant-statistical analysis. There are two main techniques which have been employed in tephra correlation procedures; Discriminant Function Analysis (DFA) and Principle Component Analysis (PCA). DFA aims to pull two or more samples apart in a multivariant (multi-elemental) space by the greatest statistical distance possible. PCA is a statistical means of detecting the element(s) which show the greatest variability between samples, within a particular dataset. These two techniques have been used by Pollard et al. (2006) and Bourne et al. (2010) to discriminate samples from a training set of data. The technique has the advantages of presenting all the elements in a single concise diagram (or in a single

statistic), producing a numerical value for a correlation (see Lowe et al. 2011 and references therein), and is very time efficient.

Multi-variant analyses were not considered here to be an appropriate technique to apply within this project as there are several difficulties in its application to tephra geochemical data. The technique can occasionally pull apart two samples from the same deposit, based on the least abundant, least accurately measured elements such as Mn or Ti or when the analytical technique varies slightly (but within accepted limits) (M.Pollard pers. comm.). This effect is particularly common in samples represented by low numbers of shards (such as is common with very far travelled tephra deposits). In addition, the multi-variant techniques of DFA and PCA necessarily assume the datasets to be both normally distributed and uni-modal. Both assumptions are demonstrably untrue for some volcanic deposits. For example, a sample may contain two populations of tephra from two near synchronous eruptions, or one eruption may have two geochemical groups (e.g. Younger Toba Tuff- Smith et al.2011, or Rotorua, New Zealand- Shane et al.2008). Combining these two modes into one statistical value will generate an artificial magma composition.

Bi-plots.

A series of element vs element bi-plots is conceptually the simplest way to present geochemical data, and to assess the similarity of two or more tephra deposits. They have the advantage over other methods of presentation by showing all the data points of all deposits of interest, rather than summarising them before comparison. The analyst can also easily show error bars on each data point, should they choose to do so. Judicious selection of the elements plotted can also reveal magmatic processes or genetic relationships that may exist between deposits. Their main disadvantages are that they can be time-consuming to create as all the elements (perhaps as many as 32) must be plotted separately, although some software programs are now to speed up the process (eg. GCD toolkit or IgPet). It is also not insignificant that many bi-plots will monopolise much of the available space in an academic journal, so generally only selected bi-plots are presented (although now many journals now allow for a supplementary data section to be published online). Bi-plots are therefore the comparison method of choice for this thesis.

5.7.3 Adopted Identification Procedure for This Thesis

The identification of a source eruption for a tephra deposit in this thesis is a two stage process.

a) **Identification of source volcanic system.**

When a tephra deposit is found, it is very useful to first reduce the number of possible eruptions it could possibly correlate to. To do this, a source region for the tephra can be identified. Having decided whether the shards in that deposit are Si-saturated or Si-undersaturated (the two are mutually exclusive), the shards can be plotted onto a High Field Strength Element (HFSE) bi-plot. Such a plot exploits characteristics which are likely to be both different between and relatively constant for, each of the possible source regions. This is because the HFSE concentrations are likely to be dominantly a function of region specific processes (mechanism/extent of mantle melting and efficiency of fluid flow respectively, see Pearce & Peate 1995 and Tatsumi & Kogiso 1997).

In this thesis, the HFSEs Zr and Nb are used. These are consistently the most abundant HFSEs in the samples and thus are measured with the highest precision. As mentioned previously, the HFSEs are strongly resistant to fractionation by precipitating mineral phases. Thus, they form strong, linear compositional trends in a magma system, which should in theory, remain constant for the duration of the life of the magma chamber.

Correlation to eruption

After the source system was deduced by this method, the tephra shards from this system for a particular core have been plotted onto bi-plots with the data of the proximal deposits also from that system. By this means, the correlation can be refined from the "system/volcano" level to the "eruption" level. The interpretation of the data should not rely exclusively on the geochemical bi-plots however, as certain correlations are impossible due to tephrostratigraphic constraints; it is not possible for isochrons to cross one other.

5.7.4 Reproducibility and Analytical uncertainty in correlations.

Reproducibility.

The most important consideration for any tephra study is to ensure that the analyses of different samples run at different times are comparable with one another. If the cloud of values produced for a particular sample is reproducible over several analytical batches, then the variation **between** batches (due to small changes in analytical setup) is small enough to be ignored. If the values are not reproducible, then the analytical uncertainty becomes significant and it is necessary to accommodate it when proposing correlations between two different samples.

Analytical Uncertainty.

The variation in the values attained by geochemical analysis within a sample can have several causes, which could be summarised and shown in different ways. These are shown in table 5.6

Variation or Uncertainty Source	Quantified by.....	Shown by.....	Potential Problems with showing variation/uncertainty this way.
1. Natural chemical variation **within** an eruption deposit due to magma in-homogeneity or mixing	Comprehensive analysis of all of the proximal deposit associated with that eruption.	Trend of values on bi-plot.	Involves some unavoidable interpolation between points, and an inherent visual assessment of the modality of the proximal deposit.
2. Natural chemical variation within a single tephra shard, due to magma in-homogeneity or mixing or post-depositional alteration.	2SD/√n for shard, minus 2SD/√n for standards will give estimate for the LA-ICP-MS. Not possible for EPMA or SIMS.	Uncertainty bars on individual points (for LA-ICP-MS only	The 2SD of analysis of single tephra shard incorporates both the real variation within the shard, and the analytical uncertainty of the system.
3.Analytical uncertainty within a single run on the EPMA, LA-ICP-MS or SIMS.	2SD/√n for standards for that run. (where n= the number of available readings per standard analysis)	Uncertainty bars from standards.	Highly relevant for comparisons between samples analysed within one run on the analytical system, but not so relevant for comparisons between samples analysed in different runs.
4.Analytical uncertainty due to the variations in analytical setup and analytical uncertainty between the analyses of the two (or more) samples to be compared.	2SD of all standard analyses attained on a particular machine, over the time period of interest.	Uncertainty bars on standards.	Can be very difficult to attain for reference data and to process the information of which standards are relevant to which shard analyses. Sometimes the elemental composition of the standard is significantly different to the elemental composition of the sample.

Table 5.6 Assessment of the potential sources of natural variation or analytical uncertainty in tephrostratigraphy, and the problems associated with their graphical illustration and any subsequent assessment of consanguinity between two or more samples.

In some geochemical investigations it is important to display error bars on the individual geochemical data points (scenario 1 and 2- table 5.6), to indicate if the difference between two or more data points from the same sample is statistically significant, or simply could be a function of the inherent variability of the analytical setup. This might be the case if analysing the different zones of a mineral crystal, or layers in a speleothem for example.

As it is the difference between two samples (each with their own cloud of data points) in this thesis is crucial to the conclusions, it is scenarios 3 and 4 in table 5.6 which should be

considered. It is crucial to establish how much of the variation in the values attained for a sample is due to analytical variability (machine error) and how much is real. This is assessed here by comparison of the 2SD of the standards to the cloud of values for sample.

For EPMA.

Several samples in this thesis were analysed in 2 or 3 batches on the EPMA. This provides the opportunity to test the reproducibility of sample values. It also can be used to compare the variation in the values for that sample (the data cloud) to the variability of the measurements of the standards. Figure 5.11 illustrates how (in theory) natural "real" variability in a sample can be semi-quantitatively distinguished from analytical uncertainty. The spread of the data points represents the natural variability in the sample plus the variability of the EPMA. If the natural variability in the sample is greater than the variability in the EPMA measurement, the data points will be spread about a line (fig 5.11 a). This line describes the heterogeneity within the magma prior the eruption represented by the sample (Wilson 1993). If the natural variability in the sample is equal to or less than the variability of the EPMA (2SD of the homogenous standards), then the data points will plot as a cloud, the dimensions of which are approximately equal to the variability of the EPMA (defined by the analyses of the standards) (fig 5.11b).

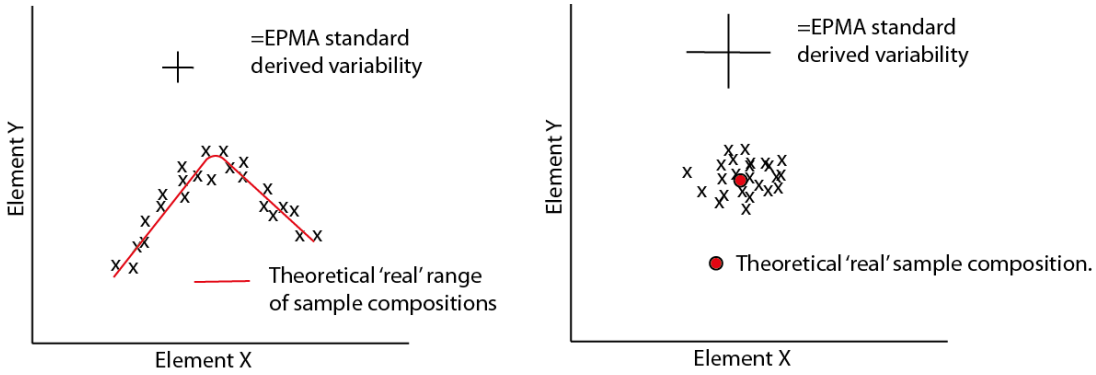

Figure 5.11 A conceptual assessment of the errors from a geochemical analysis. Black crosses indicate data points from a hypothetical sample. The variation superimposed on the real composition of the sample has both X and Y axes components, resulting in a spread of data points about the real composition, proportional to the variability of the analytical system **A)** an example for a sample with a large real compositional range (highly heterogeneous). **B)** a sample with a very restricted real geochemical range (nearly homogenous).

The 2SD defined by the standards (which are assumed to be homogenous) is the best available assessment of how much EPMA variability is inherent in the spread of data points of any particular sample, but it is a best estimate only. This is because the 2σ value for an analysis is inversely proportional to the abundance of the element and this abundance in

the sample may be somewhat different to its abundance in the standard. The 2σ value for any particular element is also a function of the analyte matrix, which also may be considerably different in the standards in comparison to the samples. It is this caveat which renders their use in assessing the data cloud of the sample semi-quantitative only.

Figure 5.12 demonstrates that the values produced from the **EPMA** are highly replicable over several analytical batches.

In addition, the spread of the sample data clouds appears to be very similar to the 2SD range of the standards (cf. fig. 5.11 and 5.12). This implies that most of the variation in the values displayed by these particular samples is due to analytical variability rather than natural 'real' variability (fig. 5.11a rather than fig. 5.11b) and that the sample (in this case) is nearly homogenous. Therefore, crucially, the uncertainty of the EPMA is captured by the spread of the data points for any particular sample. Samples with larger variability will display clouds larger than the analytical uncertainty (fig. 5.11b)

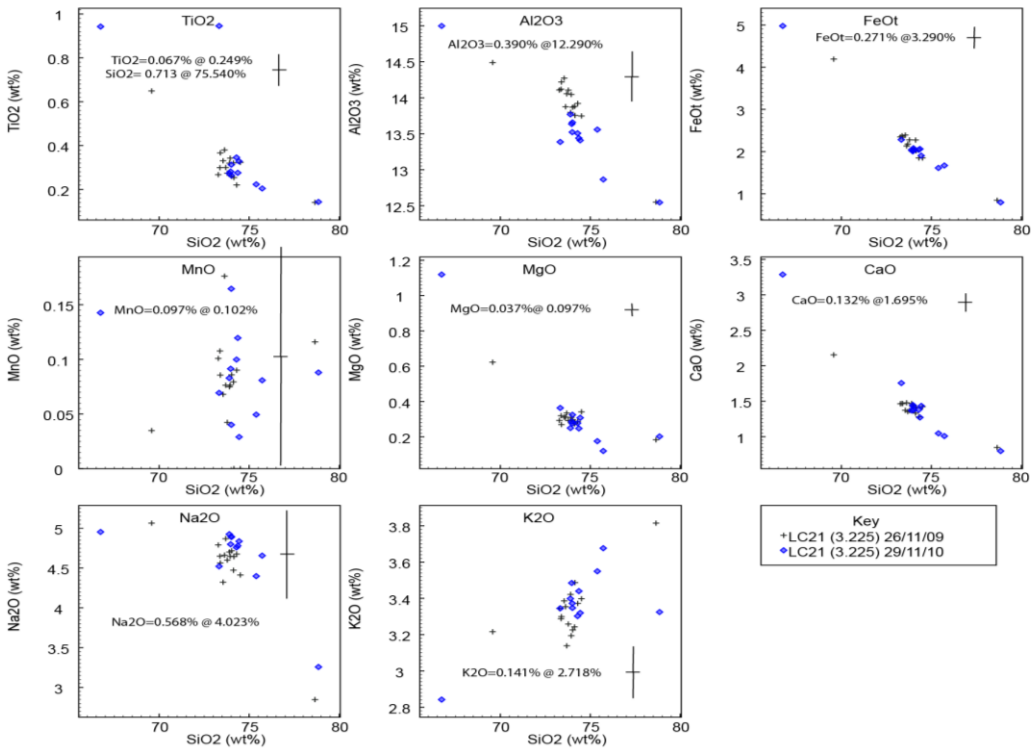

a)

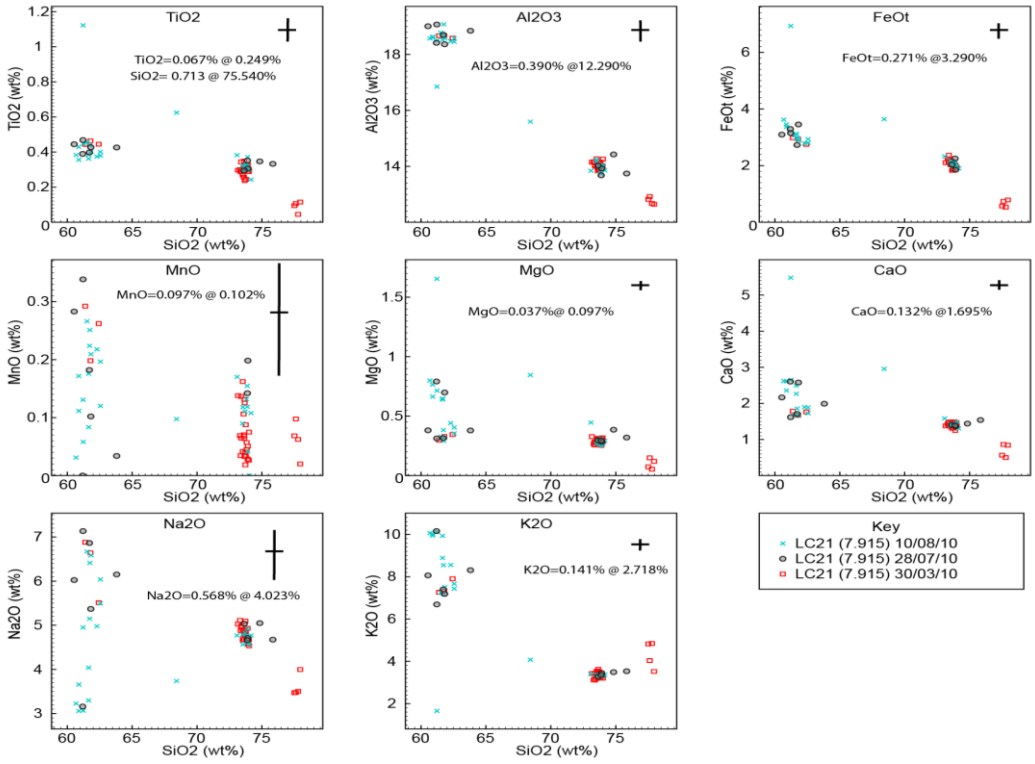

b)

Figure 5.12. Comparison of the data from a) one sample LC21 (3.225) run on two different days (26/11/09 and 29/11/10) and b) another sample LC21 (7.195) run on three different days on the EPMA demonstrating both that the EPMA produces highly replicable values over time (proof of the comparability of data produced on different dates) and that the variation in the cloud of data produced for the sample is nearly identical to the 2SD variation in measurements of the homogenous standard ATHO-G (implying that machine induced uncertainty in the value for the composition of the sample is represented by the cloud of data). NB: LC21 (7.195) is multi-modal in composition and so the error bars should be compared to each of the different modes rather than the sample as a whole.

The reproduction of almost identical values, on 2 or 3 different dates, for the samples shown in figure 5.12 demonstrates that the EPMA can be relied upon to produce comparable values for samples over different analytical batches for all 9 of the major elements. The variability of the samples from ideal/theoretical values is approximately equal to the 2SD measured on the standards (fig. 5.12). The uncertainty in the EPMA measurement is therefore mostly represented by the spread of the sample data. This practice is supported by the evidence of very good reproducibility of the values for a sample between batches (fig. 5.12), implying that any difference in the positions of data clouds for samples on a bi-plot are likely to be real, rather than a result of analytical variability. Nevertheless, the standard data are still published graphically here (appendix 1). If two samples show a very slight difference in composition in one or two elements, the analyst can refer to these analyses to judge if there is the same systematic difference in the composition of the standard analyses.

For LA-ICP-MS

The precision is an important statistic in LA-ICP-MS for analyses of materials which are thought to be in-homogenous and the composition change is the analyst's parameter of interest. This is because in such an investigation, it is the changes in the composition throughout a single analysis which must be distinguished from the machine variability. In tephrostratigraphy however, the comparison is not between different sections of the same, single, analysis but it is between two (or more) different analyses, possibly produced on different days, where the system has been re-tuned and may be operating slightly differently. It is therefore, as with the EPMA, the reproducibility of the sample data cloud, with different spot sizes, and over time, which is the key assessment when one is making comparisons between two samples of tephra analyses on the LA-ICP-MS.

Spot Size.

To verify that the mean value of the analyses remains the same at different spot sizes, and between different batches, the values derived for the standards analysed with different spot sizes, and then in different batches, were compared (fig. 5.13). An increase in the precision of the analysis (an increase in counts due to a larger beam size) simply decreases the precision (increases the size of the uncertainty bars) while keeping the average value more or less the same (fig. 5.13). This evidence vindicates the comparison of LA-ICP-MS data from different spot sizes (with the exception of the smallest: 20 micron diameter), and produced in different batches. There is no systematic difference in the values produced.

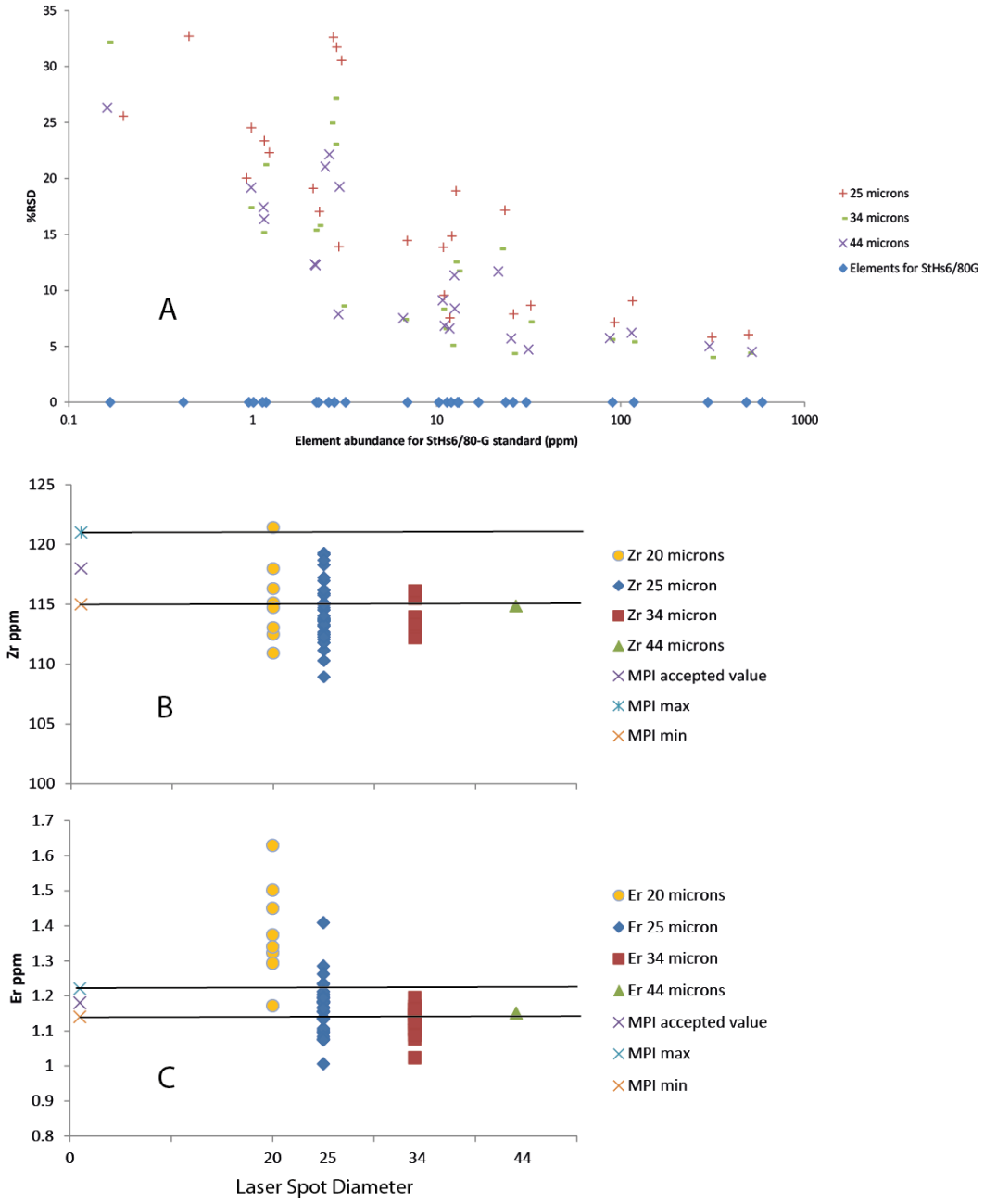

Figure 5.13 A) %RSD for StHs6/80 standards run on the LA-ICP-MS. Blue dots on the x-axis represent the ideal (MPI-DING) abundances of the trace elements in the StHs6/80 standard %RSD (per cent root standard deviation) of an analysis decreases exponentially with element abundance as the counting statistics at the detector improve. Different diameters of spot size are also indicated. Smaller spot sizes tend to produce larger uncertainties as the counting statistics decline, although the average measured concentrations do not vary systematically with spot size. **B)** Values for Zr (mid abundance element) plotted against the spot size used for the analysis (20, 25, 34 and 44 microns). There is no systematic difference between the spot sizes at this elemental abundance. **C)** Values for Er (low abundance element) plotted against the spot size used for the analysis (20, 25, 34 and 44 microns). Values are systematically higher for the smaller spot sizes (particularly 20 microns). This could be due to the limit of detection for Er being high enough to bias the measured values towards high values. Lower values would be excluded because they would be within 6SD of the backgraound count. Also shown on C and D are the maximum, minimum (2SD) and mean MPI-DING accepted values for the elements. NB: these values are derived from very high precision techniques such as Solution ICP-MS or INAA/RNAA.

Compositional heterogeneity within a tephra shard.

The precision of the LA-ICP-MS setup on any given day can be quantified using the standards. The difference between the uncertainty on the standards and that on the analysed shards could in theory be used to attain an estimate of the natural variation within each shard. As we are forced to assume in tephrostratigraphy that the chemical composition of two geographically removed deposits from a single eruption are identical, then it is inherently assumed that the variation within single shards is also identical. Two shards with identical ranges in composition will yield identical mean values. Two shards with different ranges, could in theory also yield identical compositions. However, differences in the range of compositions for individual shards would only be an important consideration if the proximal stratigraphy for that volcano showed two deposits where the fields defined by the mean shard values were indistinguishable, but the ranges on the individual shards were different. The compositional heterogeneity of individual shards is not therefore calculated in this thesis.

Analytical Uncertainty.

In the same way as previously demonstrated for the EPMA, the variability of the standards analysed with the LA-ICP-MS can be used to estimate the analytical uncertainty associated with the sample data. The principle is shown schematically in figure 5.11. If the natural sample heterogeneity is greater than the variability of the LA-ICP-MS as estimated by the standards, this will be manifested in a trend line representing the heterogeneity of the magma from which the tephra formed. If the natural heterogeneity is smaller than the analytical uncertainty (as derived from the standards) the cloud of data points will be proportional to the variability of the LA-ICP-MS system. An example of the analysis of one sample run on two different days is shown in figure 5.14. The values for the trace elements in the MPI DING standards can differ greatly from the values in the sample. As the uncertainty associated with a measurement is inversely proportional to the abundance of that element, the error bars derived from analysis of the standards may not be appropriate for the sample values. Thus, the error bars in figure 5.14 are shown with an indication of where the mean values for the standards from which they are derived would plot.

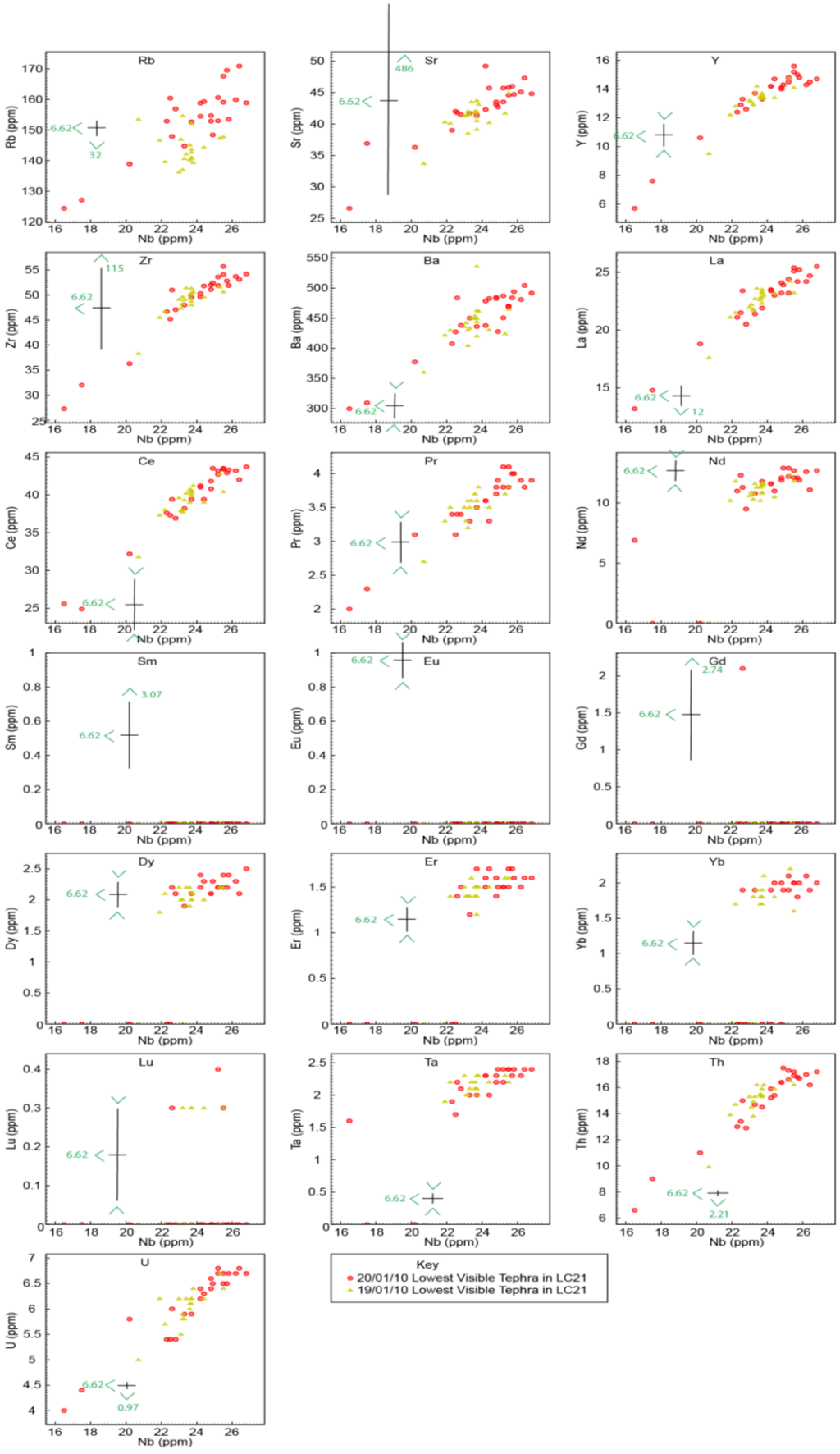
Rb
Rb (ppm)
6.62
32
Sr
Sr (ppm)
6.62
486
Y
Y (ppm)
6.62
Zr
Zr (ppm)
6.62
115
Ba
Ba (ppm)
6.62
La
La (ppm)
6.62
12
Ce
Ce (ppm)
6.62
Pr
Pr (ppm)
6.62
Nd
Nd (ppm)
6.62
Sm
Sm (ppm)
6.62
3.07
Eu
Eu (ppm)
6.62
Gd
Gd (ppm)
6.62
2.74
Dy
Dy (ppm)
6.62
Er
Er (ppm)
6.62
Yb
Yb (ppm)
6.62
Lu
Lu (ppm)
6.62
Ta
Ta (ppm)
6.62
Th
Th (ppm)
6.62
2.21
U
U (ppm)
6.62
0.97
Nb (ppm)
Key
20/01/10 Lowest Visible Tephra in LC21
19/01/10 Lowest Visible Tephra in LC21

Figure 5.14 (previous page) Replicate LA-ICP-MS analyses of the lowest visible tephra in LC21 analysed on two different days for comparison. Also shown are error bars (2SD) from the StHs6/80-G MPI-DING standard. Green arrows indicate the location of the mean standard values (green text) to which these error bars apply. Values for Y,Ba, Ce, Pr, Nd, Eu, Yb, Lu, Ta, Dy and Er plot close to the sample values and are thus comparable. For these elements the spread in the sample data is approximately equal to the error bars derived from the standards, indicating that the variation in the value of the sample is most likely due almost entirely to LA-ICP-MS uncertainty. The analytical uncertainty is thus accommodated in the spread of the sample data. Sample values for Sm,Eu and Gd are in this example below the limit of detection for the LA-ICP-MS.

In this investigation there is an extra component to the uncertainty on the LA-ICP-MS. It is possible for some tephra layers to be compositionally mixed due post-depositional mixing processes, or because two eruptions were (within sampling resolution) synchronous, so this investigation uses the SiO_2 values measured on shards during the EPMA in the calculation of the LA-ICP-MS values for those same shards. Thus, any error in the EPMA measurement is propagated into the calculation of the LA-ICP-MS trace element values. The spread of data-points on the LA-ICP-MS may therefore be slightly larger than the uncertainties as implied by the 2SD of the standards. While this may slightly affect the precision of the data points, it should not greatly affect the accuracy (fig 5.15), so the data clouds for two compositionally identical samples will still plot on top of each other on a bi-plot. This error propagation should not therefore affect the outcome of a comparison of two samples (fig 5.15).

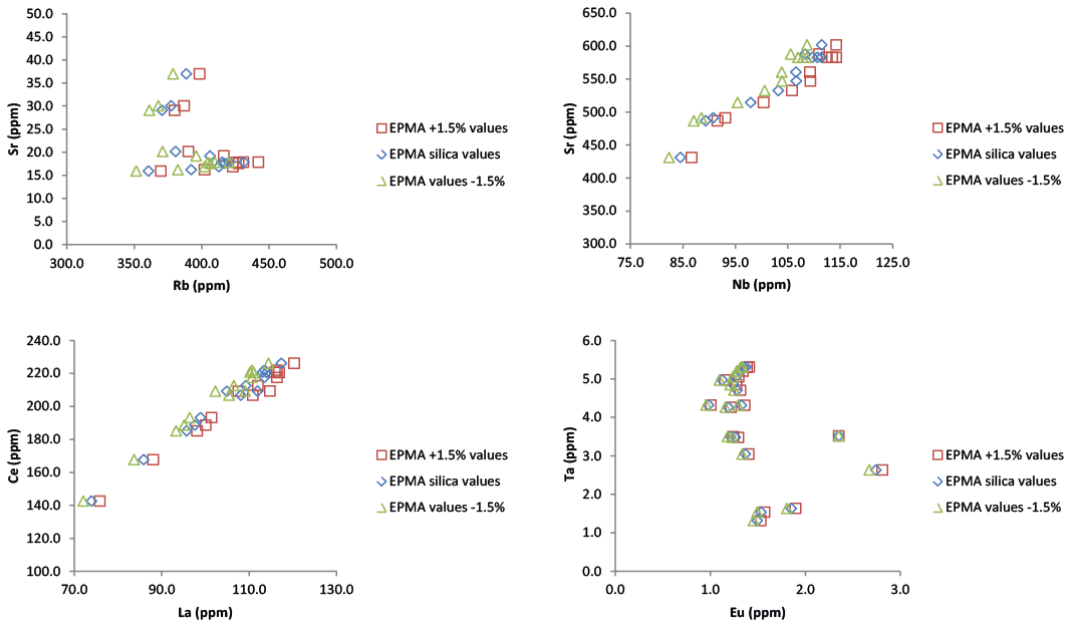

Figure 5.15 A comparison of selected LA-ICP-MS values calculated using 3 different values of SiO_2: the final, 100% normalised silica value from the EPMA, that value +1.5% and that value -1.5%.

Analytical bias.

Different spot sizes produce the same values for each of the elements, all of which carry their own analytical bias (Tomlinson et al.2010 and fig 5.16) As Si is strongly refractory (not effectively ablated) and is being used as an internal standard, the bias due to this fractionation effect (~5%) must be corrected for. This is done here in the same way as in Tomlinson et al. (2010); using the correction factor $F_{corr}= Ca_{ref}/Ca_{det}$ where Ca_{ref} is the accepted calcium in the reference standard and Ca_{det} is the Calcium value determined during the analysis of the reference standard(in this case StHs6/80 was used, due to its high enough CaO value of 5.28%, and its similar matrix to the samples). This technique does not remove the bias completely because each element has a slightly different bias (see fig.5.16) due to its own fractionation effect during the laser ablation process, and the accuracy of the machine. However, as the same correction process is applied to **all** the data in this investigation (including that produced for the proximal data), this correction will allow a fair comparison between all samples run at different times and at different spot sizes. As such, the spot size and the day of analysis are not thought to affect correlations.

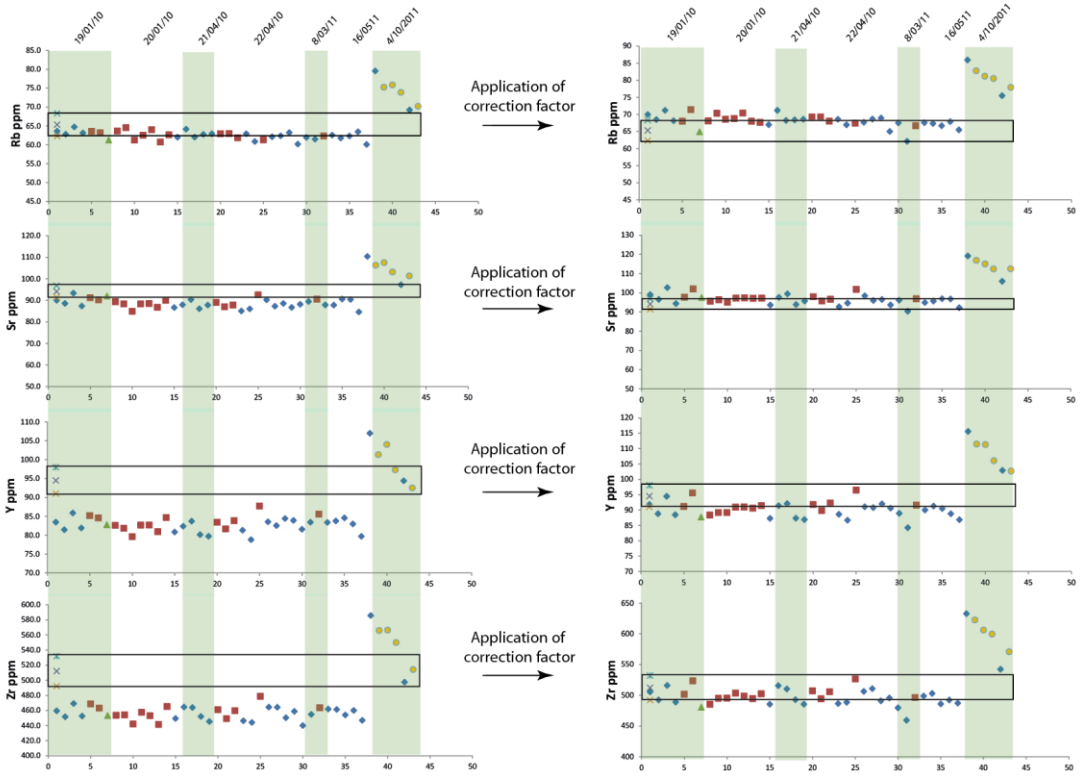

Figure 5.16 The effect of applying correction factors $F_{corr}= Ca_{ref}/Ca_{det}$ on the accuracy of the standard analyses (MPI DING standard ATHO-G), for four of the trace elements analysed on the LA-ICP-MS. Different symbols represent different laser spot sizes and the date of each set of analyses is shown at the top of each chart. Correction factors are generally ~1.09. Application of the correction factor raises all values. Analyses from

4/10/2011 should be discarded as the standards indicate high values which are out-with the range of all previous analyses and the accepted MPI-DING values.

SIMS.

The results from the secondary ion microprobe used in this thesis were supplied with a set of standard analyses which were constantly updated by the lab (University of Pavia, Italy). The data from the BCR 2G standard run with the SIMS samples from this thesis is compared to the accepted, USGS values for that standard in figure 5.17. The figure shows that the SIMS machine at Pavia produces values for this standard which are consistent with the accepted values. Therefore the data from the SIMS was considered reliable and comparable to the LA-ICP-MS data.

Figure 5.17 comparison of SIMS BCR 2G standard analyses against accepted values. 2SD shown (when larger than symbols) for measured data.

Chapter 6- Results

The tephra layers in this thesis are referred to by the core name followed by depth of sample in core in meters; e.g., LC21 (4.925). The depth refers to the base of the sample taken for analysis. In visible layers, this is the base of the visible extent of the tephra. For cryptotephra layers, it is the base of the interval that contains peak tephra shard concentrations.

This chapter describes the tephra layers and shards discovered in this thesis and their major and trace element contents. It provides little interpretation as the aim here is to provide a definitive account of the observations of the study. For each core, the shard counts are presented with photomicrographs for each of the tephra layers. Then the results of the EPMA and LA-ICP-MS or SIMS data then are presented for each tephra samples analysed. All elemental results are presented in bi-plots, the major elements are in general plotted in the format element X (wt%) vs SiO_2 (wt%), and the trace elements in the format element X (ppm) vs Nb (ppm). These two elements (Si and Nb) were selected as they are both increase systematically with the differentiation of any particular magma, and thus, in theory, should best illustrate the full range of magma compositions represented in each of the tephra layers.

6.1 LC21 results

The results of the 5cm and 1cm resolution tephra counts are presented in figure. 6.1 together with the sapropel stratigraphy and the depths of the tephra samples taken for geochemical analysis. Large volumes of cryptotephra found above a visible ash layer were interpreted as reworking by bioturbation (e.g. at the top of the core), as suggested by Watkins et al. (1978). This assertion is further tested for one visible tephra layer by comparing a geochemical analysis of shards from the visible tephra with shards from the uppermost of the mixed region of sediment and ash.

6.1.1 Results of Shard counting

The sediment processing and shard counting revealed nine cryptotephra layers to add to the 8, readily observed, visible tephra layers. These are shown in figure 6.1 and photomicrographs of shards from each sample are shown in figure 6.2.

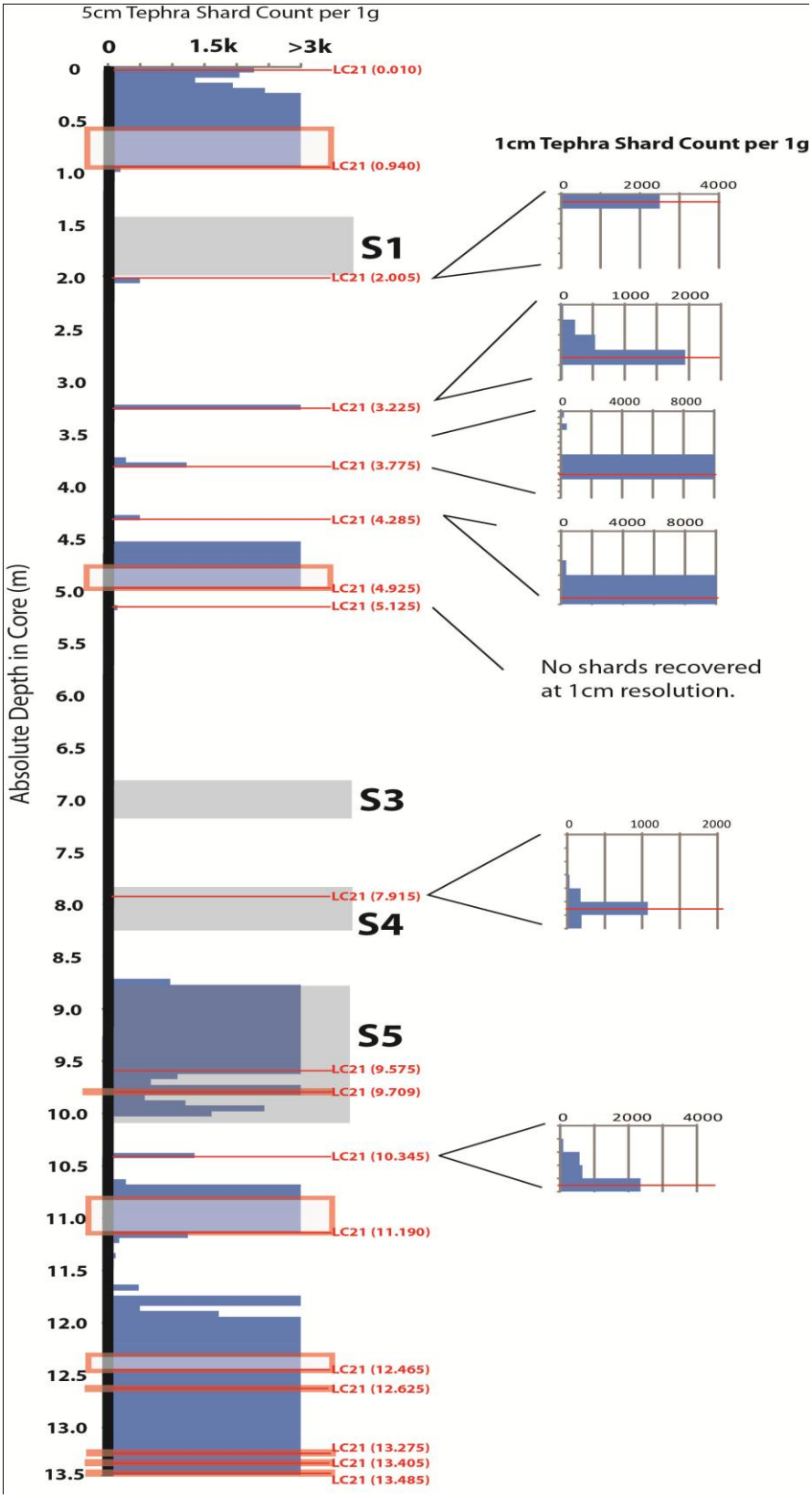

Figure 6.1 Shard count diagram for core LC21. 5cm scan counts on the left and 1cm resolution counts on the right. Red lines indicate the positions of samples extracted for geochemical analysis. Red boxes indicate the extent of visible tephra layers in the core. S1-S5 indicate visually identified sapropels. Shard counts in the 5cm samples are shown only to 3k shards per gram, in order to highlight the smaller peaks.

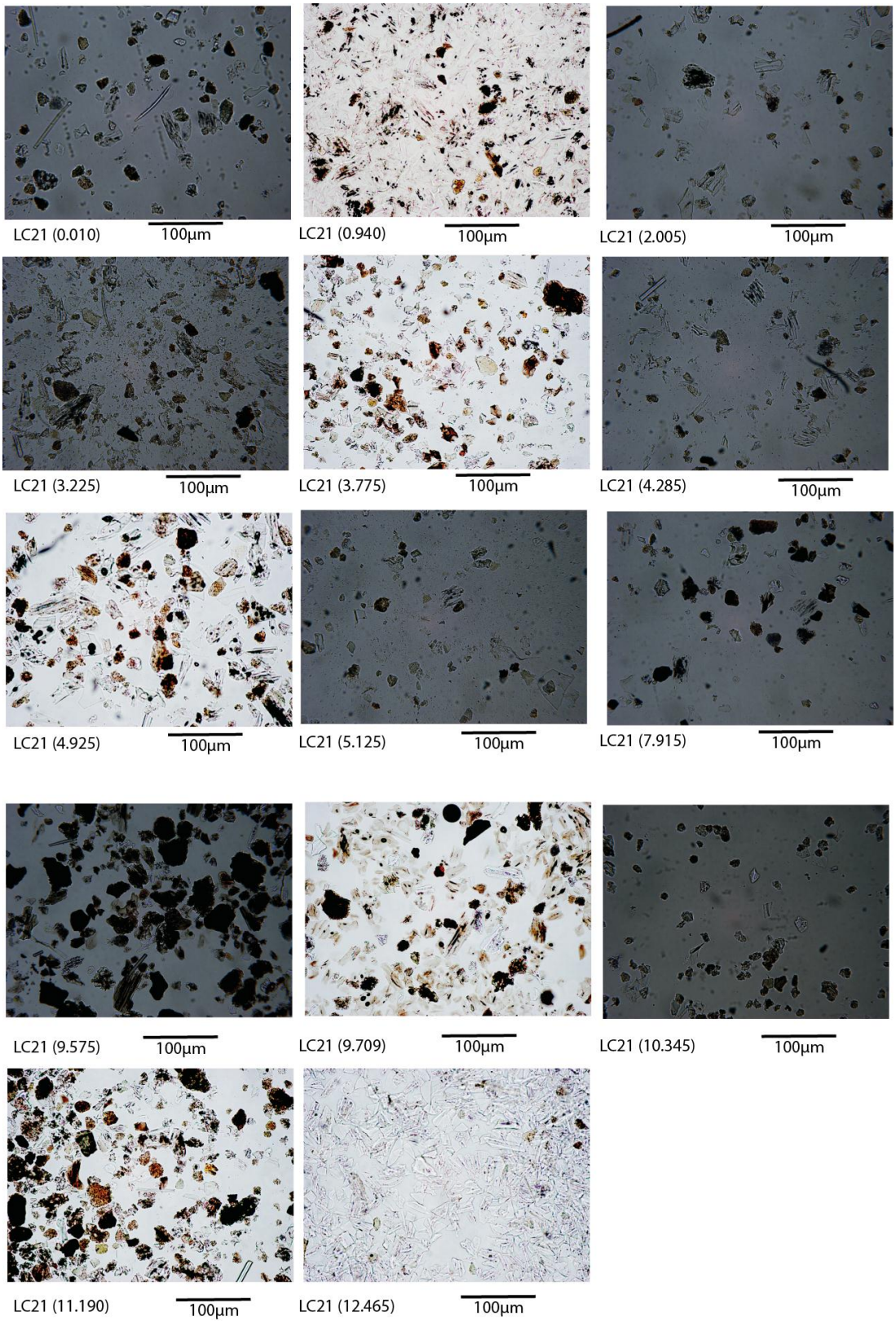

Figure 6.2 Photomicrographs of tephra shards recovered from LC21.

6.1.2 Modelled ages for LC21 tephra samples.

An innovative age modelling technique for LC21 was employed by Grant et al. (2012) which imported the highly precise, U-series age model of the Soreq Cave speleothem record (356 dates in 160ka) from Israel (Bar-Matthews et al. 2000, 2003). The technique exploits the fact that the $\delta^{18}O$ of terrestrial carbonates in the Levant is extracted from precipitation which is derived from the surface waters of the Eastern Mediterranean Sea. Therefore there is a physical link between the surface waters (and therefore planktonic foraminifera) above core LC21 and the speleothems of the Levant. By using the radiometric dates for the Minoan (Rohling et al. 2002) and Campanian Ignimbrite (Lowe et al. 2012) tephras in LC21 together with seventeen tie points between LC21 and Soreq cave $\delta^{18}O$ records, the U-series chronology was imported into the LC21 marine core. Full details of how the chronology was imported are given in Grant et al. (2012) and in Appendix 3. The resulting age model is shown (with the tephra layers marked on) in figures 6.3 and 6.4, and the dates derived for the tephra layers from this age model are given in table 6.1.

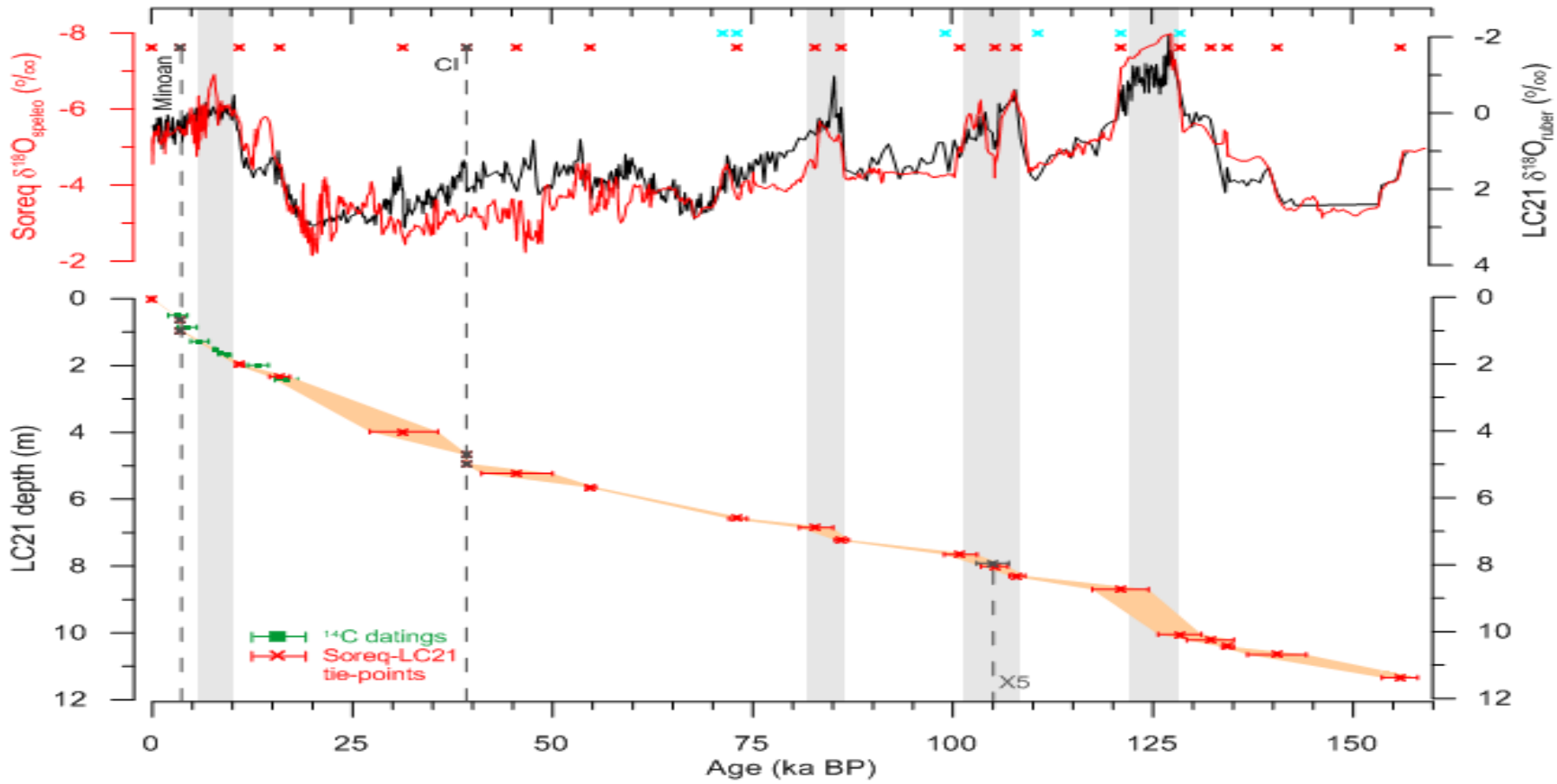

Figure 6.3a Construction of the LC21 U-series age model through the comparison of the LC21 $\delta^{18}O_{ruber}$ record to the Soreq cave $\delta^{18}O_{speleo}$ record. The top panel shows the two isotope records, tied together at points marked by red and blue crosses (see Grant et al. 2012) for details). The lower panel shows the resulting age vs depth model, with modelled error estimates, for the last ~155ka (the very bottom of the core was too poor in formainfera to attain a $\delta^{18}O$ signal).The Minoan and Campanian Ignimbrite tephras are indicated by dashed vertical lines and were used to constrain the age model. The X5 tephra was also tentatively identified in LC21 and is marked on this diagram using its radiometric date of 105±2ka (Kraml 1997), but was not used in the construction of the model. The model was further tested by 8 radiocarbon dates shown in green.

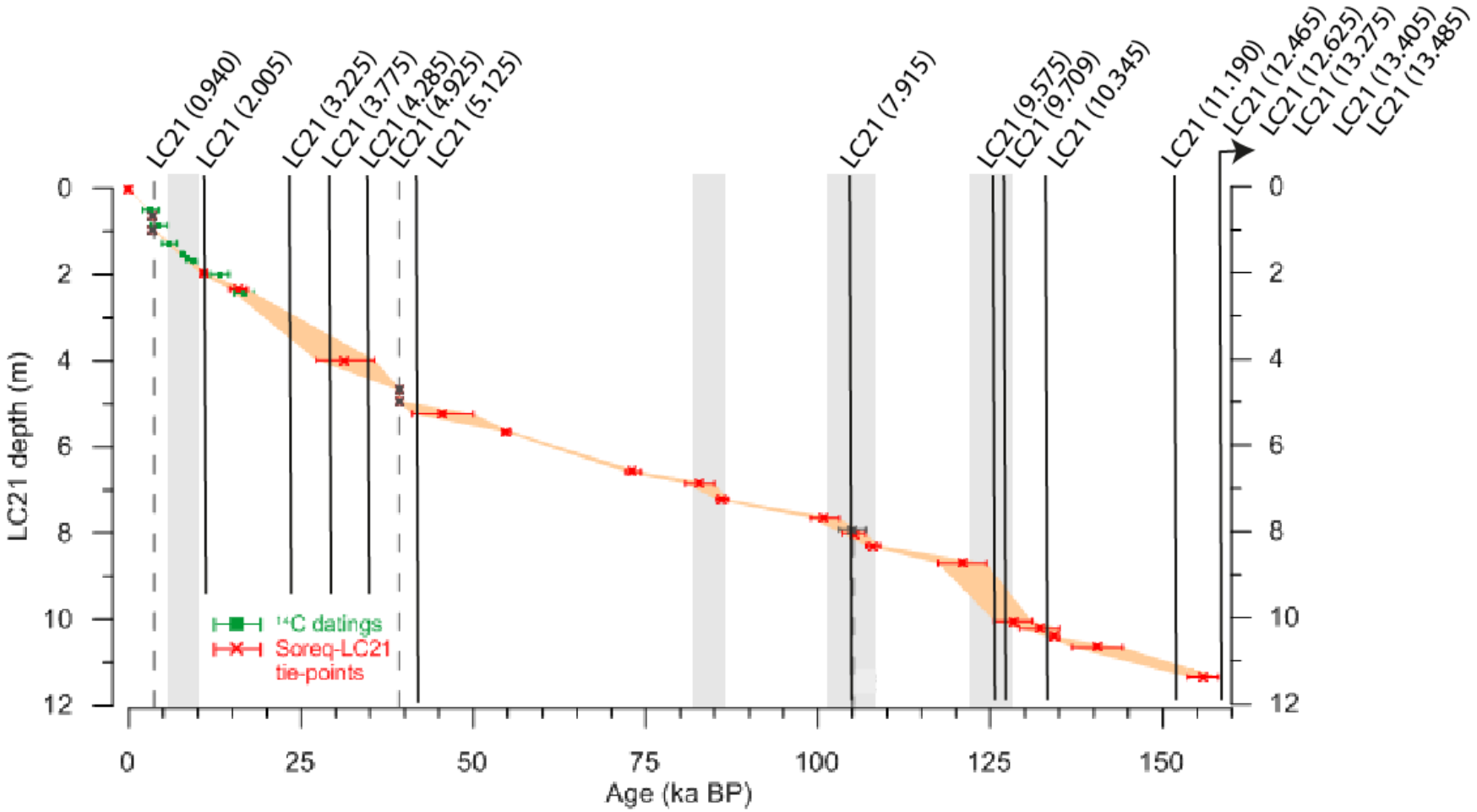

Figure 6.3b The lower panel of figure 6.3a with the positions of the tephra layer samples from LC21 plotted onto it. From this age model, dates for the unknown tephra layers in LC21 could be derived, these are shown in table 6.1. The thickness of visible tephra layers was removed from the depth scale in the construction of the age model, as tephra layers represent geologically instantaneous events.

Sample name	base depth	top depth	Age base (ka BP)	Age top (ka)	comments
LC21 (0.940)	0.94	0.716	3.59 +/- 0.14	same as base	visible layer
LC21 (2.005)	2.005	1.995	11.25 +/- 0.55	11.11 +/- 0.52	
LC21 (3.225)	3.225	3.215	24.31 +/- 2.89	24.21 +/- 2.87	
LC21 (3.775)	3.775	3.775	29.49 +/- 3.88	29.40 +/- 3.86	
LC21 (4.285)	4.285	4.275	34.86 +/- 2.47	34.75 +/- 2.53	
LC21 (4.925)	4.925	4.795	39.22 +/- 0.19	same as base	visible layer
LC21 (5.125)	5.125	5.075	43.34 +/- 2.96	42.28 +/- 2.25	
LC21 (7.915)	7.915	7.905	104.10 +/- 1.78	103.98 +/- 1.79	
LC21 (9.575)	9.575	9.565	125.77 +/- 3.00	125.72 +/- 3.01	
LC21 (9.709)	9.709	9.707	126.51 +/- 2.92	same as base	visible layer
LC21 (10.345)	10.345	10.335	133.58 +/- 1.53	133.47 +/- 1.63	
LC21 (11.190)	11.19	10.77	152.58 +/- 2.54	same as base	visible layer
LC21 (12.465)	12.465	12.455	NA	same as base	visible layer
LC21 (12.625)	12.615	12.625	NA	same as base	visible layer- skewed w.r.t core liner
LC21 (13.275)	13.265	13.275	NA	same as base	visible layer- skewed w.r.t core liner
LC21 (13.405)	13.395	13.405	NA	same as base	visible layer- skewed w.r.t core liner
LC21 (13.485)	13.475	13.485	NA	same as base	visible layer- skewed w.r.t core liner

Table 6.1 The ages of tephra layers in core LC21 defined by the age model of Grant et al. (2012). Ages for the crypto tephra layers are defined both for the base and top of the interval containing the cryptotephra. Ages for the visible layers are defined for the base of the layer.

6.1.3 Results of Geochemical Analyses.

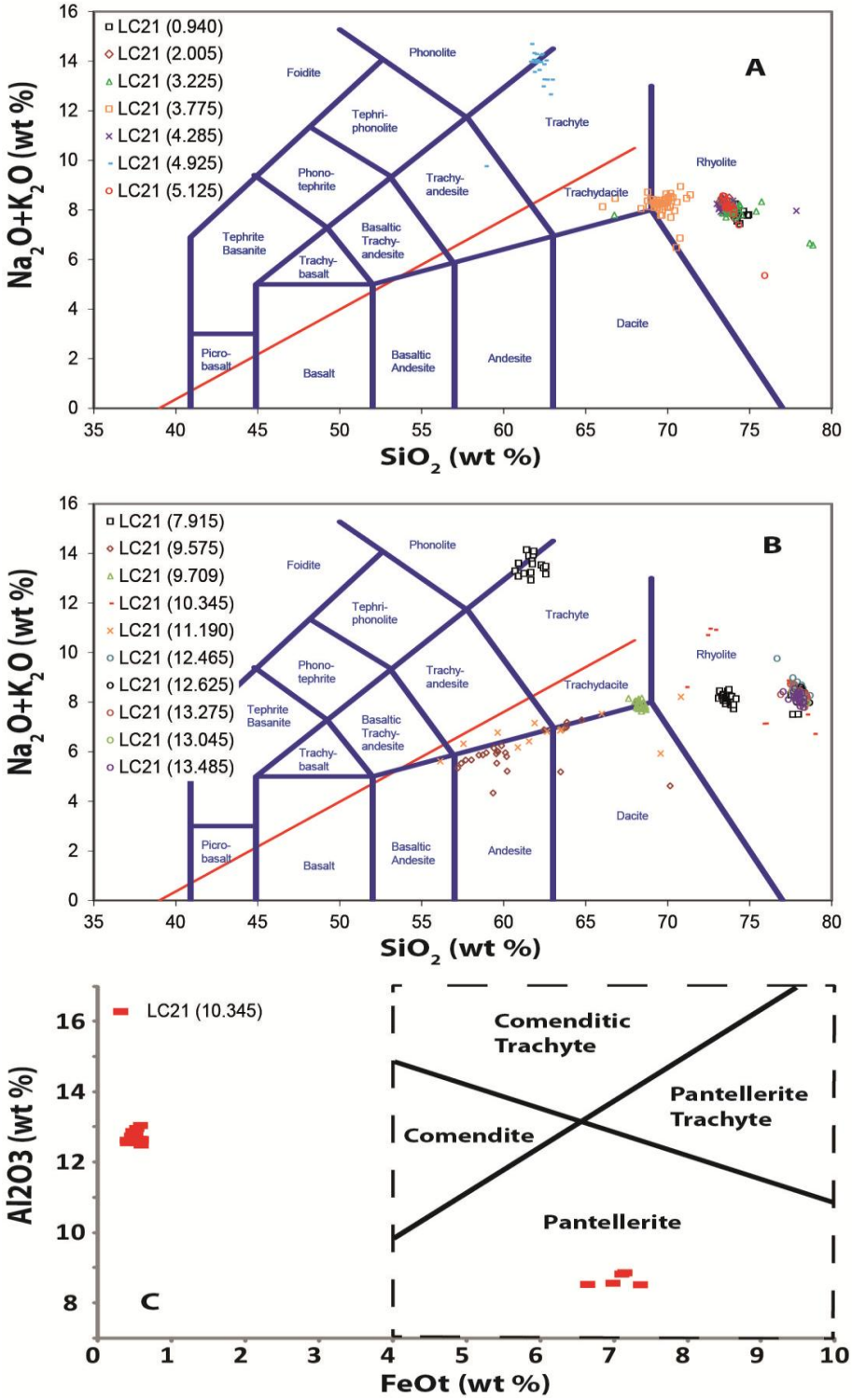

Figure 6.4 Geochemical classification diagrams for all the tephra layers found in core LC21. **A)** Tephra layers between the present day and sapropel 3; **B)** tephra layers between sapropel 3 and the base of the core; **C)** sample LC21 (10.345) which contains shards of Pantellerite.

Sample LC21 (0.01) is the very top 1cm sample from LC21, which contained a shard concentration of 4808 shards/g. This peak in cryptotephra shard concentrations is above a 22.4cm thick visible tephra layer (fig. 6.1) and there are cryptotephra shards mixed into the sediment in the interval between the two. The shards show no evidence of chemical alteration but often contain microphenocrysts which are too small to be identified under the petrological microscope (fig. 6.2). The sample was geochemically characterised to assess its relationship to this visible tephra layer: to ascertain if it constituted a separate volcanic event or reworking of the visible tephra below (as suggested by Watkins et al. 1978). It is classified as Rhyolitic by the Le Bas classification system with SiO_2 contents ranging from ~73% to 74.5% (fig. 6.5). FeOt contents of the shards are ~0.5wt% higher than CaO contents and the K_2O/Na_2O ratio is ~0.6 with Na_2O ~1wt% higher than K_2O. 24 trace element analyses show that this sample has relatively low high field strength element (HFSE) concentrations with Nb between 9 and 12 ppm (6.6). The LREE to HREE ratio (La/Y) is approximately 0.7–0.9.

Sample LC21 (0.940) was taken from the bottom 1cm of the 22.4cm thick dark grey to black tephra close to the top of core LC21 (fig. 6.1). It is possible that this sample does not represent the full range of geochemistry of the tephra deposit, however it should represent the first erupted (Plinian fall) component of the eruption as it was the first to be deposited. The shards are generally vesicular and often fluted in shape, show no evidence of chemical alteration and often contain microphenocrysts (fig. 6.2) which are too small to be identified under the petrological microscope.

The tephra shards in this sample are classified as rhyolitic by the total alkalis versus silica diagram (fig. 6.4) and the shards have a silica content of ~74-75wt%. FeOt is ~0.5wt% higher than the CaO content and Na_2O is ~1wt% higher than K_2O. The trace element concentrations from the LA-ICP-MS analyses show that the shards have relatively low HFSE concentrations (e.g. Nb~8-11ppm, Zr~ 175-300ppm, fig. 6.6) and also that the LREE to HREE ratio (La:Y) is relatively low at approximately 0.7-0.8.

Sample LC21 (0.010) was taken from the sediment above this tephra layer, to test the hypothesis that this sample represents sedimentary reworking of the visible tephra layer. This hypothesis can be falsified if the chemistries of the two samples (LC21-0.940 and LC21-0.010) are different. The results of this comparison are shown in figures 6.5 and 6.6. The two tephra samples are in fact geochemically indistinguishable from one another,

supporting the hypothesis that the shards present in LC21 (0.010) are reworked shards from the visible tephra layer represented by sample LC21 (0.940).

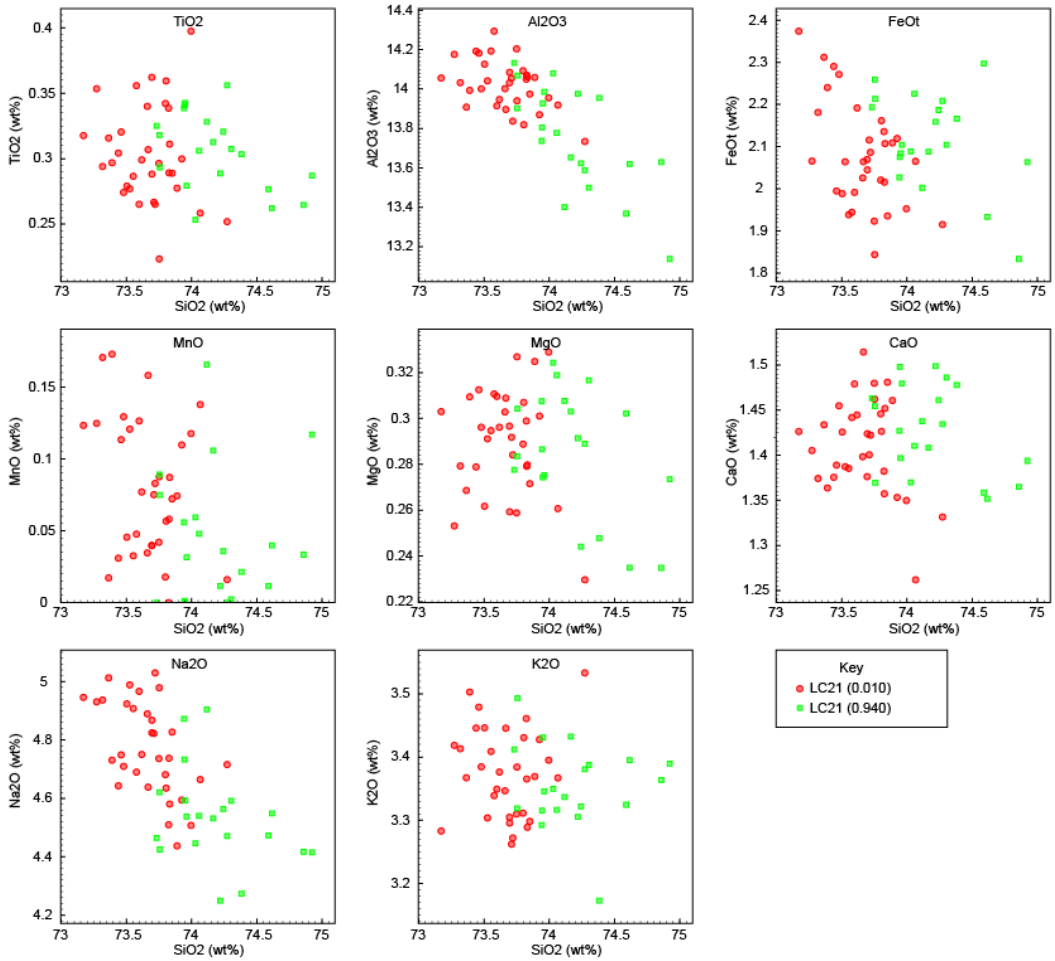

Figure 6.5 Major element analyses of LC21 (0.940) and LC21 (0.010) to test for geochemical differences between the two samples, and thus to identify reworking of the visible tephra LC21 (0.940).

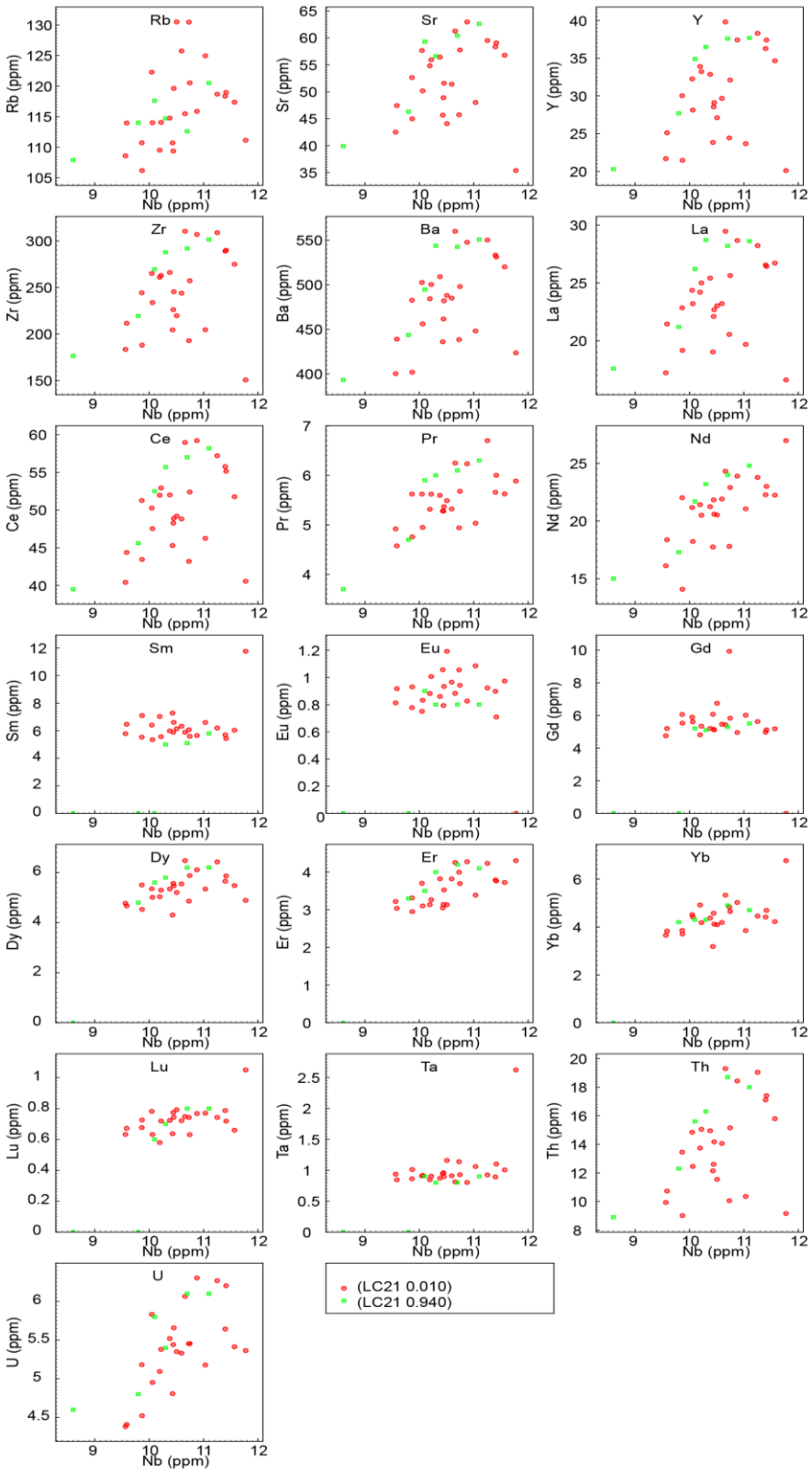

Figure 6.6 Trace element analyses of LC21 (0.940) and LC21 (0.010) to test for geochemical differences between the two samples, and thus to identify reworking of the visible tephra LC21 (0.940).

Tephra LC21 (2.005) The sample lies just below sapropel 1 (fig. 6.1) and the tephra shards from this cryptotephra are constrained within a 1cm sample showing that, if identified, this tephra layer could form a highly precise chronological marker in LC21. The shards are platy and often fluted, but rarely have abundant vesicles and are free of microphenocrysts (fig. 6.2). They are clear in colour and show no evidence of chemical alteration.

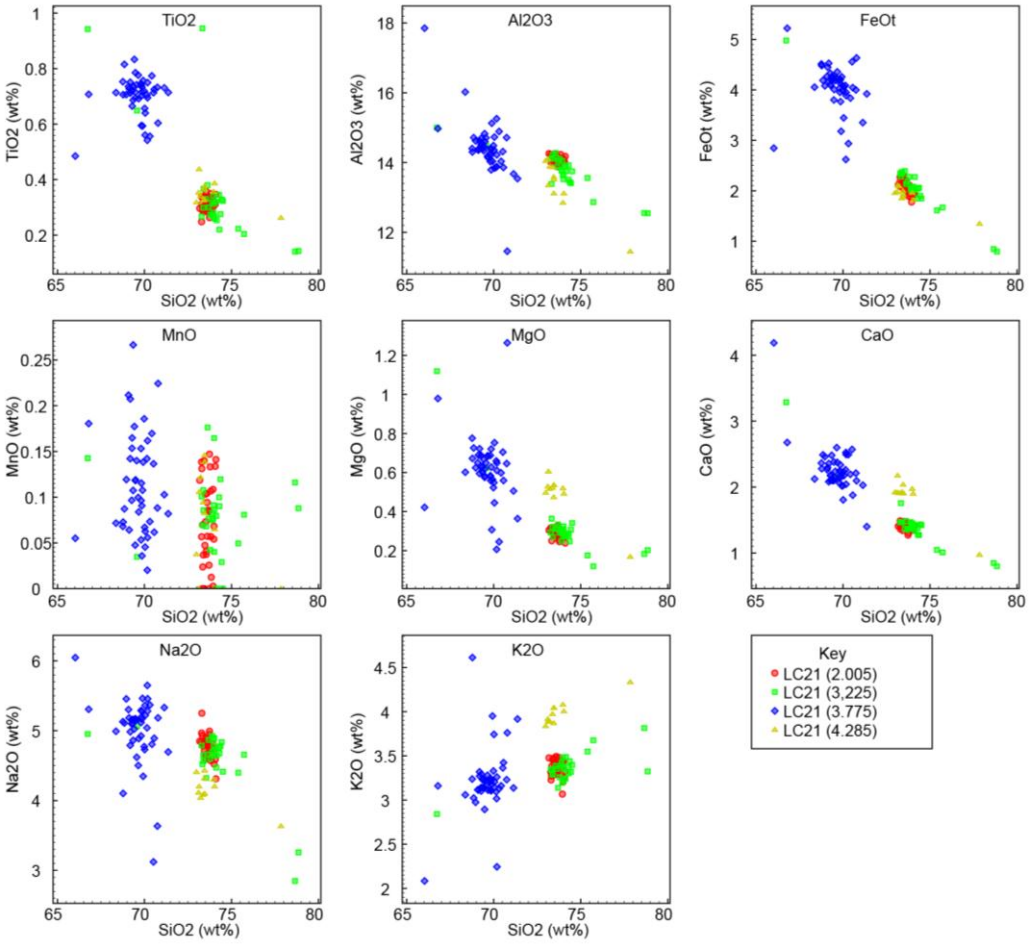

Figure 6.7 All major element analyses of shards found within sample LC21 (2.005), LC21 (3.225), LC21 (3.775) and LC21 (4.285).

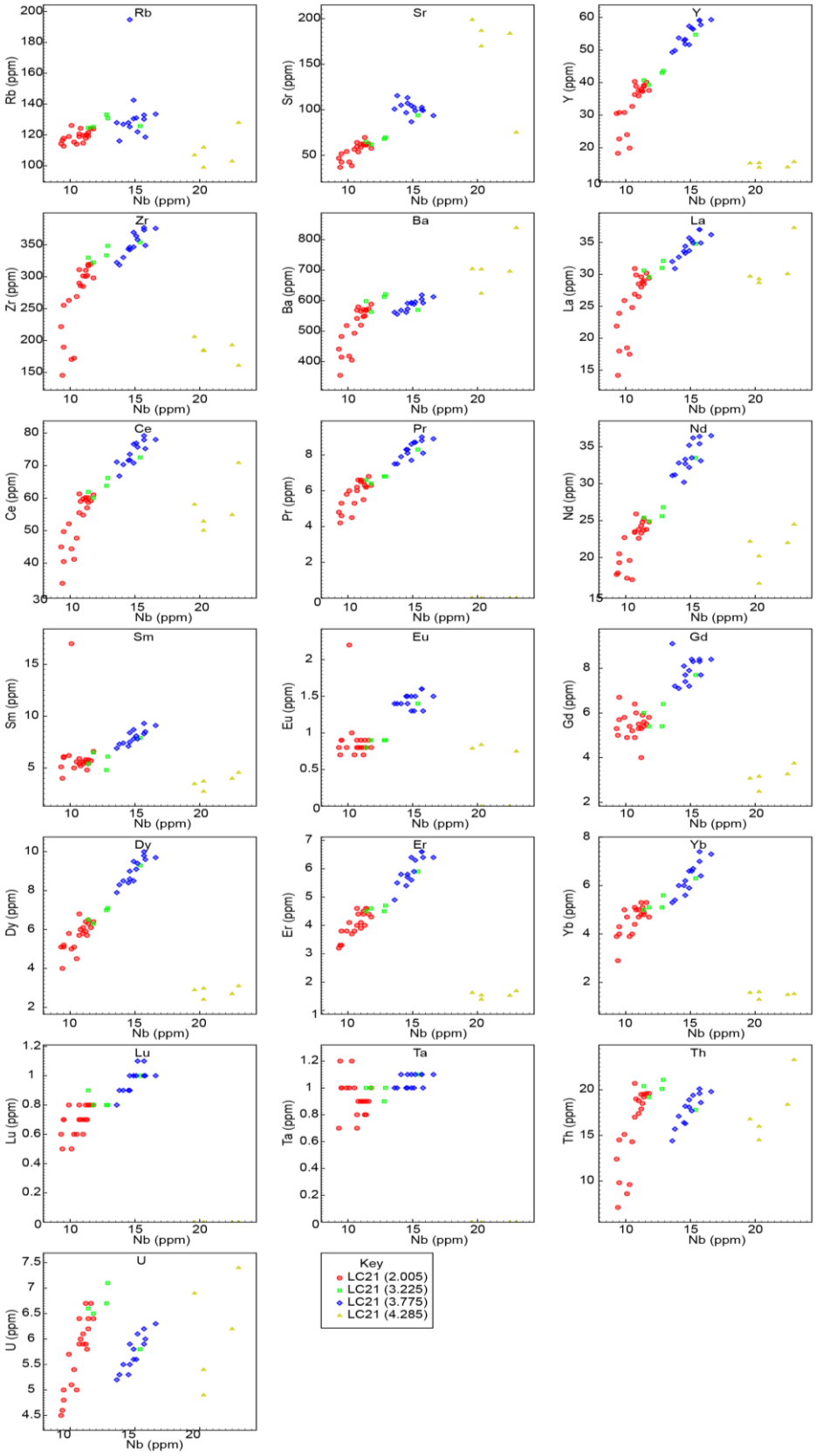

Figure 6.8 Trace element analyses of shards from tephra layers LC21 (2.005), LC21 (3.225), LC21 (3.775), and LC21 (4.285).

The EPMA analysis of thirty four of these tephra shards show that they are, as for LC21 (0.940), classified by the TAS scheme as a rhyolite (fig. 6.4). Similarly they also have FeOt ~0.5wt% higher than the CaO content and Na_2O is ~1wt% higher than K_2O (fig. 6.7). The LA-ICP-MS analyses of nineteen of the shards shows that the sample has a similar values of trace elements to LC21 (0.940) with HFSE concentrations of ~9-12ppm for Nb and ~150-300ppm for Zr (fig. 6.8). The LREE to HREE ratio is ~0.7-0.8.

Tephra LC21 (3.225) is a sample taken from a peak of cryptotephra which is the base of a 3cm depth of cryptotephra in LC21 (fig. 6.1). The shards are a mixture of platy and highly vesicular shards (fig. 6.2) and contain abundant microphenocrysts which were too small to be identified optically. They do not appear to have been geochemically altered. The EPMA analysis provided wt% concentrations for fourty shards and shows that the sample can be classified as a rhyolite (fig. 6.4) and also that the shards have more FeOt than CaO, but also show larger ranges in these two elements than the two previous samples (FeOt~3wt%, CaO~ 1%) (fig. 6.7). The LA-ICP-MS analysis was compromised by the number of micro-phenocrysts in the shards, and produced only five assessments of the trace element concentrations (fig. 6.8). These five shards show Nb values of ~9-15ppm and Zr values of ~320 to 350ppm, comparable to those of the previous two samples discussed here. The LREE to HREE ratio is approximately 0.63-0.72, a little lower than the previous samples.

Tephra LC21 (3.775) This tephra sample was taken from the base of a peak in cryptotephra shards of >10,000 shards/g (fig. 6.1). The shards are generally fluted with occasional small vesicles and no evidence of geochemical alteration. 47 EPMA analyses were attained for this sample. These analyses classify the sample as a trachydacite/rhyolite (fig. 6.4). CaO is in general lower than FeOt in concentration and N_2O is greater than K_2O. This sample has a relatively wide range of major element compositions and SiO_2 ranges from ~65% to 71% (fig. 6.7). The thirteen trace elements were attained by LA-ICP-MS and yield HFSE concentrations (fig. 6.8) intermediate between samples the preceding three samples (described above) and LC21 (4.285) (described below). Nb is ~14.5-16.5ppm and Zr is ~300-375ppm. The LREE to HREE ratio is approximately 0.61-0.66.

Tephra LC21 (4.285) Is also a sample from a peak in cryptotephra with concentrations of >10,000 shards/g, spread over 2cm (fig. 6.1) The shards are often very small (<40µm diameter) and have very large elongate vesicles within them (fig. 6.2), making them difficult to analyse using the available geochemical techniques. They do not show any evidence of

geochemical alteration. 11 EPMA analyses were achieved, describing the shards as rhyolitic (fig. 6.4) and showing that their FeOt concentrations are approximately equal to their CaO concentrations (both at ~1-2wt%). The Na_2O content of the shards is also approximately equal to the K_2O content (~3.5-4%) (fig. 6.7). The shape and size of the glass surfaces on the shards made them impossible to analyse on the 25µm diameter LA-ICP-MS system but the 5µm beam of the SIMS apparatus allowed five quantitative assessments of the trace element concentrations. Nb ranges from 19-23ppm (more enriched than all the samples previously described) while Zr is more depleted with values of ~161-206ppm (fig. 6.8). The LREE to HREE ratio is much higher than the previous samples, ranging from ~1.9-2.3.

LC21 (4.925) is a sample from the base of the 15cm thick white ash layer in LC21 (fig. 6.1). As with the other visible tephra layers in this investigation, the bottom sample may not capture the entire geochemical range of the tephra, but it should represent the initial fall deposit of the eruption. The shards from this sample are vary greatly in their morphologies. Figure 6.2 shows platy shards, fluted shards and highly vesicular shards. The shards did not show any visible micro-phenocrysts and were all clear in colour. The twenty four EPMA analyses show that this tephra is a phonolite/trachyte (fig. 6.4) and that its Na_2O values are lower than the K_2O values. CaO is always lower in concentration than FeOt (figs 6.9 and 6.10). The apparent lack of micro-phenocrysts does not guarantee abundant LA-ICP-MS analyses; which yielded only five glass-only analyses (fig. 6.11). Other analyses contained such abundant vesicle components that they had to be discarded. The five successful trace element determinations show very elevated HFSE concentrations (Nb~120-130ppm, Zr~600-700ppm) (fig. 6.11), which is far in excess of the samples previously discussed. The LREE-HREE ratio is also relatively high at 2.3-2.4 (even higher than sample LC21-4.285).

In addition to the initial sample for this visible tephra layer, three more samples were taken for the top 5cm, the middle 5cm and the base 5cm of the tephra. These were taken to test if the composition of the tephra changed with height. Major element comparisons of these samples to LC21 (4.925) are shown in figure 6.9. These samples are described further in the discussion chapter (Chapter 7).

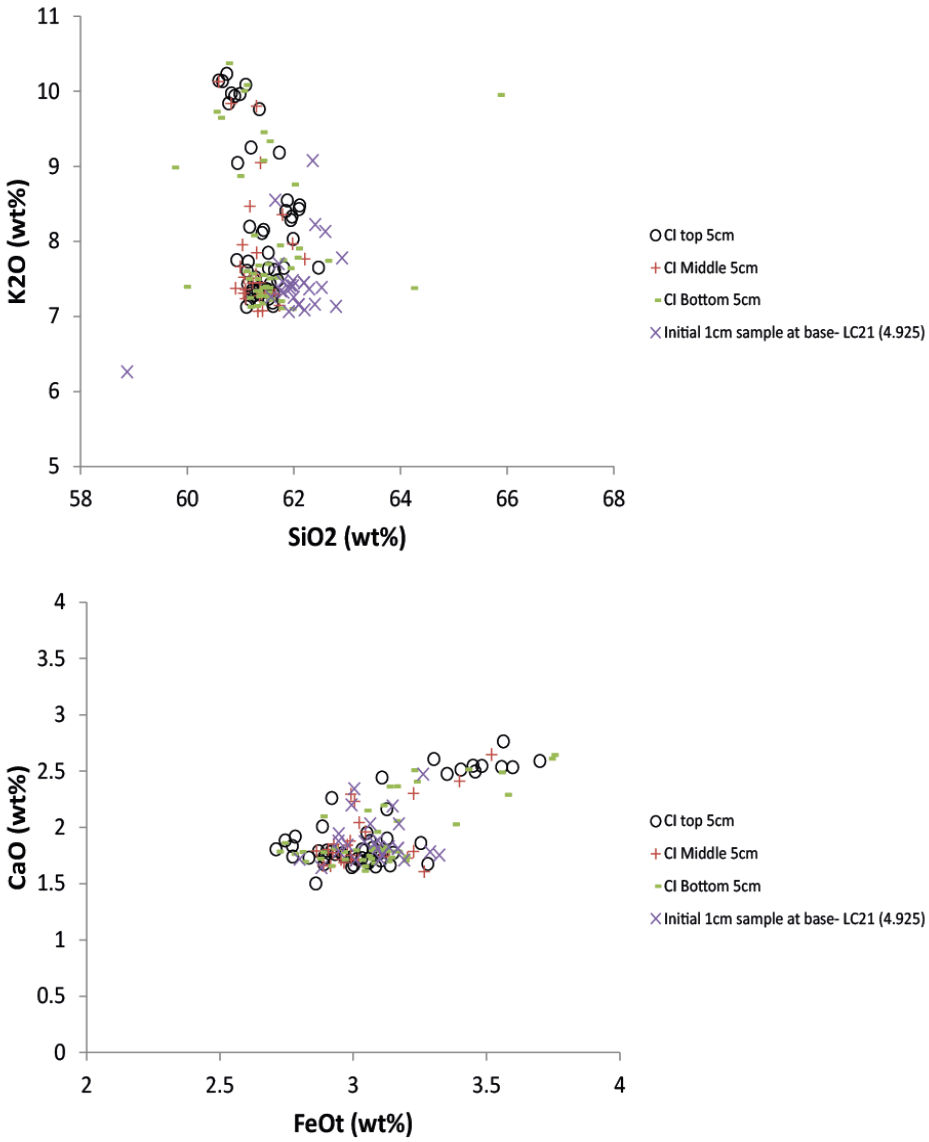

Figure 6.9 Alkali and CaO vs FeOt plots for all four samples taken from the visible tephra layer at 4.925m depth in core LC21.

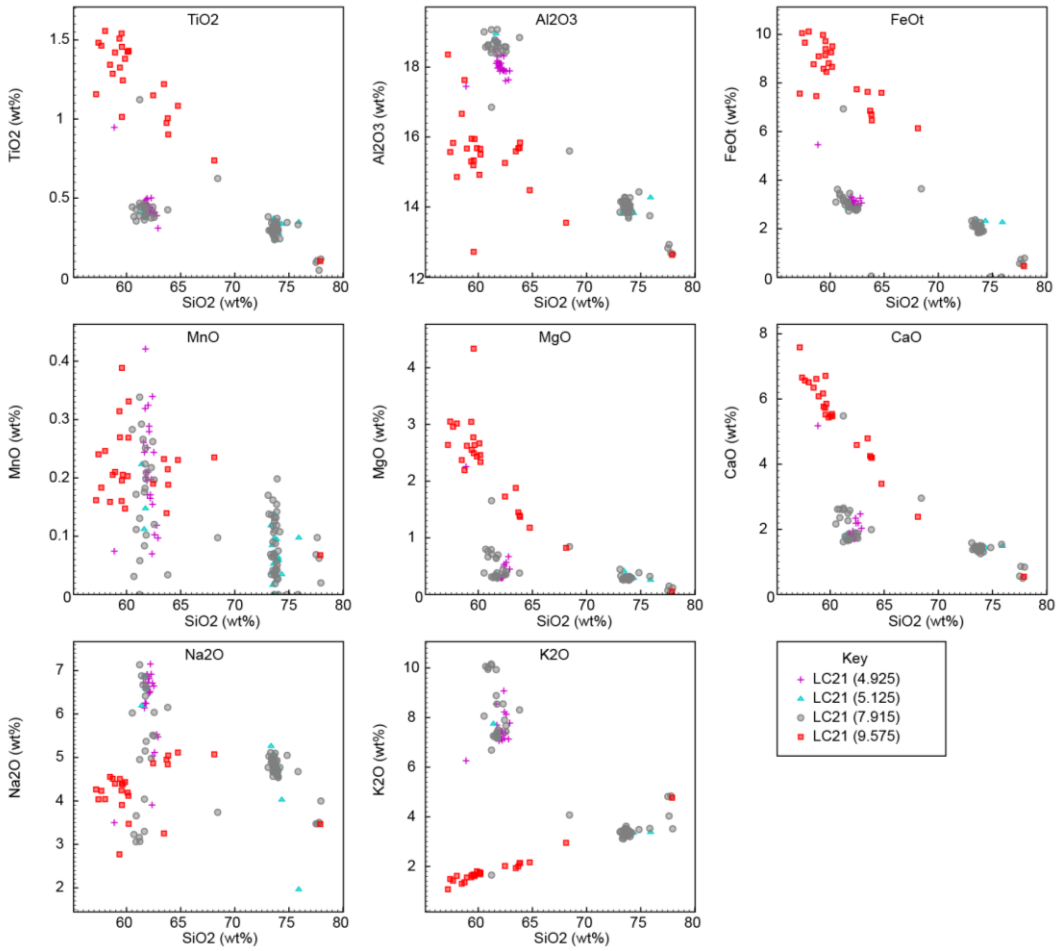

Figure 6.10 Major element analyses of samples from LC21 (4.925), (5.145), (7.915) and (9.575).

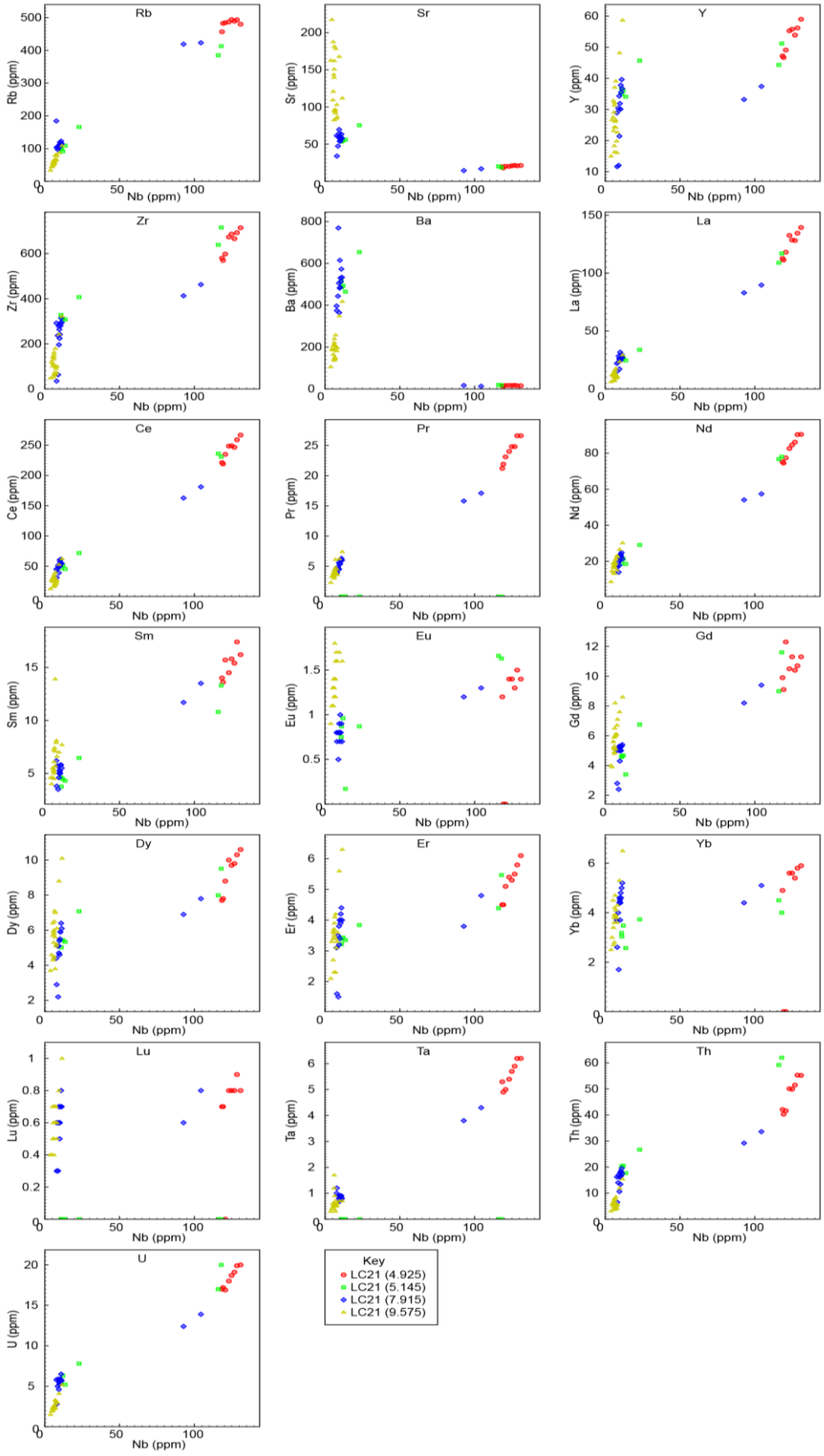

Figure 6.11 Trace element analyses of shards from samples LC21 (4.925), (5.125), (7.915), (9.575).

Sample LC21 (5.125) is a 5cm sediment sample which contains tephra shards (fig. 6.1). When the core was re-sampled at 1cm resolution, no shards were recovered. Possible explanations for this are that 1) the tephra are contamination from another sample, 2) that the shards were only present in a small 'pocket' of sediment and were not laterally ubiquitous across the core, or 3) that the tephra layer was laterally ubiquitous, but was mostly removed by the saw when the core was being cut into sections (this sample is the top sample in section 8 of LC21). In the first case, the tephra shards would be chemically and morphologically identical to those from another tephra layer found in the core, which was processed coevally with this sample. In the latter two scenarios, the shards would be different in some respect from those of the other tephra layers investigated.

The shards in this sample are either platy or highly fluted (fig. 6.2), show no visible phenocrysts or evidence of chemical alteration. The twenty one EPMA analyses revealed eighteen rhyolitic shards and 3 phonolitic shards (fig. 6.4). The rhyolitic shards have SiO_2 values of 73-76wt% and CaO values lower than the FeOt values. K_2O is lower than Na_2O (fig. 6.10). The phonolitic shards (SiO_2~61.5 wt%) also show CaO lower than FeOt, but K_2O is greater than Na_2O. The shards in this sample were mainly platy, but occasionally vesicular or fluted and all were clear in colour. Their platy morphology meant that when sectioned using the cutting and polishing techniques (Chapter 5), it was difficult to expose large surfaces for trace element analysis with the LA-ICP-MS, and so the smaller beam of the SIMS was used for this sample. Both the rhyolitic and the phonolitic shards were analysed using the SIMS. The five rhyolitic analyses show Nb values ranging from 10.9 to 23.0ppm (fig. 6.11) and Zr values from 308 to 407ppm. The La/Y (LREE to HREE ratio) is ~0.7-0.8. The phonolitic shards (2 analyses) have much higher Nb values of 118 and 116ppm, and Zr values of 716 and 639ppm (fig. 6.11). The LREE:HREE ratio is also much higher at ~2.3 and 2.5.

LC21 (7.915) is a sample from within sapropel S4a in LC21. The sample is taken from a peak in tephra shards of >1000shards/g and there are tephra shards in much lower concentrations in the 1cm sample below this peak, and the 2cms above the peak (fig. 6.1). The shards are of mixed morphologies; some are fluted, some platy and some highly vesicled (fig. 6.2). Initially the EPMA was used to attain major element data indiscriminately on all these shard morphologies. This analysis revealed seventeen trachyte/phonolitic shards and 38 rhyolitic shards (fig. 6.10). The trachyte/phonolitic shards all have CaO lower in concentration than FeOt, and K_2O greater than Na_2O. However, the trachyte/phonolitic

component of this sample is bi-modal in its Na_2O composition, with one discrete mode containing N_2O <4.5wt% and the other >4.5wt%. The rhyolitic component (68-78wt% SiO_2) has K_2O ~1wt% higher than Na_2O and FeOt exceeds CaO by <1wt% (fig. 6.10).

The 13 trace element analyses for the rhyolitic component of this sample show relatively low values of 7-11ppm Nb and LREE to HREE ratios of 0.7 and 2.4 (fig. 6.11)

The trace element analyses using the LA-ICP-MS were only possible on two of the trachyte/phonolitic shards, presumably because these shards are in general smaller than the rhyolitic shards in this sample, although no record of this was taken. Both of these shards were from the >4.5wt% N_2O mode. They show high Nb values of 92.81 and 104.44ppm but these are lower than the ~120-130ppm derived from the visible trachyte/phonolite in LC21 (sample LC21- 4.925) indicating that these shards are unlikely to be contaminants from that layer/sample. Zr values are 462.9 and 412.9ppm (fig. 6.11), also out with the ~600-700ppm range of values shown for LC21 (4.925). The LREE to HREE ratios for these two shards are 2.4 and 2.5.

The mixed morphology and chemistry of this tephra layer provided an opportunity to test if the morphology of the tephra shards was related to their chemistry. With this in mind, three additional geochemical stubs were made for this sample, one containing only platy shards, one only vesicled shards and the last only fluted shards. Each was analysed by EPMA and LA-ICP-MS. The platy shards were too thin to produce a good signal on the LA-ICP-MS and so no trace element analyses were attained for this sample, however the 3 geochemical modes are most clear using Na_2O. The results of this test are shown in the Na_2O vs SiO_2 plot in figure 6.12

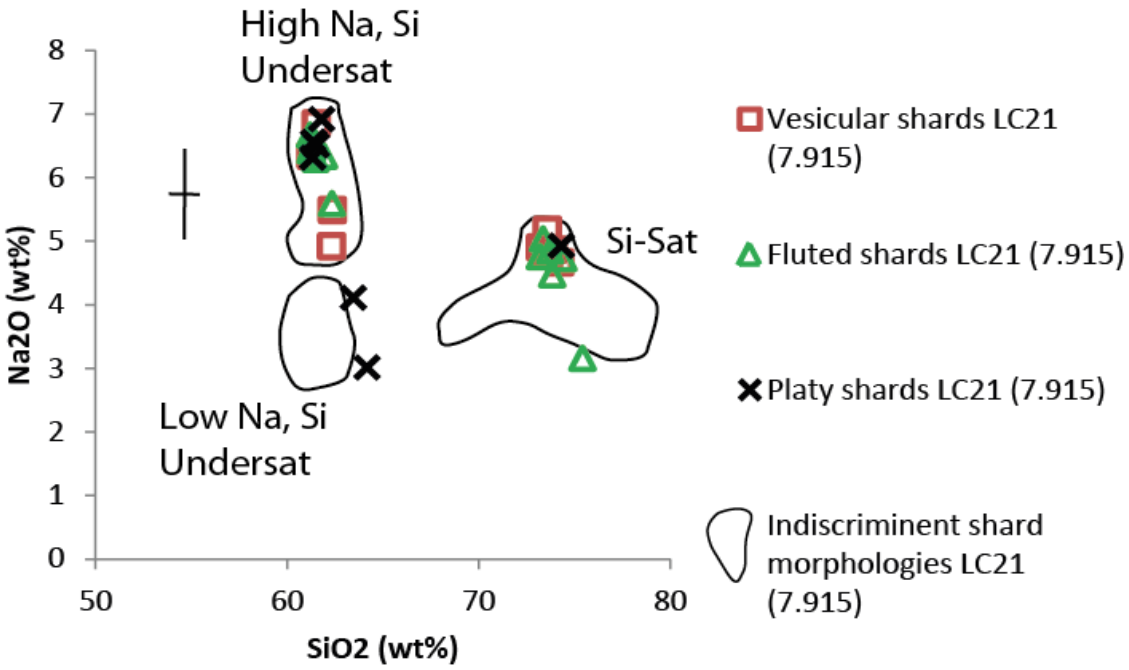

Figure 6.12 Comparison of shard morphologies and their geochemical signals for sample LC21 (7.915). The original, unsorted analyses are shown by the fields and defined by the modes described in the text. The three re-sampled subsamples of shards, discriminated this time by their morphology, are shown by the symbols. The vertical cross on the left indicates the estimated variability of the EPMA (from StHs6/80G standard).

The fluted and vesicular shards appear to yield only the silica saturated and high Na components of LC21 (7.915). It appears that the platy shards are the sole morphology associated with all three geochemical components, and the only ones to yield the low Na (<4.5wt%) geochemical component. These platy shards are the most challenging to analyse as their cut surfaces tend to be very small and thin. This micro-study also demonstrates the comparability of EPMA measurements on the same sample in two or more analytical batches.

LC21 (9.575) is the lowermost sample of many which contain >10000 shards/g of tephra in sapropel S5 in LC21. The tephra from this sample may not be representative of all the tephra in this section of the core. The shards are both brown and clear coloured in this sample, with rare phenocrysts, and can be both platy and vesicle free or thicker and contain vesicles (fig. 6.2). The EPMA analyses classify the shards as andesitic and dacitic (fig. 6.4) with a large range of SiO_2 values (~57-64wt%). The other major elements show a similarly large range in values, although FeOt is always more abundant than CaO, and Na_2O is always greater than K_2O (fig. 6.10). The Nb (~4-11pmm) and Zr (61-321ppm) values show a wide range, in contrast to the LREE to HREE ratio which is consistently low (0.38 – 0.68) (fig. 6.11).

LC21 (9.709) is a very thin (~1mm) visible tephra layer within Sapropel S5 in LC21 (fig. 6.1). Its position in the sapropel could make it an important stratigraphic marker for the correlation of LC21 to other sites. The tephra shards are generally platy with few vesicles or phenocrysts and are free of evidence of geochemical alteration (fig. 6.2). The EPMA analyses describe the shards as trachydacite/dacitic with Ca values of ~2.5-2.7wt%, always lower than the FeOt values of ~5.0-5.5wt%. Na_2O values are consistently 4.5-5.0wt% and higher than the 2.0-3.5wt% K_2O values (fig. 6.10). These are relationships which appear to be consistent for all the silica-saturated samples discussed thus far for core LC21 (with the exception of LC21 4.285). The Nb content ranges from ~4-12pmm and Zr from 312-345ppm (fig. 6.11), which is also consistent with all the silica-saturated samples discussed so far for this core (again with the exception of LC21 4.285). LREE to HREE ratios are confined to the range 0.50-0.53 for all the shards in this sample.

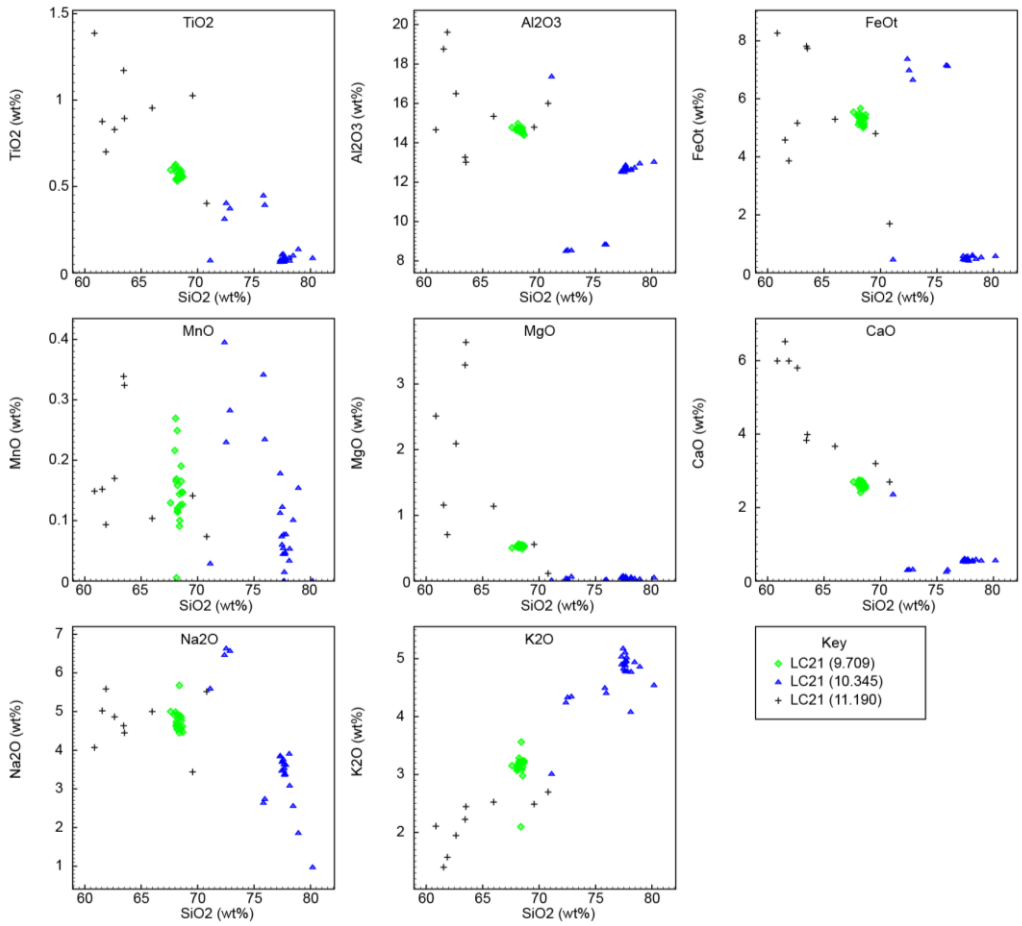

Figure 6.13 Major element analyses of tephra shards from samples LC21 (9.709), (10.345) and (11.190).

LC21 (10.345) represents a peak in tephra shard concentrations of 2357 shards/g at the base of a 4cm interval containing cryptotephra (fig. 6.1). It contains both small platy shards and larger fluted shards (fig. 6.2). No shards contain significant vesicles or phenocrysts and none show evidence of geochemical alteration. The sample contains shards of high silica rhyolite (>77wt% silica), and pantellerite (>6% FeOt and <9% Al_2O_3) although no evidence was gathered to determine if these two compositions relate to the two shard morphologies. The shards of pantellerite are highly distinctive and only the volcano of Pantelleria, after which the composition is named, is known to produce such compositions of magma. As the shards in this sample were all too small for LA-ICP-MS anlaysis, and due the distinctive nature of the Pantellerite shards, it was decided that the cost of analysis was too high to submit this sample for SIMS, therefore no trace element data exists for this sample. The shards of >77wt% SiO_2 contain more K_2O than Na_2O and thus differ from most of the other rhyolitic samples so far discussed in LC21. The shards also have very low FeOt and CaO values (<1wt%) and the two are generally equal in abundance (fig. 6.13).

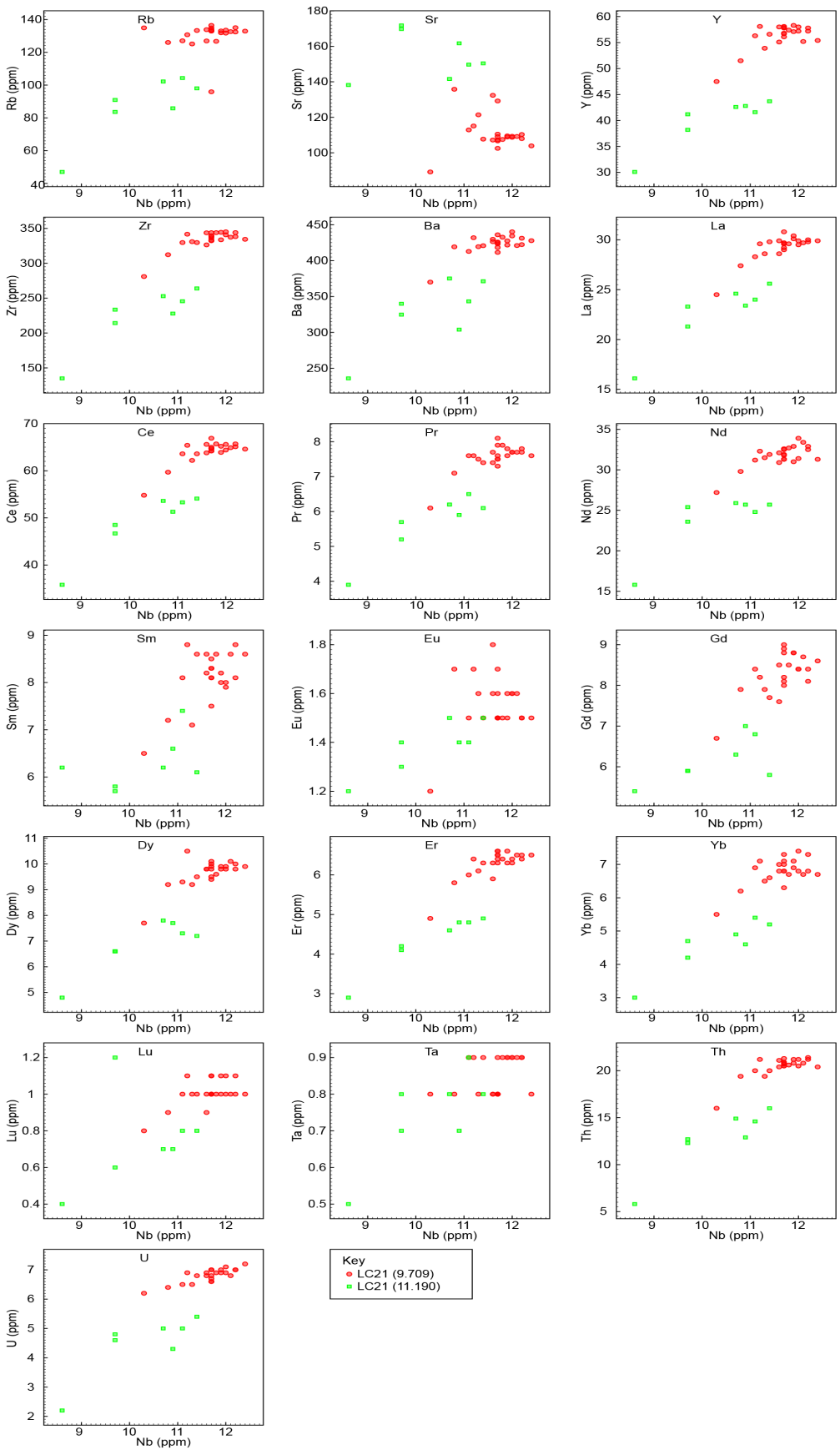

Figure 6.14 Trace element analyses of tephra shards from LC21 (9.709) and LC21 (11.190).

LC21 (11.190) is a sample from the base of the 42cm thick visible tephra below S5 in LC21. The shards are highly vesicle rich and vesicular. 9 EPMA analyses of the phenocrysts rich shards in this sample show that it has a very variable chemistry ranging from ~57-70wt% SiO_2 classifying the shards as basaltic andesite to rhyolite (fig. 6.4). The Na_2O values are always in excess of the K_2O values but there is no consistent difference in the abundance of CaO and FeOt (fig. 6.13). These EPMA analyses are not thought to contain a mineral component, as the electron backscatter facility on the EPMA was used to avoid minerals (see chapter 5) These variable chemical analyses may reflect the influence of the phenocrysts such as ortho or clinopyroxenes, or amphiboles on the glass chemistry. The abundant phenocrysts inhibited the LA-ICP-MS measurements as often there were mineral components in the analysis. As a result, only 6 trace element analyses could be achieved for this visible tephra. These trace element analyses show Nb values of 8-11% and consistent La/Y ratios of 0.53-0.58 (fig. 6.14)

Tephras LC21 (12.465), (12.625), (13.275), (13.405) and (13.485). These 5 visible tephras are all contained within the lowermost core section (section 3) of LC21. The sediment between and above all 5 is very rich in tephra shards (>10,000 shards). In addition the lower 4 tephra layers are all inclined within the core and have an unusual geometry (table 6.1) All five have platy shards and are phenocrysts free (fig. 6.2). The elemental abundances ascertained by EPMA (fig. 6.15) and LA-ICP-MS (fig. 6.16) are identical for all 5 of these tephra samples and so they are all described concurrently here.

The 140 EPMA analysis of the shards in these 5 samples shows that they have a very homogenous major element composition and are classified as high silica rhyolites (>77% SiO_2) (fig. 6.4). The shards of all these five samples have indistinguishable major element compositions with very low and virtually equal CaO and FeOt values (~0.4-0.6wt%). K_2O (~4.5-5.0wt%) is always greater than Na_2O (3.5-4.0wt%) (fig. 6.15).

The micro-phenocrysts free nature of the samples meant that many LA-ICP-MS analyses were achieved. 113 LA-ICP-MS analyses were achieved and show that the Nb varies between 20 and 24ppm, while Zr has values between ~44 and 56ppm (fig. 6.16). The LREE to HREE ratio is consistently 1.5-2.0.

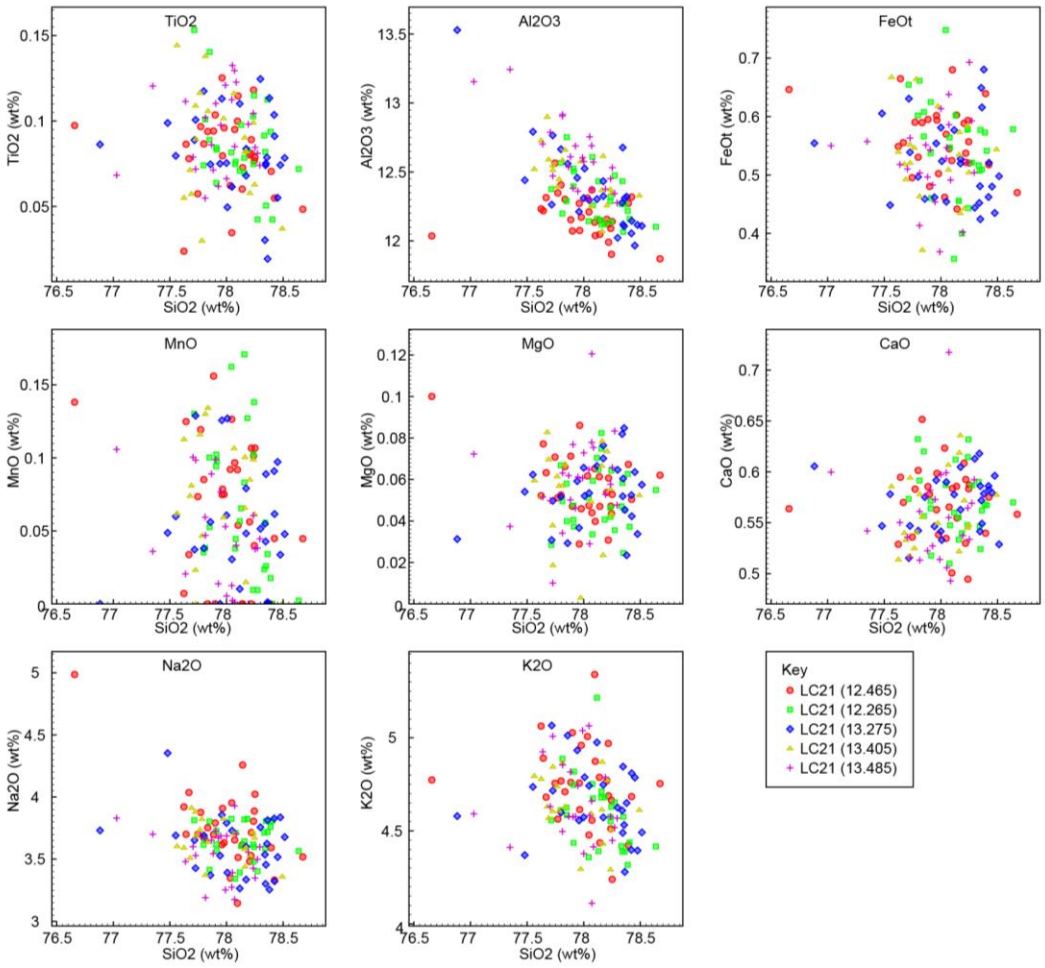

Figure 6.15 Major element analyses for samples LC21 (12.465), (12.625), (13.275), (13.405), (13.485).

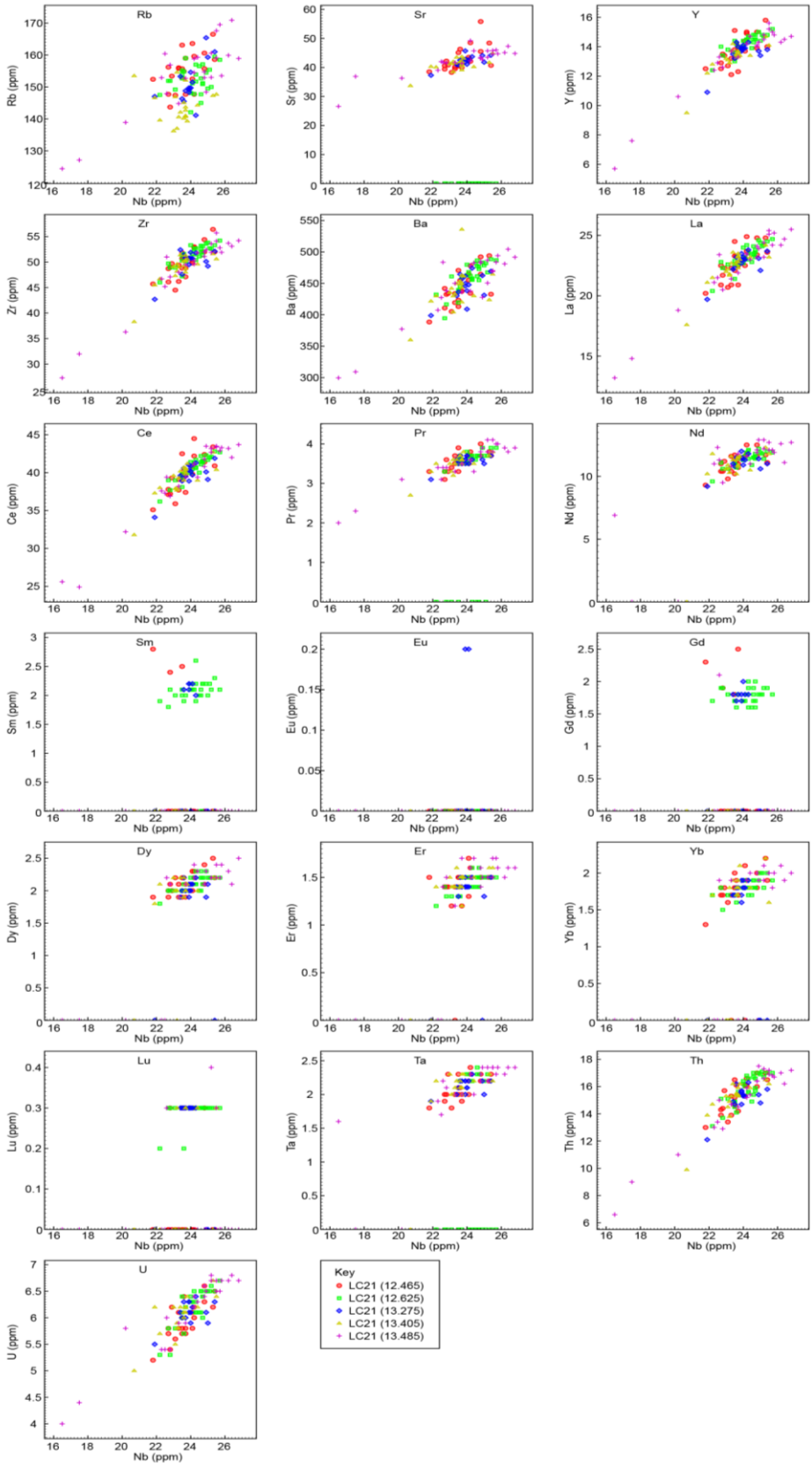

Figure 6.16 Trace element analysis of tephra shards from samples LC21 (12.465), (12.625), 13.275), (13.405), (13.485).

6.2 ODP967-Results.

6.2.1 Shard count results.

Work on ODP967 was compromised by time constraints which forced the sampling to be targeted to specific time periods of interest defined by the existing age model (Larrasoana et al.2003) and the sapropel stratigraphy. The core was chosen to potentially allow comparison of its proxy record with that of core LC21, via the tephra layers. As the tephra work on LC21 was complete, the sampling of ODP967 was targeted in an attempt to find the same tephras as were found in LC21. LC21 tephras were targeted in ODP967 using dates defined by the LC21 age model (fig. 6.3, table 6.1) and the dates in the corresponding, orbitally tuned, ODP967 age model (Larrasoana et al.2003), with additional qualitative stratigraphic information from the sapropel stratigraphy. As there was potential for error derived from the orbitally tuned Larrasoana age model within this targeting strategy, samples were taken for 20-30cm (depending on the target date in question, table 6.2) either side of the targeted age depth in ODP967. This 20cm accounts for an error of approximately ±7-12 ka either side of the predicted age according to the Larrasoana et al. (2003) age model.

LC21 tephra	Date for tephra from LC21 age model (Grant et al. 2012) Or (where stated) from literature.	Depth of date in ODP967 according to age model of Larrasoana et al. (2003)	Depth sampled (and dates according to Larraoana et al.age model).
LC21 (2.005)	11.25±0.55ka 11.11±0.52ka	1.43m=11.25ka	Sampled continuously from 3.36ka to 40.28ka as predicted by the Larrasoana age model*
Cape Riva eruption (not found in LC21)	21,705 ± 311 cal BP (Eriksen et al. 1990	1.94m=21.69ka	Sampled continuously from 3.36ka to 40.28ka as predicted by the Larrasoana age model*
LC21 (3.225)	24.31±2.89ka 24.21±2.87ka	2.01m=24.34ka	Sampled continuously from 3.36ka to 40.28ka as predicted by the Larrasoana age model*
LC21 (3.775)	29.49±3.88ka	2.15m=29.45ka	Sampled continuously from 3.36ka to 40.28ka as predicted by the

	29.40±3.86ka		Larrasoana age model*
LC21 (4.285)	34.86±2.47ka 34.75±2.53ka	2.30m=34.92ka	Sampled continuously from 3.36ka to 40.28ka as predicted by the Larrasoana age model.*
LC21 (4.925)	39.22±0.19ka (de Vivo et al.2001).	2.42m=39.07ka	Sampled continuously from 3.36ka to 40.28ka as predicted by the Larrasoana age model.*
LC21 (5.125)	43.34±2.94ka 42.28±2.25ka	2.50m=42.08ka	Not targeted as was a very minor tephra in LC21 and unlikely to be found in ODP967.
LC21 (7.915) (within sapropel 4 in LC21)	103.98±1.79ka 104.10±1.78ka	5.59m=103.93ka	Sampled all of Sapropel 4 and 13cm below and 4cm above.
LC21 (9.575) (within Sapropel S5 in LC21)	125.72±3.01ka 125.77±3.00ka	7.66m=125.82ka	Sampled all of sapropel S5 in ODP967 and 3cm below and 8cm above.
LC21 (9.709) (within Sapropel S5 in LC21)	126.51±2.92ka	7.70m=126.55ka	Sampled all of sapropel S5 in ODP967 and 3cm below and 8cm above.
LC21 (10.345)	133.47±1.63ka 133.58±1.53ka	8.00m=133.45ka	Not targeted as Pantelleria eruptions were thought unlikely to be preserved in this core.
LC21 (11.190)	152.58±2.54ka	8.83m=152.54ka	Targeted at 142.54ka* in ODP967 with 15cm above and below.

Table 6.2 The predicted depths in ODP967 of tephras found in LC21 and the sampling strategy associated with each tephra. *Some tephras were targeted 7-10ka above the depth predicted by the Larrasoana age model, as initial analyses of the two visible layers in the core, indicated that these were likely to be the Kos Plateau Tuff and the Cape Riva tephra- both of which had predicted ages from the Larrasoana age model which were 7-10ka older than the radiometric ages for these tephras.

Although this sampling strategy is fallible as it relies on the existing age model (which is to be tested using any tephra layers found), it was considered that the ~14-24ka window of sampling would accommodate any error in the age model of Larrasoana et al. (2003). Should the tephra not be found in the sampling window it would mean either that the age model of Larrasoana was wrong by > 7-12ka, or that the tephra was not deposited at the location of this core and was thus not preserved within it.

The results of both scan (10 or 5cm resolution) and 1cm resolution are shown in figure 6.18 and the samples are shown against the existing (unpublished) proxy records produced by K. Grant in figure 6.17.

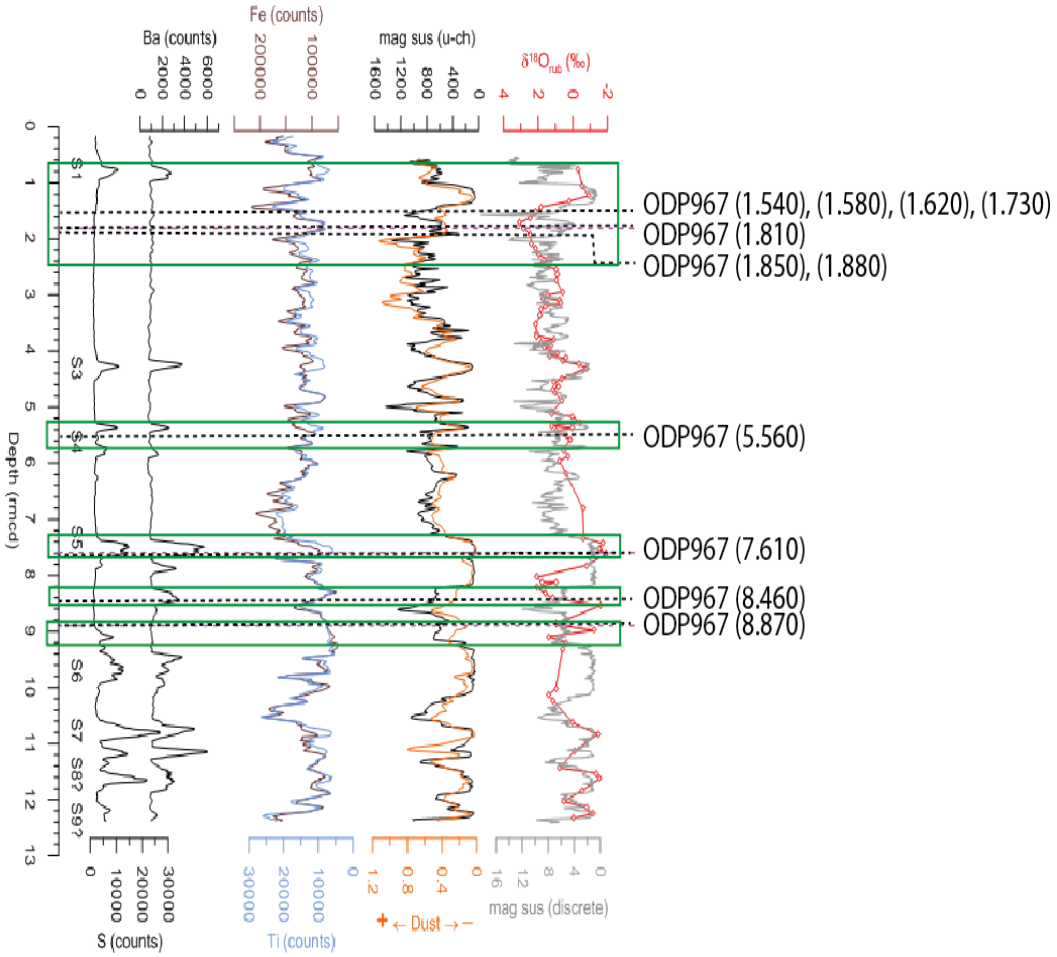

Figure 6.17 ODP967 proxies (produced with K. Grant of NOCS) shown with the locations of the tephra samples selected for geochemical analysis (dotted horizontal lines). Sections of the core targeted for tephra are shown by the green boxes. Other sections of this core were not processed and therefore may contain tephra layers undiscovered by this study. Sapropels are defined by the peaks in the S and Ba counts and are numbered S1 to S9 on the left on the diagram. Shard counts for all of these tephra samples can be seen on figure 6.18 and their TAS classifications are shown on figure 6.20, 6.21 and 6.22.

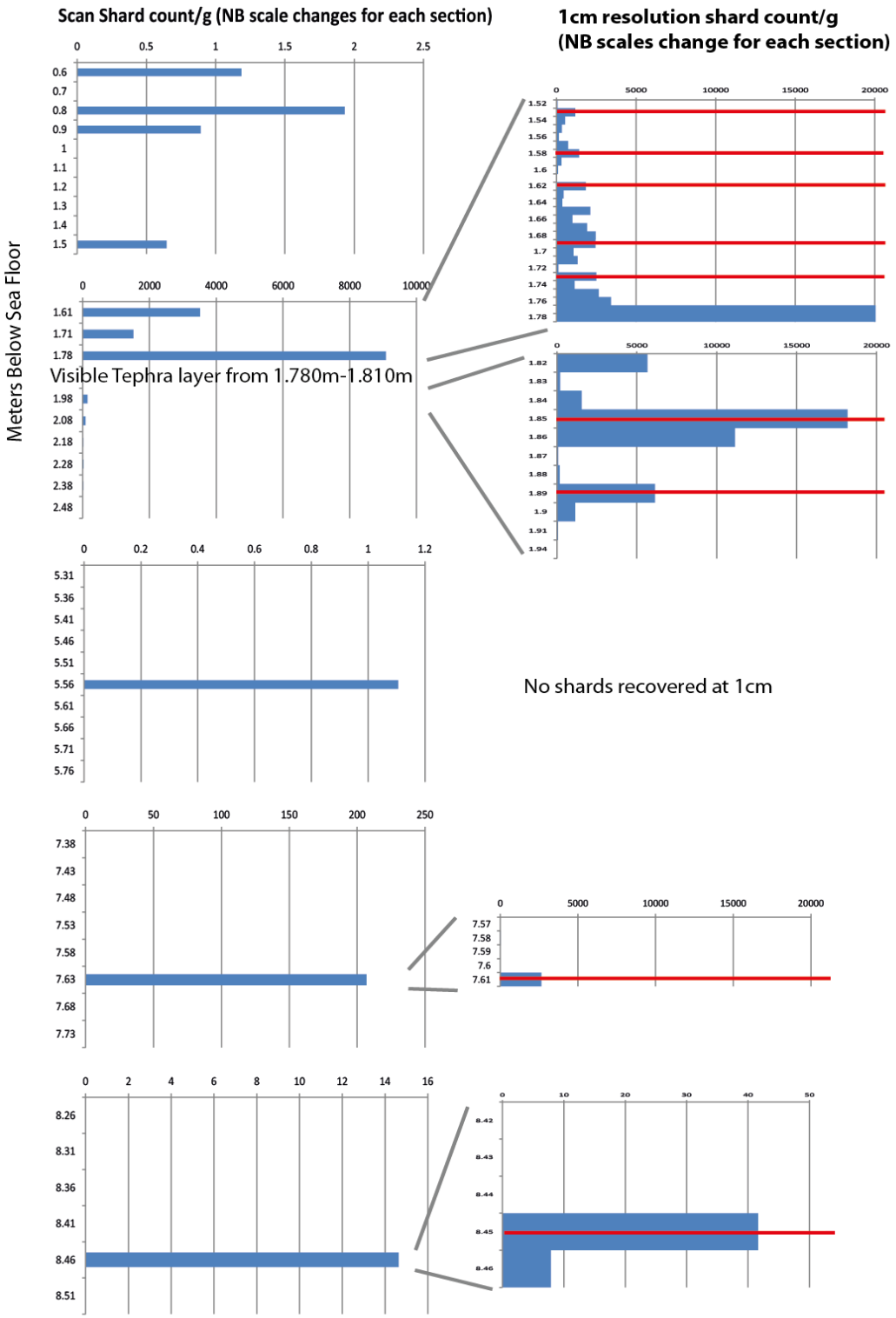

Figure 6.18 Scan and 1cm shard counts for ODP967, with the locations selected for tephra sampling shown by the red lines. NB: scale bars for both the depth and shard counts are variable between each section.

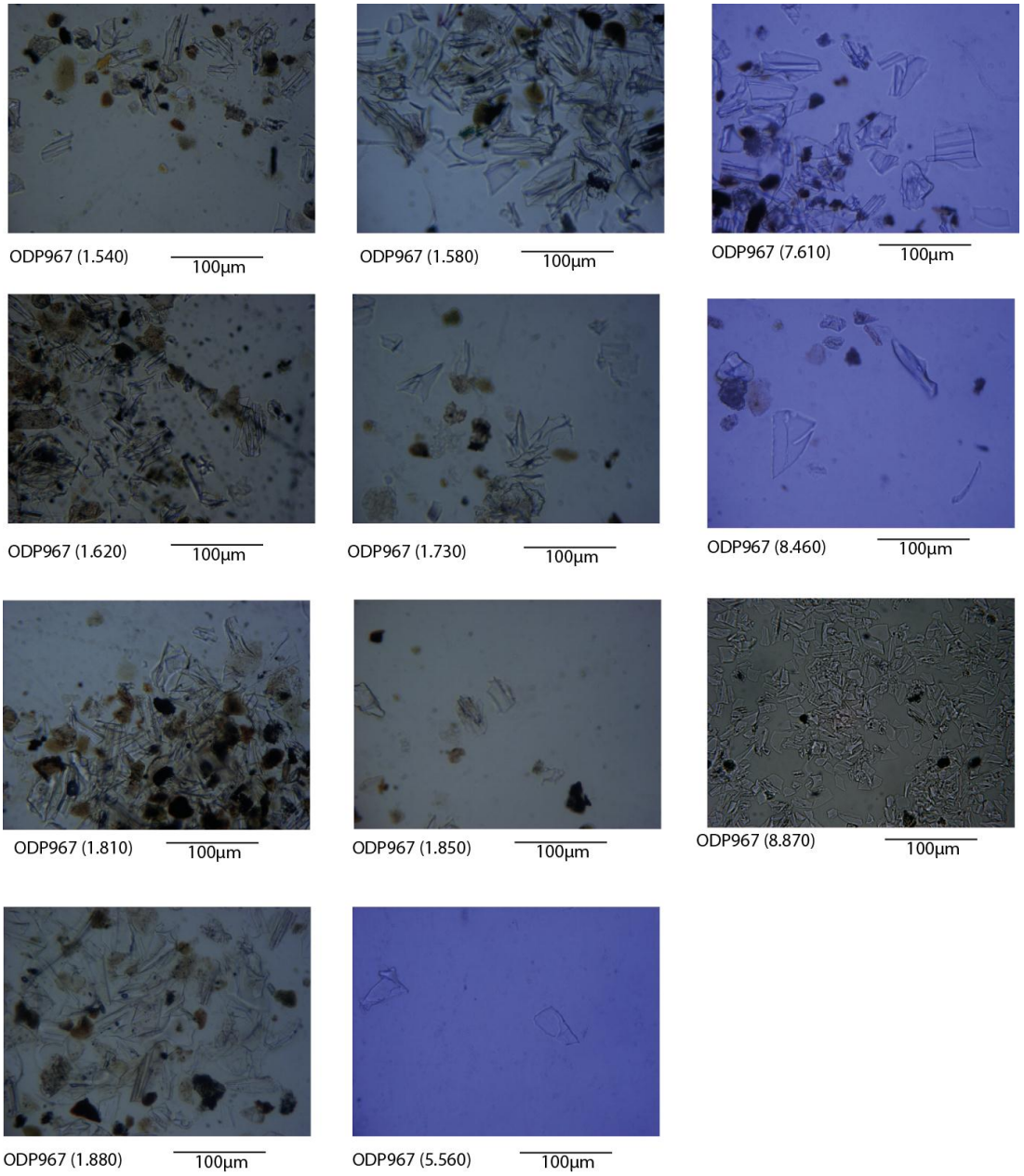

Figure 6.19 Photomicrographs of tephra shards from samples in core ODP967.

The tephrostratigraphy of ODP967 consists of two visible tephra layers, one at 1.81-1.78m depth and one at 8.87-8.86m depth (figs 6.17 and 6.18). Both of these white tephra layers consist of clear, occasionally fluted, shards with low numbers of vesicles (fig. 6.19).

There is an additional, well defined cryptotephra layer within the 1cm sample at 7.61-7.60m (figs 6.17 and 6.18). This sample yielded shard concentrations of 2638 shards/g (210 shards in sample) and is concentrated within the one cm sample with no tephra in the 1cm samples above or below. The shards are clear, occasionally fluted and with few vesicles (fig. 6.19).

Two peaks in cryptotephra also occur below the uppermost visible tephra layer, in the samples at 1.84-1.85 cm and 1.87-1.88cm, yielding shard concentrations of 18197 shards/g and 6137 shards/g respectively (fig. 6.18). Each peak has tephra in the 1cm sample above and below it, but the large (>100shards/g) concentrations are restricted to 3cm sections. Both of these peaks are thought likely to constitute eruptions as they are nearly discrete from one another, and from the visible tephra (ODP967 1.810) above them.

Above this visible layer (ODP967 1.810), there are cryptotephra shards in the sediment from 1.52m to the level of the visible tephra at 1.78m. Within this region of cryptotephra there are several peaks in shard concentrations (fig. 6.18). These peaks were sampled for chemical analysis to determine if they constitute separate eruptions from the visible tephra below them (ODP967 1.810), or, conversely if they represent reworking of this tephra into the sediment above it (as proposed by Watkins et al. 1978). Should the chemical compositions of all these layers be identical to the visible layer it is highly likely that they are reworked artefacts of the visible layer. Should the composition be different it is unlikely that they are reworked, and therefore would represent distinct eruptions.

6.2.2 Results of Geochemistry from ODP967

Eleven samples were extracted for geochemical analysis from core ODP967. The locations of these samples are shown in figures 6.17 and 6.18, and the details of each sample are given in table 6.2 The geochemistry of the samples is summarised by figures 6.20-6.26.

ODP967 (1.540) is a rhyolitic tephra (fig. 6.20) with a homogenous chemical composition, and is the top-most sample from a region of the core which contains tephra through a depth of 30cm. Although LA-ICP-MS analyses were taken from this sample using a 20, the standard analyses indicate that the data was not accurate and thus it was rejected. The shards are in general highly fluted, have very few inclusions and are clear (fig. 6.19).

ODP967 (1.580) is also a sample from a peak in shard concentrations within this depth of tephra shards. It has a homogenous rhyolitic composition (fig. 6.19), low HFSE concentrations and low LREE to HREE ratio of approximately 0.5 to 0.8. Although LA-ICP-MS analyses were taken from this sample, the standard analyses indicate that the data was not accurate (appendix 2) and thus it was rejected. The shards in this sample are either platy or highly fluted, and are clear in colour (fig. 6.19) inclusions are very rare.

ODP967 (1.620) is a sample from a peak in shards (fig. 6.18), but the sample above the top of this peak is missing. The peak in shard concentrations could therefore be in this upper sample. The shards analysed from the lower sample are homogenous in chemical composition and are rhyolitic. No LA-ICP-MS analyses were achieved for this sample as the shard surfaces were too small, and the shards were too thin. They are all platy or highly fluted and clear in colour (fig. 6.19) and inclusions are very rare.

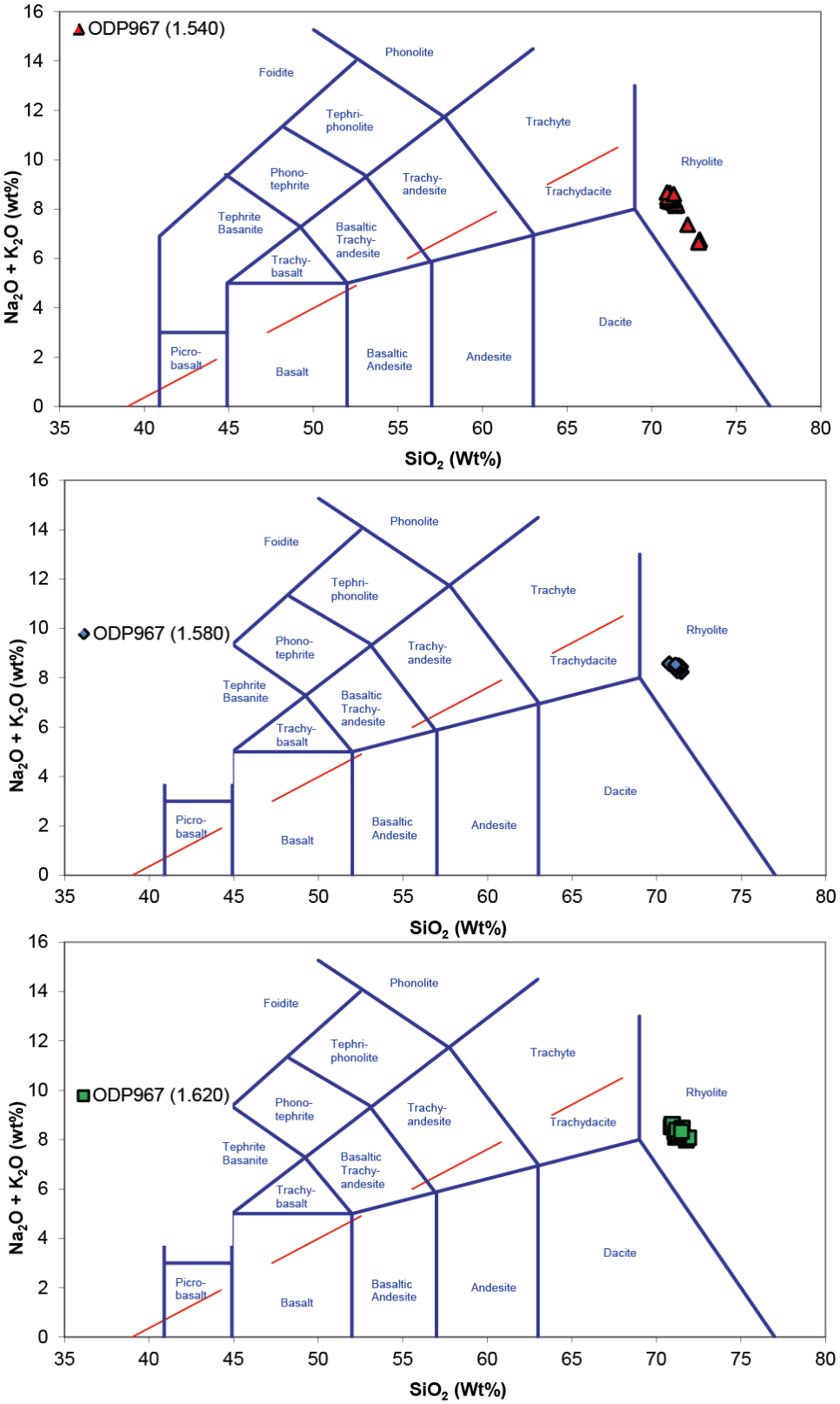

Figure 6.20 Total Alkali vs Silica diagrams for samples ODP967 (1.540), (1.580) and (1.620) The positions of these samples relative to the proxy record can be seen in figure 6.17 and the shard counts for these samples can be seen in figure 6.18.

ODP967 (1.730) yields a homogenous population of rhyolitic shards (figs 6.21 and 6.22), from the lowermost peak in shard concentrations in a section full of tephra shards (fig. 6.18). N_2O values are higher than K_2O values, and FeOt exceeds CaO. The morphology of the shards is generally platy, without many vesicles, they are clear in colour (fig 6.19) and inclusions are very rare.

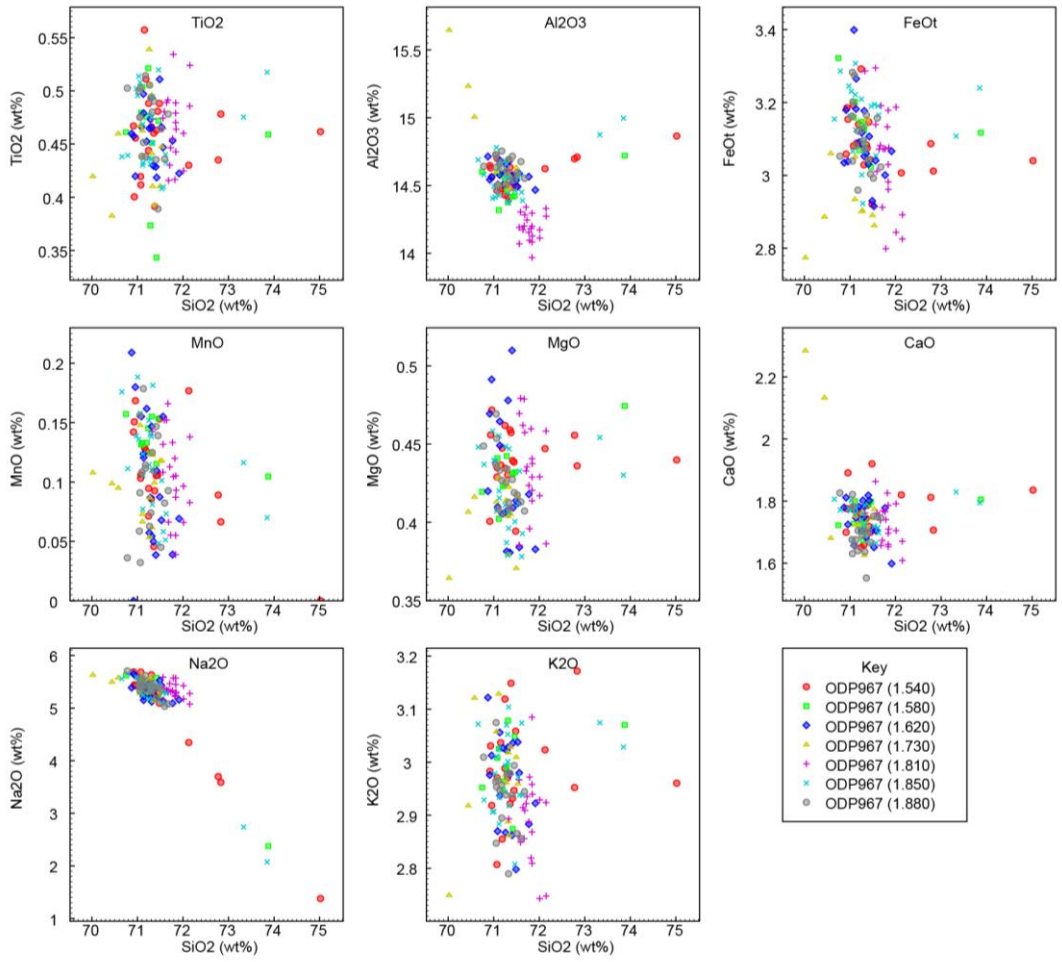

Figure 6.21 Major element bi-plots showing all data for tephra found in samples ODP967 (1.540), (1.580), (1.620), (1.730), (1.810), (1.850), (1.880).

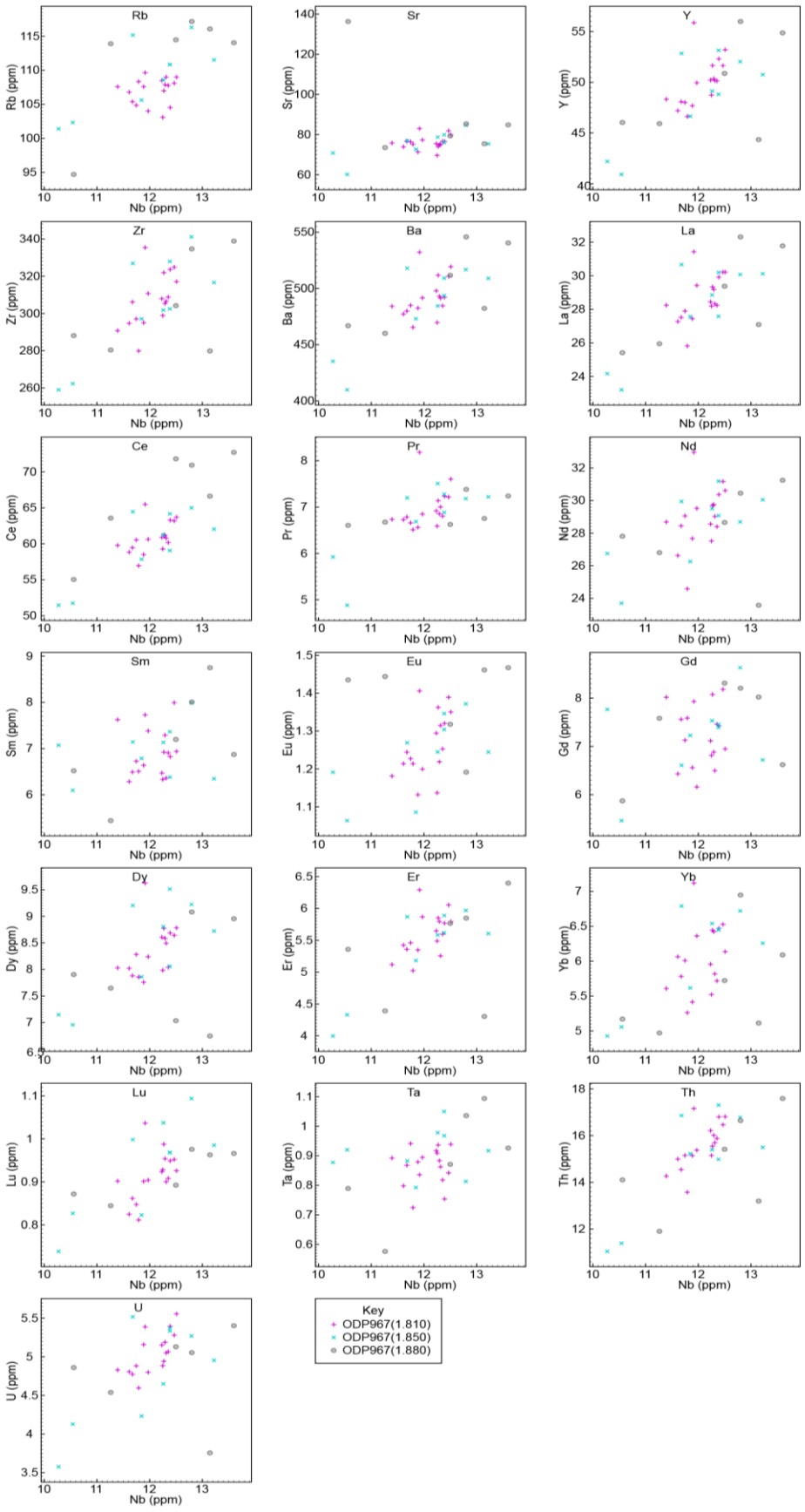

Figure 6.22 Trace element data for tephra samples ODP967 (1.810), (1.850) and (1.880).

ODP967 (1.810) is a sample from a visible tephra layer in ODP967. The tephra layer is ~3cm thick and composed of white ash. It is chemically homogenous and rhyolitic in composition. The shards have low HFSE concentrations (fig. 6.22) and a low LREE to HREE ratio of 0.55-0.58. The shards are vesicle poor, but occasionally highly fluted, and are clear in colour and inclusions are very rare (fig. 6.19)

ODP967 (1.850) is a sample from the peak in cryptotephra concentrations 4cm below the visible tephra layer ODP967 (1.810). Again the sample is geochemically homogenous and rhyolitic in composition (fig 6.23), with CaO lower than FeOt and Na_2O exceeding K_2O. The HFSE concentration are low (Nb~10-12ppm, fig. 6.22) and the HREE to LREE ratio ranges from 0.55-0.58. The shards are generally platy, with occasional vesicles, but very few fluted shards (fig. 6.19). All shards are clear in colour and inclusions are very rare.

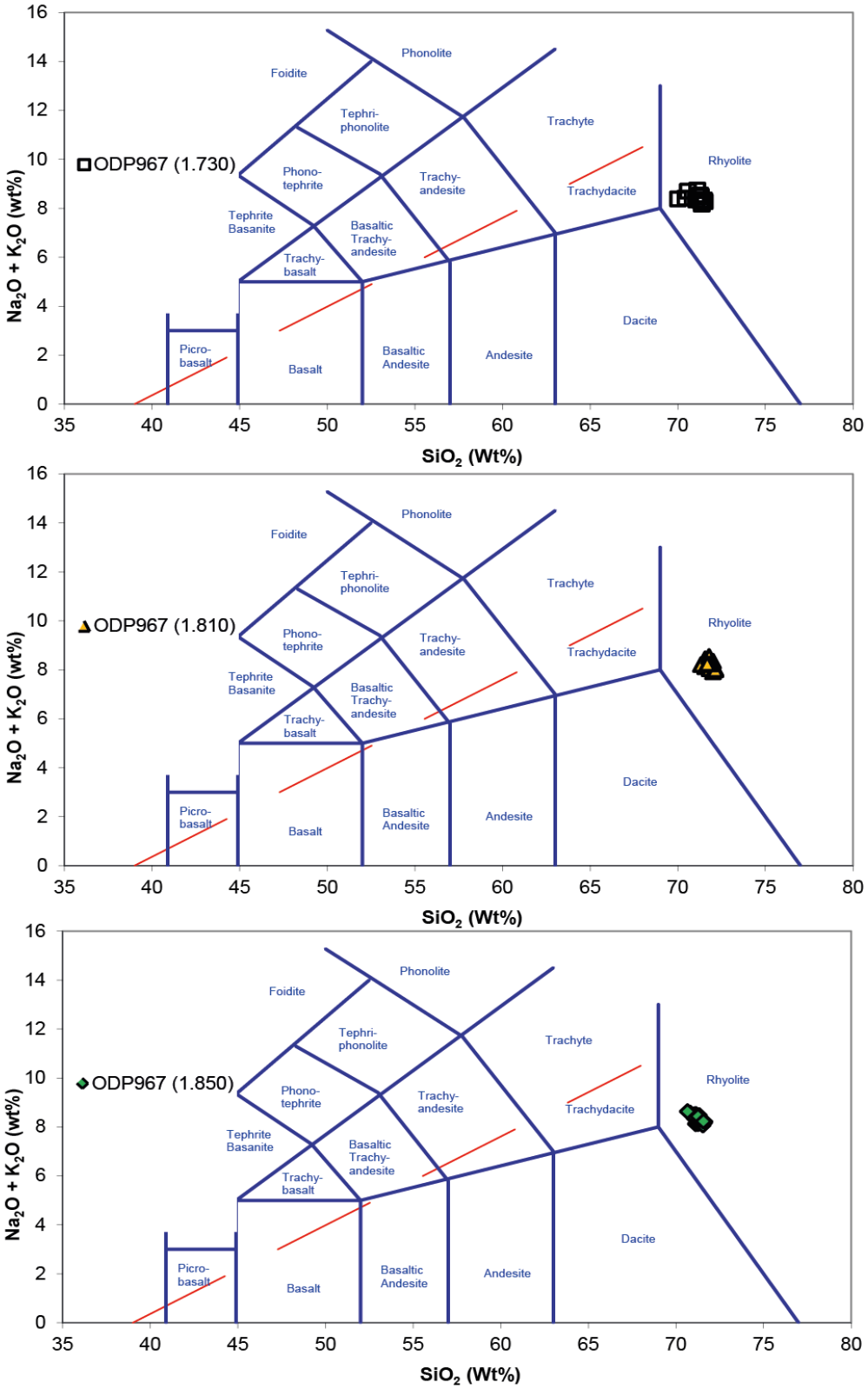

Figure 6.23 Total Alkali vs Silica diagrams for samples ODP967 (1.730), (1.810) and (1.850). The positions of these samples relative to the proxy record can be seen in figure 6.17. and the shard counts for these samples can be seen in figure 6.18.

ODP967 (1.880) contains rhyolitic tephra shards (fig. 6.24) from a peak in cryptotephra concentrations (fig. 6.18). Again, CaO is lower than FeOt and Na_2O exceeds K_2O (fig. 6.21). The six LA-ICP-MS analyses demonstrate that it has low HFSE concentrations (e.g. Nb~10-13ppm) (fig. 6.22), and a low ratio of LREE to HREE (0.50-0.61). The shards are platy, occasionally vesicle or flute rich and inclusions are very rare (fig. 6.19).

ODP967 (5.560) is a sample of a single shard from a 5cm resolution sample at the top of sapropel S4b. Two EPMA analyses were attained on this single shard (figs 6.24 and6.25). Both of these analyses yielded rhyolitic chemical signatures (fig. 6.24) with $Na_2O>K_2O$ and FeOt > CaO. This shard could not be analysed for trace elements with the LA-ICP-MS as it was too thin and the exposed surfaces were too small. The SIMS was not used to attain trace elements either, due to time constraints and expense. The shard is platy, has no vesicles or inclusions and has notably non-smooth edges indicating possible physical or chemical damage (fig. 6.19).

ODP967 (7.610) is a well-defined peak of cryptotephra within sapropel S4 (fig. 6.17 and 6.18). The sample is geochemically homogenous and very high in silica (~77%), classifying the shards as high silica rhyolitic shards (fig. 6.23) although one shard plots at 70.8wt% SiO_2. K_2O is greater in concentration than Na_2O (in contrast to all preceding sample descriptions) and CaO concentrations are only slightly higher than FeOt (fig. 6.24). HFSE concentrations are higher than all the samples described above (Nb~23-25ppm, Zr~ 52-55ppm, fig. 6.25) and the LREE to HREE ratio is also higher at ~1.4-1.6. The shards are clear in colour, platy and occasionally fluted with no vesicles or inclusions (fig. 6.19).

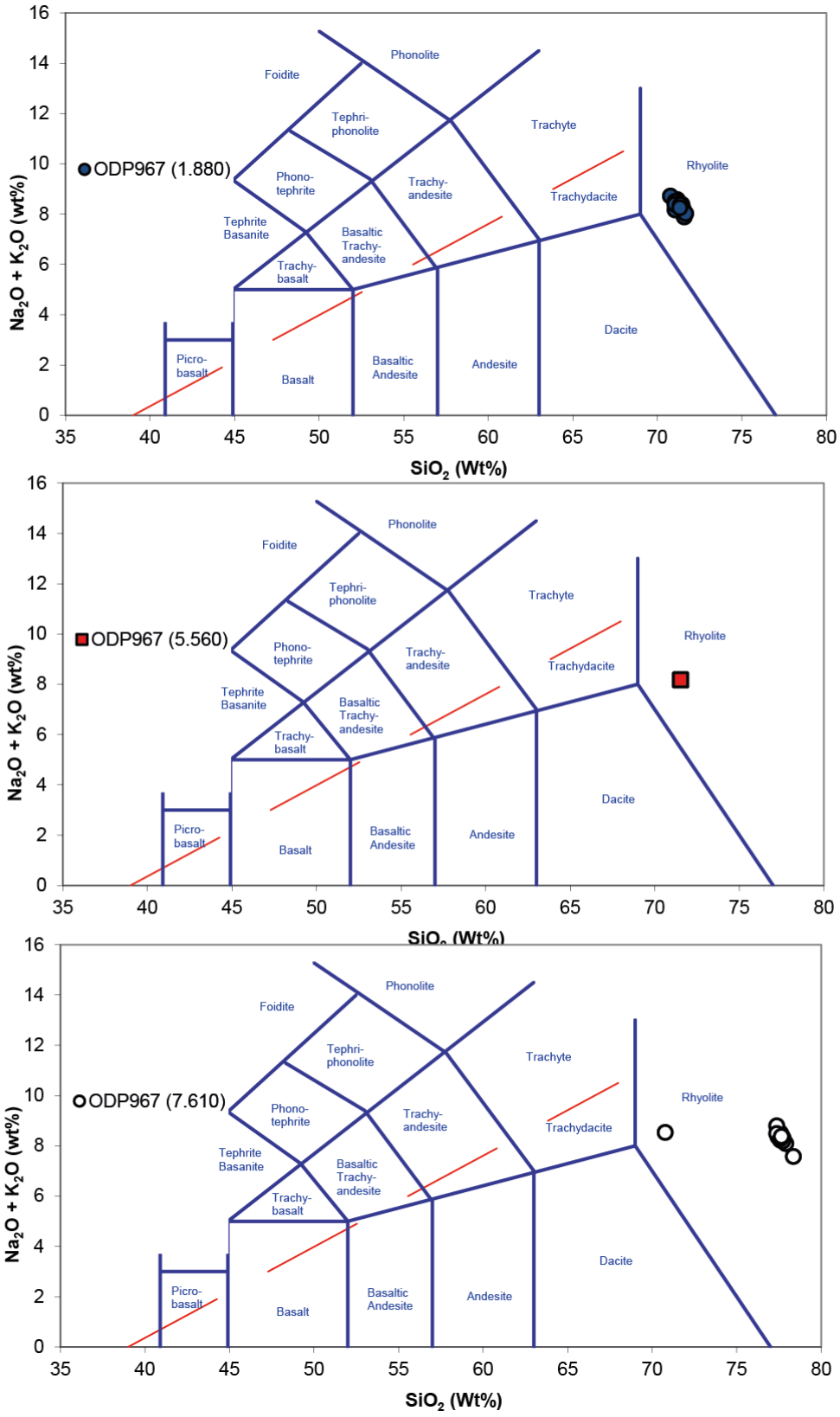

Figure 6.24 Total Alkali vs Silica diagrams for samples ODP967 (1.880), (5.560) and (7.610). The positions of these samples relative to the proxy record can be seen in figure 6.17 and the shard counts for these samples can be seen in figure 6.18.

ODP967 (8.460) is sample from a very small peak in shard concentrations of only 42 shards/g (figs 6.17 and 6.18). This concentration is derived from only 5 shards being found within this <1g sample. As a result, shards from the sample below (3 shards, or 7shards/g) were also incorporated into the sample taken for geochemistry, to increase the chance of a successful analysis. Only two of the 8 shards extracted from these two samples were successfully analysed on the EPMA. Both of these shards have rhyolitic chemistry (high silica of ~77-78%) (fig. 6.26 and 6.24). The Ca concentration (0.50 and 0.54%) is slightly higher than the FeOt concentration (0.42 and 0.39%), and K_2O >Na_2O (as with ODP967 7.610) (fig. 6.24). No trace element analyses were attained from these shards, as they were too small for the LA-ICP-MS and there was no time available, and the expense was too great, to analyse them on the SIMS. The shards were all platy and clear (fig. 6.19) and showed no evidence of chemical or physical damage.

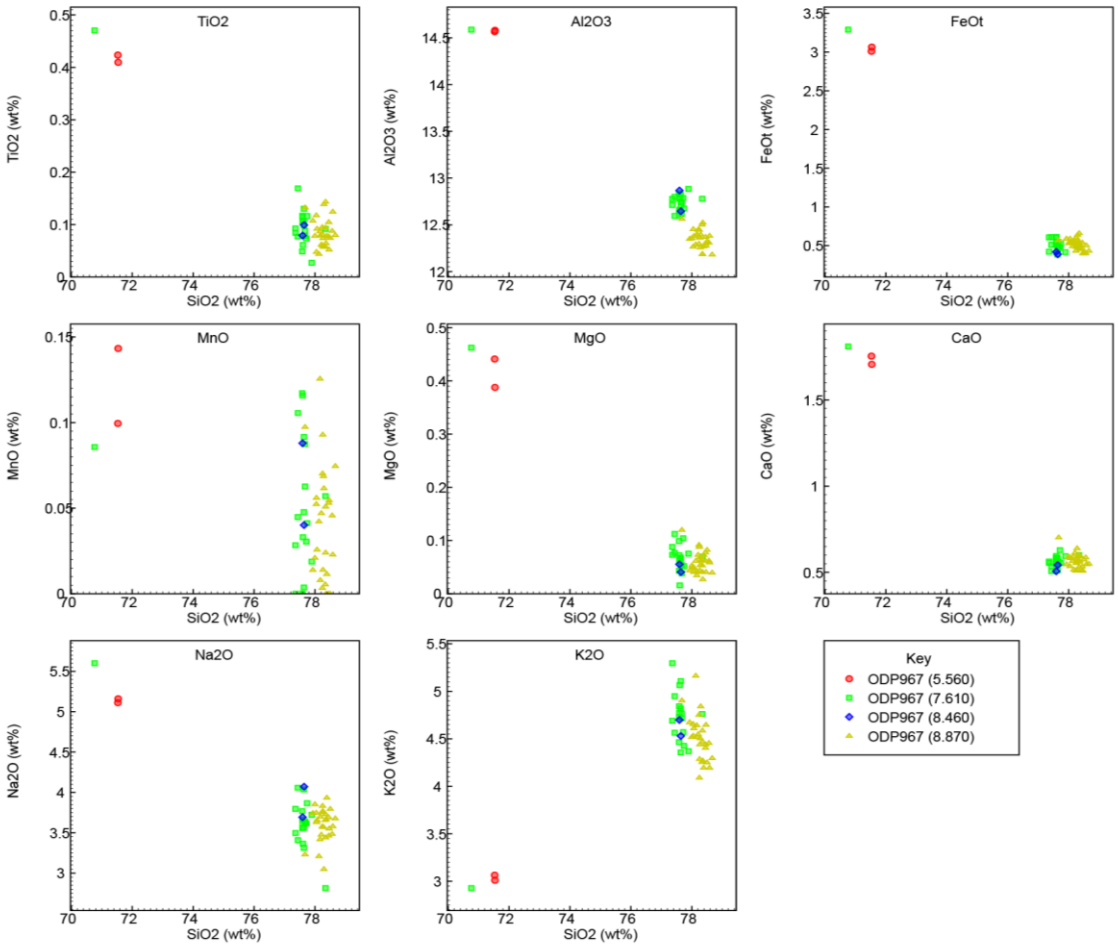

Figure 6.25 Major element bi-plots for samples ODP967 (5.560), (7.610), (8.460), (8.870).

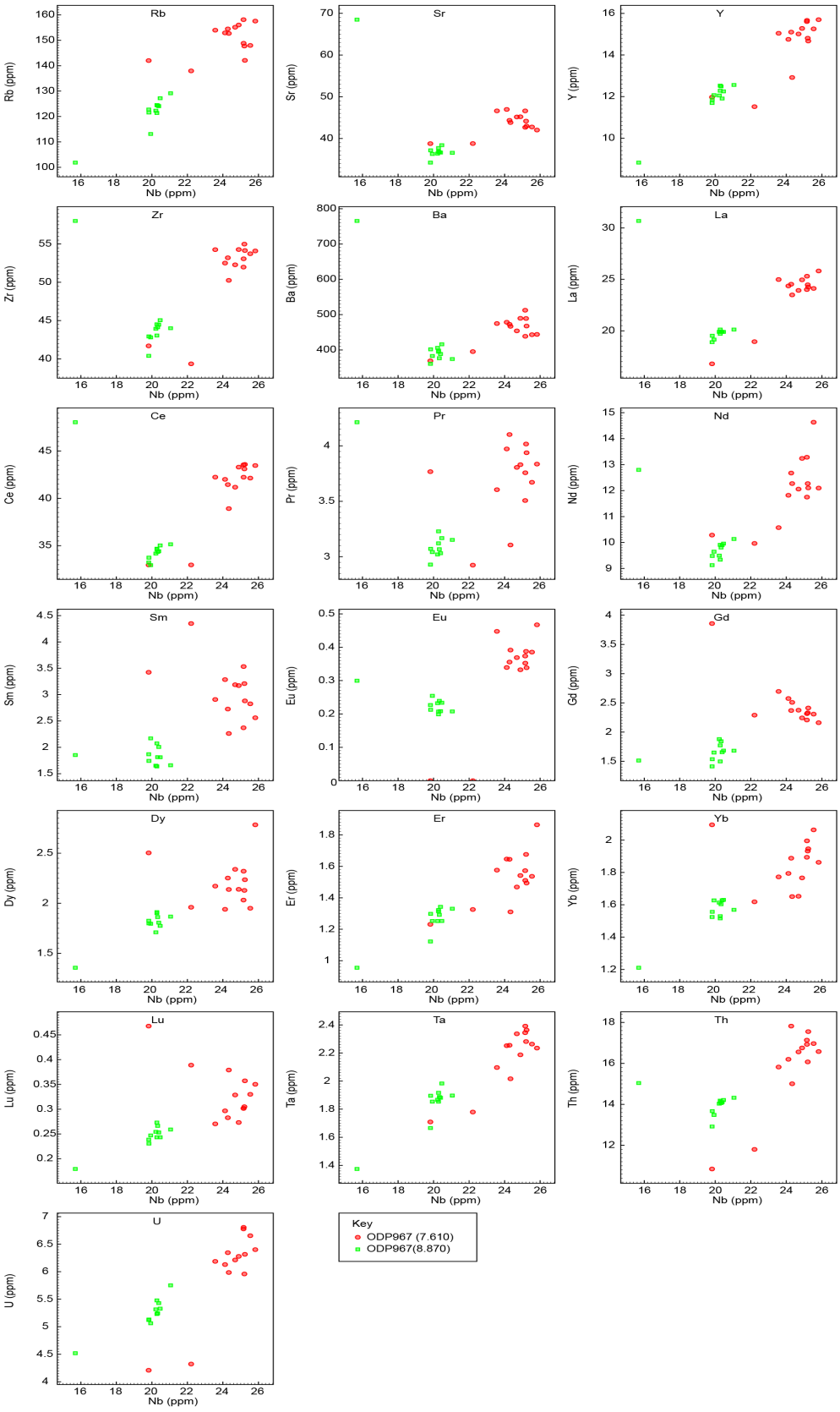

Figure 6.26 Trace element analyses of shards from samples ODP967 (7.610) and ODP967 (8.870).

ODP967 (8.870) is a sample from a 1cm thick visible layer of white ash, with a chemical composition of ~77-78% silica; a high silica rhyolite (fig. 6.26). The FeOt and CaO values are approximately equal (~0.55%) and K_2O is greater than Na_2O (fig. 6.24). The shards have HFSE concentrations of Nb~19-20ppm, Zr~40-45ppm (fig. 6.25) and an La/Y ratio of ~1.5-1.6. The shards are platy with few vesicles or phenocrysts and show no evidence of geochemical or physical alteration (fig. 6.19).

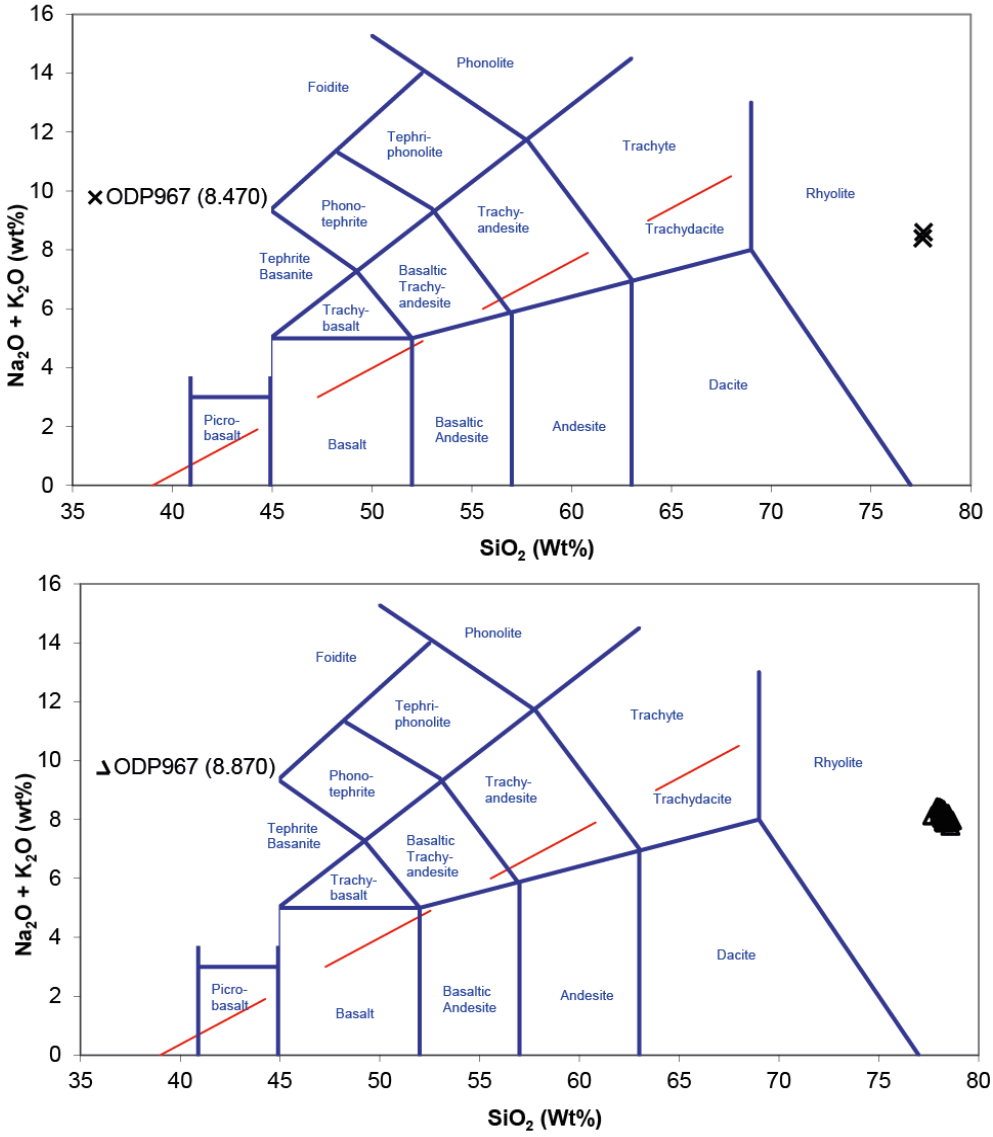

Figure 6.27 Total Alkali vs Silica diagrams for samples ODP967 (8.470) and (8.870). The positions of these samples relative to the proxy record can be seen in figure 6.17 and the shard counts for these samples can be seen in figure 6.18.

6.3 ODP975 Results

6.3.1 Shard count results.

While the whole of ODP975 was contiguously sampled and processed for cryptotephra, only 3 possible shards were identified in the 1cm sampling. These are shown in figures 6.27 and 6.28 and were found in samples D1H1 3-4cm and D1H2 73-74cm. 4 other possible

shards were also identified in the 5cm resolution samples and these were also extracted for chemical analysis (fig. 6.28). Table 6.3 summarises the tephra samples from ODP967 and which of these were analysed for major elements concentrations using the EPMA.

The very low concentrations of tephra in this western Mediterranean core are likely to be a consequence of the cores position up-wind from the major volcanic sources of the Mediterranean region (Campanian, Aeolian and Hellenic volcanic systems), and very far downwind from the Atlantic volcanic systems of Iceland, the Azores and the Canary Islands.

5cm sampling possible shards extracted	1cm sampling possible shards extracted
D 1H1 0-5cm EPMA-2 analyses on one shard	D1H1 3-4cm EPMA- 1 analysis
D 1H1 40-45cm lost in preparation of stub	
	D1H2 72-73cm EPMA- 1 analysis
	D-1H2 73-74cm EPMA- 1 analysis
D 1H2 135-140cm lost in preparation of stub	
D 1H5 75-80cm EPMA- 1 analysis	

Table 6.3 Summary of possible tephra shards recovered and analysed from core ODP975. Photo-micrographs of these potential shards can be seen in figure 6.19.

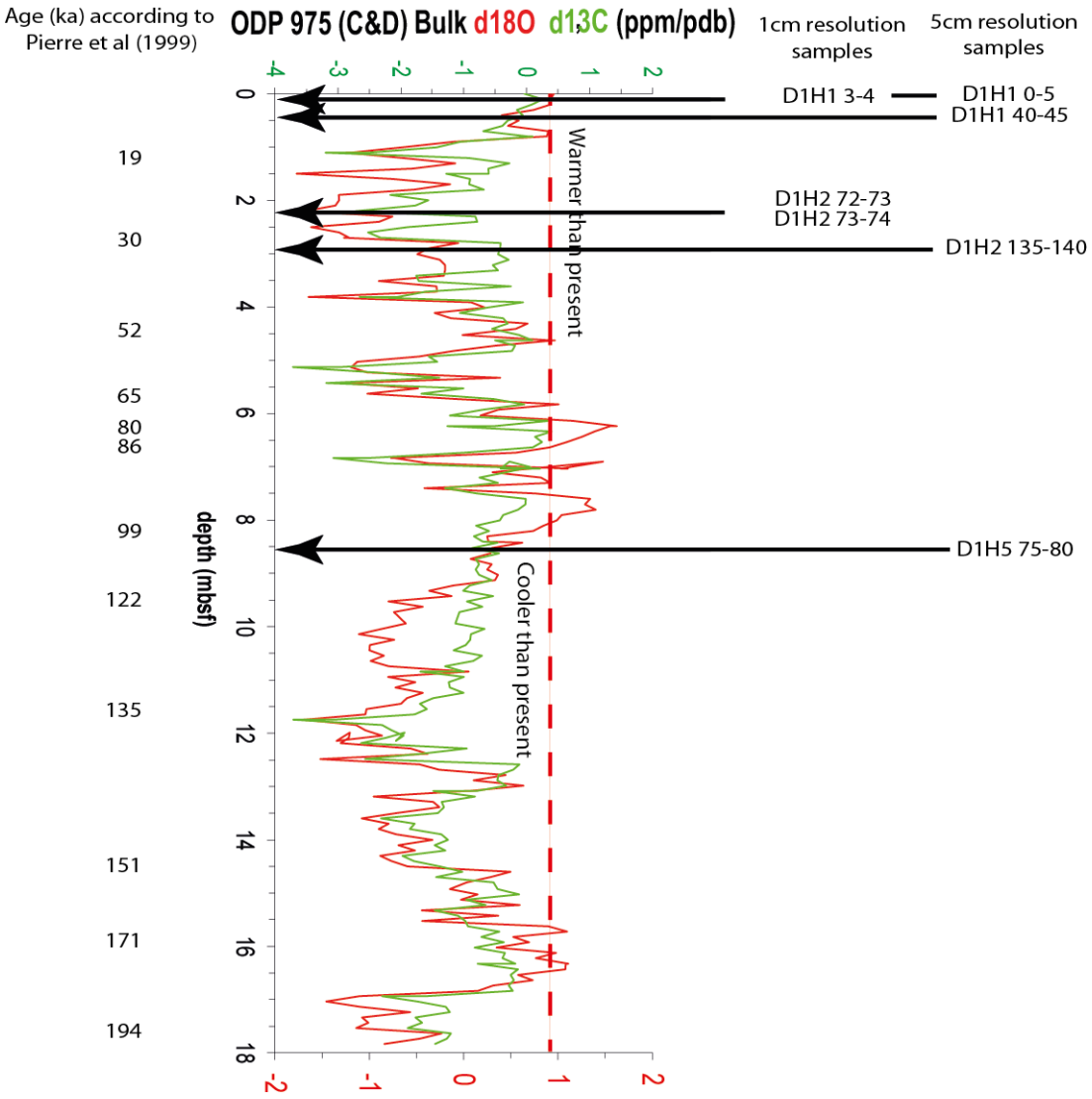

Figure 6.28 Locations of possible tephra shards extracted from ODP975 shown against depth below the sea floor, the age model of Pierre et al. (1999) and the $\delta^{18}O$ and $\delta^{13}C$ data produced by K. Grant (NOCS). The whole of the section of ODP975 shown here was scanned at 5cm resolution for cryptotephra. The possible shards which were extracted are shown in figure 6.29.

a) ODP975D 1H1 0-5cm

b) ODP975D 1H1 40-45cm

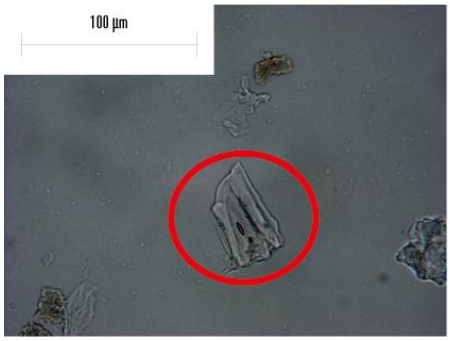

c) ODP975D 1H2 135-140cm

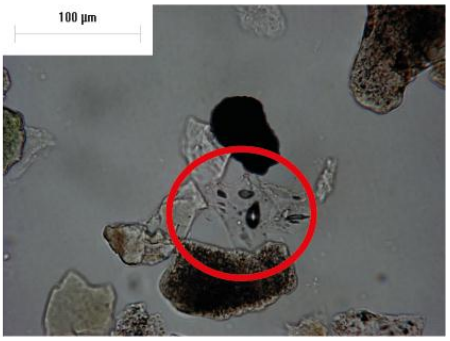

d) ODP975D 1H5 70-80 cm

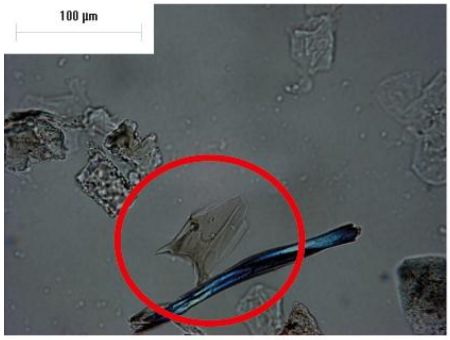

e) ODP975D 1H1 3-4 cm

f) ODP975D 72-73cm

f) ODP975D 73-74cm

Figure 6.29 Photographs of possible tephra shards recovered from ODP975D; the shards are highlighted by the red circles.

6.3.2 Results of Geochemistry from ODP975 (from EPMA only).

All the shards extracted from ODP975 were too small or thin to be analysed by the LA-ICP-MS, and were not analysed by SIMS due to a long waiting time for the SIMS instrument at the time of preparation of these samples. Therefore only EPMA data is available. In addition, for sample D1H1 3-4cm, a 3µm diameter EPMA beam at the University of Edinburgh had to be used as the largest surface area which could be cut was less than the minimum 10µm diameter EPMA beam used at the University of Oxford. This sample was analysed by A. Macleod. The standard analyses relevant to this sample are given in table 6.4 and were run before and after the sample, also using the 3µm beam at the University of Edinburgh. All other samples were run on the EPMA at the University of Oxford, and the standard values are shown in appendix 1.

ODP975 1H1 0-5cm appears to be a thin clear shard, about 30µm in diameter, with two stretched vesicles (fig. 6.28a). The surface area was large enough to attain two EPMA analyses. Both of these analyses indicate that it is unlikely that this particle is a tephra shard. While the silica values of 72.7 and 72.6% are possible for rhyolitic shards, the TiO_2 values (both 0%), FeOt values (<0.1%) and alkali values (Na_2O >13%, K_2O ~1%) are not viable values for tephra shards. More likely this particle is a mineral phase, or some form of biogenic silica.

ODP975 1H5 75-80cm (figure 6.28d) appears to be a small (~40µm) shard with a large vesicle in the centre. The EPMA analysis however indicates that it is unlikely to be tephra. The values for all of the elements are very similar to those of ODP975 1H1 0-5cm, indicating that it too is more likely to be a mineral phase, or a form of biogenic silica.

ODP967D 1H1 3-4cm (fig. 6.28e) is a sample from very close to the top of the core (fig. 6.27). The particle is shown in figure 6.28.e and is brown in colour, very thin and has concoidal edges. The EPMA analysis indicates that this is a tephra shard and it is classified as a rhyolite by the TAS diagram in figure 6.29. The shard has a SiO_2 value of 71.5% and $Na_2O > K_2O$. FeO is also greater than CaO. This shard is from a sample close to the top of the core and therefore is likely to represent a late Holocene eruption. This shard is the first evidence for tephra found in the Western Mediterranean Sea.

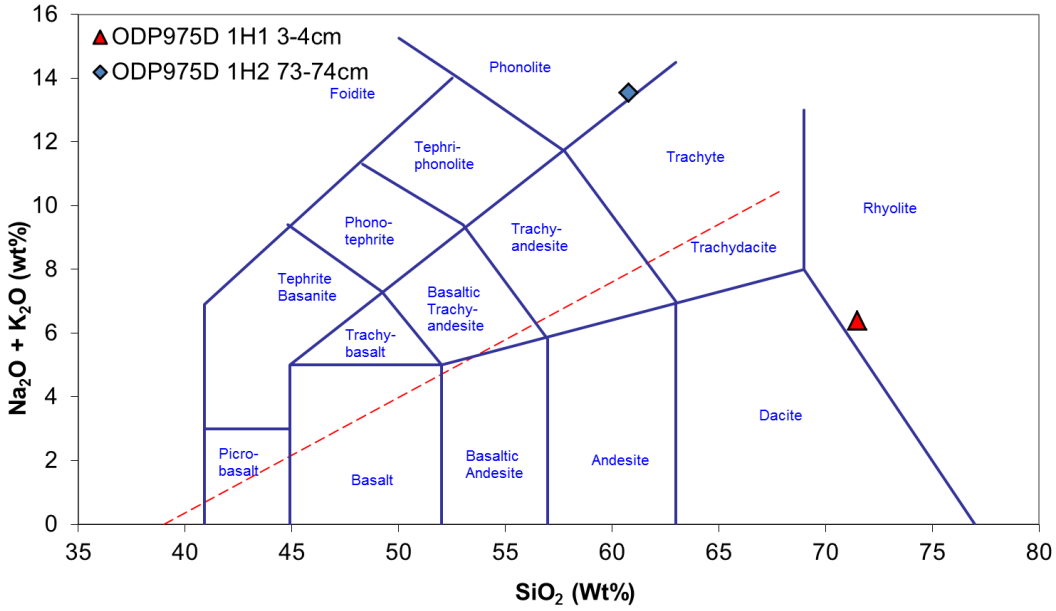

Figure 6.30 Total alkalis vs Silica diagram for the two tephra shards found in ODP975D.

ODP975D 1H2 72-73cm (fig. 6.28f) is a clear and very vesicular particle measuring about 150µm by 100µm. The particle is also deep, as demonstrated by the parts of the image which are out of focus. The EPMA analysis indicates that this particle is unlikely to be a tephra shard. The SiO_2 value of 98% indicates that this particle is most likely bio-genic silica.

Sample ODP975D 1H2 73-74cm (fig. 6.28g) is a clear particle with two elongate vesicles in it. The particle is about 75µm long and 50µm wide. The EPMA data indicates that this is a tephra shard, with phonolitic chemistry (fig. 6.29). The 100% normalised SiO_2 value is 60.8%, FeOt is greater than CaO and K_2O is greater than N_2O. Unlike sample ODP967D 1H1 3-4cm, this shard is not located close to the top of the core, and therefore may represent the first tantalising evidence that important regional chronological markers could be found in the western Mediterraean, and link ODP975 with other RESET sites in the Western Mediterranean.

Analysis number	SIO2	Ti2O	Al2O3	FeOt	MnO	MgO	CaO	Na2O	K2O	P2O5	SO2	F	Cl		Analysis Name
24 / 1 .	64.2636	0.7347	17.5959	4.4515	0.0776	2.0346	5.2693	4.7979	1.3114	0.149	0.0053	0.0217	0.0226	100.7351	STHS
25 / 1 .	63.105	0.7279	17.9277	4.4125	0.0746	1.8885	5.2744	4.6541	1.3419	0.1411	0.0027	0.0328	0.0224	99.6056	STHS
26 / 1 .	63.6749	0.7397	17.8468	4.4649	0.0734	1.8949	5.2222	4.7847	1.3523	0.1569	0.0112	0.0244	0.02	100.2663	STHS
27 / 1 .	73.7902	0.0794	13.1088	1.5114	0.0697	0.0352	0.7367	4.116	5.264	0.0064	0.0086	0.1854	0.3713	99.2831	LIPARI
28 / 1 .	74.4665	0.0744	13.1461	1.6027	0.0589	0.027	0.8291	4.0757	5.1553	0.0061	0.0028	0.1974	0.379	100.021	LIPARI
29 / 1 .	73.5342	0.083	13.194	1.5487	0.069	0.0458	0.702	3.9665	4.9914	-0.0033	-0.0045	0.1942	0.3572	98.6782	LIPARI
31 / 1 .	**71.106**	**0.9146**	**13.2914**	**3.7988**	**0.1057**	**0.7569**	**2.8112**	**4.0092**	**2.3524**	**0.1766**	**0.0307**	**0.0592**	**0.0628**	**99.4754**	**RH0349_1**
57 / 1 .	74.0845	0.078	12.9988	1.6204	0.0641	0.0418	0.715	4.4088	5.2341	0.0062	0.0054	0.1922	0.3768	99.8261	LIPARI
58 / 1 .	74.0123	0.0655	13.2226	1.5751	0.078	0.0305	0.7771	4.1543	5.0496	0.0125	0.0003	0.1774	0.3706	99.5258	LIPARI
59 / 1 .	73.9569	0.0837	13.2235	1.5217	0.0569	0.0224	0.7157	4.0669	5.3205	0.001	0.0014	0.1793	0.3749	99.5249	LIPARI

Table 6.4 Standard analyses of StHs6/80G and Lipari standards using a 3µm EPMA beam at the University of Edinburgh together with the single shard from sample ODP975D 1H1 3-4cm (highlighted in yellow) and the accepted values for both the StHs6/80G and Lipari standards.

6.4 Lago Grande di Monticchio results.

During this investigation one sample was found (LC21-7.915) which was hypothesised to contain shards relating to the X-5 tephra layer found previously in the central Ionian, Tyrrhenian and Adriatic Seas (chapter 2). If this could be demonstrated, it would be by far the furthest occurrence of the X-5 tephra found thus far, and would, for the first time, allow the correlation of sediment cores (and sapropel S4) the four basins of the Mediterranean Sea.

This marine X-5 tephra layer has been correlated to the TM24 sequence of tephra layers in the Lago Grande di Monticcio sequence (Bourne et al.2010, Vogel et al.2010, Wulf pers.comm.) The three major tephra layers from the TM24 sequence were kindly supplied by Sabine Wulf for EPMA and LA-ICP-MS analysis. These are, in descending stratigraphic order; TM24a-1, TM24a-3+4 and TM24b-15. TM26 was also analysed, as this has been correlated to the X-6 tephra; another major regional tephra marker.

Should these tephra layers be correlated geochemically, the Aegean, Ionian, Tyrrhenian and Adriatic seas could all be directly compared chronologically. In addition, the LGdM record could provide a terrestrial environmental record for comparison to the marine environmental records, and also provides a varve supported age model to assess the timings of the environmental events.

The tephras were analysed using the EPMA and LA-ICP-MS under the same conditions as all of the marine core samples. The results were as follows.

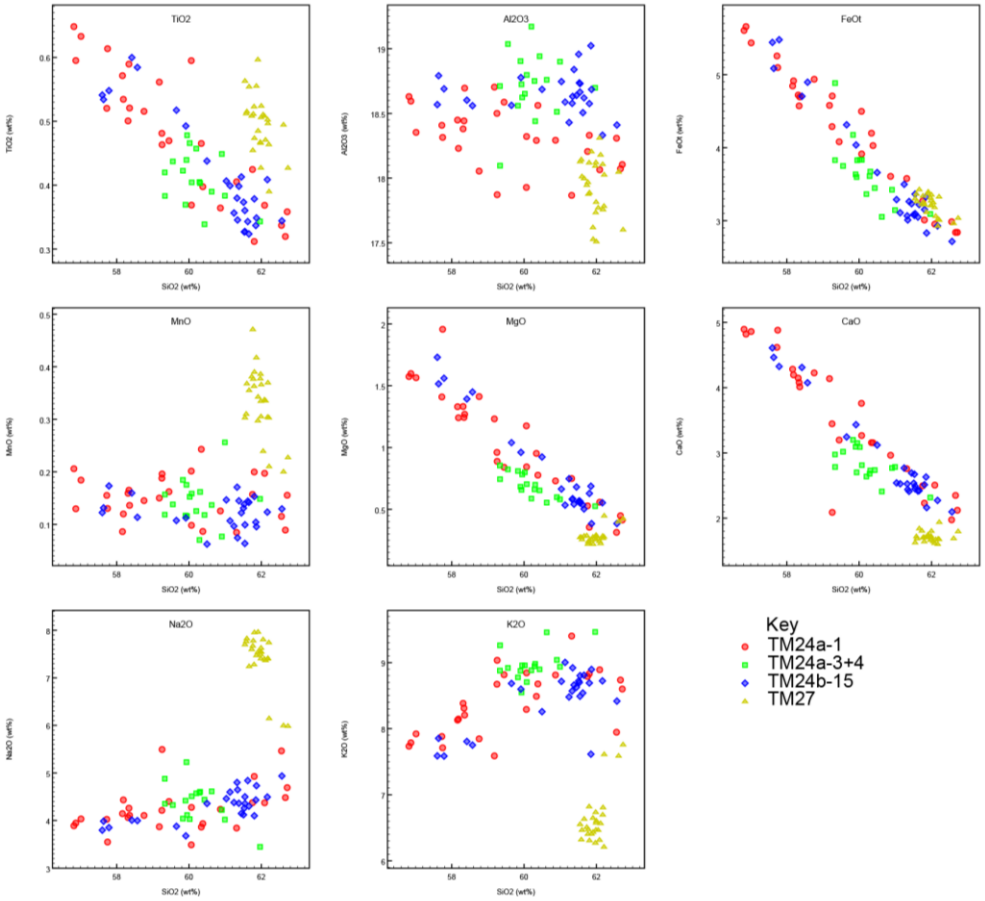

Figure 6.31 Major element analyses of the tephra layers from Lago Grande di Monticchio analysed for comparison to the tephras found in the marine cores. All analyses are plotted after normalisation to 100%; on an anhydrous basis.

TM24a-1

This tephra is the uppermost tephra of the TM24 sequence in LGdiM. SiO_2 values range from 56-62wt% and the Na_2O values (~4wt%) are consistently about half those for K_2O (~8wt%) while FeOt values are always marginally higher than CaO values (by ~0.4%) (fig. 6.30). An important trace element in alkaline magma systems is Ba as it is strongly controlled by the amount of alkali feldspar crystallisation. In this sample, Ba is very high at 526ppm to 3151ppm while Nb is ~40-60ppm (fig. 6.31) The sample has a high La/Y ratio at 2.4-2.6.

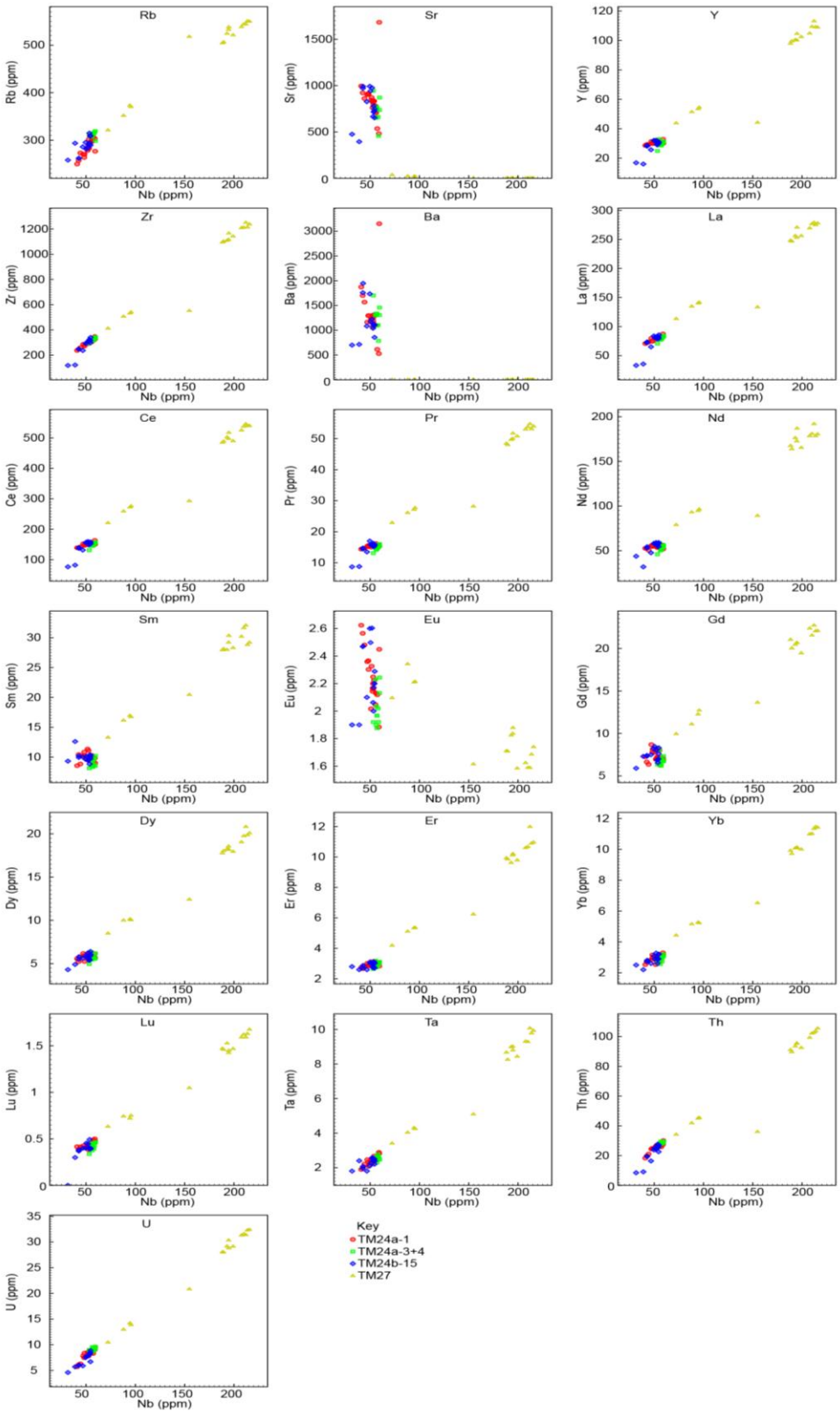

Figure 6.32 Trace element analyses of the tephra layers from Lago Grande di Monticchio analysed for comparison to the tephras found in the marine cores.

TM24a-3+4.

This sample is stratigraphically below TM24a-1 and is the combination of two types of volcanic deposit. The sample has a much more restricted geochemical range than TM24a-1 with SiO_2 ranging only from ~58-61wt% (fig. 6.30). This more restricted range is particularly evident in FeOt and CaO (fig. 6.30) which have 2SDs of 0.87 and 0.49 respectively (compared with 1.75 and 1.92 for TM24a-1). Ba values are again very enriched ranging from 785ppm-1702ppm (fig. 6.31) and the LREE to HREE ratio is very similar to TM24a-1 at ~2.5-2.7.

TM24b-15.

This trachytic/phonolitic sample is from a thick tephra layer stratigraphically below the two samples described above. This sample is chemically indistinguishable from TM24a-1 in all respects, showing the same range of values for every element (fig. 6.30 and 6.31). Even those elements which might be expected to be sensitive to fractional crystallisation in a trachytic/phonolitic magma such as Ba, K, Na, Y or La have no significant difference between these two samples. This fact illustrates that a volcanic system can produce two identical tephras very closely in time. The two tephras are separated by only 1000 varve years in LGdiM (TM24b is dated at 102,770 ± 5140ka while TM24a is dated at 101,780 ± 5090 by the LGdiM varve supported chronology).

TM27 is also a trachytic/phonolitic tephra and, as shown on figure 6.30, SiO_2 values are relatively homogenous as they range only from 61wt% to 62wt%. The relative proportions of K_2O and Na_2O differ from the three tephra samples previously described, with K_2O concentrations approximately equal to those of Na_2O (fig. 6.30). Ba contents are dramatically different from those in the preceding three samples and do not exceed 10ppm, more than two orders of magnitude less than the TM24 tephras (fig. 6.31). The LREE to HREE ratio is however very similar at 2.5-2.7.

The results shown here indicate that TM24a-1 and TM24b-15 cannot be geochemically distinguished from one another, but that TM24a-3+4 and TM27 may be distinguished from one another and from TM24a-1 and TM24b-15. The implications of these results are that should a distal tephra geochemically match TM24a-1 and TM24b-15 it cannot be used for correlations unless the required resolution of the correlation is greater than the age

difference between these two tephras (~1000years). Should the unknown distal tephra geochemically match either of TM24a-3+4 or TM27, it may be used as a correlative marker.

7. Discussions

7.1 Defining Source Volcanic Systems for an Unknown Tephra Sample.

This thesis utilises a large geochemical reference database constructed for the RESET project. This database contains data from samples representing many of the major eruptions, from the major volcanoes of the Mediterranean region. The database is constantly updated as more data is produced. As the source volcano for these proximally derived samples is known for certain, it is possible to compare to it the data from the distally derived tephra samples to define their sources (and thus which stratigraphy should be examined for the proximal correlative). It is however recognised that the proximal database may not be complete. The data may not yet be produced, the material may not have been sampled or the relevant deposits may simply not be present within the proximal stratigraphy at all (Clift and Blusztajin 1999).

To go some way to accommodate this problem, the high field strength elements can be used to infer two magmatic processes of fractional crystallisation and magma mixing. In this way, the range of possible compositions for each magma batch contributing to the eruptions of a source volcano (and therefore to its volcanic stratigraphy) can be inferred from an incomplete proximal database.

The source magma for a tephra can be defined by its position on bi-plots constructed using the high field strength elements, Zr, Ta, Hf and Nb. These elements have high ionic charges of +4, 5 or 6 which makes them highly incompatible in the lattices of the major mineral phases. As a result, these elements will increase in concentration linearly as fractional crystallisation of any particular magma batch proceeds. Some small variability will be imposed by accessory phases such as zircon or apatite, but these do not constitute major phases in most magma compositions. This principle allows a ‘magma batch’ to be defined on a HFSE-HFSE bi-plot by virtue of its trend line. Unknown samples plotting on that trend-line or it’s extension are highly likely to be derived from that source magma batch, revealing the source volcano for an unidentified tephra sample (figure 7.1 A).

The principle is complicated slightly by the fact that each source region may have more than one magma batch contributing (with mixing) to each eruption (e.g. Martin et al.2010, Druitt et al.2012). However, mixed magmas are compositionally constrained by the end member compositions shown by each magma batch. These can be known provided that each magma batch (end member) is represented individually at some point in the stratigraphy (fig. 7.1 B)

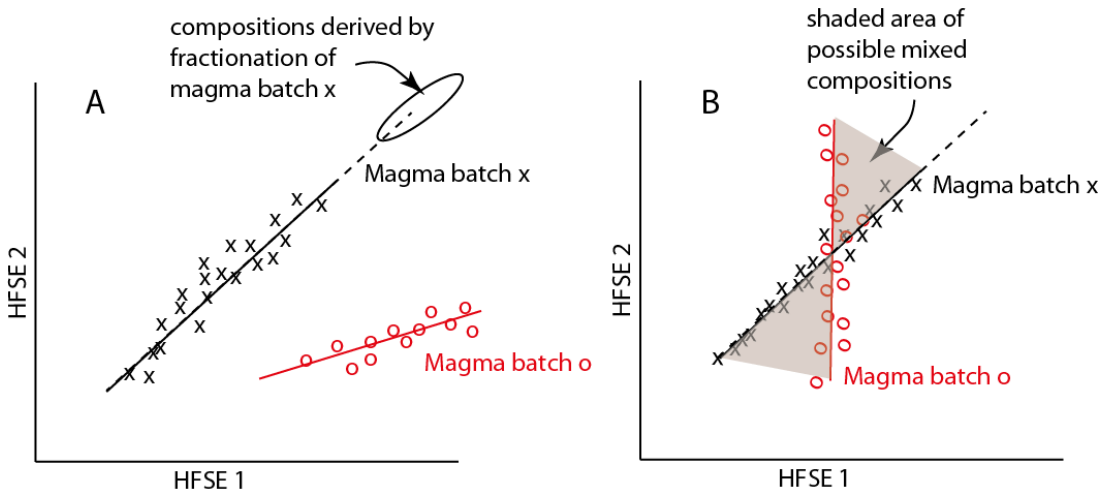

Figure 7.1 Hypothetical diagram showing the principles of using the HFSE concentrations of proximal volcanic samples to define the source volcano of an unknown tephra. **A)** demonstrates the simple situation of two sources (x and o) which have only one magma batch each contributing to the eruptions. A tephra sample from that source will plot on top of the data from the proximal samples (shown with x or o), or at the extension of that line (indicated for magma batch x by the oval and the dotted line). **B)** demonstrates the situation for a single volcano with *two* magma batches (x and o) contributing to the eruptions. In this case there is a possibility of mixing between the two batches to create a hybrid magma composition (indicated by the grey area). If an unknown tephra lies within this shaded area, it is possible that it originates from this particular volcanic system but represents a mix of the system's two magma batches. These principles mean it is possible to infer the source of an unknown distal tephra, even if the proximal deposit is missing or not yet discovered or studied (Tomlinson et al. 2012).

An unknown tephra will therefore either plot within the known proximal data (revealing the source magma batch) on such a diagram, at the extension of the fractionation trend for a batch (implying the source magma batch), or between the two trend lines indicating that the magma composition could, in theory, have formed from mixing of the two magma batches at a particular volcano (Druitt et al.2012, St.Seymour and Vassopoulos 1992). These scenarios are illustrated hypothetically in figure 7.1. If the distal sample does not satisfy any of these criteria, it cannot be inferred to originate from that particular volcano. If this is the case for all the available volcanic sources and their known magma batches, then more work is required on the proximal stratigraphies of the volcanoes to find

evidence of the source magma batch before a source assignation for the unknown tephra can be made.

All tephra samples with trace element analyses have been plotted onto HFSE plots (Zr vs Nb) to help define the source regions for each of the tephras. Zr and Nb were chosen as their abundances within the samples were high enough to yield low uncertainties. Ta often had concentrations of <1ppm and would thus yield much higher uncertainties. Hf was not analysed. These plots are shown in figure 7.2 for LC21 and figure 7.30 for ODP967 with the available proximal data from each of the major Mediterranean volcanic systems. No trace element data was generated from tephra shards found in ODP975. After being assigned a source volcano using the Zr vs Nb plot, the tephra geochemistry is then compared to that of the proximal stratigraphy for that volcano, to identify the eruption represented by the sample.

7.2 – Discussion for tephra layers found in LC21.

All tephra layers have been assigned to a source region based on the evidence of their silica saturated or under-saturated classification (fig. 6.4) and their positions on the Zr vs Nb plot (fig. 7.2).

Using Zr vs Nb plots for both silica under-saturated and silica-saturated compositions (fig. 7.2), the proximal deposits from the Aeolian Islands, Santorini, the Campanian System, Western, Eastern and Central Anatolian provinces and the Yali/Nisyros system can be clearly distinguished from one another.

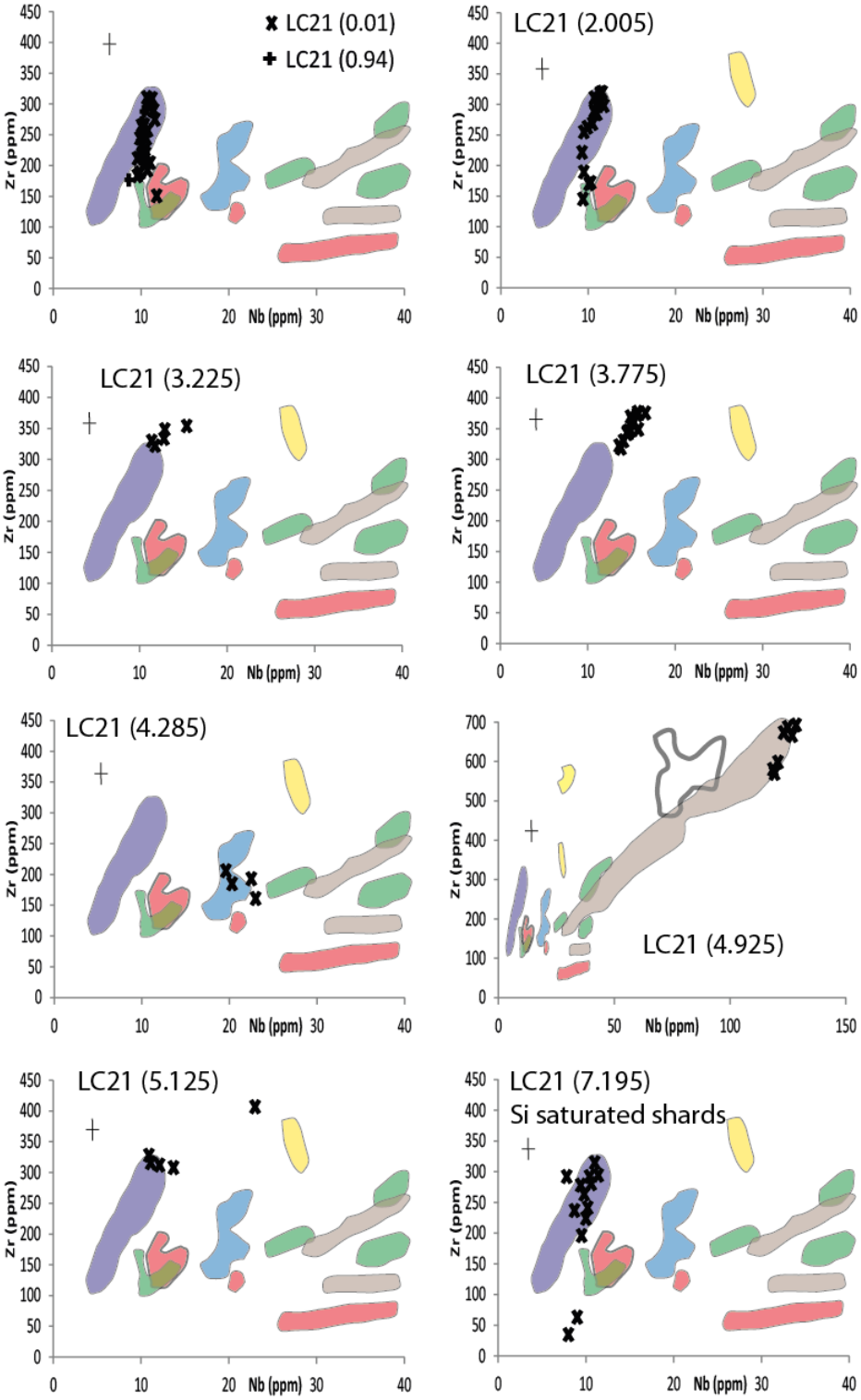

Figure 7.2 HFSE (Zr vs Nb) plots for LC21 samples with trace element analyses (sample 10.345, does not have trace element determinations). These plots can help to inform on which volcano each tephra layer could originate from, and thus inform on which stratigraphy to investigate for a proximal correlative.

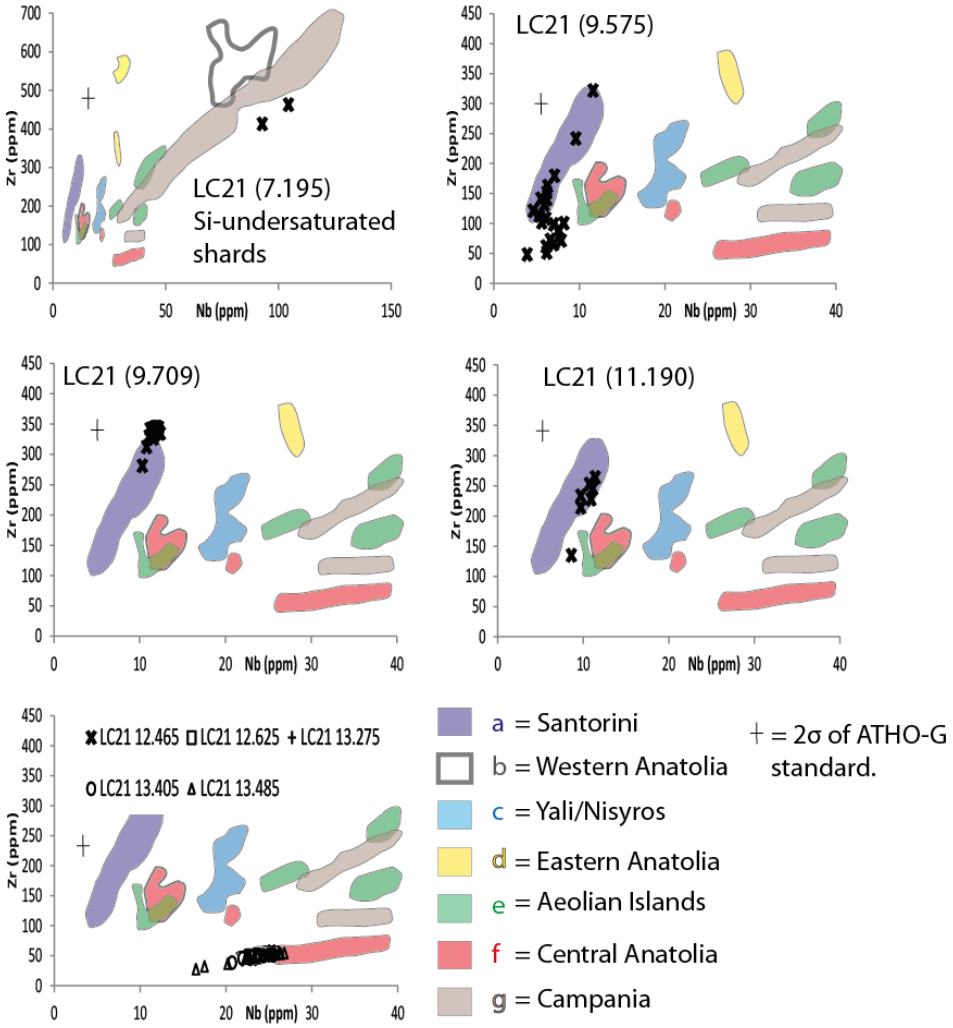

Figure 7.2 continued HFSE (Zr vs Nb) plots for LC21 samples with trace element analyses (sample 10.345, does not have trace element determinations). These plots can help to inform on which volcano each tephra layer could originate from, and thus inform on which stratigraphy to investigate for a proximal correlative.

Tephra LC21 (0.940) is the uppermost tephra from Santorini (fig. 7.2) represented in LC21. It is here proposed to be a marine deposit from the Minoan eruption, based on its position close to the top of the core (fig 6.1), its visible thickness of 24.2cm, its close approximation of the age of the Minoan eruption (3344.9 ± 7.5 cal BP -Manning et al. 2006) based on AMS14C dates from LC21 of ~3139.5 cal BP (Rohling et al. 2002a, Casford et al. 2007) and its inferred origin, from the HFSE plot, of the island of Santorini (fig. 7.2). It is important to note however that the points of on figure define a slightly different, but overlapping, trend line. This led to the hypothesis that the proximal data available for the Minoan eruption may not be fully representative of the full range of compositions for this eruption, and prompted the analysis of a pumice type which is very rare in the proximal stratigraphy. This analysis was completed by E. Tomlinson towards the completion of this thesis and is

explored more fully in section 7.5.1. The Minoan eruption is an important regional marker in the Aegean (Asku et al. 2008). It has importance not just as a regional tephra horizon, but it is also thought to have precipitated the end of the Minoan culture on Crete (see Cashman and Giordano 2008 and references therein).

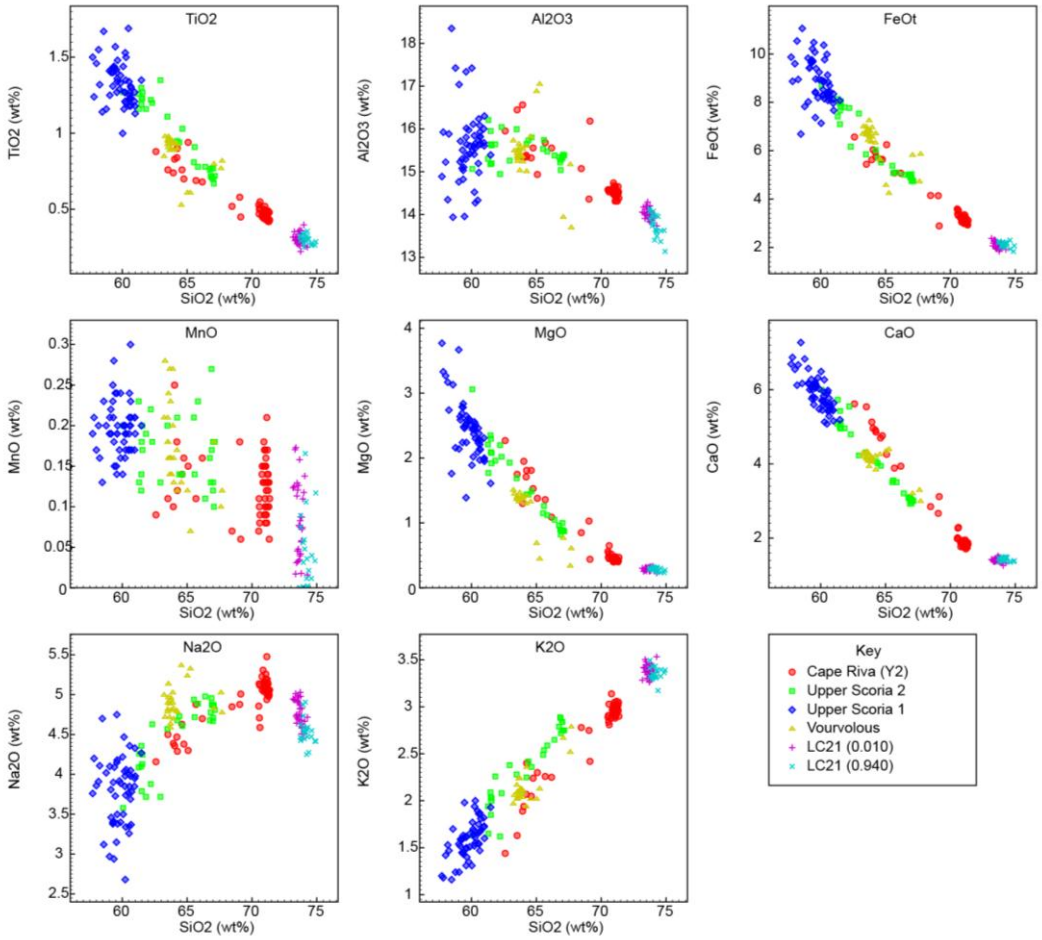

Figure 7.3 Major element comparison of LC21 (0.010) and (0.940) to the proximal stratigraphy of Santorini.

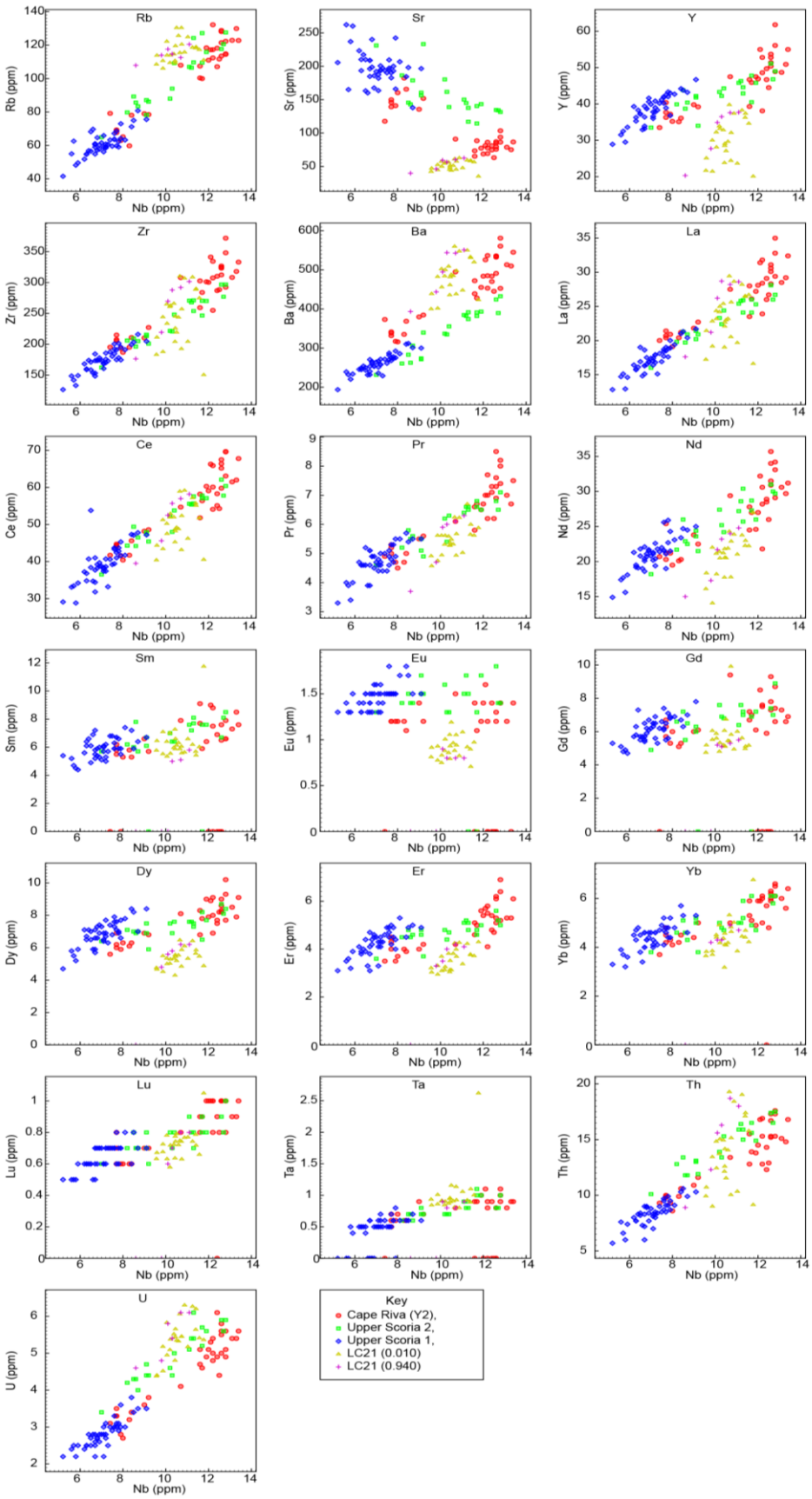

Figure 7.4 Trace element comparison of LC21 (0.010) and (0.940) to the proximal stratigraphy of Santorini.

Tephra LC21 (2.005) is stratigraphically below the Minoan deposit and dated by the chronostratigraphy at ~11.11-11.25ka (fig. 6.3, table 6.2). It is a potentially important marker for environmental correlations because it is found just below sapropel S1 in LC21 (see fig 6.2). It is inferred here that this tephra is sourced from Santorini, based on its position overlapping the Santorini field on the Zr vs Nb plot (fig. 7.2) and the calc-alkali major element chemistry (fig. 6.4). Although the shards do not all plot directly in the Santorini field of fig7.2, they do plot on the same trend line as the samples LC21 (0.01) and (0.940) which are here inferred to represent the Minoan eruption of Santorini. Through the principles discussed in figure 7.1 the tephra can be inferred to originate from the same source as the Minoan tephra- LC21 (0.940). This evidence further supported the need to analyse a rare component of the proximal stratigraphy (discussed previously with reference to LC21 0.01 and 0.940) and this is shown more fully in section 7.5.1.

The tephra lies geochemically closest to the Cape Riva proximal deposits (figs. 7.5 and 7.6), but is significantly different on many elements. The stratigraphic position just below Holocene sapropel S1 (and a calibrated 14C date in LC21 from Casford et al. 2007 at 1.990cm depth of 11,885-14,495 years BP) are inconsistent with the proximal date of the Cape Riva eruption of ~21,950 cal BP (Wulf et al. 2002 and references therein). Unfortunately this tephra cannot be chemically correlated to any other proximal Santorini deposits shown here (figs. 7.5 and 7.6) but St Seymour et al. (2004) found a Santorini eruption in a similar stratigraphic position in the Philippi peat basin, Northern Greece. While this tephra has a lower SiO_2 content than LC21 (2.005) (70-72wt% and 73-75wt% respectively) it is possible, from their similar stratigraphic positions, that these two tephras are both associated with inter-plinian activity on Santorini between the Cape Riva and Minoan eruptions (phase M12 of Vespa et al. 2006). Alternatively, each could represent a different geochemical component of the same eruption.

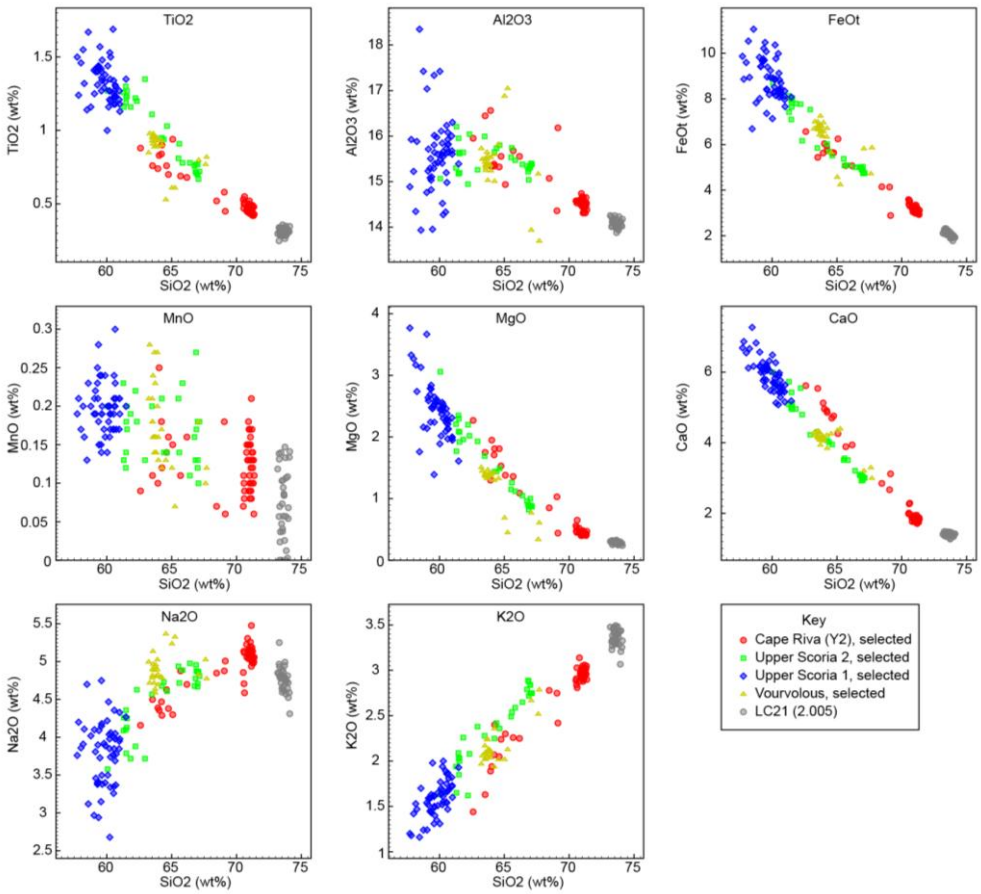

Figure 7.5 Major element comparison of LC21 (2.005) to the proximal stratigraphy of Santorini.

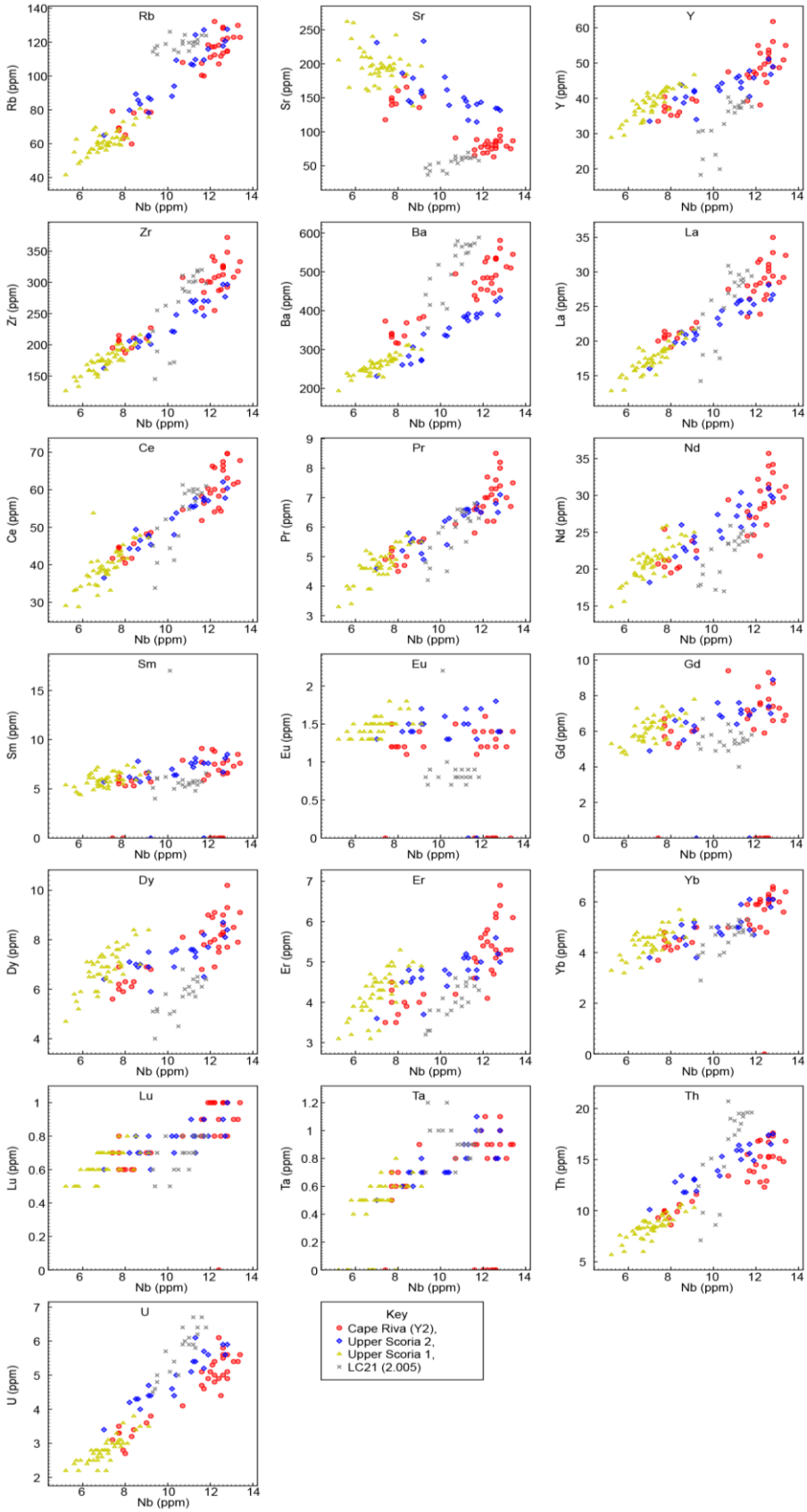

Figure 7.6 Trace element comparison of LC21 (2.005) to the proximal stratigraphy of Santorini.

Tephra LC21 (3.225) is nearly identical in chemical composition to LC21 (2.005), and by the same reasoning is inferred to most likely originate from the island of Santorini (fig. 7.2). While it's chemical composition overlaps but does not lie within the proximal Santorini field on fig. 7.2, it plots in an almost identical position to LC21 (0.940) which represents the Minoan eruption (Rohling et al. 2002b, this study). The chronostratigraphy of Grant et al. (2012) gives a date of ~24.21-24.31ka (table 6.1) for LC21 (3.225). The chemistry obtained from two of the shards matches the Cape Riva proximal deposits (fig. 7.6 and 7.7) while all the other shards are higher in SiO_2 and lower in FeOt and CaO. LC21 (3.225) is substantially below a calibrated AMS 14C date of ~ 17,000 cal BP at 2.525m (Casford et al. 2007) and the proximal deposits for the Cape Riva have a 14C date of 21,705 ± 311 cal BP (Eriksen et al. 1990), so this correlation is stratigraphically possible. Assuming, however, that that tephra layers preserve identical geochemistry in every location where they are found, it is not possible to correlate LC21 (3.225) to the Cape Riva Eruption. It is very surprising that a major eruption such as the Cape Riva from Santorini would be absent from a core only ~100km downwind from the island. In addition to LC21 (2.005), this tephra LC21 (3.225) probably represents an eruption of Santorini which is not included in the geochemical analysis of the proximal deposits.

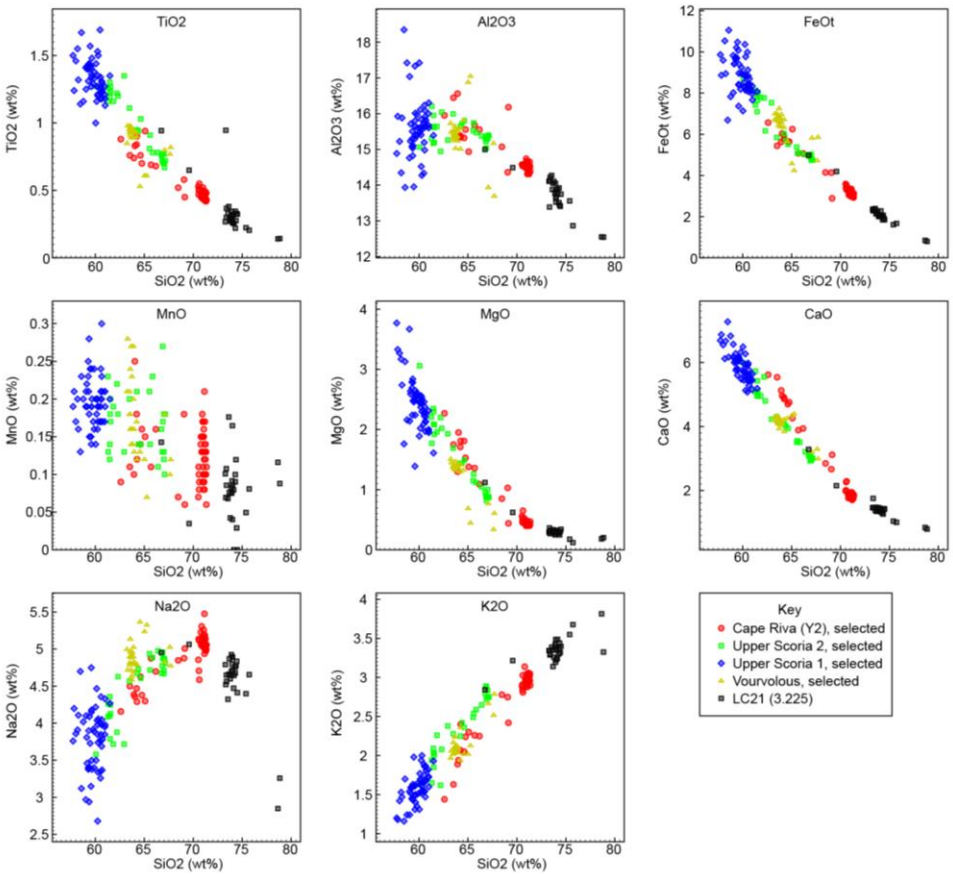

Figure 7.7 Major element comparison of LC21 (3.225) to the proximal stratigraphy of Santorini.

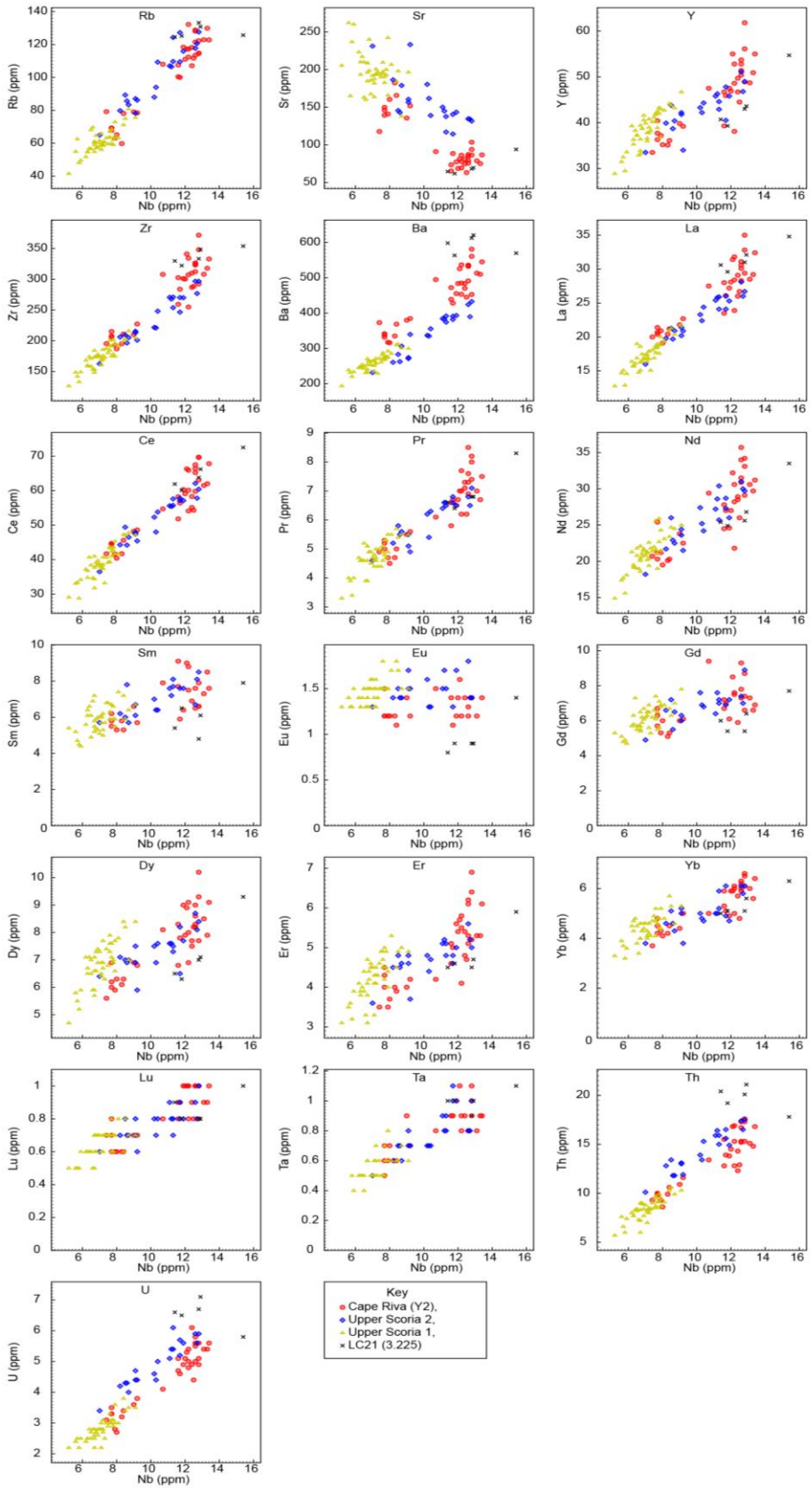

Figure 7.8 Trace element comparison of LC21 (3.225) to the proximal stratigraphy of Santorini.

Tephra LC21 (3.775) has a very different chemical composition to LC21 (3.225), being significantly lower in SiO2 (~70%). Figure 7.2 suggests that the shards in this sample most likely originate from Santorini, although the chemical data lie on the extension of, rather than within, the proximally defined geochemical field for Santorini and so this attribution is an inference rather than a deduction (fig. 7.1). The sample is here compared to the Santorini stratigraphy as this is the most likely source. The LC21 age model of Grant et al. (2012) (fig. 6.3, table 6.1) gives an age of ~29.40 – 29.49ka which is chronologically consistent with the Y4 tephra (group 4) of Aksu et al. (2008), the age of which is estimated at ~30ka BP.

The sample does not geochemically match any of the proximal deposits well. Although it is geochemically most similar to the Cape Riva eruption, it is significantly different on Ti, Ce, Nb, U and Th. The modelled age of this tephra (~29.40 – 29.49ka) is too old to be compatible with the proximally derived date for the Cape Riva (21,705±311 cal BP, Eriksen et al. 1990). No robust date is available for the Upper Scoria 2 eruption, although Druitt et al. (1999) cite a whole-rock $^{40}Ar:^{39}Ar$ age of 54 ± 3ka. This date would be valid if the crystals all held the same closure age, but Martin et al. (2010) demonstrate that the Upper Scoria 2 has two populations of crystals, one juvenile while the other is inherited. This could give a 'too old' whole-rock radiometric date for Upper Scoria 2. Druitt et al. (1989) give an approximate 14C date of 37.9ka BP from charcoal. While it is possible that this tephra layer originates from the Upper Scoria 2 eruption, the proximally defined geochemistry is so different from that of LC21 (3.775) that it is not possible to support this hypothesis with the currently available data. Perhaps (as discussed previously for the Minoan eruption) the proximal deposit relating to this tephra layer is very rare and has not yet been located on Santorini. Alternatively this tephra layer may represent an eruption for which proximal data does not yet exist.

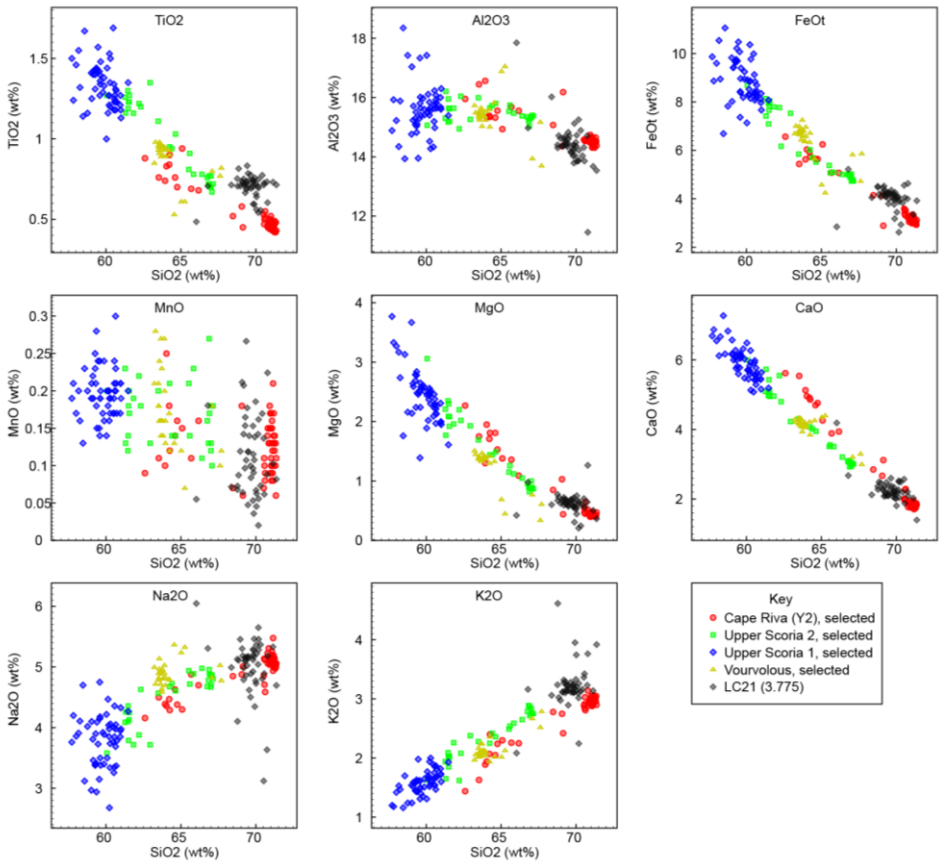

Figure 7.9 Major element comparison of LC21 (3.775) to the proximal stratigraphy of Santorini.

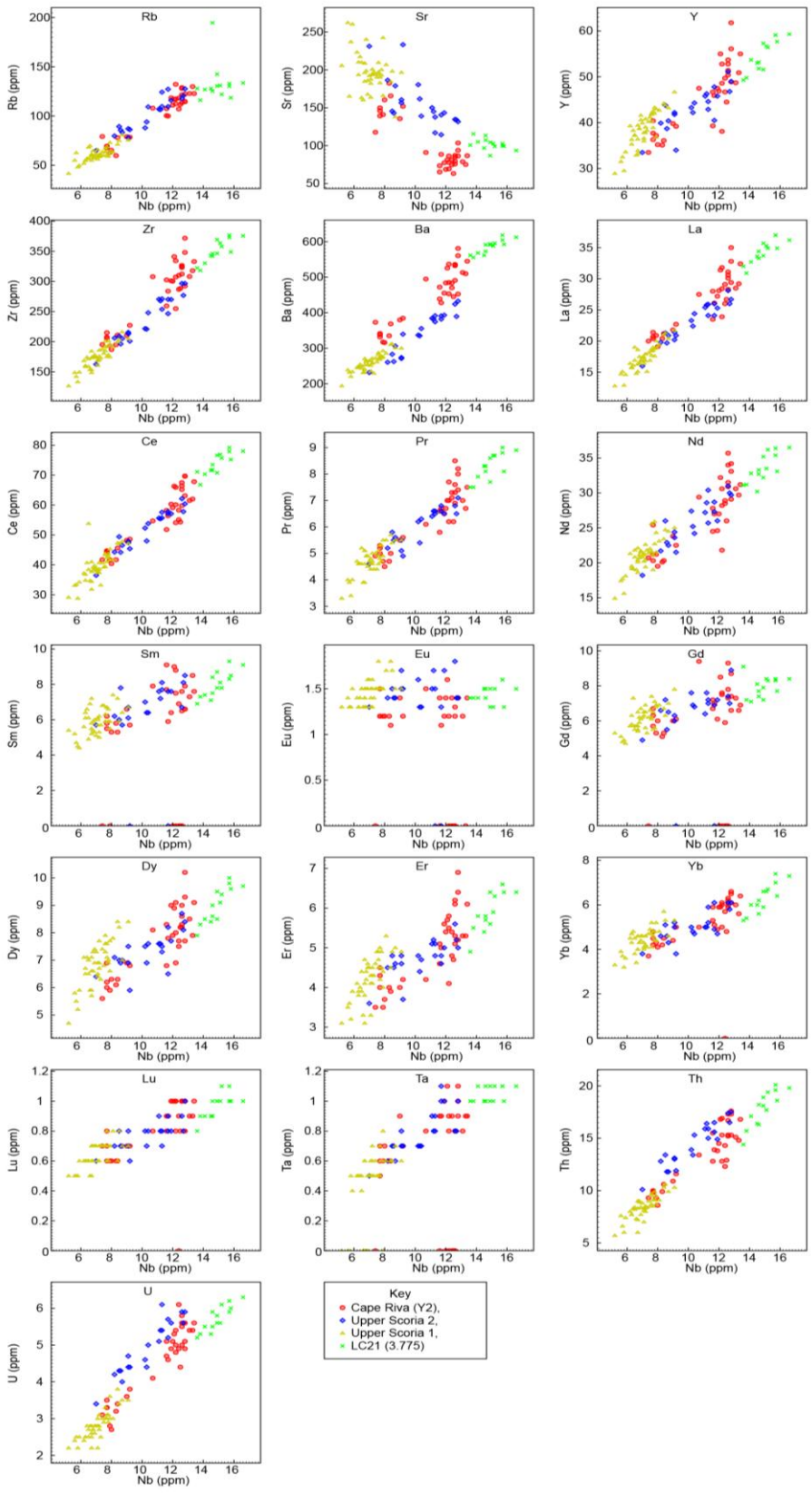

Figure 7.10 Trace element comparison of LC21 (3.775) to the proximal stratigraphy of Santorini.

Tephra LC21 (4.285) lies stratigraphically above the Campanian Ignimbrite deposit (discussed below and in Lowe et al. 2012) and has a date from the chronostratigraphy of ~34.75-34.86ka (table 2). HFSEs elements from the SIMS perfectly indicate a source from the Yali/Nisyros centre (fig. 7.2). To the knowledge of the authors, there have been only 4 known tephra-producing eruptions from the Kos/Yali/Nisyros system in the last 166ka; the Kos Plateau Tuff (~166ka, Bachmann et al. 2010), the Lower and Upper Nisyros pumices, and the Yali-2 eruption. LC21 (4.285) is too young to be the Kos Plateau tuff, as we find it stratigraphically above the Campanian Ignimbrite. It does not match the proximal data for either of the Nisyros eruptions (fig. 7.10 and 7.11) However, it does match very well to a sample of the Yali-2 pumice collected from the Nisyros caldera (this study, fig. 7.10 and 7.11). Differences exist in Al_2O_3 and SiO_2 contents (fig. 7.10) as well as U, Th and Rb (fig. 7.11). However the major element differences can be accommodated by the variation in the EPMA performance between these two batches run on 23.09.11 for proximal Yali-2 and 25.11.09 for LC21 (4.285). The 23.09.11 batch shows an anomalously low SiO_2 value for the Atho-G standard (but still within the accepted range for the EPMA). After normalisation, this difference would add to the Al_2O_3 values making them appear too high. This pattern is reflected in the comparison of these two samples. The trace element differences are not as simply explained away by analytical error. They do however represent a comparison between LA-ICP-MS method (for the proximal Yali-2 pumice) and SIMS (for sample LC21 - 4.285). It is possible that the small differences observed in the values of U,Th and Rb between the two are due to unquantifiable uncertainties in the SIMS procedure (see chapter 4). It remains possible that this tephra layer represents a hitherto unknown eruption of Yali, although this is thought unlikely here, as the stratigraphy of the Island is very well defined (Allen and McPhie 2000).

Intriguingly, one shard plots as an outlier and close to the Nisyros Upper Pumice, implying that there may be a link between the two magma batches which contributed to the LC21 (4.285) eruption.

A marine oxygen isotope stratigraphic age of 31 ka (Federman and Carey 1980, in Bachmann et al. 2010) has been assigned to the Yali-2 eruption due to a lack of appropriate material for proximal radiometric dating. Asku et al. (2008) cite an orbitally tuned age of ~35 ka for the Yali-2 tephra (Smith et al. 1996). No robust, independent date has yet been derived.

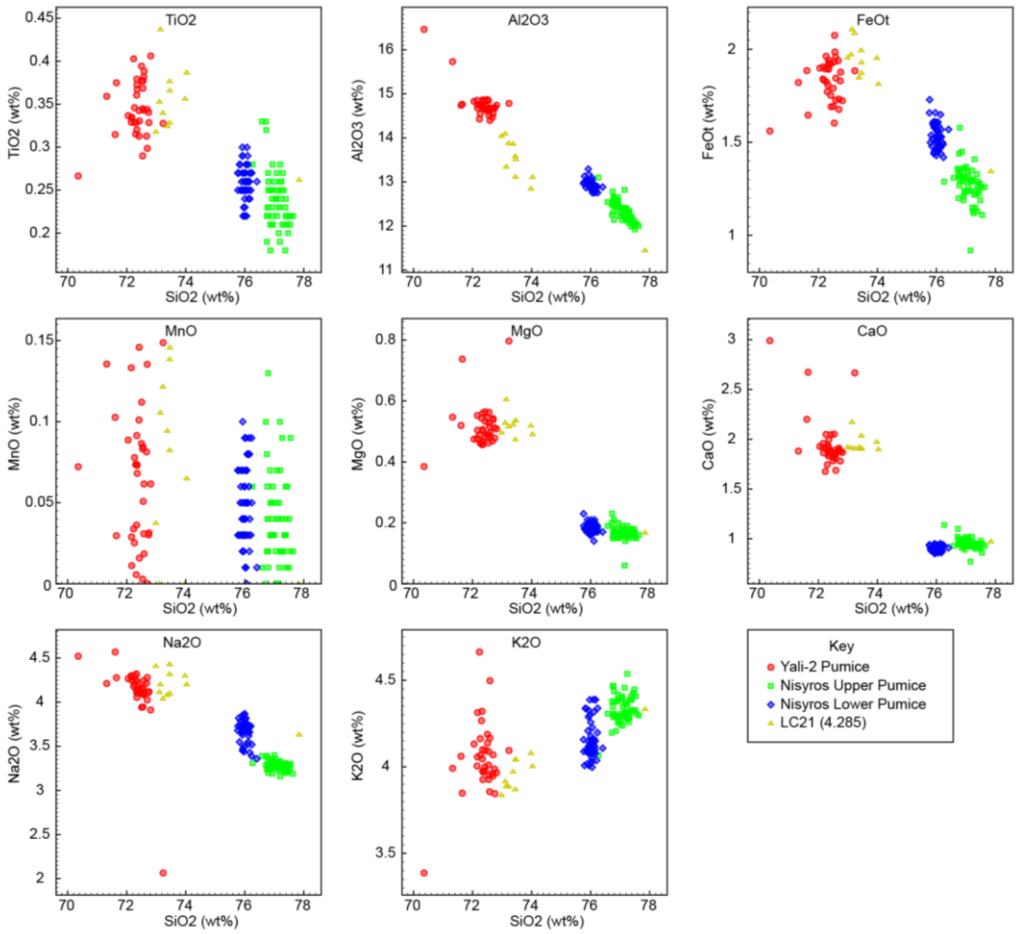

Figure 7.11 Major element comparison of LC21 (4.285) with proximal deposits of the Yali-2 pumice, the Nisyros Upper Pumice and the Nisyros Lower Pumice.

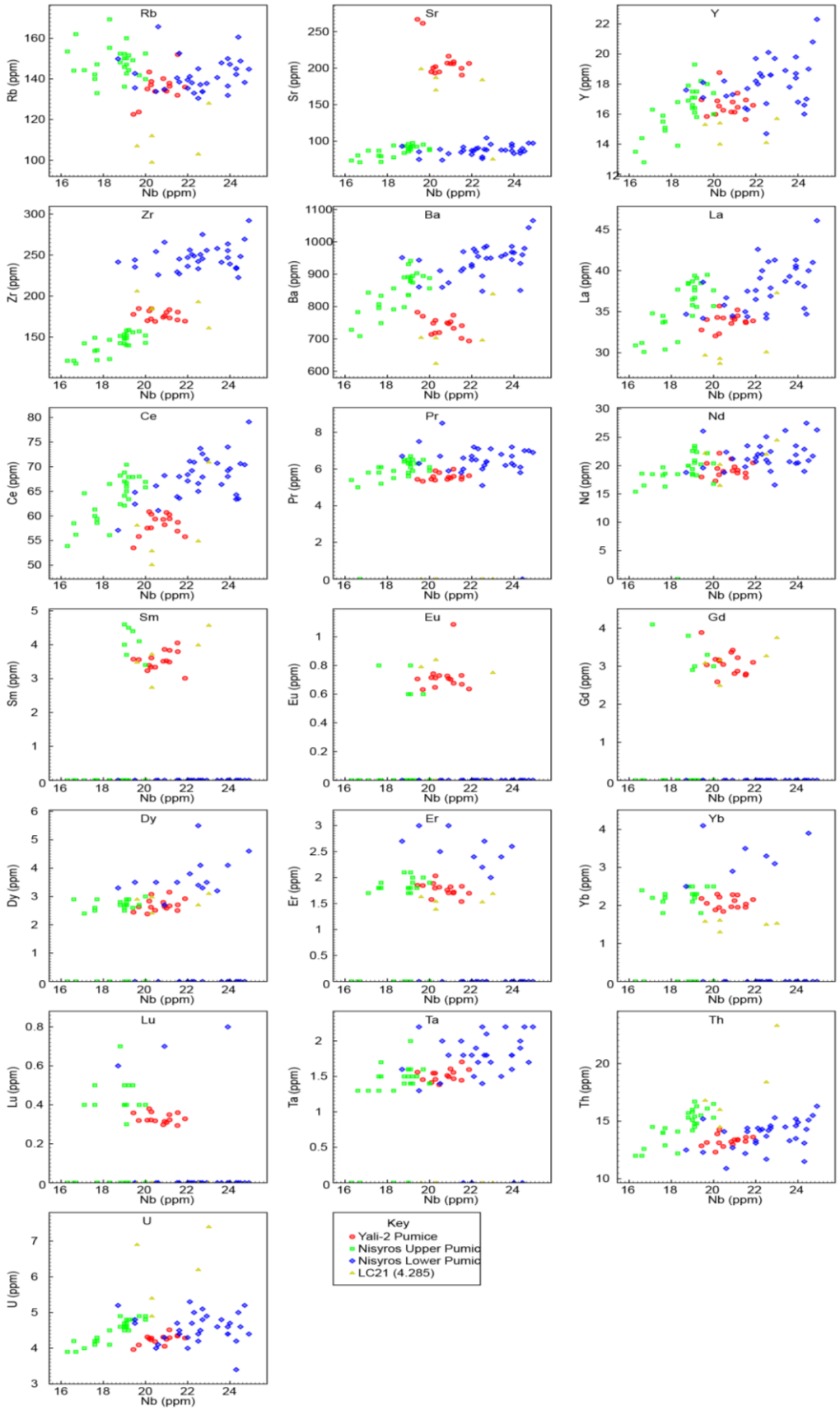

Figure 7.12 Trace element analyses of sample LC21 (4.285) with analyses from proximal deposits of Yali and Nisyros: the Yali-2 pumice, the Nisyros Upper Pumice and the Nisyros Lower Pumice.

Tephra LC21 (4.925) represents a visible layer of 15cm thickness. Its phonolitic chemistry (fig. 6.4), position in the Campanian HFSE composition field in figure 7.10 , together with its thickness indicate that this tephra is likely to be the most widespread tephra in the Mediterranean region, the Y5 tephra. This tephra is chemically identical to the proximal deposits of the Campanian Ignimbrite (figs 7.12 and 7.13). LC21 (4.925) is therefore correlated to the Campanian Ignimbrite eruption from the Campanian Fields in Italy. The CI has been $^{40}Ar:^{39}Ar$ dated to 39.28 +/- 0.11 ka (De Vivo et al. 2001). A date for this sample cannot be defined from the LC21 chronostratigraphy (Grant et al. 2012), as the date of De Vivo et al. (2001) was used to construct this age model.

In addition to the single, 1cm sample taken from the bottom of this visible tephra layer, three more, 5cm resolution samples were taken; one from the bottom 5cm, one from the middle 5cm and one from the top 5cm of the deposit. These samples were taken because the initial 1cm sample (described above) unexpectedly contained shards relating to the 'upper flow' component of the CI, a component of the eruption which was thought not to escape the confines of the Campi Phlegrei caldera. This component is the last (uppermost) in the Campanian Ignimbrite deposits, and so these samples were taken to test if this component was more abundant, higher up the deposit in LC21. The Upper Flow is characterised by K_2O values >8wt% (proximal data from E.Tomlinson). Thus, to begin to test the hypothesis that this upper flow is more abundant higher up in the stratigraphy, the K_2O values can be plotted vs SiO_2 for each of the samples representing the different levels in the deposit (fig. 7.15). A plot of the percentage of shards comprising the upper flow in each of the samples is also shown, in figure 7.15. If this is not the case, then the tephra found in visible distal marine deposits must be well mixed, either during its decent through the water column, or after deposition.

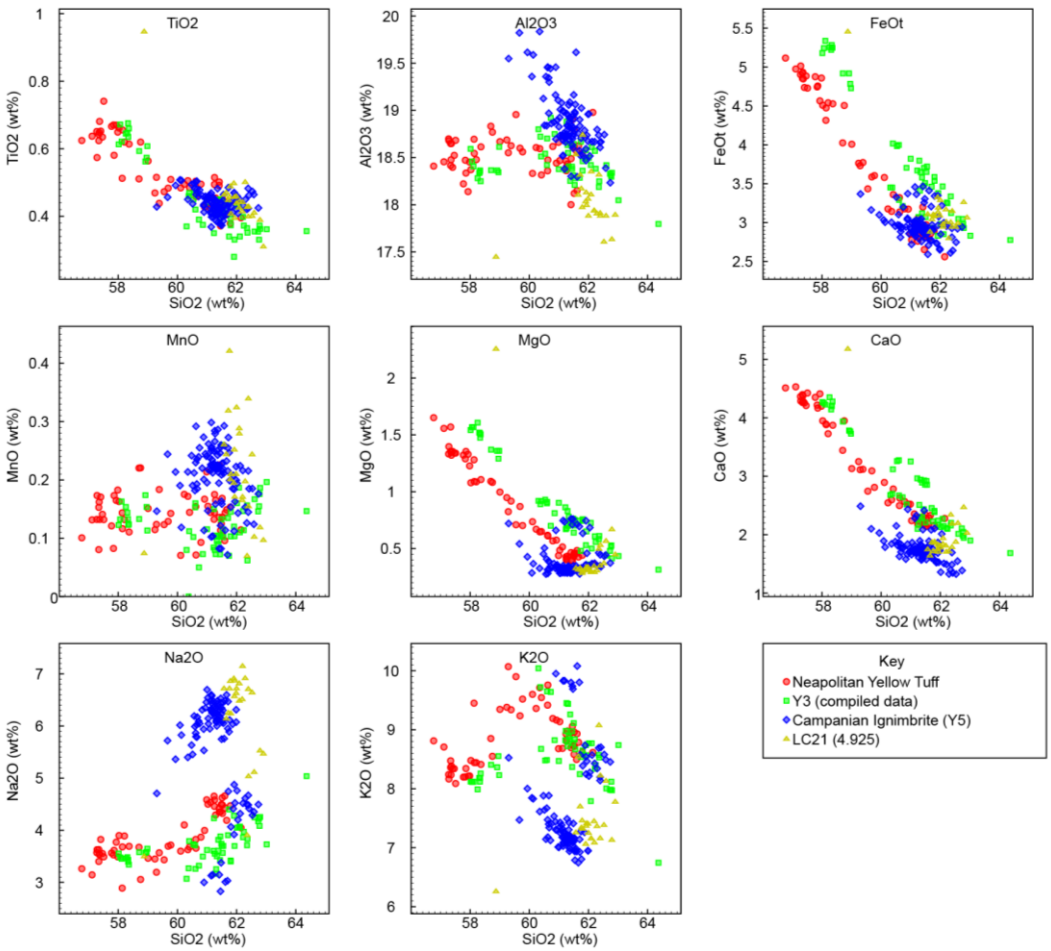

Figure 7.13 Major element comparison of LC21 (4.925) to Plinian eruptions from the proximal stratigraphy of Campania.

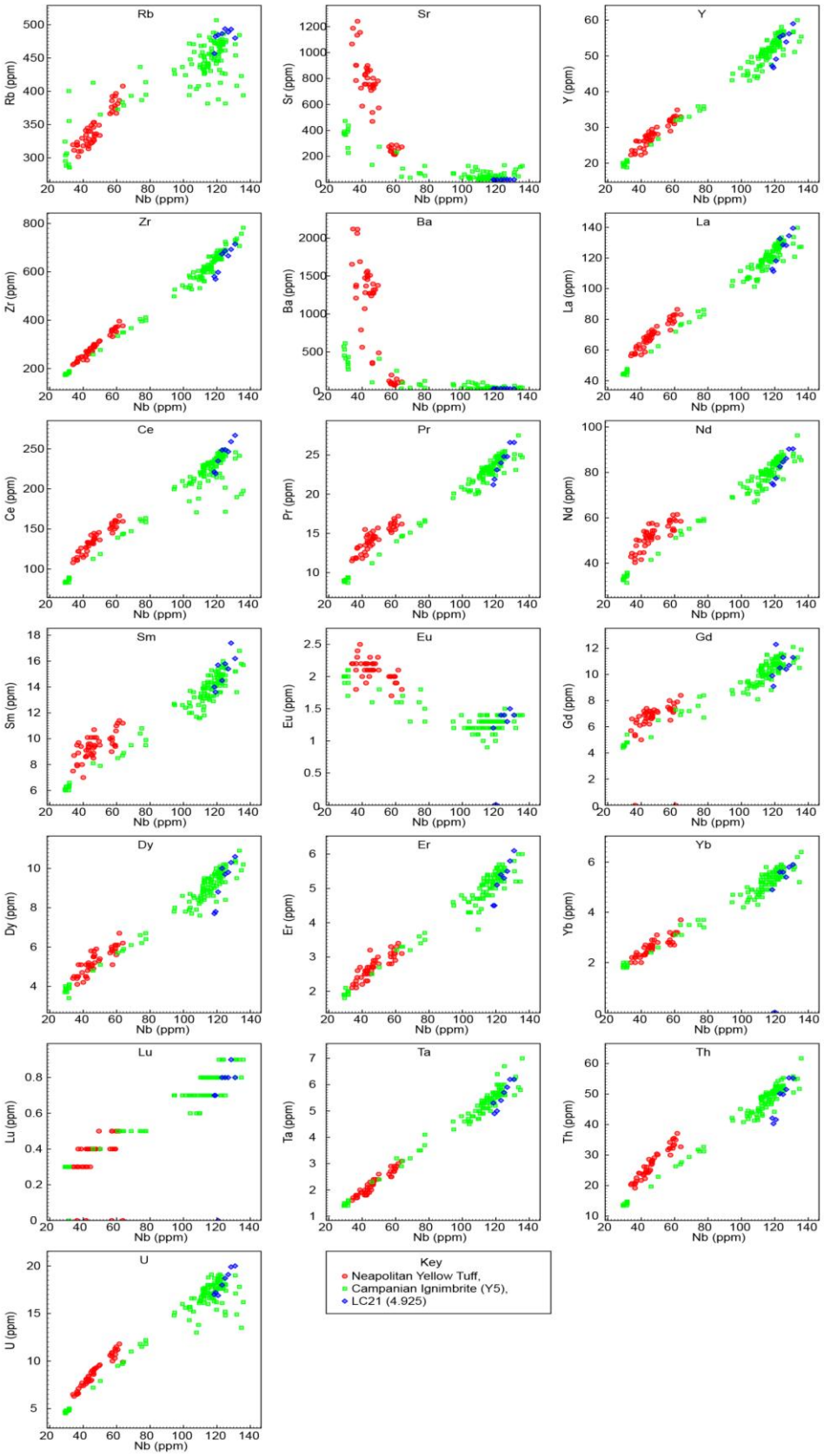

Figure 7.14 Trace element comparison of LC21 (4.925) to Plinian eruptions from the proximal stratigraphy of Campania.

Figures 7.14 and 7.15 indicate that tephra shards representing the upper flow may be more common in the upper part of the LC21 Campanian Ignimbrite deposit, corroborating the proximal stratigraphy. The fact that this component is found all the way through the deposit however, suggests that there is significant mixing of the tephra either during its transport from the volcano to the ocean floor, or after deposition on the ocean floor.

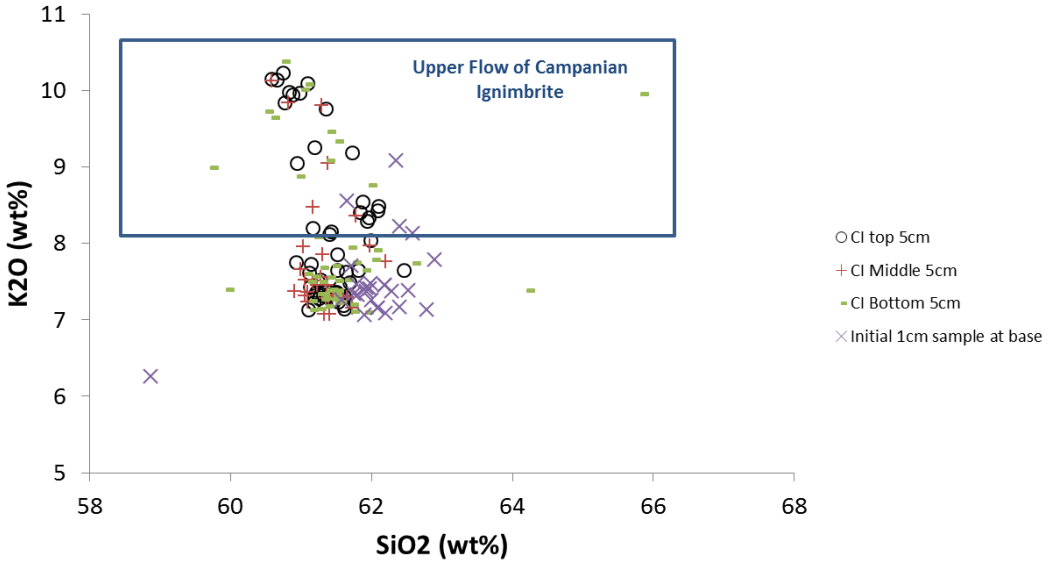

Figure 7.15 K_2O vs SiO_2 values for four samples of Campanian Ignimbrite representing the bottom 1cm, the bottom 5cm, the middle 5cm and the top 5cm. Compositions >8wt% K_2O represent the upper flow component of the Campanian Ignimbrite and are represented by the blue box.

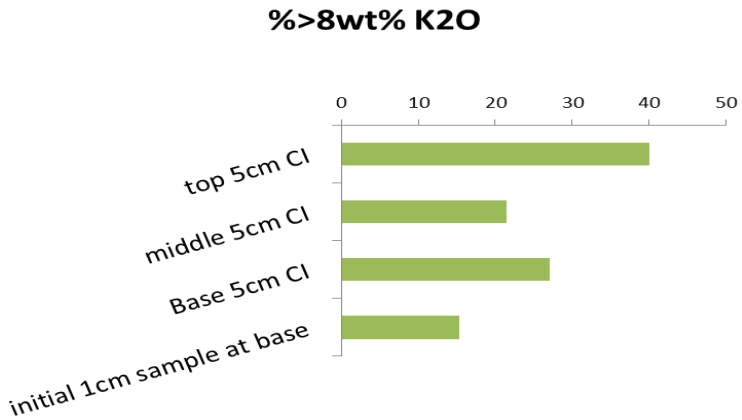

Figure 7.16 Bar chart showing the percentage of 'Upper Flow' (>8wt%) shards analysed within each sample from the Campanian Ignimbrite deposit in LC21. Most Upper Flow shards were detected in the top 5cm of the LC21 deposit, and the least were detected in the bottom 1cm. The fact that any at all were detected in the bottom 1cm indicates that some mixing of the tephra shards has occurred either during transport from the volcano to the sea floor, or after deposition.

It is possible that this sub-study may suffer from some bias introduced as a result of possible differences in the shard cutting depths between the sample stubs. More shards of the Upper Flow could have been analysed in the top 5cm sample if this stub had been cut to a lower level, exposing more of the (theoretically smaller) shards of the Upper Flow. Nonetheless the results show that both flow and fall components of eruptions can distribute ash shards over very large distances.

LC21 (5.125) plots close to the Santorini geochemical field in figures 7.16 and 7.17. Shards were only recovered from the 5cm sampling and not from the 1cm sampling. As the sample is located right at the top of a core section, it is possible that most of the tephra layer was removed during the cutting up of the core (only 101 shards were counted in the 5cm sample). Geochemically, the sample does not match any of the Santorini proximal deposits from our database (fig. 7.16 and 7.17). The deposit may be a distal component of the inter-plinian activity between the Upper Scoria 1 and Upper Scoria 2 events (phase M10 of Vespa et al. 2006). The sample is dated by our chronostratigraphy at ~42.28-43.34ka (table 6.1).

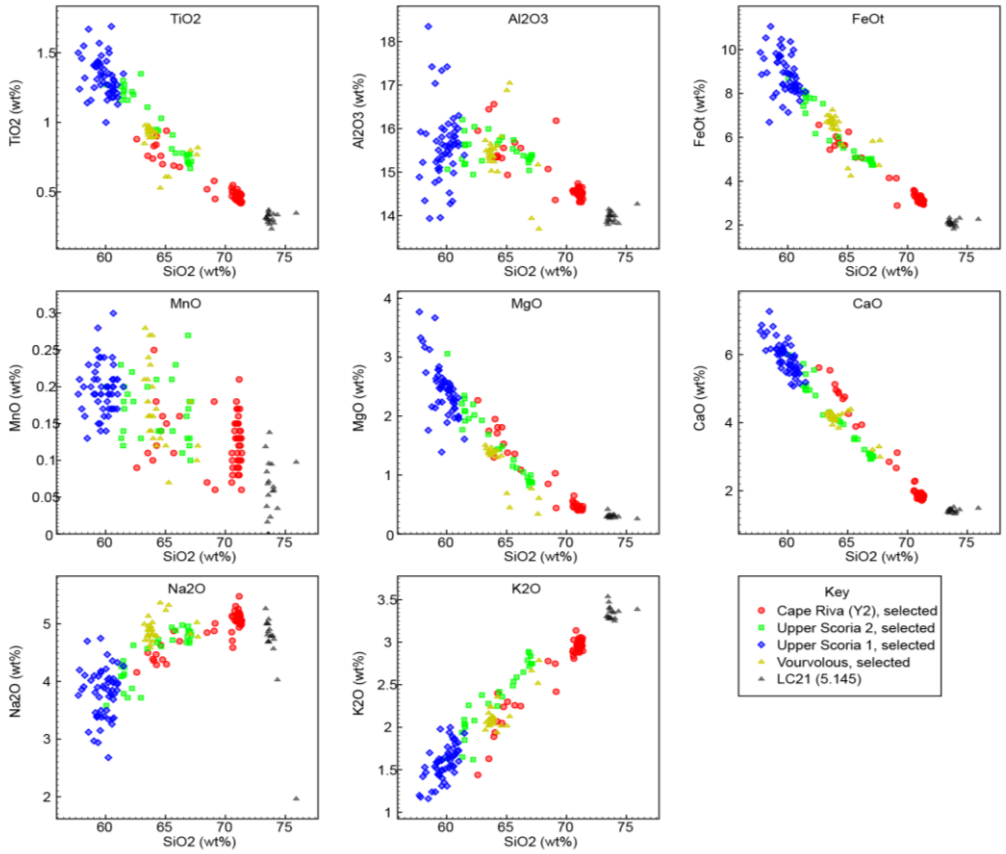

Figure 7.17 Major element comparison of the silica saturated shards from LC21 (5.125) to the proximal stratigraphy of Santorini.

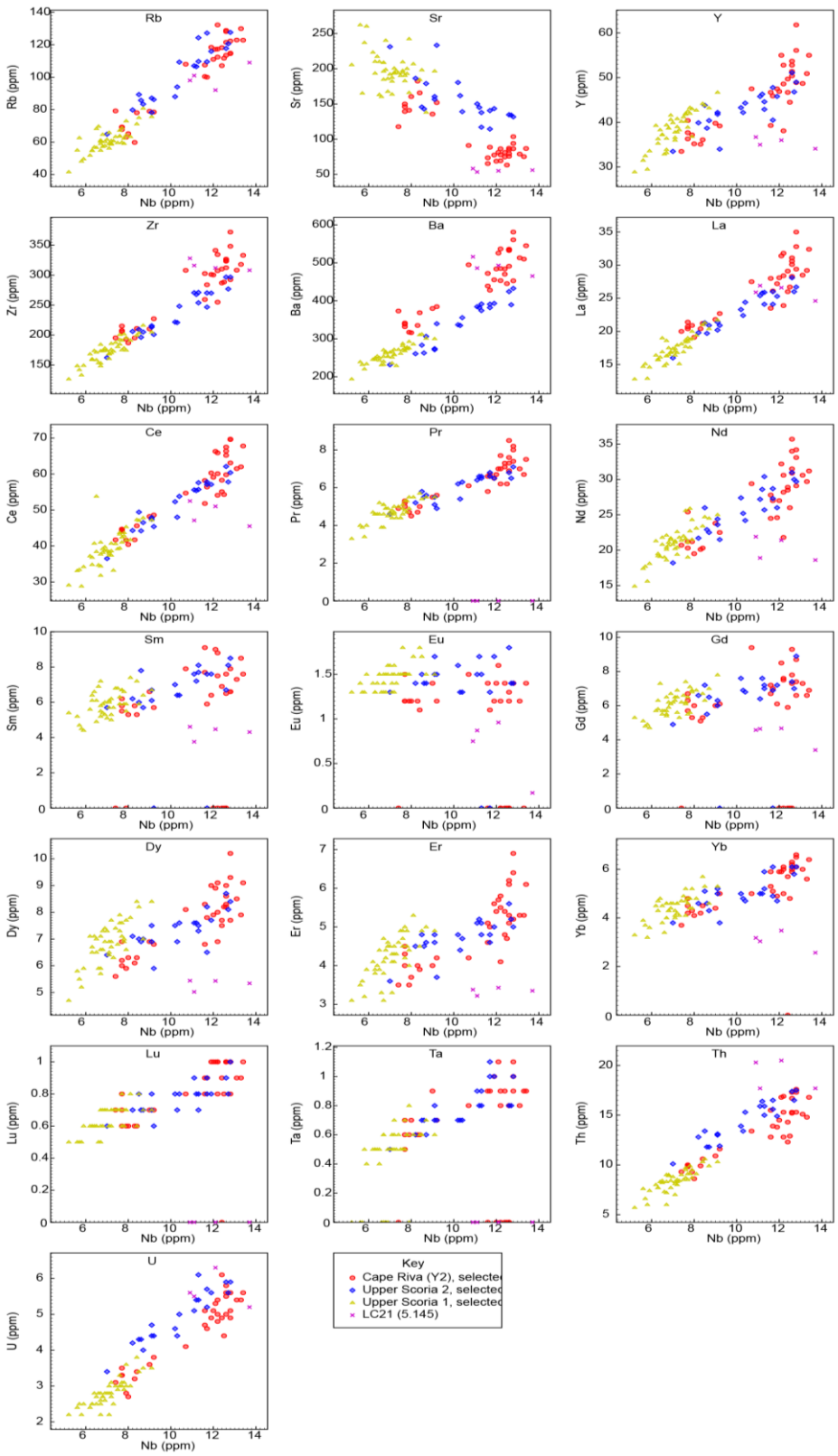

Figure 7.18 Trace element comparison of the silica saturate shards LC21 (5.125) to the proximal stratigraphy of Santorini.

LC21 (7.915) is dated by the chronostratigraphy at ~103.98 – 104.10ka (table 6.1) and contains both sub-alkaline and alkaline components (figures 6.10). The sub-alkaline component is considered to originate from Santorini as the majority of the shards plot close to the field in figure 7.2, although it is noted that one shard plots close to the Yali/Nisyros proximal deposits, and one close to the Aeolian Island proximal deposits. It does not match any of the proximal plinian deposits for Santorini and therefore may correlate to part of the interplinian eruption phases described by Vespa et al. (2006). Whatever the origin of the tephra, it shares the same date (within sample resolution) as the alkaline component of the same sample.

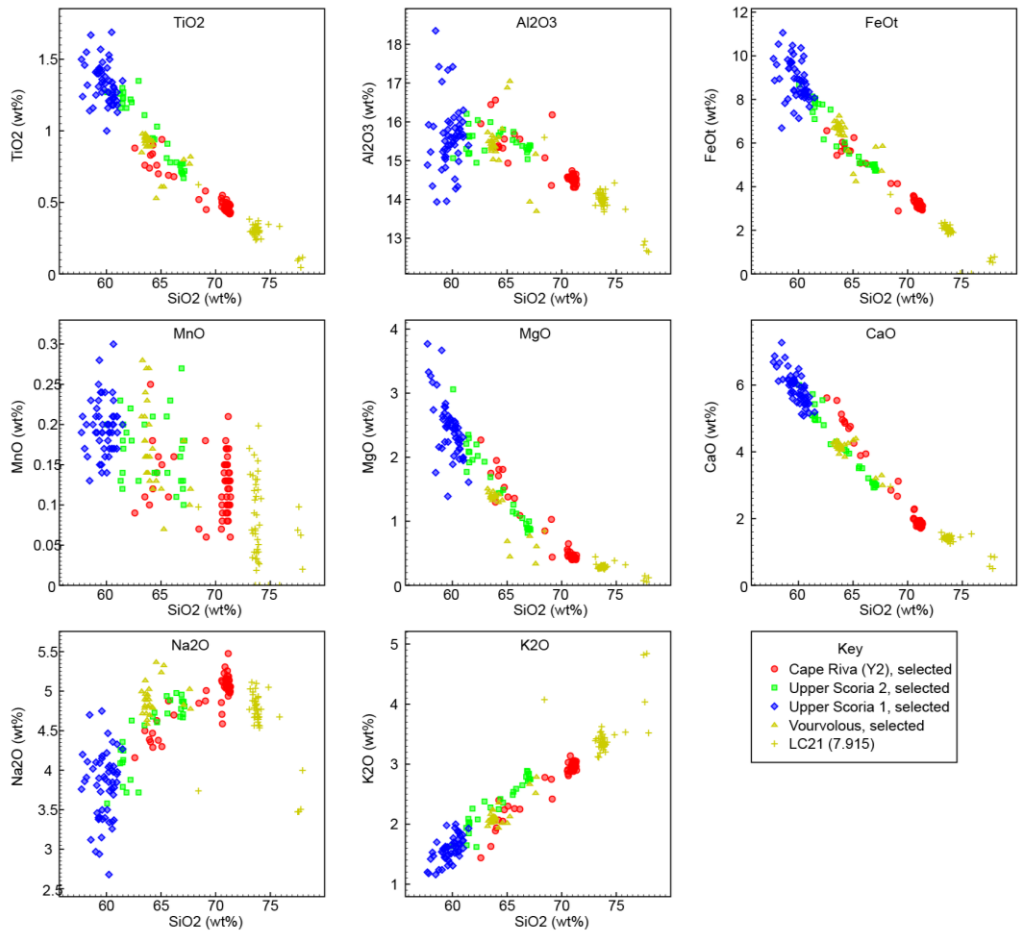

Figure 7.19 Major element comparison of the silica saturated shards from LC21 (7.915) to the proximal stratigraphy of Santorini.

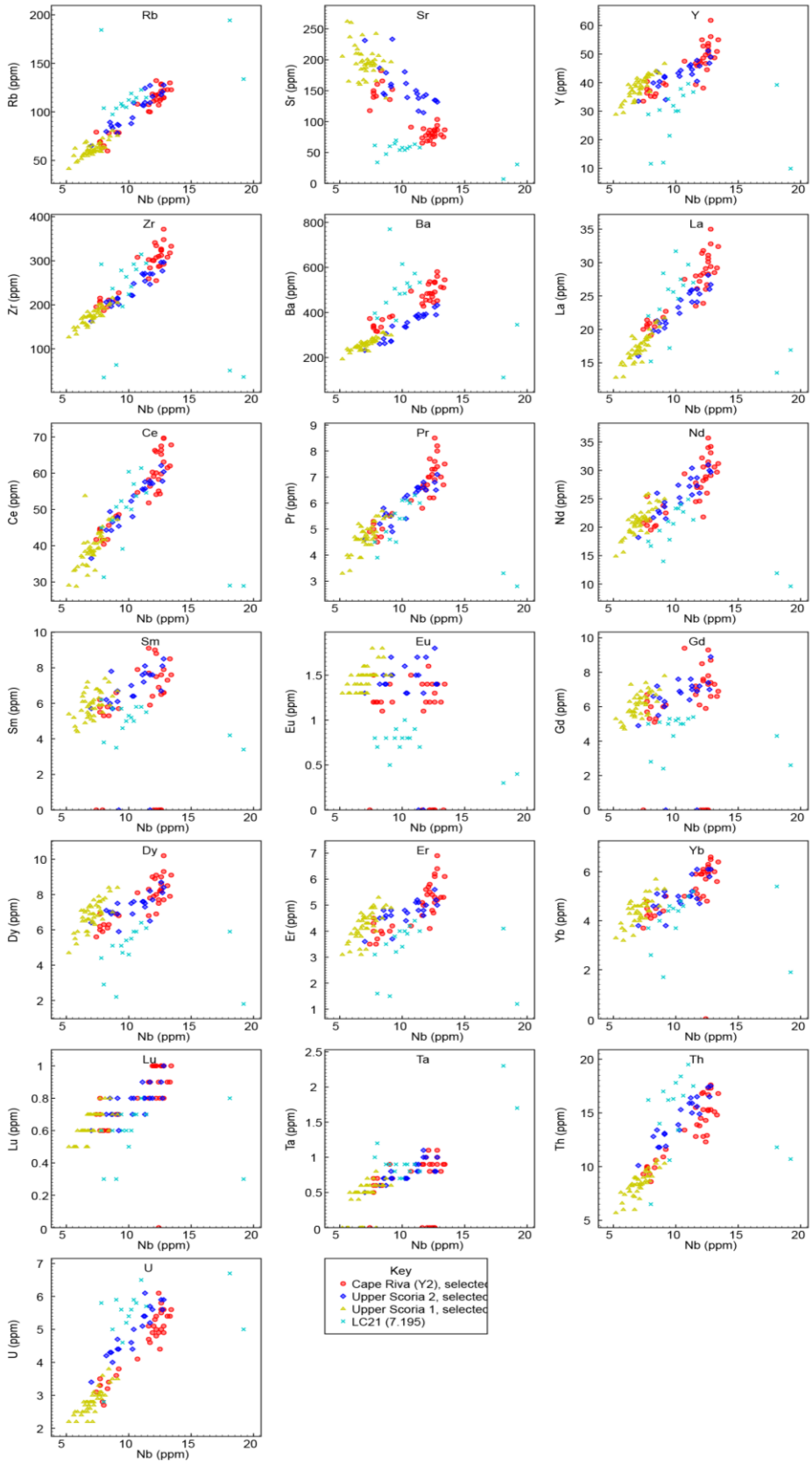

Figure 7.20 Trace element comparison of the silica saturated shards LC21 (7.915) to the proximal stratigraphy of Santorini.

The alkaline component indicates an Italian source, and the Zr vs Nb plot (fig. 7.2) is also most similar to that of the Campanian Region, although only two trace element analyses of the alkaline component of LC21 (7.915) were achieved due to the small size of the shards. Figures 7.21 and 7.22 show that some shards of the alkaline (phonolitic) component of LC21 (7.915) are in very good agreement with the TM 24a or b tephras in Lago Grande di Monticchio (this study), while the other shards are similar to, but not identical to TM27. These other shards (a high Na_2O component of the sample) do not match TM24a or b. These shards cannot represent contamination from the other Campanian tephra layer in LC21, the Campanian Ignimbrite (discussed above), as they do not match it geochemically. Perhaps then, this high Na_2O component represents another magma batch contributing to the eruption, but not preserved in the LGdM sequence, or a separate Campanian eruption occurring very soon before or after TM24.

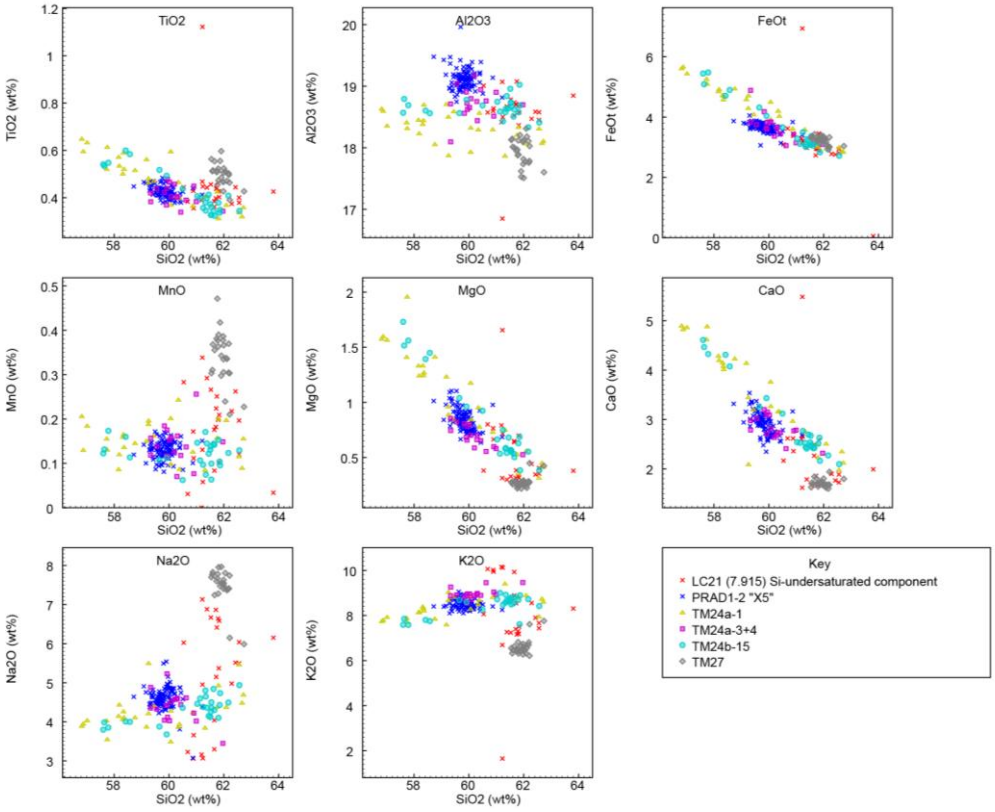

Figure 7.21 Major element comparison of silica under-saturated shards from LC21 (7.915) to the proximal stratigraphy of Campania.

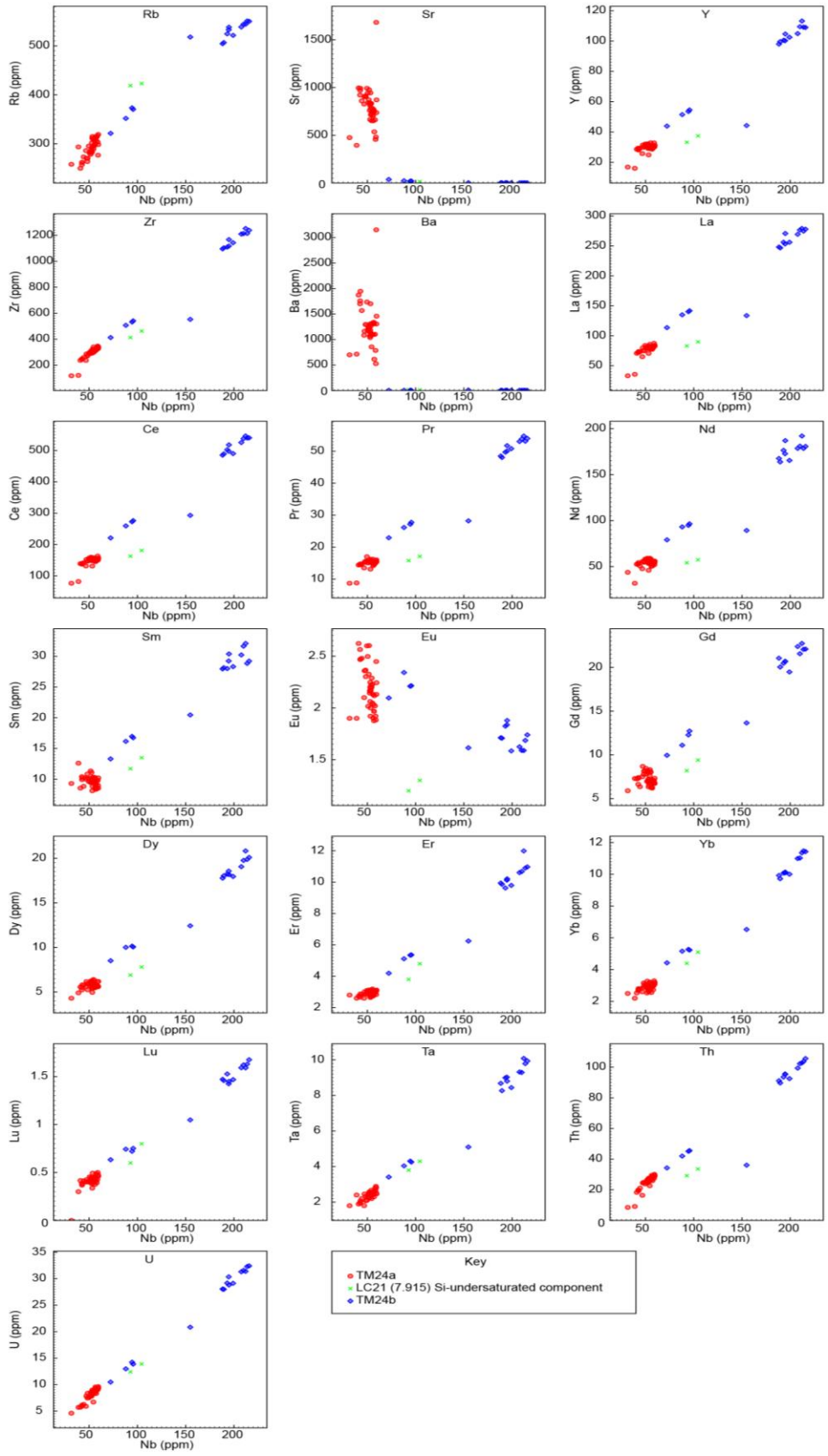

Figure 7.22 Trace element comparison of silica under-saturated shards from LC21 (7.915) to the proximal stratigraphy of Campania.

The TM24a and b tephras are both correlated to the X5 tephra (Vogel et al. 2010 and Bourne et al. 2010). This observation is by far the furthest east (~1200 km) that X5 shards have been found. X5 is dated to 105±2 ka on the basis of Kraml (1997). This tephra is found here with shards from a hitherto unknown Campanian eruption of very similar age to TM24a or b, and thus by extension, the age of the X5 tephra in the Ionian Sea of 105±2ka, Kraml 1997. This age is in good agreement with the modelled age for LC21 (7.915) of ~103.98 – 104.10ka. This correlation is explored further with reference to the proxy record in section 7.5.2.

LC21 (9.575) is a sample at the base of a large amount of crypto-tephra in the core (see fig. 6.1) and lies within sapropel 5 (S5). It is likely that the exaggerated thickness of S5 in LC21 (Marino et al. 2007) and the increase in the sedimentation rate in this part of the core is due, at least in part to the input of tephra into the core site at this time. It is also clear (fig. 6.1) that the tephra must have been emplaced nearly throughout the period of formation of S5, and it is therefore suggested that sample LC21 (9.575) represents the start of a period of interplinian activity of Santorini. Some shards closely match the Upper Scoria 1 proximal deposits, but also has some shards plotting within the proximal Vourvolous proximal deposits (figure 7.23and 7.24). It is therefore possible that this sample represents the start of the inter-plinian activity, perhaps between these two major eruptions. If this is so then the deposits of tephra shards within sapropel S1 correspond to the M9 interplinian deposits detailed by Vespa et al. (2006). LC21 (9.575) cannot represent reworking of the thin visible layer below it –LC21 (9.709), as the two differ in composition (cf fig. 7.23 and 7.25). The sample is dated by our chronostratigraphic framework at ~125.72-125.77ka (table 2).

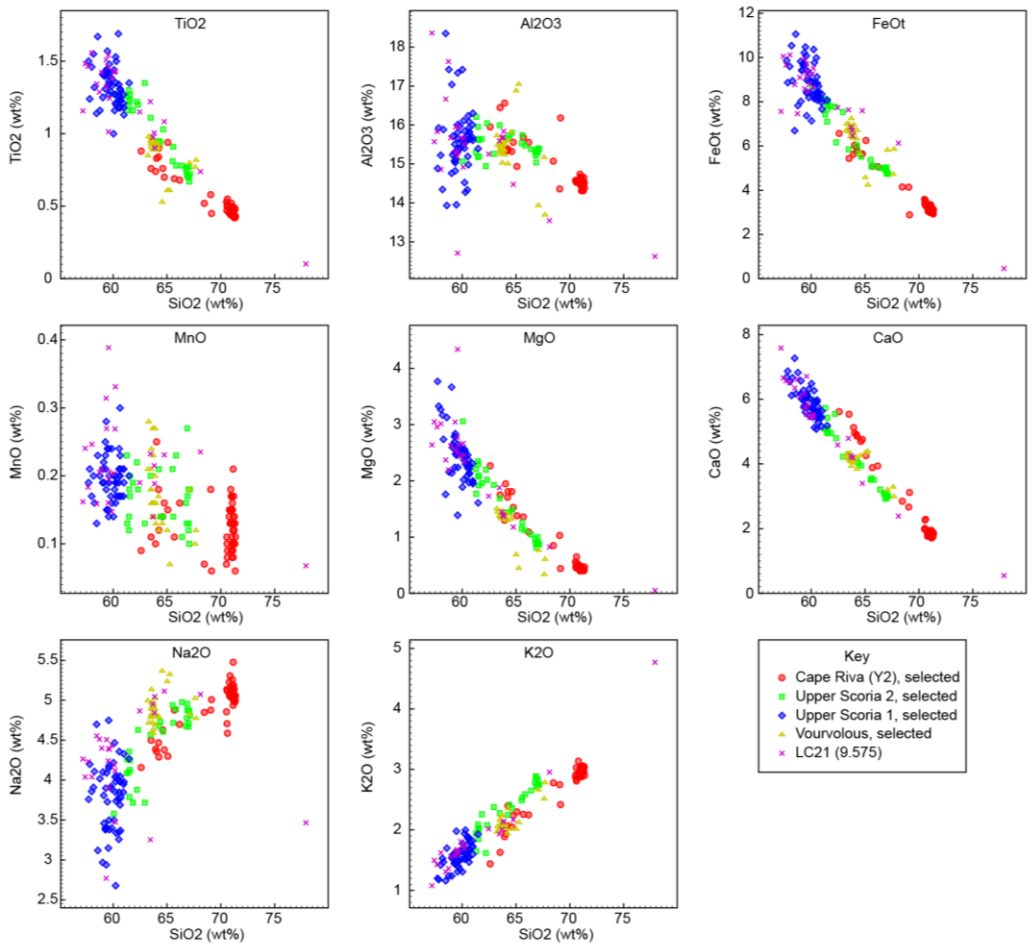

Figure 7.23 Major element comparison of LC21 (9.575) to the proximal stratigraphy of Santorini.

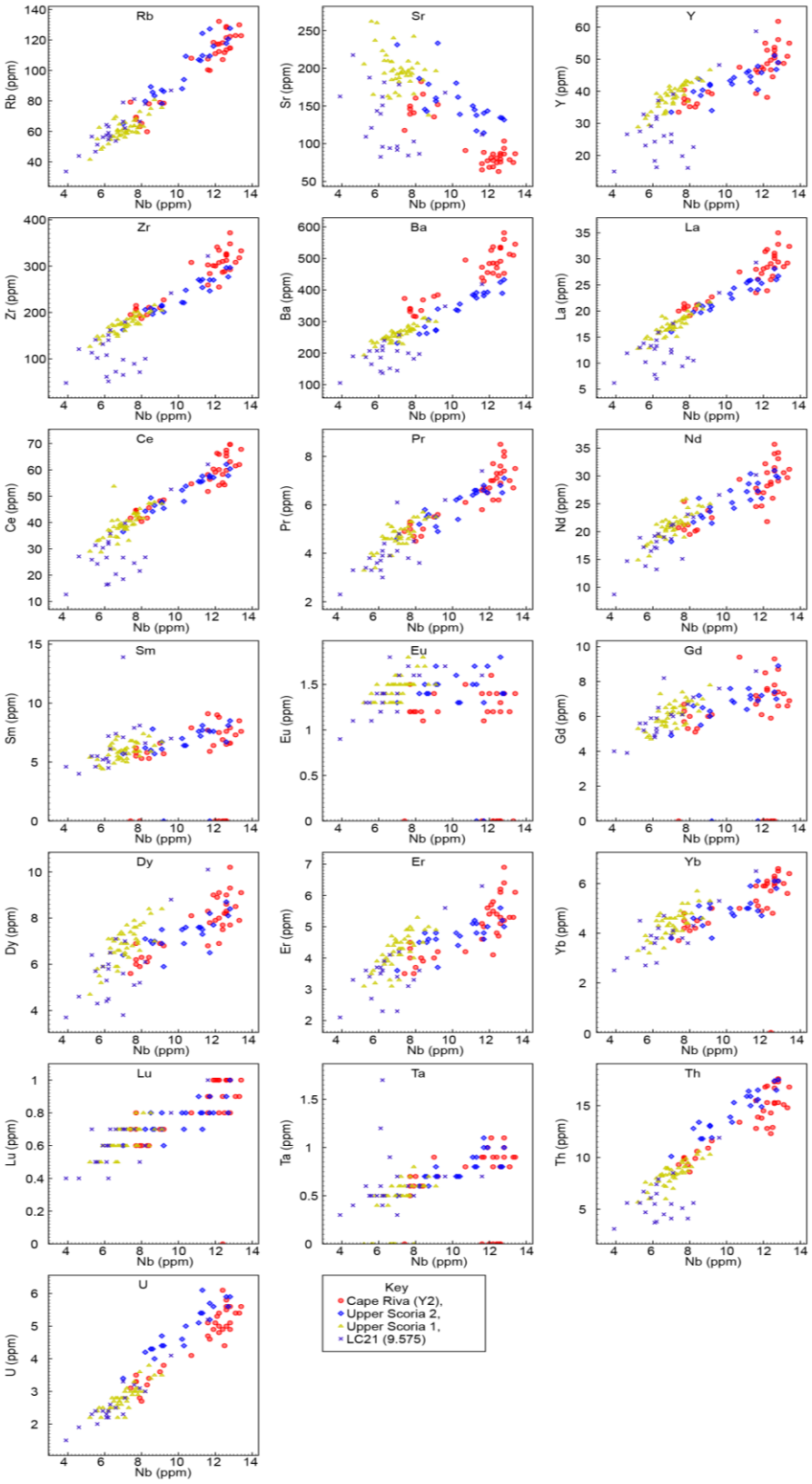

Figure 7.24 Trace element comparison of LC21 (9.575) to the proximal stratigraphy of Santorini.

LC21 (9.709) is a visible, silica saturated tephra within sapropel S5 which lies within and on the HFSE trend-line of the proximal deposits from Santorini (fig. 7.2). It must be older than the X5 tephra (the calc-alkaline component of LC21 (7.915)) dated at 105±2 ka, as it is stratigraphically below it. Geochemically the sample does not match well any of the proximal deposits from Santorini (figs 7.24 and 7.25). Given that there are no other known, silica saturated sources from which this tephra could originate, and that the HFSE plot strongly indicates an origin from Santorini, it is therefore probable that this tephra layer is another Santorini eruption which is preserved in LC21, but not found on land. The sample is dated at ~126.51ka BP by our chronostratigraphy (table 6.1).

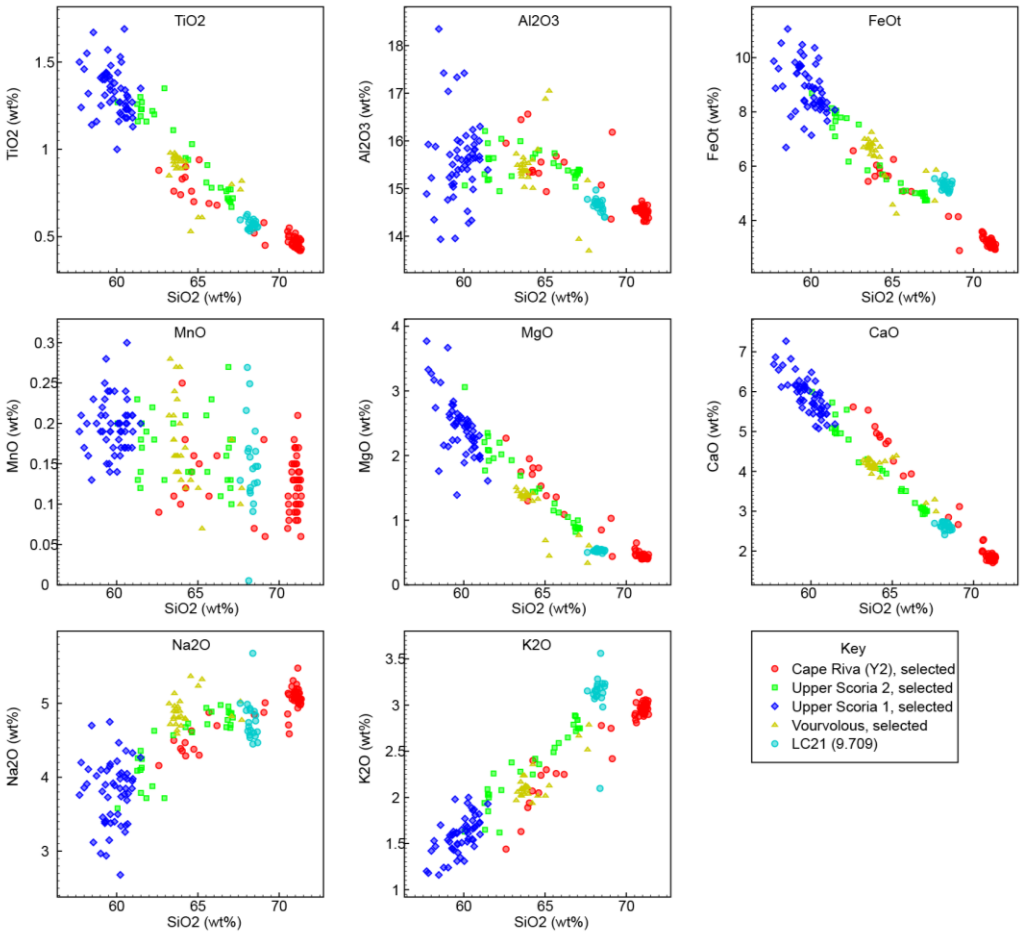

Figure 7.25 Major element comparison of LC21 (9.709) to the proximal stratigraphy of Santorini.

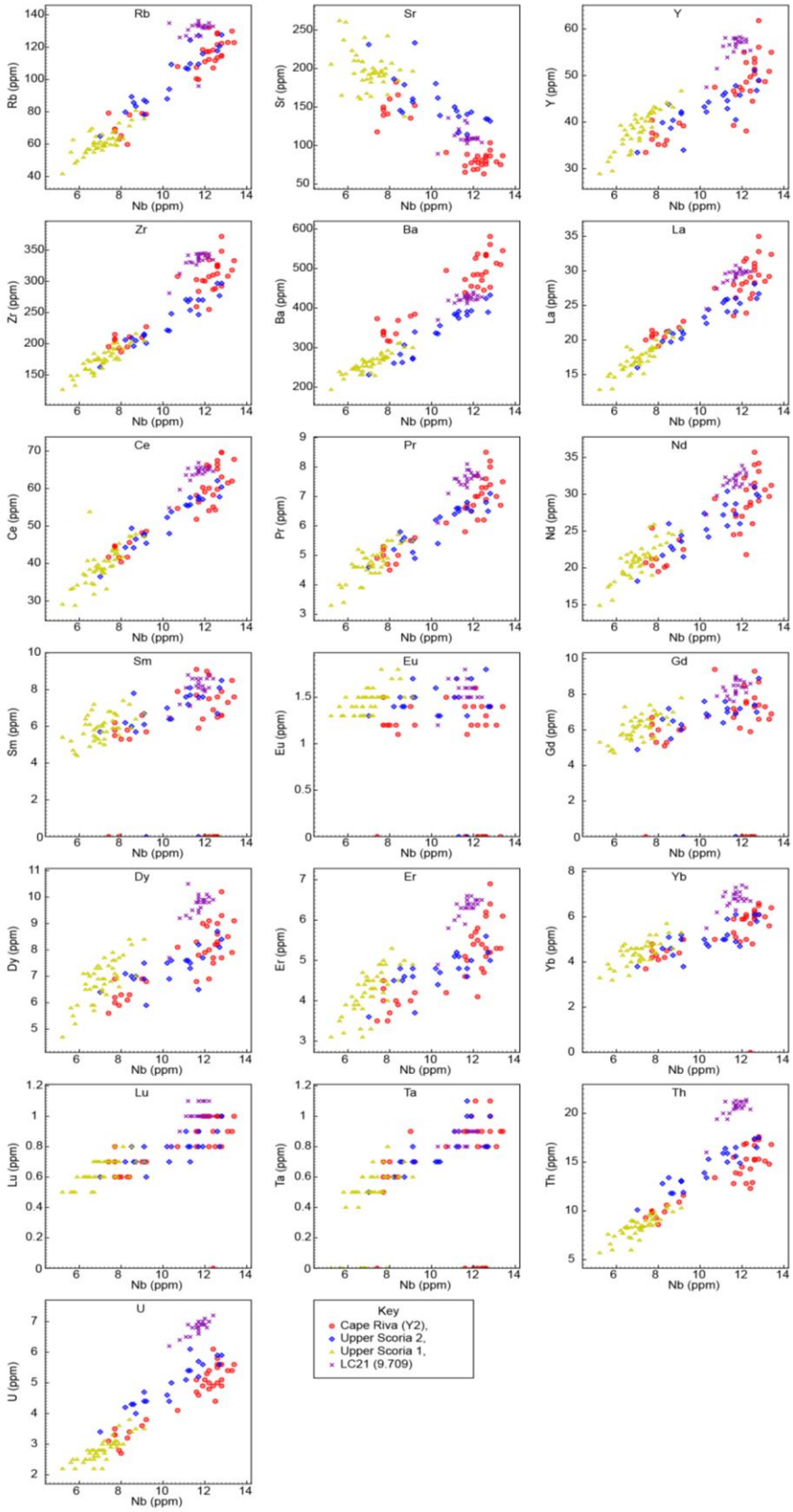

Figure 7.26 Trace element comparison of LC21 (9.709) to the proximal stratigraphy of Santorini.

LC21 (10.345) contains shards of Pantellerite composition (figure 7.26) This strongly indicates an origin from Pantelleria, as no other Mediterranean volcano is known to produce such magma compositions. The sample is from below sapropel S5 in LC21 and must therefore be older than its date of 124-119ka (Bar-Matthews et al. 2000). It cannot therefore represent either the Green Tuff (48.5±3.5ka, Cornette et al. 1983), or the Ante-Green Tuff (79,250ka, Mahood et al. 1986) eruptions as these are far too young. The stratigraphic position of the tephra prior to sapropel 5 and post Kos Plateau Tuff (see below) indicates that this may be the easternmost occurrence yet found of marine tephra P-11 (Paterne et al. 2008). No independent proximal dates exist for this tephra, but Paterne et al. (2008) cite an age of ~131 ka, unfortunately without details on how this age was derived. Our chronostratigraphy derives an age of ~133.47-133.58ka, which is excellent agreement with a date of 132.3±5.7 to 133.5±6.2ka for the proposed proximal deposit (named Unit-P) (Mahood and Hildreth 1986). This proposed correlation is tested further in section 7.5.5.

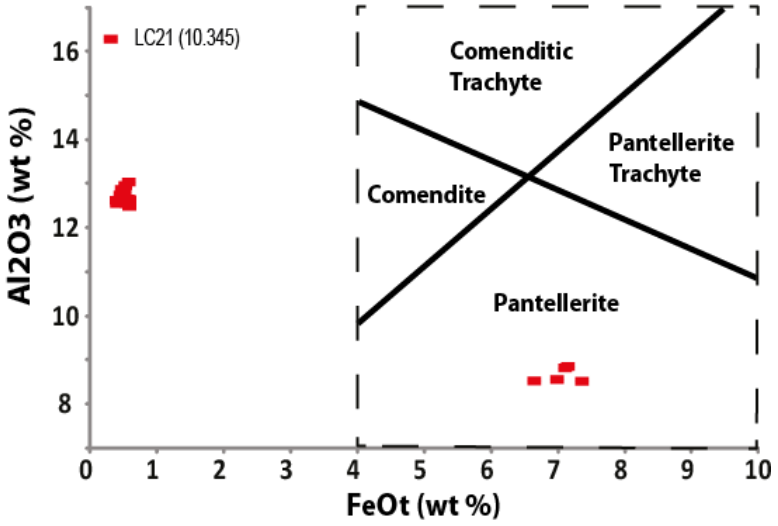

Figure 7.27 Plot showing 5 shards of LC21 (10.345) classified in the Pantellerite geochemical field (after Tamburrino et al. 2012).

The majority of the shards in the sample are not Pantellerite composition and have very high silica contents (>77wt%). These high silica contents indicate an origin of either Central Anatolia or Kos or Nisyros. As trace element data was not recovered from these very small shards, figure 7.27 shows the major element comparison of the available data for these regions, and the composition of LC21 (12.465) which, as discussed below, is implied to represent the Kos Plateau Tuff in LC21. The non-Pantelleria shards in LC21 (10.345) are

indistinguishable from the Kos Plateau Tuff in LC21. However these shards cannot originate from the KPT eruption as they are found together with the Pantelleria P-11 tephra which gives the sample a date of ~133ka (see above), which is ~30ka younger than the date for the Kos Plateau Tuff of 161±1ka (Bachmann et al.2010).

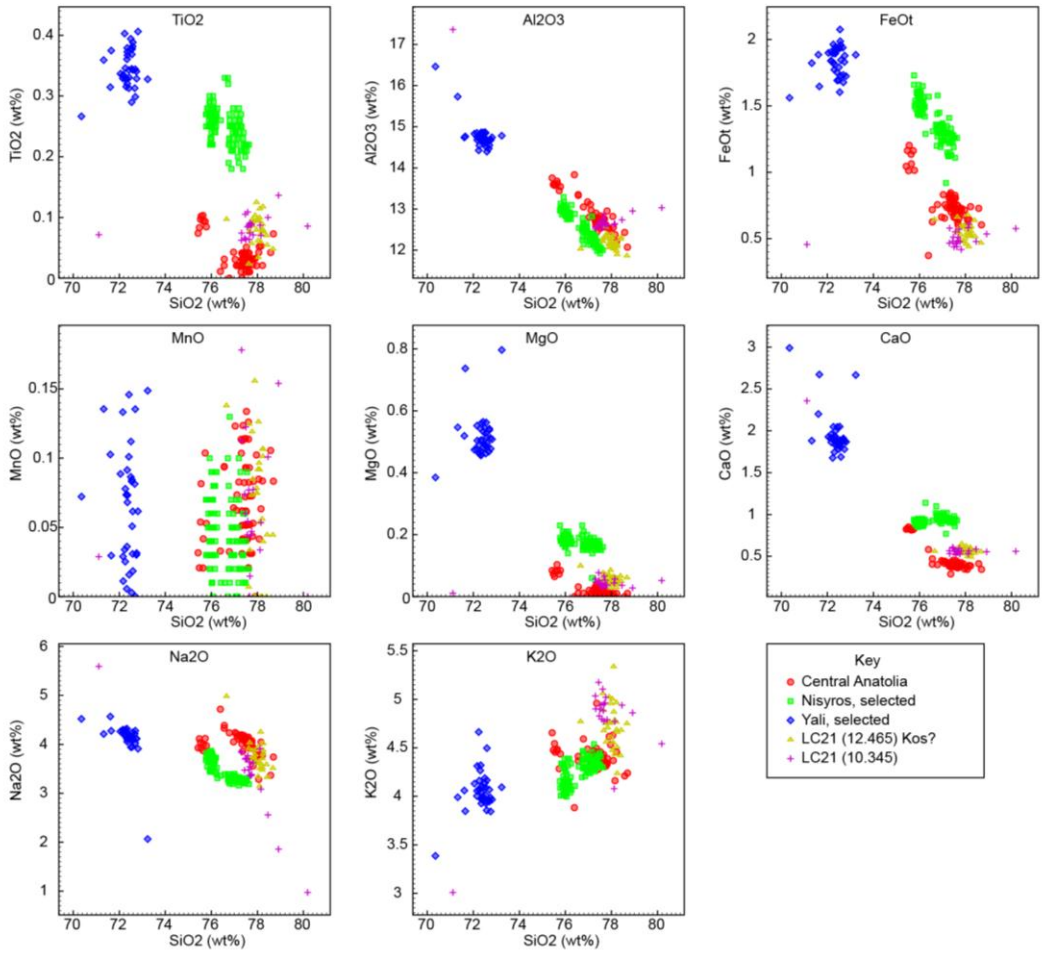

Figure 7.28 Major element comparison of LC21 (10.345) (without Pantelleria component) to the proximal stratigraphies of Central Anatolia, Nisyros, Yali and Kos (using LC21 12.465).

These shards are highly unlikely to be contaminants from LC21 (12.645) because they were processed 4months after LC21 (12.465). The shards must therefore represent a hitherto unknown eruption of Kos, Nisyros or Central Anatolia which has a major element composition identical to the Kos Plateau Tuff. This eruption must have been coincident (within sampling resolution) with the Pantelleria eruption found within the same sample.

LC21 (11.190) is a thick (42cm) visible tephra layer with a very broad major element classification ranging from basaltic andesite to rhyolite (Figure. 3b). It predates the Pantelleria tephra which is found above it -LC21 (10.345) and has a date from our

chronostratigraphy of ~152.58ka (table 6.1) The deposit most likely originates from Santorini, due to its position on figure 7.2 and its thickness. Federman and Carey (1980) note that the only (visible) marine tephra in their cores with this broad range of compositions (fig. 7.28) is the W2 tephra, attributed to the Middle Pumice Series of Santorini, dated by orbital tuning to ~150 ka (Narsici and Vezzoli 1999). This is considered this to be the most likely source of LC21 (11.190), however proximal data for the Middle Pumice eruption was not produced for RESET, so this hypothesis remains untested.

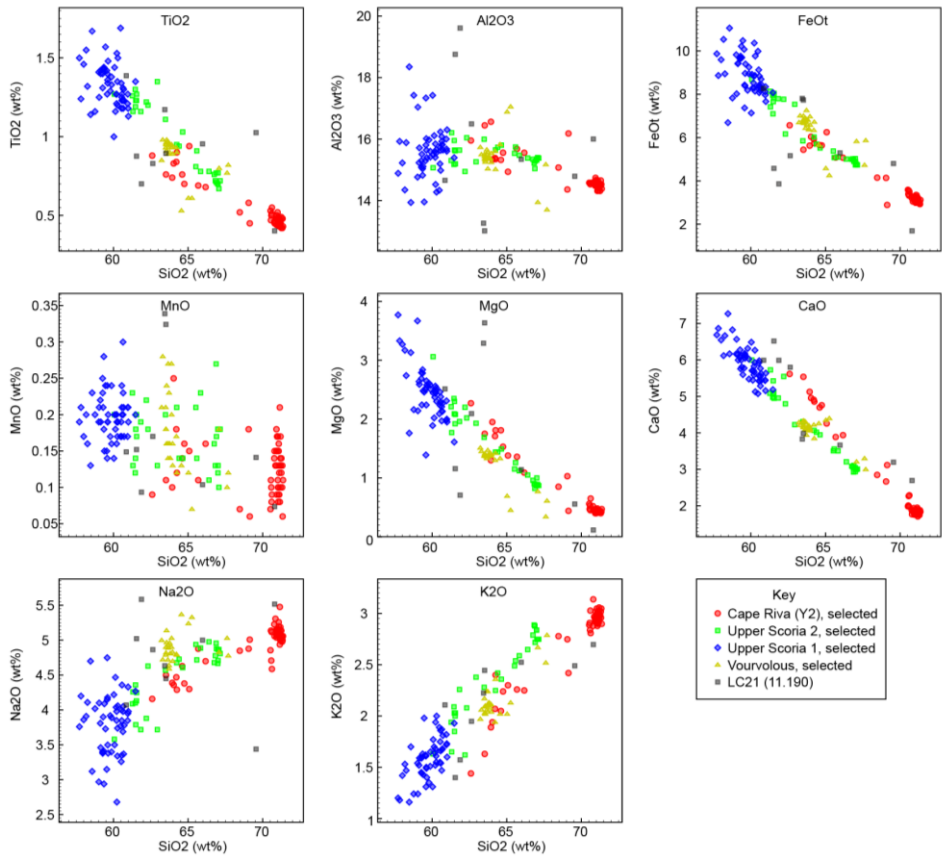

Figure 7.29 Major element comparison of LC21 (11.190) to the proximal stratigraphy of Santorini.

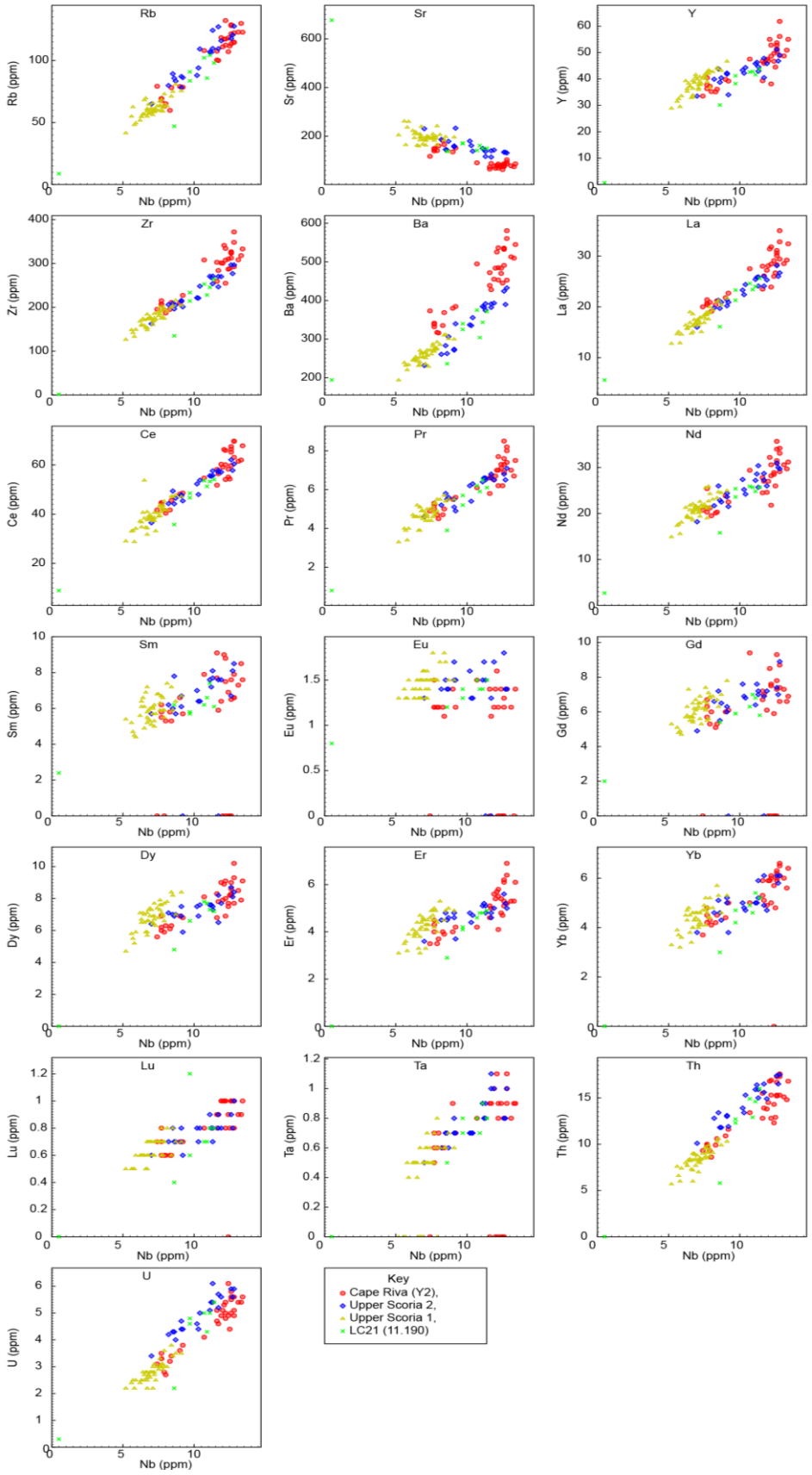

Figure 7.30 Trace element comparison of LC21 (11.190) to the proximal stratigraphy of Santorini.

Tephras LC21 (12.465), (12.625), (13.275), (13.405) and (13.485). These tephras are chemically indistinguishable from one another (figs 6.15 and 6.16) and span a region rich with tephra shards at the base of the core. They are consequently addressed together.

Given the identical geochemical nature of the tephras, some suggested hypotheses to explain their relationship are that: 1) each of the tephras represents a separate eruption (or stage of the KPT); 2) the tephras are related by reworking; or 3) the tephras represent a coring artefact at the base of the core.

In hypothesis 1, one would expect the trace elements to show some differences, but this is not the case. Hypothesis 2 is supported by the strange geometry of the bottom four tephra layers with respect to the rest of the sediment and that the sediment between the tephras is full of tephra shards. This hypothesis is also supported by the scanning XRF data (appendix 4) which shows that the elemental abundances are constant in this section of the core, implying homogenisation of the sediment by mixing. Hypothesis 3 is impossible to support as all the tephras are contained in the same core section. The isotopically defined chronostratigraphic framework (Grant et al.2012) could not derive dates for these tephras due to the lack of foraminifera in this section of the core (fig. 6.3, table 6.1), implying that the material is mainly clastic and must represent an interruption to normal hemipelagic sedimentation. Hypothesis 2 (sediment re-working) is therefore proposed here to explain the strange architecture of the tephra layers in this part of the core, and so only tephra layer LC21 (12.465) is taken to represent the position of the eruption within LC21. This is the only one of the five tephra layers which lies horizontally across the core, and after this point the scanning XRF elemental data start to vary as they normally do in the rest of the core (Appendix 4). The inferred slumping and reworking, which must be contemporary with the eruption (as the 5 tephra layers are intercalated with the reworked sediment) could have taken place as a consequence of some seismic activity associated with the source eruption.

LC21 (12.465) lies far below LC21 (7.915), the phonolitic component of which is assigned here to the X5 (TM24a or b) tephra, and also below the Pantellerite shards of LC21 (10.345) and is dated by the LC21 age model of Grant et al. (2012) (fig. 6.3) to be >155ka. The Zr vs Nb plot (fig. 7.2) implies that this tephra could originate from the Central Anatolian volcanic system as all the shards lie on an extension of the trend line for the proximal deposits. The high SiO_2 values of 77-78wt% are also consistent with an origin from the

Central Anatolian volcanic system. However a major regional Aegean tephra found by Hardiman (1999), Federman and Carey (1980) and Vinci (1985) with very high SiO_2 values is attributed (using major element analyses) to the Kos Plateau Tuff eruption from the island of Kos. The proximal deposits of the eruption have been extensively studied by Bachmann et al. (2007,2010), Allen et al. (1999) and Allen and Cas (1998), but unfortunately no single grain trace element data yet exists for this eruption, preventing a comparison to the data produced here.

There are therefore two possible sources for the shards in this tephra layer, Kos or Central Anatolia. It is extremely unlikely that of the two possible sources of Central Anatolia (~900km to the NE of LC21) or Kos (~140km to the NE of LC21), the former would be the source. This argument is particularly persuasive given that the proximally derived ^{40}Ar:^{39}Ar date of 161±1ka is in agreement with the position of the tephra in LC21 (just below the age model date of ~155ka- Grant et al. 2012), and the implication from the reworking apparent in the sedimentology that the deposition of this tephra could have been accompanied by seismic activity. Occam's razor demands that these five LC21 tephra layers (four re-worked) most likely relate to the eruption of the Kos Plateau Tuff at 161±1 ka (Bachmann et al. 2010), although no proximal single shard trace element dataset yet exists for a definitive test of this hypothesis.

7.3 Discussion for tephra layers found in ODP967.

Figure 7.31 implies that the tephras in ODP967 are derived from 2 or 3 volcanic sources; Santorini, Kos/Yali/Nisyros and/or Central Anatolia. The tephras are discussed in stratigraphic order.

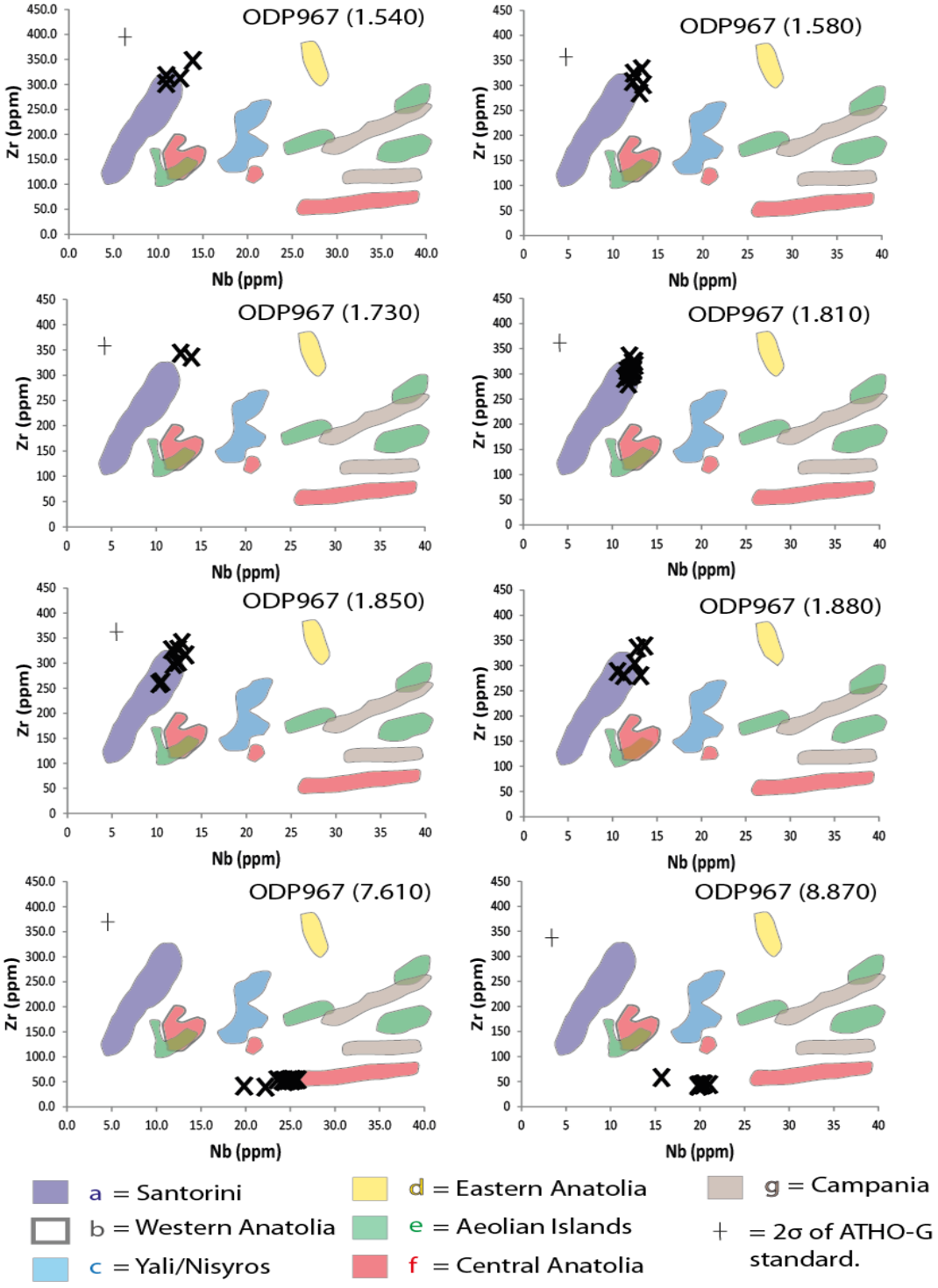

Figure 7.31 HFSE (Zr vs Nb) plots for all ODP967 with trace element analyses (samples 1.620, 5.560 and 8.460 do not have trace element abundances). These plots can help to inform on which volcano each tephra layer could originate from, and thus inform on which stratigraphy to investigate for a proximal correlative.

ODP967 (1.540), ODP967 (1.580), **ODP967 (1.620)**, and **ODP967 (1.730)** all show nearly identical major element chemical compositions (fig. 7.31) and are samples from peaks in a

continuum of crypto-tephra in ODP967 (fig. 6.2) They are therefore discussed together here.

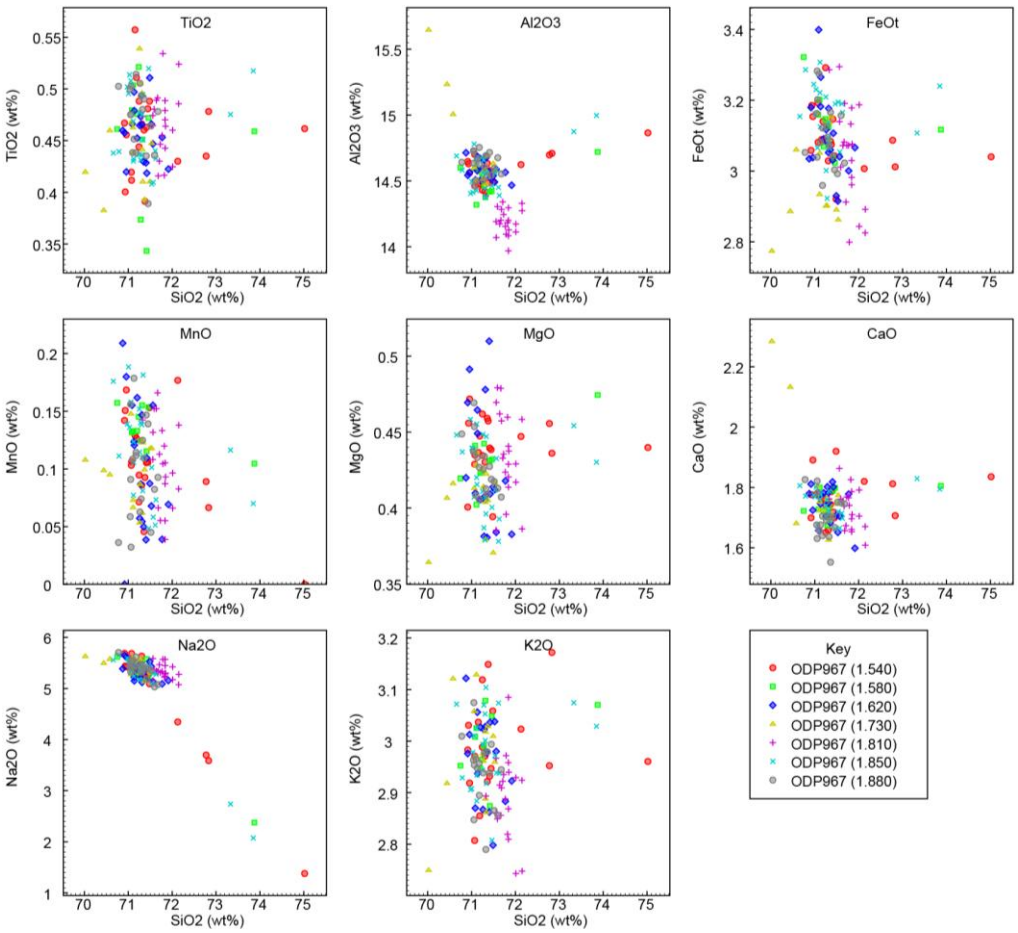

Figure 7.32 Major element geochemistry of ODP967 (1.810) and crypto-tephra layers above and below this visible tephra.

Test for upwards reworking of ODP967 (1.810). The shard count diagram for these samples indicated that they may all represent reworking of the visible tephra layer ODP967 (1.810) as implied by Watkins et al. (1978). The dates assigned to the depths of these samples by the age model of Larrasoana et al. (2003) are 12.70-12.57ka at 1.540m, 13.46-13.34ka at 1.580m, 13.97-13.85ka at 1.620m and 15.38-15.52ka at 1.730m. If any of these peaks in tephra shards represents the Cape Riva tephra (dated at 21,705 ± 311 cal BP by Eriksen et al. 1990), the age model of Larrasoana et al. (2003) is too young by 6-9ka at this point in the core. The distribution of tephra through the sediment implies that a likely interpretation could be that these peaks in tephra shard concentrations represent reworking of the visible tephra (ODP967-1.810), upwards though the sediment column.

This effect has been noted by other authors for the sediment immediately above a visible tephra layer (Watkins et al. 1978, Bourne et al.2010) and can be tested using the available major element geochemistry (fig. 7.31).

The majority of chemical compositions of all these tephra samples are indistinguishable from one another (fig. 7.32). ODP967 (1.540) and (1.580) however show additional geochemical compositions not shown in the visible tephra ODP967 (1.810), or the crypto-tephras at 1.730m or 1.620m. The majority of shards in ODP967 (1.540) and (1.580) are identical to those in ODP967 (1.810), but there are in addition several more evolved (higher SiO_2) tephra shards. This additional component may indicate that some shards in crypto-tephra samples at 1.540m and 1.580m in ODP967 may represent, at least in part, different eruptions of Santorini to that represented by the visible tephra at 1.810m depth in the core. The sedimentology (fig. 6.18) and the majority of the geochemical analyses however, strongly imply vertical re-working of the visible tephra at 1.810m depth.

This interpretation does not however preclude the existence of other eruptions of Santorini contributing to the stratigraphy. This may explain some of the 'non-Cape Riva like' tephra shard chemistries in samples ODP967 (1.540) and (1.580). St Seymour et al. (2004) found a sedimentologically well defined tephra layer derived from Santorini and dated to ~13ka, in the Phillippon peat basin in northern Greece. They conclude that this tephra is from a Santorini eruption which does not have any proximally defined deposits. Similarly, in this study, a tephra with a most likely provenance of Santorini (but demonstrably not of Cape Riva chemistry) was found in core LC21 (sample LC21 2.005). This sample is dated by the LC21 age model at ~11.25-11.11ka. These two tephras indicate that there must have been ash producing, rhyolitic eruptions from Santorini between the Cape Riva and Minoan Plinian eruptions, and that these eruptions are not yet geochemically characterised in the proximal stratigraphy.

Comparison of ODP967 (1.810), ODP967 (1.850) and ODP (1.880) to proximal deposits from Santorini.

To infer the eruptions from which these three geochemically identical (fig. 7.32), but sedimentologically discrete (fig. 6.18) layers originated, the shards were all plotted with the chemistry of the proximal deposits on Santorini (fig. 7.32 and 7.33). All shards in all 3 of these distinct tephra layers are geochemically co-incident with the major and trace

element geochemistry of the Cape Riva proximal deposits from Santorini and are discussed individually below.

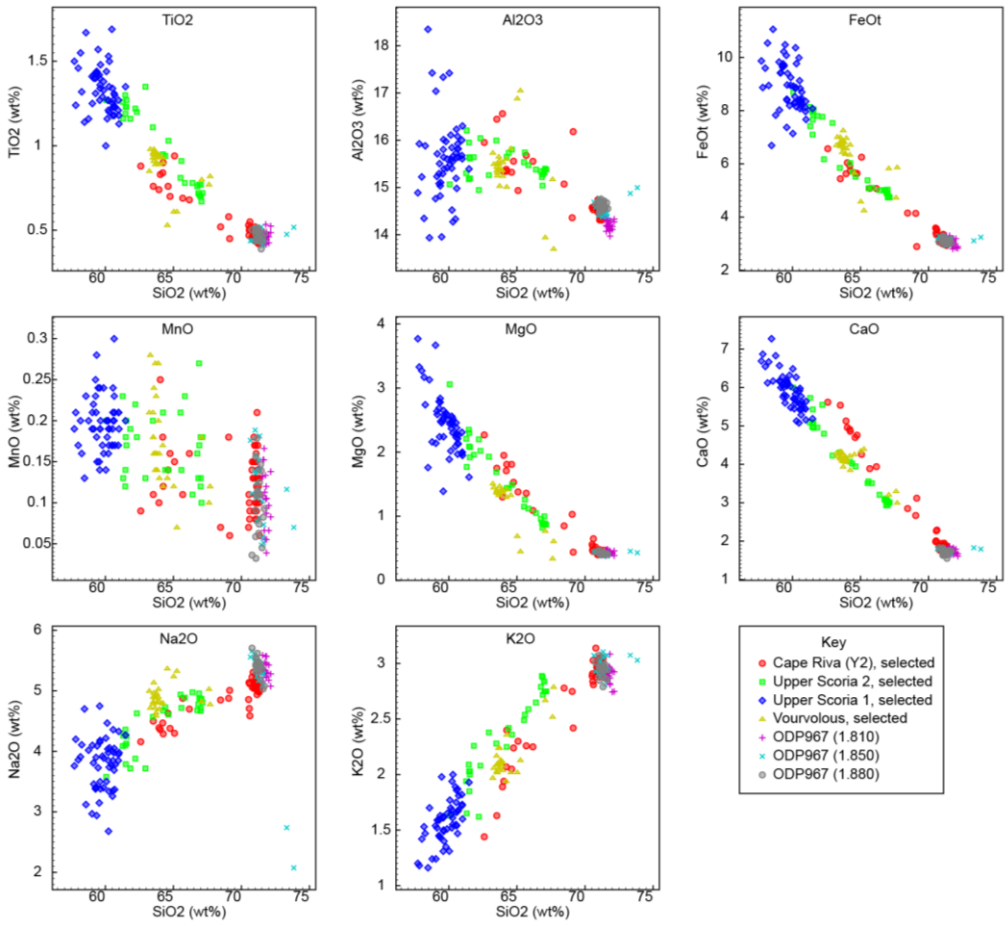

Figure 7.33 Santorini proximal deposit major element bi-plots with ODP967 (1.810), ODP967 (1.850) and ODP967 (1.880).

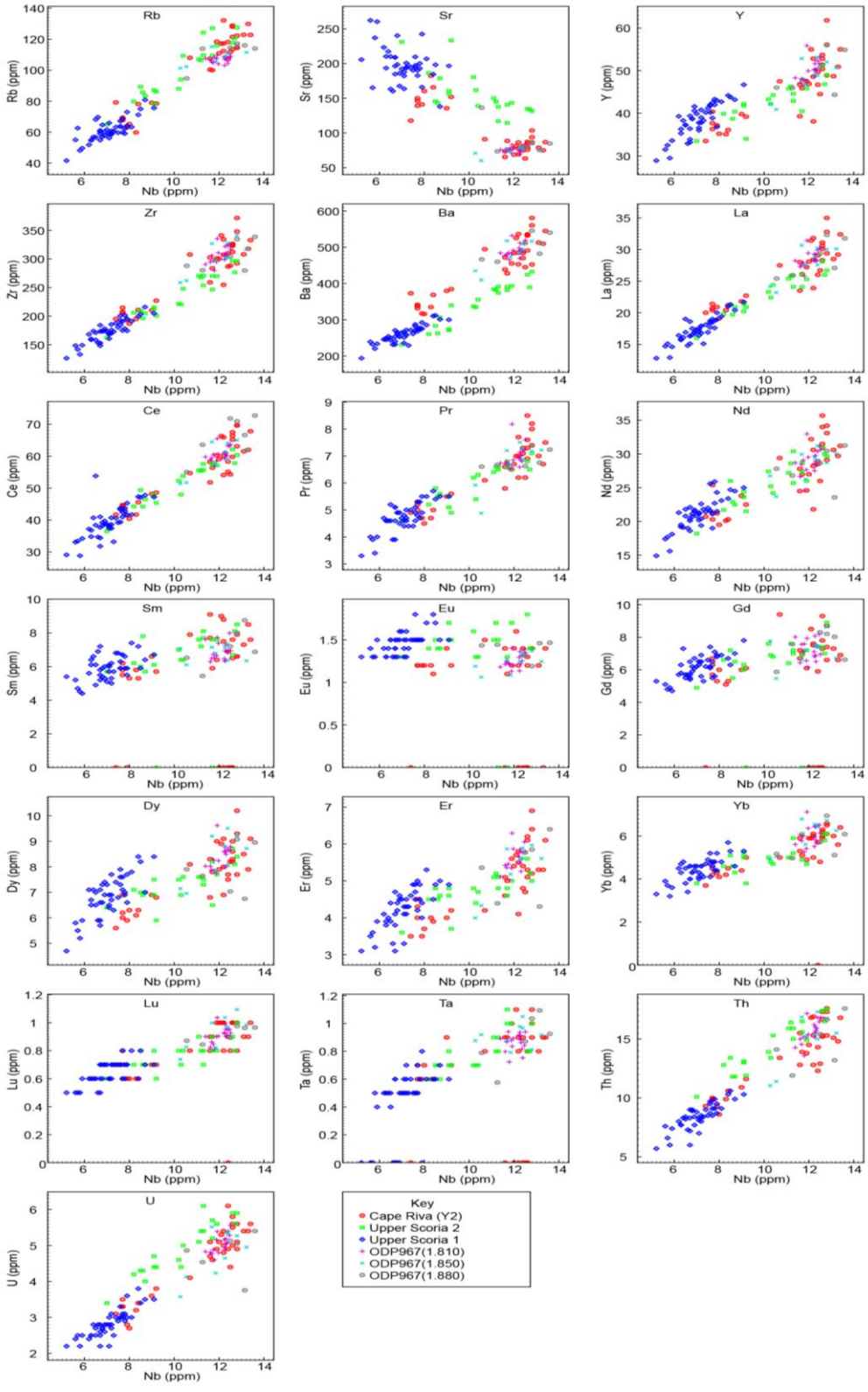

Figure 7.34 Trace element plots showing proximal Santorini deposits and the tephra samples from ODP967 at 1.810, 1.840 and 1.880m. All three tephras are geochemically indistinguishable are co-incident with the Cape Riva proximal deposits on Santorini.

ODP967 (1.810). This visible layer is deduced to originate from Santorini on the basis of its HFSE concentrations (fig. 7.30) and calc-alkali geochemistry (fig. 6.22). A visible tephra of 3cm thickness, over 700km from its source implies that it is related to a large volume eruption. The chemistry is identical to that of the Cape Riva proximal deposits (figs 7.32 and 7.33) and thus it is intuitive to suggest that this tephra layer represents the Plinian Cape Riva eruption, in ODP967. However the date from the ODP967 age model of ~17ka is 4-5ka younger than the 21,705 ± 311 cal BP date attributed to the proximal Cape Riva deposits (Eriksen et al. 1990). This inconsistency means that either this tephra does not represent the Cape Riva eruption and represents a large, younger but geochemically identical eruption, the age model of Larrasoana et al. (2003) is wrong or the proximally defined age of 21,705 ± 311ka (Eriksen et al. 1990) is wrong, or any combination of these two possibilities.

To resolve this question, ^{14}C dates should be taken above and below this tephra, and the two samples found below it (see below for a discussion of these samples.)

ODP967 (1.850) is a sample from the peak in crypto-tephra of >10000 shards/g below the visible layer at 1.810m in ODP967 (fig. 6.18). The HFSE geochemistry indicates Santorini as the most likely origin for the shards in this sample (fig. 7.30). Crypto tephra is present in the 1cm sample above and below this peak. There is crypto-tephra continuously present between the visible tephra above (at 1.810m) and this sample however the concentrations reduce to only 190 shards/g at 1.83-1.82cm. The results from the EPMA and LA-ICP-MS show that the shards within this sample are geochemically indistinguishable from ODP967 (1.810) and the proximal Cape Riva deposits (fig. 7.32 and 7.33). The date of this sample according to the age model provided by Larrasoana et al. (2003) is 18.38-18.05ka. This sample therefore represents either reworking of the visible tephra layer above it (ODP967 1.810) or another 'Cape Riva like' eruption which preceded that which deposited the ODP967 1.810. The same chronological hypotheses discussed for ODP967 (1.810) also apply to this sample. Radiocarbon dating of this section of the core may help to resolve which of these hypotheses is correct.

ODP967 (1.880) Similarly, this peak in crypto-tephra is geochemically identical to the Cape Riva proximal deposits, and also to the two samples at 1.850m and 1.810m described above (figs 7.32 and 7.33). The tephra counts show a neat peak in crypto-tephra shards of 6138 shards/g (fig. 6.18). The shard counts reduce to only 74 shards/g between this peak

and the peak above it, indicating that the sample is unlikely to represent a reworking artefact of either the visible tephra layer at 1.180m, or the crypto-tephra layer at 1.850m.

The implication of having three, apparently sedimentologically distinct (fig. 6.18) tephra layers all with chemical compositions identical to that of the Cape Riva proximal deposits from Santorini is that it is impossible to define which of these represents the Cape Riva eruption event (and thus the associated date of 21,950 cal BP- Wulf et al. 2002 and references therein). It also raises the possibility that there may be more than one 'Cape Riva like' eruption from Santorini. It is most intuitive to assign the thickest tephra layer (the 3cm thick visible tephra at 1.810m depth) to the Cape Riva event. This is not a very robust inference however, as core LC21 has shown that large eruption events can be completely absent from marine cores situated very close to the volcano: the Cape Riva eruption is entirely absent from LC21. In addition a comparison of the Italian Campanian Ignimbrite tephra between LC21 and the Adriatic core PRAD1-2 (Bourne et al.2010) shows that the deposition of tephra, from even the very largest eruptions, can be sporadic: the CI tephra layer is 15cm thick in LC21, but only manifested as a crypto-tephra layer in the Adriatic, which is ~800km closer to the source.

In order to resolve which of these tephra layers represents the Cape Riva (as defined proximally) more dating information is required, perhaps by the radiocarbon dating of foraminifera. The result also demonstrates that there must be addition eruptions preserved somewhere in the proximal stratigraphy which share the same geochemical signature as the definitive Cape Riva proximal deposits.

ODP967 (5.560) is a sample from sapropel 4 (fig. 6.17). The two shards recovered from this layer are thought to originate from Santorini, given the major element geochemical similarity to the proximal Santorini deposits (fig. 7.35). No trace element data was attained to further test this assumption due to the small size of the shard surfaces (too small for LA-ICP-MS) and the long waiting list for SIMS. The EPMA data for these two shards are shown together with the major element proximal data for Santorini in figure 7.35 and are again indistinguishable from the Cape Riva Proximal deposits.

These two shards could be either evidence of another 'Cape Riva like' Santorini eruption, or they could constitute contamination of the sample during processing. To ascertain if the latter is true, we can examine the dates of sample processing. This sample was processed 6 months after the visible tephra at 1.810m was sampled, and 3 weeks after the processing

of the other crypto-tephra samples from ODP967 (described above) yielding this chemistry. As the sieves are changed regularly and the lab is cleaned after every session, it is considered unlikely (but not impossible) that these two shards represent contamination of the sample. They are therefore thought to be tantalising (but not good) evidence of an eruption of Santorini. This eruption would have been identical in major element composition to the Cape Riva eruption of Santorini, and would have occurred during the deposition of sapropel 4. This sapropel is dated by the LC21 age model at ~105ka.

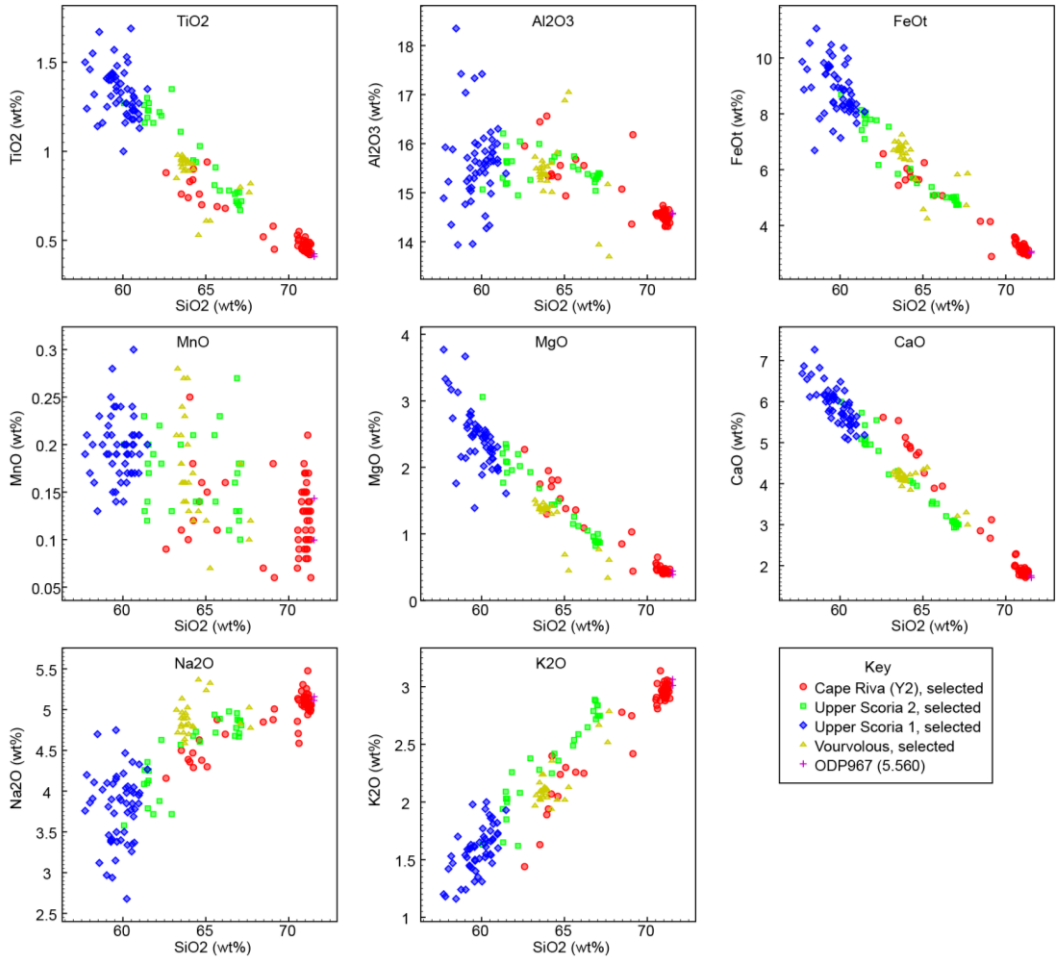

Figure 7.35 Major element analyses of the two tephra shards from sample ODP967 (5.560) shown with proximal deposits from Santorini.

ODP967 (7.610) The shards in this part of the core are all preserved neatly within a 1cm sample (fig 6.18) This demonstrates a lack of bioturbation in this section of the core. The sample is from sapropel 5, and so a well preserved (non-bioturbated) crypto-tephra layer is consistent with the theory that the sapropels represent periods of bottom water anoxia thus a reduction in the benthic marine life (Cramp and O'Sulliven 1999 and references

therein). The shards do not plot within the fields described by any of the proximal data used here to define the source of the tephras, so the sample cannot correlate to any of these eruptions, from any of the volcanic systems. The sample does however plot on the well-defined trend line defined by the Zr vs Nb plot of Acigol (Central Anatolia) (fig. 7.30). This ratio is likely to remain constant for a magma batch through time (Tomlinson et al. 2012). Thus it is proposed here that sample ODP967 (7.610) could originate from the Acigol Guneydag volcano of Central Anatolia, Turkey, but that the equivalent proximal deposits have either not been sampled, or are absent from the proximal stratigraphy.

An alternative hypothesis concerning the origin of ODP967 (7.610) is also considered here. It is noted that the sample LC21 (12.465) also plots on the trend line defined by the Acigol Guneydag proximal samples on the Zr:Nb diagram. It is argued in section 7.2 that this sample represents the Kos Plateau Tuff, found proximally on the island of Kos. ODP967 (7.610) is indistinguishable from LC21 (12.465) on all major and trace elements (figs 7.36 and 7.37). Providing therefore that LC21 (12.465) is indeed derived from island of Kos, this unknown tephra –ODP967 (7.610) could also be derived from Kos, rather than Central Anatolia. If however it is much younger than the ~161ka date of the Kos Plateau Tuff (Bachmann et al.2010), it is unlikely that an eruption could have originated from an already evacuated magma chamber. Extruded products tend to change significantly in composition after a caldera forming event (Tomlinson et al. 2012). The origin of this tephra layer cannot be further constrained here: it originates from either Kos or Central Anatolia.

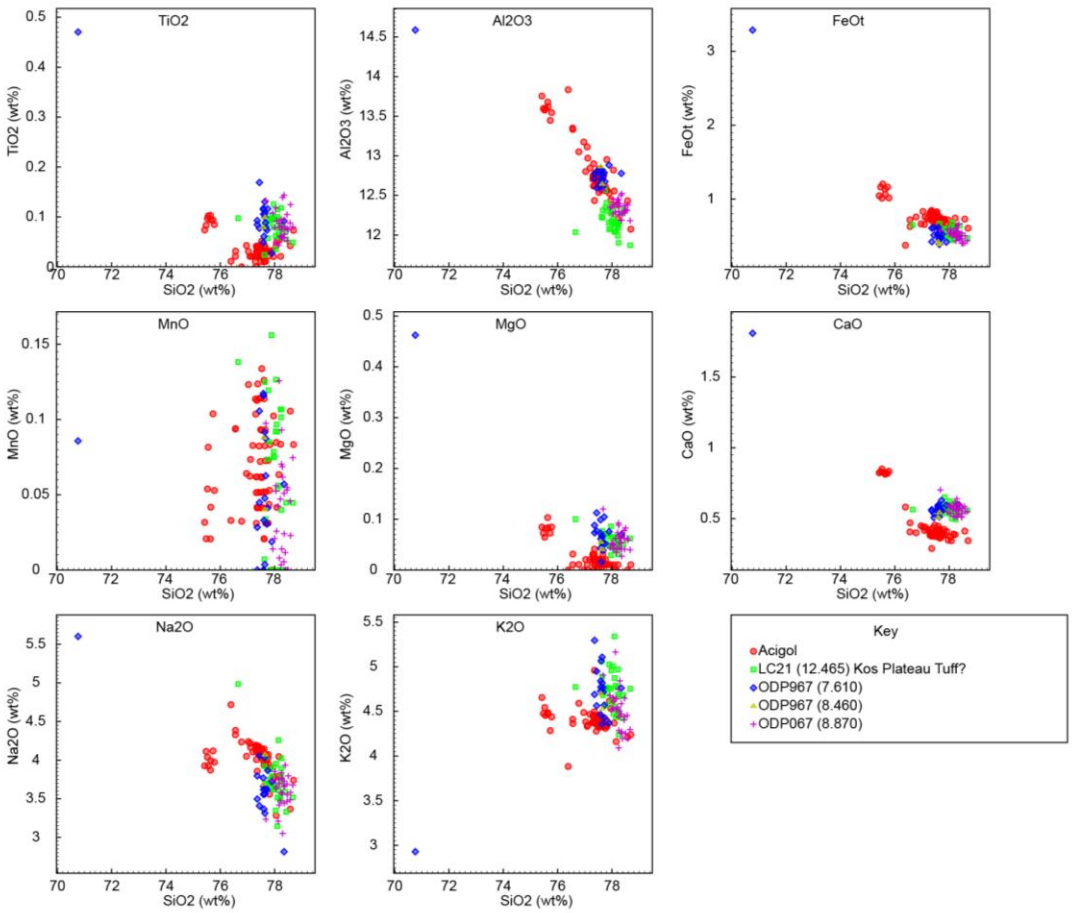

Figure 7.36 major element analyses of ODP967 (7.610), (8.460) and (8.870) plotted with proximal data from three eruptions from Acigol, central Anatolia –Kogidag (undated), Guneyday-23,800 cal BP (Schmitt et al. 2011) and Korudag- 24900 cal BP (Schmitt et al. 2011) and LC21 (12.465), here attributed to the Kos Plateau Tuff eruption.

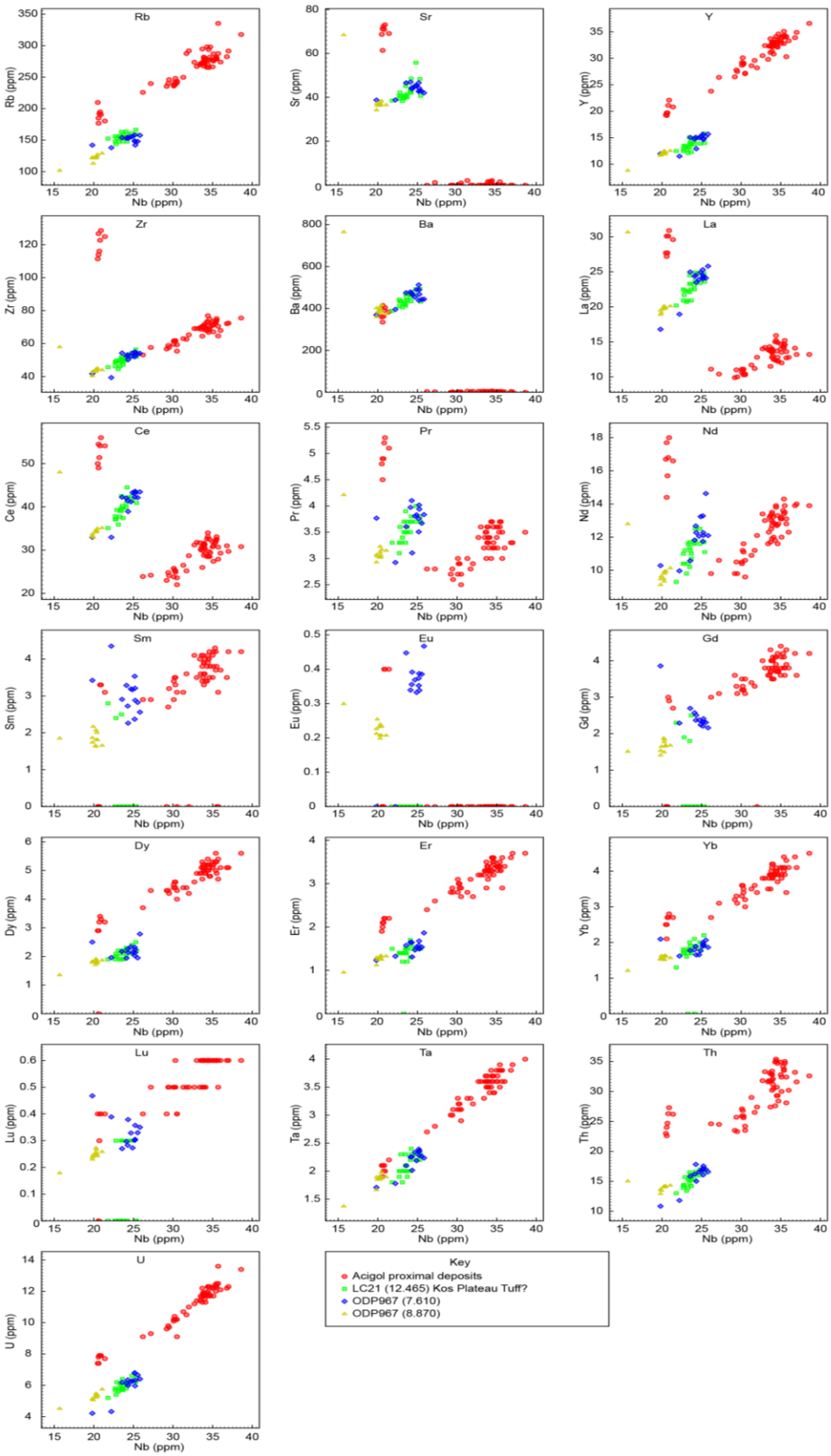

Figure 7.37 Trace element analyses from proximal deposits on Acigol (Central Anatolia), LC21 (12.465) considered in this study to represent the Kos Plateau Tuff, and ODP967 (7.610) and (8.870).

ODP967 (8.460). This sample has silica values of >77wt% a value which only proximal data from Central Anatolia, Yali/Nisyros, and the sample LC21 (12.465) (argued in chapter 6 to be from Kos) share. These high silica values therefore indicate that the shards found in this sample most likely originate from one of these volcanic centres. The two shards are here compared to both the proximal major element data from Central Anatolia, Yali/Nisyros, and the marine core sample LC21 (12.465); the Kos Plateau Tuff. These plots show that these shards are indistinguishable from ODP967 (7.610), LC21 (12.465) and the sample discussed below, ODP967 (8.870). Thus, as with sample OPD967 (5.560) these shards could demonstrate contamination of the sample with shards from another. The sample was processed over two years after LC21 (12.465), making this an unlikely source of contamination. Sample ODP967 (8.870) was processed 6 months prior to this sample, making it also an unlikely candidate. Sample ODP967(7.610) was however sampled in the same batch as ODP967 (8.460) making it a possible candidate for a contamination source. It cannot therefore be ruled out that these two shards are a product of contamination rather than representing a real eruption. Intriguingly however, Hardiman (1999) found two chemically identical tephras (both assigned to the Kos Plateau Tuff) in the Aegean cores TR172-25PC and TR172-26PC. The result would need to be replicated in cores between Cyprus and Crete to be confirmed and here these shards are considered likely to represent contamination of the sample.

ODP967 (8.870). The lowermost visible tephra in ODP967 is geochemically very similar to the crypto-tephra preserved within sapropel S5 (ODP967-7.610) (figs. 7.36 and 7.37) but the two are unlikely to be related by reworking, as they are separated by over a meter in the core and both occupy discrete, well preserved sections of sediment. The high silica content of these shards, and their position on the Zr:Nb diagram (fig. 7.30) indicate that this tephra may originate from the Central Anatolian volcanic system, or Kos. The shards also plot in a nearly identical position to those from LC21 (12.465) (fig. 7.2) which is interpreted to represent the Kos Plateau Tuff, due to its thickness and proximity to Kos and high SiO_2 content. Unfortunately no proximal, single shard, trace element geochemical data yet exists to test this assumption, and thus to determine definitively from where either of these tephras (LC21 12.465 and ODP967 8.870) originate. The two samples do however match geochemically (within error). The LA-ICP-MS results show that ODP967 (8.870) is lower in Nb, Rb, Sr,Zr,La, Ce and Pr than LC21 (12.465), however when the standards for the appropriate days are also examined (fig. 7.37), it is apparent that these discrepancies

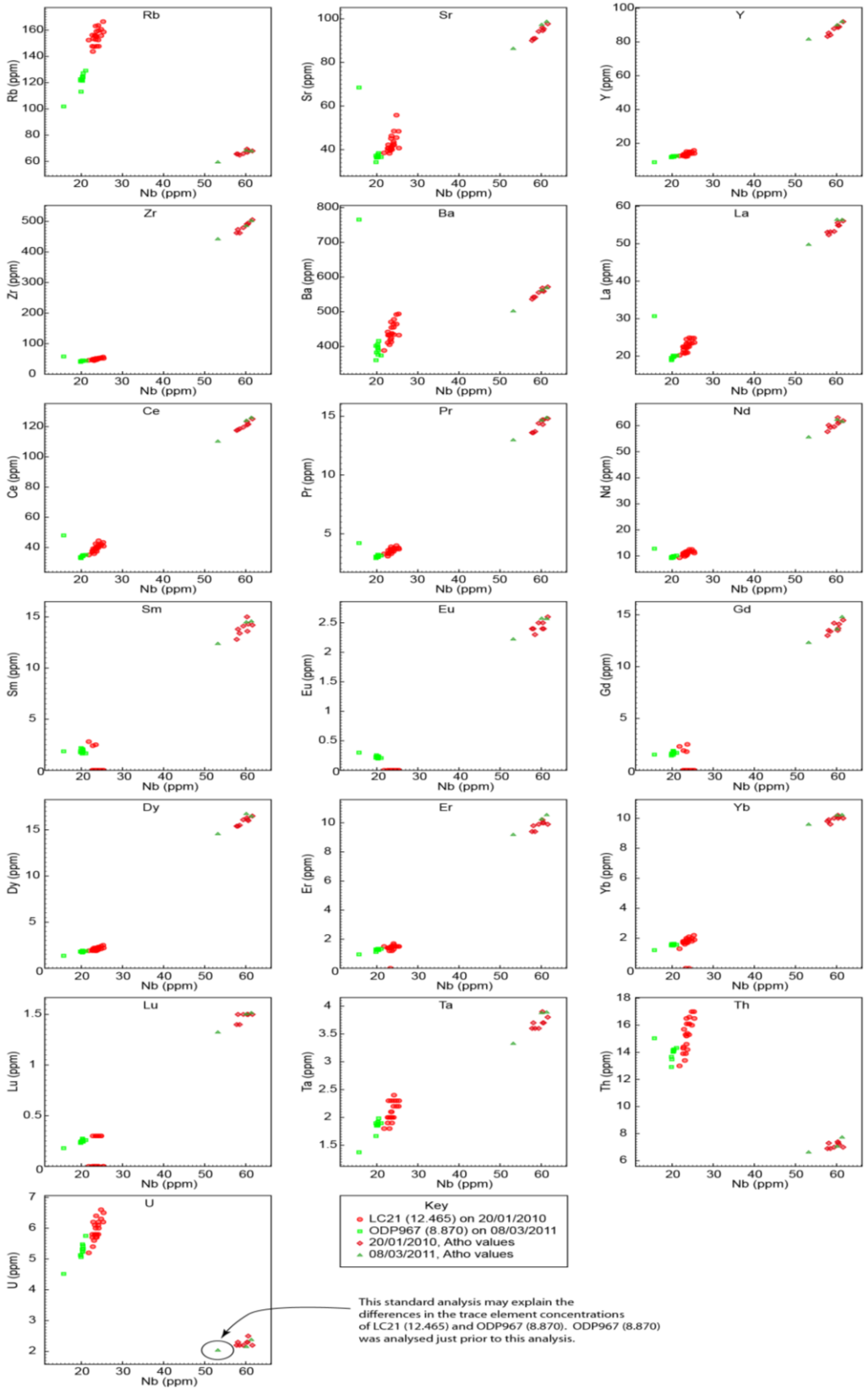

Figure 7.38 trace element analyses for samples LC21 (12.465) and ODP967 (8.870), and their corresponding standard values. One standard value for ODP967 (8.870) is significantly different from the others and was analysed directly after ODP967 (8.870), and may therefore explain the differences in Nb, Rb, Sr,Zr,La, Ce and Pr from LC21 (12.465).

can be accommodated by differences are replicated in the standard measurements and thus are not real.

This means that cores LC21 and ODP967 can potentially be linked with a tephra layer. There is some difficulty with such a correlation however, as ODP967 contains two younger tephras which also have identical chemistry to LC21 (12.465) (the Kos Plateau Tuff), as shown in figures 7.25 and 7.36. ODP967 yielded three samples of tephra shards which are all indistinguishable from one another. Attribution of the lowermost of these-ODP967 (8.870) to the Kos Plateau Tuff eruption to is based only on the fact that it is visible tephra of 1cm thickness and thus is most likely to represent a large eruption.

7.4 Discussion of tephra shards found in ODP975.

ODP975 contained only 2 tephra shards from which EPMA data could be generated (fig. 6.7). Each of these came from different depths in the core. The EPMA data demonstrated that one was rhyolitic and the other phonolitic (fig. 6.29). Both of these shards are discussed here.

ODP975D 1H1 3-4cm contains a shard from close to the top of the core and must therefore be from a relatively recent eruption (Late Holocene). Several possible sources exist for this tephra shard. Rhyolitic eruptions have occurred in the Late Holocene in Iceland, the Aeolian Islands and Santorini.

The only known ash producing eruption from Santorini in the Late Holocene is the Minoan eruption dated to 3344.9 ± 7.5 cal BP by Manning et al. (2006). It seems unlikely that this sample at only 3-4cm into the core could be so old (requiring a very slow sedimentation rate of ~1000 years/cm). In addition the shard is very platy (fig. 6.29) with none of the vesicles normally associated with volcanic regions high in volatiles such as water or carbon dioxide. In addition, the Minoan eruption has not been found to the East of the Aegean Sea previously. Core ODP975 is ~2000km to the West (upwind) of Santorini, and thus is considered to be a highly unlikely repository for tephra from the island. Santorini is not further considered here.

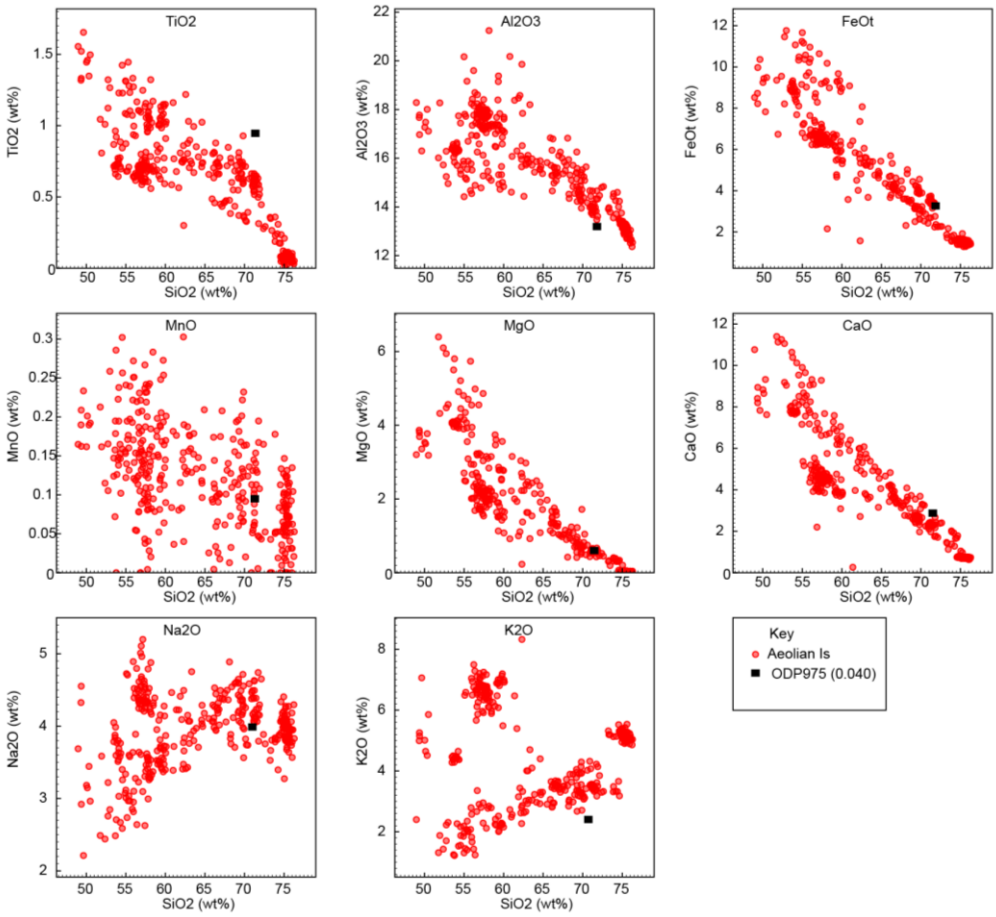

Figure 7.39 Major element data from Late Holocene eruptions from the Aeolian Islands and ODP975 (0.040).

The Aeolian Islands have been active throughout the Holocene (Albert et al. 2012), but only one major silica-saturated eruption has taken place during this time (the Monte Pilato eruption of Lipari, dated to 776 cal AD- see Keller et al. 2002, in Albert et al. 2012). The only other data available from silica-saturated eruptions from the Aeolian Islands was from the Lower Polara eruption of Salina (29,300 cal BP, Keller et al. 1980) and the Grey Porri Tuff of Salina (68,500 cal BP Lucchi et al. 2008) both impossible sources due to their ages. However the shard geochemistry was compared to the geochemistry all three of these eruptions, as this was the only data available to characterise the geochemistry of the silica-saturated eruptions from the Aeolian Islands. The comparison is shown in figure 7.39.

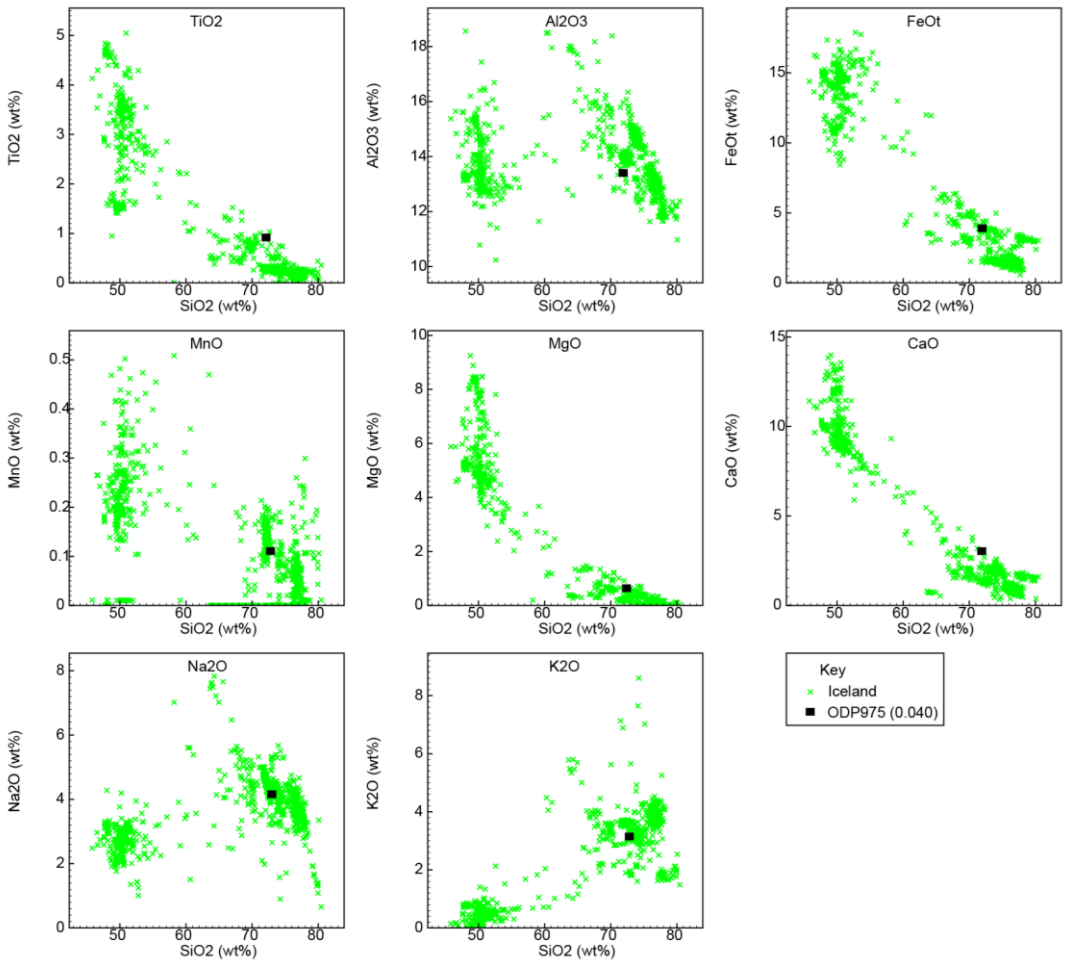

Figure 7.40 Major element analyses of Late Holocene eruptions from Iceland and sample ODP975 (0.040).

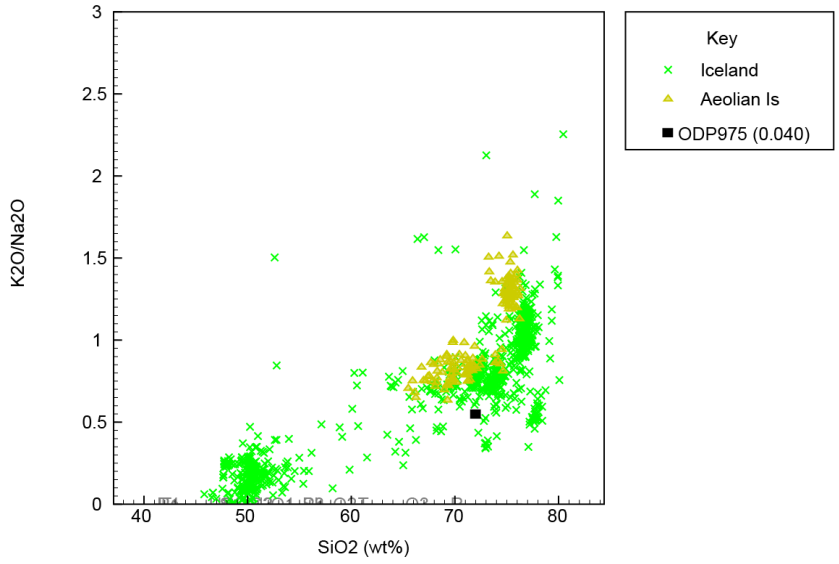

Figure 7.41 Alkali ratio vs SiO_2 plot for si-saturated, Late Holocene eruptions from the Iceland and the Aeolian Islands with ODP975 (0.040), indicating that the single shard found in sample ODP975 (0.040) is most likely from Iceland.

Icelandic distal tephra is in general vesicle poor due to the low volatile content of the magmas (Thordarson and Larsen, 2007), like the shard found in ODP975 (0.040) (fig. 6.28e). In addition, the distribution of shards from recent Icelandic eruptions of Grimsvotn (May 2011) and Eyjafjallajokull (March 2010) imply that ash from previous Icelandic eruptions could conceivably be found in the western Mediterranean Sea (Davies et al. 2010, Matthias et al. 2012). No attempt to attribute this shard to a specific eruption is made here as comprehensive geochemical data is not yet available for the complicated late Holocene volcanic stratigraphy of Iceland. There are however many rhyolitic tephra layers which may be viable candidates (Larsen et al.2002, Jagan 2010). Those available from the RESET database were compared to the geochemistry of the shard found in ODP975 (0.040) in figures 7.40 and 7.41. These indicate that the shard is most likely from an eruption in Iceland and not from the Aeolian Islands. In addition, as the sample is located only 3-4cm from the top of the core, it will not constitute a tephra which is useful to define the timing of either abrupt environmental transitions or hominin evolution which are the central aims of the RESET project.

It could be proposed that the occurrence of an Icelandic shard in this core could be due to laboratory contamination. If this is so, the contamination cannot be from any of the other tephra layers described in this thesis. This core was processed in a clean lab where distal

crypto-tephra layers originating from Iceland have been found by other workers. It is possible therefore that the shard could originate from one of these layers, but this is considered unlikely here, given the vigilant cleaning procedures employed in the lab.

If confirmed by subsequent studies, this tephra shard would be the first tephra from an Icelandic eruption to be found in the Mediterranean Sea. It could provide the first opportunity to compare the marine proxy records of the Mediterranean Sea and the North Atlantic Ocean, using a proxy-independent correlation tool. It is unfortunate however that this correlation marker lies so close to the present day, in a relatively stable period of climate.

The tephra shard in sample **ODP975D 1H2 73-74cm (2.23-2.24mbsf)** is a phonolitic shard. An estimated sedimentation rate of 146years/cm (Alves-Marron. 1999) gives an estimated date for this sample of 32704-32558 ka and an oxygen isotope date of 30ka at 2.65m (Pierre et al. 1999). These two dates indicate that the sample may lie in a time period relevant to hominin evolution and abrupt climate changes (the central interests of the RESET consortium). The phonolitic classification implies an origin from the alkaline volcanic systems of the Campanian Fields, the Aeolian Islands or the Azores. The major element geochemistries of these alkaline sources are plotted in figures 7.42a and 7.42b. The very high FeOt:CaO ratio of the Azores implies that this is an unlikely source for this tephra shard (fig 7.42a). The Aeolian Islands and the Campanian region can be distinguished by their total alkali content (fig 7.42b). This shows that the shard is most likely derived from the Campanian volcanic region.

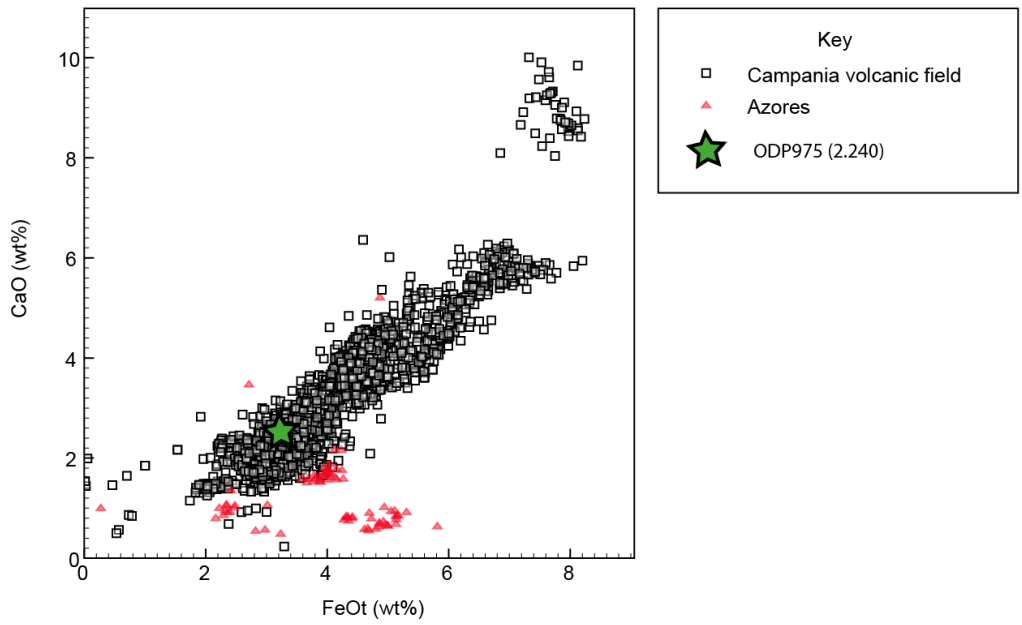

Figure 7.42a FeOt vs CaO plot for ODP975 (2.240) and proximal data from the Azores and Campania (E.Tomlinson).

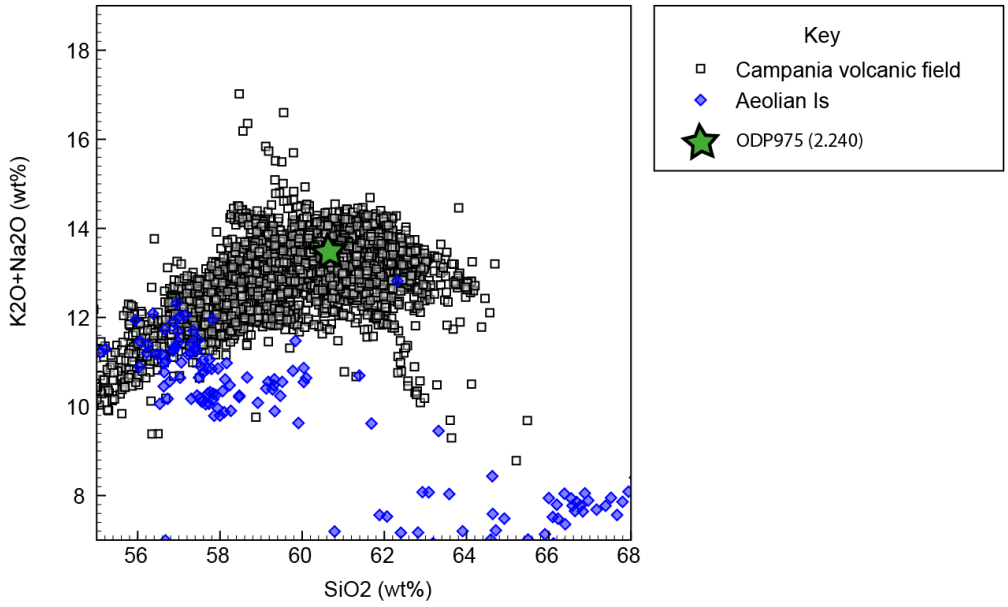

Figure 7.42b total alkali vs Silica plot for ODP975 (2.240) and proximal data from the Aeolian Islands (P.Albert) and Campania (E.Tomlinson).

As described in chapters 2 and 3, several Plinian eruptions have occurred in the Campanian region in the last 50ka. The largest of these were the Campanian Ignimbrite, the Neapolitan Yellow Tuff, and the widespread, but as yet unassigned eruption which produced the marine Y3 tephra layer. The EPMA major element chemistry for these three eruptions is plotted on figure 7.43 with the EPMA data from the shard found in this sample. This shows that the shard closely matches the Campanian Ignimbrite and NYT data, but does not

match the Y3 as defined in Lago Grande di Monticchio as TM15. However it does not match either of these perfectly, with differences most clear in Na_2O and Al_2O_3, although these differences are not out-with the variability of the EPMA. More data would be needed to assess this shard. Tephra matching the CI and NYT eruptions are both found in the Adriatic Sea (Bourne et al.2010), thus potentially providing for the first time an opportunity to explore the relationships of the proxy records in these basins, through the two possible correlation scenarios. This would be the first time that the Eastern and the western Mediterranean proxy records could be compared using a proxy-independent correlation tool. Should this tephra prove to be the Campanian Ignimbrite tephra, the comparison could be extended to the proxy record of the Aegean Sea, where the Campanian Ignimbrite has been identified in this study (see LC21 discussion). The identification of the eruption would be aided by dating of the sediment using radiocarbon dating of foraminfera.

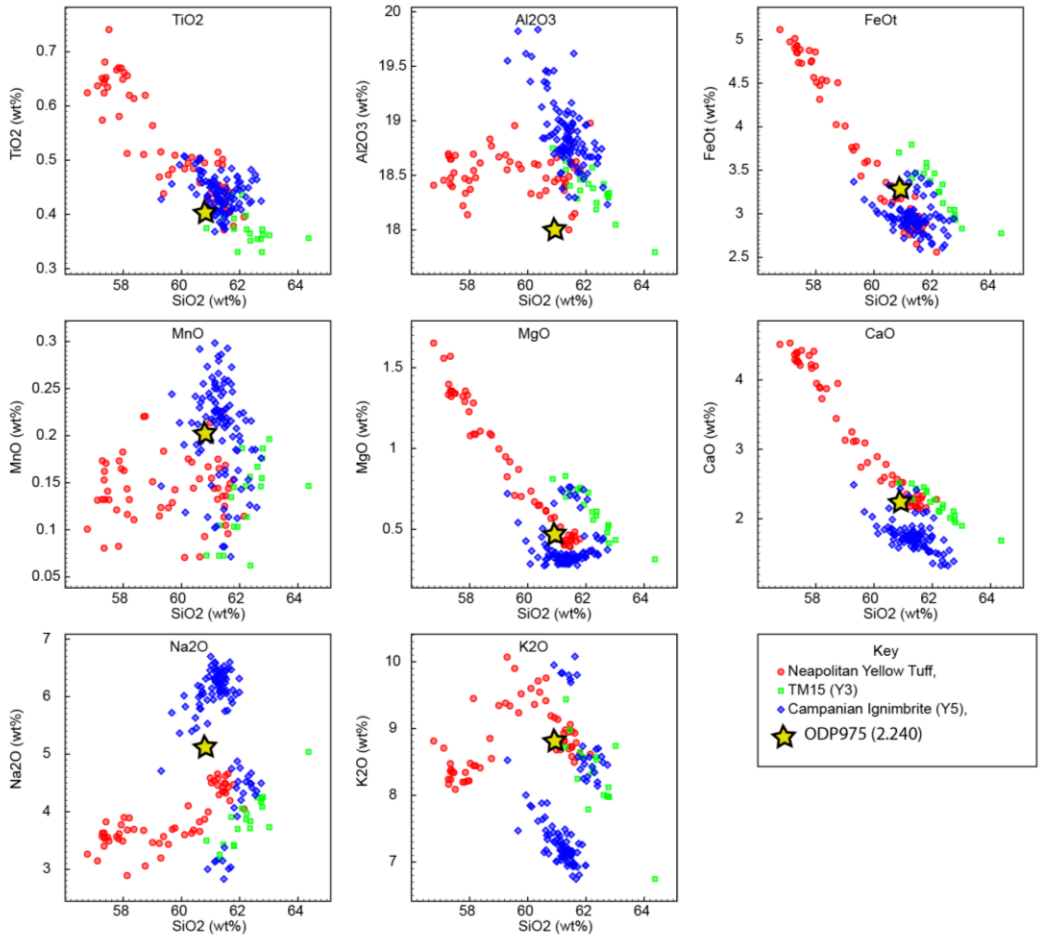

Figure 7.43 Major element plots for ODP975 (2.240) and data from major Plinian eruptions from Campania. Neapolitan Yellow Tuff and Campanian Ignimbrite data are from proximal deposits. The data from the widespread distal Y3 tephra layer from the TM15 tephra layer of Wulf et al. (2004).

7.5 Correlations and integration with literature data.

In this section the tephra geochemistries are compared where possible to geochemical analyses published in the literature. This is not possible in many cases as the raw data from many published tephra studies are often not published. The data may also be produced by an EDS-EPMA system (less precise analyses than the WDS used in this investigation) and/or lack associated standard analyses to assess data quality. Even when tephra data is published in its raw form, it is rare for authors to publish raw proxy data for comparison to that produced by the RESET consortium. The only single shard trace element determinations in the literature are by Aksu et al. (2008) (mean and 2SD only), Bourne et al. (2010) and Tamburrino et al. (2012). Table 7.1 summarises both the tephra and proxy datasets available for comparison in the literature, for each of the tephra layers found in this study.

Core Site Name	Sample base depth	Proximal Correlation	Majors for comparison?	Traces for Comparison?	Proxies freely available?	Proxies unpublished but potentially available
LC21	0.94	**Santorini-Minoan**	Aksu et al. (2008) mean and 2SD	Aksu et al. (2007) Mean and 2SD	x	Aksu et al. (2008)
LC21	2.005	**Santorini**	x	x	x	x
LC21	3.225	**Santorini**	x	x	x	x
LC21	3.775	**Santorini**	x	x	x	x
LC21	4.285	**Yali- Yali-2**	Aksu et al. (2008) mean and 2SD	Aksu et al. (2007) Mean and 2SD	x	Aksu et al. (2008)
LC21	4.925	**Campania-Campanian Ignimbrite**	Aksu et al. (2008) mean and 2SD and Bourne et al. (2010), Wulf et al. (2004)	Aksu et al. (2007) Mean and 2SD	x	Aksu et al. (2008), Piva et al. (2008)
LC21	5.125	**Santorini**	x	x	x	x
LC21	7.915	**Campania-X5 + Santorini**	Keller (unpublished)	x	visual stratigraphy of sapropels wrt tephra	Jorg Keller (unpublished)
LC21	9.575	**Santorini-Interplinian**	x	x	x	x
LC21	9.709	**Santorini**	x	x	x	x
LC21	10.345	**Pantelleria P-11**	Tamburrino et al. (2012), Margari et al. (2007)	Tamburrino et al. (2012)	x	Margari et al. (2007)
LC21	11.19	**Santorini**	x	x	x	x
LC21	12.465	**Kos- Plateau Tuff?**	Margari et al. (2007)	x	x	Margari et al. (2007)
ODP967	1.81	**Santorini-Cape Riva**	Wulf et al. (2002)+Margari et al. (2007), St Seymour et al. (2004)	x	x	Margari et al. (2007)+St Seymour et al. (2004)
ODP967	1.85	**Santorini-Cape Riva**	Wulf et al. (2002)+Margari et al. (2007), St Seymour et al. (2004)	x	x	Margari et al. (2007)+St Seymour et al. (2004)
ODP967	1.88	**Santorini-Cape Riva**	Wulf et al. (2002)+Margari et al. (2007), St Seymour et al. (2004)	x	x	Margari et al. (2007)+St Seymour et al. (2004)
ODP967	8.46	**Kos?**	x	x	x	x
ODP967	8.87	**Kos Plateau Tuff?**	Margari et al. (2007)	x	x	Margari et al. (2007)
ODP975	0.040	**Iceland?**	Yes, but stratigraphy not well defined (Jagan 2010).	(Jagan et al. 2010)	x	x
ODP975	2.24	**Campania- CI or Y3?**	Aksu et al. (2008) mean and 2SD and Bourne et al. (2010), Wulf et al. (2004)	Aksu et al. (2007) Mean and 2SD	x	Aksu et al. (2008), Piva et al. (2008)

Table 7.1 Summary of data available for comparison to the tephra layers discovered in cores LC21 and ODP967. Green references indicate terrestrial studies, blue references indicate marine studies.

7.5.1 Tephras originating from Santorini.

Tephras originating from Santorini are the most common in the three cores examined in this thesis and are found in both LC21 and ODP967. This is perhaps not surprising due to the proximity of LC21 to Santorini, and the downwind location of core ODP967. These tephras can contribute to the volcanic history of Santorini.

Minoan tephra.

The Minoan tephra was identified in core LC21 as sample LC21 (0.940). Tephra LC21 (0.940) is the uppermost tephra from Santorini represented in LC21. This marine deposit is highly likely to be from the Minoan eruption, based on (i) its position close to the top of the core, (ii) its visible thickness of 24.2cm and (iii) the close approximation of its age to that of the Minoan eruption (3344.9 ± 7.5 cal BP -Manning et al. 2006), based on AMS14C datings in LC21 (date of 3146-5558cal BP at 0.955m depth in Casford et al. 2007), and geochemical composition overlapping that of the proximal deposits of Santorini (fig. 7.2). Asku et al. (2008) also found this tephra in the Aegean Sea; in the Skiros and Ikaria basins, but it is absent in their study of visible tephras from the Marmara Sea. The discovery here of a thick Minoan tephra layers in the southeast Aegean Sea indicates that this eruption likely had a wide area of deposition both to the north and to the southeast of Santorini (fig. 7.54).

The tephra was not however found in ODP967. This could be due either to the targeted sampling strategy employed for this core (fig. 6.17 and 6.18, table 6.2), or to the tephra from this eruption simply not reaching this site.

The Minoan tephra has been extensively studied. Gulchard et al. (1993) and Kwiecien et al. (2008) discovered the tephra in the sediments of the Black Sea. It has also been identified in in terrestrial sites in Western Turkey (Sullivan 1990 and Eastwood et al. 2008) and in the Eastern Mediterranean Sea (Keller et al. 1978) (figs 7.44 and 7.45).

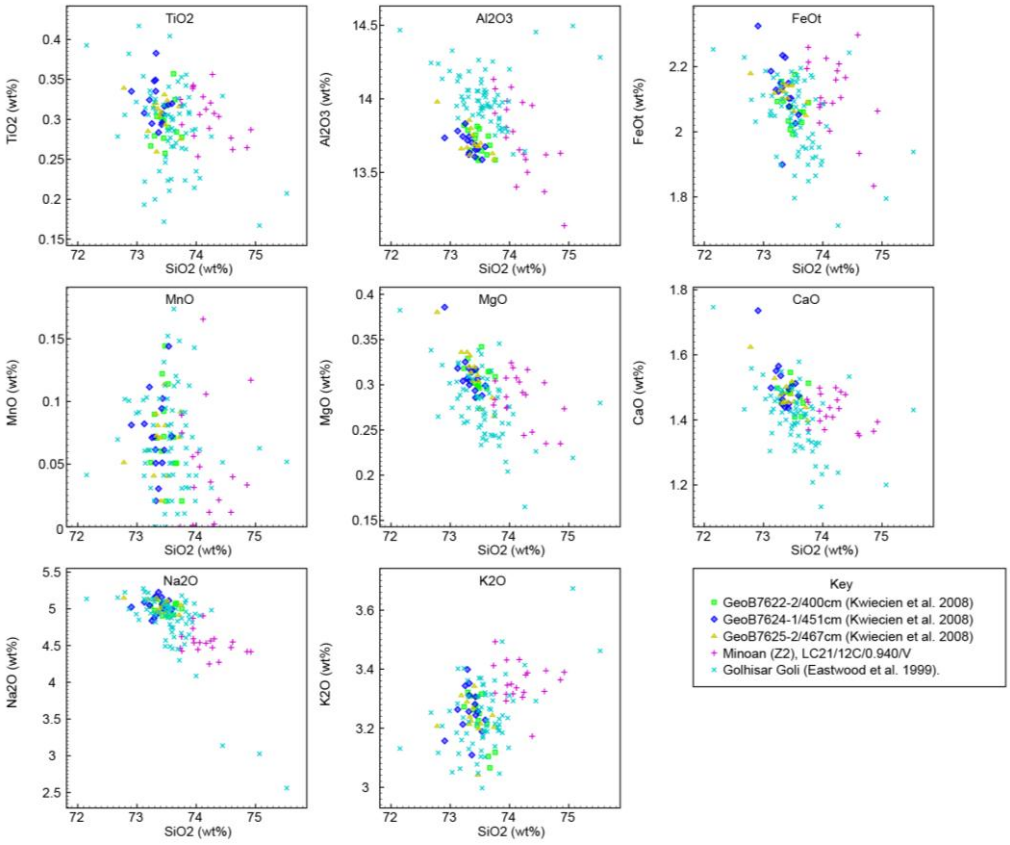

Figure 7.44 Comparison of the major element geochemistry of the distal Minoan tephra deposits, as defined in the literature, to that defined in this study, sample LC21 (0.940).

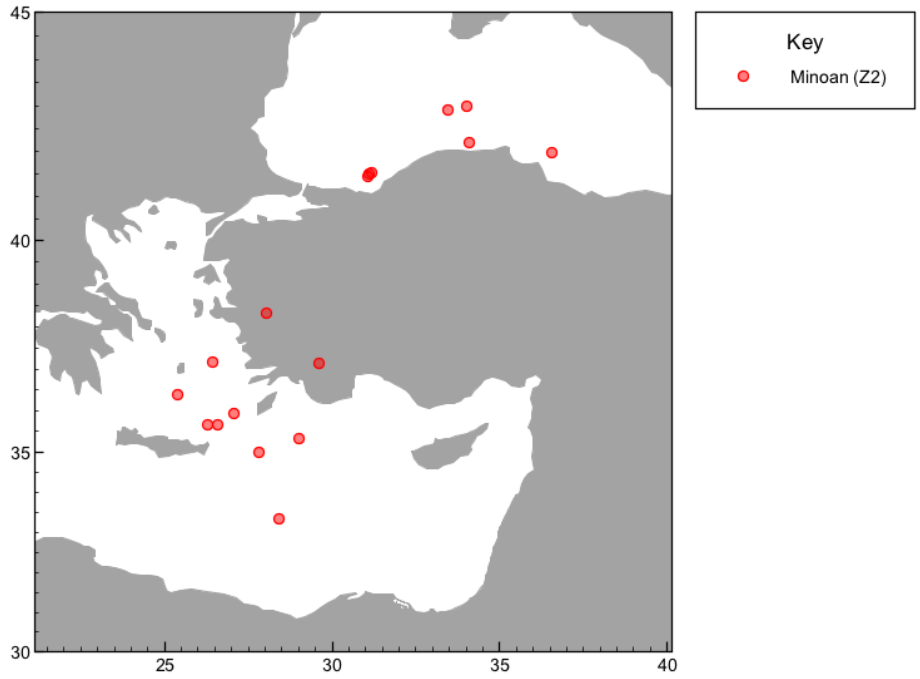

Figure 7.45 literature and RESET project reported discoveries of shards originating from the Minoan eruption of Santorini, from the RESET database.

Cape Riva Tephra.

Three tephras with the identical major element chemistry to the Cape Riva eruption are found in ODP967. These are at 1.810, 1.850 and 1.880m depth (fig. 7.32 and 7.33). It is intuitive that the uppermost tephra of these 3, tephra layer ODP967 (1.810) is the most likely to correlate to the Plinian Cape Riva proximal deposits, as it is a visible tephra 3cm thick, and that the two crypto-tephras stratigraphically below this visible layer are previously unknown precursors to the main Cape Riva eruption. Similar assumptions have been made by Sparks et al. (1983) and Pyle et al. (2006) and these are discussed further in the text below.

Interestingly however, the Cape Riva tephra is not preserved from core LC21 which is only ~100km from the island of Santorini. Vinci (1985) found this tephra as a visible layer in core MC12 located ~50km west north west of LC21 but also noted its absence in core MC09 only ~25km to the west of LC21. The distribution of the tephra from this eruption appears to be highly sporadic, even close to Santorini, implying that the distribution was strongly influenced by the wind direction at the time of the eruption. As the Cape Riva tephra is also found in ODP967 (~700km from Santorini), most likely as a visible layer, the tephra emphasises the importance of wind direction, ocean current direction and the sedimentary environment on the distribution of marine tephras, and warns against making assumptions relating thickness of deposit to distance from source (e.g. Sparks et al. 1983).

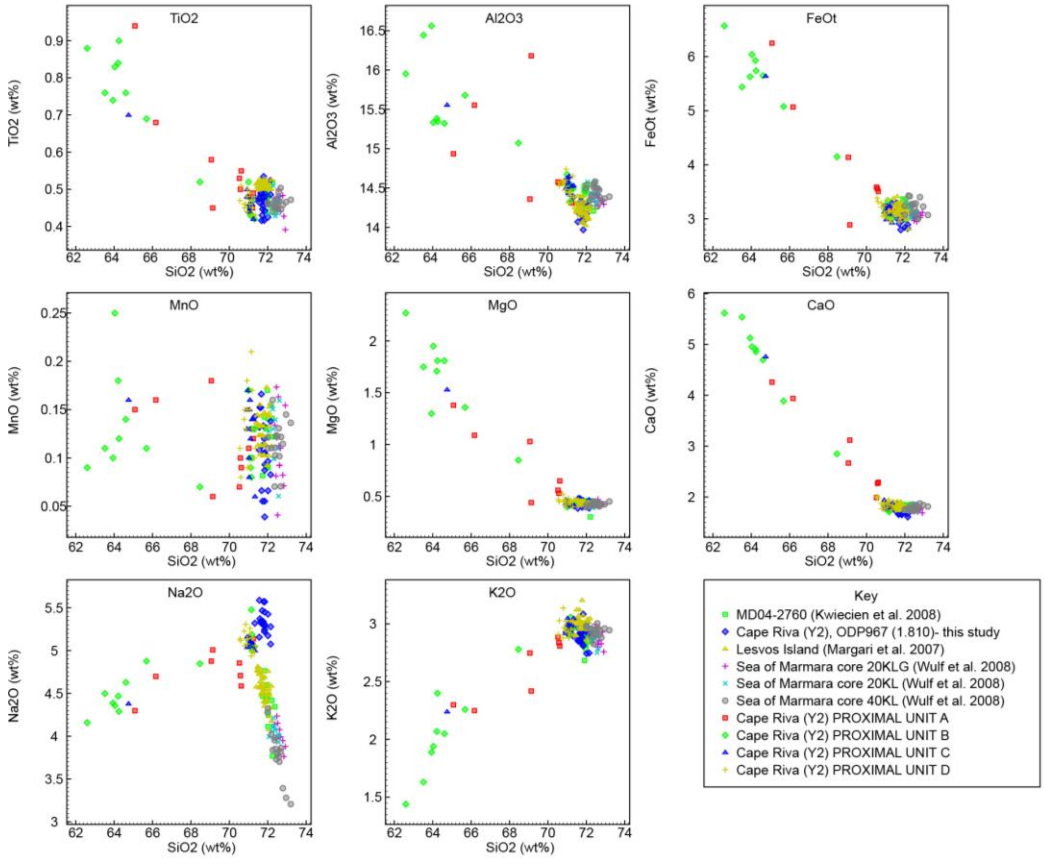

Figure 7.46 major element analyses of distal tephra shards attributed to the Cape Riva eruption of Santorini published in the literature and available on the RESET database together with ODP967 (1.810) from this study and proximal data from the Cape Riva eruption (Tomlinson, unpublished).

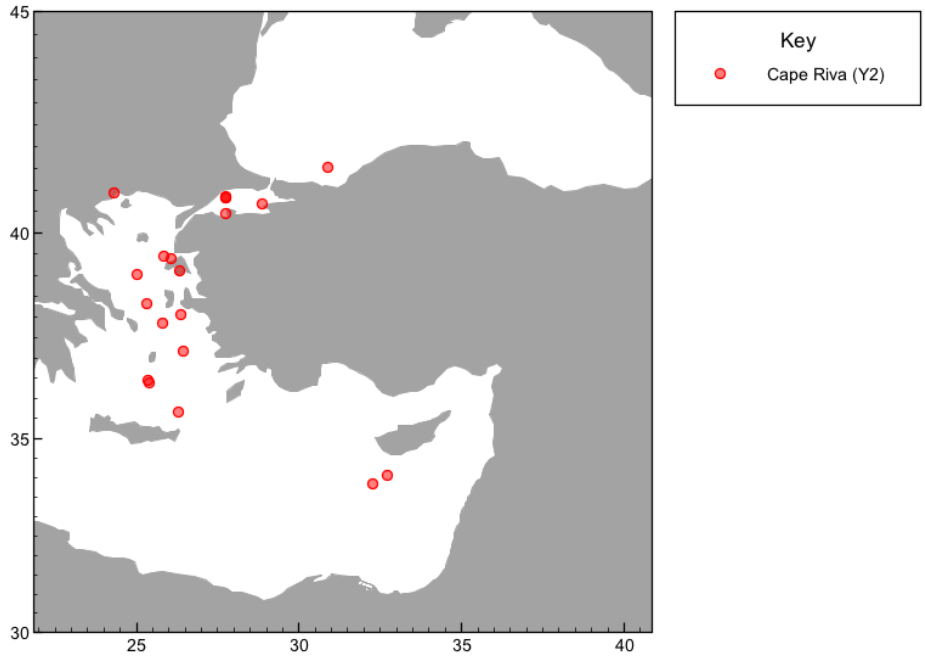

Figure 7.47 map showing reported occurrences of the Cape Riva tephra from this study and the literature (data from the RESET database).

The Cape Riva has been identified by Wulf et al. (2002) in the Sea of Marmara and the Black Sea, and on Lesvos Island (Margari et al. 2007) indicating a north easterly dispersion of the tephra. The discovery also in the Eastern Mediterranean Sea allows the potential correlation of deep sea sediments from the Aegean (Vinci 1985), the Sea of Marmara (Wulf et al. 2002), the Black Sea (Kwiecien et al. 2008) and the Eastern Mediterranean Sea (this study) and in the Nile Delta (Dacassou et al. 2007). Intriguingly the study of Aksu et al. (2008) found two or three tephra layers, all with identical geochemistry to the Cape Riva, inter-bedded with marine muds in the same Maramara Sea core, but the authors interpreted these layers as being reworked.

Upper Scoria 2 eruption

Tephra matching the Upper Scoria 2 proximal deposits was not present in any of the cores studied in this thesis. Distal tephra relating to this eruption has never been identified in the literature, although the Y4 tephra (Keller et al. 1978, Vinci 1985) is cited to originate from Santorini, but is not attributed to a specific proximal deposit. Aksu et al. (2008) tentatively suggest that their 'group 4' tephra (~35ka) may correlate to the geochemically heterogeneous marine Y4 tephra of Keller et al. (1978) and Vinci (1985). Unfortunately they provide only summary geochemical data, impeding a meaningful comparison with the data produced here. If this hypothesis is correct it may be that the sample dated at ~35ka in this study- LC21 (3.775) might also form part of this geochemically enigmatic deposit. The assumption that all tephra produced by a single eruption have identical geochemistry is the same would be compromised by this example. The Y4 tephra (Vinci 1985) is found to the southeast of Santorini (cores MC10 and MC12), within 30km of LC21.

Upper Scoria 1 and Vourvolous eruptions.

Sample LC21 (9.575) has a geochemistry which overlaps the proximal Upper Scoria 1 deposits (fig. 7.22 and 7.23). LC21 (9.575) is a sample at the base of a large amount of crypto-tephra in the core (see fig. 6.1) and lies within sapropel 5. It is likely that the exaggerated thickness of S5 in LC21 and the increase in the sedimentation rates this part of the core (Marino et al. 2007) is partly due to the input of tephra into the core site at this time. It is also clear (fig. 6.18) that the tephra must have been emplaced nearly throughout the period of formation of S5, and it is therefore suggested that sample LC21 (9.575) represents the start of a period of inter-plinian activity of Santorini. The sample closely matches the Upper Scoria 1 proximal deposits, but also has some shards plotting within the

proximal Vourvolous proximal deposits (figs. 7.22 and 7.23) It is therefore infered here that this sample represents a period of inter-plinian activity between these two major eruptions: perhaps M9 of Vespa et al. (2006).

The Upper Scoria 1 has not been identified as a distal tephra in the literature. Aksu et al. (2008) however identify a tephra (their 'group 6') which they propose to be the X1 tephra of Keller et al. (1978), derived from the Aeolian Islands. This 12cm thick tephra in the Aegean Sea seems highly unlikely to originate from the Aeolian Islands (~900km to the West of core MAR03-25 in which it was found). Furthermore, mean Nb and Zr concentration of 7.94ppm and 198.71ppm (Aksu et al. 2008) respectively are consistent with the Santorini proximal deposit data used in this thesis and inconsistent with the Aeolian Island proximal deposit data (fig. 7.2 or 7.30). The 'group 6' tephra of Aksu et al. (2008) is therefore here hypothesised to correlate to the Upper Scoria 1 eruption of Santorini, but as no single shard data is published by Aksu et al. (2008) this hypothesis cannot be tested further.

Middle Pumice eruption.

The Middle Pumice eruption does not have any available proximally derived glass data for comparison. It does however have one marine tephra example in the literature which is attributed to the Middle Pumice eruption through its stratigraphic position and the large range in major element geochemistry (Federman and Carey 1980) ranging from andesite to rhyolite in classification. LC21 (11.190) is a 42cm thick visible tephra layer with a very broad major element classification ranging from basaltic andesite to rhyolite in composition. It has a date from our chronostratigraphy of ~152.58 ka BP (table 6.1). Federman and Carey (1980) note that the only (visible) marine tephra in their cores with this broad range of compositions (fig. 7.28 and 7.29) is the W2 tephra, attributed by them to the Middle Pumice Series of Santorini and dated by orbital tuning to ~150 ka (Narsici and Vezzoli 1999, Federman and Carey 1980). This is considered here to be the most likely identity of the visible tephra LC21 (11.190).

Unidentified tephras originating from Santorini.

LC21 contains six tephra deposits originating from Santorini which do not geochemically match any of the proximal deposits. More data was thus need, both to test the implication

that these tephra layers were indeed derived from Santorini, and in order to provide an explanation of their geochemistry.

Druitt et al. (2012) proposed a model for the production of magma during the Minoan eruption (fig. 8) of Santorini, dated to 3344.9 ± 7.5 cal BP (Manning et al. 2006). They used the geochemical composition of the pumice and the plagioclase crystals inside the pumice to infer a two stage magma mixing process, which preceded the Minoan eruption. The paper expounds the timescales involved in this mixing; cleverly exploiting the diffusion rates of various trace elements, concluding that the mixing event occurred less than 100 years prior to the Minoan eruption. These observations imply that there are at least two separate magma bodies present below the island of Santorini -magma type 1 and magma type 2 (fig. 7.48). It was thus thought that the model and its associated geochemical dataset could further the understanding of the unknown Santorini derived tephra layers in core LC21.

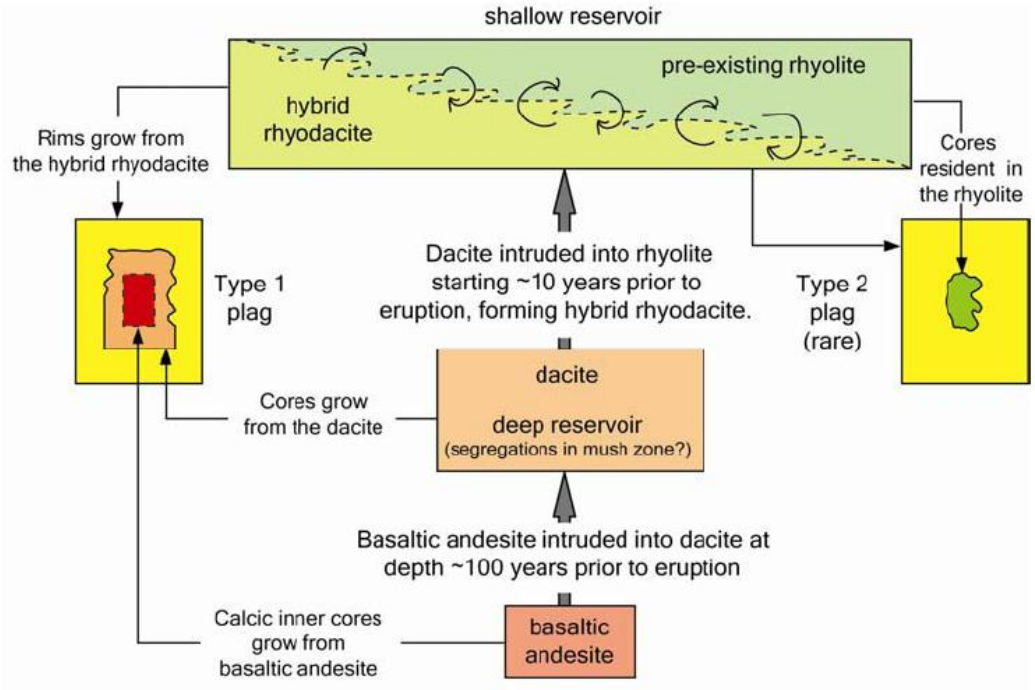

Figure 7.48 the Druitt et al. (2012) model of magma production for the Minoan eruption of Santorini. This model implies three separate magma sources, a basaltic andesite (base of diagram), a dacite magma (middle of diagram), and a rhyolite magma at the top of the diagram. The chemistry of the Minoan eruptive products (glass and crystal chemistries) implies this model for Santorini.

These tephra layers in LC21 are chemically very similar to the Minoan eruption of Santorini, but must be older and do not correlate to any of the known proximal deposits (section 7.2). In order to answer the question of whether or not these tephras did originate from

Santorini, and thus whether or not they constitute newly discovered eruptions from this source, a hypothesis was set up.

As the Minoan eruption is thought best represent the geochemical diversity of the Santorini magmas (Martin et al. 2010), using data from this eruption should provide the best comparison for the unidentified Santorini tephra layers found in LC21. Druitt et al. (2012) describe the Minoan deposits using a model (fig. 7.48). As many of the LC21 tephra layers which cannot be correlated are rhyolitic, it is intuitive to hypothesise that they may derive from the rhyolitic 'type-2' magma of Druitt et al. (2012). Proximal deposits derived from this magma batch are rare, and are concentrated at the base of the Minoan deposits as a white- crystal rich pumice (Martin et al. 2010), but no geochemical data has yet been published from this apparently minor component of the eruption. As this rhyolitic magma batch was thought to be the most likely origin for the unknown LC21 tephra layers, the following hypothesis was set up: if the unidentified LC21 tephra layers originate from the rhyolitic 'type 2' magma batch of the Druitt et al. (2012) model, then the proximal deposits of this magma batch will lie on the same high field strength element trend line as the distal LC21 deposits. The initial results of the analyses of the two end members of the Minoan deposits (by E. Tomlinson) are shown together with the geochemical data from all the Santorini derived tephra layers from LC21 in figure 7.49.

These HFSE diagrams show five data trends. Three of these trends can be explained by fractionation (fig. 7.49) of the magma batches: the trends F1, F2 and F3. The other two trends cannot be created by fractionation, as the incompatible HFSE do not increase with silica content (fig. 7.49).

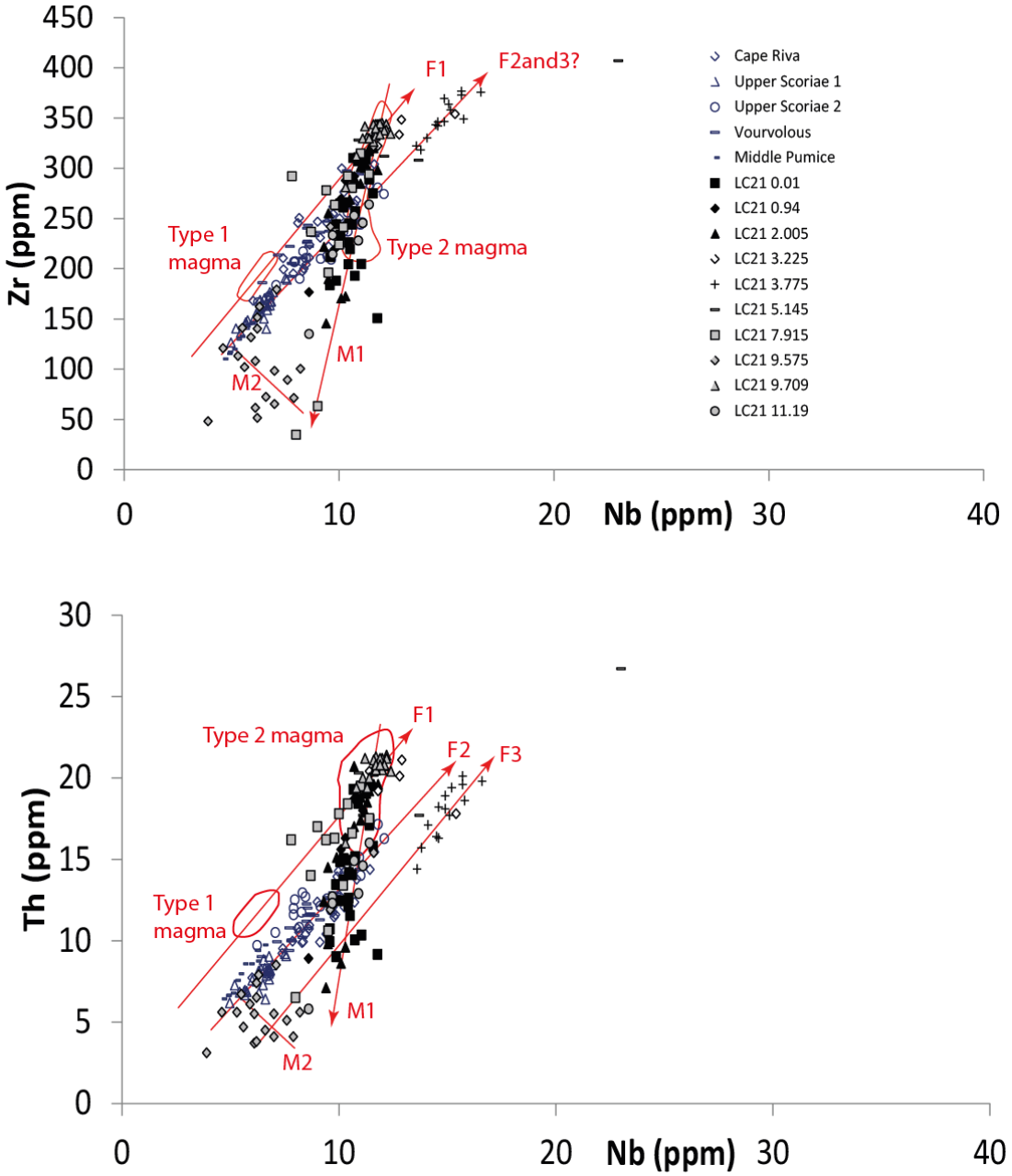

Figure 7.49 HFSE comparison of Santorini type 1 (dacitic) and type 2 (rhyolitic) magmas of (Druitt et al. 2012) (unpublished data from Emma Tomlinson) shown by red fields, with proximal deposits (Emma Tomlinson, unpublished) shown in blue symbols, and deposits from LC21 shown in grey/black (this study). Visually defined geochemical trends are imposed as red lines with, importantly, increasing silica content shown by the arrows. Four or five trends are identified within the data, implying two or three fractionation trends (F1,F2 and F3) and two possible mixing trends (M1 and M2). Mixing line M2 for sample LC21 (9.575) does not systematically increase in SiO_2 content with respect to the HFSEs and thus has no arrow. Trend lines are defined only by eye and thus are approximations only.

Figure 7.49 shows, using HFSE plots, the type1 and 2 magmas of Druitt et al. (2012) and the Santorini tephra layers from LC21. These samples define either fractionation (F1,F2 or F3 on fig. 7.49) or mixing trends (M1 or M2 on fig. 7.49). Fractionation trends are only possible where all the incompatible, HFSE concentrations increase with SiO_2 increase.

Where the values decrease while SiO_2 values increase, this violates the principles of Raleigh fractionation, so the trend lines M1 and M2 must therefore be due to magma mixing. All distal tephra samples from LC21 lie on either fractionation trend F3 or mixing trends M1 or M2. All proximal deposits (for Plinian eruptions, apart from the Minoan) fall on fractionation line F2. The Minoan deposits define fractionation trend F1 and mixing trend M1.

As all the proximal Plinian eruptions (except the Minoan) fall on fractionation trends F2, the inference is that these products from these eruptions are derived exclusively from a single magma chamber. As most of the more minor eruptions of Santorini (represented by the LC21 tephra layers) lie on mixing line M1 or M2, the products of these inter-plinian eruptions are inferred to be derived from hybrid/mixed magmas. As the majority of the samples which comprise this trend are highly evolved magmas (SiO2 of 72-75wt%), if these compositions were produced by magma mixing, the magma with which they mixed would have to be even higher in SiO_2, perhaps of 77-78wt%. Tephra layer LC21 (3.775) defines its own trend line F3 implying that this tephra may be derived exclusively from a single magma batch.

Sample/Eruption	**Date (reference)**	**Magma batch involved (from fig 7.49)**	**Comments**
Minoan	3344.9 ± 7.5 cal BP (Manning et al. 2006)	F1 (proximal) and M1 (proximal and distal)	Plinian, Caldera forming.
LC21 (2.005)	11.25±0.55 – 11.11±0.25 ka (this study)	M1	Sub-Plinian? Not detected proximally
Cape Riva	21,705 ± 311 cal BP (Eriksen et al.1990),	F2	Plinian, three eruptions of identical chemistry found in ODP967
LC21 (3.225)	24.31±2.89 – 24.21±2.87 ka	F1 + F3	Sub-Plinian? Not detected proximally
LC21 (3.775)	29.49±3.88 – 29.40±3.86 ka	F3	Sub-Plinian? Not detected proximally
LC21 (5.145)	43.34±2.96 – 42.28±2.25 ka	F1+F3	Sub-Plinian? Not detected proximally
LC21 (7.915)	104.10±1.78 – 103.98±1.79 ka	F1 and/or M1	Sub-Plinian? Not detected proximally
LC21 (9.575)	Start at 125.77±3.00 – 125.72±3.00 ka	M2	Sub-Plinian? Not detected proximally

LC21 (9.709)	126.51±2.92 ka	F1	Sub-Plinian? Not detected proximally
LC21 (11.190)	152.58±2.54 ka	F2 and/or M2	Likely Plinian due to depth of deposit in LC21. Possibly a distal facies of the Middle Pumice?
Upper Scoria 1	?	F2	Plinian
Upper Scoria 2	?	F2	Plinian
Vourvolous	?	F2	Plinian
Middle Pumice.	?	F2	Plinian

Table 7.2 Summary of how the eruptions of Santorini relate to the fractionation trends (F1,2 or 3) and mixing trends (M1 or 2) shown by the HFSEs on figure 7.49.

The question remains as to the identity of the magma that the rhyolitic (type 1) magma mixed with to produce the chemical composition on mixing trend M1. As it is known that the tephra shards with the highest HFSE values have the lowest SiO_2 values (fig. 7.49) it must be that the magma that mixed with this end member composition was higher in SiO_2 and lower in HFSE concentrations. Evidence for such a magma contributing to the Hellenic Arc does exist, as very high SiO_2 concentration magmas have been extruded in the Kos/Yali/Nisyros stratigraphy and in Central Anatolia. In addition, the fractionation trend lines of both Kos and Central Anatolia could originate from a composition which, when mixed with the rhyolitic component of the Minoan eruption, would produce the mixed composition trend M1 (fig 7.50). Alternatively this mixing line (M1, figs. 7.49 and 7.50) may be the result of crustal contamination of the rhyolitic magma. This hypothesis could be tested using isotopic data, perhaps from Sr or Nd isotopes which may reveal a crustal component.

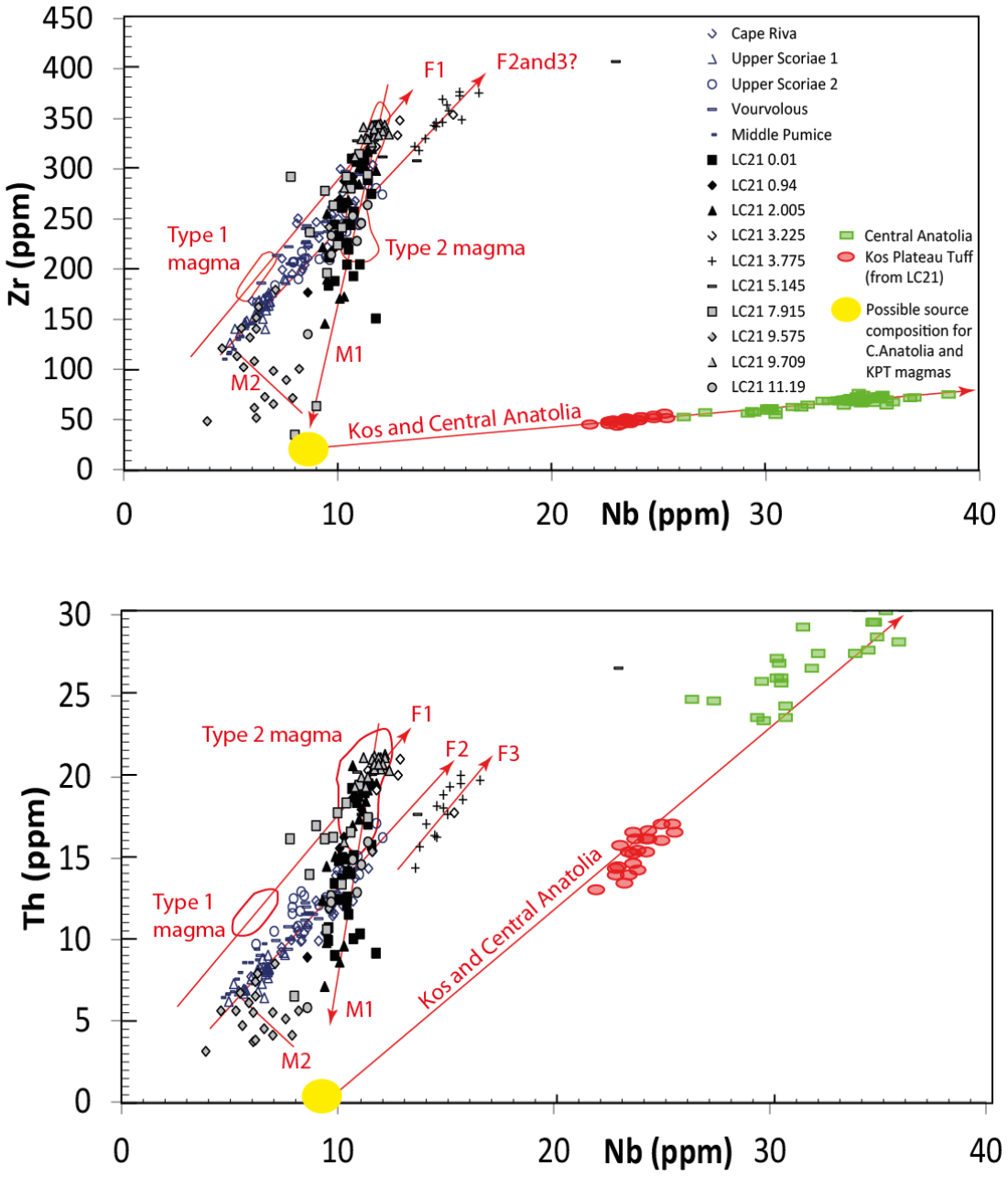

Figure 7.50. Figure 7.49 with the addition of data representing the Kos Plateau Tuff and the Central Anatolian volcanic system. The diagram illustrates a possible source melt composition from which the magmas contributing to the Kos and Central Anatolian Volcanic systems may be derived (shown by yellow spot). This highly silicic composition is proposed as the magma which mixed with the most silicic compositions of the F1 fractionation trend to create the M1 mixing trend. Trend lines are defined only by eye and are thus approximations only.

Druitt et al. (2012) also produced calculations of the SiO_2 content of the melt from their measured plagioclase Sr data. The measured melt compositions (glass analyses) from this study are compared to the calculations of Druitt et al. (2012) in figures 7.51-7.60. Druitt et al. (2012) used the anorthite content of the plagioclase crystals in the various magma

batches to calculate the Sr and SiO_2 contents in the host melts. As this study produced measured Sr and SiO_2 contents for individual shards, the process of Druitt et al. (2012) can be reversed to derive the anorthite content of the plagioclases from these measured compositions. As the anorthite component is strongly controlled by pressure and temperature (Kudo et al. 1970), this process gives a qualitative estimate of the depths of the magma batches from which the tephra shards originated (with the not unreasonable assumption that pressure and temperature increase with depth.) The trace element data from the tephra layers will therefore inform on the magma batches contributing to Santorini (figs 7.49 and 7.50) and, when combined with the work of Druitt et al. (2012) also implies the depths (figs. 7.51 to 7.60) of each of the magma batches.

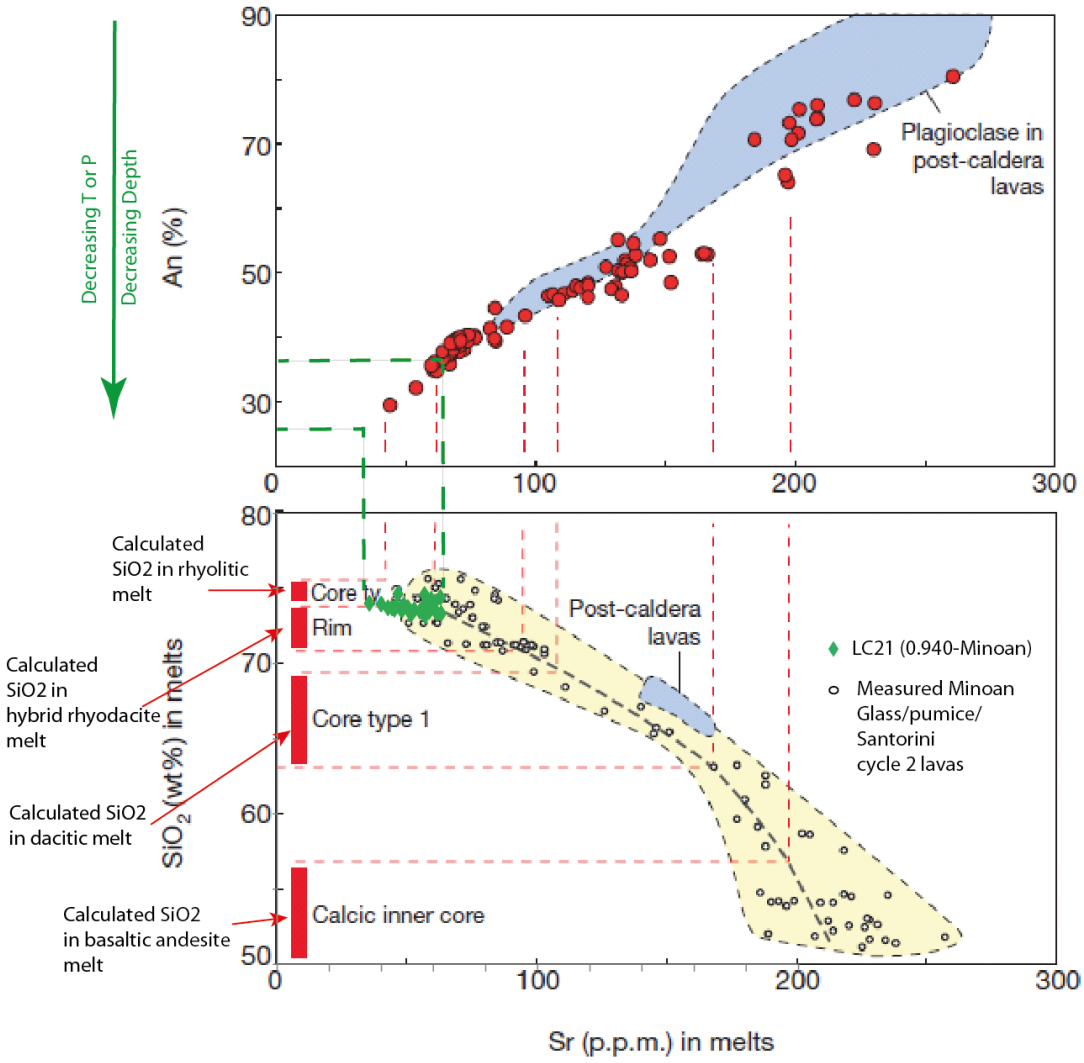

Figure 7.51 Use of figure 3 from Druitt et al. (2012) to attain an estimate of the plagioclase composition (%An) and thus the depth of the rhyolitic magma batch (batch M1) which contributed to the eruption represented by LC21 (0.940) in LC21: the Minoan eruption. The tephra preserved in LC21 erupted from a shallow magma batch. NB the tephra in LC21 does not illustrate the full range of compositions for the Minoan

eruption. Another dacitic component was also involved (fig 7.49). It is not possible to plot this data onto this diagram however, as the Sr values cannot be directly related to the SiO_2 values for the proximal samples. The diagram also shows the excellent agreement of the data produced by Druitt et al. (2012) and that produced in this study.

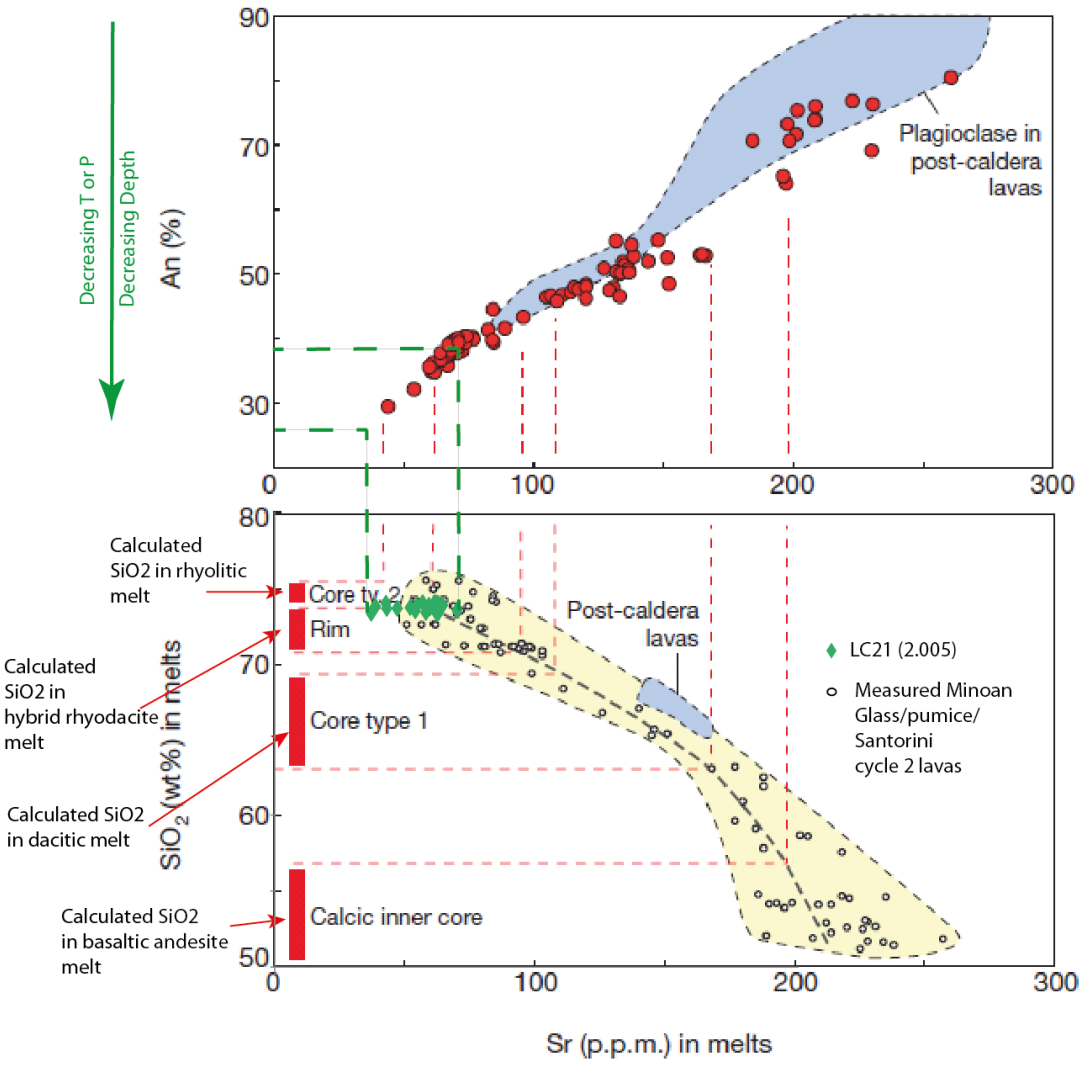

Figure 7.52. Use of figure 3 from Druitt et al. (2012) to attain an estimate of the plagioclase composition (%An) and thus the depth of the rhyolitic magma batch (batch M1) which contributed to the eruption represented by LC21 (2.005) in LC21: an unknown Santorini eruption. Magma batch M1 is inferred to be a shallow magma batch, corroborating the result from figure 7.52.

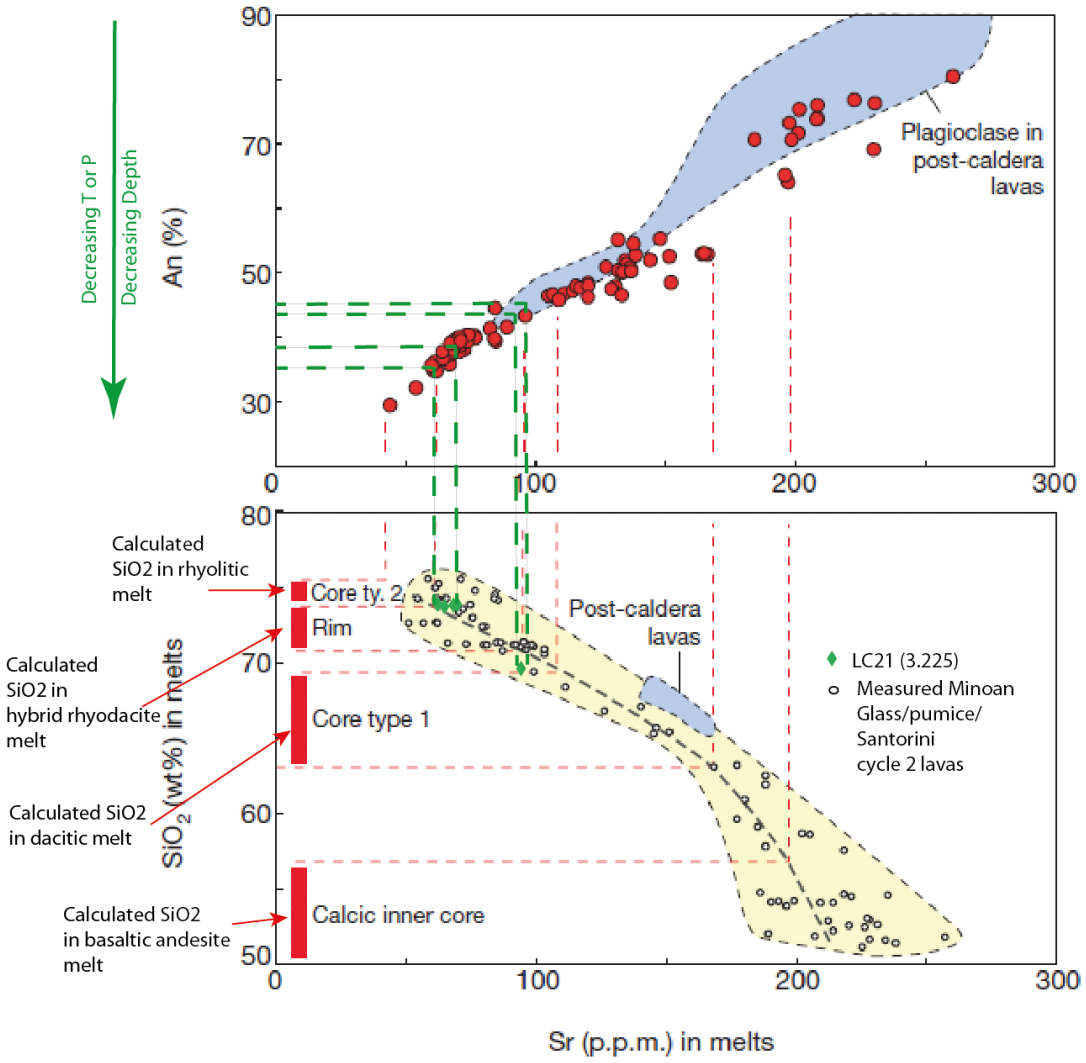

Figure 7.53 Use of figure 3 from Druitt et al. (2012) to attain an estimate of the depth of the plagioclase composition (%An) and thus the magma batches (batches F1 and F3) which contributed to the eruption represented by LC21 (3.225) in LC21: an unknown Santorini eruption. Magma batch F1 is inferred to be a shallow magma batch while the single data point from batch F3 implies a magma batch at intermediate depth. As the other diagram for batch F1 (fig.…) indicates an intermediate depth, the inference is that an evolved fraction of F1 migrated to a shallow level, to coexist with the F3 magma. Batch F1 must have arrived in that chamber first to give it time for the Sr content to equilibrate to the new ambient pressure (shown by the Sr content in this diagram). F3 must have arrived just prior to eruption, without time to equilibrate, as the Sr content for this batch still preserves its intermediate depth signature.

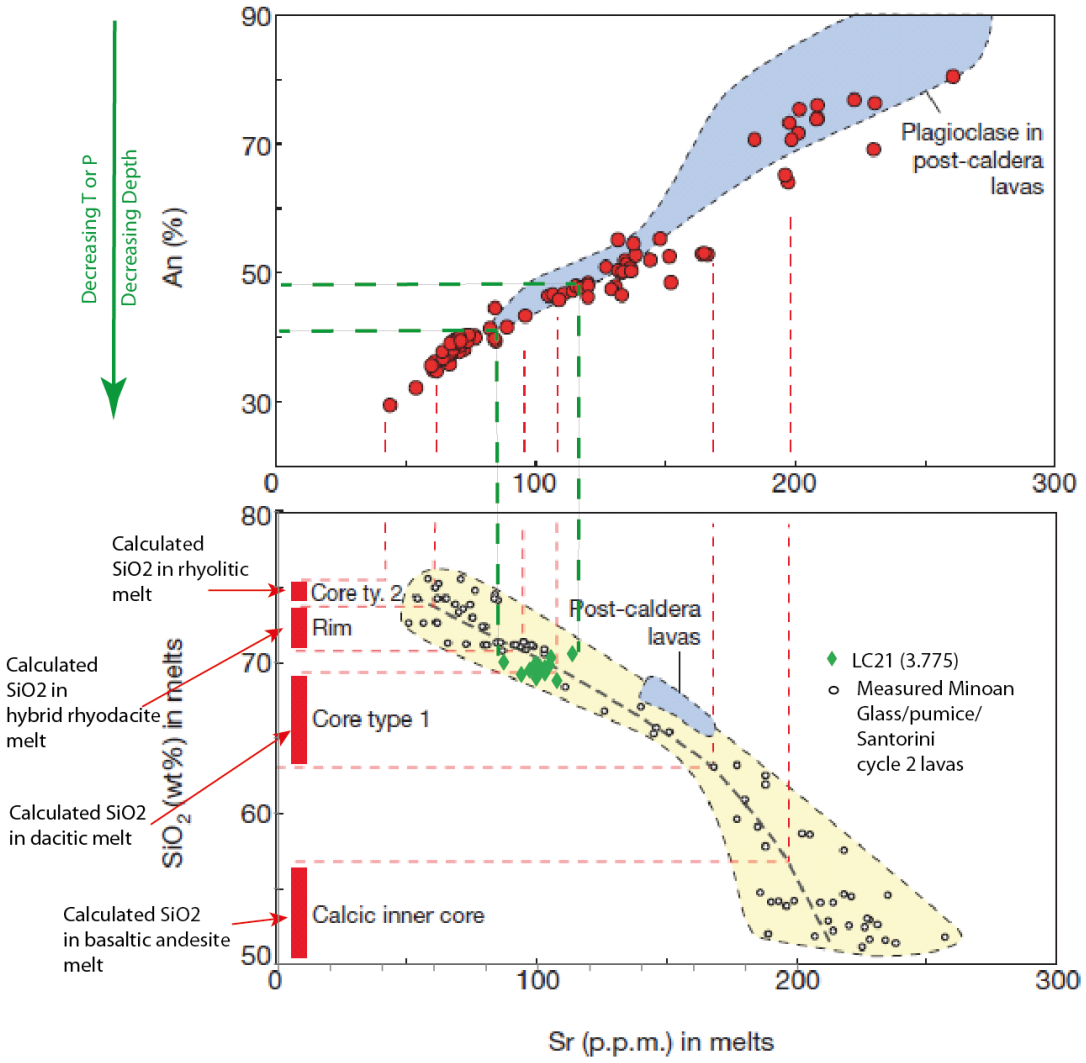

Figure 7.54 Use of figure 3 from Druitt et al. (2012) to attain an estimate of the plagioclase composition (%An) and thus the depth of the magma batch (batch F3) which contributed to the eruption represented by LC21 (3.775): an unknown Santorini eruption. The figure indicates that this magma erupted from an intermediate depth chamber, consistent with the observation for the same magma batch in figure 7.53.

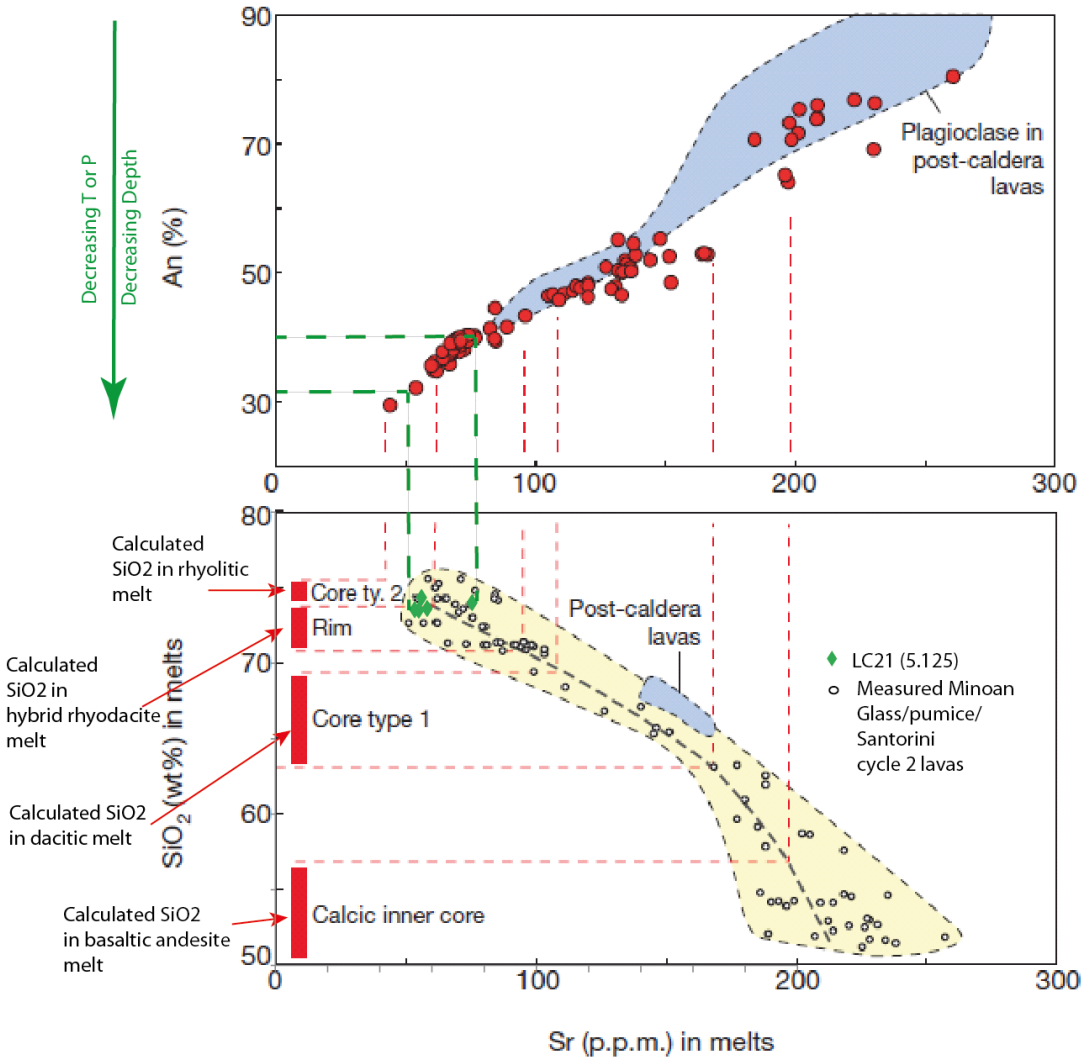

Figure 7.55 Use of figure 3 from Druitt et al. (2012) to attain an estimate of the plagioclase composition (%An) and thus the depth of the rhyolitic magma batches (batches F1 and F3) which contributed to the eruption represented by LC21 (5.125) in LC21: an unknown Santorini eruption. Both batches show evidence for having existed at intermediate depths (figs 7.55 and 7.54) Both these batches indicate in this figure that they both were resident in a shallow magma chamber for enough time for the Sr contents to equilibrate to the lower pressure.

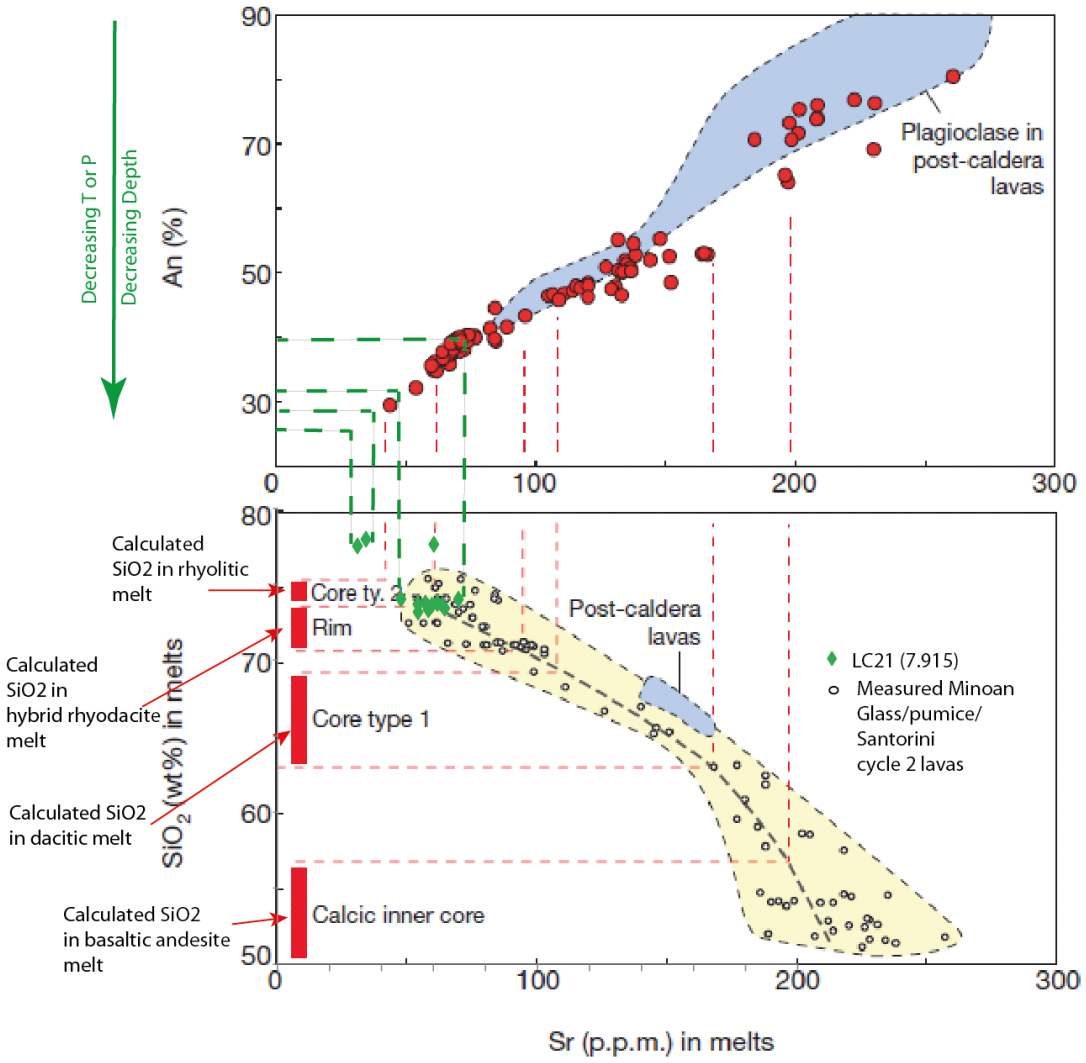

Figure 7.56 Use of figure 3 from Druitt et al. (2012) to attain an estimate of the plagioclase composition (%An) and thus the depth of the rhyolitic magma batch (batch M1) which contributed to the eruption represented by LC21 (7.915) in LC21: an unknown Santorini eruption which must be nearly synchronous with the X5 Campanian eruption. The data shows two groups in SiO_2 vs Sr space, indicating that the magma was at two different depths (two magma chambers) until very shortly before eruption, as the Sr content has not had time to equilibrate between the two magmas. These two batches mixed to form the M1 magma (fig 7.49). Batch M1 is comprised of a fractionated end member of F1 batch, and a highly silica rich magma which must be from a shallow level. The end member of the F1 magma must have been resident at a shallow depth for long enough for the Sr contents to equilibrate to the shallow level P/T conditions. The two magmas mixed prior to eruption (M2 shows a mixing trend on fig 7.49) but did not fully mix as evidenced by the two populations in this figure.

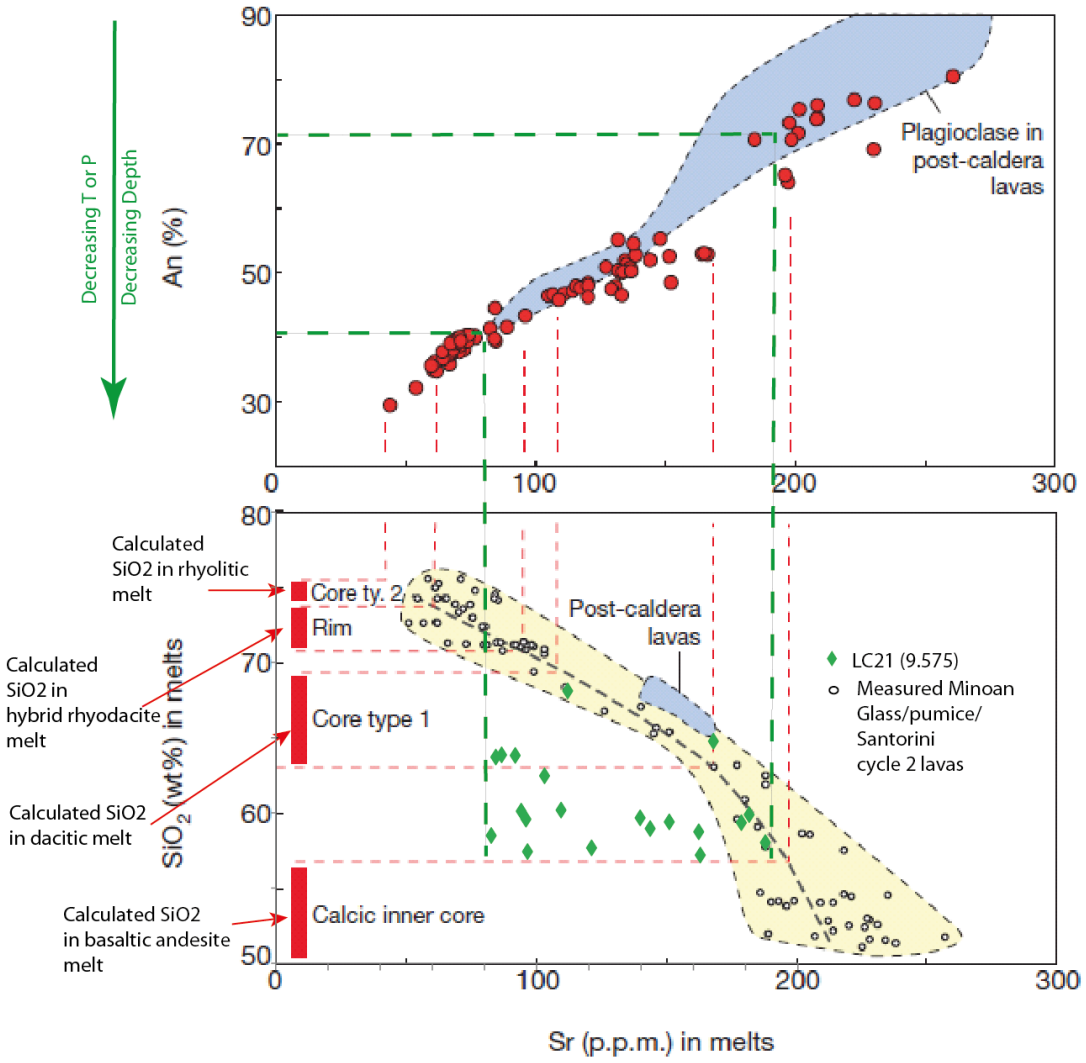

Figure 7.57- Use of figure 3 from Druitt et al. (2012) to attain an estimate of the plagioclase composition (%An) and thus the depth of the magma batch (batch M2) which contributed to the eruption represented by LC21 (9.575) in LC21: the start of a period of inter-plinian activity for Santorini. This SiO_2 vs Sr plot corroborates the assertion that this sample represents a continuous period of volcanic activity: the Sr shows a very broad composition indicating that the magma did not remain in one place for long enough for it to equilibrate completely with the ambient P/T.

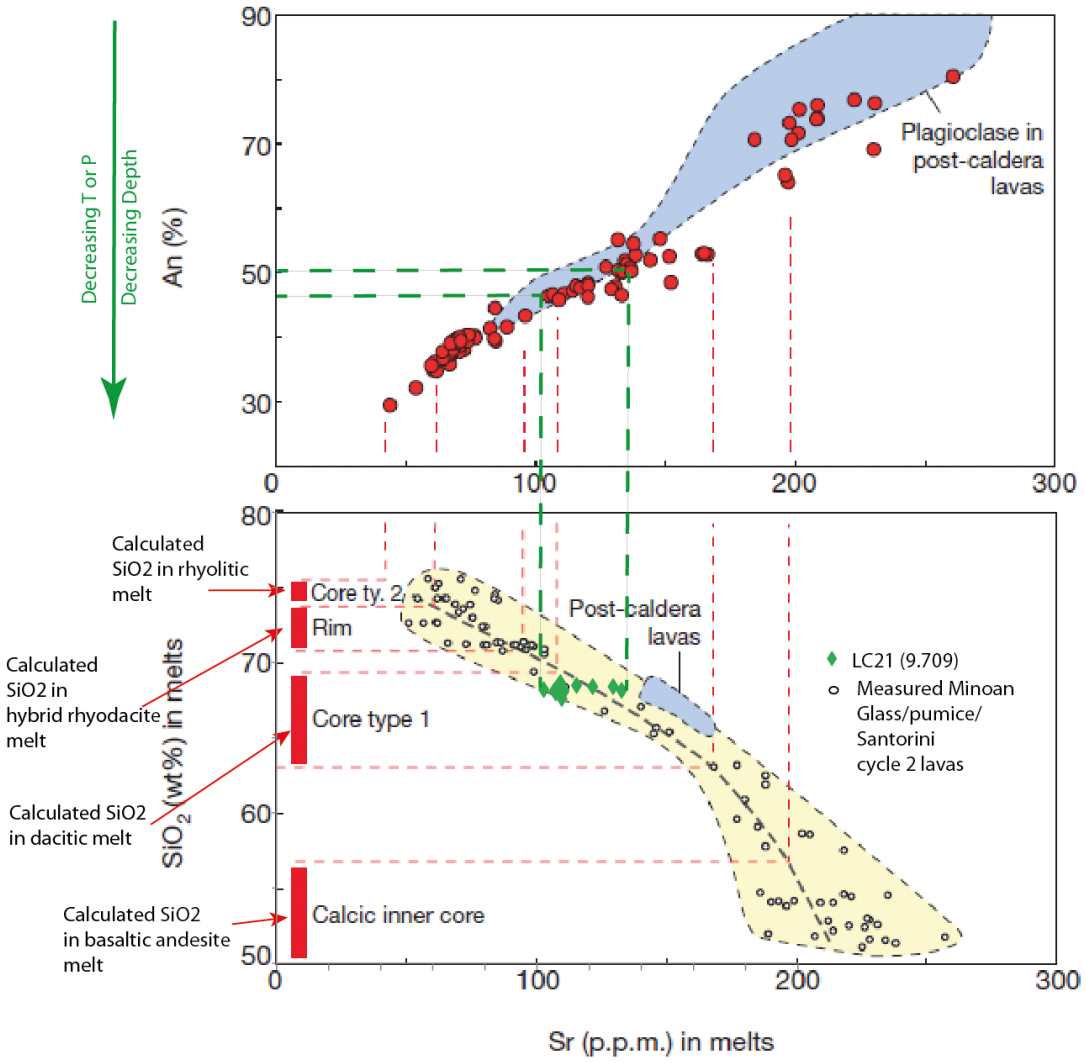

Figure 7.58 Use of figure 3 from Druitt et al. (2012) to attain an estimate of the plagioclase composition (%An) and thus the depth of the magma batch (batch F1) which contributed to the eruption represented by LC21 (9.709) in LC21: an unknown eruption from Santorini. The diagram indicates that the magma was resident in a chamber at intermediate depth until shortly prior to eruption.

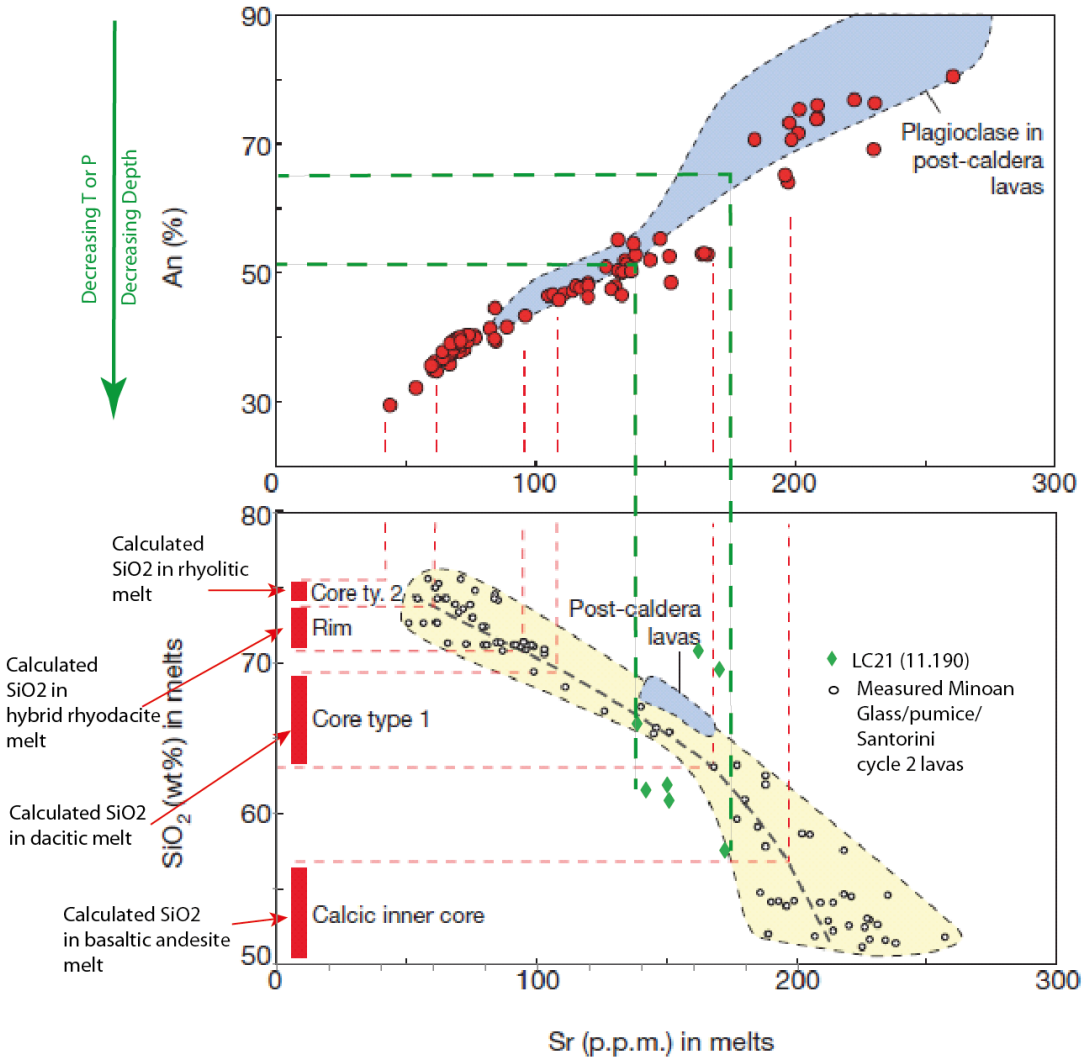

Figure 7.59 Use of figure 3 from Druitt et al. (2012) to attain an estimate of the plagioclase composition (%An) and thus the depth of the magma batch (batch F2 or M1) which contributed to the eruption represented by LC21 (11.190) in LC21: proposed (but not confirmed) here to correlated to the Middle Pumice eruption of Santorini. The figure indicates a highly heterogeneous magma chamber (corroborating the major element diversity, fig. 6.4), which existed at an intermediate depth below Santorini. As such a diversity of magma was erupted during this eruption it is thought likely here that

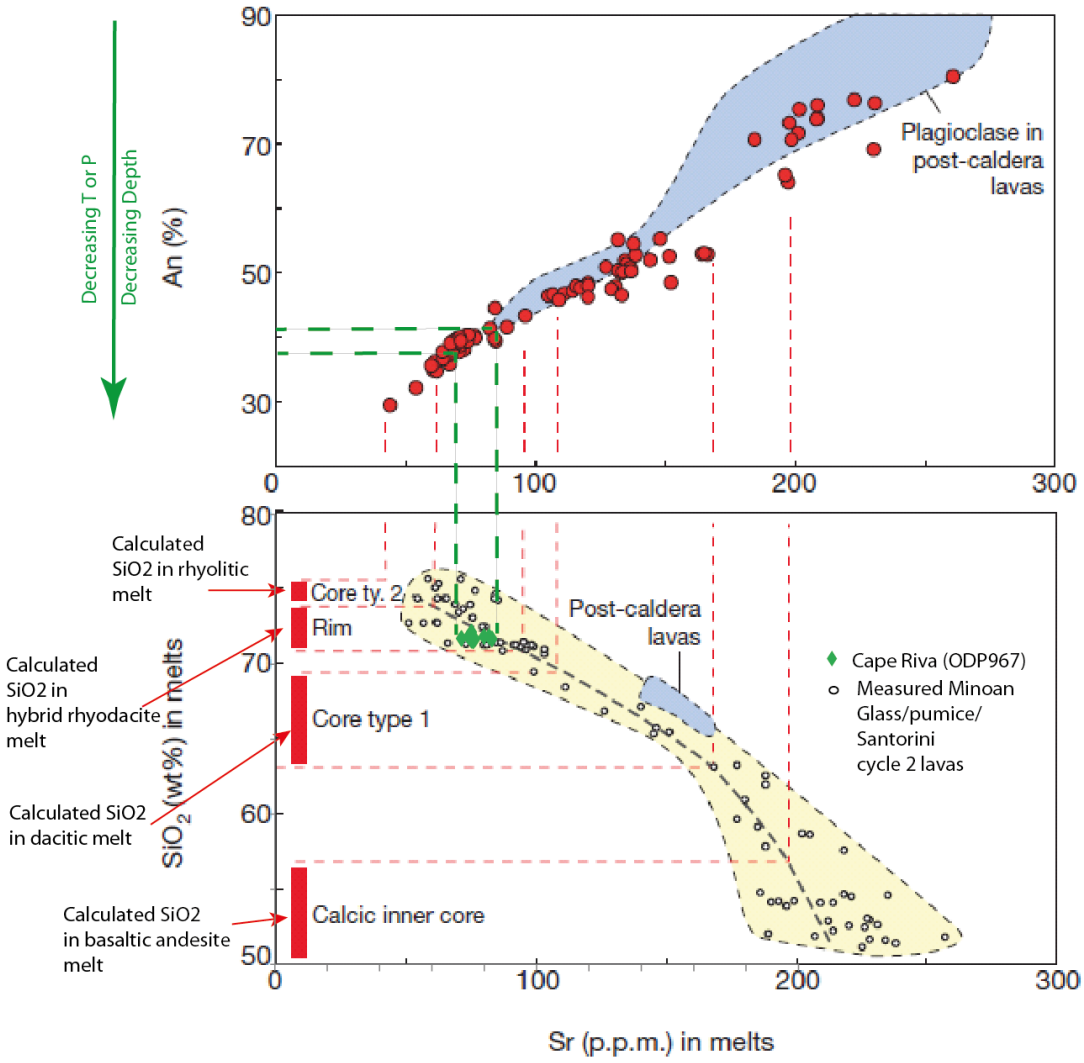

Figure 7.60 Use of figure 3 from Druitt et al. (2012) to attain an estimate of the plagioclase composition (%An) and thus the depth of the magma batch (batch F2) which contributed to the Cape Riva eruption represented by the tephra layer ODP967 (1.810). The data indicates that this magma was present at an intermediate to shallow level prior to eruption.

This information can be combined to produce a new, conceptual model of the magmatic plumbing system below Santorini (fig 7.61).

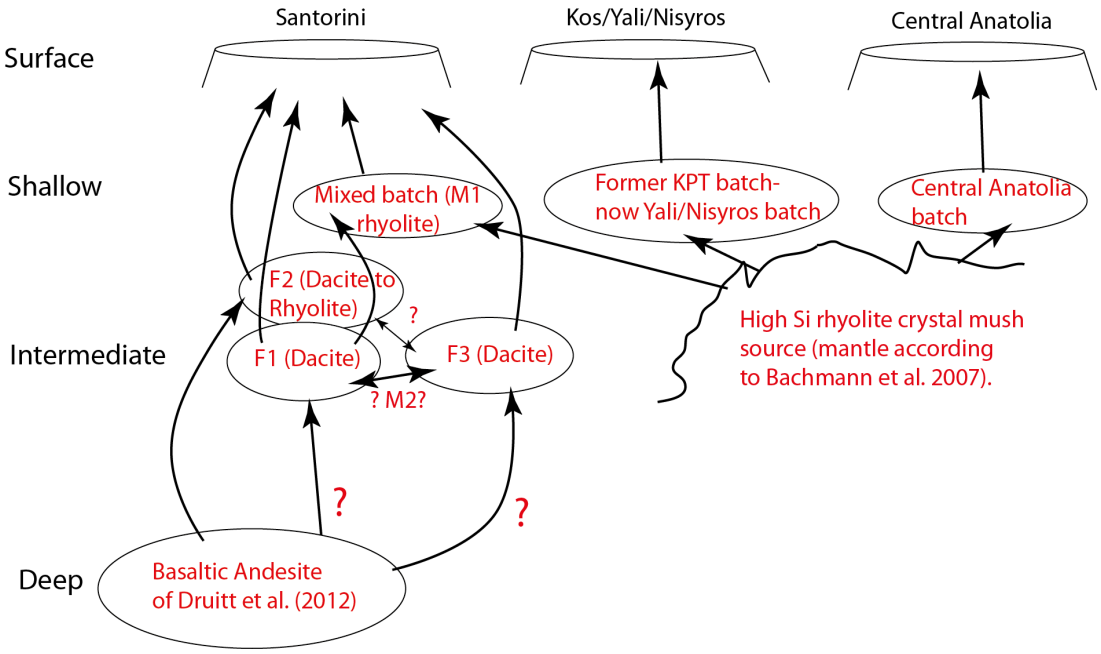

Figure 7.61 a proposed magma batch model for Santorini, with reference to Kos/Yali/Nisyros system and the Central Anatolian System. The magma batches and the links between them are defined by figures 7.49 and 7.50. The relative depths of the magma batches are qualitative and are inferred from figures 7.51-7.60 Bachmann et al. (2010) define the Kos magma chamber at only 2kb (about 8km depth) from eutectic modelling. The M1 batch is also likely to be very shallow at 0.5kb (2-3km) (Cottrell et al. 1999). Batches F1, F2 and F3 are inferred to be deeper (from figs 7.51-7.59). The basaltic andesite of the Druitt et al. (2012) model (fig.7.48) is the deepest of all (as inferred from fig 7.48) The depth of the proposed high silica crystal mush source feeding all three systems is not known, but must be shallow if the silica content is high, as higher pressures would stabilise quartz (Bachmann et al. 2007) and reduce the SiO_2 content of the melt. Interestingly Zhu et al. (2012) define a low seismic velocity region underneath Kos at a very shallow depth which could provide supporting evidence for this shallow melt source.

Magma batch F1 is a dacitic magma batch which produced eruptions both autonomously (such as LC21- 9.709, fig 7.49, table 7.2) or in conjunction with other batches (notably for the Minoan eruption, fig 7.49). It has been active since at least 126.51±2.92ka, the date derived for LC21 (9.709) by the age model of Grant et al. (2012) and its most recent contribution was to the Minoan eruption (3344.9±7.5ka, Manning et al. 2006). The magma originated from an intermediate magma chamber (fig 7.58) but can also feed a shallower magma chamber and reside there long enough to become equilibrated with the ambient P/T conditions (figs 7.53, 7.56 and 7.57).

Magma batch F2 is a dacitic to rhyolitic magma batch which apparently only contributes autonomously to eruptions of Santorini (fig. 7.49). When this batch erupts however it produces the Plinian eruptions which are prominent in the proximal stratigraphy. It is the eruptions from this batch which form all of the documented Plinian deposits on the island with the exception of the Minoan. The fact that this batch can erupt autonomously (it is 'ready-to-erupt' without mixing) and produce Plininan eruptions implies that Santorini is a

volcano which should be closely monitored. Figure 7.61 evidences that this magma batch probably resides at an intermediate depth below Santorini.

Magma batch F3 contributed LC21 (3.775) to the tephra record investigated here. It erupted without mixing for this eruption, but also contributed to eruptions LC21 (3.225) and LC21 (5.125) in conjunction with batch F1, implying some kind of link between these batches (indicated by a question mark on fig 7.61). The batch did not contribute to the major eruptions shown in the proximal stratigraphy as it is only found (thus far) in the marine archive. Figure 7.55 indicates that this magma originates from an intermediate depth magma chamber, at a similar depth to batches F1 and F2.

Magma mix M1 is implied here (fig 7.50 and 7.57) to be a mix of an evolved component of magma batch F1 and a high SiO_2 rhyolite source which contributes magmas to Santorini, Kos/Yali/Nisyros and Central Anatolia (fig 7.50 and 7.61) This mixing process is investigated by Druitt et al. (2012) for the Minoan eruption and is thought to occur on timescales only of months to decades. For the first time, it is shown here that the magmatic circumstances leading to the Minoan eruption were not unique and that this mixing processed happened at least twice before to produce tephra layers LC21 (7.915) and LC21 (2.005) at ~104.10-103.98ka and 11.25-11.11ka respectively.

Magma mix M2 is enigmatic and only evidenced by one tephra sample, LC21 (9.575). This sample was taken from the base of a large depth of tephra shards which were disseminated within sapropel 5 in LC21. This indicates the sample represents the start of an extended period of inter-plinian activity for Santorini and so the chemistry of magma mix M2 could be a consequence of continuous movement of this batch within the plumbing system. This claim is corroborated by the broad range of depths indicated by the sample on figure 7.61.

The **basaltic andesite** of Druitt et al. (2012) which is implied by them to have fed the dacitic batch F1 prior to the Minoan eruption is probably the feeder batch for F1, F2 and F3 (as indicated on fig 7.61) but no evidence to test this assertion could be derived here.

This section of the thesis has explored the relationships of the distal deposits which originate from Santorini to the proximal deposits of the island. There is evidence for more eruptions in the distal stratigraphy of LC21 (this study) than is implied from the proximal volcanic stratigraphy alone (Druitt et al. 1999, 2012). It has also been shown that in the

case of the Minoan eruption two geochemical components (dacite and rhyolite) are preserved proximally where only the rhyolite is preserved in the marine record. The component preserved in the marine record is very rare within the proximal deposits (Druitt et al. 2012, Martin et al. 2010), but forms a 22.4cm thick visible tephra in LC21, which is ~100km from the volcano. The evidence presented here indicates a complex magmatic system contributing to the eruptions of Santorini, corroborating and expanding upon the isotopically derived conclusions of Martin et al. (2010). The evidence also shows that distal marine cores can contain a crucial yet unexploited record of volcanic events.

The addition of grain size data (e.g. Sparks et al. 1983) from distal deposits could also help test models of ash production. It is the fine grained, buoyant ash which is the greatest hazard to aeroplane engines and the size of the ash particles are related to the fragmentation depth of the magma (Dufek et al. 2012). Integrating data on the physical and chemical characteristics of distal tephra deposits could contribute directly to an assessment of the volcanic hazards to aircraft.

7.5.2 Tephras originating from Campania.

There are two or possibly three samples from the cores in this study which contain tephra shards originating from the Campanian region. Two of these were found in LC21 and one in ODP975.

The Campanian Ignimbrite.

Tephra LC21 (4.925) represents a visible layer of 13cm thickness. This tephra is chemically identical to the proximal deposits of the Campanian Ignimbrite (figs 7.12 and 7.13). LC21 (4.925) is therefore correlated to the Campanian Ignimbrite eruption from the Campanian Fields in Italy (Lowe et al. 2012). The CI has been $^{39}Ar:^{40}Ar$ dated to 39.28 ± 0.11 ka (De Vivo et al. 2001). This date was used to construct the age model for LC21 (fig. 7.3). Interestingly, the comparison to the major elements of the Campanian Ignimbrite found by Bourne et al. (2010) shows significant differences in the composition. The two distal deposits do not match geochemically, but both fall within the proximal volcanic geochemical field (fig. 7.63). Had only the two distal deposits been compared to one another, without the proximal data (as is often the case in the tephrochronology literature), they may not have been assigned to the same eruption.

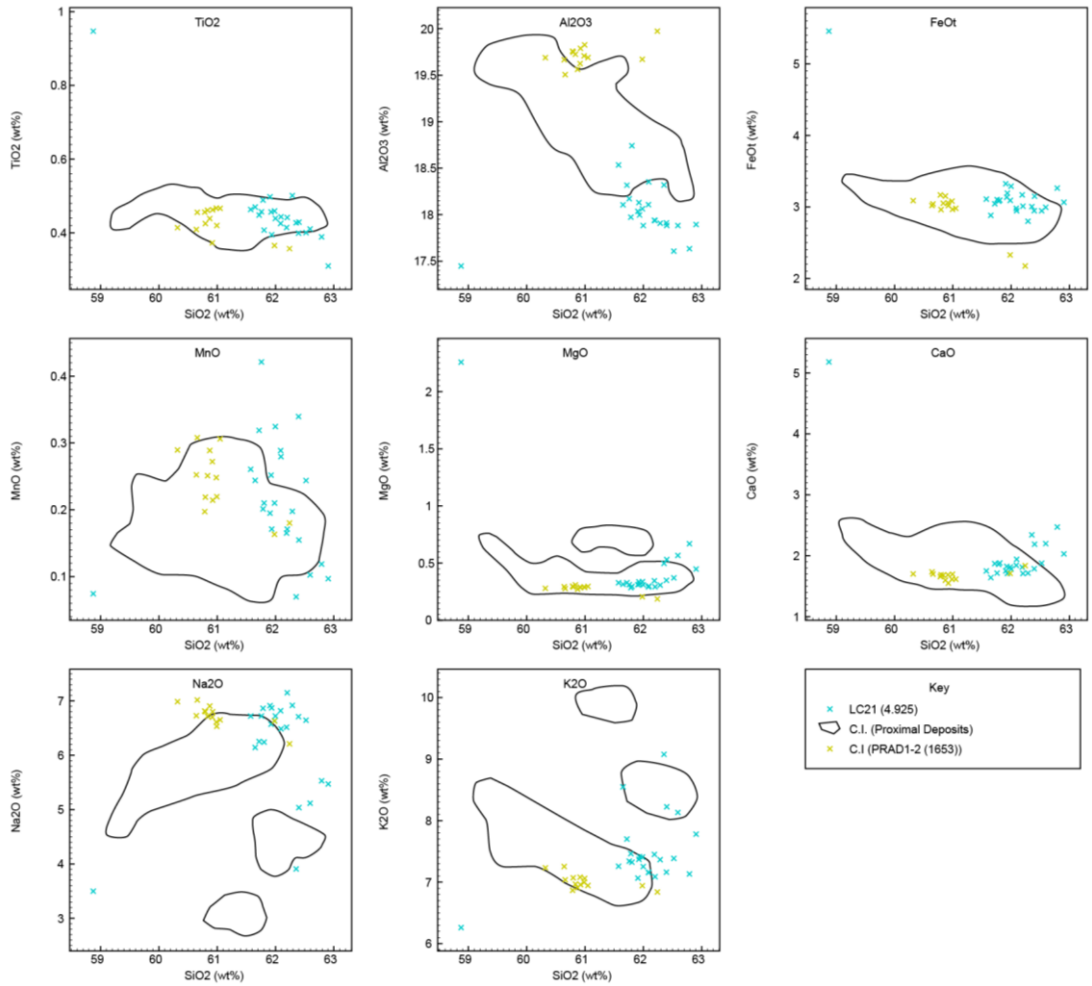

Figure 7.62 Major element omparison of LC21 (4.925) to Campanian Ignimbrite proximal deposits and the Campanian Ignimbrite of Bourne et al. (2010)- PRAD 1-2 (1653).

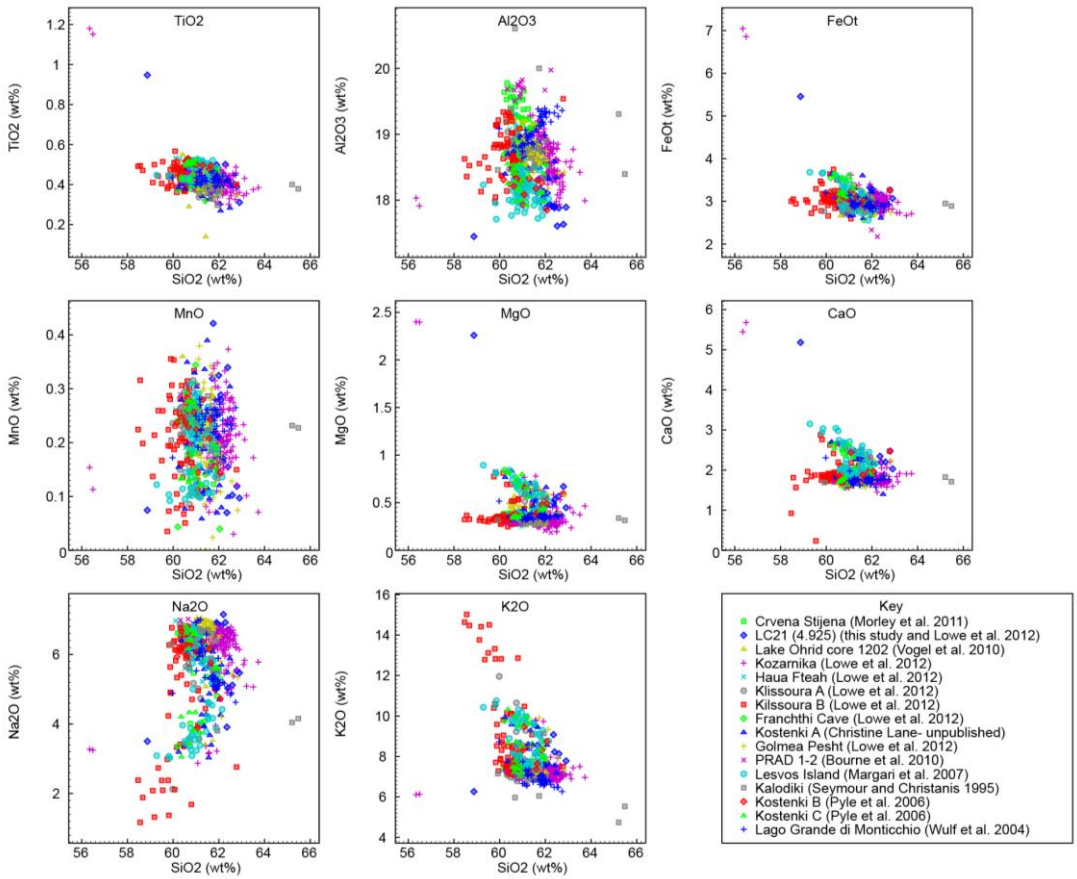

Figure 7.63 Major element analyses reported for the Campanian Ignimbrite from the literature (from the RESET database), this study –LC21 (4.925).

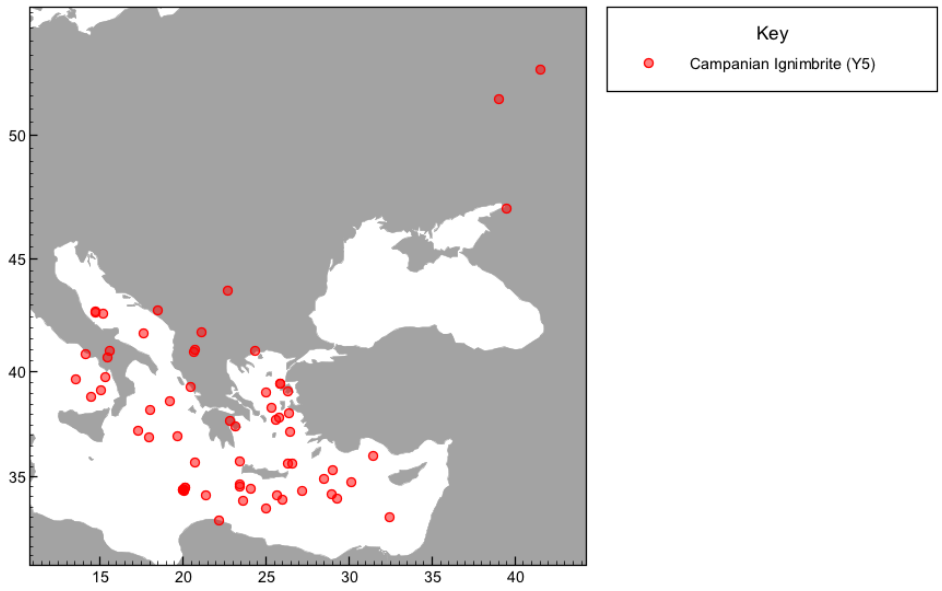

Figure 7.64 map showing the reported occurrences of the Campanian Ignimbrite tephra from the literature and reported by the RESET consortium. Data from RESET database.

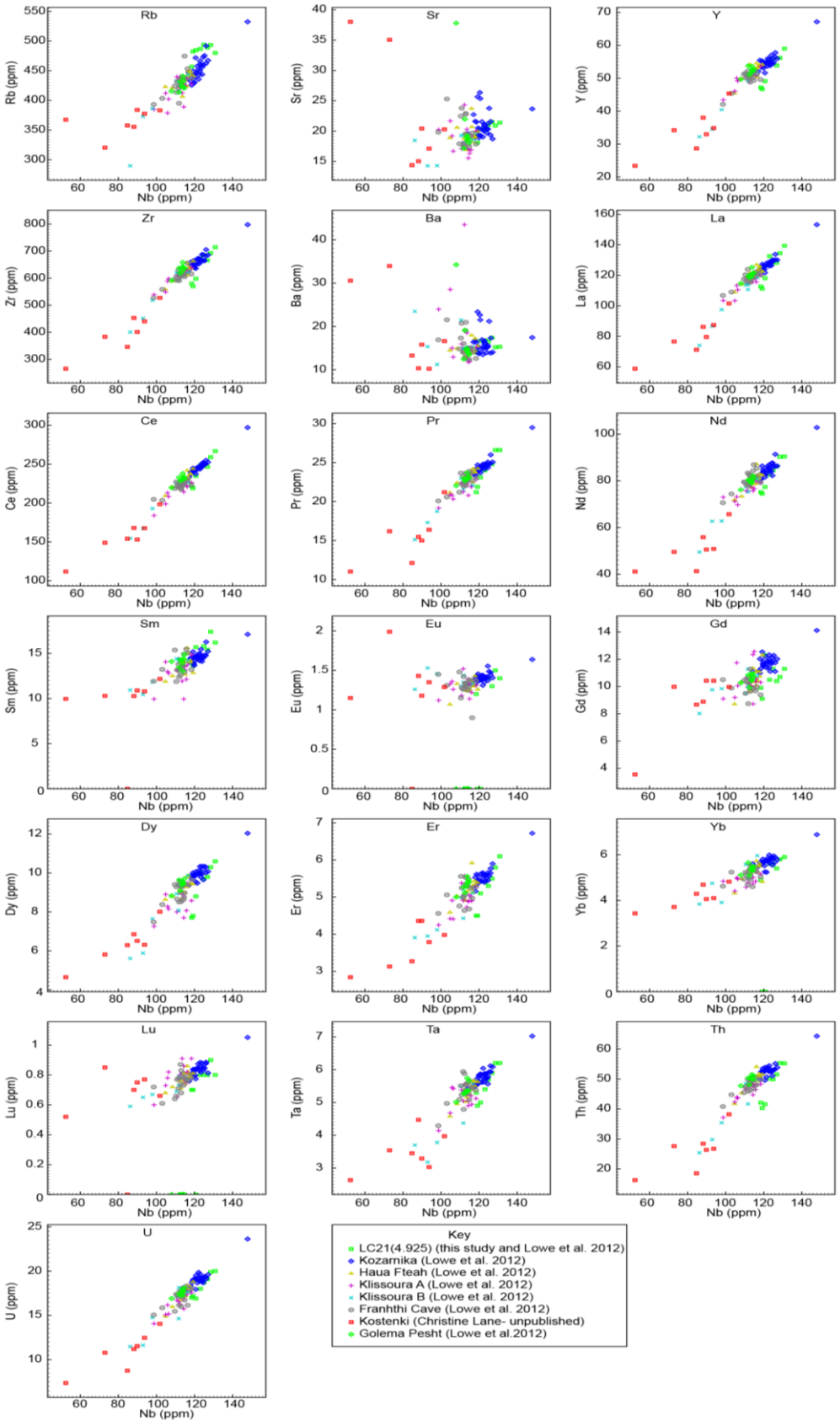

Figure 7.65 Trace element analyses of tephra shards attributed to the Campanian Ignimbrite, from the RESET database.

In addition, for the first time, evidence of Campanian tephra shards reaching the sediments of the Western Mediterranean Sea was found in this study. Core ODP975 yielded one shard of phonolitic composition at a depth of 2.24 mbsl. This shard was shown to be geochemically close to both the Neapolitan Yellow Tuff and the Campanian Ignimbrite proximal deposits (using major elements only). Should this shard originate from the CI eruption, it would allow, for the first time, a pan-Mediterranean comparison of marine proxy records with very precise stratigraphic control. More shards would need to be recovered and analysed however, to corroborate or disprove this hypothesis.

Alternatively, should this shard originate from the Neapolitan Yellow Tuff eruption, it would in the same way allow comparison of marine records from the Adriatic, Ionian and Tyrrhenian Seas with that of the Western Mediterranean Sea.

The X5 marine tephra (TM24 from Lago Grande di Monticchio) is found in core LC21. The alkaline shards in LC21 (7.195) imply an Italian source, and the Zr vs Nb plot (fig. 7.2) is also most similar to that of the Campanian Region, although only two trace element analyses of the alkaline component of LC21 (7.915) were achieved due to the small size of the shards. Figs 7.20 and 7.21 show that some shards of the alkaline (phonolitic) component of LC21 (7.915) are in very good agreement with the TM24a and TM24b tephras in Lago Grande di Monticchio (this study), while the other shards are similar to, but, crucially, not identical to TM27. The TM24a and TM24b tephras have both been correlated to the X5 marine tephra (Bourne et al. 2010, Vogel et al. 2010) and so its discovery in LC21 is by far the furthest east (~1200 km) that X5 shards have been found. X5 is dated to 105±2 ka on the basis of Kraml (1997). Given that TM24a and TM24 b (X5) and TM27 are separated by ~6000 varve years in the Monticchio stratigraphy (Wulf pers.com.), it is unlikely that these two tephras would be found in the same 1cm sample in LC21. More likely, the X5 tephra is found here with a hitherto unknown Campanian eruption of very similar age to TM24a and b.

7.5.2.1 Complexities in Sapropel 4 and the 'X5' tephra.

The use of tephra layers as stratigraphic markers is demonstrated here through the example of sapropel 4 and the marine X5 tephra (Bourne et al. 2010, Paterne et al. 2008). The sapropel is in some places separated by an interruption producing sapropels 4a and 4b, but in other locations consists of a single organic layer. Although the visual extent of a sapropel is not necessarily definitive of anoxic conditions in the bottom waters (Grant, pers comm.), it has been used to coarsely correlate marine cores from across the Mediterranean

Sea (Emeis et al. 1991) and from those cores to terrestrial environmental records (Piva et al.2008b, Bar-Matthews et al. 2000).

The X5 has been correlated to the TM24 tephras of the Lago Grande di Monticchio record in Southern Italy (Wulf et al. 2004). However this section of tephra in LGdM contains many layers of ash, and spans ~1000 years in the LGdM varve supported chronology. The discovery of tephra matching the TM24 tephras in the Aegean Sea (core LC21, this study), in the Adriatic Sea (Bourne et al. 2010) and in the Ionian Sea (Keller et al. 1978) now allows the sapropel layers in these basins to be stratigraphically related to one another, independently and at very high resolution, providing that the tephra layers comprising TM24 can be distinguished from one another.

Firstly it demonstrated how the tephra samples in the Adriatic, Ionian and Aegean Seas geochemically relate to the TM24 tephras of Lago Grande di Monticchio. Then these relationships are used to stratigraphically relate the visual extent of the organic sapropel layers to one another, and also to the Lago Grande di Monticchio climatic record.

7.5.2.2 The relationship of the tephra layers in the Mediterranean marine cores to the Lago Grande di Monticchio tephras.

As only major element data is available for the Aegean and the Ionian Seas (courtesy of Jorg Keller- unpublished data), trace element data cannot be used here for correlations.

The tephras TM24a and TM24b are both related to the marine tephra X5 in the literature (Bourne et al. 2010, Vogel et al. 2010, Allen et al. 1999). However, these two tephras are ~1000 years apart in the Lago Grande di Monticchio chronology (Wulf pers.com). This time difference may be insignificant for low resolution correlations, and it is actually less than the uncertainty on the radiometric age for the X5 tephra (105 ± 2ka). For high resolution (sub millennial) comparison of records however, it is important to attempt to determine which of these two Monticchio tephras relates to the marine tephras. TM27 is ruled out as a possible correlative for any of the Ionian Sea 'X5' tephra layers, as it has been correlated to the X6 tephra layers which are found stratigraphically below the X5 in the Ionian Sea (Keller et al. 1978 and Anna Bourne pers. comm). It has also been ruled out as a possible correlative for the Aegean 'X5' (LC21 7.915), on the evidence of the trace element concentrations in this thesis (fig. 7.13)

To uncover any elemental differences between TM24a and TM24b, 3 samples from these two layers were compared on all major and trace elements (figs 7.20 and 7.21) TM24a was split into TM24a-1 and TM24a 3+4, and sample TM24b-15 represents TM24b. These samples were selected by S. Wulf as the thickest layers in these two tephras and those most likely to relate to widespread, voluminous eruptions. Figures 7.20 and 7.21 show that only TM24a-3+4 can be distinguished from the other two samples through its more restricted composition and very slight differences in Si, Fe and Ca. TM24a-1 and TM24b-15 are indistinguishable on all elements, and have identical ranges. Therefore, if a marine tephra geochemically matches TM24a-3+4, we can be confident that it relates to TM24a. If it matches TM24a-1 and TM24b-15 we cannot yet be certain which of these is present in the marine record.

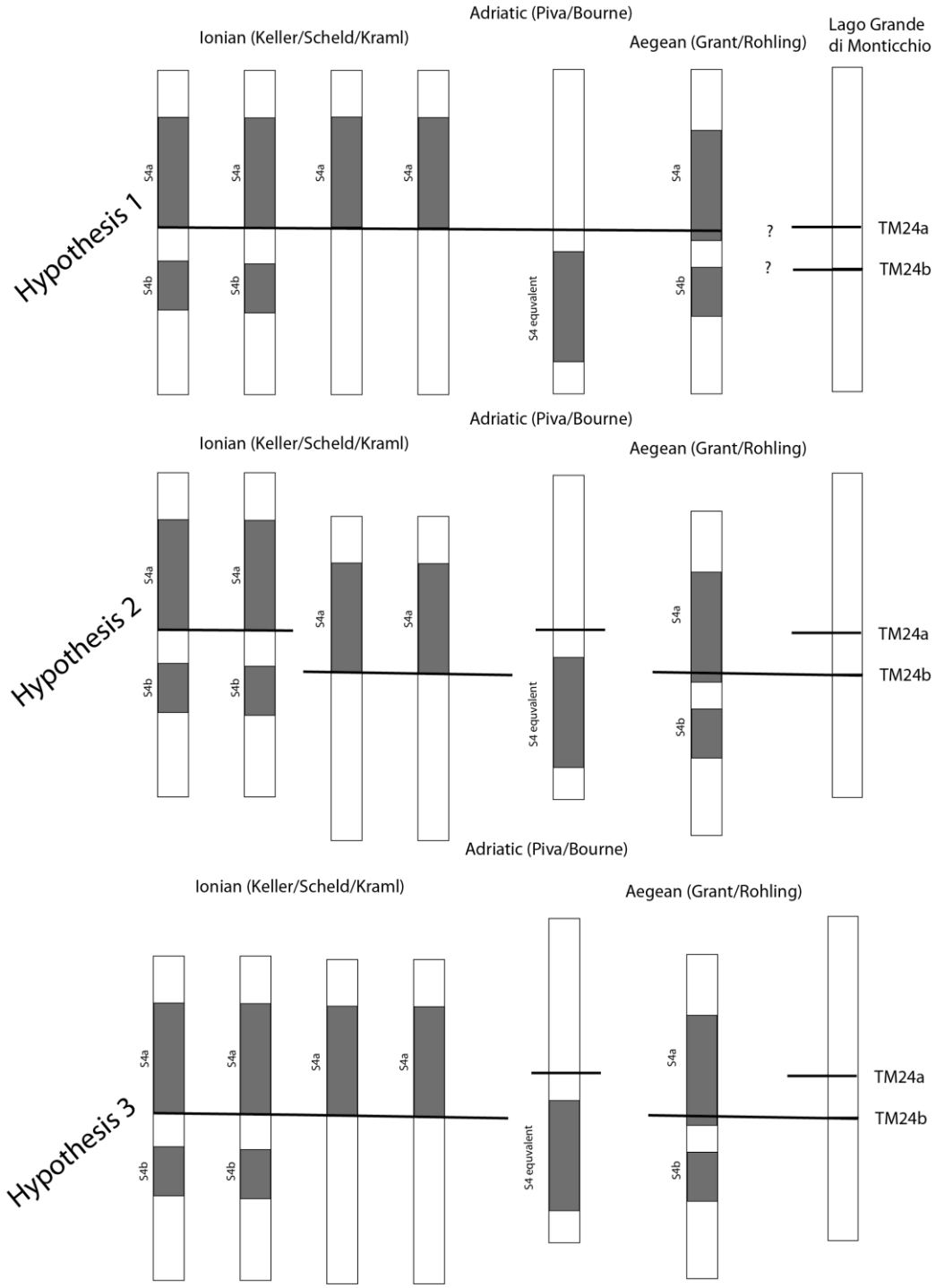

Figure 7.66 three likely hypotheses for the correlation of the tephras in and around sapropel S4 in the Ionian, Adriatic and Aegean Seas and the TM24 tephra layers of Lago Grande di Monticchio. Hypothesis 1- all the marine tephra layers correlate to one another and to either one of TM24a or TM24b. The implication if this hypothesis is true is that the Aegean Sea leads the Ionian sea in the formation of sapropels and that the Adriatic only preserves the equivalent of S4b. Hypothesis 2 states that some of the marine tephra layers correlate to TM24a and some to TM24b (there are multiple variants on this hypothesis), but with no consistency within a basin. The implications of this hypothesis are that sapropels are a-synchronous within a basin, and between basins. Hypothesis 3 states that the Ionian and Aegean Sea 'X5' tephras correlate with TM24b but that the 'X5' in the Adriatic correlates with TM24a. This hypothesis is predicated on the assumption that the sapropel stratigraphy synchronous (or almost synchronous) across the Mediterranean Sea. The implication is that sapropel formation in the Aegean Sea, slightly precludes that of the Ionian Sea, but that the formation of sapropels is synchronous within a basin.

The next step is to compare marine tephras designated as 'X5' to the Monticchio tephras. This geochemical comparison is shown in figure 7.67. Only major elements were available for many of the marine tephra layers. However, as the differences between the Monticchio tephras are in Si, Ca and Fe (fig. 7.67), these should be sufficient to test the correlations.

The data show that the Adriatic Sea 'X5' of Bourne et al. (2010) (PRAD 1-2 2517) correlates to the TM24a-3+4 sample, and that the 'X5' tephra layers of the Ionian and Aegean Seas, correlate with the TM24a-1 and TM24b-15 samples. So while the Adriatic tephra can be confidently assigned to TM24a, the Ionian and Aegean tephras are still unresolved between TM24a-1 and TM24b3+4 (fig. 7.67).

Extra information is available to resolve the correlation as the Aegean Sea sample LC21 (7.915) and some of the Ionian Sea samples contain an extra geochemical component (high Na_2O, low K_2O) not found in the LGdiM samples. The presence of this component in both the Aegean Sea and some of the Ionian Sea tephras supports the correlation of the 'X5' between these regions. This component is also found proximally, stratigraphically contemporary with tephra correlated to the Ionian Sea 'X5' (Albert pers.com). In addition, another tephra is found *above* this proximal 'X5' tephra (Albert, unpublished), which correlates to TM24a-3+4 (and also therefore to PRAD1-2- 2517). Therefore stratigraphically, the Ionian Sea and Aegean Sea 'X5' tephras cannot correlate with TM24a-1 and must therefore by default relate to TM24b-15, while the 'X5' tephra of the Adriatic (PRAD 1-2 2517 of Bourne et al. 2010) correlates to TM24a-3+4. These stratigraphic relationships demonstrates that scenario 3 in figure 7.66 must therefore be correct.

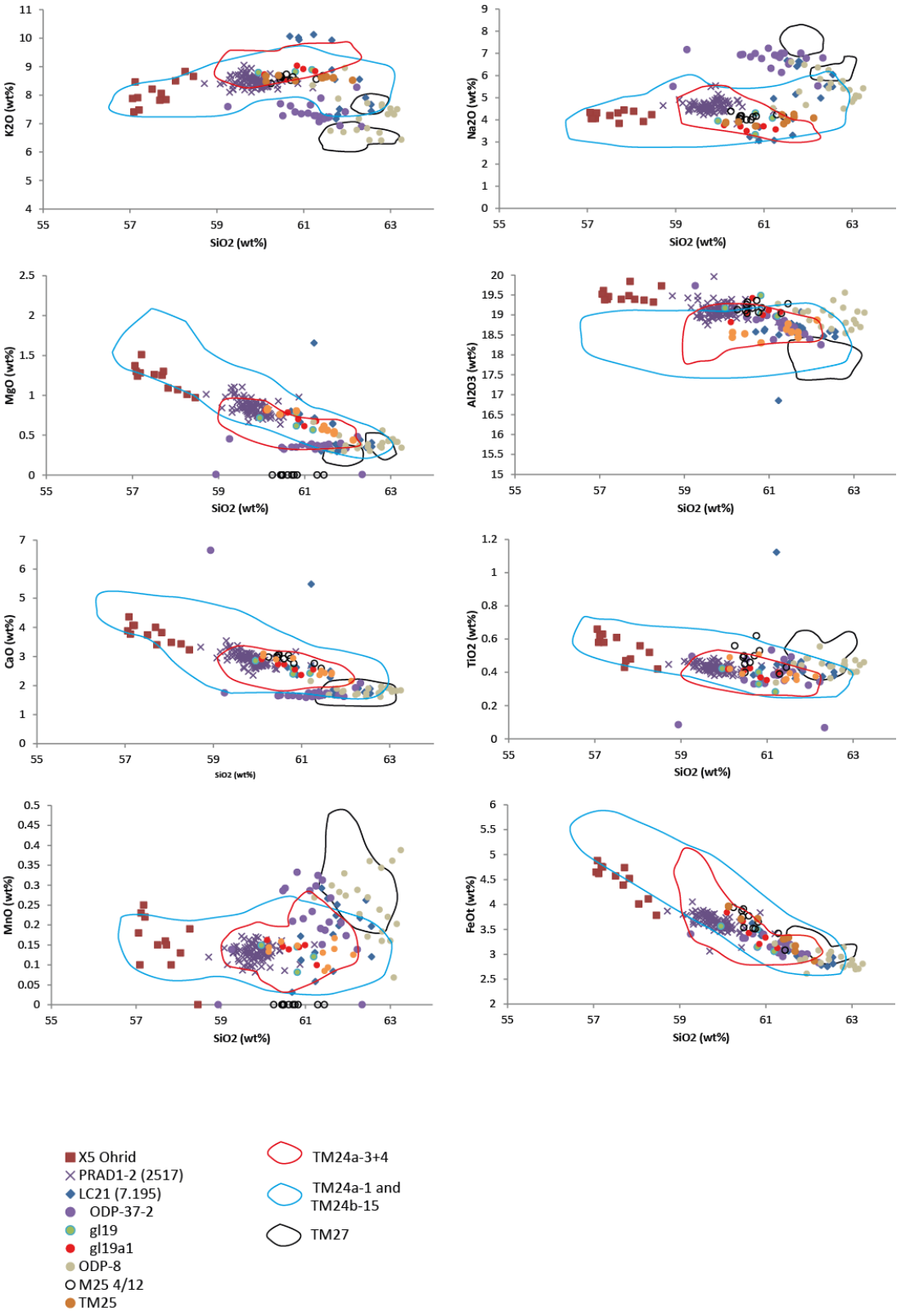

Figure 7.67 Major element data from 'X5' assigned tephras from various cores in the Adriatic, Aegean and Ionian Seas, and Lake Ohrid in Macedonia (Vogel et al. 2010) plotted with the data from TM24 tephra samples from Lago Grande did Monticchio produced in this study. TM24a-1 and TM24b-15 are indistinguishable and have thus been grouped together for clarity.

The implications of these correlations are important, both for tephrochronology, and for oceanography. In the case of the former, the result indicates that the tephra record in the Mediterranean can be very complicated, and that geochemically similar eruptions, when spaced closely in time, could potentially lead to incorrect correlations and, by extension, incorrect conclusions regarding the relationships of proxies between different sites. It also shows that a particular tephra can be preserved in one site but not in a site relatively close by.

An implication for Mediterranean oceanography is that the sapropels do not necessarily constitute absolutely synchronous marker horizons. This study shows that the Aegean sapropel S4a occurs (at least visually) before S4a in the Ionian Sea. The TM24b tephra occurs exactly at the base of S4a in the Ionian Sea, but actually within S4a in LC21 in the Aegean Sea. As S4a extends visually 1-2cm below TM24a in LC21, this implies (with a sedimentation rate of ~1cm= 47years from Casford et al. 2007) that the anoxic conditions of the Aegean occurred perhaps as much as 100 years before that of the Ionian Sea. This is consistent with the work of Marino et al. (2007), who conclude that anoxia in the deep Aegean Sea may precede that in the open Mediterranean Sea by 100 ± 40 to 300 ± 120 yr.

7.5.3 Tephras originating from Yali/Nisyros.

The tephra from the Yali/Nisyros system was found in core LC21.

The Yali-2 tephra.

Analysis of the proximal deposits of the Yali-2 eruption from the Nisyros Caldera allowed the assignation of distal tephra in sample LC21 (4.925) to this eruption. The sample has a date from our chronostratigraphy of ~34.75-34.86ka (table 6.1). Trace elements perfectly indicate a source from the Yali/Nisyros centre (fig. 7.2), and the stratigraphy of the Yali/Nisyros proximal deposits has been well documented (Allen and McPhee 2000) implying that this can be a confident correlation. A marine oxygen isotope stratigraphic age of 31 ka (Federman and Carey 1980, in Bachmann et al. 2010) has been assigned to the Yali-2 eruption due to a lack of appropriate material for proximal radiometric dating. Asku et al. (2008) cite an orbitally tuned age of ~35 ka for the Yali-2 tephra (Smith et al. 1996). The new age model for LC21 (Grant et al. 2012) defines an imported U-series age of ~34.75-34.86ka (table 6.1).

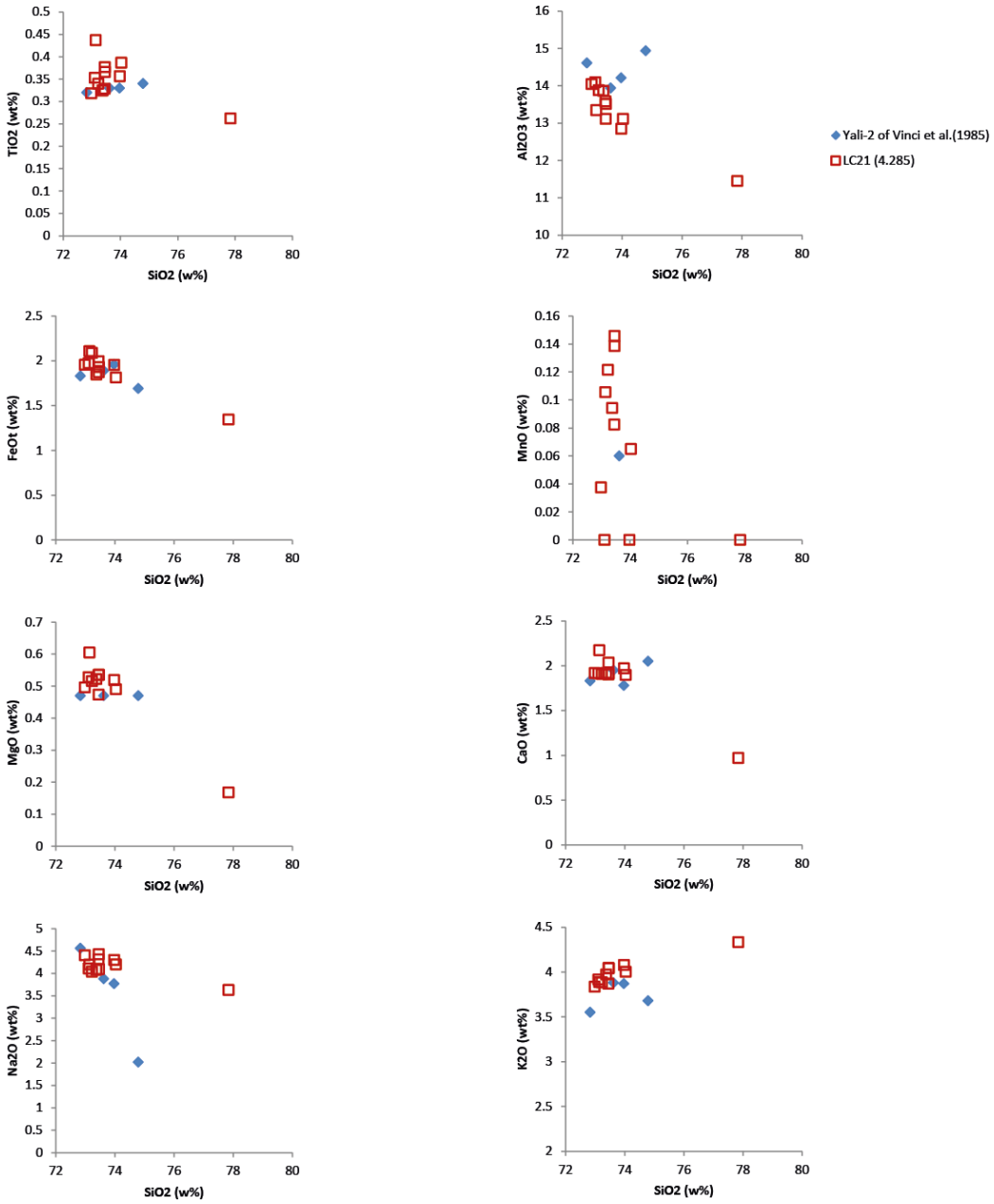

Figure 7.68 major element comparison of LC21 (4.285) with the geochemical data from shards attributed to the Yali-2 eruption of Yali from the literature (Vinci 1985).

The only single shard EPMA major element data available for comparison to that produced in this study is from Vinci et al. (1985), although the Yali-2 pumice has also been identified by Federman and Carey (1980) and Aksu et al. (2008). Federman and Carey describe a distribution to the south east of Yali, where the layer remains visible for about 300km distance from the Island (fig. 7.70),

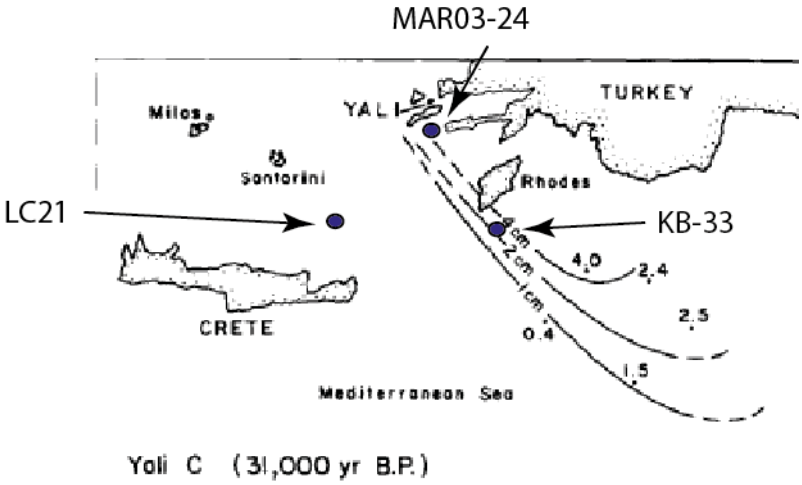

Figure 7.69 Map showing the reported extent of the Yali-2 tephra from Federman and Carey (1980), updated with the identification of the tephra in cores MAR-03-24 (Aksu et al. 2008), KB-33 (Vinci et al. 1985) and as a crypto-tephra in LC21 (this study).

7.5.4 Tephras originating from Kos or Central Anatolia

In all, 4 tephra layers (and another one which could represent contamination) have chemistries which are identical, and these are likely to originate from either Kos or Central Anatolia. Two of these tephras are in the Aegean core LC21 and two are from the Eastern Mediterranean core ODP967. The most likely source volcano for these tephra shards is Kos (as explained in chapters 7.2 and 7.3). As the chemistry of all four samples is identical, it is not possible to propose correlations between them based only on the geochemical evidence (as might be ideal). Thus other evidence (from the proxy record) must be employed to assess the likelihood of correlations.

It could be hypothesised, using the sapropel stratigraphy that ODP967 (7.640), which lies within sapropel S5 may correlate to one of the tephras within S5 in LC21. Both these tephra samples (LC21 9.575 and 9.709) are however considered to be derived from Santorini (see section 7.2), so while the deposition of these may indeed be nearly synchronous with ODP967 (7.640), they are impossible correlatives.

There is another tephra sample below S5 in LC21 does not have trace element analyses associated with it due to the small size of the shards. This sample (LC21 10.345) contains a minor component of shards of Pantellerite, which can be derived only from the Island of Pantelleria. However, the major component of this sample shows the same high silica values as ODP967 (7.640), and is consistent with it on all 9 major elements (fig. 7.35). It is

possible that these two tephras are correlatives, but unfortunately the hypothesis cannot be further interrogated without attaining trace element analyses.

Should these two tephras be correlatives, then the implications for the stratigraphy would be as follows:

Sapropel 5 would be demonstrably a-synchronous between ODP967 (E.Med) and LC21 (Aegean Sea), as the deposition would start pre- ODP967 (7.640) in the Eastern Mediterranean Sea, and post LC21 (10.345) the Aegean Sea. This would contradict or at least complicate the assertion of Marino et al. (2007) that the Aegean Sea is the driver of sapropel formation in the Mediterranean as it would implicate that sapropel 5 started to form in the Eastern Med before it started in the Aegean.

The isotope (planktonic foram $\delta^{18}O$) stratigraphies for the two cores are hard to reconcile if these two tephra samples are correlated to one another. ODP967 (7.640) is associated with isotopically high values (warm SST), but LC21 (10.345) is associated with very low (cold SST) isotope values (cf. fig. 6.17 and 6.3). While it is the marine proxy record which should be tested using the tephra, it is hard to imagine a mechanism which might cause such an enormous vast disparity in isotopic values between the Aegean and the Eastern Mediterranean.

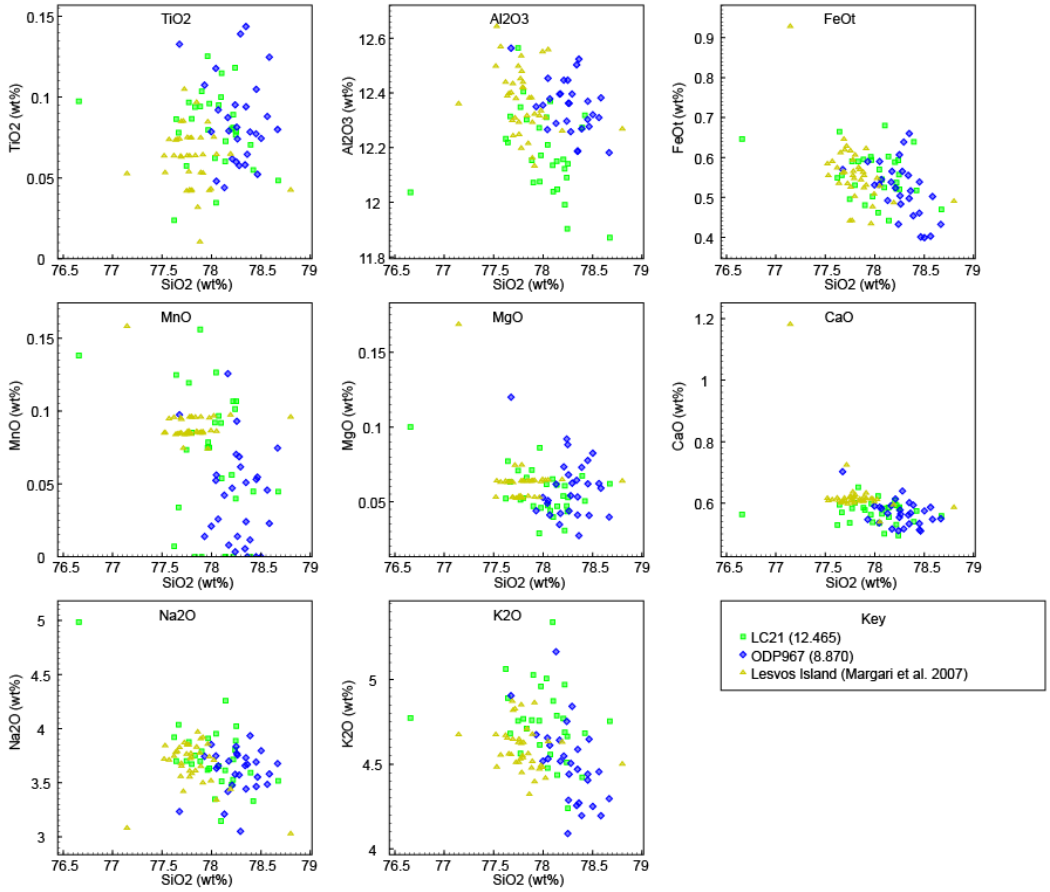

Figure 7.70 Major element comparison of tephra shards from LC21 (12.465), ODP967 (8.870) and the Kos Plateau Tuff from Lesvos Island (ML6 of Margari et al. 2007).

The geochemistry of ODP967 (7.640) is also coincident with LC21 (12.465) (figs 7.35 and 7.36). The major and trace element geochemistry thus supports the hypothesis that these two samples correlate. This hypothesis is however hard to reconcile with the stratigraphic positions of these two samples in their respective cores. ODP967 (7.640) lies within sapropel S5, while LC21 (12.465) lies over 2m below S5 in ODP967 and is dated at >152ka by the LC21 age model. Sapropel 5 is dated at ~122-127ka in LC21. While the age from the LC21 age model is an estimate which relies on the accurate correlation of two isotope stratigraphies, it is very unlikely that it is wrong by 20-30ka, given that it predicts an age 133ka for the P-11 tephra in LC21 which is indistinguishable from the radiometric age for this eruption.

Alternatively, if the two tephras originate from different sources, one from the Island of Kos, and the other from the Central Anatolian system) the striking geochemical similarity of these two deposits may suggest a geochemical link between these two volcanic centres. Perhaps both are fed by the same magma at depth or are produced by very similar

processes. More work on the proximal deposits of both centres is required to explore this idea.

If any of these tephras did originate from Turkey, it would be only the second Turkish tephra to be discovered in the Eastern Mediterranean Sea. Hamann et al. (2011) discovered a visible, early Holocene tephra which they correlated to the Central Anatolian Dikkarin eruption at ~8.8ka. These tephras have the potential to link archaeological records, or terrestrial environmental records from Turkey and possibly Cyprus (which lies between the Turkish mainland and ODP967) directly to marine cores in the Eastern Mediterranean Sea.

7.5.5 Tephras originating from Pantelleria.

The distinctive chemistry of tephra shards originating from Pantelleria was found only in shards from core LC21. Five shards in sample LC21 (10.345) are of Pantellerite composition (FeOt 6-8%, Al_2O_3 8-10%). These shards are unmistakably derived from Pantelleria. They are found in this sample with rhyolitic shards, which may originate from Yali/Nisyros and are discussed in section 7.5.4 below. The stratigraphy of Pantelleria prior to the Green Tuff (45-50ka Cornette et al.1983, White et al.2009, Avanzinelli et al.2004) is not well studied. However, the marine tephra P-11 is attributed to Pantelleria (Paterne et al. 2008) and is dated (by the orbital tuning method) to ~133ka. This tephra is also found in the Albanian lake core from Lake Ohrid (Vogel et al. 2010), and likely on the north Aegean island of Lesvos, although this tephra (ML5 from Margari et al. 2007) is misidentified as the Green Tuff (Vogel et al. 2010). TM22 from Lago Grande Di Monticchio (Wulf et al. 2004) is also assigned to the Ante-Green Tuff from Pantelleria, and is dated at 85,320 by their varve supported chronology.

The best stratigraphy for a comparison to the tephra shards discovered here is the marine core stratigraphy of Tamburrino et al. (2012). This is located just offshore from the Island of Pantelleria and should thus provide a detailed stratigraphy of the islands eruptions. Three of the tephras found in Tamburrino et al. (2012) are candidates to correlate with LC21 (10.345). These are ODP2,3 and 4 and the major elements are shown together with LC21 (10.345) and the P-11 as assigned in Lake Ohrid (Vogel et al. 2010) in figure 7.71

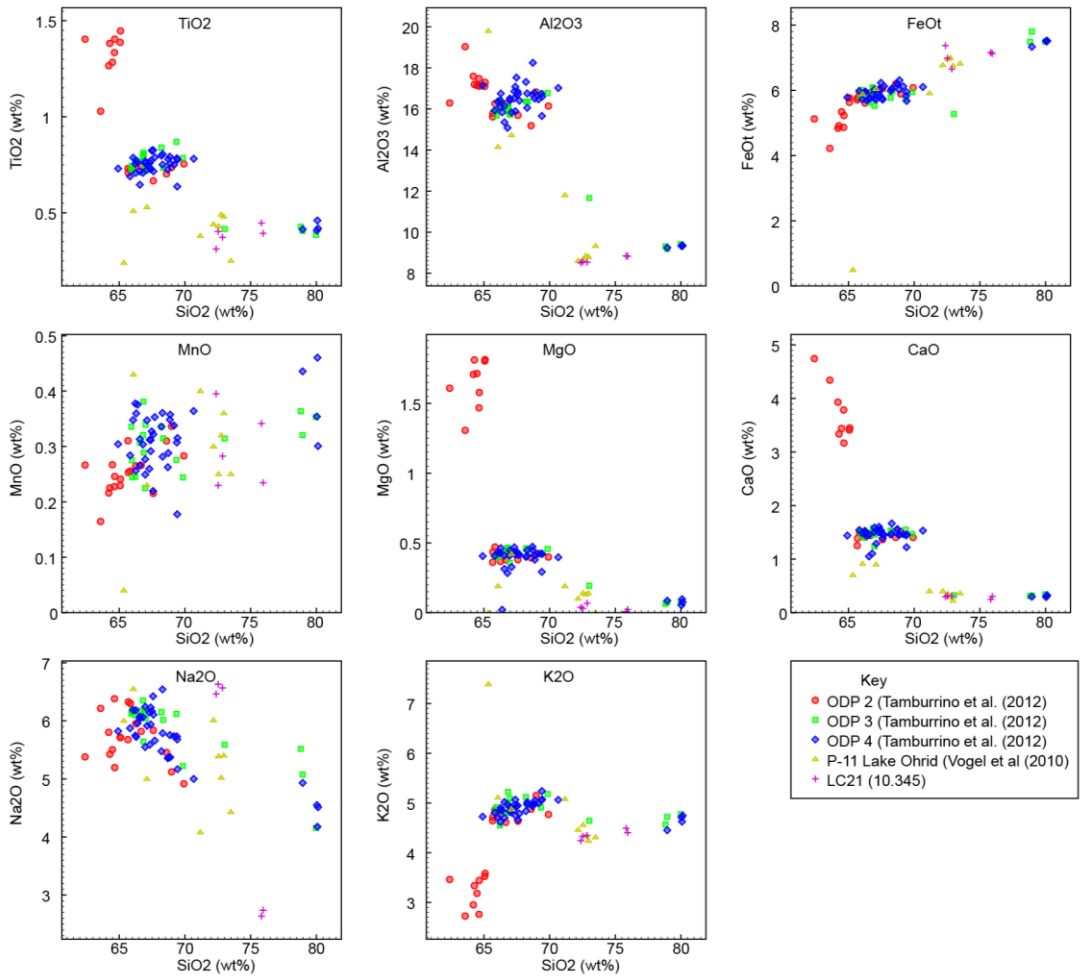

Figure 7.71 Major element comparison of shards attributed to the P-11 tephra from Lake Ohrid, tephra layers ODP2,3 and 4 from Tamburrion et al. (2012) and shards derived from Pantelleria, in LC21 (10.345) (this study).

The Pantellerite shards from LC21 (10.345) and Lake Ohrid (Vogel et al. 2010) overlap in geochemical composition with one shard of ODP3 of Tamburrino et al. (2012 which is attributed there to the P-11 tephra of Paterne et al. (2008). Although tenuous, this is the best match of the three tephra layer options from Tamburrino et al. (2012). ODP3 does however have additional higher and lower SiO_2 components to LC21 (10.345), and an additional higher SiO_2 component to the Lake Ohrid 'P-11'. This evidence indicates that the geochemistry of the Pantellerian products is diverse, and may not be identical across a range of sites, a severe hindrance to the application of tephrostratigraphy. ODP3 is dated by the oxygen isotope stratigraphy of Tamburrio et al. (2012) to 128.1ka, the P-11 of Paterne et al. (2008) is dated 130.6ka, and the Unit-P (to which ODP3 is correlated by Tamburrino et al 2008) is dated by the ^{40}Ar:^{40}Ar method to 132.3 ± 5.7ka to 133.5 ± 6.2 ka. LC21 (10.345) is dated at ~133ka by the imported age U-series age model of Grant et al. (2012). These dates are broadly in agreement and corroborate the geochemical evidence for the identification of LC21 (10.345) as the P-11 tephra layer.

7.5.6 Tephras of Unknown Origin.

The single tephra shard found at 3-4cm depth in core ODP975 is of unknown origin. Possible sources include Iceland, the Canary Islands and the French Massive Central. Iceland is thought here to be the most likely origin (as discussed in chapter 7.4). The origin of this tephra shard would be intriguing to confirm as, if it is derived from Iceland it could corroborate observations of recent ash plumes from both the Grimsvotn and Eyjafjallajökull volcanoes (Langmann et al. 2012, Matthias et al. 2012), and be the first evidence from the palaeo-record that Icelandic tephra plumes travelled as far as the Mediterranean Sea. It is in itself the first evidence of tephra in the Western Mediterranean Sea.

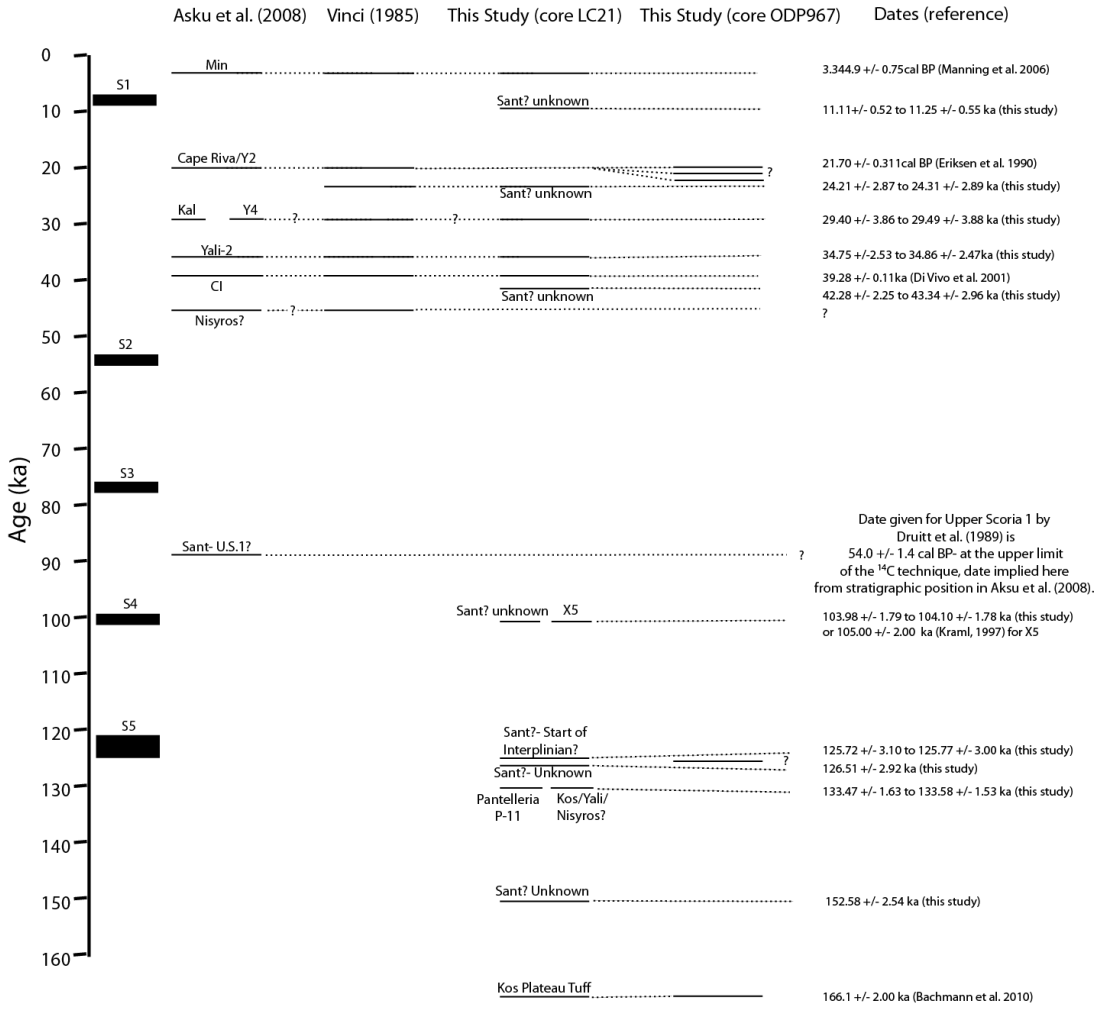

Figure 7.72 A composite tephrostratigraphy for the Aegean and the Eastern Mediterranean Sea, merging the work of Aksu et al. (2008) and Vinci et al. (1985) with this study. NB there is no stratigraphic control to relate the chronological order of tephras where they are inferred by dotted lines. The positions of the tephra layers in these cases are related on the basis of the available dating evidence.

8. Synthesis, suggestions for further work and conclusions.

8.1 Reappraisal of the thesis aims.

This thesis set out four aims in chapter 1. These are re-stated below together with a synopsis of the degree to which each of these has been met.

Aim 1 - to contribute to an assessment of the geographical extent of Mediterranean volcanic products. *The distribution of the tephra found in this investigation will be placed in the context of those already known from the literature.*

The study identified 22 tephra deposits in Mediterranean marine cores, representing 18 to 20 separate eruptions originating from Santorini (12 eruptions), Kos/Yali/Nisyros (3 or 4 eruptions), Campania (2 or 3 eruptions), Pantelleria (1 eruption), and one possible eruption from Iceland represented by a single tephra shard only. These tephra layers were set within the context of those already published in the literature, contributing to an assessment of the geographical distribution of volcanic products in the Mediterranean.

Aim 2 - to initiate the development of a regional tephrostratigraphy for the eastern Mediterranean. *This will help future investigators to identify the tephras preserved in their records, and to subsequently link those records into a regional tephrostratigraphic framework or lattice. Such a lattice could allow an assessment of the synchronicity (or otherwise) of some of the environmental events or archaeological information in the various records.*

This thesis represents the first cryptotephra investigation of Eastern Mediterranean marine sediments. As such it has geochemically characterised 11 previously undiscovered tephra layers and extended the known range of 2 other tephra layers (one from Campania, the other from Pantelleria) into the eastern Mediterranean Sea. It has also provided the first trace element concentration assessments for 7 tephra layers which were previously characterised only by their major element concentrations. These discoveries and analyses have been integrated with the literature to develop an embryonic tephrostratigraphy for the Eastern Mediterranean Sea (fig 7.72).

Aim 3 - to develop and test a regional tephrochronology for the Eastern Mediterranean. *Such a chronology would a) allow dates to be imported into all other records where the known tephras are found and b) provide dates for the often poorly dated volcanic events of the region. Aim 3 thus has an environmental application and a volcanological application.*

Aim 3 has not been fully met. Only three of the tephra layers characterised in this study had proximally defined radiometric dates and geochemistry to which the distal deposits could be compared. These were the Minoan eruption of Santorini, the Campanian Ignimbrite and the Kos Plateau Tuff. All of these were found in core LC21 but the construction of an age model spanning 161ka using only 3 dates would not yield any reliable dating information for other events (environmental or volcanic) recorded within the core. Instead, an imported U-series age model for LC21 was constructed by Grant et al. (2012) by tying the $\delta^{18}O$ record for LC21 to the $\delta^{18}O$ record of Soreq cave, Israel, with the aid of the precisely dated Minoan and Campanian Ignimbrite tephra layers as additional tie points. This age model defined ages and modelled uncertainties for all the other tephra layers found within LC21 (Table 6.1) and thus addresses aim 1.2.3b for LC21. No age models were created for ODP967 or ODP975 due to both the lack of radiometric dates and tephra layers which could be confidently assigned to dated volcanic eruptions. The unknown tephra layers in these records could not therefore be assigned dates.

Aim 4 - to develop synchronised age models for each of the cores investigated *and to subsequently compare dates produced for oceanographic events of interest.*

As it was only possible to generate an age model for one of the core sequences (LC21) studied, and no tephra layers were found to be common to two or more of the cores with associated proxy records, it was not possible to synchronise the proxy records for the cores using tephra layers.

However, an important and kind provision of geochemical and stratigraphic data by Jorg Keller relating the X5 tephra layer in the Ionian Sea to the visible depth of sapropel 4 in the same cores allowed an initial investigation into the chronological relationship of the sapropel between the Aegean and Ionian Seas. The fortuitous position of this tephra (the marine defined X-5 tephra) close to the base of sapropel S4a allowed the inference that the formation of the sapropel (anoxia of the bottom water) is not synchronous across all the basins of the Mediterranean. The Aegean appears to precede the Ionian Sea in anoxia by about 100 years. This tephra layer correlation needs to be tested further with the

acquisition of trace element geochemistry from the Ionian Sea X-5 deposits of Keller et al. (1978)

8.2. The contribution of this thesis to the earth sciences.

The work presented in this thesis yielded several important new results, each contributing new knowledge or ideas to a different realm of the earth sciences. Several of the tephra layers presented for the first time in this thesis are evidence of hitherto unstudied, most likely inter-plinian, eruptions of Santorini. These data can therefore potentially contribute to the volcanic and petrogenic history of the island. This has been demonstrated here with a comparison of the proximal data for the caldera-forming Minoan eruption (chapter 8). The Santorini derived tephra layers found in LC21 and ODP967 were compared to the magma batch model for Santorini proposed by Druitt et al. (2012). This distal tephra data from the ocean cores implies that the chemistry of the Minoan eruption was not unique in the history of Santorini, and that the 3 magma sources of Druitt et al. (2012) cannot explain the geochemistry of all the eruptive products from the island. The marine cores show evidence of more eruptions of Santorini than are evidenced by the proximal stratigraphy. This implies that marine cores are vitally important repositories of volcanic ejecta and should form a standard part of future volcanological studies.

This thesis investigated a marine core (ODP975) in the Western Mediterranean. The core yielded four possible tephra shards, two of which were confirmed by EPMA analysis. The first of these is most likely from Iceland, and could represent the first evidence of Icelandic ash reaching the Western Mediterranean Sea (albeit in very low concentrations). This raises the possibility that the North Atlantic proxy records (where Icelandic tephras abound) and the Mediterranean Sea proxy records may be able to be directly correlated, using tephra layers. The tephra shard is unlikely to represent laboratory contamination, for the reasons outlined in section 7.4. The second shard is most likely from the Italian Campanian volcanic system, and similarly may represent the first evidence of volcanic products from Italy to be preserved to the west of Sardinia. This discovery implies that it may be possible to link the Eastern and the Western Mediterranean seas using tephrostratigraphy.

8.3 Problems encountered during the research

8.3.1 Multiple tephra layers with identical geochemical compositions.

Marine core ODP967 shows 3 tephra layers of identical chemical composition (that of Santorini's Cape Riva eruption), very closely spaced in time. It is impossible to determine which of these distal tephra layers represents the proximal (dated) Cape Riva deposits without further dating information (most likely from radiocarbon dating of the foraminifera). Intuitively one might suggest that this is only a problem where the environmental events of interest must be resolved at a higher chronological resolution than the time period represented by the multiple, identical tephra layers. However, once one of the foundation principles of tephrochronology (that every eruption has a unique chemical composition) is challenged, the reliability of tephra layers for the dating and correlation of records is dramatically compromised.

This is a very severe impediment to tephrochronology and tephrostratigraphy. It is not possible to use any of those repeated tephra layers as a chronological or stratigraphic markers. Of greatest concern is that there are potentially many more (as yet undiscovered) tephra layers with identical geochemistry, but different dates, to the deposits which are currently known. Potentially, therefore no tephra layer is a reliable chronological or stratigraphic marker. In radiometric chronological techniques, the more knowledge that is gained the better the method is understood and the more precise and accurate the technique becomes. This cannot presently happen for tephrochronology however as we do not know for certain if two geochemically identical deposits originate from the same eruption. In the short term future of tephrostratigraphy, the more tephra layers that are discovered, the less precise the technique will become. "Unknown unknowns" are very significant in tephrochronology; how do we know what is yet to be discovered? This problem is also cited by Blaauw et al. (2012) with reference to dating via the tuning of proxy records. "Unknown unknowns" are a major problem for any dating technique which relies on correlations.

Smith et al. (2011) also encountered the problem of identical glass phase geochemical compositions for the eruptions of Toba, and went some way to addressing the issue by using biotite phenocrysts compositions instead of the geochemistry of the glass. The three eruptions which they investigate span >700ka however, which is ample time for the

chemistry of phenocrysts to change and is also an unlikely timescale for which tephrochronology could provide useful information. In the present study the three identical tephra layers probably span no more than 2ka (a period of time over which tephrochronology should, in theory, be highly useful) which leaves very little time for a significant change in either the glass or the phenocrysts compositions. In addition the work of Smith et al. (2011) relies on the presence of phenocrysts in the distal glass shards. These are not present in most crypto-tephra shards.

8.3.2 Differences between the geochemical analyses of proximal and distal tephra deposits.

During this study the Minoan eruption was identified both in marine core LC21 and in the proximal volcanic stratigraphy of Santorini. The correlation of the two deposits is highly likely, given the dating and depth information alone. A comparison of the proximal and distal geochemical compositions shows that the proximal deposits are mostly rhyodacitic in composition, with a very rare rhyolitic component, while the distal deposits are entirely comprised of the rhyolitic component. The deposits of the Minoan eruption are the best preserved and by far the most abundant deposits in the proximal stratigraphy (Druitt et al. 1989, 1999, 2012). Had the very rare rhyolitic component not been preserved proximally, there would be no geochemical justification for correlating these two deposits. It is entirely possible that this is the case for other, older eruptions with less well preserved proximal deposits. An extension of this problem of proximal-distal differences in chemical composition is that geochemically different distal tephra deposits could originate from the same eruption.

8.3.3 Differences in the geochemical composition of deposits from a single eruption between sites.

Just as it is possible for there to be differences in the geochemical composition of deposits from one eruption, between the proximal stratigraphy and a distal stratigraphy, it has been shown here that the Campanian Ignimbrite tephra layer has a different geochemical composition in the Adriatic Sea (Bourne et al. 2010) to the Aegean Sea (this study). The two can only be correlated with knowledge of the proximal geochemistry (fig 7.60). The result implies that the comprehensive sampling and analysis of proximal volcanic stratigraphies is crucial to tephrochronology.

8.3.4 The absence of deposits from apparently very voluminous, Plinian eruptions in a marine core close to the source volcano.

The work completed on marine core LC21 shows that the Plinian Cape Riva, Upper Scoria 2, Upper Scoria 1 and Vourvolous eruptions are not represented in this marine core, despite it being only ~100km from the volcano. The identification of the Cape Riva eruption as a visible tephra layer in the Sea of Marmara and the Black Sea, up to 1,100km from the volcano (Wulf et al. 2002 and pers.comm.) indicates that the deposition of tephra layers is highly geographically variable and that the deposition of ash is probably highly dependent on wind direction. This result shows that it is difficult to predict which records may be fruitful for cryptotephra studies. As such a study can be labour, time, materials and money intensive, the selection of a site can be highly risky.

8.4 Suggestions for further work

8.4.1 Construction of volcanic stratigraphies.

In order to remove the latent uncertainties described above, a comprehensive knowledge of the eruptive histories for each volcano must first be defined. Marine cores surrounding the volcanoes provide an excellent opportunity to build up these volcanic histories for island volcanoes such as Santorini (this study), Pantelleria (Tamburrino et al. 2012), or Iceland (Guðmundsdóttir et al. 2011). The cores could be tied together using the marine proxy records, which can safely be assumed to be synchronous over short distances. This work could be integrated with work on the proximal deposits to define a comprehensive record of ash production from each volcano. Only after this work is complete can we confidently use tephra layers as isochrons, and make inferences about the synchronicity of proxy records.

Comprehensive crypto and visible tephra work on marine cores taken from locations surrounding Santorini is needed to compose a complete volcanic stratigraphy for the island. As any tephra layers found could be dated using the oxygen isotope stratigraphy and with an imported U-series chronology from Soreq cave, the resulting tephrostratigraphy would comprise a fully dated geochemical record of volcanic activity on Santorini. Such a record would also infer the plume directions for each of the eruptions.

Such a detailed volcanic history has never before been constructed for any of the world's volcanoes and may be crucial for defining magma eruption rates and (as attempted in this

thesis) magmatic plumbing systems. In addition, as marine cores also preserve climatic proxy records, this work could be vital to investigations of relationships between volcanic activity and climate. It is suggested here therefore that marine core tephra work should, where possible, be included as part of volcanic history research projects.

None of the problems elucidated for tephra based correlations in section 8.3 impinge on the construction of volcanic histories. The more tephra layers we discover, the more complete the knowledge of a volcanic system becomes. This contrasts with the use of tephra layers for dating or for correlation purposes where the more layers we discover, the greater the uncertainty associated with the date or correlation.

8.4.2 Tephra investigations in the Western Mediterranean Sea.

This study recovered and analysed two tephra shards from the Western Mediterranean core ODP975. These shards are most likely derived from Iceland and Campania. This core is only the second record in which shards from both of these volcanic systems have been found (the first is Lake Bled in Slovenia- Lane et al. 2011). The core hints that the Western Mediterranean Sea may be a suitable place to relate the volcanic histories of Iceland and Italy. In addition, notwithstanding the problems expounded in section 8.2, any Icelandic tephra found in the sediments of the Western Mediterranean could be used to link the western Mediterranean proxy records with those of the North Atlantic and possibly the Greenland ice cores. Such a comparison would be the first independent comparison of proxy records between the important environmental records.

Icelandic tephra may be more abundant in the more northern cores of the Mediterranean, while Campanian tephra shards should be more abundant closer to Italy. A good core location would therefore be off the western coast of Sardinia or Corsica, or in the Gulf of Lions.

8.4.3- Contribution to the RESET project and suggestions for the progression of the project.

This PhD has revealed several tephra layers which may correlate to tephra layers discovered in other sites by co-workers on the RESET project. Tephra layers geochemically matching the Campanian Ignimbrite were discovered in archaeological and terrestrial environmental records in the Eastern Mediterranean, allowing the proxy record from

marine core LC21 from this study to be linked to these sites (Lowe et al. 2012). This showed that the Neanderthals and Modern Humans were not directly affected by either the CI eruption itself, or the climatic cooling around this time. If the single shard in Western Mediterranean marine core ODP975 relating to the Campanian Ignimbrite could be corroborated by more work on cores close by, then the proxy record from this site could similarly be compared to these same archaeological and terrestrial environmental sites.

Four tephra layers matching the Cape Riva proximal deposits were found by M. Hardiman (RHUL) in the Phillippi Basin in Northern Greece, and he identified a further two in a core from Lesvos Island. These Cape Riva-like tephras can be added to the three found in ODP967 in this study, to corroborate the assertion made here that different eruptions from one volcano can have identical geochemical attributes. These tephra layers may with more dating work contribute to the volcanic history of Santorini.

Tephra shards matching LC21 (12.465), the Kos Plateau Tuff were found in Lesvos by M. Hardiman (RHUL). The Lesvos terrestrial proxy record could therefore be directly compared with both the proxy record from marine cores LC21 and ODP967, where this tephra layer is also found.

Shards relating to the P-11 tephra layer were identified in LC21, and also on the island of Lesvos by M. Hardiman (RHUL), and in Klissora Cave archaeological record on mainland Greece by D. White (Natural History Museum). This eruption could potentially therefore link the Neanderthal archaeology at Klissora with an environmental record.

8.5 Conclusions.

This thesis has investigated the tephrostratigraphies of three Late Quaternary, Mediterranean marine sediment cores. 22 tephra layers were discovered in these cores, corresponding to 19 volcanic eruptions. 11 of these eruptions are characterised for the first time here. The study shows that, at present, there are significant problems with using tephra layers as coherent stratigraphic markers. The problems outlined in section 8.2 currently preclude the use of tephra layers as reliable isochrons. However, if comprehensive volcanic stratigraphies can be constructed (as is attempted in this thesis for Santorini) then many of these problems will be addressed.

It has been shown that marine cores can provide excellent volcanic stratigraphies. A comprehensive study of several cores surrounding an island volcano such as Santorini could

provide a highly detailed geochemical and chronological volcanic history for the island. As a result of this construction, the ash layers could then be confidently used as isochrons to link the proxy records of environmental and archaeological sites. Such a history would also be invaluable for volcanologists who are interested in defining magma eruption and recharge rates, and those interested in hazard assessments. In particular, the use of the high field strength elements to define the source magma batch within a volcanic system has been demonstrated here for Santorini. Sr, Ti and Mg from plagioclase analyses can be used to provide further information on the depth history of a particular magma batch (Druitt et al. 2012).

This study has also extended the geographical extent of crypto-tephra studies into the Eastern and Western Mediterranean Seas. The Eastern Mediterranean preserves eruptions from Santorini, Kos and Central Anatolia (Hamann et al. 2010) while the Western sediments studied here yielded two shards of tephra, one most likely derived from Iceland and the other from Campania in Italy.

This tephra study has uncovered previously unknown complications in the use of tephra layers as dating markers or stratigraphic correlation tools. It has also explored the application of tephra layers preserved in marine cores (particularly crypto-tephra layers) to volcanology and implies that important information about volcanic systems may be revealed though this method.

References.

Alban Defleur. A, White. T., Valensi. P., Slimak. L. and Cre´gut-Bonnoure. E. (2006) Neanderthal Cannibalism at Moula-Guercy, Arde`che, France. *Science* **286** pp128–31.

Albert.P.G.; Tomlinson.E.L.; Smith.V.C.; Di Roberto.A.; Todman.A.; Rosi.M.; Marani.M.; Muller.W. and Menzies.M.A. (2012) Marine-continental tephra correlations: Volcanic glass geochemistry from the Marsili Basin and the Aeolian Islands, Southern Tyrrhenian Sea, Italy. *Journal of Volcanology and Geothermal Research* **229-230** pp74-94.

Alici.P.; Temel.A.; Gourgaud.A. (2002) Pb-Nd-Sr isotope and trace element geochemistry of Quaternary extension-related alkaine volcanism: a case study of Kula region (western Anatolia, Turkey). *Journal of Volcanology and Geothermal Research* **115** pp487-510.

Allen.S.R. and Cas.R.A.F. (1998) Rhyolitic fallout and pyroclastic density current deposits from a phreatoplinian eruption in the eastern Aegean Sea, Greece. *Journal of Volcanology and Geothermal Research*. **86** pp219-251.

Allen.S.R.; Stadlbauer.E. and Keller.J. (1999) Stratigraphy of the Kos Plateau Tuff: product of a major Quaternary explosive rhyolitic eruption in the eastern Aegean, Greece. *International Journal of Earth Sciences* **88** pp132-156.

Allen.S.R. and McPhie.J. (2000) Water-settling and resedimentation of submarine rhyolitic pumice at Yali, eastern Aegean, Greece. *Journal of Volcanology and Geothermal Research*. **95** pp285-307.

Allen.J.M.; Brandt.U.; Brauer.A.; Hubberten.H-W; Huntley.B.; Keller.J.; Kraml.M.; Mackensen.A.; Mingram.J.; Negenbank.J.F.W.; Norwaczyk.N.R.; Oberhansli.H.; Watts.W.A. Wulf.S. and Zolitschka.B. (1999) Rapid environmental changes in the southern Europe during the last interglacial period. *Nature* **400** pp740-743.

Alvarez-Marron.J. (1999) Pliocene to Holocene structure of the eastern Alboran Sea (Western Mediterranean) *Proceedings of the Ocean Drilling Program* **161** pp 345-355

Appenzeller.C.; Stocker.T.F. and Anklin.M. (1998) North Atlantic Oscillation Dynamics Recorded in Greenland Ice Cores. *Science* **282** pp446-449.

Avanzinelli.R.; Bindi.L.; Menchetti.S. and Conticelli.S. (2003) Crystalisation and genesis of peralkaline magmas from Pantelleria Volcano, Italy: an integrated petrological and crystal-chemical study. *Lithos* **73** pp41-69.

Aydar.E. (1998) Early Miocene to Quaternary evolution of volcanism and basin formation in western Anatolia: a review. *Journal of Volcanology and Geothermal Research* **85** pp 69-82

Bachmann.O.; Schoene.B.; Schnyder.C. and Spikings.R. (2010) The $^{40}Ar/^{39}Ar$ and U/Pb dating of young rhyolites in the Kos-Nisyros volcanic complex, Eastern Aegean Arc, Greece: Age discordance due to excess ^{40}Ar in biotite. *Geochemistry, Geophysics, Geosystems*. **11** pp1525-2027.

Bachmann.O.; Charlier.B.L.A.; Lowenstern.J.B.; (2007) Zircon crystallisation and recycling in the magma chamber of the Kos Plateau Tuff (Aegean Arc). *Geology* **35** pp73-76.

Banks.W.E.; d'Errico.F.; Townsend Peterson.A.; Kageyama.M.; Sima.A. and Sanchez-Goni M-F. (2008)Neanderthal extinction by competitive exclusion. *PLoS One* **3** e3972.

Barrat.J.A.; Keller.F.; Amosse.J.; Taylor.R.N.; Nesbitt.R.W. and Hirta.T. (2007) "Determination of rare earth elements in sixteen silicate reference samples by ICP-MS after Tm addition and ion exchange separation." *Geostandards and Geoanalytical Research.* **20** pp133-139.

Bar-Matthews.M.; Ayalon.A.; Kaufman.A. (2000) Timing and hydrological condition ofSapropel events in the eastern Mediterranean, as evident from speleothems, Soreq cave, Israel. *Chemical Geology* **169** pp145-156.

Barker.S.; Knorr.G.; Edwards.L.R.; Parrenin.F.; Putnam.A.E.; Skinner.L.C.; Wolff.E. and Ziegler.M. (2011) 800,000years of abrupt climate variability. *Science* **334** pp347-351.

Beaulieu.J.L.; Tzedakis.P.; Ponel.P. and Frederic.G. (2007) Pollen records, Late Pleistocene/Southern Europe. *Encyclopaedia of Quaternary Science* pp 2661-2668.

Bigazzi.G.; Yegingil.Z.; Ercan.T.; Oddone.M. and Ozdogan.M. (1993) Fission track dating obsidian in Central and N. Anatolia. *Bulletin of Volcanology*. **55** p588-595.

Blaauw.M. (2012) Out of tune: the dangers of aligning proxy archives. *Quaternary Science Reviews* **36** pp38-49.

Blockley.S.P.E.; Pyne-O' Donnel, Lowe.J.J. Matthews.I.P., Stone.A., Pollard.A.M., Turney.C.S.M. and Molyneux.E.G. (2005) A new and less destructive laboratory procedure for the physical separation of distal glass shards from sediments. *Quaternary Science Reviews* **24** pp1952-1960.

Bourne.A.; Lowe.J.J.; Trincardi.F.; Asioli.A.; Blockley.S.P.E.; Wulf.S.; Matthews.I.P.; Piva.A. and Vigliotti.L. (2010) Distal tephra record for the last ca 105,000 years from core PRAD 1-2 in the central Adriatic Sea: implications for marine tephrostratigraphy. *Quaternary Science Reviews* **29** pp3079-3094.

Bond.G.; Broeker.W.; Johnsen.S.; McManus.J.; Laberie.L.; Jouzel.J. and Bonani.G. (1993) Correlations between climate records from the North Atlantic sediments and Greenland ice. *Nature* **365** pp 143-147

Buettner.A. Kleinhanns.I.C. Ruffer.D. Hunziker.J.C. and Villa.I.M. (2005) Magma generation at the easternmost section of the Hellenic arc: Hf, Nd, Pb and Sr isotope geochemistry of Nisyros and Yali volcanones (Greece). *Lithos* **83** pp29-46.

Cacho.I.; Grimalt.; Pelejero.C.; Canals.M.; Sierro.F.J.; Flores.J.A. and Shakleton.N.J. (1999) Dansgaard-Oeschger and Heinrich event imprints in Alboran Sea paleotemperatures. *Palaeoceanography*. **14** pp698-705.

Cacho.I.; Grimalt.J.O.; Sierro.F.J. Shackleton.N. and Canals.M. (2000) Evidence for enhanced Mediterranean thermohaline circulation during rapid climatic coolings. *Earth and Planetary Science Letters* **183** pp 417-429.

Cacho.I.; Canals.M.; Sbaffi.L.; Shakleton.N.J.; Schonfeld.J. and Zahn.R. (2001) Variability of the western Mediterranean sea surface temperatures during the last 25,000 years and its connection with the northern hemisphere climatic changes. *Palaeoceanography* **16** pp40-52.

Cacho.I.; Grimalt.J.O. and Canals.M. (2002) Response of the Western Mediterranean Sea to rapid climatic variability during the last 50,000 years: a molecular biomarker approach. *Journal of Marine Systems* **33-34** pp253-272.

Calanchi.N.; Cattaneo.A.; Dinelli.E.; Gasparotto.G. and Lucchini.F. (1998) Tephra layers in Late Quaternary sediments of the central Adriatic Sea. *Marine Geology* **149** pp191-209.

Capotondi.L. and Vigliotti.L. (1999) Magnetic and micro-faunal characterisation of late quaternary sediments from the western Mediterranean: inferences about sapropel formation and paleaoceanographic implications. *Proceedings of the Ocean Drilling Program, Scientific Reports*. **161** pp505-518.

Carminati. & Doglioni (2004) Mediterranean Tectonics. *Encyclopaedia of Geology.* Elsevier, Amsterdam.

Carracedo.J.C.; Day.S.; Guillou.H.; Rodriguez Badiolas.E.; Canas.J.A.; Perez Torrado.F.J. (1998). Hotspot volcanism close to a passive continental margin: the Canary Islands. *Geological Magazine* **135** pp591-604.

Cashman.K.V. (2008) Volcanoes and Human History. *Journal of Volcanology and Geothermal Research* **176** pp 325-329.

Casford.J.S.L.; Rohling.E.J.; Abu-Zied.R.; Cooke.S.; Fontanier.C.; Leng.M.; and Lykousis.V. (2002) Circulation changes and nutrient concentrations in the late Quaternary Aegean Sea: A nonsteady state concept for sapropel formation. *Paleoceanography* **17** pp14.1-14.11

Casford.J.S.L.; Rohling.E.J.; Abu-Zied.R.H.; Fontanier.C.; Jorissen.F.J.; Leng.M.J.; Schmiedl.G. and Thomson.J. (2003) A dynamic concept for eastern Mediterranean circulation and oxygenation during sapropel formation. *Palaeogeography, Palaeoclimatology, Palaeoecology* **190** pp103-119.

Casford.J.S.L.; Abu-Zied.R.; Rohling.E.J.; Cooke.S.; Fontanier.C.; Leng.M.; Millard.A.; Thomson.J. (2007) A stratigraphically controlled multiproxy chronostratigraphy for the eastern Mediterranean. *Palaeoceanography* **22** PA4251.

Cioni.R.; Santacroce.R. and Sbrana.A. (1999) Pyroclastic deposits as a guide for reconstructing the multi-stage evolution of the Somma-Vesuvius Caldera. *Bulletin of Volcanology* **60** pp20-222.

Clift.P. and Blusztajin.J. (1999) The trace-element characteristics of Agean and Aeolian volcanic arc tephra. *Journal of Volcanology and Geothermal Research* **92** pp321-347.

Comas.M.C.; Zahn.R.; Klaus.A. and the ODP Shipboard Party of leg 161. Chapter 5 *Proceedings of the Ocean Drilling Program* **161** pp113-177

Cornette.Y.; Crisci.G.M.; Gillot.P.Y. and Orsi.G. (1983) Recent volcanic history of Pantelleria: a new interpretation. *Journal of Volcanology and Geothermal Research* **17** pp361-373.

Cottrell.E.; Gardner.J.E.; Rutherford.M.J. (1999) Petrologica and experiemental evidence for the movement and heating of the pre-eruptive Minoan rhyodacite (Santorini, Greece) *Contributions to Mineraology and Petrology* **135** pp315-331.

Capotondi. L. and Vigliotti.L. (1999) Magnetic and microfaunal characterization of Late Quaternary sediments from the western Mediterranean: Inferences about sapropel formation and paleoceanographic implications. *Proceedings of the Ocean Drilling Program Scientific Results*. **161** pp505-518.

Cramp.A., Collins.M.B. and West.R. (1988) Late Pleistocene-Holocene sedimentation in the NW Aegean Sea. : a paleoclimatic, paleoceanographic reconstruction. *Palaeogeography, Palaeoclimatology, Palaeoecology* **68,** pp 61-77.

Cramp.A. and O'Sullivan.G. (1999) Neogene sapropels in the Mediterranean: a review. *Marine Geology* **153** pp11-28.

Dacassou.E.; Capotanodi.; Murat.A.; Bernasconi.S.M.; Mulder.T.; Gonthier.E.; Migeon.S.; Duprat.J.; Giraudeau.J. and Mascale.J. (2007). Multiproxy Late Quaternary stratigraphy of the Nile deep-sea turbidite system- Towards a chronology of deep-sea terrigenous systems. *Sedimentary Geology* **200** pp1-13.

Davies.S.M.; Larsen.G.; Wastegard.S.; Turney.C.S.M.; Hall.V.A.; Coyle.L. and Thordarson.T. Widespread dispersal of Icelandic tephra: how does the Eyjafjoll eruption of 2010 compare to past Icelandic events? *Journal of Quaternary Science* **25** pp605-611.

De Vivo.B. Rolandi.G.; Gans.P.B.; Calvert.A.; Bohrson.W.A.; Spera.F.J. & Belkin.H.E. (2001) New constraints on the pyroclastic eruptive history of the Campanian volcanic Plain (Italy) *Mineralogy and Petrology* **73** pp 47-65.

Deino.A.L.; Orsi.G.; de Vita.S. and Piochi.M. (2004) The age of the Neapolitan Yellow Tuff caldera-forming eruption (Campi Flegrei caldera-Italy) assessed by $^{40}Ar/^{39}Ar$ dating method. *Journal of Volcanology and Geothermal Research* **133** pp157-170.

Della Vedova.B.; Lucazeau.F.; Pasquale.V.; Pellis.G. and Verdoya.M. (1995) Heat flow in the tectonic provinces crossed by the southern segment of the European Geotraverse. *Tectonophysics* **244** pp57-74.

d'Errico.F.; Zilhao.; Julien.M.; Baffier.D.; and Pelegrin.J. (1998) Neanderthal acculturation in Western Europe? *Current Anthropology* **39** pp1-44.

Doose.H.; Zahn.R.; bernasconi.S.; Pika-Biolzi.M.; Murat.A.; Pierre.C. and Belanger.P. (1999) Planktonic $\delta^{18}O$ and $U^{k'}_{37}$ temperature estimates from organic rich sediments at sites 974 and 975, Tyrrhenian Sea and Balearic Rise. *Proceedings of the Ocean Drilling Program, Scientific Results.* **161** pp489-503

Druitt.T.H.; Mellors.R.A.; Pyle.D.M. and Sparks.R.S.J. (1989). Explosive Volcanism on Santorini, Greece. *Geological Magazine.* **126** pp95-126.

Druitt.T.H., Edwards.L.; Mellors.R.M.; Pyle.D.M.; Sparks.R.S.J.; Lanphere.M.; Davies.; M and Barriero.B. (1999). Santorini Volcano. *Geological Society Memoir* **19**.

Druitt.T.H.; Costa.F.; Deloule.E.; Duggan.M. and Scaillet.B. (2012) Decadal to monthly timescales of magma transfer and reservoir growth and a caldera volcano. *Nature* **482** pp77-82.

Duarte.C.; Mauricio.J.; Pettitt.P.B.; Souto.P.; Trinkhaus.E.; Plicht.H. and Zilhau.J. (1999) The early Upper Palaeolithic human skeleton from the Abrigo do Lagar Velho (Portugal) and modern human emergence in Iberia. *Proceedings of the National Academy of Sciences*. **96** pp7604-7609.

Dufek.J.; Manga.M. and Patel.A. (2012) Granular disruption during explosive volcanic eruptions. *Nature Geoscience* **5** pp561-564.

Eastwood, W. J., Pearce, N. J. G., Westgate, J. A., Perkins, W. T., Lamb, H. F., & Roberts, N. (1999). Geochemistry of Santorini tephra in lake sediments from southwest turkey. Global *and Planetary Change*, **21(1-3)** pp17-29.

Emeis. K-C.; Camerlenghi.A.; MacKenzie.J.A.; Rio.Domenico and Sprovieri.R. (1991) The occurrence and significance of Pleistocene and Upper Pliocene sapropels in the Tyrrhenian Sea. *Marine Geology* **100** pp155-182.

Emeis.K.C.; Robertson.A.H.F.; Richter.C. and the shipboard crew of ODP leg 160 (1996). Chapter 8, Site 967.*Proceedings of the Ocean Drilling Program, Initial Reports* **160** pp215-287.

Emeis.K.C.; Schulz.H.M.; Struck.U.; Sakamoto.T.; Doose.H.; Erlenkeuser.H.; Howell.M.; Kroon.D. and Paterne.M. (1998) Stable isotope and alkenone temperature records of sapropels from sites 964 and 967: constraining the physical environment of sapropel formation in the eastern Mediterranean Sea. *Proceedings of the Ocean Drilling Program, Scientific Results* **160** pp309-331.

Federman.A.N. and Carey.S.N. (1980) Electron Microprobe correlation of tephra layers from Eastern Mediterranean. *Quaternary Research* **13** pp160-171.

Francalanci.L.; Vougioukalakis.G.E. and Fytikas.M. (2007) Petrology and Volcanology of Kimolos and Polyegos volcanoes within the context of the South Aegean arc, Greece. *Geological Society of America Special paper* **418** pp 33-65.

Frumkin.A.; Bar-Yosef.O. and Schwarcz.H.P. (2011) Possible paleohydrologic and paleoclimatic effects on hominin migration and occupation of the Levantine Middle Paleolithic. *Journal of Human Evolution* **60** pp437-451.

Follieri.M.; Giardini.M.; Magri.D. and Sadori.L. (1998) Palynostratigraphy of the last glacial-interglacial period in the volcanic region of central Italy. *Quaternary International* **47** pp3-80.

Fujimaki.H. (186) partition coefficients of Hf,Zr, and REE between zircon, apatite and liquid. *Contributions to Mineral Petrology* **94** pp42-45.

Ganssen.G.; and Troelstra. S.R. (1987) Paleoenvironmental changes from stable isotopes in planktonic formaninfera from eastern Mediterranean sapropels. *Marine Geology* **75** pp221-230.

Ghorbel.N.; Fakhfakh.S.; Jbara.O.; Odof.S.; Rondot.S.; Fakhfakh.Z. and Kallel. A (2005) "EPMA analysis of insulating materials: Monte Carlo Simulations and Experiments. " *Journal of Physics D: Applied Physics* **38** pp1239-1247.

Giaccio, B.; Hajdas, I.; Peresani, M.; Fedele, F. G. & Isaia, R. (2006) The Campanian Ignimbrite Tephra and its relevance for the timing of the Middle to Upper Palaeolithic shift.

In Conard, N. J. (ed.), *When Neanderthals and Modern Humans Met*, Tübingen: Kerns Verlag pp343–375.

Gill.R. (1997) Modern Analytical Geochemistry, Longman Geochemistry series pp215-233.

Grant.K.M.; Rohling.E.J.; Bar-Matthews.M.; Ayalon.A.; Medina-Elizalde.M.; Brink-Ramsey.C.; Satow.C. and Roberts.A.P. (2012). Rapid coupling between ice volume and polar temperature over the past 150,000 years. *Nature* **in press**. DOI- 10.1038/nature11593

Gray.A.L. (1985) Solid sample introduction by laser ablation inductively coupled plasma mass spectrometry. *Analyst* **61** pp551-556

Green.R.E. and co-authors (2010) A draft sequence of the Neanderthal genome. *Science* **328** pp710-722.

Golovanova.L.V.; Doronichev.B.V, Cleghorn.N.E.; Koulkova.M.A.; Sapelko.T.V. and Shackley.M.S (2010) Significance of ecological factors in the Middle to Upper Paleolithic Transition. *Current Anthorpology*. **51** pp 655-691.

Gonzalez-Donoso.J.M.; Serrano.F. and Linares.D. (2000) Sea surface temperature during the Quaternary at ODP sites 976 and 975 (western Mediterranean). Palaeogeography, Palaeoclimatology, Palaeoecology **162** pp17-44.

Gulchard.F.; Carey.S.; Arthur.M.A.; Sigurdsson.H. and Arnold.M. (1993) Tephra from the Minoan eruption of Santorini in sediments of the Black Sea. *Nature* **363** p610-612.

Guðmundsdóttir.E.R.; Larsen.G. and Eiriksson.J. (2011) New tephra layers identified in sediments on the North Icelandic shelf. *Abstracts for Marine Tephrochronology Meeting, Geological Society of London* 26th October 2011.

Hamann.Y.; Wulf.S.; Ersoy.O.; Ehermann.W.; Aydar.E. and Schmiedl.G. (2010) First evidence of a distal early Holocene ash layer in Eastern Mediterranean deep-sea sediments derived from the Anatolian province. *Quaternary Research* **73** pp497-506

Hardiman.J.C. (1999) Deep sea tephra from Nisyros Island, eastern Aegean Sea, Greece. *Geological Society Special Publications* **161** pp69-88.

Hayes.A.; Rohling.E.J.; De Rijk.S.; Kroon.D. and Zachariesse.W.J. (1999) Mediterranean planktonic foraminferal faunas during the last glacial cycle. *Marine Geology* **153** pp239-252.

Hayward.B.W.; Sabaa.A.T.; Kawagata.S. and Grenfell.H.R. (2009) The Early Pliocene re-colonisation of the deep Mediterranean Sea by benthic foraminfera and their pulsed Late Pliocene-Middle Pleistocene decline. *Marine Micropaleontology* **71** pp97-112.

Henderson.G.M. (2002) New oceanic proxies for paleoclimate. *Earth and Planetary Science Letters* **203** pp1-13.

Herrera.K.J.; Somarelli.J.A.; Lowery.R.K.; Herrera.R. (2009) To what extent did Neanderthals and modern humans interact? *Biological Reviews* **84** pp245-257.

Houk.R.S.; Velmer.A.; Fassel.V.A.; Flesch.G.D. and Svec.H. (1980) "Inductively coupled argon plasma as an ion source for mass spectrometric determination of trace elements." *Analytical Chemistry* **52** pp2283-2289.

Hublin.J.J.; Spoor.M.; Braun.M. Zonneveld.F. and Condemi.S. (1996) A late Neanderthal associated with Upper Palaeolithic artefacts. *Nature* **381** pp224-226.

Hunt.J.B.; Clift.P.D.; Lacasse.C.; Vallier.T.L. and Werner.R. (1998) Interlaboratory comparison of electron probe microanalysis of glass geochemistry. *Proceedings of the Ocean Drilling Program, Scientific Results* **152** pp85-91.

Jagan.A. (2010) Tephra stratigraphy and geochemistry from three Icelandic lake cores: a new method for determining source volcano of tephra layers. *Unpublished MPhil Thesis, University of Edinburgh*.

Jarvis. K.E. (1997) Inductively couples plasma mass spectrometry. Chapter 10 in Gill.R. (1997) Modern Analytical Geochemistry, Longman Geochemistry series pp215-233.

Jimenez-Espejo.; Ruiz.F.M.; Finlayson.C.; Paytan.A.; Sakamoto.T.; Ortega-Huertas.M.; Finlayson.G.; Iijima.K.; Gallego-Torres.D. and Fa.D. (2007) Climate forcing and Neanderthal extinction in Southern Iberia: insights from a multiproxy marine record. *Quaternary Science Reviews* **26** pp836-852.

Joannin.S.; Ciaranfi.N. and Stefanelli.S. (2008) Vegetation changes during the late early Pleistocene at Montalbano Jonico (Province of Matera, southern Italy) based on pollen analysis. *Palaeogeography, Palaeoclimatology, Palaeoecology* **270** pp92-101.

Jochum.P.K.; Willbold,M.; Raczek.I.; Stoll.B. and Herwig.K. (2006) Chemical Characterisation of the USGS reference glasses GSA-1G, GSC-1G, GSD-1G, GSE-1G, BCR-2G, BHVO-2G and

BIR-1G Using EPMA,ID-TIMS, ID-ICP-MS and LA-ICP-MS. *Geostandards and Geoanalytical Research* **29** pp285-302.

Jochum, K.P.; Stoll, B.; Herwig, K.; Willbold, M.; Hofmann, A.W.; Amini, M.; Aarburg, S.; Abouchami, W.; Hellebrand, E.; Mocek, B.; Raczek, I.; Stracke, A.; Alard, O.; Bouman, C.; Becker, S.; Ducking, M.; Bratz, H.; Klemd, R.; de Bruin, D.; Canil, D.; Cornell, D.; de Hoog, C.J.; Dalpe, C.; Danyushevsky, L.; Eisenhauer, A.; Gao, Y.J.; Snow, J.E.; Goschopf, N.; Gunther, D.; Latkoczy, C.; Guillong, M.; Hauri, E.H.; Hofer, H.E.; Lahaye, Y.; Horz, K.; Jacob, D.E.; Kassemann, S.A.; Kent, A.J.R.; Ludwig, T.; Zack, T.; Mason, P.R.D.; Meixner, A.; Rosner, M.; Misawa, K.J.; Nash, B.P.; Pfander, J.; Premo, W.R.; Sun, W.D.D.; Tiepolo, M.; Vannucci, R.; Vennemann, T.; Wayne, D. and Woodhead, J.D. (2006) MPI-DING reference glasses for in situ microanalysis: new reference values for element concentrations and isotope ratios. *Geochemistry Geophysics Geosystems,* **7**(2).

Juvigne. E.H. (1992) Distribution of widespread late glacial and Holocene tephra beds in the French Central Massif. *Quaternary International*. **13** pp181-185

Kallel. N.; Duplessy.J.C.; labeyrie.L. Fontugne.M. Paterne.M. and Montacer.M. (2000) Mediterranean pluvial periods and sapropel formation over the last 200,000 years. *Palaeogeography, Palaeoclimatology, Palaeoecology.* **157** pp 45-58.

Karaoglu.O.; Ozdemir.Y.; Umit Tolluoglu.A.; Karabiyikoglu.M.; Kose.O and Froger.J-L (2005) Stratigraphy of the volcanic products around the Nemrut caldera: implications for reconstruction of the caldera formation. *Turkish Journal of Earth Sciences* **14** pp123-143.

Keller.J.; Ryan.W.B.F.; Ninkovich.D. and Altherr.R. (1978) Explosive volcanic activity in the Mediterranean over the past 20,000 year as recorded in deep sea sediments. *Geological Society of America Bulletin* **89** pp591-604.

Keller. J. (1980) The island of Salina. *Rendiconti della Società Italiana di Mineralogiae Petrologia*. **36**, pp 489–524.

Klein.B.; Rother. W. Manca.B.B.; Breagant.D.; Beitzel.V.; Kovacevic.V. and Luchetta.A. (1999) The large deep water transient in the eastern Mediterranean. *Deep Sea Research* **46** pp371-414.

Klein.R.G. (2003) Wither the Neanderthals. *Science* **299** pp1525-1527.

Kocyigit.A. and Beyhan.A. (1998) A new intercontinental transcurrent structure: the central Anatolian Fault Zone, Turkey. *Tectonophysics* **284** pp317-336.

Kraml, M., (1997). Laser-40Ar/39Ar-Datierungen an distalen marinen Tephren des jung-quartaren mediterranen Vulkanismus (Ionisches Meer, METEOR-Fahrt 25/4). Ph.D. thesis, Albert-Ludwigs-Universitat Freiburg i.Br., 216pp.

Kroon.D.; Alexander.I.; Little.M.; Lourens.L.J.; Matthewson.A.; Robertson.A.H.F. and Sakamoto.T. (1998) Oxygen isotope and sapropel stratigraphy in the Eastern Mediterranean during the last 3.2 million years. *Proceedings of the Ocean Drilling Program* **160** pp181-189.

Kudo.A.M. and Weill.D.F. (1970) An igneous plagioclase thermometer. *Contributions to Mineralogy and Petrology* **25** pp 52-65

Kwiecien, O., Arz, H. W., Lamy, F., Wulf, S., Bahr, A., Rohl, U., & Haug, G. H. (2008). Estimated reservoir ages of the Black Sea since the Last Glacial. *Radiocarbon*, **50(1),** pp99-118.

Larrasoana. J.C.; Roberts.A.P.; Rohling.E.J.; Winklhofer.M. and Wehausen.R. (2003). Three million years of monsoon variability over the northern Sahara. *Climate Dynamics* **21** pp689-698.

Larsen.G.; Erikiksson.J.; Knudsen.K.L. and Heinemeier.J. (2002) Correlation of late Holocene terrestrial and marine tephra markers, north Iceland: implications for reservoir age changes. *Polar Research* **21** pp283-290.

Lane.C. (2009) Exploring the variability of microtephra deposits: chemical characterisation and discrimination methods. PhD thesis, University of Oxford.

Lane.C.; Andric.M.; Cullen.V. and Blockley.S. (2011) The occurrence of distal Icelandic and Italian tephra in the Lateglacial of Lake Bled, Slovenia. *Quaternary Science Reviews*. **30** pp1013-1018.

Langmann. B.; Folch.A.; Hensch.M. and Matthias (2012) Volcanic ash over Europe during the eruption of Eyjafjallajökull on Iceland, April-May 2010. *Atmospheric Environment* **48** pp1-8.

Lowe.D. (2011) Tephrochronology and its application: a review. *Quaternary Geochronology* **6** pp107-153.

Lowe.J.J. and Walker.M.J.C. (1997) Reconstructing Quaternary Environments. 2nd edtion. Prentice Hall.

Lustrino.M. and Wilson.M. (2006) The circum-Mediterranean anorogenic Cenozoic igneous province. *Earth Science Reviews* **81** pp1-65.

Lucchi, F., Tranne, C. A., Astis, D. G., Keller, J., Losito, R., & Morche, W. (2008). Stratigraphy and significance of Brown Tuffs on the Aeolian Islands (southern Italy). *Journal of Volcanology and Geothermal Research*, **177(1),** pp 49-70.

Macrae, N.D. (1995) Secondary-ion mass spectrometry and geology. *Canadian Mineralogist,* **33** pp. 219-236.

Mahood.G and Hildreth.W. (1983) Large partition coefficients for trace elements in high silica rhyolites. *Geochimica et Cosmochimica Acta* **47** pp11-30.

Mahood.M and Hildreth.W. (1986) Geology of the paeralkaline volcano at Pantelleria. *Bulletin of Volcanology* **48** pp143-172.

Marchitto.T.M. (2007) Nutrient Proxies- Paleooceanography, physical and chemical proxies. *Encyclopaedia of Quaternary Science* pp1732-1740.

Margari.V.; Pyle.D.M.; Bryant.C. and Gibbard.P.L. (2007) Medterranean tephra stratigraphy revisited: Results from a long terrestrial sequence on Lesvos Island, Greece. *Journal of Volcanology and Geothermal Research* **163** pp34-54.

Margari.V.; Gibbard.P.L.; Bryant.C.L. and Tzedakis.P.C. (2009) Character and environmental changes in southern Europe during the last glacial period: evidence from Lesvos Island, Greece. *Quaternary Science Reviews* **28** pp 1317-1339.

Martin.V.M.; Davidson.J.; Morgan.D. and Jerram.A (2010) Using the Sr isotope compositions of feldspars and glass to distinguish magma system components and dynamics. *Geology* **38** pp539-542.

Martin-Puertas.C.; Matthes.K.; Brauer.A.; Muscheler.R.; Hansen.F.; Pertrick.C.; Aldahan.A.; Possnert.G.; and Van Geel.B. (2012). Regional atmospheric circulation shifts induced by a grand solar minimum. *Nature Geoscience* **5** pp397-401.

Marino.G.; Rohling.E.J.; Rijpstra.W.I.C.; Sangiorgi.F.; Schouten.S. and Sininghe Damste.J.S. (2007) Aegean Sea as driver of hydrographic and ecological changes in the eastern Mediterranean. *Geology* **35** pp675-678.

Marino.G.; Rohling.E.J.; Sangiorgi.F.; Hayes.A.; Casford.L.J.; Lotter.A.F.; Kucera.M. and Brinkhuis.H. (2009) Easrly and middle Holocene in the Aegean Sea: interplay between high and low latitude climate variability. *Quaternary Science Reviews* **28** pp3246-3262.

Matthias.V. Aulinger.A.; Bieser.J.; Cuesta.J.; Geyer.B.; Langmann.B.; Serikov.I.; Mattis.I.; Minikin.A.; Mona.L.; Quante.M.; Schumann.U. and Weinzier.B. (2012). The ash dispersion over Europe during the Eyjafjallajökull eruption-Comparison of CMAQ simulations to remote sensing and air-borne in-situ observations. *Atmospheric Environment* **48** pp184-194.

McPhail, D.S. (2006) Applications of Secondary Ion Mass Spectrometry (SIMS) in materials science. *Journal of Materials Science,* **41** pp. 873-903.

Menzel.D.; Schouten.S.; van Bergen.P.F. and Sinninghe Damste.J.S. (2004) Higher plant vegetation changes during Pliocene sapropel formation. *Organic Geochemistry* **35** pp1343-1353

Molisso.F.; Insinga.D.; Marzaioli.F.; Sacchi.M. and Lubritto.C. (2010) Radiocarbon dating versus volcanic event stratigraphy: Age modelling of Quaternary marine sequences in the coastal region of the Eastern Tyrrenian Sea. *Nuclear Instruments and Methods in Physics Research B* **268** pp1236-1240.

Moore.R.B. (1990) Volcanic geology and eruption frequency, Sao Miguel, Azores. *Bulletin of Volcanology* **52** pp602-614.

Morgan.G.B. and London. D. (1996) “Optimizing the electron microprobe analysis of hydrous alkali aluminosilicate glasses”. *American Mineraologist* **81** pp1176-1185.

Morigi.C. (2009) Benthic environmental changes in the Eastern Mediterranean sea during sapropel S5 deposition. *Palaeogeography, Palaeoclimatology, Palaeoecology* **273** pp258-271.

Morley, W, M., & Woodward, J. C. (2011). The Campanian Ignimbrite (Y5) tephra at Crvena Stijena Rockshelter, Montenegro. *Quaternary Research* **75** pp683-696.

Müller, U.C.; Pross, J.; Tzedakis, P.C.; Gamble, C.; Kotthoff, U.; Schmiedl, G.; Wulf, S.; Christanis, K. (2011): The role of climate in the spread of modern humans into Europe. *Quaternary Science Reviews* **30** pp273-279.

Murat.A. (1999) Plio-Pleistocene occurrence of sapropels in the western Mediterranean Sea and their relation to Eastern Mediterranean Sapropels. *Proceedings of the Ocean Drilling Program, Scientific Results.* **161** pp 519-527.

Munno.R. and Petrosino.P (2004) New constraints on the occurrence of the Y-3 Upper Pleistocene tephra marker layer in the Tyrrhenian Sea. *Il Quaternario* **17** pp11-20.

Munno.R. and Petrosino.P. (2006) The late Quaternary tephrostratigraphical record of the san Gregorio Magno basin (southern Italy). *Journal of Quaternary Science* **22** pp247-266.

Muscheler.R.; Beer.J.; Kubik.P.W. and Synal.H-A. (2005) Geomagnetic field intensity during the last 60,000 years based on ^{10}Be and ^{36}Cl from the summit ice cores and ^{14}C. *Quaternary Science Reviews* **24** pp1849-1860.

Narcisi.B. & Vezzoli.L. (1999) Quaternary stratigraphy of distal tephra layers in the Mediterranean-an overview. *Global and Planetary Change* **21** pp31-50.

Neilsen.C.H. and Sigurdsson.H. (1981) "Quantitative methods for electron microprobe analysis of sodium in natural and synthetic glasses" *American Mineralogist* **66** pp547-552.

Notsu.K.; Fujitani.T.; Ui.T.; Matsuda.J. and Ercan.T. (1995) Geochemical features of collision-related rocks in Central and Eastern Anatolia, Turkey. *Journal of Volcanology and Geothermal Research* **64** pp171-192.

Oppenheimer.C and Pyle (2009). Volcanoes, in J.C. Woodward (ed.) The Physical Geography of the Mediterranean. Oxford University Press, Oxford pp 435-468.

Orsi.G. De Vita.S. and di Vito.M. (1996) The restless, resurgent Campi Flegrei nested caldera (Italy): constraints on its evolution and configuration. *Journal of Volcanology and Geothermal Research* **74** pp179-214.

Pabst.S.; Worner.G.; Civetta.L. and Tesoro.R. (2008). Magma chamber evolution prior to the Campanian Ignimbrite and Neapolitan Yellow Tuff eruptions (Campi Flegrei, Italy) *Bulletin of Volcanology* **70** pp961-976.

Pappalardo.L.; Civetta.L.; D'Antonio.M.D. Deino.A.; Di Vito.M.; Orsi.G.; Carandente.A.; de Vita.S.; Isaia.R. and Piochi.M. (1999) Chemical and Sr-isotopical evolution of the Phlegrean magmatic system before the Campanian Ignimbrite and the Neapolitan Yellow Tuff eruptions. *Journal of Volcanology and Geothermal Research* **91** pp141-166.

Paterne.M.; Guchard.F.; Labeyrie.J.; Gillot.P.Y. and Duplessy.J.C. (1986) Tyrrhenian Sea tephrochronology of the oxygen isotope record for the past 60,000 years. *Marine Geology* **72** pp259-285.

Paterne.M.; Labeyrie.J.; Guichard.F.; Mazaud.A. and Maitre.F (1990) Fluctuations of the Campanian explosive volcanic activity (Southern Italy) during the past 190,000 years, as determined by marine tephrochronology. *Earth and Planetary Science Letters* **98** pp166-174.

Paterne.M.; Guichard.F.; Duplessy.J.C.; Siani.G.; Sulpizio.R. and Labeyrie.J. (2008) A 90,000-200,000 yrs marine tephra record of Italian volcanic activity in the central Mediterranean Sea. *Journal of Volcanology and Geothermal Research* **177** pp187-196

Pearce.J.A. and Peate.D.W. (1995) Tectonic implications of the composition of volcanic arc magmas. *Annual Reviews of Earth and Planetary Sciences* **23** pp251-285.

Pearce.J.G.; Denton.J.S.; Perkins.W.T.; Westgate.J.A. and Alloway.B.V. (2007) Correlation and characterisation of individual glass shards from tephra deposits using trace element laser ablation ICP-MS analyses: current status and future potential. *Journal of Quaternary Science* **22** pp721-736.

Pedersen.T.F. and Calvert.S.E. (1990) Anoxia vs. productivity: what controls the formation of organic-carbon rich sedimentary rocks? *American Association of Petrologists and Geologists Bulletin.***74** pp 454-466.

Perissoratis.C. and Piper.D.J.W. (1992) Age, regional variation and shallowest occurrence of the S1 sapropel in the Northern Aegean Sea. *Geo-Marine Letters*. **12** pp 49-53.

Pettitt.P.B. and Pike.A.W.G. (2001) Blind in a cloud of data: problems with the chronology of Neanderthal extinction and anatomically modern human expansion. *Aniquity* **75** pp415-420.

Pierce.N.J.G.; Perkins.W.T.; Abell.I.; Duller.G.A.T. and Fuge.R. (1992) "Mineral microanalysis by laser ablation inductively coupled plasma mass spectrometry. *Journal of Analytical Atomic Spectrometry* **7** pp53-57.

Pierce. N.J.G.; Westgate.J.A.; Preece.S.J.; Eastwood.W.J. and Perkins.W.T. Identification of Aniakchak (Alaska) tephra in Greenland ice core challenges the 1645 BC date for the Minoan eruption of Santorini. *Geochemistry, Geophysics, Geosystems* **5** pp ??

Pierce.N.J.G.; Denton.J.S.; Perkins.W.T.; Westgate.J.A. and Alloway.B.V. (2007) "Correlation and characterisation of individual glass shards from tephra deposits using trace element laser ablation ICP-MS analyses: current status and future potential." *Journal of Quaternary Science* **22** pp721-736

Pierce.N.J.S.; Bendall.C.A. and Westgate.J.A. (2008) Comment on "Some numerical considerations in the geochemical analysis of distal microtephra" by A.M.Pollard, S.P.E.Blockley and C.S. Lane. *Applied Geochemistry* **23** pp1353-1364.

Piva.A.; Asiolo.A.; Trincardi, F.; Schneider.R.R. and Vigliotti.L. (2008a) Late Holocene Climate variability in the Adriatic Sea (Central Mediterranean). *The Holocene* **18** pp 153-167.

Piva, A.; Asioli, A.; Andersen, N.; Grimalt, J.O.; Schneider, R.R.; Trincardi, F.; 2008b. Climatic cycles as expressed in sediments of the PROMESS1 borehole PRAD1-2, central Adriatic, for the last 370 ka: 2. Paleoenvironmental evolution.*Geochemistry, Geophysics, Geosystems* **9** (3), pp1-21.

Platevoet.B.; Scaillet.S.; Guillou.H.; Blamart.D.; Nomade.S.; Massault.M.; Poisson.A.; Elitok.O. Ozgur.N.; Yagmurlu.F. and Yilmaz.K. (2008). Pleistocene eruptive chronology of the Golcuk volcano, Isparta Angle, Turkey. *Quaternaire* **19** pp147-156.

Poli.S.; Chiesa.S. Gillot.P.Y.; Gregnanin.A. and Guichard.F. (1987) Chemistry versus time in the volcanic complex of Ishia (Gulf of Nales, Italy): evidence for successive magmatic cycles. *Contributions to Mineralogy and Petrology* **95** pp322-335.

Pollard.A.M.; Blockley.S.P.E. and Lane.C.S. (2006) Some numerical considerations in the geochemical analysis of distal microtephra. *Applied Geochemistry* **21** pp 1692-1714.

Potts.J.P. (1987) "A handbook of silicate rock analysis" Blackie and Son Ltd pp326-374

Pouchou, J.L.; Pichoir, F. (1985) PAP'Xy(rz) procedure for improved quantitative microanalysis. Microbeam Analysis, pp. 104-106

Pyle.D.M.; Rickets.G.M.; Margari.V.; van Andel.T.H.; Sinitsyn.A.A.; Praslov.N.D. and Lisitsyn.S. (2006) Wide dispersal and deposition of distal tephra during the Pleistocene 'Campanian Ignimbrite/Y5' eruption, Italy. *Quaternary Science Reviews* **25** pp2713-2728.

Reed.S.J.B. (1996) Electron Microprobe Analysis and Scanning Electron Microscopy in Geology. *Cambridge University Press*, Cambridge.

Roberta.M.; Rosalba.M.; Paola.P.; Nicoletta.S.; Antonio.S. and Igor.V. (2008) Late Quaternary tephra layers along the Cilento coastline (southern Italy) *Journal of Volcanology and Geothermal Research* **177** pp277-243.

Roberts.P.A.; Stoner.J.S. and Richter.C. (1999) Diagenetic magnetic enhancement of sapropels from the eastern Mediterranean Sea. *Marine Geology*. **153** pp103-116.

Rohling.E.J. and Thunnell.R.C. (1999) Five decades of Mediterranean palaeoclimate and sapropel studies. *Marine Geology* **153** pp7-10.

Rohling .E.J. (1994) Review and new aspects concerning the formation of eastern Mediterranean sapropels. *Marine Geology* **122** pp1-28.

Rohling.E.J.; Hayes.A.; Kroon.S.; Zachariasse.W.J.; and Eisma.D. (1998) Abrupt cold spells in the northwest Mediterranean. *Palaeoceanography* **13** pp316-322.

Rohling.E.J.; Mayewski.P.A. and Challenor.P. (2003) On the timing and mechanism of millennial-scale climate variability during the last interglacial cycle. *Climate Dynamics* **20** pp257-267.

Rohling. E.J.; Abu-Zied.R.H.; Casford.J.S.L.; Hayes.A. and Hoogakker.B.A.A. (2009) The marine environment: present and past, in J.C.Woodward (ed.) *The Physical Geography of the Mediterranean.* Oxford University Press. Oxford pp33-67.

Rohling.E.J.; Cane.T.R.; Cooke.S.; Sprovieri.M. Bouloubassi.I; Emeis.K.C.; Schiebel.R.; Kroon.D.; Jorissen.F.J.; Lorre.A. and Kemp.A.E.S. (2002a) African monsoon variability during the previous interglacial maximum. *Earth and Planetary Science Letters* **202** pp61-75.

Rohling.E.J.; Mayewski.P.A.; Abu-Zied.R.H.; Casford.J.S.L. and Hayes.A. (2002b) Holocene atmosphere-ocean interations: records from Greenland and the Aegean Sea. *Climate Dynamics* **18** pp587-593.

Sancetta.C. (1994) Mediterranean sapropels: seasonal stratification yields high production and carbon flux. *Palaeoceanography* **9** pp 195-196.

Sanchez-Goni.M.F.; Sierro.F.J.; Peypouquet.J.P.; Grimalt.J.O.; Shackleton.N.J.; Cacho.I.; Turon.J.L. and Guiot.J. (2002). Synchroneity between marine and terrestrial responses to millennial scale climate variability during the last glacial period in the Mediterranean region. *Climate Dynamics* **19** pp95-105.

Sandler.A. & Herut.B. (2000) Composition of clays along the continental shelf off Israel: contribution of the Nile versus local sources. *Marine Geology* **167** pp339-354.

Schaldach.G.; Razilov.I. and Bernt.H. (2003) "Optimization of the geometry of a double-path spray chamber forinductively coupled plasma-atomic emission spectrometry by computer simulation and an evolutionary strategy" *Spectrochimica Acta Part B* **58** pp1807-1819

Schminke.H-U.; Park.C. and Harms (1999) Evolution and environmental impacts of the eruption of Laacher See Volcano (germany) 12,900 a BP. *Quaternary International* **61** pp61-72.

Schmitt, A., Danisik, M., Evans, N., Siebel, W., Kiemele, E., Aydin, F., & Harvey, J. (2011). Acigol rhyolite field, Central Anatolia (part 1): high-resolution dating of eruption episodes and zircon growth rates. *Contributions to Mineralogy and Petrology*, **162(6)** pp1215-1231.

Sen.E.; Kurkcuoglu.B.; Aydar.E.; Gourgaud.A. and Vincent.P.M. (2003) Volcanological evolution of Mount Erciyes stratovolcano and origin of the Valibaba Tepe ignimbrite (Central Anatolia, Turkey).*Journal of Volcanology and Geothermal Research* **125** pp225-246.

Shane.P. (2000) Tephrochronology- A New Zealand case study. *Earth Science Reviews* **49** pp223-259

Seymour, K. S. K. S., & Christanis, K. (1995). Correlation of a tephra layer in western Greece with a late Pleistocene eruption in the Campanian province of Italy. *Quaternary Research*, **43(1)** pp46-54.

Siani.G.; Sulpizio.R.; Paterne.M. and Sbrana.A. (2004) Tephrostratigraphy study for the last 18,000^{14}C years in a deep sea sediment sequence for the South Adriatic. *Quaternary Science Reviews* **23** pp2485-2500.

Shane.P.; Nairn.I.A.; Martin.B.S. and Smith.V. (2008) Compositional heterogeneity in tephra deposits resulting from the eruption of multiple magma bodies: implications for tephrochronology. *Quaternary International* **178** pp 44-53.

Shea.J.J. (2003) Neanderthals, competition and the origin of Modern Human behaviour in the Levant. *Evolutionary Anthropology* **12** pp173-187.

Smith.V.; Pearce.J.G.; Matthews.N.E.; Westgate.J.A.; Petraglia.M.D.; Haslam.M.; Lane.C.S.; Korisettar.R. and Pal.J.N. (2011) Geochemical fingerprinting of the widespread Toba tephra using biotite compositions. *Quaternary International*

Sparks.R.J.S.; Brazier.S; Huang.T.C. and Muerder.D. (1984) Sedimentology of the Minoan Deep-Sea Tephra Layer in the Aegean and eastern Mediterranean. *Marine Geology* **54** pp131-167

Spray. J.G. and Rae.D.A. (1995) "Quantitative electron-microprobe analysis of alkali silicate glasses, a revies and user guide" *The Canadian Mineralogist* **33** pp323-332.

Straus.L.G. (2005) On the demise of the Neanderthals. *Quaternary International* **137** pp1-5.

St Seymour. K. and Vlassopoulos.D. (1992) Magma mixing at Nisyros volcano, as inferred from incompatible trace-element systematics. *Journal of Volcanology and Geothermal Research* **50** pp 273-299.

Sullivan.D. (1990) The discovery of Santorini Minoan tephra in western Turkey. *Nature* **333** pp552-554.

Tatsumi.Y. and Kogiso.T. (1997) Trace element transport during dehydration processes in the subducted oceanic crust: 2. Origin of chemical and physical characteristics in arc magmatism.*Earth and Planetary Science Letters* **148** pp207-221.

Tamburrino.S.; Insignia.D.D.; Sprovieri.M.; Petrosino.P. and Tiepolo.M. (2012) Major and trace element characterisation of tephra layers offshore Pantelleria Island: insights into the last 200ka of volcanic activity and the contribution to the Mediterranean tephrochronology. *Journal of Quaternary Science* **27** pp129-140.

Thomas.J.B. Bodnar.R.J. Shmizu.N. and Sinha.A.K. (2002) Determination of zircon/melt trace element partition coefficients from SIMS analysis of melt inclusions in zircon. *Geochimica et Cosmochimica Acta* **66** pp2887-2901.

Thompson.W.G. and Goldstein.S.L. (2006) A radiometric calibration of the SPECMAP timescale. *Quaternary Science Reviews* **25** pp3207-3215.

Thordarson.T. and Larsen.G. (2007) Volcanism in Iceland in historical time: Volcano types eruption styles and eruptive history. *Journal of Geodynamics* **43** pp118-152.

Tomlinson.E.L.; Thordarson.T.; Muller.W.; Thirlwall.; Thirlwall.M. and Menzies.M.A. (2010) Microanalysis of tephra by LA-ICP-MS-Strategies, advantages and limitations assessed using the Thorsmork ignimbrite (Southern Iceland). *Chemical Geology* **279** pp73-89.

Trauth.M.H.; Larrasoana.J.C.; Mudelsee.M. (2009). Trends, rhythms and events in Plio-Pleistocene African Climate. *Quaternary Science Reviews* **28** pp399-411.

Trinkaus.E (2007) European early modern humans and the fate of the Neanderthals. *Proceedings of the National Academy of Sciences* **104** pp7367-7372.

Tsimplis.M.N. and Josey.S.A. (2001) Forcing of the Mediterranean Sea by atmospheric conditions over the North Atlantic. *Geophysical Research Letters*. **28** pp803-806.

Tzedakis.P.C.; Frogley.M.R.; Lawson.I.T.; Preece.R.C.; Cacho.I. and de Abreu.L. (2004) Ecological thresholds and patterns of millennial-scale climate variability: the response of vegetation in Greece during the last glacial period. *Geology* **32** pp109-112.

Tzedakis.P. (2005) Towards an understanding of the response of southern European vegetation to orbital and suborbital climate variability. *Quaternary Science Reviews* **24** pp1585-1599.

Tzedakis.P.C.; Hooghiemstra.H.and Palike.H. (2006) The last 1.35 million year at Tenaghi Philippon: revised chronostratigraphy and long term vegetation trends. *Quaternary Science Reviews* **25** pp3416-3430.

Tzedakis.P.C.; Palike.H.; Roucoux.K.H. and de Abreu.L. (2009) Atmospheric vegetation and low latitude links on orbital and millennial timescales. *Earth and Planetary Science Letters* **277** pp307-317.

Underdown.S. (2008) A potential role for transmissible spongiform encephalopathies in Neanderthal extinction. *Medical Hypothesis* **71** pp4-7.

Van Geel.B.; Buurman.J. and waterbolk.T.H. (1996) Archaeological and palaeoecological indications of an abrupt climate change in the Netherlands and evidence for climatological teleconnections around 2650 BP. *Journal of Quaternary Science* **11** pp451-460.

Vespa.M. Keller.J. Gertisser.R. (2006). Interplinian explosive activity of Santorini volcano (Greece) during the past 150,000 years. *Journal of Volcanology and Geothermal Research* **153** pp262-286.

Vinci.A. (1985) Distribution and chemical composition of tephra layers from eastern Mediterranean abyssal sediments. *Marine Geology* **64** pp143-155.

Vezzani.L.; Festa.A. and Ghisetti.F.C. (2010) Geology and tectonic evolution of the central-southern Apennines, Italy. *The Geological Society of America, Special Paper* **469** pp1-58.

Vogel.H.; Zanchetta.G.; Sulpizio.R.; Wagner.B. and Nowaczk.N. (2010) A tephrostratigraphic record for the last glacial-interglacial cycle from lake Ohrid, Albania and Macedonia. *Journal of Quaternary Science* **25** pp320-338.

Volentik.A.; Vanderkluysen.L. and Principe.C. (2002) Stratigraphy of the Caldera walls of Nisyros volcano, Greece. *Eclogae Geolgicae Helvetiae* **95** pp223-235.

Watkins.N.D.; Sparks.R.S.J.; Sigurdsson.H.; Huang.T.C.; Federman.A.; Carey.S. and Ninkovich.D. (1978). Volume and extent of the Minoan tephra from the Santorini volcano: new evidence from deep sea cores. *Nature*. **271** pp122-126.

Wilson.M. (1993) Magmatic differentiation. *Journal of the Geological Society* **150** pp611-624.

Weldeab.S.; Emeis.K-C.; Hemleben.C.; Schmiedl.G.; Shulz.H. (2003) Spatial productivity variations during the formation of sapropels S5 and S6 in the Mediterranean Sea: evidence from Ba contents. *Palaeogeography, Palaeoclimatology, Palaeoecology* **191** pp169-190.

White.J.C.; Parker.D.F. and Ren.M. (2009) The origin of trachyte and pantellerite from Pantelleria, Italy: Insights from major element, trace element and thermodynamic modelling. *Journal of Volcanology and Geothermal Research* **179** pp33-55.

WoldeGabriel.G.; Hart.W.K.; Katoh.S.; Beyene.Y. and Suwa (2005) Correlation of Plio-Pleistocene Tephra in Ethiopian and Kenyan rift basins: Temporal calibration of geological features and hominid fossil records. *Journal of Volcanology and Geothermal Research* **147** pp81-108.

Wulf.S.; Kraml.M.; Kuhn.T.; Schwarz.M.; Inthorn.M.; Keller.J.; Kuscu.I. and Halback.P. (2002) Marine tephra from the Cape Riva Eruption (22ka) of Santorini in the Sea of Marmara. *Marine Geology* **183** p131-141.

Wulf.S.; Kraml.M.; Brauer.A.; Keller.J. and Negendank.J.F.W. (2004) Tephrochronology of the 100ka lacustrine sediment record of Lago Grande di Monticchio (southern Italy). *Quaternary International* **122** pp7-30.

Wulf.S.; Kraml.M. and Keller.J. (2008) Towards a detailed distal tephrostratigraphy in the Central Mediterranean: The last 20,000yrs record of Lago Grande di Monticchio. *Journal of Volcanilogy and Geothermal Research* **177** pp118-132.

Wulf.S.; Keller .J.; Paterne.M.; Mingram.J.; Lauterbach.S.; Opitz.S.; Sottili.G.; Giaccio.B.; Albert.P.G.; Satow.C.; Tomlinson.E.; Viccaro.M. and Brauer.A. (2012) The 100-133ka record of Italian explosive volcanism and revised tephrochronology of Lago Grande di Monticchio. *Quaternary Science Reviews* **58** pp 104-123.

Yang, W.-H.A. and Kirkpatrick, R.J (1990) Hydrothermal reaction of a rhyolitic composition glass: a solid-state NMR study. *American. Mineralologist*. **75**, pp 1009–1019.

Zahran.N.F.; Helal.A.I.; Amr.M.A.; Abdel-Hafiez.A.; and Mohsen.H.T. (2003) "Formation of polyatomic ions from the skimmer cone in the inductively coupled plasma mass spectrometry." *International Journal of Mass Spectrometry* **226** pp271-278.

Zanchetta.G, Drysdale.R.N.; Hellstrom.J.C.; Fallick.A.E.; Isola.I.; Gagan.M.K.; Pareschi.M.T. (2007) Enhanced rainfall in the Western Mediterranean during deposition of Sapropel S1: stalagmite evidence from Corchia cave (Central Italy). *Quaternary Science Reviews* **26** pp179-286.

Zhu. H.; Bozdag.E.; Peter.D. and Tromp.J. (2012) Structure of the European upper mantle revealed by adjoint tomography. *Nature Geoscience* **5** pp489-498.

Zielinski. G.; Germani M.S (1998) New ice-core evidence challenges the 1620s BC age for the Santorini (Minoan) eruption. *Journal of Archaeological Science* **25** pp279–289.

Zolitschka, B.; Negendank, J.F.W.; (1996). Sedimentology, dating and palaeoclimatic interpretation of a 76.3 ka record from Lago Grande di Monticchio, southern Italy. *Quaternary Science Reviews* **15** pp101‑112.

Appendix 1 Standard analyses for EPMA analyses.

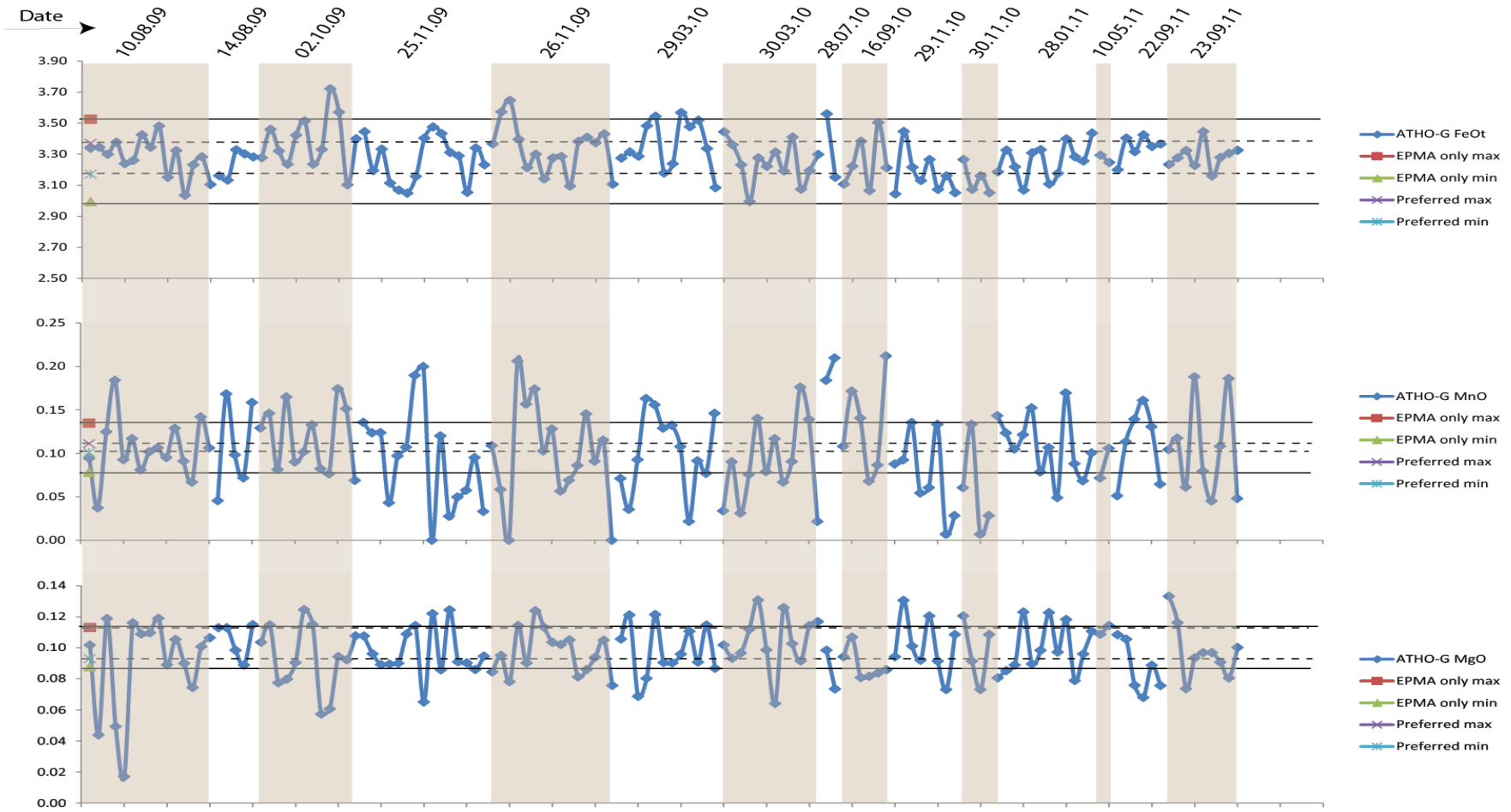

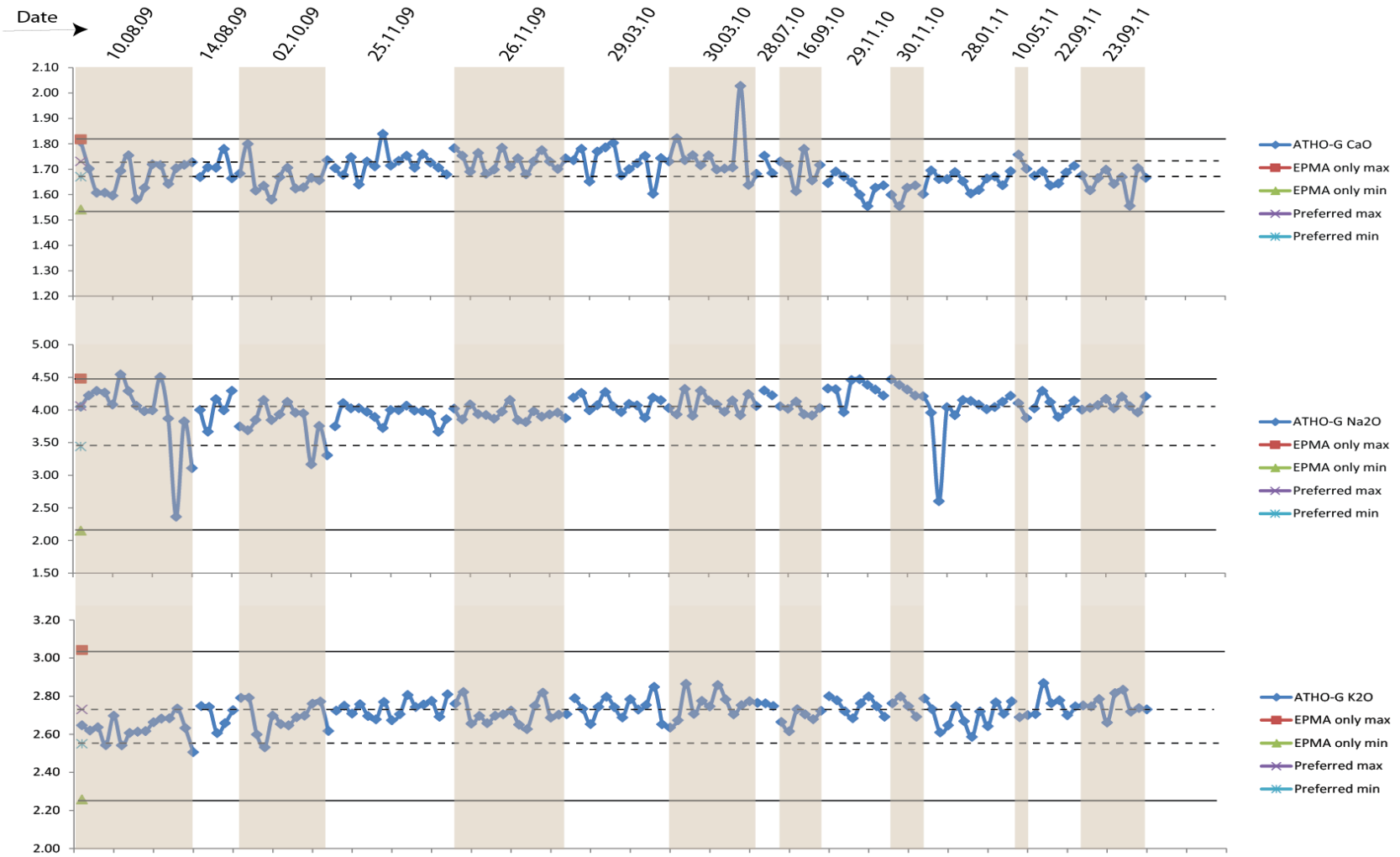
Date
10.08.09
14.08.09
02.10.09
25.11.09
26.11.09
29.03.10
30.03.10
28.07.10
16.09.10
29.11.10
30.11.10
28.01.11
10.05.11
22.09.11
23.09.11
2.10
2.00
1.90
1.80
1.70
1.60
1.50
1.40
1.30
1.20
ATHO-G CaO
EPMA only max
EPMA only min
Preferred max
Preferred min
5.00
4.50
4.00
3.50
3.00
2.50
2.00
1.50
ATHO-G Na2O
EPMA only max
EPMA only min
Preferred max
Preferred min
3.20
3.00
2.80
2.60
2.40
2.20
2.00
ATHO-G K2O
EPMA only max
EPMA only min
Preferred max
Preferred min

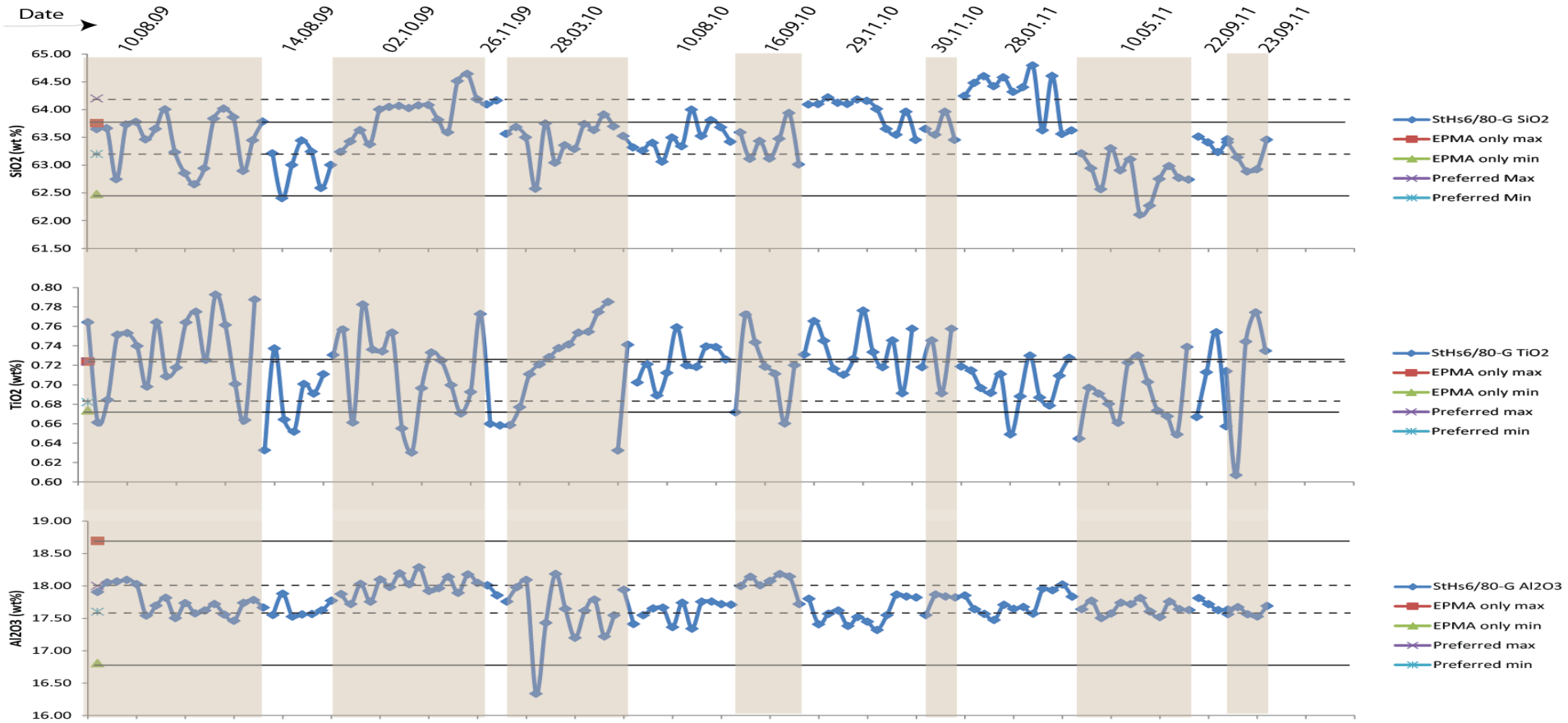
Date
10.08.09
14.08.09
02.10.09
26.11.09
28.03.10
10.08.10
16.09.10
29.11.10
30.11.10
28.01.11
10.05.11
22.09.11
23.09.11
SiO2 (wt %)
65.00
64.50
64.00
63.50
63.00
62.50
62.00
61.50
StHs6/80-G SiO2
EPMA only max
EPMA only min
Preferred Max
Preferred Min
TiO2 (wt%)
0.80
0.78
0.76
0.74
0.72
0.70
0.68
0.66
0.64
0.62
0.60
StHs6/80-G TiO2
EPMA only max
EPMA only min
Preferred max
Preferred min
Al2O3 (wt%)
19.00
18.50
18.00
17.50
17.00
16.50
16.00
StHs6/80-G Al2O3
EPMA only max
EPMA only min
Preferred max
Preferred min

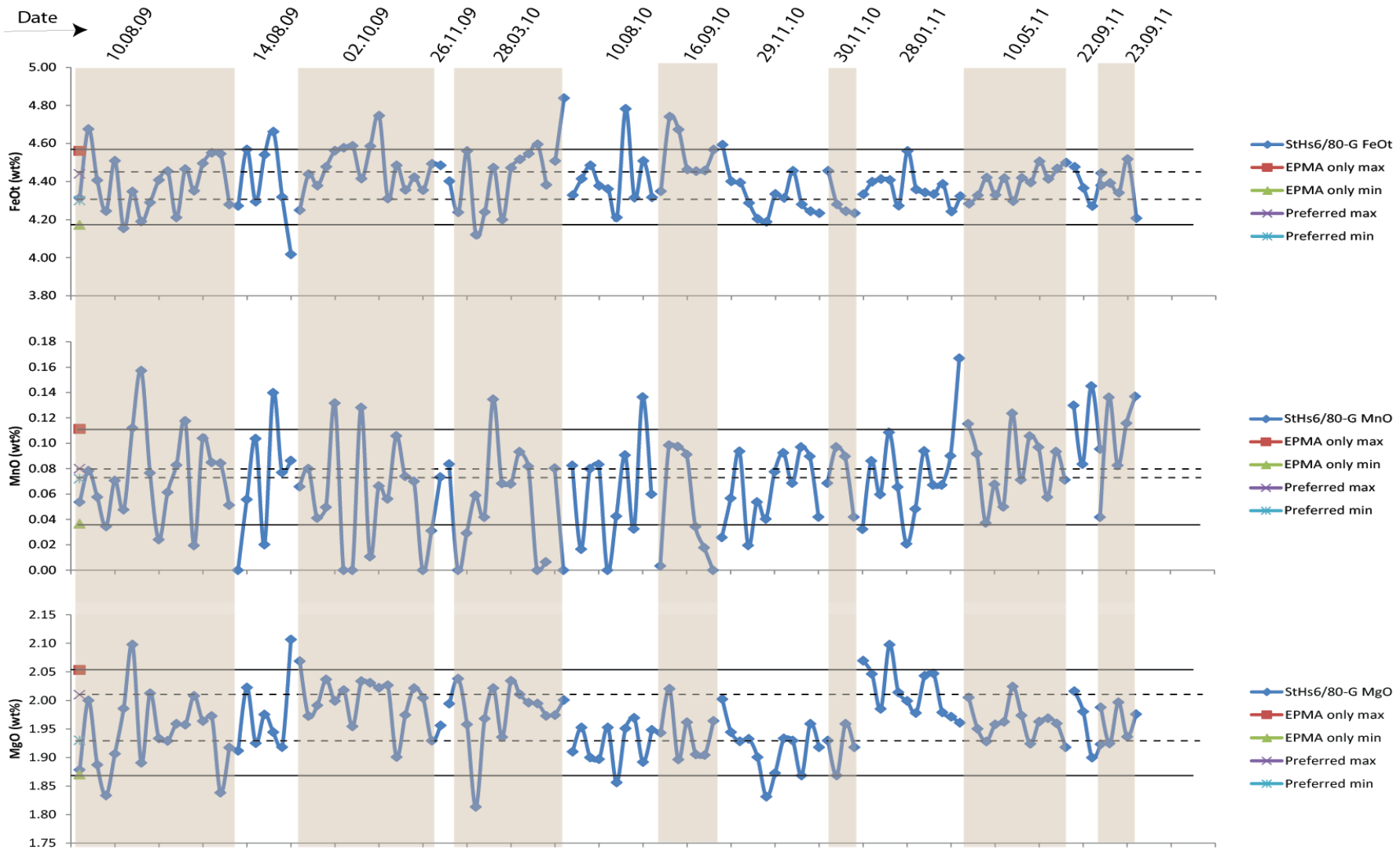
Date
10.08.09
14.08.09
02.10.09
26.11.09
28.03.10
10.08.10
16.09.10
29.11.10
30.11.10
28.01.11
10.05.11
22.09.11
23.09.11
FeOt (wt%)
5.00
4.80
4.60
4.40
4.20
4.00
3.80
StHs6/80-G FeOt
EPMA only max
EPMA only min
Preferred max
Preferred min
MnO (wt%)
0.18
0.16
0.14
0.12
0.10
0.08
0.06
0.04
0.02
0.00
StHs6/80-G MnO
EPMA only max
EPMA only min
Preferred max
Preferred min
MgO (wt%)
2.15
2.10
2.05
2.00
1.95
1.90
1.85
1.80
1.75
StHs6/80-G MgO
EPMA only max
EPMA only min
Preferred max
Preferred min

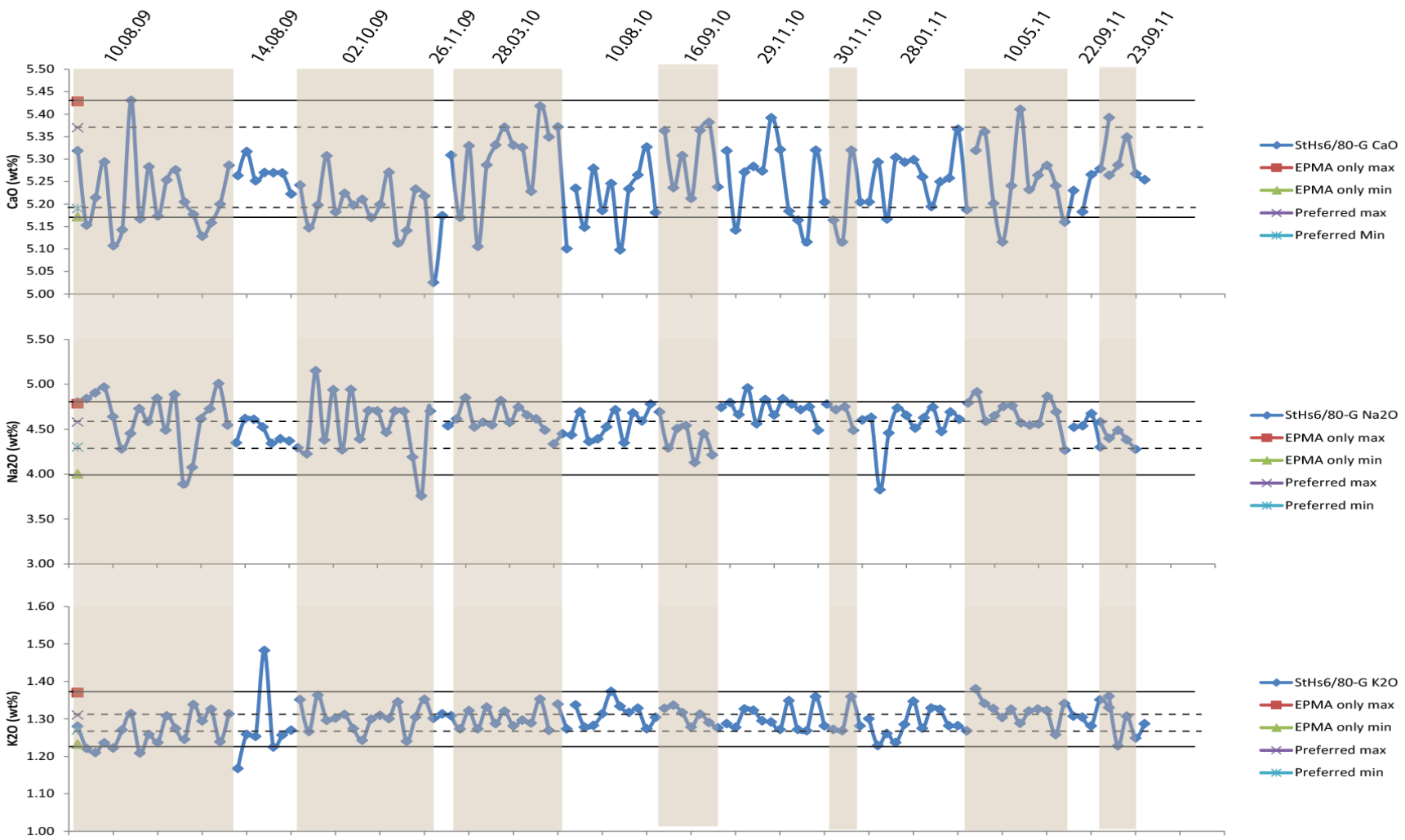
10.08.09
14.08.09
02.10.09
26.11.09
28.03.10
10.08.10
16.09.10
29.11.10
30.11.10
28.01.11
10.05.11
22.09.11
23.09.11
CaO (wt%)
5.50
5.45
5.40
5.35
5.30
5.25
5.20
5.15
5.10
5.05
5.00
StHs6/80-G CaO
EPMA only max
EPMA only min
Preferred max
Preferred Min
Na2O (wt%)
5.50
5.00
4.50
4.00
3.50
3.00
StHs6/80-G Na2O
EPMA only max
EPMA only min
Preferred max
Preferred min
K2O (wt%)
1.60
1.50
1.40
1.30
1.20
1.10
1.00
StHs6/80-G K2O
EPMA only max
EPMA only min
Preferred max
Preferred min

Appendix 2 - Atho-G standard analyses (bias corrected) from LA-ICP-MS.

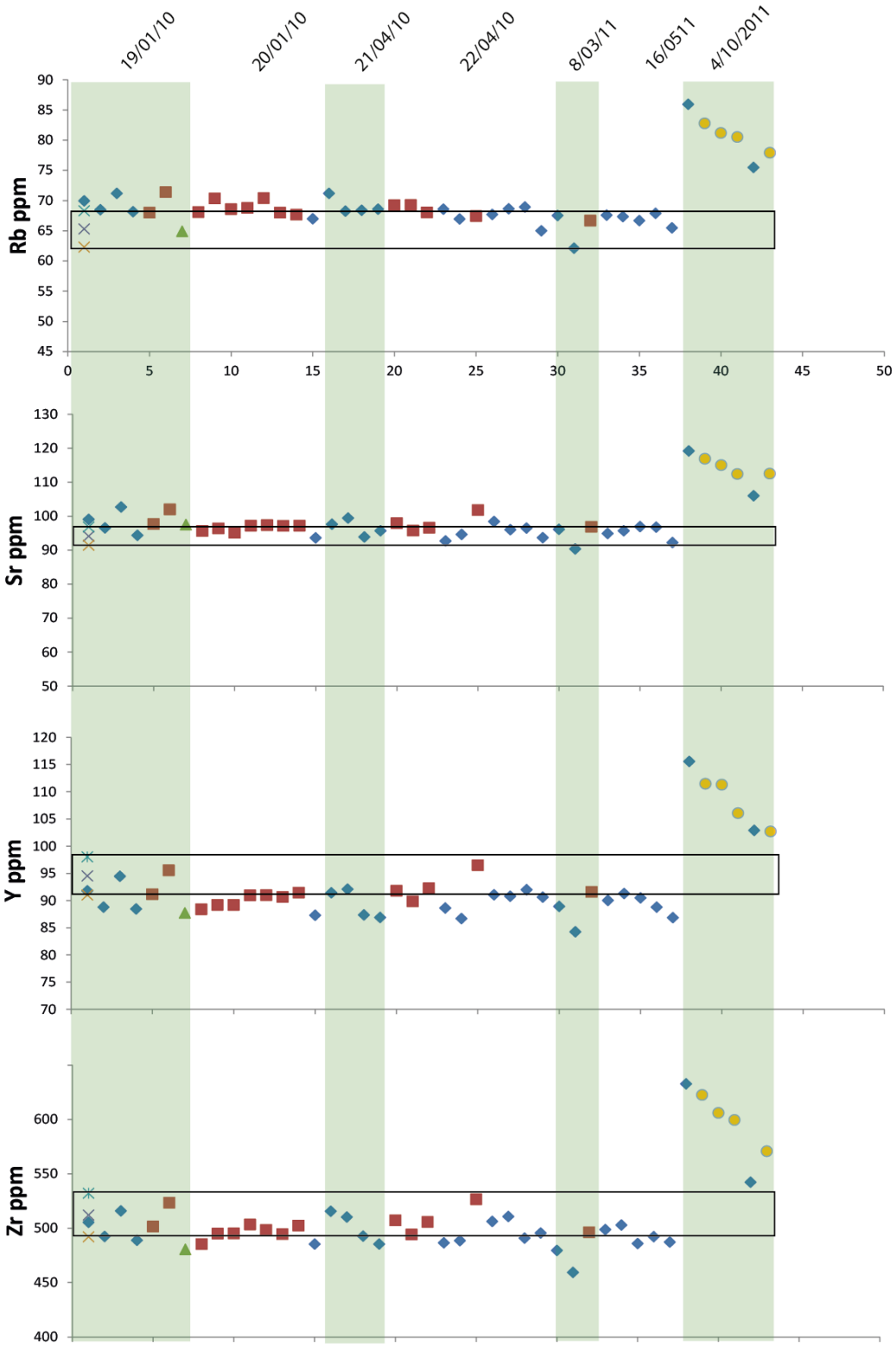

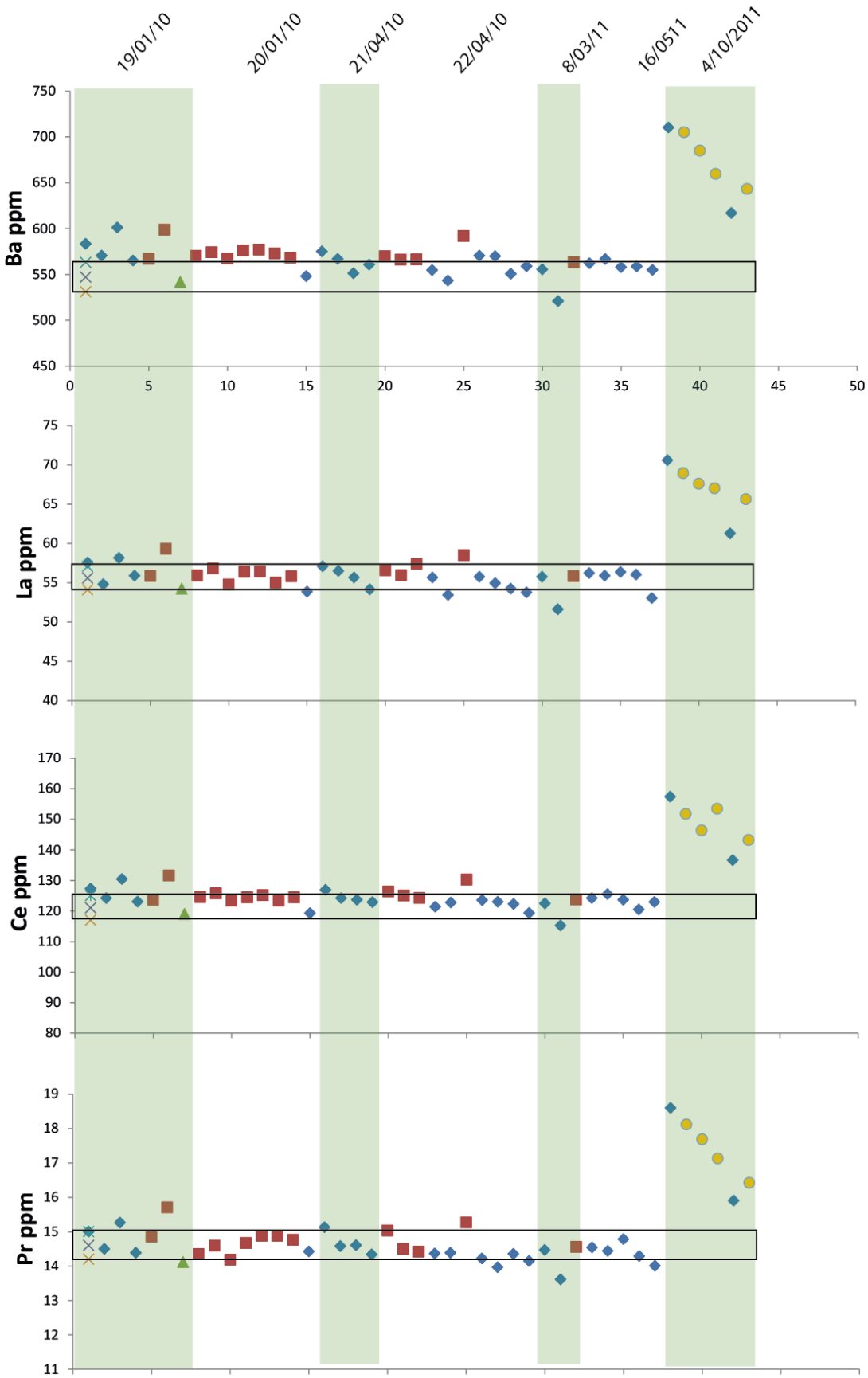
19/01/10
20/01/10
21/04/10
22/04/10
8/03/11
16/0511
4/10/2011
Ba ppm
La ppm
Ce ppm
Pr ppm

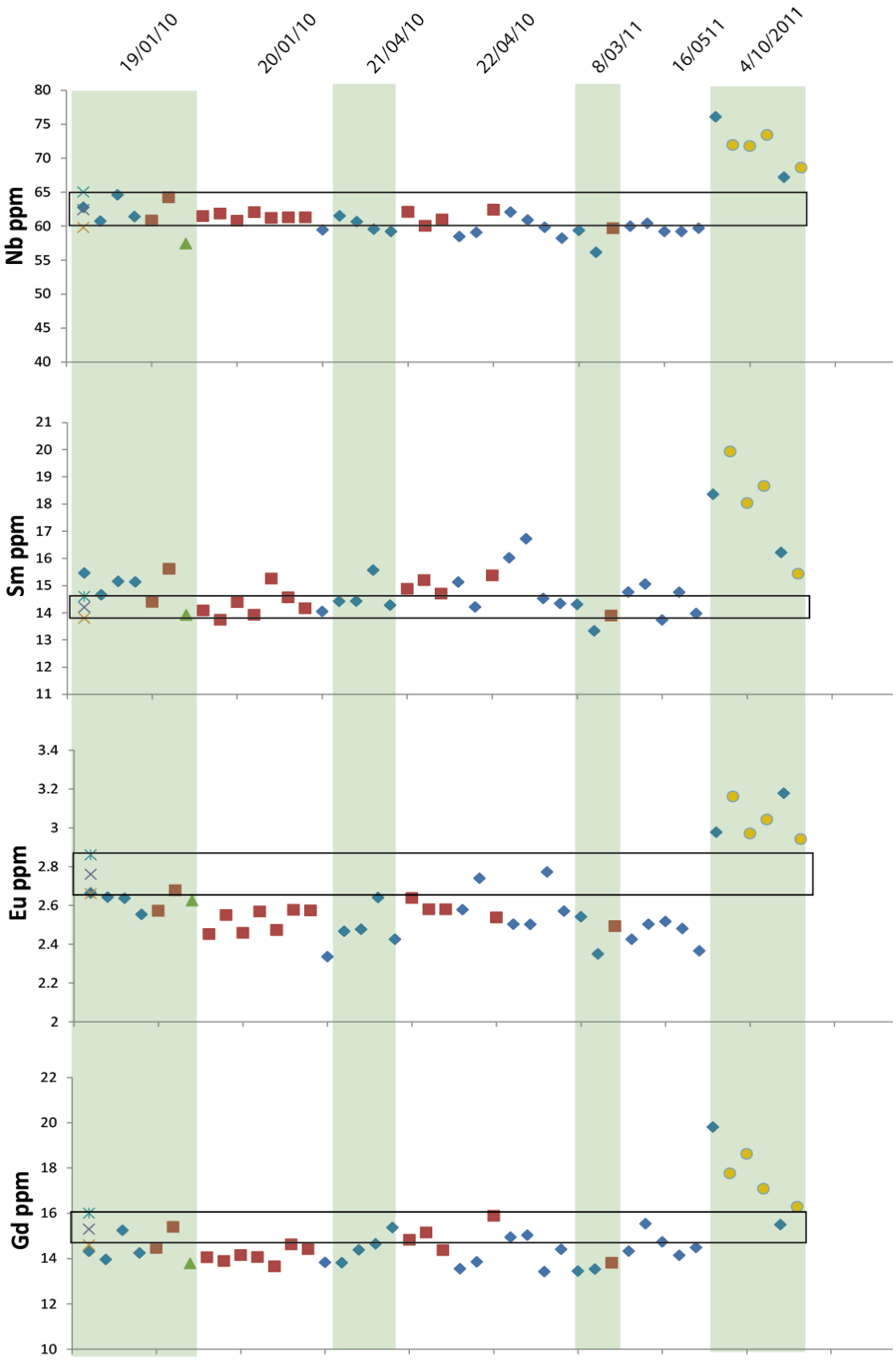
19/01/10
20/01/10
21/04/10
22/04/10
8/03/11
16/0511
4/10/2011
Nb ppm
80
75
70
65
60
55
50
45
40
Sm ppm
21
20
19
18
17
16
15
14
13
12
11
Eu ppm
3.4
3.2
3
2.8
2.6
2.4
2.2
2
Gd ppm
22
20
18
16
14
12
10

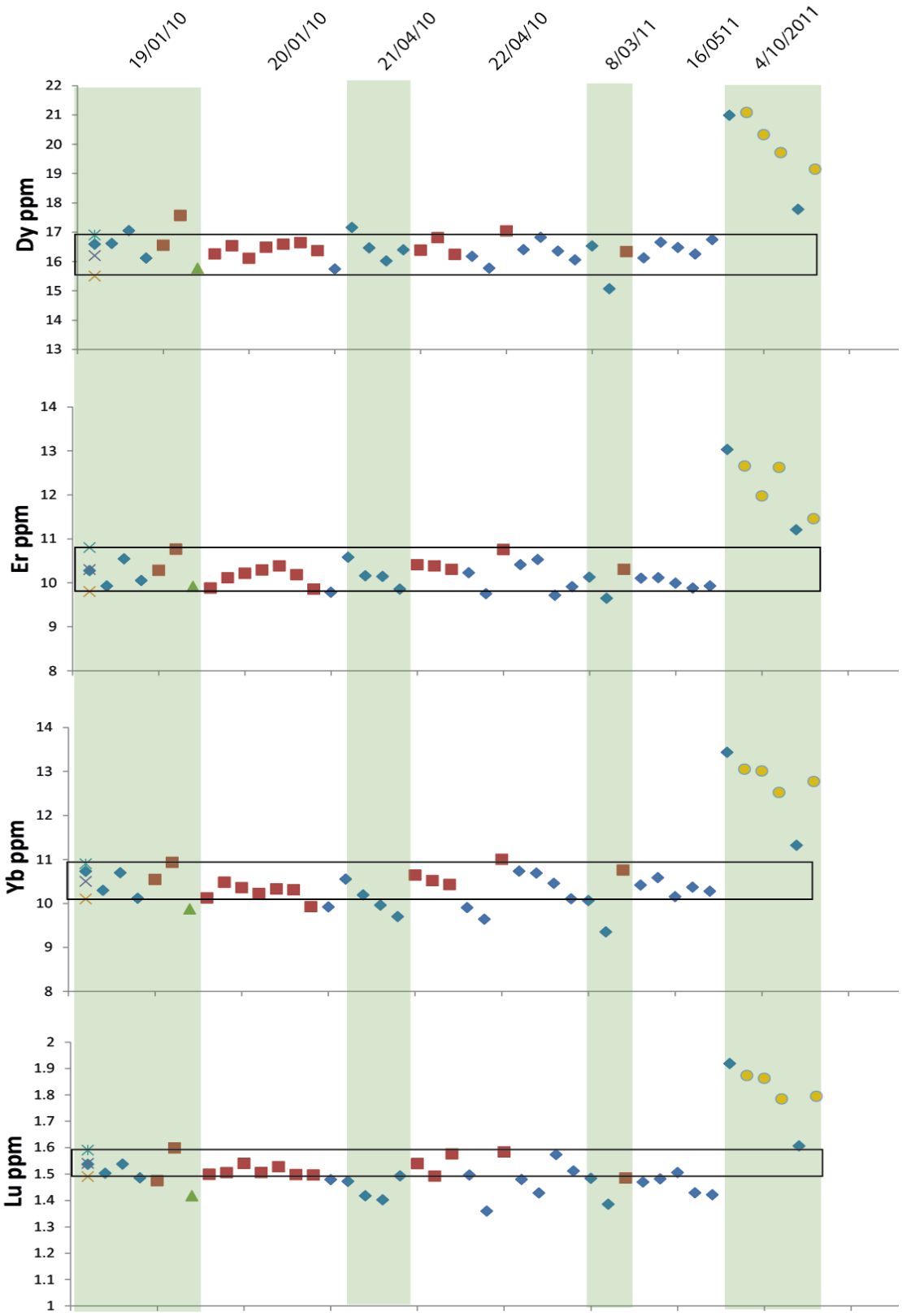
19/01/10
20/01/10
21/04/10
22/04/10
8/03/11
16/0511
4/10/2011
Dy ppm
Er ppm
Yb ppm
Lu ppm

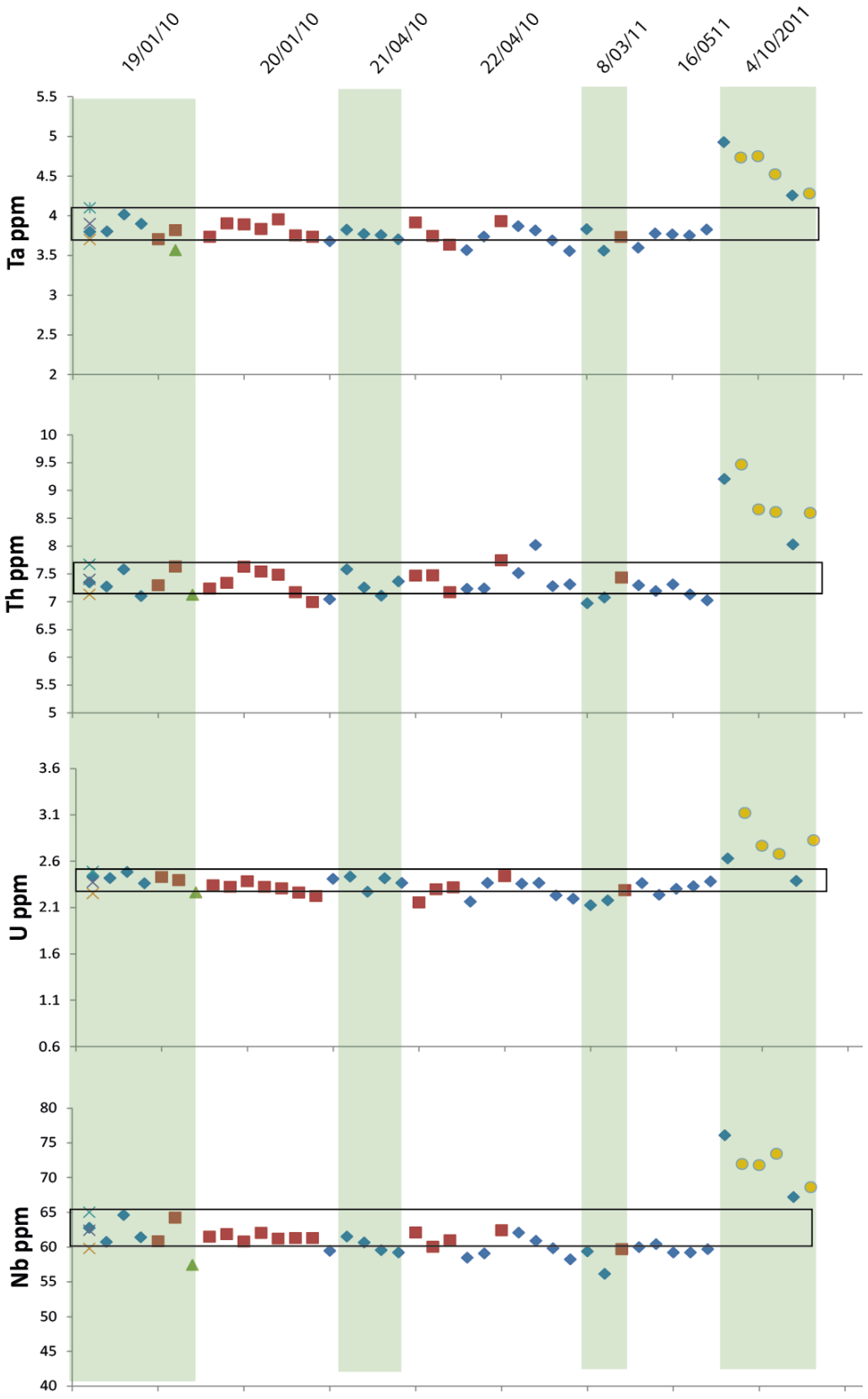
19/01/10
20/01/10
21/04/10
22/04/10
8/03/11
16/0511
4/10/2011
Ta ppm
5.5
5
4.5
4
3.5
3
2.5
2
Th ppm
10
9.5
9
8.5
8
7.5
7
6.5
6
5.5
5
U ppm
3.6
3.1
2.6
2.1
1.6
1.1
0.6
Nb ppm
80
75
70
65
60
55
50
45
40

StHs6/80 standard analyses (bias corrected) from LA-ICP-MS

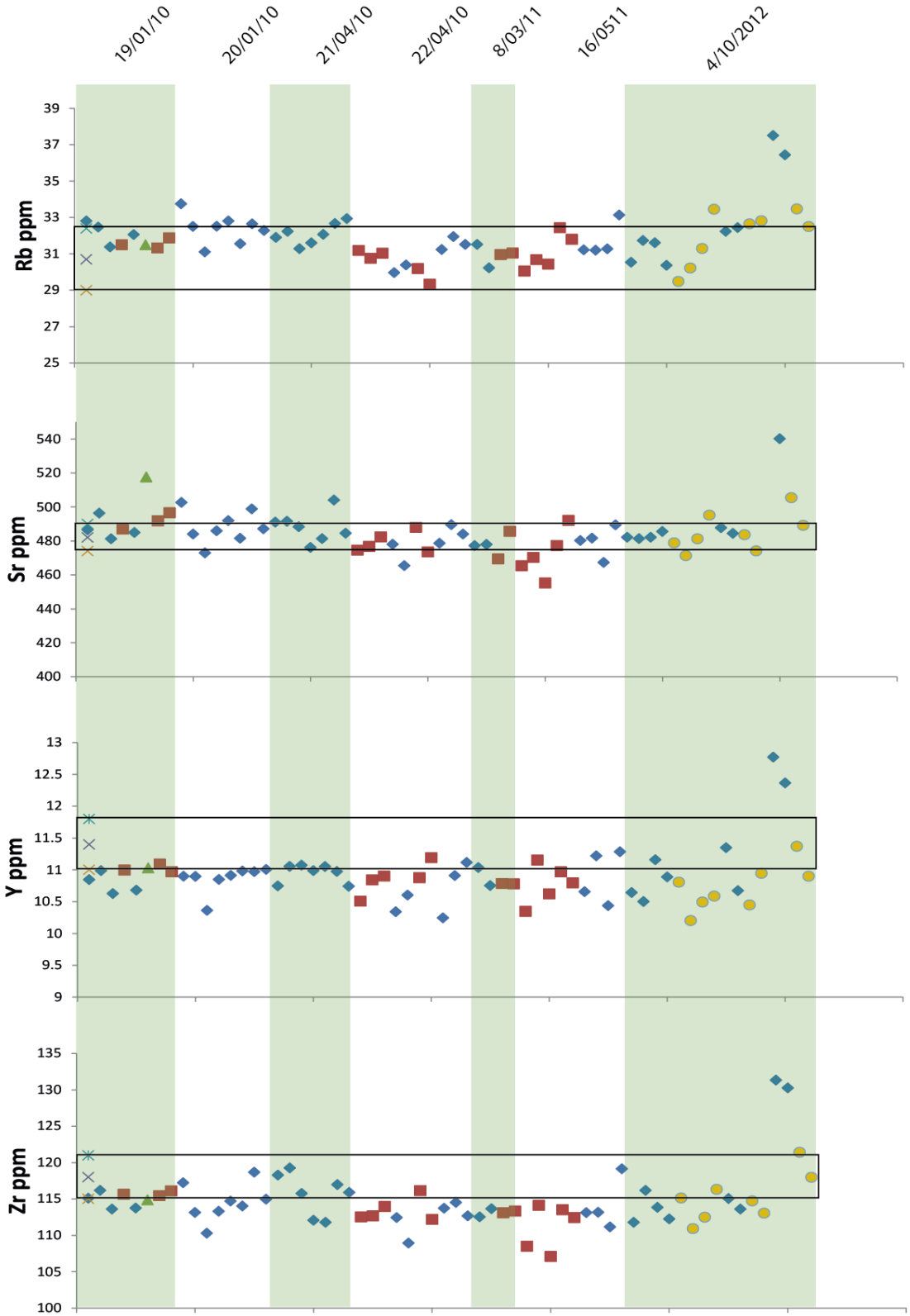

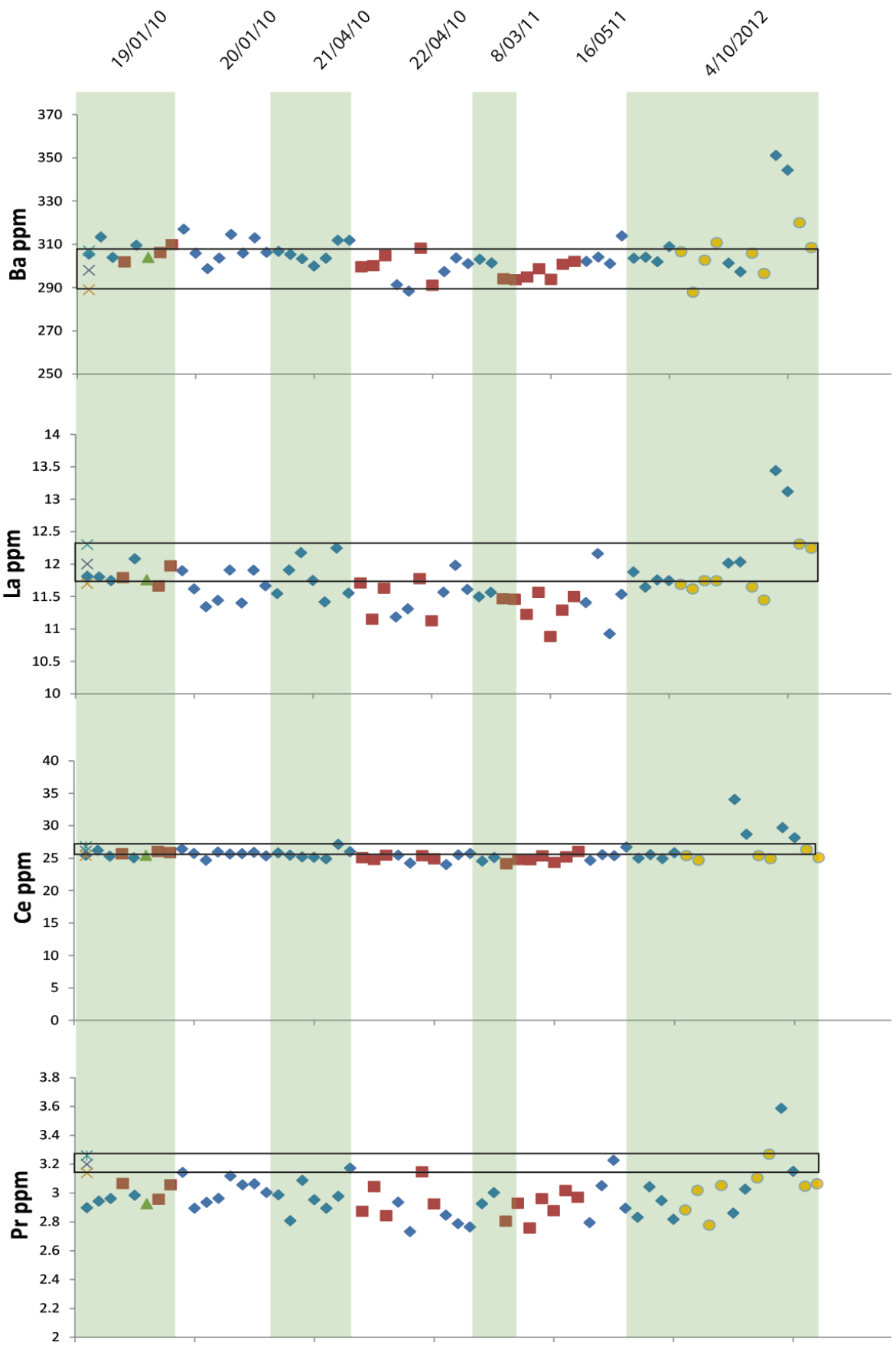
19/01/10
20/01/10
21/04/10
22/04/10
8/03/11
16/0511
4/10/2012
Ba ppm
370
350
330
310
290
270
250
La ppm
14
13.5
13
12.5
12
11.5
11
10.5
10
Ce ppm
40
35
30
25
20
15
10
5
0
Pr ppm
3.8
3.6
3.4
3.2
3
2.8
2.6
2.4
2.2
2

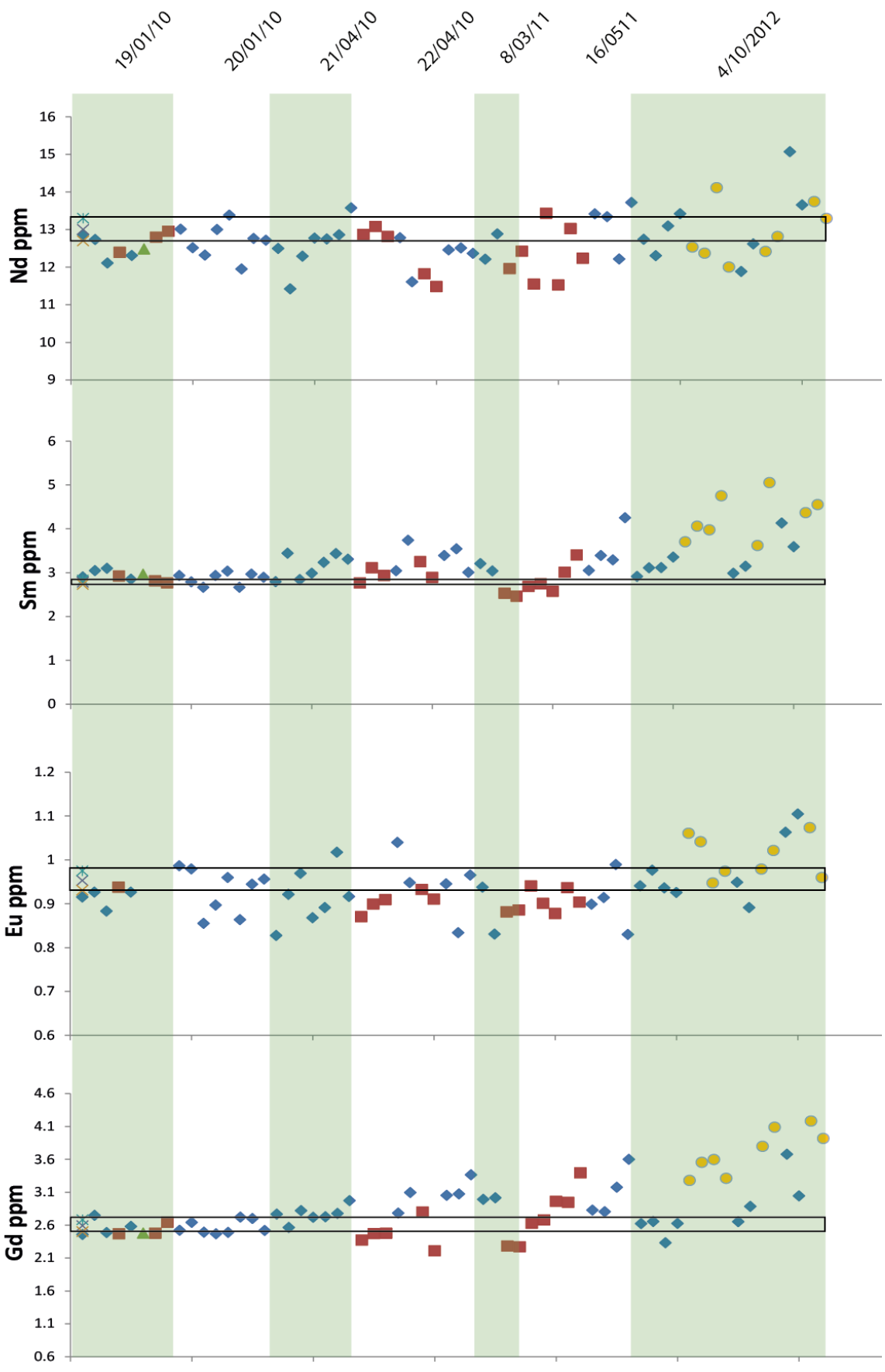
19/01/10
20/01/10
21/04/10
22/04/10
8/03/11
16/0511
4/10/2012
Nd ppm
16
15
14
13
12
11
10
9
Sm ppm
6
5
4
3
2
1
0
Eu ppm
1.2
1.1
1
0.9
0.8
0.7
0.6
Gd ppm
4.6
4.1
3.6
3.1
2.6
2.1
1.6
1.1
0.6

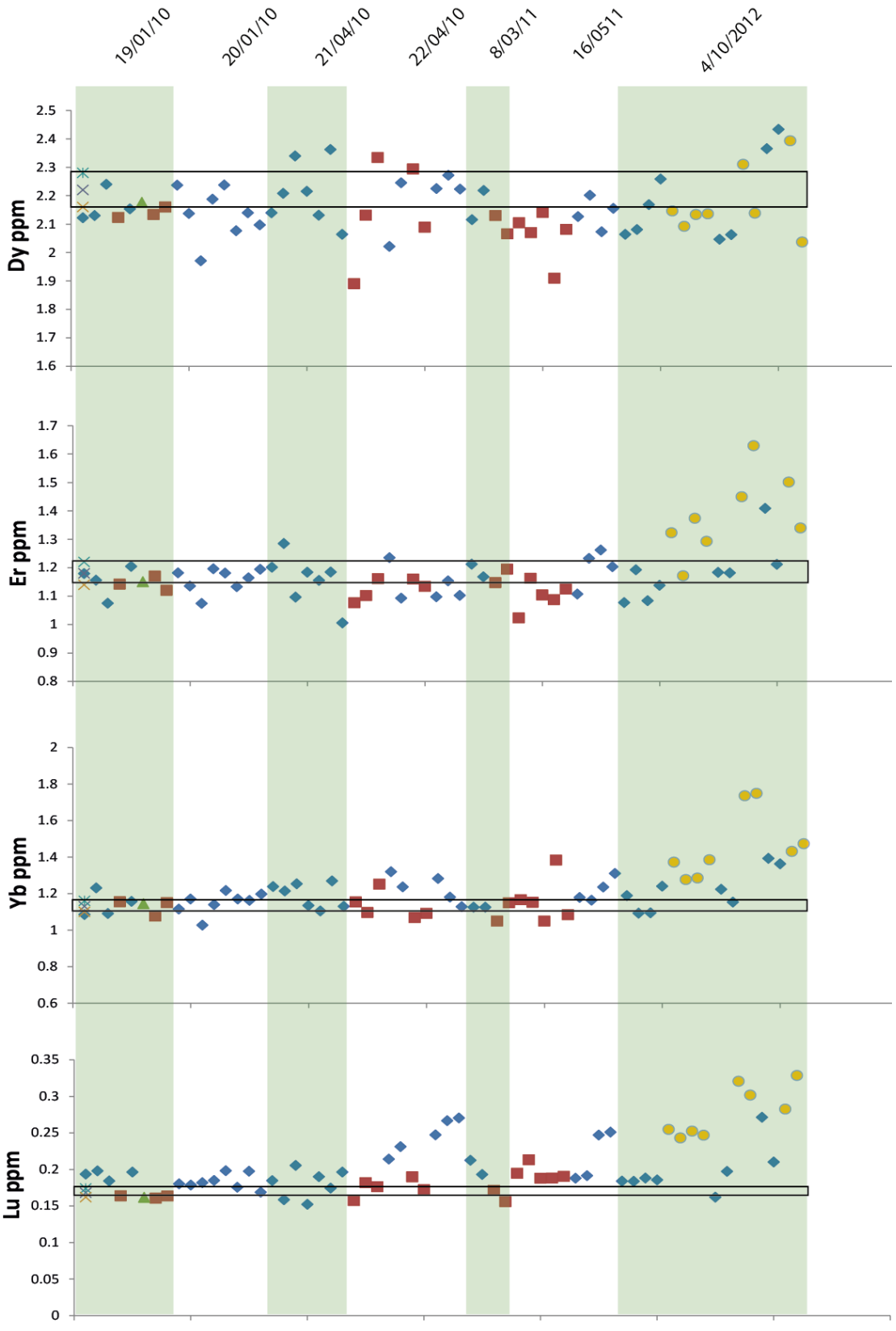
19/01/10
20/01/10
21/04/10
22/04/10
8/03/11
16/0511
4/10/2012
Dy ppm
Er ppm
Yb ppm
Lu ppm

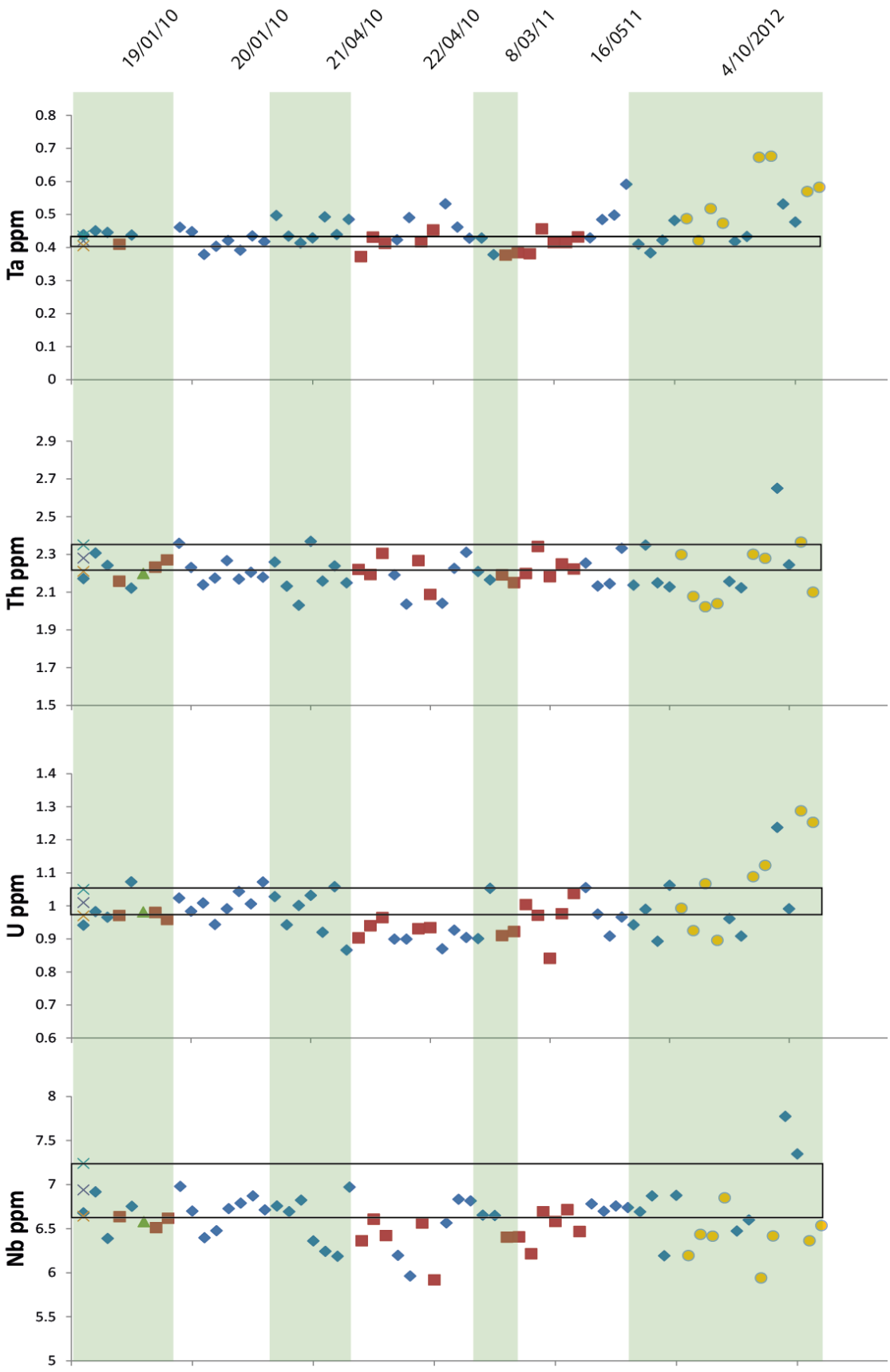
19/01/10
20/01/10
21/04/10
22/04/10
8/03/11
16/0511
4/10/2012
Ta ppm
0.8
0.7
0.6
0.5
0.4
0.3
0.2
0.1
0
Th ppm
2.9
2.7
2.5
2.3
2.1
1.9
1.7
1.5
U ppm
1.4
1.3
1.2
1.1
1
0.9
0.8
0.7
0.6
Nb ppm
8
7.5
7
6.5
6
5.5
5

Appendix 3- details of the construction of the chronology for core LC21 through correlation with the Soreq Cave speleothem.

The following is extracted directly from a submission to Nature by K. Grant on 4th September 2012.

Age model for core LC21

For the interval 0-40 ka BP, the LC21 age model is constrained by five previously generated radiocarbon datings (Casford et al., 2007), 9 new radiocarbon datings (Table S1), and conclusive identification of two well-dated tephra horizons (the Minoan and the Campanian Ignimbrite, CI, tephra layers) (Fig. S4). New ^{14}C datings (this study) were performed at the University of Oxford Radiocarbon Accelerator Unit on clean, hand-picked planktonic foraminiferal tests with no evidence of pyritization or overgrowth (see Bronk Ramsey et al. (2002) for details of the chemical pretreatment, target preparation and AMS measurement). Calibration of ^{14}C datings into calendar years requires a reservoir age correction, which is a combination of the averaged whole ocean reservoir age (405 yrs) and a local correction ("ΔR"). For Mediterranean marine calcite, ΔR is commonly taken to be 58±85 yrs (Reimer and McCormac, 2002) or 149±30 yrs (Facorellis et al., 1998) depending on whether dated samples were extracted from non-sapropel or sapropel horizons, respectively. A higher ΔR value for periods of sapropel deposition reflects decreased rates of Mediterranean intermediate- and deep-water ventilation associated with such intervals. Three of our ^{14}C-dated samples were picked from a sapropel, so we use a ΔR value of 149±30 yrs to calibrate these samples and a ΔR value of 58±85 yrs for all other samples (Table S1). All datings (including those of Casford et al. (2007) were calibrated with OxCal (Bronk Ramsey, 2008) using the Marine09 radiocarbon calibration curve. The accuracy of our calibrated ^{14}C datings is further improved by combining sample age and depth information in a Bayesian deposition model (Section 4).

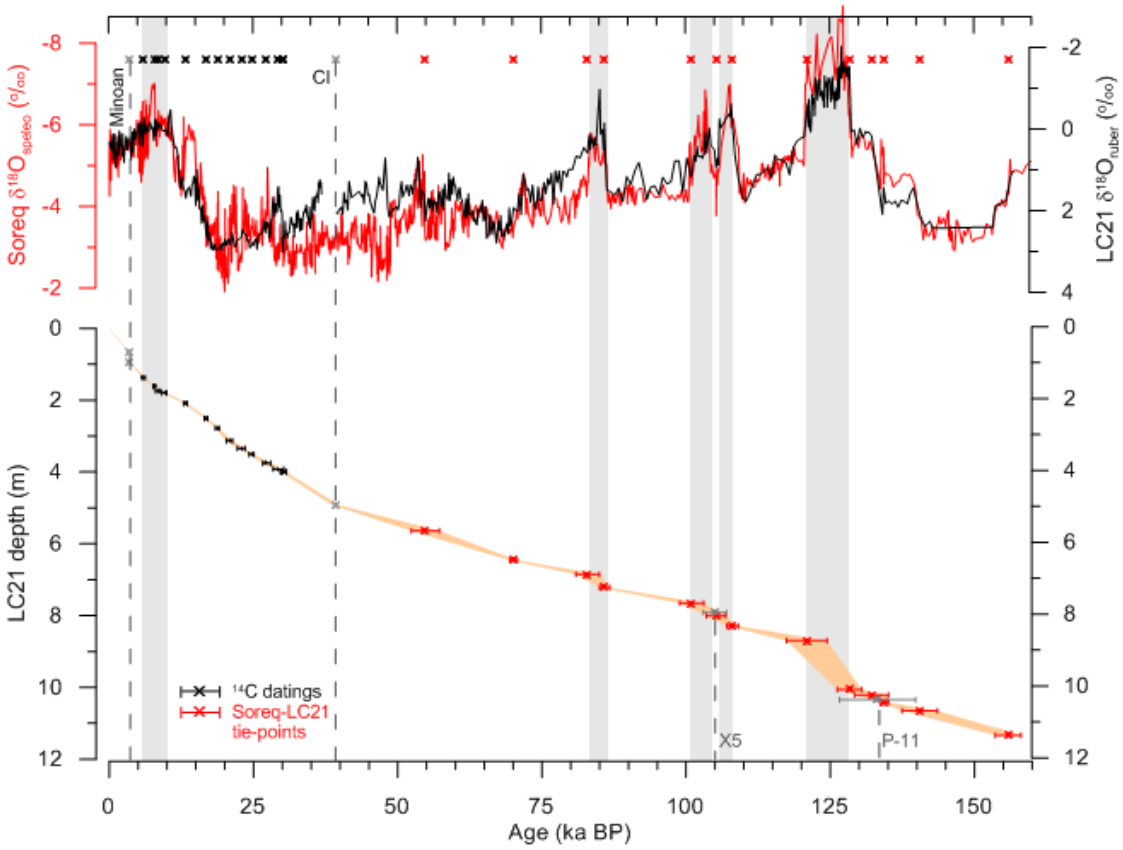

Figure S4 Construction of the LC21 age model. LC21 ^{14}C datings (black crosses) and correlation of the LC21 $\delta^{18}O_{ruber}$ (black) and Soreq Cave $\delta^{18}O_{speleo}$ (red) records, with OxCal-modelled correlation tie-points (red crosses). The Minoan, Campanian Ignimbrite (CI), X5 and P-11 tephra horizons (grey crosses and dashed lines) and intervals of sapropel deposition (grey rectangles) are also indicated. Superimposed on the LC21 age-depth model (orange fill) are the error margins of the ^{14}C datings, Soreq-LC21 tie-points and tephra horizons (black, red and grey error bars (2σ), respectively).

For the interval 40-150 ka BP, we used Analyseries (Paillard, 1996) to graphically correlate the $\delta^{18}O_{ruber}$ and $\delta^{18}O_{speleo}$ records (Fig. S4). As mentioned above, there is a direct physical process linking the $\delta^{18}O$ of calcite precipitated in eMed surface waters and in Levantine caves. It follows that there will be a signal common to both $\delta^{18}O_{ruber}$ and $\delta^{18}O_{speleo}$ on which any local $\delta^{18}O$ variations are superimposed. On long (orbital) timescales, eMed surface waters are periodically affected by intense freshening, and thus $\delta^{18}O$ depletion, caused by flooding of the Nile and North African wadi systems as a result of intensification and northward penetration of the African monsoon during precession minima (Rohling et al., 2002, 2004; Larrasoaña et al., 2003). These $\delta^{18}O$ depletions, together with sea level-controlled variations in $\delta^{18}O_{Med}$, are clearly evidenced by the good general agreement between $\delta^{18}O_{ruber}$ and $\delta^{18}O_{speleo}$. We therefore only correlate these major transitions in $\delta^{18}O_{ruber}$ and $\delta^{18}O_{speleo}$. In this way we transfer the U-series speleothem chronology to core LC21.

Our Soreq-LC21 correlation is validated by identification of two further tephra horizons at 7.915 m and 10.345 m in core LC21. These correlate with the X5 and P-11 tephras that have been dated at 105 ±2 ka BP (Kraml, 1997) and, indirectly, at 132.3 ±5.7 to 133.5 ±6.2 ka BP (Mahood and Hildreth, 1986), respectively (Fig. S4). Next, we applied a Bayesian deposition model using the OxCal programme (Bronk Ramsey, 2008), to derive a best-case chronology for LC21 with well-defined uncertainties.

OxCal Bayesian models

The chronostratigraphy of a sediment core is, in effect, a series of probability functions, and information of a probabilistic nature can be mathematically combined using the Bayes Theorem. OxCal achieves this using the Markov Chain Monte Carlo (MCMC) sampling method (Gilks et al., 1996) and Bayesian algorithms to create "*posterior*" probability densities for each point in a sedimentary sequence. Specifically, OxCal builds a "*prior*" model from information about the deposition of the sequence and the actual dates. Here we use the "Sequence" and "Poisson" OxCal models. The simple Sequence model allows wide variations in sedimentation rate and makes minimal *a priori* assumptions, assuming only that there are no age reversals in the sedimentary sequence. The Sequence model is also applicable when coherent depth information is lacking, as is the case for the Soreq Cave composite speleothem record. The Poisson model includes depth information and is therefore more appropriate for the LC21 datings. Previous studies have demonstrated that the Sequence and Poisson models can significantly improve the precision of an age model whilst retaining accuracy (Bronk Ramsey 2000; Blockley et al., 2007).

Our prior models consist of dates and uncertainties in the form of a normal (Gaussian) probability distribution (the "*likelihood*"), with an uncertainty σ about the mean μ. The dating information is from Soreq Cave (Supplementary Data), LC21 (Table S1) and from the Minoan (Manning et al., 2006) and CI (De Vivo et al., 2001) tephra horizons). The Soreq-LC21 tie-points were inserted into the OxCal Sequence model as a blank age and uncertainty at the relevant chronostratigraphic level obtained from the correlation, in order to determine a posterior probability density distribution for each tie-point.

OxCal assesses the statistical robustness of a model run by calculating an "Agreement Index" (AI), which is determined by the area of overlap between the probability density distributions of the *prior* (unmodelled) data and the posteriors. The higher the AI, the better the agreement, and the acceptance threshold for a posterior density is an AI >60% (Bronk Ramsey, 2008). In both of our models, overall agreement between the priors and the posteriors is high (AI >99% for most [97%] of the dates in the Sequence model; AI >87% for all dates in the Poisson model), which implies that our modelled ages and uncertainties are statistically robust. The final Soreq Cave chronology is accurate

to within ±500 years for most of the dates (72%), and has a maximum uncertainty of ±2686 years. Only 3% of the dates have an uncertainty >1500 years.

The modelled ^{14}C dates and tephra ages were then used to establish the LC21 chronology (by linear interpolation) for the interval 0-40 ka BP. After rescaling the $\delta^{18}O_{speleo}$ record using the modelled U/Th dates, the $\delta^{18}O_{rub}$ and $\delta^{18}O_{speleo}$ records were re-synchronised for the interval 40-150 ka BP (see main-text Fig. 1a).

Appendix 4- Section 3 (base of core LC21) scanning XRF data.

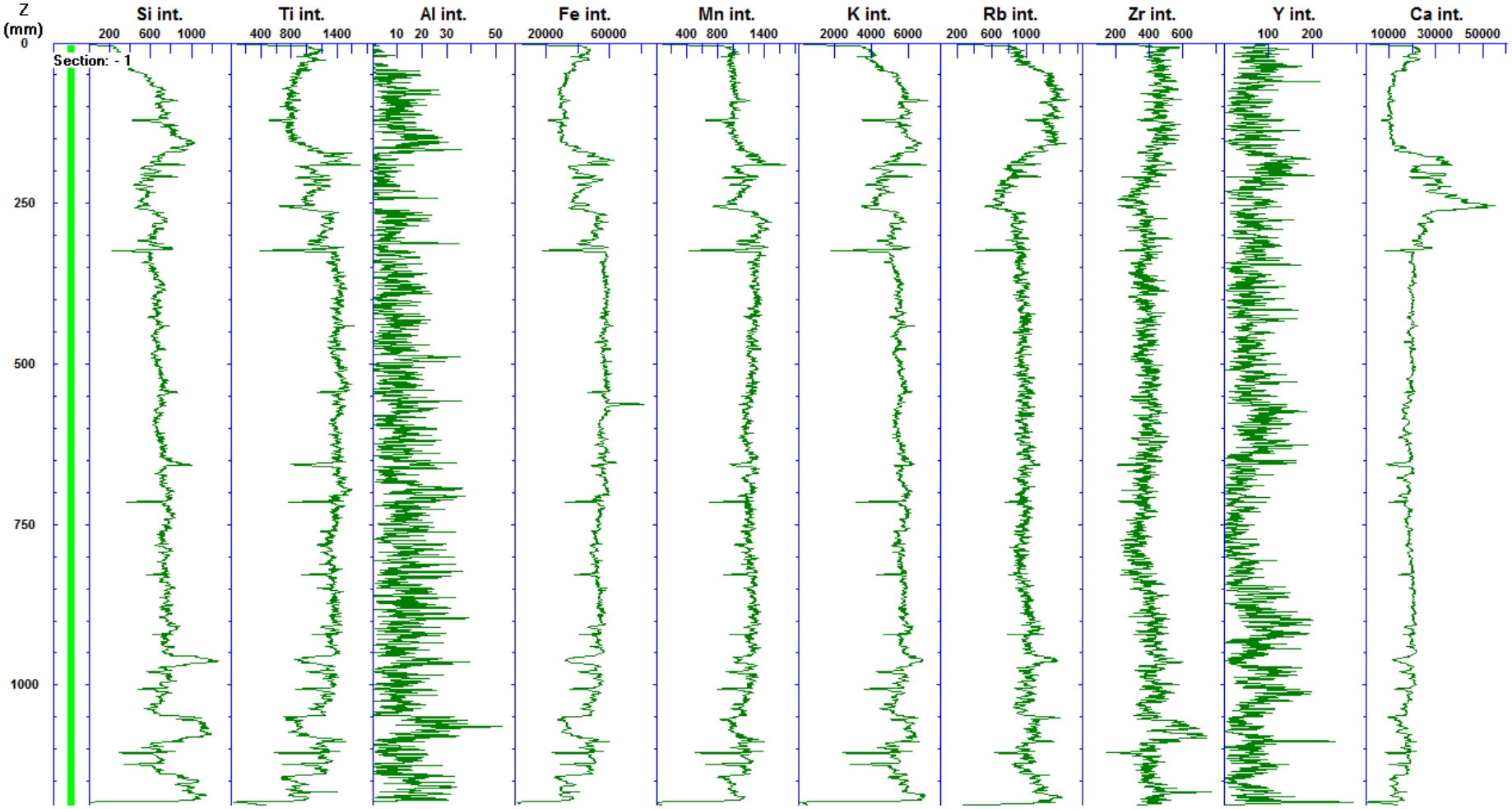

Core: LC21	Section: - 1	User:	Date: 00/00/0
X-Ray tube: target		Filename: Section 3	Data produced by the NOC Itrax
X-radiograph Conditions	,	Step Size: 500 microns	Dwell time: 0 /increment